Seventh International Workshop on Microgravity Combustion and Chemically Reacting Systems

The NASA STI Program Office . . . in Profile

Since its founding, NASA has been dedicated to the advancement of aeronautics and space science. The NASA Scientific and Technical Information (STI) Program Office plays a key part in helping NASA maintain this important role.

The NASA STI Program Office is operated by Langley Research Center, the Lead Center for NASA's scientific and technical information. The NASA STI Program Office provides access to the NASA STI Database, the largest collection of aeronautical and space science STI in the world. The Program Office is also NASA's institutional mechanism for disseminating the results of its research and development activities. These results are published by NASA in the NASA STI Report Series, which includes the following report types:

- TECHNICAL PUBLICATION. Reports of completed research or a major significant phase of research that present the results of NASA programs and include extensive data or theoretical analysis. Includes compilations of significant scientific and technical data and information deemed to be of continuing reference value. NASA's counterpart of peer-reviewed formal professional papers but has less stringent limitations on manuscript length and extent of graphic presentations.

- TECHNICAL MEMORANDUM. Scientific and technical findings that are preliminary or of specialized interest, e.g., quick release reports, working papers, and bibliographies that contain minimal annotation. Does not contain extensive analysis.

- CONTRACTOR REPORT. Scientific and technical findings by NASA-sponsored contractors and grantees.

- CONFERENCE PUBLICATION. Collected papers from scientific and technical conferences, symposia, seminars, or other meetings sponsored or cosponsored by NASA.

- SPECIAL PUBLICATION. Scientific, technical, or historical information from NASA programs, projects, and missions, often concerned with subjects having substantial public interest.

- TECHNICAL TRANSLATION. English-language translations of foreign scientific and technical material pertinent to NASA's mission.

Specialized services that complement the STI Program Office's diverse offerings include creating custom thesauri, building customized databases, organizing and publishing research results . . . even providing videos.

For more information about the NASA STI Program Office, see the following:

- Access the NASA STI Program Home Page at *http://www.sti.nasa.gov*

- E-mail your question via the Internet to help@sti.nasa.gov

- Fax your question to the NASA Access Help Desk at 301–621–0134

- Telephone the NASA Access Help Desk at 301–621–0390

- Write to:
  NASA Access Help Desk
  NASA Center for AeroSpace Information
  7121 Standard Drive
  Hanover, MD 21076

Seventh International Workshop on Microgravity Combustion and Chemically Reacting Systems

National Aeronautics and
Space Administration

Glenn Research Center

Document Change History

PREFACE

Since February 1, 2003, we have heard questions about the worth of our research compared to the risks associated with going into Earth orbit to do what cannot be done in the ground-based facilities. By the words of those among us that knew and trained the crew of the Spaceship Columbia for STS–107, I am convinced that the crew understood the sometimes unquantifiable value of basic research and viewed their participation and contributions to it with excitement despite the well-known dangers. While combustion scientists are sometimes motivated by the aesthetics of equations or flames, most argue persuasively that their work contributes to the improved well-being of planet Earth and its inhabitants. So, to the recent questions my answer is partly in the contents of this book and the scientific achievement it represents, but also in the informed decision of the Columbia crew to fly and the scores of astronauts and cosmonauts who eagerly await the opportunity to carry on in their flightpath.

The Seventh International Workshop on Microgravity Combustion and Chemically Reacting Systems is planned for June 3–6, 2003, in Cleveland, Ohio, near the NASA John H. Glenn Research Center at Lewis Field. The new name for the workshop is based on the decision to broaden our scope to encompass support for future space exploration through basic and applied research in reacting systems that in some cases may not look like combustion. The workshop has been lengthened to 4 days with focus sessions on spacecraft fire safety and exploration-related research. We believe that the microgravity combustion science community is almost uniquely positioned to make substantial contributions to this new effort and we hope you will consider making the attempt to do so.

As before, the workshop is intended to be 4 days of learning, teaching, and creativity. We are grateful to the National Center for Microgravity Research (NCMR) for their remarkable technical and organizational contributions to the workshop. Led by its director, Professor Simon Ostrach, the deputy director, Tom Jacobson, and the chief combustion scientist, Professor James S. T'ien, the conference staff of the NCMR has created another wonderful environment for our work. I would like to specifically thank Norm Weinberg, Evan Halprin, William Yanis, Sandi Jones, Cindy Rosenberger, Beatrix Norton, Maria Upton, and the conference director, Dr. Christine Gorecki. I would also like to thank the Microgravity Combustion Discipline Working Group (DWG) for their contributed wisdom including Professors Robert Altenkirch, Gerard Faeth, Jack Howard, Mitchell Smooke, and Forman Williams; Drs. Meredith Colket and Julian Tishkoff; DWG chair, Professor Chung K. Law and Dr. Merrill K. King of NASA Headquarters. On behalf of everyone, but especially the tardy authors, I would like to thank the NCMR staff and the NASA Glenn Logistics and Technical Information Division and its contractors, particularly Caroline Rist, Amy Fennell, and Lori Feher for their expert production of this book.

I note with fondness and best wishes the retirement of two bedrock contributors to the Microgravity Combustion Science program. Dr. Thomas Labus retired as the deputy director of the NCMR. Among his many contributions is the achievement in 1982, as a section head in the NASA Lewis Space Propulsion Division, of elevating to "space-flight" program status the first Combustion Science Shuttle experiments: those of Professors Williams, Dryer, Berlad, and Altenkirch. Mr. Michael Johnston retired as the creator of truly countless experimental devices for operations in the NASA Lewis/Glenn drop towers and parabolic aircraft. We could paper the drop tower with the "thank you" letters from student experimenters for Mike's hand in their graduate research. The contributions of Tom and Mike, often overlooked, affect much of the content of this book.

Finally, in the spirit of honoring the courage, effort, and sacrifice of those that have given so much to advancing the science displayed in this book, I hope that you find the workshop educational, stimulating, and even useful.

Kurt Sacksteder
NASA Glenn Research Center
April 2003

TABLE OF CONTENTS

COMBUSTION OF INTERACTING DROPLET ARRAYS IN MICROGRAVITY

D.L. Dietrich, P.M. Struk

NASA John H. Glenn Research Center

M. Ikegami and G. Xu

National Institute for Advanced Industrial Science and Technology

Introduction

Theory and experiments involving single droplet combustion date back to 1953[1], with the first microgravity work appearing in 1956[2]. The problem of a spherical droplet burning in an infinite, quiescent microgravity environment is a classical problem in combustion research with the classical solution appearing in nearly every textbook on combustion. The microgravity environment offered by ground-based facilities such as drop towers and space-based facilities is ideal for studying the problem experimentally. A recent review by Choi and Dryer [3] shows significant advances in droplet combustion have been made by studying the problem experimentally in microgravity and comparing the results to one dimensional theoretical and numerical treatments of the problem.

Studying small numbers of interacting droplets in a well-controlled geometry represents a logical step in extending single droplet investigations to more practical spray configurations. Studies of droplet interactions date back to Rex and co-workers [4], and were recently summarized by Annamalai and Ryan [5]. All previous studies determined the change in the burning rate constant, k, or the flame characteristics as a result of interactions. There exists almost no information on how droplet interactions affect extinction limits, and if the extinction limits change if the array is in the diffusive[6] or the radiative[7] extinction regime.

Thus, this study examined experimentally the effect that droplet interactions have on the extinction process by investigating the simplest array configuration, a binary droplet array. The studies were both in normal gravity, reduced pressure ambients and microgravity facilities. The microgravity facilities were the 2.2 and 5.2 second drop towers at the NASA Glenn Research Center and the 10 second drop tower at the Japan Microgravity Center. The experimental apparatus [8] and the data analysis techniques [9] are discussed in detail elsewhere.

Experimental Results

Extensive testing in normal gravity showed that interaction effects have a stronger influence on the extinction behavior of a binary array than the quasi-steady burning behavior. In normal gravity, k is only a very weak function of the inter-droplet spacing at initial non-dimensional separation distances (L/D) greater than 5. The extinction droplet diameter, D_{ext}, however, is much smaller (if it existed) for the droplet array at an instantaneous L/D of approximately 20. These low pressure, normal gravity environment minimized, but did not altogether eliminate, the effects of buoyancy. Initial drop tower tests [10] showed that the reduced pressure, air ambients that yield a finite extinction droplet diameter in normal gravity do not produce a finite extinction droplet diameter in microgravity. In fact, at pressures down to the ignitable limit, the droplets burned to completion. Thus in order to observe extinction at finite droplet sizes, we performed the microgravity experiments in reduced oxygen mole fraction, reduced pressure ambients.

The flame did extinguish at a finite droplet diameter at an ambient oxygen mole fraction of 0.15 (depending on the pressure). Figure 1a shows the burning behavior for a single droplet and a binary array $(L \approx 3mm)$ in a 0.15 oxygen mole fraction, $190mmHg$ ambient in microgravity. This oxygen mole fraction ambient condition was not flammable in normal gravity at ambient pressures up to $760mmHg$. The burning behavior is non-linear, with k increasing throughout the flame

lifetime. Finally, this figure shows that the flame size initially grew with time, reached a plateau, then decreased with time until extinction. The flame standoff ratio, however, increased nearly linearly with time throughout the burn.
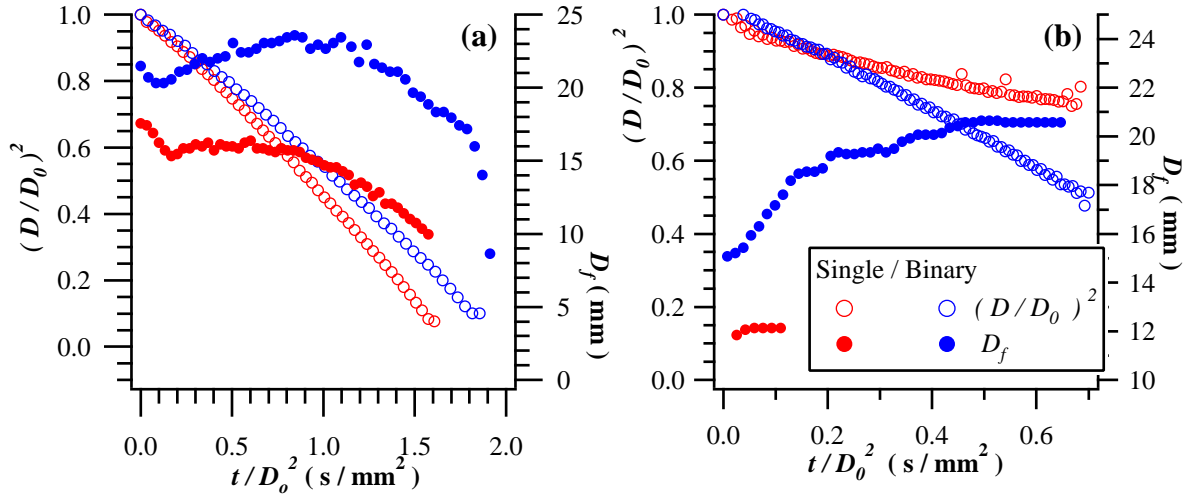
Figure 1: Droplet and flame histories as a function of time for a single droplet and a binary droplet array ($L \approx 4mm$) in (a) 0.15 oxygen mole fraction, $380mmHg$, nitrogen ambient; (b) 0.25 oxygen mole fraction, $190mmHg$, helium ambient in microgravity.

In the 0.15 mole fraction ambient and all pressures ($90 \rightarrow 760mmHg$), the flame surrounding the binary array extinguished at a finite droplet diameter. Figure 1a shows that while the single droplet burned to completion, the flame surrounding the array extinguished approximately one second after the igniter withdrew. The D_{ext} was approximately $1.1mm$ for both droplets of the array. Further, the flame size was nearly 50 percent larger than the flame surrounding the single droplet and the flame was much dimmer. In the binary array test, the flame size increased, reached a maximum, and extinguished. The above trends were consistent over a range of inter-droplet spacings and ambient pressures. In the 0.15 oxygen mole fraction ambient, the flame surrounding the binary array always extinguished at a finite droplet size that was larger than the single droplet extinction diameter.

The results cited above display an opposite trend to the normal gravity test results. That is, interactions diminished flammability in the microgravity tests, whereas in the normal gravity tests, interactions enhanced flammability. The large, weak flames in the microgravity tests were probably more influenced by radiative losses (spectral, due to the lack of soot) from the flame zone than the normal gravity tests.

Recent droplet combustion experiments on the Space Shuttle[11] showed that droplets burning in helium-oxygen ambients exhibited large burning rates, smaller flame standoff ratios and finite-sized extinction droplet diameters. The experiments further demonstrated both modes, diffusive and radiative, of flame extinction. Figure 1b shows the burning history of a single droplet and a binary array in a $190mmHg$, 0.25 oxygen mole fraction (balance helium) ambient in microgravity. The droplet histories were more linear and was much higher for the helium diluted experiments than those in the nitrogen diluted experiments (Fig. 1a). Also, the flames were much brighter in the helium-diluted ambients and the flame sizes and standoff distances in the helium-diluted ambients

were approximately 50 percent smaller. The flame surrounding the single droplet extinguishes quickly after ignition. The flame surrounding the binary array, however, burns much longer, with $D_{ext} \approx 1.1mm$. This extinction trend is opposite to that displayed in nitrogen-diluted experiments, but in agreement with the normal gravity experiments. The k for the binary array (0.75 mm^2/s) was smaller than k for the single droplet (0.90 mm^2/s), although there is only a short time period in the single droplet experiment to calculate k. The flame height for the binary array was larger than the flame height for the single droplet. Further tests showed that the flames surrounding the binary droplet array at $L \approx 8, 12\ mm$ (merged flames existed for both spacings) both extinguished at droplet diameters smaller than the single droplet. The extinction behavior at $L \approx 24mm$, however, was nearly identical to that of a single droplet.

The observed difference between the two ambients is attributed to the importance of radiative loss. The nitrogen/oxygen tests had larger, weaker flames, and smaller burning rates and consequently were affected more significantly by radiative loss from the flame zone compared to the helium/oxygen tests.

Numerical Modeling

The numerical model of the single droplet (numerical modeling of the binary array is in progress) is based on the model of the candle flame [12]. The model is one-dimensional and transient in both the liquid and gas phase. The gas-phase model assumes: one-step, second-order overall Arrhenius reaction, constant specific heats and thermal conductivity, constant Lewis number for each species (although different species can have different, constant Lewis numbers), ideal gas behavior, and no buoyant force. Flame radiative losses from carbon dioxide and water vapor are accounted for by a gray gas treatment. Dietrich and co-workers [13] provide complete details about the numerical model, solution procedure and a more complete listing of the results.

Figure 2 shows a comparison of an experiment in a $120mmHg$, 0.15 oxygen mole fraction ambient with the predictions of the numerical model. The D_{ext} are $0.76mm$ and $0.69mm$ for the experiment and model, respectively. The agreement between the model and experiment is very good. The predicted flame diameter and temporal behavior of the flame size are very close to the experiment. The only exception is near the end of the test when the model predicts that the flame size and standoff decrease until extinction, whereas the experiment shows that the flame standoff increases continuously until extinction.

The numerical model correctly predicts many of the observed experimental trends. Furthermore, quantitative agreement is good for the temporal behavior of both the droplet and flame. This agreement requires suitable values for the average gas-phase thermo-physical and chemical kinetic properties. The fact that the droplet history agrees is not surprising, since even the simplest formulation will produce good estimates of the burning rate constant as long as reasonable properties are used in the formulation. Simplified models, however, do not predict accurate flame sizes, and the current model provides reasonable agreement for flame size as a function of time. The model does not predict the experimentally observed pressure dependence of extinction. This is due to the simplified kinetics scheme, although it may be possible to change the pressure dependence of the single step scheme to get better agreement. One surprising result of the model was the sensitivity of the extinction conditions to the ignition parameters. The igniter location, energy and duration must closely match the experimental values such that the model accurately predicts both the pre-ignition vaporization behavior and ignition time (first appearance of a flame).
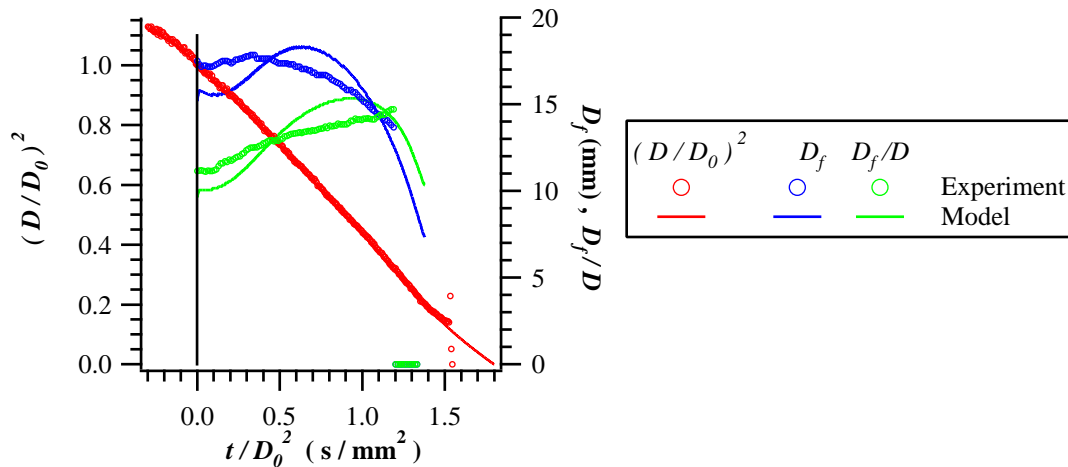
Figure 2: Experiment and numerical model comparison for a single ($D_0 \approx 1.8mm$) droplet burning in a 0.15 oxygen mole fraction, $120mmHg$, nitrogen-diluted ambient in microgravity.

References

[1] G.A.E. Godsave *Proc. Comb. Inst.* **4**:818-830 (1952).

[2] S. Kumagai and H. Isoda *Proc. Comb. Inst.* **6**:726-731 (1956).

[3] M.Y. Choi and F.L. Dryer *Microgravity Combustion, Fires in Free Fall*, Ch. 4, Academic Press, New York (2001).

[4] J.F. Rex, A.E. Fuhs and S.S. Penner, *Jet Propulsion* **26**: 179 (1956).

[5] K. Annamalai and W. Ryan, *Prog. Energy Combust. Sci.* **18**: 221 (1992).

[6] C.K. Law *Combust. Flame* **24**: 89 (1975).

[7] B.H. Chao, C.K. Law and J.S. Tien *Proc. Comb. Inst.* **23**: 523 (1990).

[8] P.M. Struk, D.L. Dietrich, M. Ikegami and G. Xu, *Proc. Comb. Inst.* **29**: to appear (2002).

[9] P.M. Struk, M. Ackerman, V. Nayagam and D.L. Dietrich, *Microgravity Sci. Tech.* **XI/4**: 144 (1998).

[10] J. Easton, *Large Diameter Radiative Extinction Experiments with Decane Droplets in Microgravity*, MS Thesis, Case Western Reserve University (1998).

[11] V. Nayagam, J.B. Haggard, R. Colantonio, A.J. Marchese, B.L. Zhang and F.L. Dryer and F.A. Williams *AIAA J.* textbf26: 1369 (1998).

[12] D.L. Dietrich, H.D. Ross, Y. Shu, P. Chang and J.S. T'ien, *Combust. Sci. Tech.* **156**:1 (2000).

[13] D.L. Dietrich, P.M. Struk, M. Ikegami and G. Xu, Proceedings of the Third Joint Meeting of the US Sections of the Combustion Institute, March 16-19, Chicago, Illinois (2003).

Droplet Vaporization in a Levitating Acoustic Field

G. A. Ruff[1], S. Liu[2], and I. Ciobanescu[2]

[1]NASA Glenn Research Center, Cleveland, OH

[2]Mechanical Engineering and Mechanics Department, Drexel University,
Philadelphia, PA

INTRODUCTION

Combustion experiments using arrays of droplets seek to provide a link between single droplet combustion phenomena and the behavior of complex spray combustion systems. Both single droplet and droplet array studies have been conducted in microgravity to better isolate the droplet interaction phenomena[1-3] and eliminate or reduce the effects of buoyancy-induced convection. In most experiments involving droplet arrays, the droplets are supported on fibers to keep them stationary and close together before the combustion event. The presence of the fiber, however, disturbs the combustion process by introducing a source of heat transfer and asymmetry into the configuration. As the number of drops in a droplet array increases, supporting the drops on fibers becomes less practical because of the cumulative effect of the fibers on the combustion process. To eliminate the effect of the fiber, several researchers have conducted microgravity experiments using unsupported droplets. Jackson and Avedisian[4] investigated single, unsupported drops while Nomura *et al.*[5] studied droplet clouds formed by a condensation technique.

The overall objective of this research is to extend the study of unsupported drops by investigating the combustion of well-characterized drop clusters in a microgravity environment. Direct experimental observations and measurements of the combustion of droplet clusters would provide unique experimental data for the verification and improvement of spray combustion models. In this work, the formation of drop clusters is precisely controlled using an acoustic levitation system so that dilute, as well as dense clusters can be created and stabilized before combustion in microgravity is begun.

While the low-gravity test facility is being completed, tests have been conducted in 1-g to characterize the effect of the acoustic field on the vaporization of single and multiple droplets. This is important because in the combustion experiment, the droplets will be formed and levitated prior to ignition. Therefore, the droplets will begin to vaporize in the acoustic field thus forming the "initial conditions" for the combustion process. Understanding droplet vaporization in the acoustic field of this levitator is a necessary step that will help to interpret the experimental results obtained in low-gravity.

EXPERIMENTAL METHODS

The acoustic levitator, shown in Fig. 1, is a single-axis driver assembly consisting of two piezoelectric transducers in a sandwich configuration similar to that developed by Cao *et al.*[6] Aluminum transmitter blocks are placed on both sides of the sandwich transducer and sized to create a plane standing wave in the material when oscillating at 20 kHz. A titanium acoustic horn is coupled to the forward transmitter to amplify the transducer displacement. The tip of the horn is 29 mm in diameter and directs the acoustic wave towards a concave reflector (50-mm diameter). The reflector focuses the acoustic pressure field to produce an axially- and radially-varying pressure field between the driver and reflector.

The droplet evaporation tests were conducted by first producing an acoustic field and then dispensing a droplet to the end of a 90-micron hypodermic needle from a 0.1 ml syringe. Single droplets were simply pulled off the needle by the acoustic field as the needle was

withdrawn. Multiple droplets were produced by rapidly moving the reflector up approximately 2 mm and returning it to its original position. The disturbance in the acoustic field broke up the parent drop into a number of smaller droplets that were then captured and stabilized in the acoustic antinode. The droplets are imaged through a window in the reflector using a CCD camera and recorded on video tape. The time history of the diameter of the droplet (or droplets) is determined by first digitizing the video and then analyzing sequential images using image analysis software.

VAPORIZATION IN ONE-G

As in several other microgravity investigations, methanol has been used in our initial tests of the acoustic levitator/droplet generator system.[1,2] The first tests were to determine the effect of the acoustic field on droplet vaporization rate for methanol. Table 1 shows the measured vaporization rate for an isolated methanol droplet at different sound pressure levels (SPL). The evaporation rate was found to be relatively independent of the strength of the acoustic field, at least for the levels used in this experiment. Also, the vaporization rate compares very well to the theoretical value for diffusion-controlled, quasi-steady droplet evaporation calculated to be 0.00331 mm^2/s. Seaver et $al.$[7] and Tian and Apfel[8] used acoustic fields similar in strength to those used in this experiment and drew similar conclusions. Yarin et $al.$[9] evaluated droplet vaporization at higher SPL (160 dB and above) and found the effect to be significant. Although stronger fields could be applied, the strength of the field was maintained at the minimum required to levitate the droplets.

Table 1. Isolated Droplet Vaporization at Varying Sound Pressure Level

SPL (dB)	d_o (mm)	-K (mm^2/s)
119	0.463	0.00352
123	0.476	0.00354
128.3	0.562	0.00400

Tests were also conducted using ethanol droplets to confirm consistent behavior with drops having a different composition. Figure 2 shows the vaporization rate data obtained for isolated ethanol and methanol drops. As expected, ethanol evaporates at a faster rate and, as shown in the legend, both yield values of the vaporization rate constant, K, that compare well with that predicted by the d^2-law. Similar experiments were conducted using two- and three-droplet clusters to develop and evaluate procedures before advancing to clusters having a greater number of droplets.

Before discussing the experimental results for multiple droplet conditions, the theoretical model to which the results are compared will be presented. A number of simplified theories of droplet vaporization and combustion have been developed to study multiple droplet effects.[10-13] Several investigations using detailed numerical simulations have also been conducted.[14-16] Labowsky[10] applied the method of images to calculate the effect of arrays of up to seven equally-sized interacting drops on combustion and evaporation process. He found that the burning rate was decreased by approximately 10% when the drops were separated by 20 droplet diameters and up to 30% as the spacing became less than 5 diameters. A more detailed, three-dimensional analysis of Kim et $al.$[15] reached a similar conclusion. The Point Source Method (PSM) developed by Annamalai and Ryan[17] determines the mass loss rate of interacting drops by treating each droplet as a point mass source and heat sink, and evaluates the steady-state mass loss of arrays of

interacting drops in a quiescent atmosphere with Le = 1 and Sh=2. For arrays up to 5 drops, results from the PSM have been shown to be in excellent agreement with the results obtained through the exact methods developed by Labowsky[10] and Brzustowski *et al.*[11] One of the primary reasons for using the PSM method for the initial comparisons with our data is that, once the appropriate equations are developed, experimentally-measured droplet diameters and spacing can be input. This yields correction factors for the vaporization rate relative to the isolated droplet vaporization rate for the unequally-sized and spaced droplets found in an experiment.

Table 2 shows the results of the PSM method for a typical three-droplet cluster. The vaporization rate of the larger droplet is shown to compare fairly well with the predictions of the PSM. The rates for the two smaller droplets are substantially less than predicted. Because of the stability of the cluster, we know all three droplets were in the same pressure well and, therefore, were exposed to relatively the same conditions. Yarin *et al.*[9] indicated that without external blowing, the accumulation of vapor in the pressure well could reduce the vaporization rate. Given that convection by acoustic streaming would be to increase the vaporization rate and the SPL for this experiment is well below the levels at which these effects are observed, vapor accumulation appears to be a plausible explanation. Other data sets are being analyzed to further evaluate these observations. Also, numerical simulations of the experimental configurations are underway using a modified version of the Fire Dynamics Simulator (FDS) code[18] to investigate this phenomenon in more detail.

Table 2. Comparisons for Three-Droplet Ethanol Cluster

Diameter (mm)	Droplet Spacing (mm)			m''/m''_{iso}	
	1 - 2	1 - 3	2 - 3	Experiment	PSM
0.512				0.860	0.884
0.476	2.96	2.52	2.41	0.672	0.875
0.293				0.281	0.822

SUMMARY

A single axis acoustic levitator has been designed and constructed. The design of the acoustic levitator provides both a vertical and lateral positioning force on the droplets and stable clusters containing between 2 and 20 drops have been generated. Results have shown that isolated droplet vaporization in a resonant acoustic field at 1-g are consistent with those of previous researchers. Current work consists of comparing vaporization rates from droplets within a cluster to predictions of the Point Source Method. Numerical simulations using the Fire Dynamic Simulator (FDS) have also begun. Meanwhile, fabrication of the drop tower test facility is progressing and should be ready for testing during the summer of 2003.

REFERENCES
1. Dietrich, D. L., Struk, P.M., Kitano, K., and Ikegami, M., "Combustion of Interacting Droplet Arrays in a Microgravity Environment," Proceedings of the Fifth International Microgravity Combustion Workshop (NASA Conference Publication 1999-208917), Cleveland, Ohio, May 18 - 20, 1999.
2. Gokalp, I., Chauveau, C., Vieille, B., Kadota, T., and Segawa, D., "High Pressure Burning of Methanol Droplets: A Comparison between Parabolic Flight and Drop Tower Experiments," Proceedings of the Fourth International Microgravity Combustion Workshop (NASA Conference Publication 10194), Cleveland, Ohio, May 19-21, 1997.
3. Wang, C. H. and Ueng, G. J., "An Experimental Investigation of Fuel Droplet Combustion Under Micro-Gravity," *Int. Comm. Heat Mass Transfer*, Vol. 24, No. 7, pp. 931-944, 1997.

4. Jackson, G. S. and Avedisian, C. T., "Combustion of Unsupported Water-in-n-Heptane Emulsion Droplets in a Convection-Free Environment," *Int. J. Heat Mass Transfer*, Vol. 41, pp. 2503-2515, 1998.

5. Nomura, H., Koyama, M., Ujiie, Y., Sato, J., Kono, M., and Yoda, S., "Microgravity Experiments on Combustion of Monodispersed and Mono-Sized Fuel Droplet Clouds," Fifth International Microgravity Combustion Workshop," Cleveland, Ohio, May 18 - 20, 1999.

6. Cao, Z., Liu, S., Li, Z., Gong, M., Ma, Y., and Wang, C., "Development of an Acoustic Levitation Reactor," *Powder Technology*, Vol. 69, pp. 125-131, 1992.

7. Seaver, M., Galloway, A., and Manuccia, T. J., "Acoustic Levitation in a Free-Jet Wind Tunnel," *Rev. Sci. Instrum.*, Vol. 60, pp. 3452-3459, 1989.

8. Tian, Y. and Apfel, R. E., "A Novel Multiple Drop Levitator for the Study of Drop Arrays," *J. Aerosol Sci.*, Vol. 27, pp. 721-737, 1996.

9. Yarin, A. L., Brenn, G., Kastner, O., Rensink, D., and Tropea, C., "Evaporation of acoustically levitated droplets," J. Fluid Mech., Vol. 399, pp. 151-204, 1999.

10. Labowsky, M., "A Formalism for Calculating the Evaporation Rates of Rapidly Evaporating Interacting Particles," *Combustion Science and Technology*, Vol. 18, pp. 145-151, 1978.

11. Brzustowski, T. A., Twardus, E. M., Wojcicki, S., and Sobiesiak, A., "Interaction of Two Burning Fuel Droplets of Arbitrary Size," *AIAA J.*, Vol. 17, No. 11, pp. 1234-1242, 1979

12. Marberry, M., Ray, A. K. and Leung, K., "Effect of Multiple Particles Interactions on Burning Droplets," Combustion and Flame, Vol. 57, pp. 237, 1984

13. Umemura, A., "Interactive Droplet Vaporization and Combustion: Approach from Asymptotics," *Progress in Energy and Combustion Science*, Vol. 20, pp. 325, 1994.

14. Raju, M. S. and Sirignano, W. A., "Interaction Between Two Vaporizing Droplets in an Intermediate-Reynolds-Number-Flow", *Physics of Fluids*, 2, pp. 1780-1796, 1990.

15. Kim, I., Elghobashi, S. E. and Sirignano, W. A., "Three-Dimensional Droplet Interactions in Dense Sprays," AIAA Paper No. AIAA-91-0073, 29th Aerospace Sciences Meeting, January 7-10, 1991, Reno, Nevada.

16. Leiroz A. and Rangel, R.H., "Numerical study of Droplet-Stream Vaporization at Zero Reynolds Number", *Numerical Heat Transfer. Part A, Applications,* Vol. 27, No. 3, pp. 273, 1995.

17. Annamalai, K. and Ryan, W., "Interactive Processes in Gasification and Combustion. Part I: Liquid Drop Arrays and Clouds," *Progress in Energy and Combustion Science*, Vol. 18, pp. 221, 1992.

18. McGrattan, K.B. and Baum, H.R. and Rehm, R.G. and Hamins, A. and Forney, G.P. and Floyd, J.E. and Hostikka, S. and Prasad, K., "Fire Dynamics Simulator, Technical Reference Guide," National Institute of Standards and Technology (NIST), 2002, NISTIR 6782, 2002 Ed., http://fire.nist.gov/bfrlpubs/
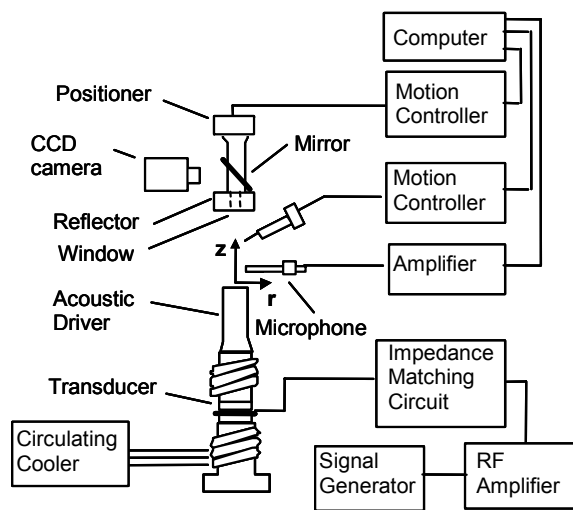
Figure 1. Droplet levitation apparatus
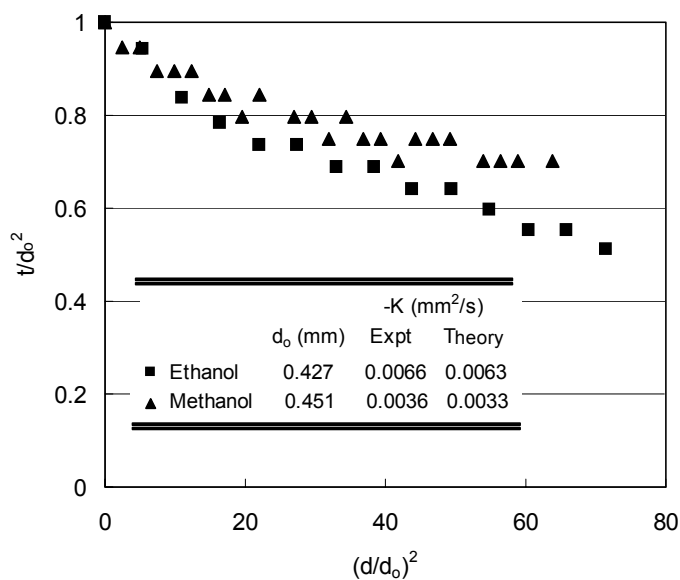
Figure 2. Comparison of ethanol and methanol evaporation

Combustion of Porous Graphite Particles in Oxygen Enriched Air[1]

Andrew J. Delisle,[†] **Fletcher J. Miller**[‡] **and Harsha K. Chelliah**[†]

[†]Mechanical and Aerospace Engineering, University of Virginia, Charlottesville, VA 22903

[‡] National Center for Microgravity Research, MS 110-3, Cleveland, OH 44135

OBJECTIVES:
Combustion of solid fuel particles has many important applications, including power generation and space propulsion systems. The current models available for describing the combustion process of these particles, especially porous solid particles, include various simplifying approximations. One of the most limiting approximations is the lumping of the physical properties of the porous fuel with the heterogeneous chemical reaction rate constants [1]. The primary objective of the present work is to develop a rigorous modeling approach that could decouple such physical and chemical effects from the global heterogeneous reaction rates. For the purpose of validating this model, experiments with porous graphite particles of varying sizes and porosity are being performed under normal and micro gravity.

EXPERIMENTAL APPROACH:
As reported in the previous Microgravity Workshop [2], the major experimental challenges of this project were particle deployment, ignition, and obtaining *self-sustained oxidation* under normal and reduced gravity conditions. The typical char particle temperature that support self-sustained oxidation is over 1600 K [3]. In practical coal combustors, because of the high temperature environment containing oxygen and hot vitiated products, porous char particles undergo self-sustained oxidation. Replicating such an high temperature environment in reduced gravity facilities is difficult and has not been pursued yet. The main challenges of creating an high-temperature environment in microgravity are related to the temperature decay due to heat losses (during 20 seconds of reduced gravity in KC135 aircraft) and avoiding buouyancy driven currents in the process of creating high-temperature environment.

(i) An Alternate Method of Self-Sustained Oxidation: O_2 Enrichment:
In air at room temperature, the convective and radiative heat losses from the particle to the surroundings are significant compared to the heat release; consequently, self-sustained combustion was never realized. In addition, the heat losses associated with particle mounting can further inhibit the particle oxidation. Under such conditions, an external energy source in the form of a focused CO_2 laser beam, with a minimum heat flux of 88 W/mm^2 was needed to burn the particle in less than 25 secs.

In order to attain self-sustained heterogeneous combustion of porous carbon particles, oxygen enriched air was considered. With the enclosed chamber designed for this project [4], under normal and reduced gravity room temperature conditions enriched air provided self-sustained combustion when the oxygen mass fraction was above 55%. Similar enriched conditions were used by Ubhayakar and Williams [5], in the context of combustion of a coal char particle (about 125 microns in diameter) under normal gravity conditions.

(ii) KC135 Aircraft Experimental Setup:
The first KC135 reduced gravity experiments with 1 mm size porous carbon spheres (porosity

---

31%) in air were performed in October 2001, with follow-up experiments in oxygen enriched air in March and April 2002 [6]. The experimental rig consists of an enclosed chamber certified for pure oxygen environment, CO_2 laser and associated optics for rapid particle ignition, Cohu monochrome camera with an Optem Zoom70 microscope lens, together with a Mini-DV recorder to record the particle image at 30 fr/s (adequate for carbon particle oxidation with burning rate constants of the order of 0.1 mm^2/s), fiber optic coupled spectrometer for particle temperature measurement, and oxygen sensor to monitor the enrichment level. All the above components were mounted on 4ft× 2ft optical bread board, with a separate equipment rack for power supply of the laser, water cooling system for the laser, laptop, etc.

(iii) Particle Mounting:
Laser drilled porous carbon particles, tethered with a 12 micron alumina (Al_2O_3) fiber as shown in Fig. 1 were used in the present experiments. Because of the large aspect ratio (i.e. 1 mm sphere with a 15 micron diameter hole), the laser drilled holes were far from the desired 15 micron straight holes. Laser drilling of the particles were performed by several commercial vendors, as well as the NASA Glenn Research Center micromachining laboratory. In all these attempts, the drilled holes took an hour-glass shape (with 75 micron at the ends and about 50 micron at the neck hole) because of the large aspect ratio involved. To maximize the number of reduced gravity experiments in the KC135 aircraft, a rotary table with five particle holders was designed [2,6].
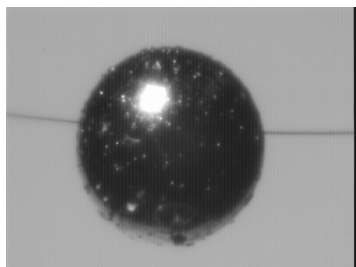
Figure 1: 1 mm carbon particle mounted on 15 μm alumina fiber [6].
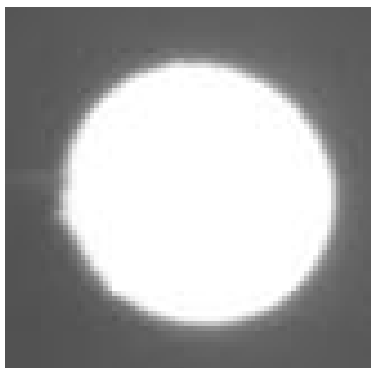
Figure 2: Image of the oxidizing particle in enriched air, using a OD 8 neutral density filter [6].
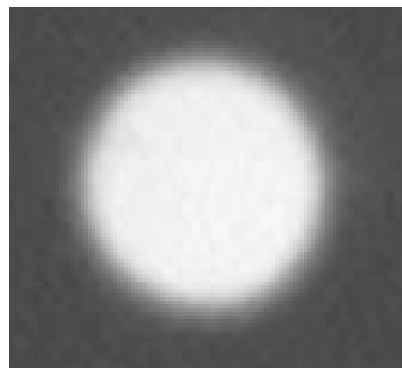
Figure 3: Image of the oxidizing particle in enriched air, using 410± 10 nm band-pass filter [6].

(iv) Regression Rate and Surface Temperature Measurements:
Once ignited by the focused CO_2 laser beam, with a typical spot size of about 200 μm diameter, the carbon particles oxidized in about 5-10 sec in oxygen enriched air. In the past research we demonstrated the use of a microscope CCD camera for particle imaging [2] and a fiber optic coupled spectrometer to measure the particle surface temperature [7]. From the camera images, we were able to track the particle diameter vs. time using specialized tracking software developed at NASA Glenn. Unlike droplet combustion which typically uses a backlit view of the droplet, in our case the graphite particle was sufficiently self-luminous that we were able to image it directly. That led, however, to an uncertainty in the data analysis when the question arose as to whether the camera was imaging only the particle emission, or whether there could have been an influence of a CO gas-phase flame that changed the apparent particle size. Limited tests with optical filters (eg. OD 8 neutral density filter to reduce broad-band

emission vs. 410±10 nm band-pass filter to capture CO emission) failed to conclusively answer this question. Figure 2 shows an image of the luminous particle obtained with the OD 8 neutral density filter, while Fig. 3 shows that obtained with 410 nm band-pass filter. The latter shows a more diffusive image, indicative of the CO diffusive-reactive layer outside the particle.

A miniature fiber-optic coupled spectrometer (Ocean Optics S2000) was used to acquire the emission spectrum from the particle in order to determine its temperature. This method requires only that the particle emissivity be constant over the spectral region measured, but not necessarily a black body. The recorded spectral emission in the range from 767 to 937 nm was considered, with fitting the resulting intensity vs. wavelength data to a black body curve to obtain the temperature. To obtain the spectrometer sensitivity function, it was used to measure a calibrated black body source at $1000^{o}C$ [6].

(v) Experimental Results:
Figure 4 shows the variation of the square of the normalized particle diameter vs. time, for three enriched air experiments (60%, 65% and 70% oxygen) at room temperature, with glassy carbon spheres (31% porosity) under normal gravity. These experiments were performed with the 410 nm band-pass filter. The increase of the slope of the line with increasing O_2 level indicates a distinct effect on the mass burning rate with oxygen concentration. This means the combustion is in a diffusion-controlled regime, which is expected for the large particle size. When oxygen mole fraction was below 55%, no emissions were observed indicating that self-sustained oxidation is not possible. Limited porous carbon particle oxidation experiments were performed under reduced gravity conditions, under similar oxygen enrichment conditions. After each burn in the KC135 aircraft, a fresh particle on the rotary table was brought into a preselected position in the camera field of view and the laser focus. However, minute shifts of the
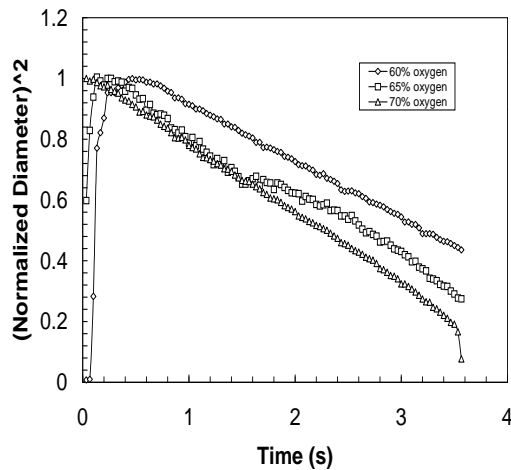
Figure 4: Comparison of the normalized equivalent particle diameter square vs. time, for oxygen enriched air under normal gravity.
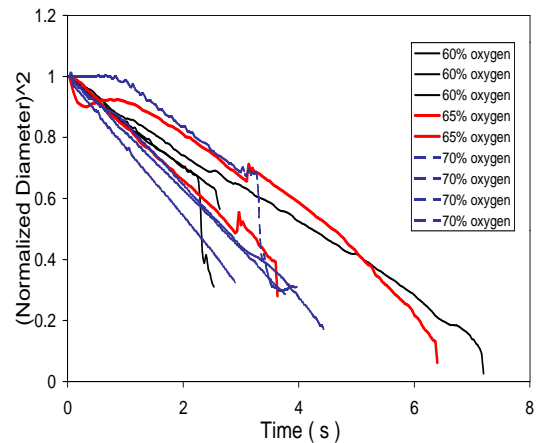
Figure 5: Comparison of the normalized equivalent particle diameter square vs. time, for oxygen enriched air under reduced gravity.

particle requiring fine adjustments of the CO_2 laser and camera, necessitated the use of OD 8 neutral density filter in reduced gravity experiments, instead of the 410 nm band-pass filter used in normal gravity.

As expected, the carbon particles oxidized in enriched air without any difficulty in reduced gravity, as shown in Fig. 5. Analysis of these data have indicated a slightly lower burning rate constant compared to the normal gravity conditions. However, the results shown in Fig. 5 indicate no clear trend with oxygen enrichment, as summarized in Table 1. Also the results shown in Fig. 5 indicate abrupt changes at some instances in time. These sudden changes are believed to be due to g-jitter effects, but for these preliminary experiments we had no accelerometer data. Even at these highly enriched air conditions, it is clear that the reduced gravity oxidation time exceed that of the NASA 5.2 sec drop tower. Considering the initial transition effects associated with particle heat up and ignition, the KC135 aircraft is the best choice for experiments with solid fuel particles.

Table 1: A Preliminary Comparison of Particle Burning Rate Const. (mm^2/s)

Oxygen mole fraction in air	60 %	65%	70%
1g experiments (with 410 nm filter — Fig. 4)	0.189	0.210	0.231
1g experiments (with the OD 8 neutral density filter)	0.191	0.162	—
reduced g experiments (with the OD 8 neutral density filter — Fig.5)	0.140	0.137	0.147

NUMERICAL APPROACH:

The details of the *unsteady* solid particle combustion model that is being developed were presented at the previous microgravity workshop [8]. The goal of this effort was to (a) couple the internal pore combustion to external homogeneous combustion, (b) develop a set of consistent inter-phase conditions for scalar variables, (c) investigate the transient effects, including extinction of particle oxidation, and (d) validate the model with experimental data. While the unsteady model predicted the ignition and subsequent quasi-steady state oxidation process comparable to early experiments, calculations have not been performed for the oxygen enriched air at room temperature. Because the experiments indicate a quasi-steady burning trend, for both normal and reduced gravity, the goal here is to first perform the quasi-steady modeling calculations first as described by Chelliah [3], before undertaking the computationally expensive transient calculations.

REFERENCES:

[1] Laurendeau, N.M., *Prog. Energy Comb. Sci.* **4**:221 (1978).
[2] Chelliah, H.K. Miller, F.J., and Delisle, A.J., *Sixth Int. Microgravity Combustion Workshop*, Cleveland, OH, May 2001
[3] Chelliah, H.K., *Combust. and Flame* **104**:81-94 (1996).
[4] Pantano, D., MS Thesis, University of Virginia, May, 1999.
[5] Ubhayakar and Williams, F.A., *J. Electrochem Soc.* **123**(4):747-756 (1976).
[6] Delisle, A.J., MS Thesis, University of Virginia, August, 2002.
[7] Miller, F.J., "Multi-wavelength Optical Pyrometry for Solid-Phase Temperature Measurements, WSS Meeting Paper, The Combustion Institute, Spring 2000.
[8] Chelliah, H.K., Miller, F.J., Pantano, D., and Kasimov, A.K., *Fifth Int. Microgravity Combustion Workshop*, Cleveland, OH, May 1999.

Liquid Flame: Combustion of Metal Suspensions in Liquid Sulfur.

Sam Goroshin, Lorena Camargo, and John Lee
McGill University, Montreal, Quebec, Canada

Combustion of the majority of solid heterogeneous systems such as pyrotechnics or SHS is accompanied by phase change: melting or/and vaporization of initial reactants and formation of intermediate combustion products in a liquid or gaseous state. Most of the known binary heterogeneous systems are also loose or compacted powder mixtures and are porous. Flows that are induced by volume change during phase transitions, capillary forces, and evolution of gases trapped in pores complicate the flame propagation process and the study of the high-temperature combustion chemistry. The system described in the present paper is the first observation of a non-gaseous "uniphase" flame when the initial mixture, flame and combustion products are all in liquid state. Combustion of suspensions of iron and manganese powders in liquid sulfur does not release gases and produces products (metal sulfides) that remain liquid in the wake of the flame front. Though free from the flows induced by the phase transitions, the liquid flame fronts are strongly influenced by gravity forces. Buoyancy-driven convection in cooling combustion products and sedimentation of metal particles in the liquid sulfur matrix complicates the study of the system at normal gravity conditions. The use of very fine, micron-sized metal powders and the shallow-pool flame technique allowed the authors to provide some observations at normal gravity conditions, though the study of this unique system in a wide range of parameters is possible only under a microgravity environment.

Thermodynamics of the gasless metal-sulfur combustion

Our previous thermodynamic calculations [1] have indicated that some metal-sulfur reactions form very small amounts of gas products, i.e. they are practically gasless. Thus, for example, stoichiometric compositions of Cr-S and Fe-S have pressures of gas products of about 6.5 and 10^{-2} mbar at adiabatic flame temperatures of 2168 K and 1462 K correspondingly (constant volume combustion calculations). Due to intensive "sparkling" demonstrated by the Cr-S mixtures that leads to creation of multiple flame fronts, it was difficult to use Cr-S for the present open-pool flame experiments. The other candidate, Fe-S, has a very low flame temperature and readily quenches when burned in thin layers. By combining energetic, although gas producing mixture such as Mn-S, with gasless but low-energy Fe-S composition, ternary combustion compositions might be designed that are gasless and posses, at the same time, sufficiently high flame temperatures. Thus, thermodynamic calculations presented in Fig.1 shows that Mn-Fe-S compositions demonstrate virtually gasless flames when the concentration of Mn-S in the mixture is below 50 %.
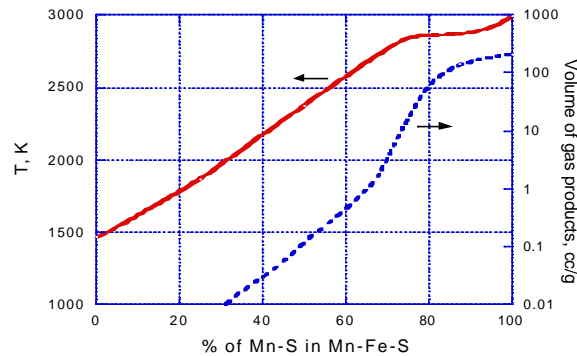
Figure 1 Adiabatic flame temperature and production of gas products in Mn-Fe-S mixtures as a function of composition.

Mixture preparation and shallow-pool flame experimental technique.

Stochiometric compositions of micron-sized ($d_{32} < 10$ microns) Mn, Fe and S powders were blended in a rotating tumbler for several hours. The powder mixture was then placed in a Pyrex beaker and heated in a heating mantle. Upon melting of sulfur, at around 115? C, the mixture transforms into a uniform, free from gas bubbles, low-viscosity suspension of metal powders in liquid sulfur.

Our previous experiments on flame propagation in solidified Me-S suspensions in wide cylindrical tubes have indicated unstable flame fronts with irregular flame propagation velocity [1,2]. Apparently, this behavior is the result of a very strong convection induced by buoyancy forces in high-temperature liquid combustion products [3]. To avoid development of the convective flow, thin-layer, two-dimensional combustion fronts were used in present experiments.

The 1-mm or 2-mm deep cylindrical cavity, machined in a massive steel plate, was uniformly filled with metal-sulfur suspension. In order to prevent solidification of the suspension, the plate was heated to the temperature above the melting point of sulfur. Protective argon flow was maintained above the pool surface to prevent possible ignition of sulfur vapor in air. The mixture was ignited at the center of the pool by a thin tungsten glowing wire. The flame propagation process was recorded with a digital video camera through a 45? inclined mirror. A schematic of the experimental setup and a photo of the flame in a 1-mm deep pool of Mn-Fe-S suspension are shown in Fig. 2.
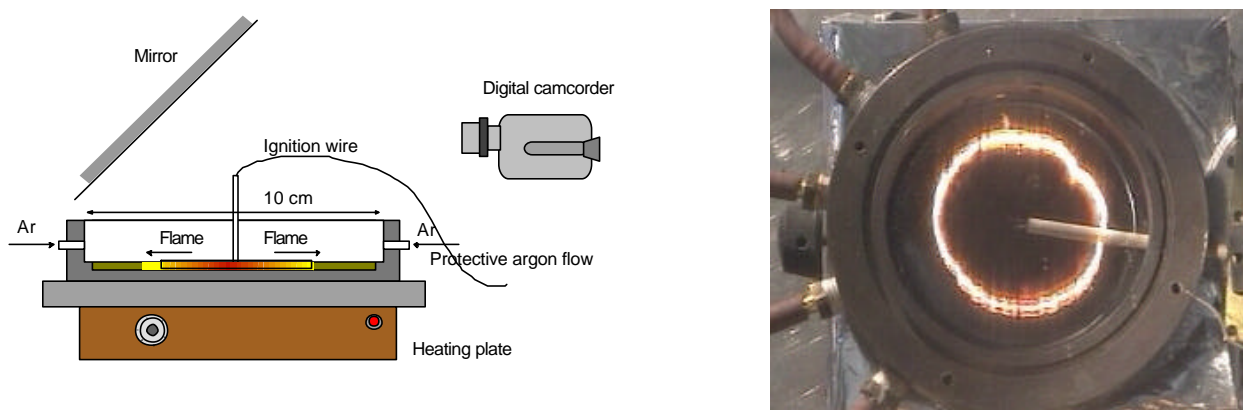
Figure 2 Schematics of experimental set-up and photo of the liquid flame in the 1-mm deep pool.

Flame speed measurements.

Fairly symmetrical circular flame fronts (see photo in Fig. 2) moving with practically constant speeds were observed in all studied compositions with the exception of the pure Fe-S mixture. The heat of reaction in the Fe-S composition is very low and the flame quenches easily. Thus, flame circles in thin 1-mm Fe-S layers were often discontinued leaving behind patches of unburned mixture. The flame speed was quite reproducible in all compositions and, as a rule, noticeably higher in shallower 1-mm pools (see Fig. 3). Flame fronts in both 1-mm and 2-mm pools were also sharp and well defined with no evidence of sulfur evaporation or boiling ahead of the flame front. However, in several experiments that were performed with deeper 4 to 5 mm pools, boiling of the sulfur was observed at distances of about 3-4 mm ahead of the flame front. Formation of oblique combustion fronts due to faster flame speed at the bottom of the pool is clearly responsible for this phenomenon and was also confirmed by thermocouple measurements (see the next paragraph).

Flame speed data in mixtures of different compositions (Fig. 4) show that, contrary to expectations, flame speed decreases with the increase of the manganese content in the Fe-Mn-S stoichiometric ternary mixture, i.e., higher flame speeds are observed in less energetic mixtures with lower calculated flame temperatures (see Fig. 1). Mixtures diluted with powdered inert products of Mn-Fe-S combustion also

exhibit similar paradoxical behavior: flame speed practically remains the same in diluted mixtures in spite of the decrease in calculated adiabatic flame temperature by almost 500 K (Fig. 5).
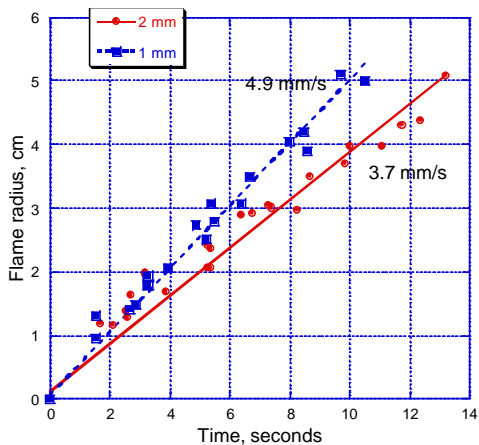
Figure 3 Flame trajectories in 1-mm deep and 2-mm deep pools plotted from six different shots (50% (Mn-S) and 50% (Fe-S) stoichiometric composition).
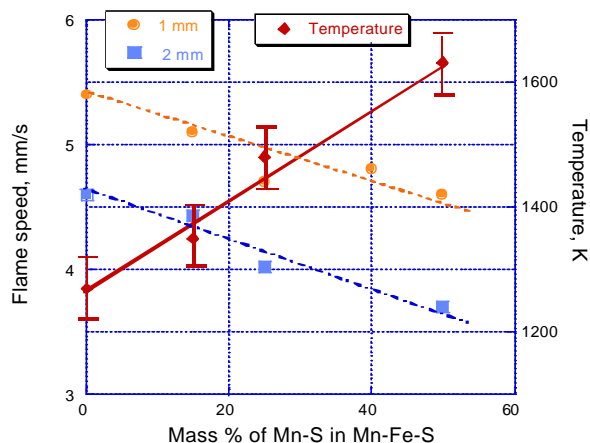
Figure 4 Flame speed and measured peak flame temperature as a function of the mixture composition in 1-mm and 2-mm deep pools.
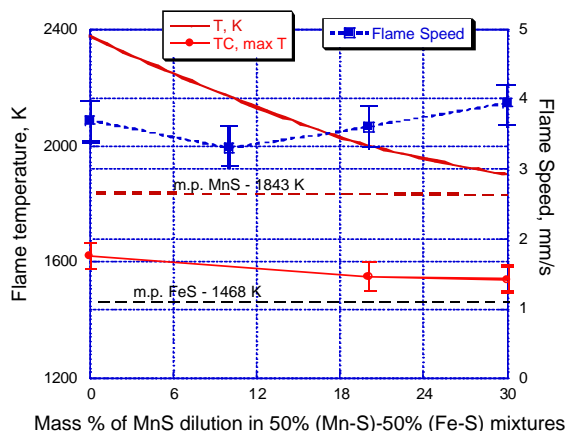
Figure 5 Flame speed, calculated adiabatic flame temperature, and measured peak flame temperatures (line with points) as a function of the mixture dilution by the MnS combustion product.

Flame temperature measurements.

Apparently, anomalous dependencies of flame speeds on mixture compositions reported above indicate that calculated adiabatic flame temperatures do not define characteristic reaction rates in combustion fronts. Hence, direct flame temperature measurements are required to correlate actual flame temperature with the measured flame speed. Temperature profiles in flame fronts were registered by an array of three C-type W-Re thermocouples positioned along the pool radius at distances of about 14, 28, and 42 mm from the pool's center. The thermocouple beads were submerged to about 0.5 mm below the surface of the liquid combustible mixture. Thermocouples with three different bead sizes of about 0.5, 0.250, and 0.175 mm were used. Only the largest, 0.5 mm thermocouple can be recovered and used in multiple experiments. Smaller thermocouples were usually destroyed in attempts to extract them from solidified combustion products. The response time even for the largest thermocouple was mach smaller than the

characteristic cooling time of combustion products. Thus, the thermocouples of different bead sizes registered practically the same peak flame temperatures. On the other hand, the response time, even for the smallest thermocouple (0.175 mm), was not fast enough to resolve the temperature profile in the flame preheat zone, which is estimated to be only 0.1- 0.2 mm thick due to very low heat conductivity of the liquid sulfur. Typical temperature profiles registered by two .25 mm thermocouples are shown in Fig.6 and indicate maximum flame temperatures of only 1550-1600K compared to 2000 K that is predicted by the equilibrium calculations for this mixture (Fig. 5, 20% dilution). A similar tendency is observed practically for all other mixture compositions where measured maximum flame temperatures are much lower than those predicted by thermodynamic calculations (Fig. 4 and 5). The measured peak flame temperatures are also relatively weak functions of the mixture composition and, in general, are close to the melting point of the corresponding metal-sulfide product.
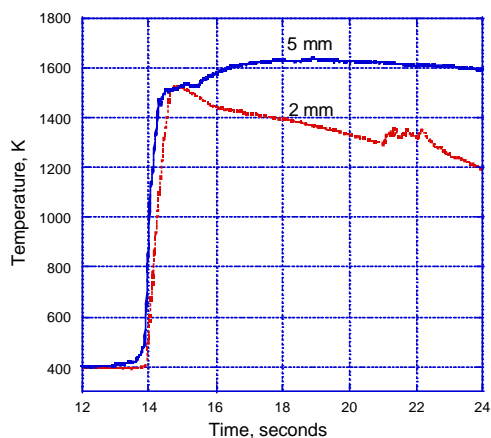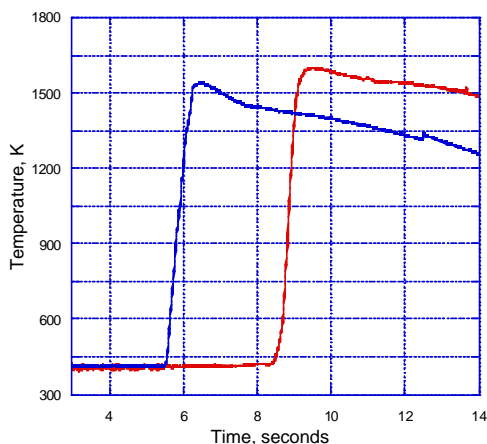
Figure 6 Temperature traces from two .25 mm thermocouples positioned 14 mm apart in the 2-mm deep pool of 50% (Mn-S)-50% Fe-S mixture diluted by 20% of MnS.

Figure 7 Comparison of temperature profiles in 2mm and 5 mm deep pools (the same mixture as in Fig 6)

The cause for such low values of flame peak temperatures becomes evident if we compare temperature traces in 2-mm and 5-mm deep pools shown in Fig. 7. The much smaller rate of heat loss in the deeper 5-mm pools reveals that the combustion front has a complex, two-stage structure. Thus, the initial and very fast combustion stage ends when the flame temperature reaches a melting point of the corresponding sulfide product. A wide reaction zone that follows demonstrates a burning rate so slow that it cannot compensate for the heat loss in the shallow 1 and 2-mm deep pools, thus producing declining temperature profiles. It reveals itself only when the rate of heat loss is sufficiently low as in the 5-mm deep pool. Only the first fast reaction zone and the flame temperature associated with the end of it can affect the flame speed. This explains the observed lack of correlation between measured flame speed and calculated adiabatic flame temperature.

References.
1. Goroshin, S., Mizera, A., Frost, D., and Lee, J.H.S. " Metal-Sulfur Combustion" *Proc. Combust. Inst.*, 26, 1996, pp. 1883-1889
2. Goroshin, S., Lee, J.H.S., Frost, D., " Combustion Synthesis of ZnS in Microgravity" " *Proc. Combust. Inst.*, 25, 1996, pp. 1651-1657
3. Goroshin, S., Lee, J.H.S., and Herring, R. "Combustion Synthesis of the Metal-Sulfides Refractory Glass Ceramics" *Proc. of the First Int. Symposium on Microgravity Research & Applications in Physical Science, Sorrento, Italy, 2000* (ESA SP-454, January 2001, pp. 251-258)

A Two-Dimensional Instability in Deflagrations with Edges

M.Chen, J.Buckmaster

University of Illinois at Urbana-Champaign

Department of Aeronautical and Astronautic al Enginering

104 S.Wright St., Urbana IL 61801

Abstract

We examine the Lewis-number-greater-than-1 stability of a deflagration sitting on a porous-plug burner with an inert coflow. The flame edges generated by the coflow influence the stability, and this influence is examined. Very wide flames display the same stabilit y characteristics as unbounded flames (flames sans edges), but for moderately wide flames the instability is suppressed. A new tw o-dimensional instability can occur for narrow flames, and this can occur for parameter values for which the unbounded flame is stable. There is a range of mass fluxes for which a monotonic decrease in burner (flame) width generates a transition from unstable flames to stable flames, to unstable flames, to quenching.

Introduction

In the present paper we examine a flame with an edge, but one that is forced by supply conditions, and so is not formally an edge-flame, although edge-flame studies might provide useful physical insights. A recen t review of edge-flames, both non-premixed and premixed, can be found in [1]. Our purpose is to examine flames that within a 1-D framework can display a pulsating instability, to see how the instability is affected by the presence of the edge.

The configuration, a planar one, is sketched in Fig.1, and corresponds, roughly, to a burner with an inert coflow. A deflagration is supported above the burner exit face of width $2L_g$, but the coflow regions, each of width L_i, create dual edges.

When L_g is large we would expect the flame to exhibit behavior c haracteristic of 1-D burner flames, and these have been studied for Lewis numbers greater than 1 (our focus here) in [4, 5]. These studies show that the flame can certainly pulsate if the Lewis number is large enough, and can even pulsate for a Lewis number of 1 if the heat loss to the burner is large enough. Here we examine what happens when L_g is not so large, so that 2-D effects are important and the presence of the edges has a global influence on the combustion field.

Model formulation

We adopt a constant densit y model (an Oseen model in the steady-state) with an assigned vertical mass flux M flowing both from the burner face and in the coflow. Non-dimensional equations can then be written in the form:

$$\frac{\partial T}{\partial t} + M\frac{\partial T}{\partial y} = \nabla^2 T + D(1 - T_\infty)Y e^{-\frac{\theta}{T}},$$

$$\frac{\partial Y}{\partial t} + M\frac{\partial Y}{\partial y} = \frac{1}{Le}\nabla^2 Y - DY e^{-\frac{\theta}{T}}, \tag{1}$$

where

$$D = \frac{(1 - T_\infty)^2 \theta^2 e^\theta}{2Le}, \ \theta = \frac{E}{RT_r}.$$ (2)

In these formulas, $(\ )_\infty$ refers to supply conditions and Le is the Lewis number. The reference mass flux M_r used in this formulation is the first order asymptotic approximation to the mass flux for an unbounded deflagration, valid in the limit $\theta \to \infty$. The reference temperature T_r is the adiabatic flame temperature for a flame sans burner.

We shall seek solutions that are symmetric in x, and then the boundary conditions are as follows:

$$x = 0: \quad \frac{\partial T}{\partial x} = 0 = \frac{\partial Y}{\partial x}$$ (3)

$$x = L_g + L_i: \quad \frac{\partial T}{\partial x} = 0 = \frac{\partial Y}{\partial x}$$ (4)

$$0 < x < L_g, \ y = 0: \quad T = T_s, \ MY - \frac{1}{Le}\frac{\partial Y}{\partial y} = M$$ (5)

$$L_g < x < L_g + L_i, \ y = 0: \quad MT - \frac{\partial T}{\partial y} = MT_\infty, \ MY - \frac{1}{Le}\frac{\partial Y}{\partial y} = 0.$$ (6)

$$y = H: \quad \frac{\partial T}{\partial y} = 0 = \frac{\partial Y}{\partial y}.$$ (7)

We adopt the parameter values

$$T_s = \frac{1}{6}, \ T_\infty = \frac{1}{6}, \ Le = 1.3, \ \theta = 7, \ H = 60$$ (8)

The adiabatic flame temperature in this formulation is equal to 1, so that if the supply temperature is 300K, the choice of T_∞ implies that the adiabatic flame temperature is 1800K.

Solutions

One-dimensional calculations show that blow-off occurs when $M = .83$; for $M \leq .14$ oscillating solutions are found; and these persist down to $M = .03$, when quenching occurs. This behavior has long been familiar.

We now examine 2-D solutions corresponding to a flame with edges. L_i, the width of the coflow, is set to the value 15. For non-premixed combustion there is a literature which implies that an edge-flame is more susceptible to the $Le > 1$ oscillating instability than is the trailing 1-D structure [1, 6], but there are no comparable results for premixed combustion. Here we have premixed combustion and a flame edge rather than an edge-flame; nevertheless, for the data (8) we set $M = .15$ (slightly greater than the critical value .14 for the onset of 1-D oscillations) and $L_g = 85$: the flame is stable. Moreover, a reduction of M to .12 and then to .08, values for which the 1-D flame is unstable, yields only stable 2-D solutions.

Although instability is not found for $L_g = 85$, the situation is different when L_g is reduced. The effects of various choices of L_g are shown in the scatter plot in the $M - L_g$ plane in Fig.2. If L_g is small enough, the flame is quenched by the coflow, and the squares identify points corresponding to quenched solutions. It is easier (occurs at larger L_g) to quench a small M flame than a large M flame, but the effect is small.

The stars in Fig.2 mark points for which the solution is oscillatory. The upper boundary (broken line) of the domain of oscillating solutions is quite a strong function of M, and the smaller the value of M, the wider the flame that can support oscillations. But in the domain of Fig.2 ($.05 \leq M \leq .3; \ 0 \leq L_g \leq 50$) a wide enough flame is always stable. There are no instabilities when $M > .3$.

The instability seen here is two-dimensional; there are significant fluctuations in the maximum reaction rate, and the position of this maximum shifts both in x and y. Fluctuations in the maximum temperature are modest but nonlinear; the peaks are sharper than the troughs.

Note that these instabilities can occur for values of M for which the 1-D flame is stable. This doesn't follow immediately from the results of the section '1-D results' as only 1-D perturbations are allowed for there, and the results of [5], for example, reveal that the 1-D burner flame can be more unstable to nonplanar disturbances than planar ones, although not excessively so. But a number of attempts to trigger instabilities by the imposition of 2-D disturbances, failed when $L_i = 0$ for values of L_g and M in the unstable band of Fig.2.

Of course, the 1-D instability, or nonplanar variations of it, can be recovered if L_g is large enough so that edge effects are small, and if M is sufficiently small.

Concluding Remarks

We have examined a deflagration sitting on a burner, one whose 1D counterpart can display oscillating instabilities, and have explored the effect of flame width (and therefore flame edges) on the stability. We find that wide but finite flames can be stable for parameter values for which the infinitely wide flame is unstable. But narrow flames can display a 2D instability that appears to have little connection with the instability of the infinitely wide flame.

It is possible that the latter result has some connection with a recently described instability seen in numerical simulations of propellant flames with edges, [7].

Acknowledgements
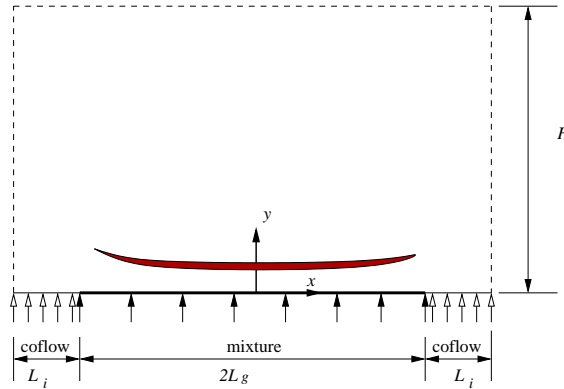
Figure 1: Flame with edges on a porous plug burner with inert coflow
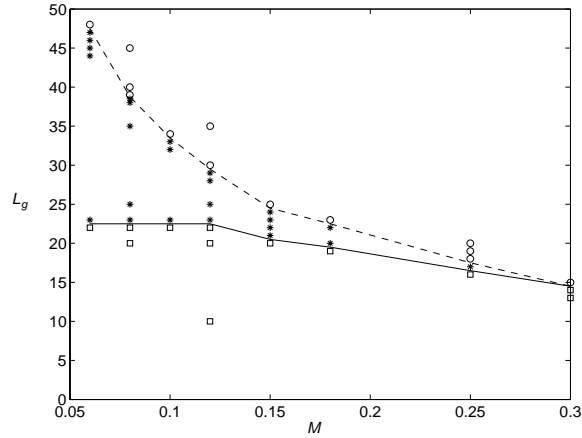
Figure 2: Stability and quenching in the $M - L_g$ plane; ◯ stable flame, ∗ oscillating flame, □ quenched flame

References

[1] J.Buckmaster. Edge-flames, *Pr ogr es in Energy and Combustion Science* **28** 435-475 2002.

[2] P .Ronney Near-limit flame structures at low Lewis number, *Combustion and Flame* **82** 1-14 1990.

[3] J.Buckmaster, M.Smooke, V.Giov angigli. Analytical and n umerical modeling of flame-balls in hydrogen-air mixtures. *Combustion and Flame* **94** 113-124 1993.

[4] S.B.Margolis. Bifurcation phenomena in burner- stabilized premixed flames. *Combustion Science and T echnolgy* **22** 143-169 1980.

[5] J.Buckmaster. Stability of the porous plug burner flame. *SIAM Journal on Applied Mathematics* **43** 1335-1349 1983.

[6] J.Buckmaster, A.Hegab, T.L.Jackson. More results on oscillating edge-flames. *Physics of Fluids* **12** 1592-1600 2000.

[7] Xu Zhou, T.L.Jackson, J.Buckmaster *Combustion and Flame* , to appear.

LEWIS-NUMBER EFFECTS ON EDGE-FLAME PROPAGATION

Vedha Nayagam[1] and Forman A. Williams[2], [1]National Center for Microgravity Research
21000 Brookpark Road, Cleveland, OH 44135, email:v.nayagam@grc.nasa.gov
[2]Center for Energy Research, University of California, San Diego, La Jolla, CA 92093

INTRODUCTION

Highly strained diffusion flames experience extinction. Strain-rate variations in nonuniform flows can lead to extinctions at some locations while the diffusion flame remains intact at others, resulting in a diffusion flame with an edge. Mixing of fuel and oxidizer in the extinguished regions can lead to triple flames. At strain rates high enough for the diffusive transport zones on each side of the diffusion flame to be comparable in size with the preheat zone of the stoichiometric premixed propagating nose of the triple flame, the two premixed flames of the triple flame disappear, merging into a propagating edge of the diffusion flame. Detailed analyses of such edge flames in general necessitate considering the multidimensional, time-dependent conservation equations. Buckmaster [1], however, identified a one-dimensional model that simplifies the analysis greatly and reveals many properties of edge flames. The present work explores further the implications of a model of this general type, addressing especially effects of the Lewis number of the fuel.

Experimental motivation for the present study stems from observations of rotating spiral edge flames in von Karman swirling flows [2]. Slow injection of fuel through a spinning porous disk into air results under suitable conditions in flat diffusion-flame spirals, separated from the disk by a distance only on the order of 1 mm, comparable with the corresponding premixed-flame preheat-zone thickness [2]. Propagation of the edge of the spiral into the oncoming flow locally resembles edge-flame propagation. Explanation of the spiral flames thus can make use of knowledge of edge-flame propagation velocities. The spirals are observed to be different for fuels of different molecular weights, thereby suggesting that the Lewis number of the fuel plays a role. It is for this reason that the present work focuses on effects of Lewis numbers. The spiral flames are observed near extinction conditions, in that a small decrease in the flow rate of the fuel completely extinguishes the flame. A mixture fraction, defined to be unity in the fuel feed stream and zero in the air, has a small value, of order 0.1, already at the external surface of the disk. The dominant heat loss from the diffusion flame therefore occurs by conduction through the steep temperature gradient from the flame to the surface of the disk. This tends to cause oxygen leakage through the diffusion flame, even on the basis of one-step activation-energy asymptotics, independent of detailed chemistry. Liñán's [3] premixed-flame regime of the diffusion flame therefore appears to be more applicable than the diffusion-flame regime addressed by Buckmaster [1].

FORMULATION

Figure 1 illustrates the edge flame steadily propagating flame in the x-direction. The edge is located at x=0, and the diffusion flame extends to x=∞. The approximate, one-dimensional

conservation equations for fuel mass fraction Y, and excess enthalpy Z, can be written in nondimensional form as

$$LV \frac{dY}{ds} - \frac{d^2 Y}{ds^2} - (1 - Y) = -L\Delta Y \exp\left[\frac{L}{\varepsilon}\left(\frac{\theta - \theta_f}{\theta / \theta_f}\right)\right], \tag{1}$$

$$\frac{d^2 Z}{ds^2} - V\frac{dZ}{ds} - Z = V\left(\frac{L-1}{L}\right)\frac{dY}{ds}. \tag{2}$$

where the non-dimensional excess enthalpy is defined as $Z = (\theta - \theta_0) - (1 - Y)/L$. The other non-dimensional variables are defined as

$$s = x / \sqrt{at}, V = v(\rho c_p / \lambda)\sqrt{at}, \theta = c_p T / q, L = \lambda/(\rho D c_p), \Delta = (\rho c_p / \lambda)atA e^{-E/RT_f}. \tag{3}$$

In Eq. (3) s is the independent variable, V is the propagation velocity, L is the Lewis number, Δ is the Damköhler number, A is a characteristic reciprocal-time rate prefactor, θ is the dimensionless temperature, D is the diffusion coefficient of the fuel, λ is the thermal conductivity, v is the kinematic viscosity, and q is the heat released per unit mass of fuel consumed. The length scales t and a denote the thickness of the reaction sheet and the thickness of the diffusion layer, respectively. The parameter $\varepsilon = LRT_f^2 /[E(q/c_p)]$, is the reciprocal of the Zel'dovich number with E representing the activation energy, R the universal gas constant, and T_f is a characteristic premixed-flame temperature, to be determined. It should be noted that we have assumed the oxidizer mass fraction is in abundance at the flame and the conservation of oxidizer need not be addressed in the premixed-flame regime for the one-dimensional model. The boundary conditions for eq. (1) and (2) are $Y \rightarrow 1$ and $Z \rightarrow 0$ as $s \rightarrow -\infty$ and $Y \rightarrow Y_\infty$ and $Z \rightarrow 0$ as $s \rightarrow \infty$. Now we seek solutions of eq. (1) and (2), assuming ε to be a small parameter and V of the order unity, using activation energy asymptotics. The details of the analysis can be found in [4] and they are not presented here due to space limitations.

RESULTS AND DISCUSSION

Solution of eq. (1) and (2) yields a relationship between the propagation velocity V, the Lewis number L, and the Damköhler number Δ. The general relationship is somewhat involved and here we consider the limit where Lewis number is near unity. We set $L=1+\varepsilon\ell$ with ℓ of order unity. In this limit, to the leading order we obtain,

$$V + \sqrt{V^2 + 4} = 2\delta \exp\left[\left(\frac{\ell V}{4\sqrt{V^2 + 4}}\right)\left(1 + \frac{V}{\sqrt{V^2 + 4}}\right)\right] \tag{4}$$

where the reduced Damköhler number δ is defined as

$$\delta = \frac{T_\infty^2 R}{E(q/c_p)}\sqrt{\frac{2\rho c_p atA}{\lambda}}\, e^{-E/(2RT_\infty)}. \tag{5}$$

Figure 2 shows the dependence of V on δ for various values of ℓ, according to eq. (4). For ℓ=0, Lewis number unity, eq. (4) reduces to $V=\delta-\delta^{-1}$, which goes to infinity as $\delta \rightarrow \infty$, minus infinity as $\delta \rightarrow 0$, and vanishes at δ=1. When V is large and positive, eq. (4) becomes $V=\delta e^{\ell/2}$, showing that Lewis number greater than unity increase V, while Lewis number less than unity decrease it.

When V is negative and large in magnitude, an expansion of equation (4) gives $V = -(1/\delta)\text{Exp}(\ell/2V^2)$, which again shows that Lewis number greater than unity increases the magnitude of V, while Lewis number less than unity decreases it. Behaviors at smaller values of V, that is, for δ closer to unity, are more interesting. Expanding eq. (4) for small values of V produces the equation

$$V + 2 = 2\delta\,e^{V\ell/8} \approx 2\delta(1 + V\ell/8). \tag{6}$$

When δ near unity the above equation becomes $V(1 - \ell/4) = 2(\delta - 1)$, which reverses its behavior for $\ell > 4$. The propagation velocity becomes a non-monotonic function of the reduced Damköhler number, there being three values of V for each value of δ in a range between a minimum $\delta < 1$ and a maximum $\delta > 1$. Static stability reasoning suggests that the middle solution is unstable. Therefore, there are two statically stable edge-flame solutions for each ℓ, one for an advancing edge and the other for a retreating edge.

The preceding analysis has addressed edge flames on the basis of a one-dimensional model. The resulting edges advance at large Damköhler numbers and retreat at small Damköhler numbers as demonstrated previously [1]. The Lewis number affects the rate of advance or retreat mainly by its influence on the excess enthalpy at the edge. For sufficiently large Lewis numbers, the dependence of the propagation velocity of the edge on the Damköhler number is not monotonic; there is a region about a propagation velocity of zero (an edge that is stationary with respect to the gas) over which the steady propagation velocity decreases with increasing Damköhler number, and the steady solution is likely to be unstable. Under these conditions there appear to be two stable steady solutions, one for an advancing edge and the other for a retreating edge. These steady solutions may apply to the leading and trailing edges observed [2] for spiral flames in von Karman swirling flows. Although the full analysis was completed only for Lewis numbers near unity, the general formulas in the solution apply for arbitrary Lewis numbers. Although the analysis was performed only for the premixed-flame regime of the downstream diffusion flame, it is clear from the literature [1] that similar results would be obtained for the diffusion-flame regime. Since only the details that are affected, the general characteristics of the solution do not depend on the specific assumptions of the problem. The present results would therefore apply to edges of both diffusion flames and premixed flames. Consideration of the diffusion-flame regime with an oxidizer Lewis number different from unity could, however, reveal different Lewis-number effects.

We have recently investigated the effects of curvature on edge-flame propagation speeds as a function of the fuel Lewis number [5]. Both negative and positive curvatures, corresponding to flame holes and flame disks, respectively, are considered. As seen before for edge flames in the diffusion-flame regime with unity Lewis number [6], we predict finite-time singular behavior for both flame-hole closing and flame-disk collapse, meaning the fronts approach their annihilation with ever-increasing speeds. As before both advancing and retreating fronts are possible for the same Damköhler number when Lewis number is sufficiently greater than one. Analytical expressions obtained in the limit of large radius of curvature show that curvature has considerably less influence on propagation speeds.

CONCLUSIONS

This study has shown how to describe steady edge-flame propagation for general Lewis numbers. The competition between fuel diffusion and conductive heat loss is responsible for these effects. Advancing edges experience fuel depletion by transverse diffusion ahead of the edge, at relative rates that increase with decreasing Lewis numbers, while receding edges have conductive heat-loss rates that increase proportionally with increasing Lewis numbers. There are conditions for sufficiently large Lewis numbers under which both advancing and receding edges may exist with the same chemical reaction-rate parameters. The existence of stable steady advancing and retreating edges at the same Damköhler number may have bearing on behaviors of experimentally observed edge flames. Spiral flames in von Karman swirling flows possess steadily propagating well-defined leading and trailing edges [2]. Equating the propagation velocity to the flow velocity at each of these edges may enable the shape of the spiral to be calculated. The positive and negative propagation velocity may apply to the leading and trailing edge, respectively. Further research therefore seems warranted, investigating relationships of predictions of this simplified model to experimental measurements of edge flames.

REFERENCES
1. Buckmaster, J., *Combust. Sci. Tech.*, 115:41-68 (1996)
2. Nayagam, V., and Williams, F. A., 6th International Microgravity Combustion Workshop, NASA/CP-2001-210826, pp. 97-100, (2001)
3. Liñán, A., *Acta Astronautica*, 1:1007-1039 (1976)
4. Nayagam, V., and Williams, F. A., *J. Fluid Mech.*, 458: 219-228 (2002)
5. Nayagam, V., and Williams, F. A., 3rd Joint Meeting of the Combustion Institute, Chicago, Illinois, March 16-19, 2003.
6. Nayagam, V., Balasubramaniam, R., Ronney, P. D., Combust. Theory Modelling 3:727-742 (1999).
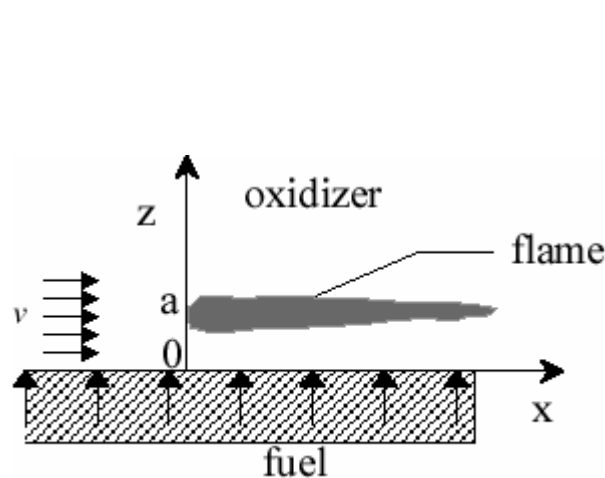
Fig. 1. Schematic illustration of the problem.
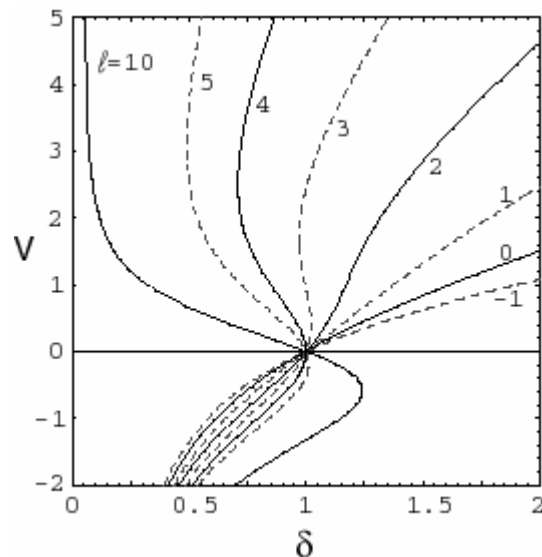
Fig. 2. Edge velocity as function of Damköhler number for various ℓ values.

FLAME OSCILLATIONS IN NON-PREMIXED SYSTEMS
DIFFUSION FLAMES AND EDGE-FLAMES

Moshe Matalon

McCormick School of Engineering & Applied Science
Northwestern University
Evanston, IL 60208-3125
matalon@northwestern.edu

Diffusive-thermal instabilities are well known features of premixed and diffusion flames. In one of its form the instability appears as spontaneous oscillations. In premixed systems oscillations are predicted to occur when the effective Lewis number, defined as the ratio of the thermal diffusivity of the mixture to the mass diffusivity of the deficient component, is sufficiently larger than one. Oscillations would therefore occur in mixtures that are deficient in the less mobile reactant, namely in lean hydrocarbon-air or rich hydrogen-air mixtures.

For diffusion flames the conditions for the onset of oscillations are more complex [1]-[2]. First, one may not speak of an effective Lewis number but rather consider two Lewis numbers, Le_F and Le_O associated with the fuel/oxidizer respectively. Furthermore unlike premixed systems, the compositions at the supply ends and the underlying flow conditions appear to be important parameters. A stability theory of a nominally planar flame shows that instabilities occur only when there is sufficient reactant leakage through the reaction zone. This would normally occur at high flow rates, or near-extinction conditions, when the Damköhler number D inversely proportional to the square of the characteristic flow speed is below a critical value D_c, so that $D_{ext} < D < D_c$ where D_{ext} identifies the extinction conditions. (A Burke Schumann flame sheet corresponding to complete combustion is therefore unconditionally stable.) Oscillations result when at least when one of the two Lewis numbers is larger than one, as shown in Figure 1, with the Lewis number of the reactant diffusing against the stream being of more relevant. We see that the parameter plane of Le_F versus Le_O is separated into two regions identified by excess/deficiency in available enthalpy in the reaction zone. Oscillations are possible only when the available enthalpy is in excess while cellular flames may occur when it is deficient. It is not necessary for both Lewis numbers to be larger than one, oscillations may occur when one of
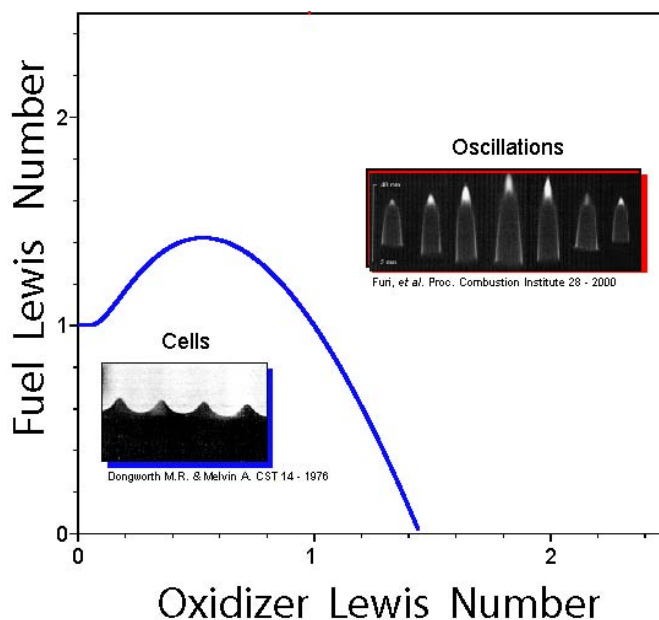
Figure 1

the two Lewis number is close to or even below one, provided the other is sufficiently larger than one. Another important parameter identified by the theory is the initial mixture strength ϕ defined as the ratio of the mass fraction of fuel supplied at the fuel boundary to the mass fraction of oxidizer supplied at the oxidizer boundary, normalized by their stoichiometric proportions. Oscillations are more likely to occur when the mixture in the reaction zone is relatively "rich" and hence characterized by an initial mixture-strength ϕ sufficiently larger than one. It should be noted that in practice ϕ is not an independent parameter; variations in mixture strength brought about by diluting the streams with an inert gas would also affect the values of the Lewis numbers. This suggests that the mixture strength is perhaps the most important parameter that determines whether oscillations will or will not occur. Finally, volumetric heat losses are also known to promote flame oscillations [2]-[4]; oscillations may occur under conditions where, in their absence, the flame remains stationary and stable.

The theoretical predictions summarized above are in general agreement with experimental results; see for example [5] where a jet configuration was used and experiments were conducted for various inert-diluted propane and methane flames burning in inert-diluted oxygen. Nitrogen, argon and SF_6 were used as inert in order to produce conditions of substantially different Lewis numbers and mixture strength. In accord with the predicted trend, it was found that oscillations arise at near extinction conditions, that for oscillations to occur it suffices that one of the two Lewis numbers be sufficiently large, and that oscillations are more likely to be observed when ϕ is relatively large.

The theoretical results reported above are based on a stability analysis of a nominally planar diffusion flame, so that when oscillations occur the flame appears to move back and forth normal to itself. Indeed, the diffusion flame surrounding a suspended fuel droplet [6] was seen to exhibit radial oscillations and for jet flames the whole flame expands and contracts during a cycle [5] in the axial direction. In other experiments where oscillations have been observed, whether in the laboratory or in microgravity environment, the flame has an edge which is seen to advance and retreat in a direction that more or less coincides with the diffusion flame trailing behind [7]-[9]. Edge-flames are two-dimensional structures that can be neither characterized as premixed nor as diffusion flames. Studies of oscillating edge-flames were carried out numerically by Buckmaster and co-workers [10] using a simple two-dimensional model of a flame traveling along an axis, with the concentrations of fuel and oxidizer specified in the transverse direction at two opposing ends. The edge results in their model from the fact that the fuel-supply is cut-off at a finite position. The calculations reveal that when the Damköhler number is sufficiently low and the fuel Lewis number sufficiently larger than one (the oxidizer Lewis number was taken to be equal to one) oscillations do occur. The results reported here are based on numerical calculations [11] that examine the dynamics of an edge-flame in a mixing layer. Two co-flowing streams, one of fuel and the other of oxidizer are separated upstream by a semi-infinite plate as shown in Figure 2. The flame established in the mixing layer formed
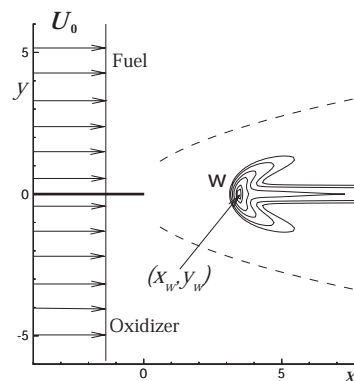
Figure 3

behind the tip of the plate consists of an edge-flame standing at some distance from the plate and a diffusion flame trailing behind. The objective is to examine the influence of the various parameters on the onset of oscillations and show that the edge-flame in this nonpremixed system possesses stability properties that share common features with those of diffusion flames reported above.

The position of the edge-flame (x_w, y_w), defined as the location where the reaction rate attains its maximum value, is plotted in Figure 3 as a function of the Damköhler number D for selected values of equal Lewis numbers both larger than one. The calculations reported in this case correspond to $\phi = 1$, so that the diffusion flame trailing behind lies along the y-axis as illustrated in Figure 2. For a given D the flame stands at a well-defined distance from the plate; it gets closer to the tip as D increases and gets attached to the plate when $D \to \infty$. The solid parts of the curve identify stable states while the dashed parts represent oscillatory states with an edge-flame advancing and retreating along the axis. Thus, oscillations occurs when $D < D_c$, or at high flow

rates. The marginal state $D = D_c$ marked by a dark circle depends on the Lewis numbers and the mixture strength; the larger the Lewis numbers the larger D_c implying that oscillations are more likely to be observed when the Lewis numbers are sufficiently large. The temperature history at various locations along the axis (representing in this case the stoichiometric surface) shows that the oscillations are damped further downstream. This implies that it is primarily the edge of the flame that oscillates and that the oscillations decay along the trailing diffusion flame. Since in the absence of radiative losses the flame extends to infinity, far downstream combustion occurs along a Burke-Schumann flame sheet that, as discussed above, is absolutely stable.
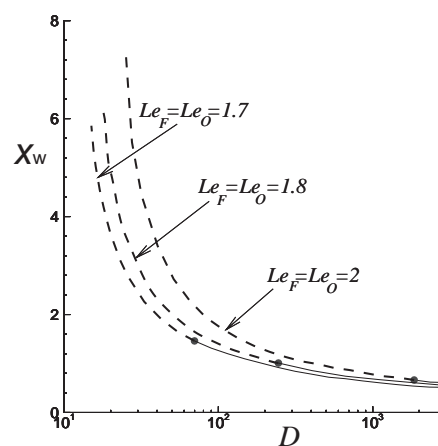
Figure 4

Although the results presented in Figure 3 considered equal Lewis numbers for both the fuel and oxidizer, they are nevertheless representative of situations where the Lewis numbers are unequal and larger than one. As suggested earlier, in non-premixed flames it is not necessary for both Lewis numbers to be larger than one; oscillations may occur even when one the two Lewis numbers is below one provided the other is sufficiently large. This is verified in Figure 4 which, similar to Figure 3 displays the position of the edge-flame as a function of D with $Le_F = 3$ and $Le_O = 0.8$. Note the sensitivity of the results to the Zeldovich number in this case. The figure in the insert shows the temporal variations of an unstable state which clearly exhibits a limit cycle with the edge moving back and forth nearly along the stoichiometric surface that lies in this case entirely in the fuel side ($y_w > 0$).
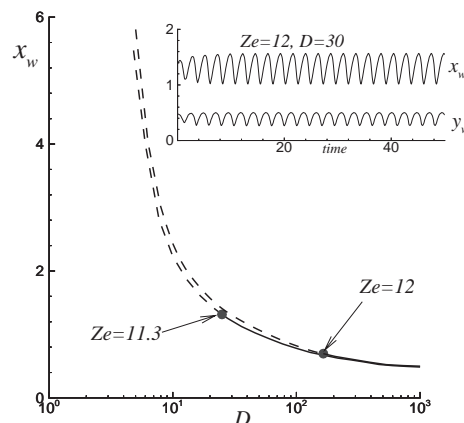
Figure 5

In the presence of radiative losses the diffusion flame trailing behind the edge-flame is quenched beyond a certain point and the flame is of finite extent. Complete extinction occurs when heat losses are excessive. This is shown in Figure 5, where the position of the edge-flame is plotted against the parameter b representing the ratio of radiative heat losses to chemical heat release. Total extinction occurs when $b \to b_{ext}$, the value of b where the curve becomes vertical. The dashed part of the curves, where to $b_c < b < b_{ext}$ correspond to oscillatory states. The calculations reported in this figure were carried out with unity Lewis numbers, in order to suppress diffusive-thermal effects [12]. The results imply that heat losses alone can trigger flame oscillations. Note that onset of oscillations requires a value of $\phi > 1$ and that oscillations occur primarily at near-extinction conditions.

Similar to diffusion flames edge-flames in mixing layers are characterized by two Lewis numbers, one associated with the fuel and the other with the oxidizer and by the mixture-strength ϕ based on the supply conditions. For oscillations to occur it is necessary for at least one of the two Lewis numbers to be larger than one and for the mixture to be "rich" in fuel. Volumetric heat losses promote and may even trigger flame oscillation. Oscillations occur only at sufficiently high flow rates, or near extinction conditions, when there is appreciable reactant leakage through the reaction zone. The mode of oscillation is a back and forth movement of the edge along the stoichiometric surface that decays further downstream along the trailing diffusion flame.
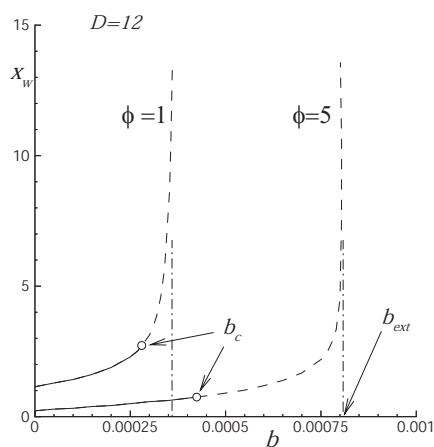
Figure 6

ACKNOWLEDGMENTS

REFERENCES

1. Cheatham S. & Matalon M. 2000, *J. Fluid Mechanics*, **414**, p. 105.
2. Kukuck S. & Matalon M. 2001, *Combustion Theory & Modeling*, **5**, p.217.
3. Cheatham S. & Matalon M. 1996, *Proceedings of the Combustion Institute*, **26**, p. 1063.
4. Sohn C.H., Kim J.S., Chung S.H. and Maruta K. 2000, *Combustion & Flame*, **123**, p.95.
5. Furi, M., Papas, P., & Monkewitz, P.A. 2000, *Proceedings of the Combustion Institute*, **28**, p. 831.
6. Nayagam, V. & Williams, F.A. 1998, 7th Int. Conference on Numerical Combustion; York, UK
7. Ross, H.D., Sotos, R.G. & T'ien, J.S., 1991, *Combustion Science & Technology*, **75**, p. 155.
8. Dietrich D., Ross H. & Tien J.S. 1994, AIAA Paper 94-0429.
9. Ross, H.D. *Progress in Energy and Combustion Science*, **1**, p.17
10. Buckmaster, J. *Progress in Energy and Combustion Science*, **28**, p. 435
11. Kurdyumov V.N. and Matalon, M. AIAA 2003 Paper number 2003-1016.
12. Kurdyumov V.N. and Matalon, M. 2002 *Proceedings of the Combustion Institute*, **29**, to appear.

Flamelet Formation in Hele-Shaw Flow

I. S. Wichman
Department of Mechanical Engineering
Michigan State University
East Lansing, Michigan 48824-1226
and
S. L. Olson
Microgravity Combustion
NASA Glenn Research Center
Cleveland, Ohio 44135

Abstract

A Hele-Shaw flow apparatus constructed at Michigan State University (MSU) produces conditions that reduce influences of buoyancy-driven flows. In addition, in the MSU Hele-Shaw apparatus it is possible to adjust the heat losses from the fuel sample (0.001" thick cellulose) and the flow speed of the approaching oxidizer flow (air) so that the "flamelet regime of flame spread" is entered. In this regime various features of the flame-to-smolder (and vice versa) transition can be studied. For the relatively wide (~ 17.5 cm) and long (~ 20 cm) samples used, approximately ten flamelets existed at all times. The flamelet behavior was studied mechanistically and statistically. A heat transfer analysis of the dominant heat transfer mechanisms was conducted. Results indicate that radiation and conduction processes are important, and that a simple 1-D model using the Broido-Shafizadeh model for cellulose decomposition chemistry can describe aspects of the flamelet spread process.

Introduction

Prior to extinction, microgravity flames on solid fuels exhibit an instability that appears to be related to extinction or the return of flame spread. This "flamelet" behavior extends the flammability range by altering the geometry of the flame thereby enhancing oxygen delivery to the flame zone. Analysis of Thermal and Hydrodynamic Instabilities in Near-limit Atmospheres (ATHINA) is a space flight project that examines near limit flame spread over materials that resemble those found in spacecraft. Quantities influencing flammability are material physical properties spacecraft atmosphere, and magnitude and geometry of the flow across the surface.

In the near-limit case [when: (1) oxygen concentration approaches flammability limits; (2) heat losses sufficiently high; (3) air flow rate sufficiently low] a complicated form of flame spread behavior occurs. This behavior shows flame front breakup into separate flamelets and propagation of fingered flamelet fronts. Systematic causes and long-term behaviors of such flamelets are not understood: whether they are benign, whether they represent nascent precursor flames, whether they represent an intermediate state between flaming and smoldering. Flamelets develop in low-gravity conditions when the influences of buoyancy are smaller than under normal gravity conditions.

Previous extended zero-*g* work includes Space-Shuttle studies of smoldering [Olson et al (1998)]. This research is a fully zero-*g* version of the smoldering process studied in an Earth-based apparatus, the precursor to the MSU Hele-Shaw facility, by Zik et al. (1998). In the work of Zik the samples lay on the substrate. Both flame spread and smoldering were possible, although attention was focused on smoldering. Both Olson et al. (1998) and Zik et al. (1998) obtained smolder front bifurcations. We note that Olson et al. (1998) did not use a substrate, and that Zik et al. (1998) used elevated O_2 concentrations (not air). Olson et al. (1998) used a potassium acetate doped cellulose fuel to promote smoldering while inhibiting flaming.

Based on this previous research, a framework for ATHINA was built upon the notion that flame spread in near-limit conditions depended upon *two* quantities, (I) the *heat losses* and (II) the *oxidizer transport rate*. Quantity (II) is varied by changing: (1) the O_2 level or (2) the opposed flow velocity. In our work we fixed the oxygen mass fraction Y_O at the level in the ISS (23% in N_2). With the Y_O fixed, near-limit conditions are created by either continually increasing the sample-to-surroundings heat losses or keeping the heat losses constant while decreasing the oxidizer transport rate (i.e., the air flow rate). See **Figure 1** for a qualitative rendering of the influences of (I) and (II) on flame/flamelet transition.

In principle, there are many ways to accomplish the heat losses from the sample. The ATHINA approach is to insert, beneath the sample, a *backing* or *substrate* material that carries heat away from the sample (mostly by conduction and

radiation). In the limit that the sample touches the substrate, Zik et al. (1998) obtained pure smoldering spread. When there is a gap, flamelet spread occurs.

Hele-Shaw Apparatus

A facility was constructed that produces zero-gravity-like conditions to provide "ground-based support" for the zero-*g* ATHINA flight project. Flamelet behaviors were observed over time periods of the order of several minutes. The Hele-Shaw apparatus resembles the apparatus built by Zik et al. (1998) to study low-*g* smolder front propagation in elevated O_2 atmospheres. The Hele-Shaw facility has a wide operating range. It yields data on flame spread analogous to present NASA drop tests. We provide a brief summary of some of the results of our research effort. In the Hele-Shaw apparatus, air flows from a plenum through a porous flow-straightening plate into the test section. Test section flow velocities are calculated using flowmeters. Tests have used the hot wire technique to measure the velocity field, which resembles a fully developed laminar channel flow.

In the test section, a backing (substrate), whose spacing can be adjusted, is placed beneath the sample, while a transparent quartz plate is placed above it. Air and combustion products are exhausted downstream to the atmosphere. Samples are ignited downstream of the inlet using a high resistance wire. Ignition of the sample occurs at a high flow velocity that is ramped down for the final test section flow speed. The ignition procedure establishes a uniform, flat flame front. Subsequent instabilities are then attributed to inherent flame dynamics, not initial irregularities of the flame front. The substrate is a heat sink made of polished copper. The samples are secured an equal distance between the copper backing and top quartz plate.

Results

At all test section/substrate heights, *h* (defined here as the distance between the sample bottom surface and the substrate), flames began as spreading uniform fronts. Reduction of airflow caused the blue front to either break apart or extinguish. The tiny flamelets remained present for most conditions. At lower oxidizer flow rates some of the cellular flames would continue spreading down the sample displaying additional instabilities. A test is shown in **Figure 2**.

Experiments indicated that for high gap spacings *h* the flamelet sizes increased and flamelets were more stable. This suggested that the flame front acts as a barrier to the oxidizer flow. Tests that were conducted in drop towers had a much larger *h* than the Hele-Shaw apparatus. Oxidizer was able to travel behind the flame front (i.e., "leak") around the flamelets, giving an oval shape. Flamelets rarely oscillated when this occurred. Only the side edges oscillated with a frequency of order 1 Hz. Oscillations either ceased and a more stable flamelet continued to spread across the fuel, or the oscillations led to extinction.

An interesting and unexpected behavior was seen for *h ~ 3,5,8 mm*. A fast flame pulse traveled across the flamelet front at frequencies ranging from *2 - 15Hz* at various flow velocities and test section heights. Pulses originated in either the middle or edge of the front and moved over the flame front. These pulsations may be related to the formation of a combustible partially premixed gas mixture of fuel vapors (volatiles) and air between adjacent flamelets that can, when "triggered," produce premixed flame propagation across the flamelet front. This mechanism requires further investigation by high-speed camera.

In some tests**,** the flamelets displayed fingering patterns like the smoldering/flame spread patterns found by Zik et al. (1998) and Olson, et al. (1998). In these cases, the flamelets were evenly spaced and rarely combined with each other. This suggested that adjacent flamelets competed for oxidizer. The substantial char-zone length before actual commencement of fingering suggests a long transition period for its occurrence. Some flamelets split and then branched, always readjusting to become evenly spaced. In cases with a single flamelet, several branches formed and burned to the end of the sample. For some tests at *5 mm* and *8 mm*, the blue thin continuous flame front did not break apart and spread to the end of the sample. The oxidizer flow was decreased but the oxygen transport was sufficient so the flame front did not corrugate. As the flame burned through the edge**,** it turned from blue to yellow and sooty and burned more vigorously, indicating either that the flame acted as a barrier to the oxidizer transport or there is oxidizer available at the edge. As the flame burned through the sample air filled the middle open section allowing oxidizer to penetrate behind the flame front. This produced a stronger burning flame since yellow soot, which forms at higher flame temperatures than in blue flames, was observed.

The research conducted in the Hele-Shaw apparatus has enabled the construction of the Hele-Shaw version of the Flammability Map (see **Figure 3**, which should be compared with the leftmost upper part of **Figure 1**).

It is possible to speculate that the instabilities are driven by reduced oxidizer transport rather than heat losses. When the sample to quartz plate gap distance is fixed and the flow velocity is constant, variation of the gap distance between sample and substrate can produce the full spectrum ranging from flame fronts to flamelet fronts. Thus, although reduced oxidizer transport is important when the gap between sample and quartz plate diminishes, the adjustment of heat losses can, without alteration of the geometry and flow of oxidizer, produce the full spectrum of flame responses.

Statistical results

Another task concerns the statistical behavior of the flamelets as they form, bifurcate and extinguish. The Hele-Shaw tests show the time progression of formation (birth) by bifurcation of an existing flamelet into two flamelets and extinguishment (death) by extinction of the flamelets as they run out of oxidizer or are starved of oxygen by their neighbors. In these tests, it required ~ 5s to establish the flow (flow speed = 5 cm/sec) which gave the precise conditions under which the flame breakup tests took place. The flamelets that formed were tracked and counted as bifurcations and extinctions occurred. The flamelets were numbered from top to bottom at the beginning of the breakup, and each one was followed through its history. The position-time data give good linear correlation for the test time period. The flamelet bifurcations and extinctions were tracked in time and the total population of flamelets as a function of time is determined from the data. Each bifurcation adds one flamelet. Each extinction subtracts one. The bifurcations and extinctions show a linear cumulative number of events, which means they occur at a nearly constant rate. The slopes are slightly different, however, which suggests a gradual increase in population (average) over the test time. However, the average population is sufficiently small that this difference is not apparent within the scatter of the population with time (avg ~12). The running average is shown for comparison. Only data after breakup are used.

In order to obtain meaningful population data, the cumulative number of events should exceed twenty (20) as a minimum. Although the flamelet spread rate seems to reach steady state quickly, it requires time to obtain population statistics. For a bifurcation and extinction rate of 0.14 Hz, 214 seconds of data after breakup are needed to observe thirty events. In addition, this sample was 18 cm wide, and flight samples will be 12 cm at most. Hence, the anticipated number of flamelets obtained will be 3-5 (based partly on drop tower experience, which gives 5 or 6 flamelets on a 15 cm wide sample). Each bifurcation and extinction (*+1* or *–1*) will strongly affect the running averages, hence more time is needed for good averages. A steady or "stable" population is one with a nearly constant value, with nearly equal "birth" and "death" rates. See **Figure 4** for representative results.

Calculations

A one-dimensional model for predicting heat and mass transfer in thin cellulosic fuels using the Broido scheme was developed in order to model heat and mass transfer during flame and flamelet spread over thermally thin cellulosic fuels. Using this model, a numerical study was performed to indicate: (1) the heat transfer mechanism that dominates flame spread; (2) the role of the "backing" or heat-loss substrate on the flame spread mechanism; (3) the influence of actual cellulose pyrolysis kinetics on the heat transfer, release of volatile combustibles and formation of char from the original solid fuel. A multi-step physical model for heat and mass transfer in cellulose decomposition was examined for the case of flamelet propagation over thin solid fuels. In this model, the cellulose decomposes to volatiles and char through active cellulose during the heating processes. The decomposition model uses the Broido-Shafizadeh mechanism.

A short temperature drop period was observed in the solid fuel during the heating and pyrolysis process. Numerical results indicated that the solid fuel temperature was sensitive to the chemical rate parameters E_v and E_c in the Broido-Shafizadeh scheme governing equations. Emissivity variation during the pyrolysis process had little influence on temperature profiles. The volatile diffusion process was numerically simulated and the results enabled the calculation of an approximate flame existence time, which agrees satisfactorily with experiments, suggesting that the parameters used in the numerical computations were reasonable

Conclusions

The Hele-Shaw facility is capable of examining numerous features of zero-**g** flamelet spread. It has the advantage of providing long test times and accurate flow field conditions. Hot-wire measurements of the velocity fields inside the test section showed good agreement with theoretical profiles. Many questions remain. Although oxidizer transport has been shown to be crucial, it remains to examine its influences when Y_O is changed keeping the flow constant. In this case, the fluid dynamical transport is unchanged but the mass transport to the flamelet is increased. This trade-off must be examined. Also, the details of the Hele-Shaw apparatus need to be scrutinized. In future experiments we will determine the degree to which simulated low-**g** conditions are attained when the present right-side-up Hele-Shaw apparatus is turned upside-down. If the upside-down tests differ greatly, **g** still plays an important role in the Hele-Shaw tests. Finally, and perhaps most importantly, we have not conclusively demonstrated (yet) that the flamelet regime is in fact a stable, non-transient (i.e., either temporary and unstable) actual intermediate physical regime lying between flaming and smoldering. To demonstrate this, long tests with many flamelets and flamelet "events" ("births" and "deaths") are required.

References

1. Olson, S. L., Baum, H. R., and Kashiwagi, T., "Finger-Like Smoldering over Thin Cellulosic Sheets in Microgravity, *"Twenty-Seventh Symposium (International) on Combustion,* The Combustion Institute, pp. 2525-2533 (1998).

2. Olson, S. L., Kashiwagi, T., Fujita, O. Kikuchi, M. and Ito, K., "Experimental Observations of Spot Radiative Ignition and Subsequent Three-Dimensional Flame Spread over Thin Cellulose Fuels," *Combustion and Flame*, Vol. 125, pp. 852-86 (2001).
3. Zik, O., Olami, Z., Moses, E., "Fingering Instability in Combustion," *Phys. Rev. Lett.,* Vol. 81, pp. 3868-3871 (1998).

Figure 1. Conceptual plot of flame spread instability process showing the stable flame spread dome surrounded on the left by the near-limit flamelet instability region and on the right by the blowoff regime.

Figure 2. Instability development during flame spread. Note that the flame front breaks into fragments that later form flamelets, which may terminate or combine or divide.

Figure 3. The Flammability Map for the Hele-Sh Rig. Also shown are data from other sources [Olson et al. (2001)].

Figure 4. Flamelet bifurcations and extinctions counted cumulatively. The flow speed is 5 cm/sec. The gap spacing was 5 mm.

LAMINAR SOOT PROCESSES (LSP) EXPERIMENT: FINDINGS FROM SPACE FLIGHT MEASUREMENTS

P.B. Sunderland, D.L. Urban and Z.G. Yuan
NASA Glenn Research Center, Cleveland, Ohio

C. Aalburg, F.J. Diez and G. M. Faeth
The University of Michigan, Ann Arbor, Michigan

INTRODUCTION

The present experimental study of soot processes in hydrocarbon-fueled laminar nonbuoyant and nonpremixed (diffusion) flames at microgravity within a spacecraft was motivated by the relevance of soot to the performance of power and propulsion systems, to the hazards of unwanted fires, and to the emission of combustion-generated pollutants. Soot processes in turbulent flames are of greatest practical interest, however, direct study of turbulent flames is not tractable because the unsteadiness and distortion of turbulent flames limit available residence times and spatial resolution within regions where soot processes are important. Thus, laminar diffusion flames are generally used to provide more tractable model flame systems to study processes relevant to turbulent diffusion flames, justified by the known similarities of gas-phase processes in laminar and turbulent diffusion flames, based on the widely-accepted laminar flamelet concept of turbulent flames [1-4]. Unfortunately, laminar diffusion flames at normal gravity are affected by buoyancy due to their relatively small flow velocities and, as discussed next, they do not have the same utility for simulating the soot processes as they do for simulating the gas phase processes of turbulent flames.

Local effects of buoyancy are small in the soot reaction region of practical turbulent flames; therefore, buoyant laminar diffusion flames can only provide a proper model flame system for turbulent flames to the extent that buoyancy does not affect soot processes. Unfortunately, soot particles are too large to diffuse like gas molecules and are primarily convected by local flow velocities; as a result, their behavior in buoyant and nonbuoyant diffusion flames is quite different [4-6]. This can be explained based on both measurements [7-12] and predictions [13,14]. In a buoyant flame, soot nucleation first occurs near the flame sheet, after which the soot convects inward to more fuel-rich regions before finally being swept out of the flame (passing from fuel-rich to fuel-lean conditions) near the flame tip. In contrast, in nonbuoyant flame, soot nucleation first occurs near the cool core of the flame, after which the soot particles are swept directly through the flame (passing from fuel-rich to fuel-lean conditions) at all points along the flame surface within the dividing streamlines. Thus, soot processes within buoyant and nonbuoyant laminar diffusion flames are very different, with results for nonbuoyant laminar diffusion flames representing soot processes of interest for practical turbulent flames (that generally are nonbuoyant due to their large flow velocities).

These differences between soot processes in buoyant and nonbuoyant laminar diffusion flames motivated the first phase of the present experiments which involved measuring soot properties within nonbuoyant laminar jet diffusion flames. These results were somewhat compromised, however, because the test flames had rather large residence times, and corresponding large radiative heat losses; this resulted in radiative quenching near the flame tip which caused tip opening phenomena and associated emissions of unburned fuel and soot along the axes of the flames. Such excessive radiative heat losses are not typical of practical turbulent diffusion flames; therefore, the present experiments emphasized conditions where the flames were nearly adiabatic. Similar to the original experiments of Refs. 15-20, the present measurements sought the shapes, the laminar smoke point properties and the soot properties of round nonbuoyant laminar jet diffusion flames.

EXPERIMENTAL METHODS

Apparatus. A sketch of the test apparatus appears in Fig. 1. The arrangement consisted of a laminar jet diffusion flame stabilized at the exit of a round fuel nozzle extending along the axis of a windowed cylindrical chamber. The chamber had a diameter of 400 mm, a maximum length of 740 mm and was capable of operating at pressures of 30-130 kPa. The chamber was filled with an O2/N2 mixture to provide the nominal composition of dry air (21 ± 1% O2 by volume) with total O2 consumption during a flame test less than 10%. The flames were ignited using a retractable hot wire. Two fuel nozzles were considered, having inside diameters of 0.8 and 0.4 mm. The larger jet exit velocities, u_o, for a given fuel flow rate, yielded characteristic flame residence times,

$$t_{ch} = 2L_f/u_o \tag{1}$$

where L_f is the luminous flame length, that were 4-16 times smaller than the conditions of Refs. 15-20. The reduced radiative heat losses yielded nearly-adiabatic flames.

Instrumentation. Laminar flame shapes were measured using a CCD video camera. Soot volume fractions and temperature distributions were measured using imaging techniques, deconvoluting laser extinction measurements for soot volume fractions, and deconvoluting two-line emission measurements to find soot temperatures and mixture fractions. Other measurements are described in Urban et al. [15].

RESULTS AND DISCUSSION

Flame Shapes. Flame shape predictions adopted the simplified approach of Lin et al. [17] yielding the following expression for the flame length:

$$L_f - L_o = (3C_f Sc/(8\pi\mu))\dot{m}/Z_{st} \tag{2}$$

where L_o is the virtual origin, C_f is an empirical coefficient to match measurements and predictions (C_f=1 (basic theory), =1.13 (soot-containing flame at the laminar smoke point, and =0.56 (soot-free flame)), Sc=0.76 is the Schmidt number, μ is the flame viscosity, $\dot{m}$ is the burner flow rate and Z_{st} is the mass fraction of the fuel in a stoichiometric mixture of the burner exit and ambient fluids (ambient fluid = air in the following). See Ref. 17 for the formulas for other flame properties.

A typical video flame image appears in Fig. 2; these conditions correspond to an ethylene/air flame for the 0.8 mm diameter burner at a pressure of 1/2 atm. This flame has a length of 109 mm and is very near the laminar smoke point but with no evidence of tip opening. A preliminary evaluation of the flame length prediction of Eq. (2) is illustrated in Fig. 3. Predictions on this figure are for smoke-point and soot-free flames, setting L_o=0, taking a mean value of μ for air at 1100 K for all the flames and using Z_{st}=0.0636 and 0.0602 for ethylene- and propane-fueled flames, respectively. The test conditions included two soot-emitting flames, several flames near the laminar smoke point, several soot-containing flames at flow rates smaller than laminar smoke point conditions, and one soot-free (blue flame). The comparison between measurements and the simplified flame length expression of Eq. (2) is remarkably good for soot emitting and laminar smoke point flames and for the soot-free flame. The other soot-containing flames fall between these limits, as expected.

Laminar Flamelet Concept. The laminar flamelet concept implies that laminar diffusion flames should have scalar gas properties that are only functions of the degree of mixing of the flow, typically represented by the local mixture fraction, for given burner exit and ambient conditions. These functions, called state relationships, are applied to turbulent diffusion flames, assuming that turbulent diffusion flames involve a collection of strained laminar flamelets. The

use of the laminar flamelet approximation is effective for buoyant and nonbuoyant soot-free flames, vastly simplifying predictions because only mixture fraction predictions are needed to find all scalar properties [1-4]. As noted earlier, however, similar state relationships are not found for soot properties in buoyant laminar diffusion flames due to soot path effects. The success of the simplified flame shape analysis discussed in connection with Figs. 2 and 3, suggests that the laminar flamelet concept might be valid for soot properties within nonbuoyant laminar diffusion flames. In particular, the simplified analysis shows that the variation of mixture fraction (and thus all scalar properties) as a function of *time* is identical for all soot paths from the burner exit to the surroundings. This also implies identical soot properties along all soot paths through the present nonbuoyant laminar diffusion flames, even when the burner flow is varied.

The potential for soot property state relationships was tested by considering maximum soot concentrations along various soot paths for experiments carried out on STS-83 and –94. These results are illustrated in Fig. 6 as ratios of maximum soot volume fractions for each path considered through a given flame to the average of all the paths through the same flame, for the four flames for these experiments where characteristic flame residence times were small enough to make radiative heat losses small. As anticipated from the simplified theory, maximum soot concentrations for all the paths through the flames, for given burner exit and ambient conditions, are essentially the same within experimental uncertainties. Given successful subsequent evaluation of the soot property state relationship concept from the STS-107 results, an important simplification for understanding, and modeling, practical soot-containing turbulent diffusion flames will be obtained.

ACKNOWLEDGMENTS

REFERENCES
1. Bilger, R.W., *Combust. Flame* 30:277 (1977).
2. Faeth, G.M. and Samuelson, G.S., *Prog. Energy Combust. Sci.* 12:305 (1986).
3. Sivathanu, Y.R. and Faeth, G.M., *Combust. Flame* 82:211 (1990).
4. Gore, J.P. and Faeth, G.M., *J. Heat Trans.* 110:173 (1988).
5. Sunderland, P.B. et al., *Combust. Flame* 96:97 (1994).
6. Law, C.K. and Faeth, G.M., *Prog. Energy Combust. Sci.* 20:65 (1994).
7. Sunderland, P.B. et al., *Combust. Flame* 100:310 (1995).
8. Lin, K.-C. et al., *Combust. Flame* 104:369 (1996).
9. Santoro et al., *Combust. Flame* 51:203 (1983).
10. Santoro et al., *Combust. Sci. Tech.* 53:89 (1987).
11. Puri, R. et al., *Combust. Flame* 92:320 (1993).
12. Puri, R. et al., *Combust. Flame* 97:125 (1994).
13. Spalding, D.B., *Combustion and Mass Transfer*, Pergamon, New York, Chapt. 10, 1979.
14. Mortazavi et al., AIAA Paper No. 93-0708, 1993.
15. Urban, D.L. et al., *AIAA J.* 36:1346 (1998).
16. Faeth, G.M., *Microgravity Combustion Science* (H.D. Ross, ed.), Academic Press, New York, p. 83, 2001.
17. Lin, K.-C. et al., *Combust. Flame* 116:415 (1999).
18. Lin, K.-C. and Faeth, G.M., *AIAA J.* 37:759 (1999).
19. Dai, Z. and Faeth, G.M., *Proc. Combust. Inst.* 28:2085 (2000).
20. Urban, D.L. et al., *Proc. Combust. Inst.* 28:1965 (2000).
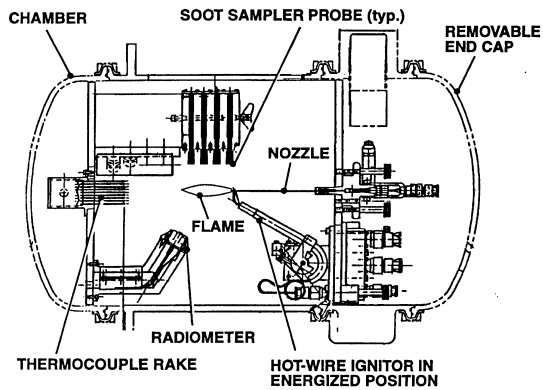
Fig. 1. Sketch of the Laminar Soot Processes (LSP) test apparatus for observations of nonbuoyant round laminar jet diffusion flames in still air at microgravity.

Fig. 3. Luminous flame lengths of round nonbuoyant and buoyant ethylene/air laminar jet diffusion flames as a function of fuel flow rate, burner diameter and pressure.

Fig. 2. Video image of a nonbuoyant round laminar jet diffusion flame in still air at microgravity (ethylene fuel jet from a 0.8 mm diameter burner port, pressure = 0.5 atm, maximum luminous flame length and diameter of 109 and 10 mm, respectively).
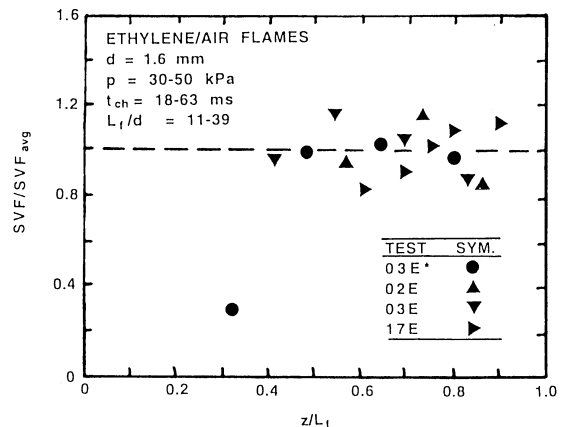
Fig. 4. Normalized maximum soot volume fractions as a function of normalized distance from the burner exit for round nonbuoyant ethylene/air laminar jet diffusion flames at microgravity.

LAMINAR SOOT PROCESSES (LSP) EXPERIMENT: FINDINGS FROM GROUND-BASED MEASUREMENTS

C. H. Kim, A. M. El-Leathy and G. M. Faeth
The University of Michigan, Ann Arbor, Michigan

F. Xu
The University of Central Florida, Orlando, Florida

INTRODUCTION

Processes of soot formation and oxidation must be understood in order to achieve reliable computational combustion calculations for nonpremixed (diffusion) flames involving hydrocarbon fuels. Motivated by this observation, the present investigation extended earlier work on soot formation and oxidation in laminar jet ethylene/air and methane/oxygen premixed and acetylene-nitrogen/air diffusion flames at atmospheric pressure in this laboratory [1-7], emphasizing soot surface growth and early soot surface oxidation in laminar diffusion flames fueled with a variety of hydrocarbons at pressures in the range 0.1-1.0 atm [8,9].

Sunderland et al. [1-3] investigated soot surface growth in laminar jet diffusion flames but were unable to evaluate available mechanisms of soot surface growth and oxidation because their measurements did not provide information about radical concentrations (e.g., H, OH and O) needed by the theories [10-14]. Xu et al. [4-6] continued the work of Sunderland et al. [1-3] by studying soot formation in laminar premixed flames. These measurements were used to evaluate the Hydrogen-Abstraction/Carbon-Addition (HACA) soot surface growth mechanisms of Kazakov et al. [10] and Colket and Hall [11]. It was found that the HACA soot surface growth mechanisms provided excellent correlations of the measurements using quite reasonable steric factors that appear in the theories. Xu and Faeth [7] extended the study of soot surface growth to diffusion flame environments, considering acetylene-nitrogen-fueled flames burning in coflowing air, and using the full suite of measurements developed during the premixed flame studies of Refs. 4-6. These results showed that soot surface growth rates in premixed and diffusion flames satisfy similar reaction rate expressions, and were well represented by the HACA mechanisms of [10] and [11]. The present investigation extends this research to consider the structure and soot surface growth and oxidation properties of laminar diffusion flames fueled with hydrocarbons other than acetylene (e.g., ethylene, propylene, propane and benzene) at pressures of 0.1-1.0 atm.

Early studies of soot surface oxidation by O_2 in nonflame environments were reported by Nagle and Strickland-Constable [12]. Subsequently, Neoh et al. [13,14] studied soot oxidation within laminar premixed flames. Soot surface oxidation in laminar diffusion flames has been studied as follows: in methane/air flames by Garo et al. [15,16], and in ethylene-nitrogen/oxygen-argon flames by Haudiquert et al. [17]. These diffusion flame studies supported the findings of Neoh et al. [13,14] of the dominant role of OH in soot oxidation at near-stoichiometric conditions in flames but yielded OH collision efficiencies that were not in particularly good agreement with the results of Neoh et al. [13,14] for premixed flames. One explanation for the disagreement was that optical scattering and extinction measurements were used to infer soot structure properties during the diffusion flame studies that were based on models that have not been very successful for representing soot optical properties [18-20]. Thus, the present investigation also sought to resolve problems of soot oxidation in diffusion flames using experimental methods developed during earlier studies of soot processes in this laboratory, which avoid the experimental problems of [15-17].

EXPERIMENTAL METHODS

The experiments considered here involved new measurements in diffusion flames at atmospheric pressure for various hydrocarbons burning in air and at pressures 0.1-1.0 atm

involving acetylene-nitrogen mixtures burning in air. Flame and soot properties in these flames were measured in the same manner as Xu and coworkers [4-7]. A total of six premixed and thirteen diffusion flames were used to evaluate mechanisms of soot surface growth and oxidation during the present study.

FLAME STRUCTURE

Typical of all flames considered thus far [1-7], soot in the present flames were aggregates of nearly spherical primary soot particles with the primary particle diameters being nearly monodisperse at given locations in a particular flame. Structure measurements (temperature, T, streamwise velocity, u; primary particle diameter, d_p; soot volume fraction, f_s; and the mole fractions of stable and some radial (H, OH and O) species) were obtained along the axes of the test flames. Results are illustrated in Fig. 1 for an ethylene/air flame at atmospheric pressure which is typical of the other flames that were studied. Different flame conditions varied the concentrations of acetylene and H in the soot formation region, species that are largely responsible for soot growth through the HACA mechanism, but did not affect the fundamental soot surface growth mechanism. Thus, soot formation began where H-atom first appeared in the presence of significant concentrations of acetylene and ended where concentrations of acetylene became small in the presence of significant concentrations of H-atom. Similarly, varying fuel type varied concentrations of O_2 and OH that are largely responsible for soot surface oxidation but did not affect the mechanism of soot surface oxidation. Finally, soot oxidizing species, mainly OH and O2, are present throughout the soot formation region so that soot formation and oxidation proceed at the same time with the former dominating fuel-rich conditions and the latter dominating near-stoichiometric and lean conditions.

SOOT SURFACE GROWTH RATE PROPERTIES

Soot surface growth rates, w_g, were interpreted using the HACA soot surface growth mechanisms of Refs. 10 and 11, expressed as follows:

$$w_g = \alpha_i R_i \tag{1}$$

where i = FW and CH denote the mechanisms of Refs. 10 and 11, respectively, the α_i are steric factors on the order of unity, and the R_i are the complex HACA reaction rate expressions given by Xu et al. [4]. As a first approximation, the R_i are proportional to the product of the concentrations of hydrogen-atom and acetylene, $[H][C_2H_2]$. Thus, measured values of $w_g/[C_2H_2]$ are plotted as a function of [H] in Fig. 2, to provide a direct test of the main features of the HACA soot surface growth mechanism without the intrusion of uncertainties due to the numerous empirical parameters in the original detailed mechanisms; the correlation is surprisingly good indicating similar soot surface growth rate behavior for premixed and diffusion flames involving various hydrocarbon fuels and pressures of 0.1-1.0 atm. A more direct evaluation of the HACA mechanism of Colket and Hall [11] appears in Fig. 3; this mechanism provides a reasonably good correlation of the measurements with a steric factor on the order of unity as expected for soot surface growth rates for premixed and diffusion flames involving various hydrocarbon fuels and pressures of 0.1-1.0 atm. Results for the HACA mechanism of Kazakov et al. [10] were similar.

SOOT SURFACE OXIDATION RATE PROPERTIES

Similar to Neoh et al. [13], soot oxidation rates (corrected for effects of soot growth) were converted into collision efficiencies, for oxidizing species, i, as follows:

$$\eta_i = 4w_{ox}/(C_i[i]\bar{v}_i) \tag{2}$$

where w_{ox} is the rate of soot surface oxidation per unit area, C_i is the mass of carbon removed from the surface per mole of species i reacting at the surface, [i] is the gas phase concentration of i adjacent to the surface, and

$$\overline{v}_i = (8R_uT/(\pi M_i))^{1/2} \qquad (3)$$

is the mean molecular velocity of species i, R_u is the universal gas constant, T is the temperature and M_i is the molecular weight of species i. The measurements indicated that O_2, CO, H_2O and O did not provide a good correlation of collision efficiencies for early soot surface oxidation. Results for OH, however, illustrated in Fig. 4, provided an excellent correlation for all the test flames, as well as for the earlier results in premixed flames due to Neoh et al. [13], yielding a steric factor of 0.13 with an uncertainty of 0.05, essentially independent of laminar flame type (premixed for diffusion), fuel type and pressures in the range 0.1-1.0 atm.

ACKNOWLEDGMENTS

REFERENCES

1. Sunderland, P.B. Koylu, U.O. and Faeth, G.M., *Combust. Flame* 100:310 (1995).
2. Sunderland, P.B. and Faeth, G.M., *Combust. Flame* 105:131 (1996).
3. Lin, K.-C., Sunderland, P.B. and Faeth, G.M., *Combust. Flame* 104:375 (1996).
4. Xu, F., Sunderland, P.B. and Faeth, G.M., *Combust. Flame* 108:471 (1997).
5. Xu, F., Lin, K.-C. and Faeth, G.M., *Combust. Flame* 115:195 (1998).
6. Xu, F. and Faeth, G.M., *Combust. Flame* 121:640 (2000).
7. Xu, F. and Faeth, G.M., *Combust. Flame* 125:804 (2001).
8. El-Leathy, A.M., Xu, F., Kim, C.-H. and Faeth, G.M., *AIAA J.*, in press.
9. Xu, F., El-Leathy, A.M., Kim, C.-H. and Faeth, G.M., *Combust. Flame* 132:58 (2003).
10. Kazakov, A., Wang, H. and Frenklach, M., *Combust. Flame* 110:111 (1995).
11. Colket, M.B. and Hall, R.J., *Soot Formation in Combustion* (H. Bockhorn, ed.), Springer-Verlag, Berlin, p. 442, 1994.
12. Nagle, I. and Strickland-Constable, R.F., *Proceedings of the Fifth Carbon Conference*, Vol. 1:154 (1962).
13. Neoh, K.G., Howard, J.B. and Sarofim, A.F., *Particulate Carbon* (D.C. Siegla and B.W. Smith, ed.), Plenum Press, New York, p. 26, 1980.
14. Neoh, K.G., Howard, J.B. and Sarofim, A.F., *Proc. Combust. Inst.* 20:951 (1984).
15. Garo, A., Lahaye, J. and Prado, G., *Proc. Combust. Inst.* 21:1023 (1986).
16. Garo, A., Prado, G. and Lahaye, J., *Combust. Flame* 79:226 (1990).
17. Haudiquert, M. et al., *Combust. Flame* 111:338 (1997).
18. Wersborg, B.L., Howard, J.B. and Williams, G.C., *Proc. Combust. Inst.* 14:929 (1972).
19. Williams, G.C., *Proc. Combust. Inst.* 14:929 (1972).
20. Koylu, U.O. and Faeth, G.M., *J. Heat Trans.* 115:409 (1993).
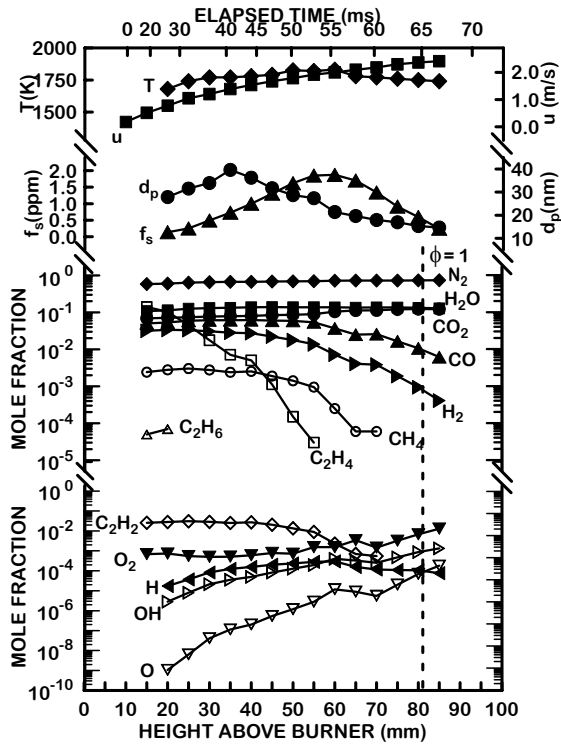
Fig. 1. Measured soot and flame properties in an ethylene/air diffusion flame at atmospheric pressure. From El-Leathy et al. [8].
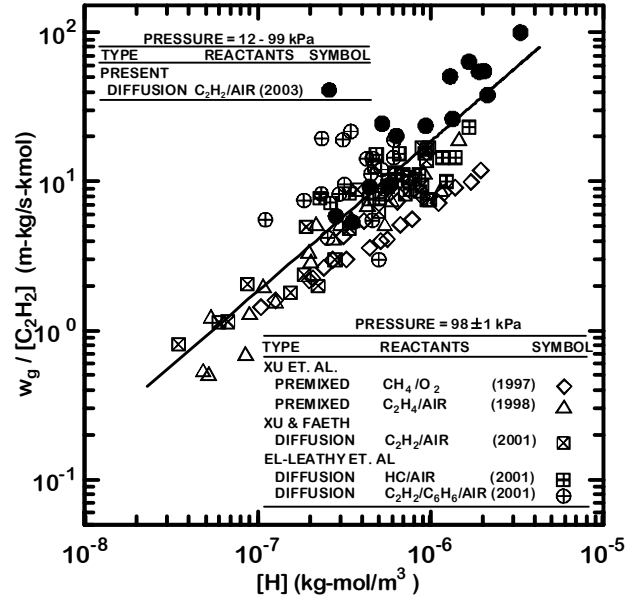
Fig. 2. Soot surface growth rates (corrected for soot surface oxidation) as a function of acetylene and hydrocarbon-atom concentrations for laminar premixed and diffusion flames (involving various fuel types and pressures).
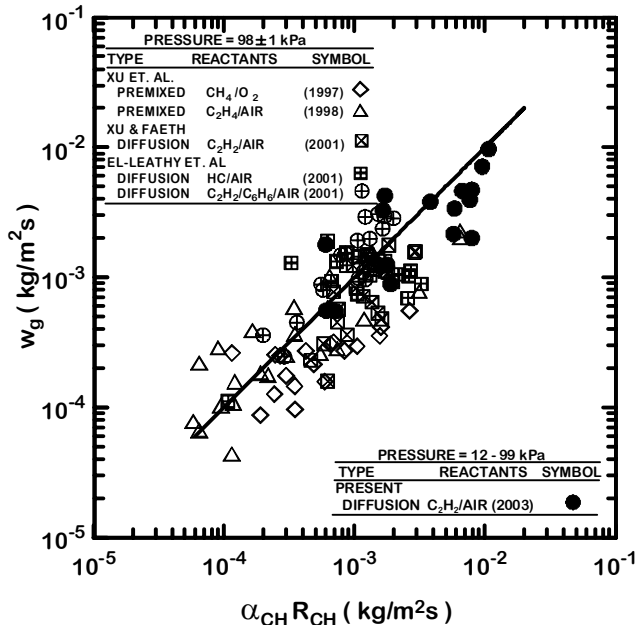
Fig. 3. Soot surface growth rates (corrected for soot surface oxidation) in terms of the HACA mechanism of Colket and Hall [11] for laminar premixed and diffusion flames involving various fuel types and pressures.
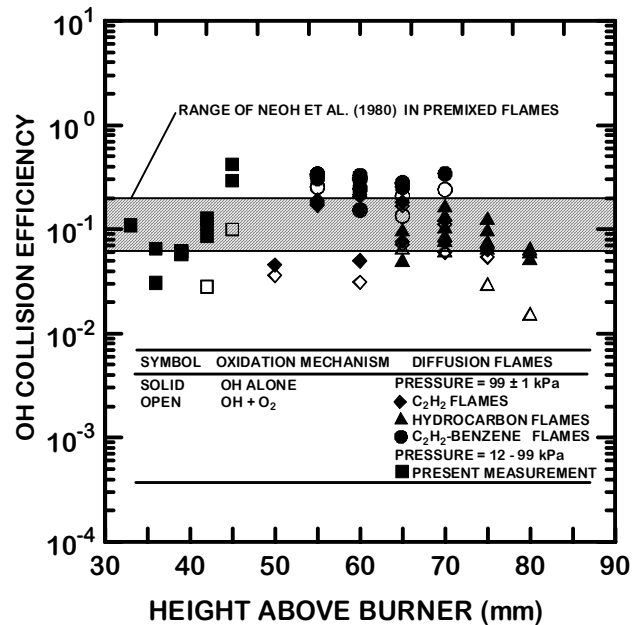
Fig. 4. Soot surface oxidation collision efficiencies for early soot oxidation assuming soot burnout due to OH and O_2 (with the O_2 rate taken from Ref. 12) for laminar premixed and diffusion flames involving various fuel types and pressures.

Soot Nanostructure and Its Impact Upon the O$_2$ Oxidation Rate

Randy L. Vander Wal, Aaron J. Tomasek
NCMR c/o NASA-Glenn
Cleveland, OH 44135

Introduction

Studies of soot oxidation have ranged from *in situ* flame studies to shock tubes to flow reactors [1]. Each of these systems possesses particular advantages and limitations related to temperature, time and chemical environments. Despite the aforementioned differences, these soot oxidation investigations share three striking features. First and foremost is the wide variation in the rates of oxidation. Reported oxidation rates vary by factors of +6 to - 20 [2] relative to the Nagle Strickland-Constable (NSC) rate for graphite oxidation [3]. Rate variations are not surprising, as the temperatures, residence times, types of oxidants and methods of oxidation differ from study to study. Nevertheless, a valid explanation for rate differences of this magnitude has yet to be presented.

Experimental

Soots possessing different nanostructures were produced by pyrolysis of acetylene, benzene or ethanol. These soots still in aerosol form were introduced into the post-flame gases produced by a lean, premixed flame supported on a sintered metal burner. A synthetic air mixture consisting of N$_2$ and O$_2$ was used for the methane premixed flame. The relative percentages of O$_2$/N$_2$ were varied to maintain the same total "air" flow rate while varying the relative O$_2$ concentration, thereby maintaining the same "air" heat capacity. To produce an oxidizing gas mixture, all flames used $\phi < 1$ with a constant methane flow rate of 1.5 slpm. In this manner the adiabatic flame temperature and post-flame gas temperature was maintained nearly constant for this given fuel flow rate. A 5 slpm co-flow of N$_2$ was used as a shroud.

The soot and a portion of the post combustion gases were directed into a 1 inch outer diameter quartz chimney of 6 inches in length, placed directly above the quartz tube. With this setup, the temperature along the chimney axis was 750 +/- 30 ℃, as measured by a type K thermocouple. This variation was within the error range of the thermocouple, +/- 25 ℃, and hence it was taken as constant at 750 ℃. With a known entrance gas velocity, the residence time of the soot within the chimney is readily calculated based on buoyant acceleration as 75 +/- 5 ms.

Oxidation was conducted well above the flame front, in the post-flame gases. Burning with phi < 1 ensures that that the OH concentration within the post-flame gases is insignificant [10]. Given vastly slower rates for oxidation of carbons by H$_2$O or CO$_2$, the primary oxidant was considered to be the excess O$_2$ [1]. The soot stream appeared as a thin cylinder with yellow C$_2$ swan band emission associated with burning soot. Partially oxidized soot was collected at the chimney exit by thermophoretic sampling directly upon a lacey TEM grid. A custom image analysis program was scripted for analysis of the HRTEM images using a windows-based, macro interface using Optimus v.6.5.

Results and Discussion

Analysis Model

The analysis of the oxidation process is based on a shrinking sphere model, where reactions with oxidizer and corresponding mass loss occur at the particle surface. With this model, changes in the primary particle diameter, as observed using TEM, are readily translated into mass loss per unit surface area. The contribution of internal surface area and pore diffusional effects are

not considered, but this appears justified as detailed in the discussion section for our experimental conditions. It should be noted that this model makes no provisions or assumptions regarding the soot particle structure, active sites, nor mechanism details of the oxidation reactions occurring at the particle surface.

Results

Figure 1 plots the mass burnout rates versus free O_2 concentration for the soots derived from the different fuels. Burnout rates are calculated relative to the initial particle size before introduction into the flame environment. The mass loss rate increases with increasing O_2 concentration as expected for all soots, yet the soots derived from benzene and acetylene exhibit a dramatic difference in their oxidation rates. As observed, the acetylene soot requires a much higher ambient O_2 concentration to achieve the same level of burnout (for any given reaction duration) as the benzene derived soot. The soot derived from ethanol exhibits a very similar rate as the benzene soot. The faster burnout rate for the benzene and ethanol derived soots is also reflected in their complete oxidation at O_2 concentrations far lower than that of the acetylene derived soot, despite similarly sized primary particles for these two soots. Plotted for reference is the calculated NSC rate at each O_2 concentration at the measured post-flame gas temperature [3]. As seen in Fig. 1, the measured rates for the graphitic acetylene soot lie much closer to the NSC rates. Notably the oxidation rates of all the soots exceed the NSC rate. HRTEM images of the soot have been obtained and reported elsewhere [4]. These images form the basis for our subsequent discussion and lattice fringe analysis as follows next.

Discussion

Soot Structure

Although the relation between carbon structure and reactivity is well-known in carbon science from thermal and oxidative studies of coal [5], char [6] and graphite [7]; the relation for soot remains unstudied. It is well-known that graphite oxidation proceeds anisotropically, i.e, the reactivity of basal plane carbon atoms is far lower than that of edge site carbon atoms. Measurements by Rosner and Allendorf observed a 10 - 100-fold reactivity difference between isotropic and pyrolytic graphite, intrepreted on the basis of the differerent reactivities of carbon atoms within basal plane versus edge site positions [7]. Similar variations in the different oxidation rates for natural graphites were observed by Thomas [8] and Henning [9]. Consequently, the observed reactivity will be an average of basal versus edge site carbon atom reactivities for graphitic layer planes of finite dimensions [3]. As the layer plane size decreases, the number of edge site carbon atoms will necessarily increase in proportion to the number of basal plane carbon atoms, allowing one to expect the overall reactivity to increase. In addition to the size of the graphene segments, their relative curvature will also impact their oxidation rate. Curvature arises from 5-membered rings within the aromatic framework [10]. This curvature imposes bond strain because the orbital overlap giving rise to the electronic resonance stabilization is lessened [12]. Therein the C-C bonds are weakened and individual atoms are more exposed, i.e. they are more susceptible to oxidative attack. It is for these same reasons that fullerenes and carbon nanotubes are less resistant towards oxidation than planar graphite [11]. A larger degree of curvature (smaller radius of curvature) increases the imposed bond strain and hence the resistance towards oxidation decreases, as has been found for carbon nanotubes of different diameters [12]. This duality of reactive sites forms the physical basis for the NSC oxidation rate expression which takes into account both edge and basal plane carbon sites and their associated reactivities [3]. However, this semi-empirical rate is based on pyrolytic graphite, a structure with extended basal planes and correspondingly few edge site carbon atoms. Consequently the overall oxidation rate

would be expected to be relatively low compared to most other carbons possessing a less graphitic structure. Notably there is no corresponding model or rate expression that takes into account the curvature of graphitic layer planes and the associated impact upon oxidative stability.

Thus the reactivity of a soot particle towards oxidation depends upon its nanostructure, i.e. the size, orientation and organization of the graphene layer planes. Variations in the graphene layer plane dimensions, curvature, and relative orientation will greatly impact the reactivity of the individual graphene segments, and hence the overall particle reactivity. Yet as discussed, little attention has been given to soot particle nanostructure and its impact upon reactivity towards oxidation within combustion systems. To the degree to which the soot nanostructure reflects a dependence upon inception and growth conditions, so too will its oxidation rate reflect a similar dependence. Our results clearly illustrate a dependence of the burnout rate upon the soot nanostructure as governed here by both the initial fuel and soot growth conditions.

Applying the above discussion to the HRTEM images of our nascent soot samples as have been reported elsewhere [13] and will be presented during the talk, we can compare structural analysis with burnout rates. The benzene derived soot with short, unaligned segments translates into a relatively high percentage of edge site carbon atoms relative to those located at basal plane sites. In contrast, the acetylene derived soot consists of longer graphene segments, which implies a smaller number of edge plane carbon atoms relative to basal plane atoms.   Finally, the ethanol derived soot produced similarly long, yet highly curved fringes, which creates high tortuosity, and structural disorder throughout the particle.

Lattice Fringe Analysis

Though the HRTEM images are helpful in revealing the nanostructure of the two soots and provide a basis for interpretation of differences in their oxidation characteristics, alone they provide only a qualitative guide for the measured oxidation rate differences. A more quantitative measure may be obtained by a lattice fringe analysis of the HRTEM images.

Figure 2 plots the histograms of fringe length for each of the three soots. As seen, the fringe length distribution for the acetylene soot extends to much longer graphene layer plane dimensions. Relative to the distribution for the benzene soot with 80% of the lamella between 0 and 1 nm in length, only 50% of the acetylene fringe length distribution lies between 0 and 1 nm. Alternatively only 2% of the benzene fringe length distribution is greater than 2 nm while 20% of the lamella in the acetylene soot are greater than 2 nm. Of particular interest is that the fringe length histogram for the ethanol derived soot is intermediate between those for the benzene and acetylene derived soots as seen in Fig. 2. (For ethanol, 60% of its fringe length histogram lies between 0 and 1 nm while 13% of the lamella are greater than 2 nm.)   Its higher burnout rate clearly points to another factor influencing its reactivity, such as curvature-induced bond strain. The curvature of the graphene segments for the ethanol versus acetylene derived soots is readily apparent upon visual comparison of the the HRTEM images which will be shown. The lattice fringe length distributions serve to quantify the data conveyed by the HRTEM images and provide a firm basis for our conclusions. Future work will be directed towards developing a correlation between the soot nanostructure, as revealed by HRTEM and quantified by fringe analysis, and the soot's oxidation rate.

Conclusions

The work reported here illustrates a dependence of the soot particle nanostructure upon synthesis conditions; namely temperature, time and initial fuel identity. Such structural variations in the graphene layer plane dimensions necessarily alters the ratio of basal plane versus edge site carbon atoms. A corresponding variation in the overall reactivity, reflecting an average of the different reactivities associated with these specific atomic sites arises. This variation is illustrated

here between a disordered soot derived from benzene and a graphitic soot derived from acetylene. Their oxidation rates differ by nearly 5-fold. Curvature of layer planes, as observed for an ethanol derived soot, is found to substantially increase oxidative reactivity. Relative to fringe length as a manifestation of graphitic structure, curvature more effectively increases reactivity towards oxidation. Larger variations in oxidation behavior may be expected, depending upon the soot synthesis conditions. Other physical properties may similarly be affected.

References
1. Kennedy, I. M., Prog. Energy Combust. Sci. 23:95-132 (1997). (and references therein).
2. Puri, R., Santoro, R. J., and Smyth, K. C., Combust. and Flame 97:125-144 (1994).
3. Nagle, J. Strickland-Constable, R. F., Proc. of the Fifth Carbon Conf. 1, p.154-164 (1962).
4. Vander Wal, R. L., and Tomasek, A. J., Combust. and Flame (in press).
5. Ljubisa, R., Walker, P. L. and Jenkins, R. G., Fuel 62:849 (1983).
6. Davis, K. A., Hurt, R. H., Yang, N. Y. C. and Headley, T. J., Combust. and Flame 100:31-40 (1995).
7. Rosner, D. E. and Allendorf, H. D., AIAA Journal 6:650-654 (1968).
8. Thomas, J. M., Microscopy studies of graphite oxidation, in The Chemistry and Physics of Carbon, (P. L. Walker, Jr., Ed.) Vol. 1, p. 121 (1965).
9. Henning, G. R., Chemistry and Physics of Carbon, (P. L. Walker, Jr., Ed.), Vol. 2 p. 1 (1966).
10. Kroto, H. W., Heath, J. R., O'Brien, S. C., Curl, R. F., and Smalley, R. E., Nature, 318:162-165 (1985).
11. Dresselhaus, M. S., Dresselhaus, G., and Eklund, P. C., Science of Fullerenes and Carbon Nanotubes, Academic Press Inc. (1996).
12. Yang, Y., Zou, H., Wu, B., Li, Q., Zhang, J., Liu, Z., Guo, X., and Du, Z., J. Phys. Chem. B 106:7160-7162 (2002).
13. Vander Wal, R. L., Tomasek, A. J., Street, K. J., and Thompson, W., Environ. Sci. and Technol. (submitted).
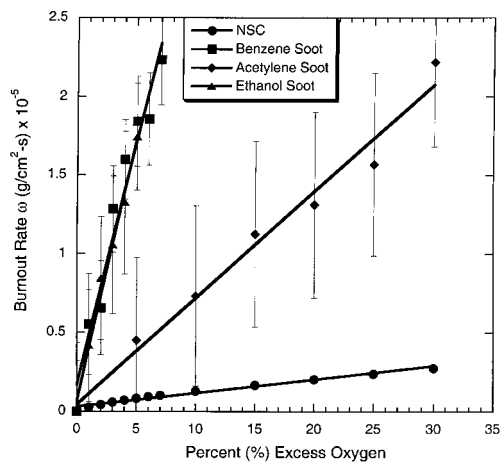
Figure 1 (above). Dependence of soot mass burnout rate with O_2 percentage in the post-flame gases. The NSC rate is also shown for comparison.

Figure 2 (right). Histograms of the lattice fringe lengths for the different indicated soots as obtained by application of the fringe analysis program to the HRTEM images from ref. 4.
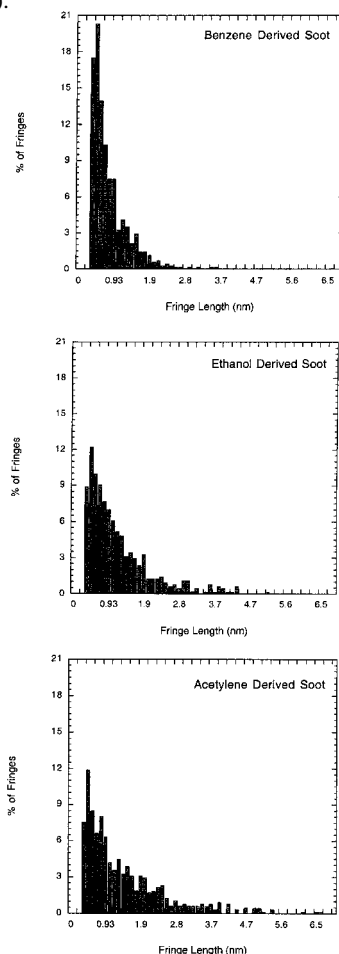
EXPERIMENTS AND MODELING OF SOOT FORMATION IN LAMINAR PREMIXED FLAMES: DETAILED PARTICLE SIZE DISTRIBUTION FUNCTION, EFFECT OF FERROCENE ADDITION, AND ROLE OF ION IN SOOT MASS GROWTH

Hai Wang
Department of Mechanical Engineering, University of Delaware, Newark, DE 19716

Chih-Jen Sung
Department of Mechanical and Aerospace Engineering, Case Western Reserve University,
Cleveland, OH 44106

INTRODUCTION

The research addressed here is a collaborative project between University of Delaware and Case Western Reserve University. There are two basic and related scientific objectives. First, we wish to demonstrate the suitability of spherical, laminar, premixed flames in the study of the fundamental chemical and physical processes of soot formation. Our reasoning is that the flame standoff distance in spherical flames under microgravity can be substantially larger than that in a flat burner-stabilized flame. Therefore the spherical flame is expected to give better spatial resolution to probe the soot inception and growth chemistry than flat flames. Second, we wish to examine the feasibility of defining the laminar flame speed of soot forming flames. Our basic assumption is that under the "adiabatic" condition (in the absence of conductive heat loss), the amount and dynamics of soot formed in the flame is unique for a given fuel/air mixture. The laminar flame speed can be rigorously defined as long as the radiative heat loss can be determined. This laminar flame speed characterizes the characteristics of soot formation and dynamics in addition to the heat release rate.

The research involves two integral parts: experiments of spherical and cylindrical sooting flames in microgravity, and the computational counterpart that aims to simulate sooting laminar flames, and the sooting limits of near adiabatic flames. During the last two years, our primary focus has been to prepare the experiments that are to be conducted in the 2.2-second Microgravity Drop Tower. The diagnostic system has been developed and tested [1]. Several experimental and computational projects have been carried out with the aim to address issues related the overall aim of the research. These projects are (a) a computational study on the role of ions in soot mass growth [2], (b) the simulation of detailed particle size distribution functions of soot formed a laminar premixed flame [3], and (c) an experimental and computational study on the role of iron additive on soot formation [4]. Status of the microgravity experiments and the results of the aforementioned projects will be reviewed below.

MICROGRAVITY EXPERIMENT STATUS

Sooting flames will be studied in the near future using spherical and cylindrical flame configurations in microgravity. These two configurations are preferable to the popular twin counterflow flame method because they prevent the sooting non-uniformity as found in the counterflow geometry. The proposed method also allows the simple determination of the unstretched burning velocity by varying the mass flow rate of the reactants and measuring the resulting flame radius. Since the flame location must be accurately known, a simple and compact optical technique first needed to be developed and tested.

In the planned study, an optical system using the Rainbow Schlieren Deflectometry (RSD) concept will be used to precisely determine the flame location. This system, shown in Fig. 1, was designed and built for use in the 2.2-second Microgravity Drop Tower at NASA Glenn. It uses a CCD color camera (operating at 30 frames per second), together with a calibrated color filter, light source, and lenses, to obtain the instantaneous temperature field of an axisymmetric flame. An on-board light source provides the necessary illumination for the RSD system.
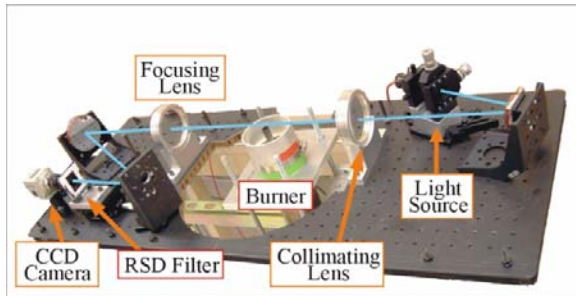
Figure 1. Picture of current drop rig RSD optical setup. Blue line indicates the path of the RSD light beam.

The entire system (optics and software) was tested using a sample premix methane/air Bunsen flame with co-flow. Figure 2 shows a sample raw RSD image obtained at an equivalence ratio of 0.75. The resulting RSD temperature data was compared to temperature measurements using a thermocouple (Fig. 3) and chemiluminescence imaging of the flame surface (Fig. 4). It was concluded that, although it is difficult to accurately measure the high temperature region, it is possible to accurately determine the flame location using this system. The flame location is obtained by locating the point of maximum temperature gradient, which is located close to the point of maximum heat release. The error in locating the flame surface was estimated to be about ±0.15 mm.
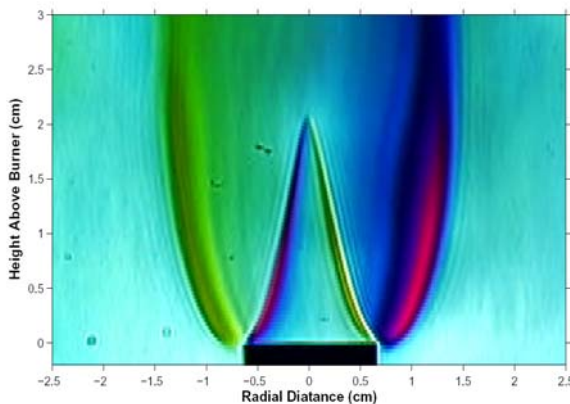
Figure 2. Raw RSD image of a methane/air flame.
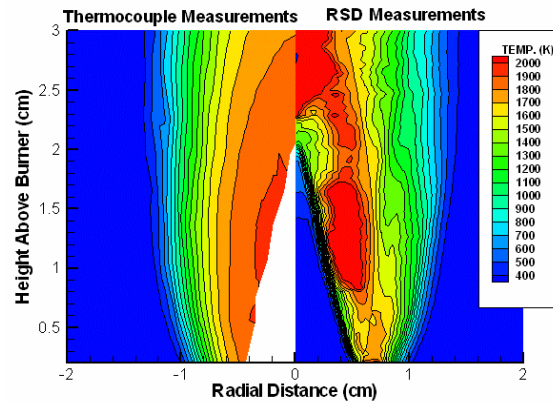
Figure 3. Comparison of temperature contours by thermocouple and by RSD at 200 flame locations.

In the lean methane case, the flame location obtained using RSD was found to be equivalent to that obtained using chemiluminescence imaging (see Fig. 4). Under moderately sooting conditions, direct imaging of the flame surface is not possible, but RSD still provides acceptable images (see Fig. 5). In the future, more work will be done to test the system using different fuels and sooting conditions. The microgravity rig is currently under construction and the first drops are scheduled for the late summer, 2003. More work still needs to be done to improve the fabrication and optimization of the RSD filters. Better filters would provide better sensitivity and therefore less error in determining the temperature field.
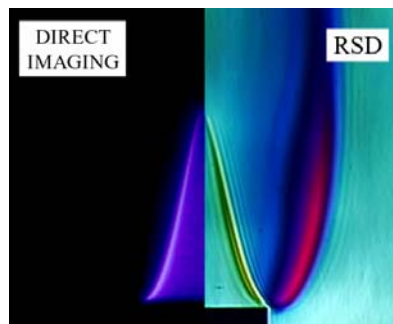
Figure 4. Comparison of chemiluminescence and RSD imaging for a $\phi = 0.75$ flame.
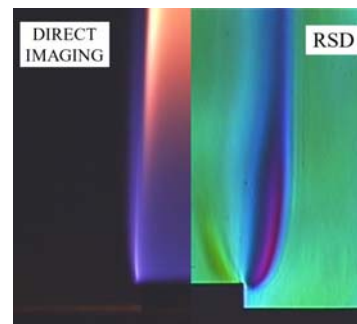
Figure 5. Comparison of chemiluminescence and RSD imaging for a fuel-rich flame.

THE ROLE OF IONS IN SOOT MASS GROWTH

In sooting flames, a large fraction of the soot particles may be charged due to thermal ionization. The density of charged particles is expected to increase exponentially with an increase in flame temperature and particle size. Due to charge interactions, the coagulation of charged-neutral particles can be notably enhanced. Furthermore, the presence of charge on the particles may also affect the surface reaction rate. Although the role of ions in soot formation has been extensively discussed, the influence of charged particles in soot mass growth has not been quantitatively examined by considering the detailed particle size distribution function.

We carried out a detailed numerical simulation study with the goal to assessing the role of charged particles in soot mass growth [2]. The results show that at 2000 K, as many as 50% of the particles are charged. A rigorous consideration of coagulation enhancement due to charge interactions gives, however, little difference in the predicted soot volume fraction. This result allowed us to conclude that as far as the simulation of soot formation is concerned, the omission of thermal ionization does not lead to significant differences in the predicted growth of soot particles. Thermal ionization would play a role in the growth of soot particles if the surface reactions between charged particles and gaseous molecules were enhanced. Nevertheless, the uncertainty associated with the omission of thermal ionization is significantly smaller than the uncertainties in the kinetics of particle inception and surface growth in most laboratory flames.

SIMULATION OF DETAILED SOOT PARTICLE SIZE DISTRIBUTION FUNCTION

In a recent study [5], detailed soot particle size distribution functions (PSDFs) were measured using a nano scanning mobility particle sizer. It was found that the PSDFs could be bimodal (Fig. 6), depending on the strength of particle nucleation in the post flame [3]. The characteristic bimodal PSDF shape is expected to be pertinent to flames with maximum flame temperature < ~1700 K.
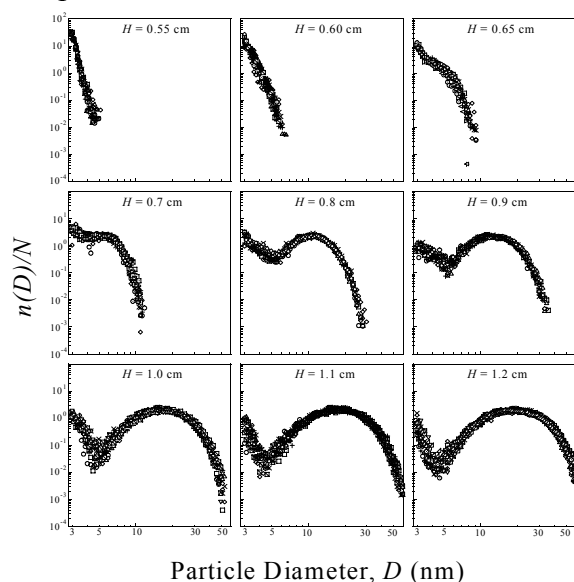
Figure 6. PSDFs measured in a $\phi = 2.07$ premixed ethylene flame.
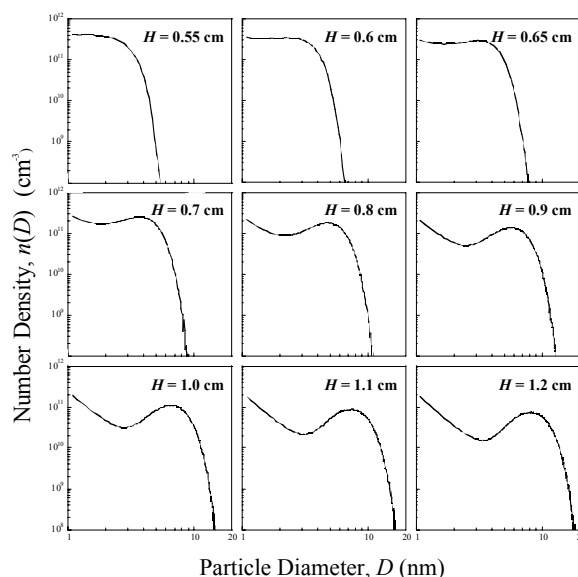
Figure 7. PSDFs computed in a $\phi = 2.07$ ethylene flame.

The bimodality poses a challenge for accurate prediction of the intensity of soot radiation, which is greatly influenced by soot surface area and thus the shape of the PSDF. Moreover, the existence of the bimodal distribution provides a stringent validation test for the soot model [6], since the bimodal behavior affects the rate of soot mass growth and thus the soot yield. For this reason, we carried out a detailed numerical simulation using a recently developed stochastic method [7]. The results show that the model predicts well the shapes of the measured PSDFs, although the particle size was somewhat under-predicted (Fig. 7). The cause for this discrepancy is currently under investigation.

THE ROLE OF FERROCENE IN SOOT FORMATION

It is known that while ferrocene suppresses soot formation in diffusion flames, it promotes soot formation in premixed flames. The consensus appears to be that in premixed flames iron or iron oxide would nucleate early into particles, which provide a substrate for carbon deposition. This phenomenon is viewed as soot nucleation induced by iron or iron oxide. In diffusion flames, however, the iron incorporation promotes the catalytic burnout of the carbon as soot transverse through the oxidizing region of the flame.
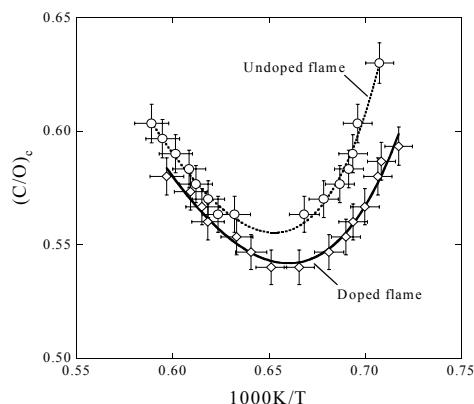
Figure 8. Measured critical C/O ratios of ethylene/oxygen/argon flames (Ar/O = 2.25) w/o ferrocene doping. The doped flames have 20 ppm ferrocene.
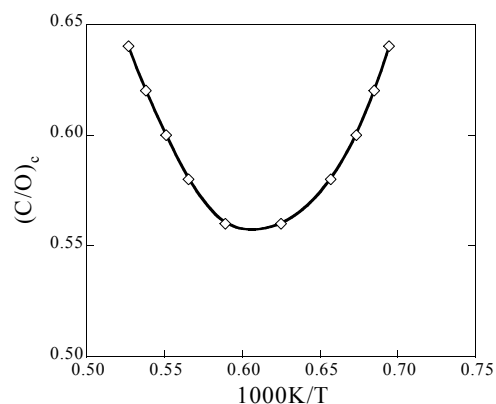
Figure 9. Computed critical C/O ratios in the undoped flames.

In this study, we examined the critical sooting limits of premixed ethylene flames with and without ferrocene doping. Figure 8 shows the experimentally measured critical C/O ratio as a function of the flame temperature. The critical C/O ratios follows a characteristic, inverted bell shape dependence. The doped flames have smaller critical C/O ratio, indicating that the soot inception is indeed promoted by ferrocene. Computationally, the possible influence of the cyclopentadienyl resulting from ferrocene decomposition is examined. The computational results reproduced well the inverted bell shape dependence (Fig. 9). The concentration of cyclopentadienyl radicals due to ferrocene pyrolysis was found to be too small to influence the PAH concentration and thus the homogeneous nucleation of soot. This result further supports the notion that, in doped flames soot nucleation is induced by iron or iron oxide particles.

REFERENCES

1. Ibarreta, A. F. and Sung, C. J. "Determination of flame location using rainbow Schlieren deflectometry," *Proceedings of Joint Meeting of the US Sections of the Combustion Institute*, Chicago, March 2003, paper P14.
2. Balthasar, M., Mauss, F. and Wang, H., *Combust. Flame*, **129**, pp.204-216 (2002).
3. Zhao, B., Yang, Z., Johnston, M. V., Wang, H., Wexler, A. S., Balthasar, M., and Kraft, M. *Combust. Flame*, in press, 2003.
4. Hirasawa, T., Sung, C. J., Yang, Z., Joshi, A. and Wang, H., "Effect of ferrocene addition on sooting limits in ethylene/oxygen/argon premixed flames," Manuscript in preparation.
5. Zhao, B., Yang, Z., Wang, J., Johnston, M. V. and Wang, H. *Aerosol Sci. Technol.*, in press, 2003.
6. Frenklach, M. and Wang, H., "Detailed mechanism and modeling of soot particle formation," in *Soot Formation in Combustion: Mechanisms and Models of Soot Formation*, (Bockhorn, H., ed.), Springer Series in Chemical Physics, vol. 59, Springer-Verlag, Berlin, 1994, pp.162-190.
7. Balthasar, M. and Kraft, M. *Combust. Flame*, in press, 2003.

SOOTING LIMITS OF DIFFUSION FLAMES WITH OXYGEN-ENRICHED AIR AND DILUTED FUEL

P.B. Sunderland[1], D.L. Urban[2], D.P. Stocker[2], B.H. Chao[3], and R.L. Axelbaum[4*]

[1]NCMR
[2]NASA Glenn Research Center
Cleveland OH

[3]Dept. of Mechanical Engr.
University of Hawaii
Honolulu HI

[4]Dept. of Mechanical Engr.
Washington University
St. Louis MO

INTRODUCTION

Oxygen-enhanced combustion permits certain benefits and flexibility that are not otherwise available in the design of practical combustors, as discussed by Baukal (1998). The cost of pure and enriched oxygen has declined to the point that oxygen-enhanced combustion is preferable to combustion in air for many applications. Carbon sequestration is greatly facilitated by oxygen enrichment because nitrogen can be eliminated from the product stream. For example, when natural gas (or natural gas diluted with CO_2) is burned in pure oxygen, the only significant products are water and CO_2. Oxygen-enhanced combustion also has important implications for soot formation, as explored in this work.

Most fundamental sooting limits have come from studies of laminar premixed flames. One reason for this is that both temperature and the C/O atom concentration ratio are nearly constant in the soot forming regions of premixed flames. The limits typically are identified by the C/O ratio at which luminous yellow emission is barely perceptible. The limits are intrinsic properties of the mixtures and offer both practical value and fundamental information about soot inception processes. When a limit occurs at a high C/O ratio for a given flame temperature this indicates conditions, e.g. fuel type, that are less conducive to forming soot. Takahashi and Glassman (1984) concluded that sooting limits in premixed flames arise from a competition between fuel pyrolysis and oxidative attack. Markatou et al. (1993) found that oxidation of light hydrocarbons (such as C_2H_3), rather than oxidation of polyaromatic hydrocarbons (PAH), is the mode of oxidation that is critical to sooting limits for premixed flames. The formation of PAH and soot is prevented by the oxidation of these light hydrocarbons.

Despite the differences between soot inception in premixed and nonpremixed flames, the C/O ratio (which varies with position in diffusion flames) is proposed here to be relevant to sooting limits in diffusion flames. Du and Axelbaum (1995) employed the C/O ratio to explain their observations of what later came to be called permanently-blue flames. The fundamental point here originates from the same reasoning as to why C/O ratio is relevant in premixed flames. When the C/O ratio is unity, there is exactly enough oxidizer to retain the carbon in the gas phase as CO, while at higher C/O ratio there is insufficient oxidation to gasify the carbon and this would be expected to lead to soot formation. Owing to finite-rate chemistry and the production of H_2O and CO_2 the measured sooting limit, $(C/O)_c$, in premixed ethylene/air combustion is less than unity. For ethylene it occurs around $(C/O)_c = 0.6$.

We propose that soot inception in nonpremixed flames requires a region where C/O ratio, temperature, and residence time are above certain critical values. Soot does not form at low temperatures, with the threshold in nonpremixed flames ranging from about 1250-1650 K, a

---

temperature referred to here as the critical temperature for soot inception, T_c. Soot inception also can be suppressed when residence time is short (equivalently, when the strain rate in counterflow flames is high). Soot induction times of 0.8-15 ms were reported by Tesner and Shurupov (1993) for acetylene/nitrogen mixtures at 1473 K.

The above reasoning is employed in Fig. 1 to explain the role of local C/O ratio and temperature, T, in unstrained nonpremixed flames. This figure depicts two diffusion flames, both with $Z_{st} = 0.226$ (where Z_{st} is the stoichiometric mixture fraction) and the same relationship between C/O and Z but with dramatically different adiabatic flame temperatures, T_{ad}, owing to different amounts of inert in the flames. For purposes of discussion, we assume here that $T_c = 1250$ K and $(C/O)_c = 1$. Consider first a flame of pure C_2H_4 and O_2 indicated by the dotted line. As indicated by the horizontal bar, a broad region exists where both $T > 1250$ K and C/O > 1; this region is expected to form soot given sufficient residence time. Consider next the other flame, shown in Fig. 1 by a dashed line, where both ethylene and oxygen have been diluted with nitrogen such that Z_{st} is unchanged but T_{ad} has been reduced until a condition is reached where C/O = 1 at the location where the local temperature is 1250 K. The conditions of the second flame characterize a flame at the sooting limit because the region where C/O ratio and temperature are both above their critical values is infinitely thin.

Burner stabilized spherical microgravity flames are employed in this work for two main reasons. First, this configuration offers unrestricted control over convection direction. Second, in steady state these flames are strain-free and thus can yield intrinsic sooting limits in diffusion flames, similar to the way past work in premixed flames has provided intrinsic values of C/O ratio associated with soot inception limits.

RESULTS AND DISCUSSION

The present experiments were conducted in microgravity in the NASA Glenn 2.2-second drop tower. The experimental apparatus is described in detail in Sunderland et al. (2003). As before, the burner is a 6.4 mm diameter porous stainless-steel sphere. All tests were conducted in quiescent ambient gas at 295 K and 0.98 bar (with an estimated uncertainty of ±0.005 bar), and ignition was performed in microgravity.

Four representative flames at or near their sooting limits are shown in Fig. 2. Typical of the flames in this study, these images reveal spherical symmetry except near the burner tube. These flames represent both convection toward oxidizer (normal flames) and convection toward fuel (inverse flames). The flames of Fig. 2b and 2d are considered here to be at the experimental sooting limits since a small reduction in reactant concentration yields blue conditions. Note that soot, when present, appears inside the flame sheet for normal flames and outside for inverse flames.

Seventeen sooting limits have been identified. The sooting limits of are presented in Fig. 3 in terms of reactant compositions. The present spherical flames allow a boundary to be identified between conditions where soot cannot form in unstrained, long residence time flames – permanently-blue flames – and conditions where soot can form given sufficient residence time. This boundary is identified by the solid curve. The dashed curves are T_{ad} isotherms, determined with CEA. Within experimental uncertainties convection direction does not have an impact on the sooting limits. Figure 3 also includes sooting limits measured in normal-gravity counterflow C_2H_4 flames in three previous studies, namely Du and Axelbaum (1995), Lin and Faeth (1996), and Hwang and Chung (2001).

Further insight can be gained by plotting the present sooting limit data in terms of T_{ad} versus Z_{st}. Recall that Fig. 1 used $(C/O)_c$ and T_c to identify where soot can and cannot form in unstrained nonpremixed flames. In other words, if $(C/O)_c$ occurs at the same location as T_c on the fuel side, conditions suitable for soot formation are infinitely thin, indicating a sooting limit given sufficient residence time. Employing the Burke-Schumann assumptions, Y_C, Y_O and T are linear in Z, as in Fig. 1. This behavior, coupled with the hypothesis that soot formation requires temperature and C/O to be above fixed critical values, predicts a linear increase in T_{ad} with Z_{st} at the sooting limit. Motivated by this analysis, the data in Fig. 3 are plotted in Fig. 4 in terms of Z_{st} versus T_{ad}, again defining a region of permanently-blue conditions. Figure 4 allows the data to be correlated with a least-squares fit, yielding the fit shown. This correlation also is included as the solid curve in Fig. 3, where the mapping from the axes of Fig. 4 to those of Fig. 3 was done using CEA. The slope of the line fit in Fig. 4 reveals the large effect of Z_{st} on sooting limits, accounting for a range in T_{ad} at the sooting limits of 1815 to 2738 K. Figure 4 shows that convection direction has no measurable effect on the sooting limits of the present flames. The normal-gravity sooting limit flames in Fig. 3 also are included in Fig. 4.

Figure 4 indicates that the mechanism for attaining a sooting limit may be different at low and high Z_{st}. The adiabatic flame temperature for the low Z_{st} sooting-limit flame is nearly equal to T_c. Thus, when inert is added to the standard fuel/air flame (low Z_{st}) the sooting limit is obtained largely because the temperature is so low that the kinetics of soot inception are too slow to produce soot. On the other hand, when Z_{st} is high, C/O ratio is high deep into the fuel side of the flame. This suggests the sooting limit is attained because there is sufficient oxygen on the fuel side of the flame to favor oxidation of light hydrocarbons over formation of soot precursors. C/O ratio is higher farther into the fuel-rich region but there the temperature is too low for soot inception to occur.

REFERENCES
Baukal, C.E., Oxygen-enhanced combustion, C.E. Baukal, Ed., CRC Press, Boca Raton, pp. 1-45 (1998).
Du, J. and Axelbaum, R.L., Combust. Flame 100:367 (1995).
Hwang, J.Y. and Chung, S.H., Combust. Flame 125:752 (2001).
Lin, K.–C. and Faeth, G.M., J. Propulsion and Power 12:691 (1996).
Markatou, P. Wang, H. and Frenklach, M., Combust. Flame 93:467 (1993).
Sunderland, P.B., Axelbaum, R.L., Urban, D.L., Chao, B.H. and Liu, S., Combust. Flame 132:25 (2003).
Takahashi, F. and Glassman, I., Combust. Sci. Tech. 37:1 (1984).
Tesner, P.A. and Shurupov, S.V., Combust. Sci. Tech. 92:71 (1993).
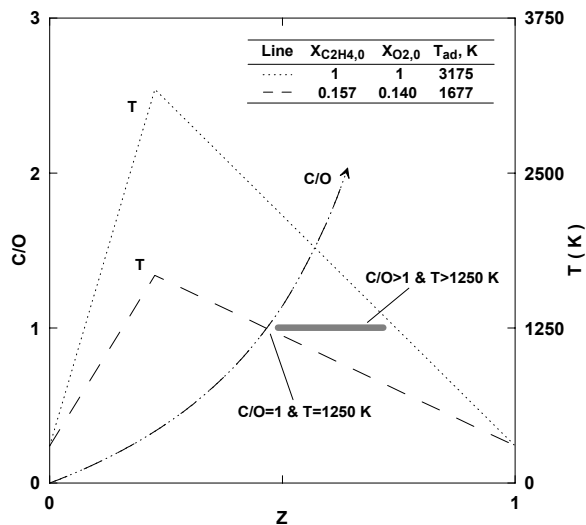
Fig. 1. Profiles in mixture-fraction space of T_{ad} and C/O ratio for two flames with $Z_{st} = 0.226$ but different flame temperatures. The Burke Schumann assumptions have been made. The horizontal bar indicates the region of potential soot inception for the high temperature flame. Such a region does not exist for the low temperature flame.
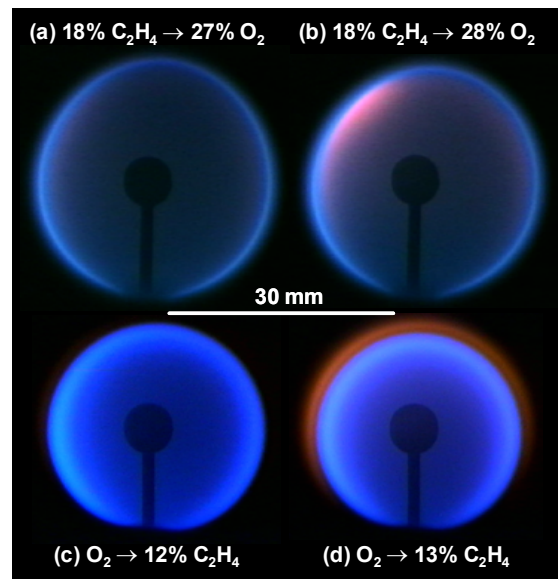
Fig. 2. Color images of representative flames below the sooting limit (a and c) and at the sooting limit (b and d) for convection toward oxidizer (a and b) and convection toward fuel (c and d). Images were taken just before drop termination.
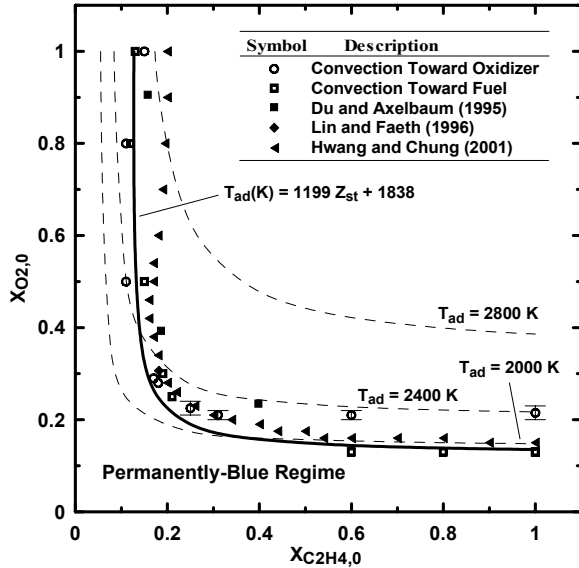
Fig. 3. Oxygen mole fraction versus ethylene mole fraction in the supply gases at the sooting limit for the present flames and for published normal-gravity flames.
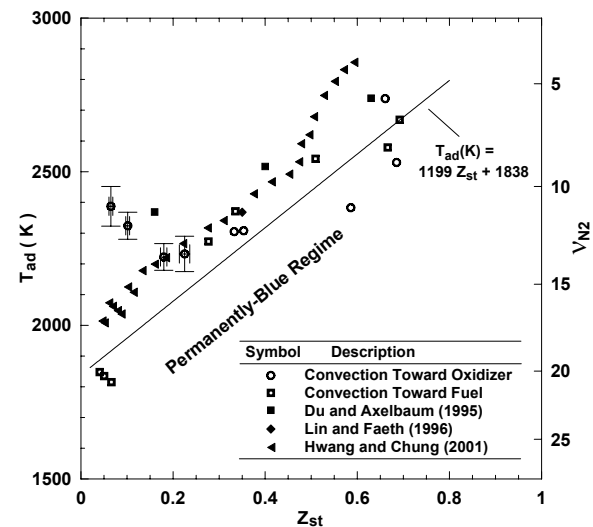
Fig. 4. Adiabatic flame temperature versus stoichiometric mixture fraction at the sooting limit for the present flames and for published normal gravity flames. The ordinate symbol ν_{N2} is associated with the stoichiometry of $C_2H_4 + 3O_2 + \nu_{N2}N2 \rightarrow$ products, and corresponds to the T_{ad} shown.

COSMIC: CARBON MONOXIDE AND SOOT IN MICROGRAVITY INVERSE COMBUSTION

Mikofski, M.A.
University of California, Berkeley
Blevins, L.G.[*]
Sandia National Laboratories
Davis, R.W., Moore, E.F., Mulholland, G.W.
National Institute of Standards and Technology

INTRODUCTION

Almost seventy percent of fire related deaths are caused by the inhalation of toxins such as CO and soot that are produced when fires become underventilated.(1) Although studies have established the importance of CO formation during underventilated burning,(2) the formation processes of CO (and soot) in underventilated fires are not well understood. The goal of the COSMIC project is to study the formation processes of CO and soot in underventilated flames. A potential way to study CO and soot production in underventilated flames is the use of inverse diffusion flames (IDFs). An IDF forms between a central air jet and a surrounding fuel jet. IDFs are related to underventilated flames because they may allow CO and soot to escape unoxidized. Experiments and numerical simulations of laminar IDFs of CH_4 and C_2H_4 were conducted in 1-g and μ-g to study CO and soot formation. Laminar flames were studied because turbulent models of underventilated fires are uncertain. Microgravity was used to alter CO and soot pathways. A IDF literature survey, providing background and establishing motivation for this research, was presented at the 5th IWMC.(3) Experimental results from 1-g C_2H_4 IDFs and comparisons with simulations, demonstrating similarities between IDFs and underventilated fires, were presented at the 6th IWMC.(4) This paper will present experimental results from μ-g and 1-g IDFs of CH_4 and C_2H_4 as well as comparisons with simulations, further supporting the relation between IDFs and underventilated flames.

EXPERIMENTAL AND COMPUTATIONAL METHODS

Microgravity was attained in the 2.2 Second Drop Tower at the NASA Glenn Research Center. Normal gravity tests were conducted at UC Berkeley. Experiments were performed using the COSMIC rig, a standard NASA drop-tower rig, on which the experimental apparatus was mounted. Flames were stabilized on a burner with a 1 cm central tube surrounded by a concentric annulus with an outer diameter of 3 cm. The burner was mounted inside a standard NASA 27 liter combustion chamber. A ni-chrome wire suspended above the burner was used to ignite the IDF. Temperature measurements were made with a fine wire S-type thermocouple positioned 3.5 cm above the burner. A thin-film thermopile radiometer with a CaF_2 window was positioned adjacent to the flame with its face parallel to the axis of symmetry in order to collect radiation from flames up to 8 cm in height. A camera mounted outside the chamber window was used to record images. Fuel and air were stored in 500 cc storage bottles. Gas flow rates were measured by mass flow meters and controlled by fine metering valves. Solenoids valves were used to open and close the fuel and air lines. A NASA Droppable Data Acquisition and Control System (DDACS) was programmed to control the rig and store data. A NASA Power Distribution

Module (PDM) distributed power to the DDACS, the camera, the igniter, pressure transducers, the mass flow meters and the solenoid valves from two 24 volt NASA batteries.

For CH_4 the mass flow rate was 41.6 mg/s (10 cm/s average velocity) with an air mass flow rate of 47.2 mg/s (50 cm/s), and for C_2H_4 the flow rate was 49.1 mg/s (7 cm/s) with an air mass flow rate of 31.9 mg/s (35 cm/s). The air to fuel velocity ratio was constant, 5:1, for both flames. The chamber was evacuated to 0.2 psia and filled with N_2 to 1 atm to prevent secondary flames from forming between the fuel and any air in the chamber. For μ-g tests, the igniter was triggered at the beginning of the drop. For 1-g tests, the igniter was triggered manually. Thermocouple and radiometer voltages were recorded during the test. After 2.1 seconds, the igniter was de-energized and the fuel and air lines closed. A post-test sampling system was then used to analyze the CO concentration of the combustion products and to collect soot samples on quartz filters. The combustion products were passed through a pump, a quartz filter, a non-dispersive IR CO analyzer, and back to the chamber in a closed loop until the CO concentration reached a steady state. The soot mass from μ-g tests was determined using a carbon burn-off technique. Filters from 1-g tests were weighed before and after sampling to deduce the soot mass.

Calculations were carried out using direct numerical simulation of the time-dependent Navier Stokes and conserved variable equations for an axisymmetric laminar flame.(5) The simulation employs assumptions of low Mach number, infinite-rate chemical kinetics, unity Lewis number, variable thermophysical properties, a semi-infinite surrounding fuel-stream, and negligible radiation heat transfer. Dilute-condition particle tracking incorporating the effects of inertial, thermophoretic, and gravitational forces is included to show basic IDF particle pathways and time-temperature histories.(6) Particles were introduced at axial positions of 0 mm, 5 mm, 10 mm, 15 mm, and 20 mm above the burner, and at radial positions corresponding to a characteristic soot formation temperature of 1250 K.(7)

RESULTS AND CONCLUSIONS

An examination of the images shown in Figs. 1 and 2 reveals that both flames were longer, more rounded, and more luminous in μ-g, and that the CH_4 flame was longer than the C_2H_4
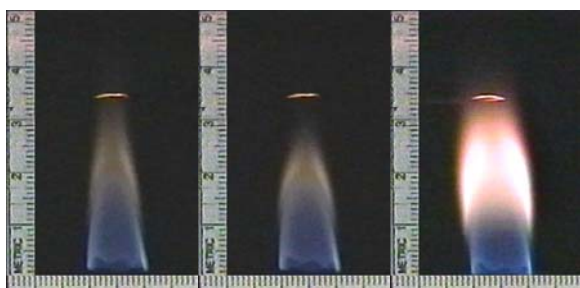
(a) 1-g   (b) 1-g   (c) μ-g

Fig. 1. CH_4 IDFs (f/#8).
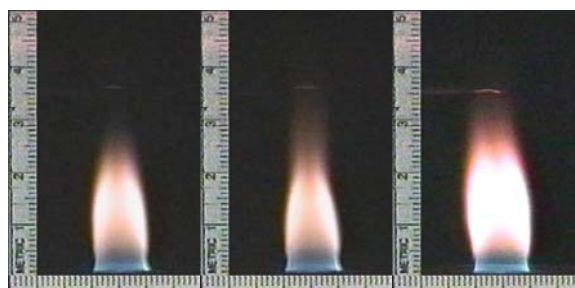
(a) 1-g   (b) 1-g   (c) μ-g

Fig 2. C_2H_4 IDFs (f/#16)

flame for both 1-g and μ-g. The CH_4 1-g flame is mostly blue and has a faint orange cap, while the C_2H_4 1-g flame is covered by an orange annular region for most of its length. Both μ-g flames are covered by a luminous orange annular region. In addition, the 1-g flames flickered (two states of flickering are shown in the figures), but the μ-g did not. The temperature and radiometer data, shown in Fig. 3 and Table 1, indicate that both flames reached steady state faster

and radiated more in μ-g. The 1-g flickering is also visible in the thermocouple signal shown in Fig. 3

Table 1. Average measured and predicted data for CH$_4$ and C$_2$H$_4$ 1-g and μ-g IDFs

T_m = measured temperature, 3.5 cm above flame, T_p = predicted temperature, 3.5 cm above flame, H_p = predicted flame height

Fuel	Gravity	Radiometer	T_m	T_p	H_p	[CO]	[CO]/[CO$_2$]	m_{soot}
		V	K	K	cm	ppm		μg
CH$_4$	1-g	0.96 ± 0.02	1209 ± 5	1699	2.1375	167 ± 3	0.80 ± 0.02	25
CH$_4$	μ-g	2.2 ± 0.02	1223 ± 51	1734	2.2725	180 ± 4	0.92 ± 0.04	12
C$_2$H$_4$	1-g	0.77 ± 0.02	1072 ± 8	1592	1.4625	261 ± 1	3.31 ± 0.05	33
C$_2$H$_4$	μ-g	1.6 ± 0.04	1129 ± 24	1653	1.5075	262 ± 6	3.52 ± 0.38	43
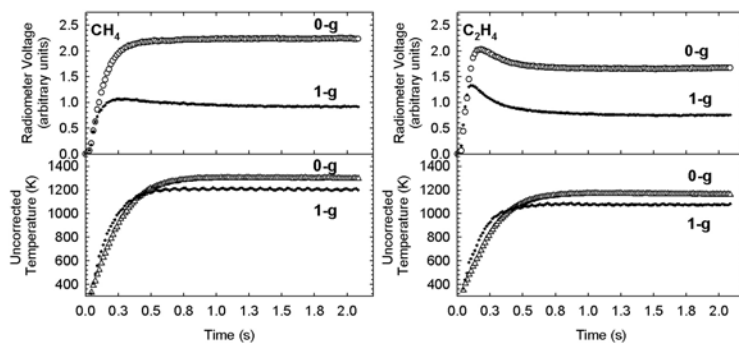
Fig. 3. Radiometer and thermocouple measurements

Post-test data are displayed in Table 1. Measured CO concentrations of the post-test gases from both flames in 1-g and μ-g were significant with [CO]/[CO$_2$] ratios on the order of 1 for CH$_4$ and 3 for C$_2$H$_4$. The CO to CO$_2$ concentration ratio of laminar, underventilated normal flames was measured to be 1:2 in a previous study.(8) Soot collected from both CH$_4$ and C$_2$H$_4$ μ-g flames displayed a spike in the low-temperature phase of the carbon burn-off analysis, qualitatively indicating that a fraction of the soot was made of volatile organics, similar to the soot of underventilated flames. The analysis of the soot from the μ-g C$_2$H$_4$ flame showed a spike in the high-temperature phase, indicating that the soot was also partially carbonized, whereas the μ-g CH$_4$ was flat in that region, indicating that it was mostly organic. The soot mass collected from C$_2$H$_4$ flames was greater in μ-g, but surprisingly the soot mass from CH$_4$ flames was less in μ-g, despite the larger CH$_4$ soot cap. However, different techniques were used to deduce the soot mass, and the number of data points was statistically insufficient for conclusions to be made.

The simulation results shown in Fig. 4 and Table 1 agree well with the experimental observations, predicting similar trends in flame height, shape, and temperature. The predicted particle pathways obtained from the simulations demonstrate that the particles move away from the flame for both flames in μ-g. The time-temperature histories shown in Fig. 5 demonstrate that the particles for both flames are accelerated by buoyancy in 1-g,
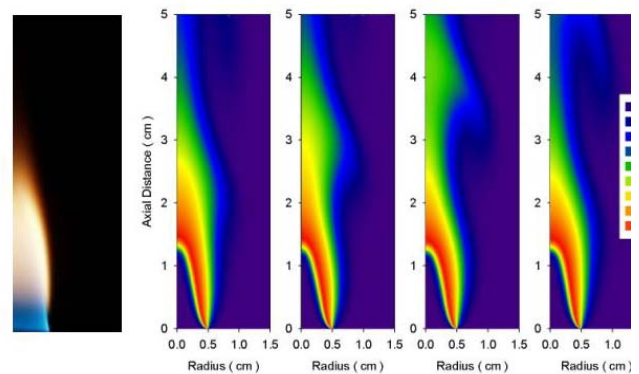
Fig. 4. Photo and calculated temperature profiles for 1-g C$_2$H$_4$ flame.

that the C_2H_4 particles experience reheating due to buoyancy-induced flickering, and that the temperatures of particles in both μ-g flames decrease monotonically with time.
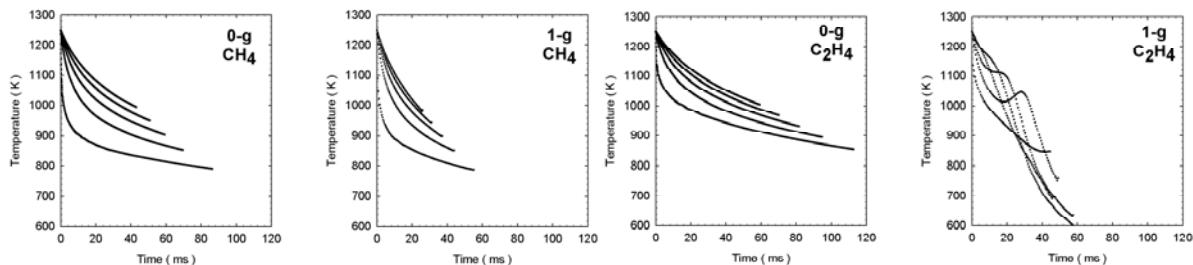
Fig. 5. Time/temperature history of particles in 0-g and 1-g CH₄ and C₂H₄ IDFs.

SUMMARY AND FUTURE PLANS

Experiments and simulations of 1-g and μ-g CH₄ and C₂H₄ IDFs have been conducted. Predicted flame heights, temperatures and shapes of IDFs correlate well with experiments. IDFs produce significant concentrations of CO, and the soot from IDFs is partially organic, which support the hypothesis that IDFs are similar to underventilated flames. Microgravity was used to alter the way IDFs behave. More drop tower experiments are planned to study soot structure and chemical composition. The results should provide insight into the formation mechanisms of undesirable CO and soot during underventilated combustion.

ACKNOWLEDGEMENTS

REFERENCES

1. Hall, J. R. Jr., National Fire Protection Association (NFPA), Quincy, MA, 1996.
2. Pitts, W. M., *Progress in Energy and Combustion Science*, Vol. 21, No. 3, 1995, pp. 197-237.
3. Blevins, L. G., Mulholland, G. W., and Davis, R. W., *Proceedings of the Fifth International Microgravity Combustion Workshop, NASA/CP-1999-208917*, NASA, Cleveland, 1999, pp. 479-481.
4. Blevins, L. G., Fernandez, M. G., Mulholland, G. W., Davis, R. W., Moore, E. F., Steel, E. B., and Scott, J. H. J., *Proceedings of the Sixth International Microgravity Combustion Workshop*, NASA, Cleveland, Ohio, 2001.
5. Davis, R. W., Moore, E. F., Santoro, R. J., and Ness, J. R., *Combustion Science and Technology*, Vol. 73, No. 4-6, 1990, pp. 625-635.
6. Davis, R. W., Moore, E. F., and Zachariah, M. R., *Journal of Crystal Growth*, Vol. 132, No. 3-4, 1993, pp. 513-522.
7. Du, J. and Axelbaum, R. L., *Combustion and Flame*, Vol. 100, No. 3, 1995, pp. 367-375.
8. Leonard, S., Mulholland, G. W., Puri, R., and Santoro, R. J., *Combustion and Flame*, Vol. 98, No. 1-2, 1994, pp. 20-34.

MICROGRAVITY SUPERAGGLOMERATES PRODUCED BY SILANE AND ACETYLENE

Matthew Bundy, George W. Mulholland, Samuel Manzello, Jiann Yang, John Henry Scott
National Institute of Standards and Technology, Gaithersburg, MD, 20899

Yudaya Sivathanu
En'Urga, Inc., West Lafayette, IN 47906.

Introduction

The size of the agglomerates produced in the in the upper portion of a flame is important for a variety of applications. Soot particle size and density effect the amount of radiative heat transfer from a fire to its surroundings. Particle size determines the lifetime of smoke in a building or in the atmosphere, and exposure hazard for smoke inhaled and deposited in the lungs. The visibility through a smoke layer and dectectability of the smoke are also greatly affected by agglomerate size. Currently there is limited understanding of soot growth with an overall dimension of 10 μm and larger. In the case of polystyrene, smoke agglomerates in excess of 1 mm have been observed "raining" out from large fires.

Unlike hydrocarbon fuels, silane has the advantage that silica particles are the major combustion product resulting in a particle volume fraction a factor of ten greater than that for a carbonaceous smoke. There are two very desirable properties of silica aero-gels that are important for both space and earth based applications. The first important property is its inertness to most oxidizing and reducing atmospheres. Therefore, silica aero-gels make excellent fire ablatives and can be used in very demanding applications. The second important property is that silica aero-gels are expected to have very high porosity (greater than 0.999), making them lightweight and ideal for aerospace applications. The added benefit of the high porosity is that they can be used as extremely efficient filters for many earth based applications as well.

Evidence of the formation of superagglomerates in a laminar acetylene/air diffusion flame was found by Sorensen et al. [1]. An interconnecting web of super-agglomerates was observed to span the width of the soot plume in the region just above the flame tip and described as a gel state. It was observed that this gel state immediately breaks up into agglomerates as larges as 100 μm due to buoyancy induced turbulence. Large soot agglomerates were observed in microgravity butane jet diffusion flames by Ito et al.[2]. Several other works to date have studied the effect of flame structure on soot volume fraction and agglomeration size in a microgravity environment.[3-4]. In microgravity the absence of buoyant convective flows increases the residence time in the flame and causes a broadening of the high temperature region in the flame. Both of these factors play a significant role in gas phase radiation and soot formation

Experimental Hardware

Experiments were performed using a combustion "drop rig" that was designed for use at NASA Glenn's 2.2 second drop tower facility. The hardware consisted of a 25 L combustion chamber, an open tube burner, a gas flow control system, an electrical system and an imaging

system. The burner consisted of a 4.52 mm diameter stainless steel tube positioned along the centerline 15 cm above the base of the chamber. Two CCD video cameras were used to image the flame and soot plume. Illumination for imaging the agglomerates was provided using a microsecond Xenon flashlamp. A 0.25 mm diameter Kanthol hot-wire was used to ignite the flame. Pressure transducers were used to monitor the fuel bottle and combustion chamber pressure. Rotary solenoids were used to position the ignition wire and TEM sampling grid.

Normal Gravity Experiments

Acetylene and silane was burned in the standard NASA cylindrical combustion chamber. A digital camera with backlighting through a diffuser was used to photograph both the flame and smoke plume as illustrated in the lower portions of the Figure 1. The photographs show the

a   b   c   d   e   f
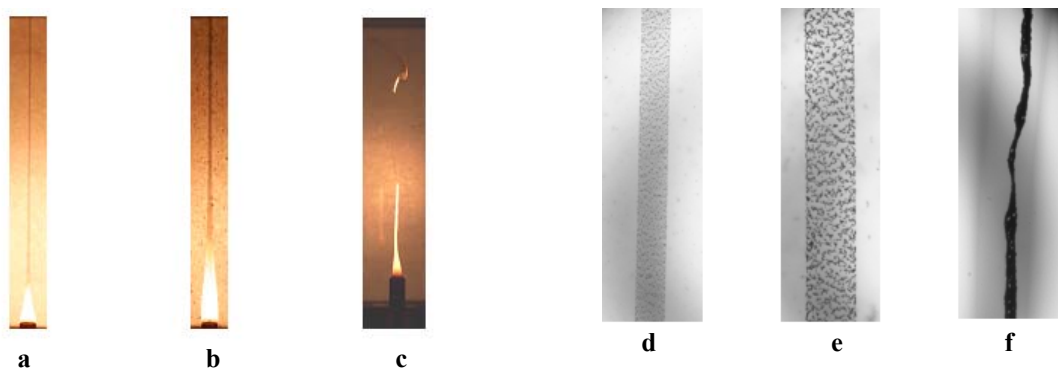
Figure 1. Photograph of acetylene and silane flames in normal gravity.

flame and plume for an acetylene fuel flow rate of 0.66 cm^3/s, 2.10 cm^3/s, and for a silane flow rate of 2.1 cm^3/s (a, b and c respectively). The series of photographs (d, e, and f) in Fig. 2 were taken at a location about 9 cm from the burner exit with the digital camera and a Xenon flash lamp with a pulse duration of 1.3 μs and a pulse energy of 0.35 J to "freeze" the motion of the soot agglomerates. At the lower flow rate the soot appears as a relatively gray background while at the larger flow, individual 50 μm to 100 μm particles appear to be connected across much of the plume. Other noteworthy features are the increasing plume width with increasing fuel flow rate and the sharpness of the smoke boundary. For the silane flames, filaments were observed leaving the flame zone rather than superagglomerates such as for acetylene. A μs flash photograph of a filament 9 cm above the flame is shown in Fig. 1c.

Fibrous particles were examined with a stereomicroscope (Fig 2a) and a field emission scanning electron microscope (Fig. 2b). The SEM micrograph shows evidence of partially fused spherule structures with diameters as small as 150 nm. We expected that the much larger particulate volume fraction for the silane flame would lead to a totally interconnected gel-like structure and were surprised to observe a fibrous material. It is likely that the combination of the higher flame temperature for silane combustion together with the lower melting point of SiO_2 particulate has resulted in the formation of the partially fused filaments. An interesting hollow cage-like structure, shown in Fig. 2c was produced when the fuel line was purged with a pulse of nitrogen at the end of the experiment. This suggests that varying the flame temperature by diluting the silane will likely be important in controlling the morphology of the silane particles.
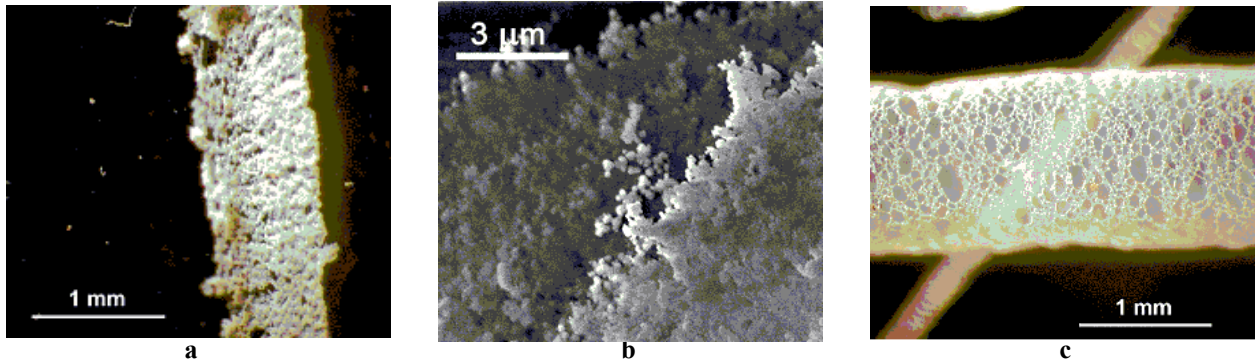
Figure. 2. Optical micrograph of silica fiber.

Microgravity Acetylene Experiments

Microgravity experiments were performed in a 2.2 second drop tower using acetylene at flow rates of 0.6 cc/s, 1.0 cc/s and 2.0 cc/s. Fig. 3 (a and b) shows images of the acetylene flames and soot plumes recorded during the microgravity experiments. The microgravity flame was three times as wide as the normal gravity flame.
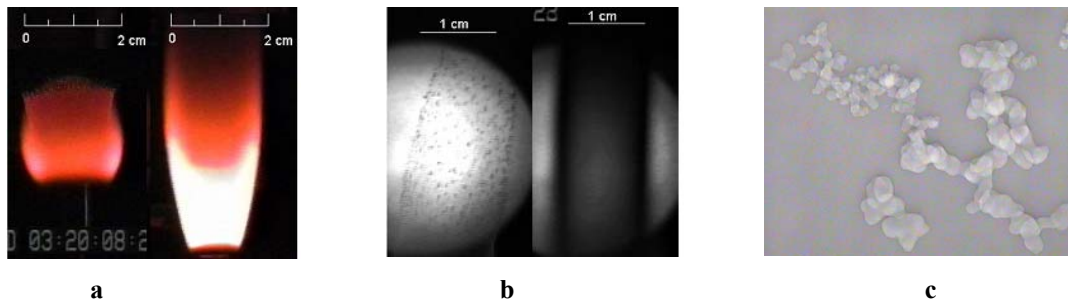
Figure 3. Images of acetylene flame and the soot plume and a TEM photo.

Although detailed measurements of the agglomerate size were not possible due to the low image resolution, approximate particle sizes were attained in the post flame region between 2.5 cm and 5.5 cm above the burner. Microgravity superagglomerates as large as (1.2 ± 200) mm were observed in these experiments. Another noteworthy observation is apparent from inspection of the flame video in slow motion. It appears that superagglomerates can be seen escaping from the open flame tip annulus in the μG flames at acetylene flow rates of 0.6 cc/s and 1.0 cc/s. This suggests that the large soot agglomerates are formed in the high temperature region of the flame. Detailed measurement of the primary particle size distribution was performed for soot sampled at three flame conditions at a location of 25 mm above the burner duct. At least 100 primary spheres were analyzed for each condition. The diameter of the primary particles for the 2.0 cc/s flame was measured to be (45.4 ± 10.2) nm in μ-g and (40.0 ± 11.4) nm in 1-g. A digitized TEM micrographs for soot particles sampled above the 1.0 cc/s acetylene flame in microgravity is shown in Fig. 9. Inspection of this image clearly shows clusters formed from 2 different primary particle sizes measured to have diameters of (16.3 ± 5) nm and (43.0 ± 9) nm. This feature was found throughout the entire TEM grid with a slightly higher number of small particle clusters, however since only a single TEM grid was collected for this condition the nature and generality of this bimodal feature is uncertain.

Numerical Simulations

Temperature and soot volume fraction contours for normal gravity and microgravity acetylene flames were calculated [8,9]. These results were consistent with the qualitative observations from the μG experiments. The calculations of the soot volume fraction and temperature field in the flame zone/plume together with the calculation of the particle position versus time provides the necessary input to estimate the agglomerate growth for the case of a 1 cm^3/s acetylene flow rate [10]. Our agglomeration simulations suggest than free molecular coagulation together with gelation are too slow to produce superagglomerates of size greater than 100 μm for 1-g experiments. The simulations predict a relatively modest enhancement in the agglomeration as the gel point is approached for the free molecular limit. For μ-g conditions, our simulation results predict a maximum agglomerate length of 35 μm based on $f_V=6.0\times10^{-6}$ and a length of 680 μm for $f_V=6.0\times10^{-4}$. For the higher density it is seen that the agglomeration model predicts that agglomerates approaching the critical gel size would form in a flame at μ-g conditions.

Conclusions

1. For the first time in μ-g the emission of soot super-agglomerates from the luminous flame was visually demonstrated by simultaneously imaging the flame and soot plume.
2. The burning of silane at 1-g results in novel structures including fibers and cage-like structures depending on the time/temperature history for the particles in the flame.
3. The flame calculations show an increased residence time in μ-g which helps explain enhanced agglomerate growth.
4. A soot agglomerate model based on Brownian motion can not account for the superagglomerates observed in acetylene flames at 1-g.

Acknowledgements

References

[1] Sorensen, C.M., Hageman, W.B., Rush, T.J., Huang, H., Oh, C., *Phys. Rev. Lett*.,80:1782 (1998).
[2] Ito, H., Fujita, O., Ito, K., *Combustion and Flame*, 99:363 (1994).
[3] Ku, J.C., Tong, L., Sun, J., Greenberg, P.S., Griffin, D.W., *Proceedings of the Second International Microgravity Combustion Workshop*, 121 (1992).
[4] Koylu, U.O. and Faeth, G.M., *Combustion and Flame*, 89:140 (1992).
[5] Sivathanu, Y.R. and Gore, J.P., *Combustion and Flame*, 97: 161 (1994).
[6] Leung, K.M., Lindsted, and Jones, W.P., *Combustion and Flame*, 87:289 (1991).
[7] Mulholland et al., *Energy and Fuels*, 2, 481-486 (1988).

EFFECT OF GRAVITY ON POROUS TRICALCIUM PHOSPHATE AND NONSTOICHIOMETRIC TITANIUM CARBIDE PRODUCED VIA COMBUSTION SYNTHESIS

M. Castillo, J. J. Moore, F.D. Schowengerdt, R.A. Ayers
Center for Commercial Applications of Combustion in Space (CCACS), Colorado School of Mines, 1500 Illinois St., Golden, Colorado 80401, USA

ABSTRACT

Novel processing techniques, such as self-propagating high temperature synthesis (SHS), have the capability to rapidly produce advanced porous materials that are difficult to fabricate by other methods. This processing technique is also capable of near net shape synthesis, while variable gravity allows the manipulation of the structure and composition of the material. The creation of porous tricalcium phosphate (TCP) is advantageous in the biomaterials field, since it is both a biocompatible material and an osteoconductive material. Porous tricalcium phosphate produced via SHS is an excellent candidate for bone scaffold material in the bone regeneration process. The porosity allows for great vascularization and ingrowth of tissue. Titanium Carbide is a nonstoichiometric biocompatible material that can be incorporated into a TiC-Ti composite system using combustion synthesis. The TiC-Ti composite exhibits a wide range of mechanical and chemical properties. Both of these material systems (TCP and TiC-Ti) can be used to advantage in designing novel bone replacement materials. Gravity plays an important role in both the pore structure and the chemical uniformity of these composite systems and offers considerable potential in advanced bone engineering.

INTRODUCTION

New and novel bone replacement materials are currently being investigated at the Colorado School of Mines through the process of self-propagating high temperature synthesis (SHS). SHS with its rapid kinetics allows the production of near net-shaped samples. This process is highly exothermic and can allow for difficult intermetallic and porous materials to easily be manufactured. The processing parameters include green density, gasifying agents, reaction stoichiometry, and gravity. Green density is the initial density of the reactants and allows for control over the final apparent porosity. Gasifying agents also allow for the generation of additional pores. Gasifying agents are selected so that they evolve and do not contaminate the sample or change the desired final stoichiometry of the products. Reaction stoichiometry controls the combustion temperature and the final composition of the sample. Furthermore, the final composition can be graded from the reaction stoichiometry. Gravity plays a role in the morphology of the pores and final graded structure. SHS performed in microgravity will affect samples that are sensitive to cooling rates. The samples manufactured in microgravity experience heat loss only through radiation since convection is lost. The addition of gravity will affect samples that have a liquid-solid reaction through gravity-driven fluid flow (in terrestrial conditions). All SHS processing parameters focus on the control of porosity and composition, which are critical when designing a biomaterial.

The current state of the art bone implants are in dire need of improved design and functionality. Current implants lack mechanical properties that match the properties of bone.

The production of porous implants will lead to a more graded implant in-vivo that will be engineered to grade the mechanical properties of the bone with those of the implant and thereby reduce the occurrence of stress shielding. Peters et al. have recently discussed the possibility of combining materials and properties to make functionally graded materials in order to improve implant material [1].

In those cases in which it may not be necessary to match the mechanical properties of the bone, a porous resorbable material can be used as the alternative. Porous resorbable materials provide a scaffold onto which the bone can remodel and resorb. An optimum level of porosity allows for easy vascularization and infiltration of tissue into the pores. Although this latter resorbable scaffold may lack the necessary mechanical properties required of an implant, this problem can be overcome with external devices that maintain the integrity of the injured area during the bone remodeling process.

EXPERIMENTAL PROCEDURE

SHS is conducted by mixing the reactants in the desired reaction stoichiometry for 8 hours to ensure thorough mixing. Prior to mixing, temperature-enthalpy calculations are performed to determine the adiabatic temperature for the reaction [2]. The adiabatic temperature is the maximum achievable theoretical temperature generated in the SHS reaction with no heat loss from the system. The TCP system requires that all processing be performed in an inert atmosphere (i.e. glovebox). TCP is created by mixing and reacting calcium oxide (CaO) and phosphorus pentoxide (P_2O_5), - a highly hygroscopic material. The mixtures are either pressed to a desired relative green density or poured into a paper mold as a loose powder mixture, depending on the desired green density. Each sample is reacted in an inert atmosphere and the reaction is initiated via a tungsten resistance coil at the bottom of the sample, with the propagation wave traveling upwards. Samples are made into cylinders that have a height of 2.54 cm and a diameter of 1.27 cm (2:1 aspect ratio). Physical data for the reactant powders are listed in Table 1:

Table 1. Physical data for the reactant powders.

	CaO	P_2O_5	Ti	C
Particule Size (μm)	<45	<94	<45	<45
Purity (%)	99.99	99.9	99.998	99.5
Melting Point (°C)	2888		1660	
Sublimation Point (°C)		631		3652 - 3697
Molecular Mass (g/mol)	56.07	141.92	47.87	12.01

All microgravity experiments were conducted aboard the NASA KC-135 low-G flight research aircraft in parabolic flight patterns that typically achieve ~15-20 seconds of low gravity and ~20 seconds of high (2G) gravity. A special flight rack (COSYM) was used to conduct the experiments and to obtain the experimental data (i.e. video, temperature, pressure). The reacted products were characterized using a Philips Quanta 600 environmental SEM. Apparent porosity measurements were conducted according to ASTM Designation C20-92.

RESULTS AND DISCUSSION

XRD analysis confirmed that the alpha phase of tricalcium phosphate had been produced via SHS. Shown below in Figure 1 (A), the scanning electron microscope (SEM) photomicrograph exhibits the highly porous morphology of the SHS-produced TCP. Typical bone exhibits a bimodal distribution of pores in which the finer pores range from 100-300 microns and the larger ones are on the order of millimeters. The SHS produced TCP exhibits both ranges of pores. Figure 1 (B) shows TCP produced aboard the NASA KC-135 (low-G flight) while the Figure 1 (C) shows TCP produced under terrestrial conditions (1G). SHS of TCP in microgravity displays typical hexagonal type grain growth and the lack of gravity allows nuclei to be unrestrained. TCP produced in terrestrial conditions exhibits lamellar type growth, where gravity dictates the pattern or direction of lamellar grains. The characteristic spots shown in Figure 1 (C) were determined by Valdés et al. to be calcium pyrophosphate ($Ca_2P_2O_7$) quenched at the surface [3].
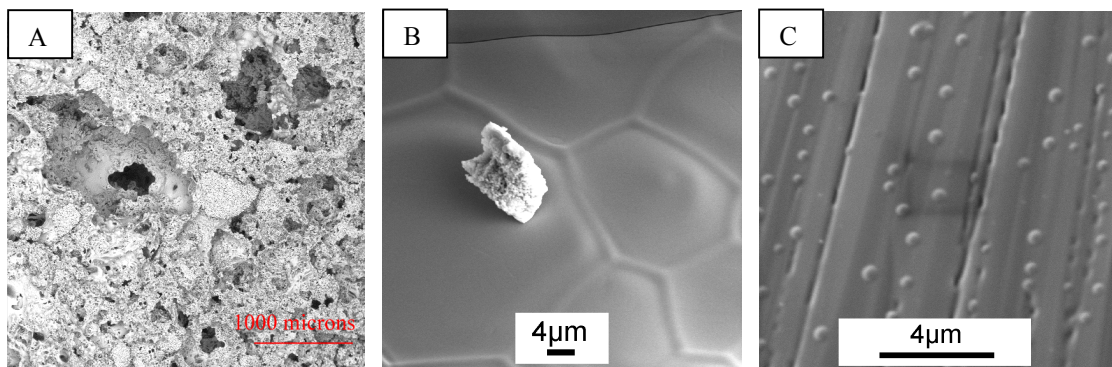
Figure 1. SEM photomicrograph of SHS produced TCP. A and C are manufactured in terrestrial conditions and B is produced aboard the NASA KC-135 (low-G plane).

SHS was conducted on TiC type materials under terrestrial conditions at the Colorado School of Mines. The SHS reactant system studied is $(1+x)Ti + C$, where $x = 0, 0.5, 1.0,$ and 1.5. Reactions that are able to propagate are shown below in the Table 2. Due to the high thermal conductivity of the reactants, this system is able to react in relatively loose powder conditions that generates a 30% relative green density. Higher relative green densities would not sustain the SHS reaction in propagating mode due to heat being dissipated too rapidly from the combustion front.

Table 2. Successful SHS reactant combinations for the TiC_x system.

	Relative Green Density			
x	30%	40%	45%	50%
0.0	X	X	X	X
0.5	X	X	X	
1.0	X	X		
1.5	X			

It has been shown from previous research that these reactant combinations have the potential to produce nonstoichiometric TiC_x [2]. The phase diagram for TiC shows a homogeneous region where TiC_x can be produced in the range of $0.47 \leq x \leq 1.0$ [3]. The composition of the SHS-produced TiC is currently under investigation to produce evidence of nonstoichiometric titanium

carbide and the possibility of a gravity-driven, functionally graded material (FGM). There is a significant amount of liquid Ti formed during the reaction and it may be expected to see a gradient of Ti that would settle towards the bottom of the sample due to gravity.
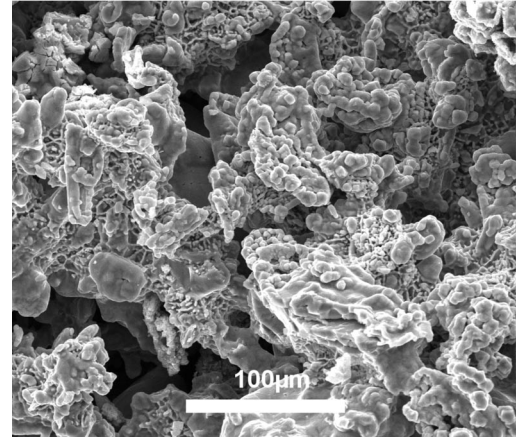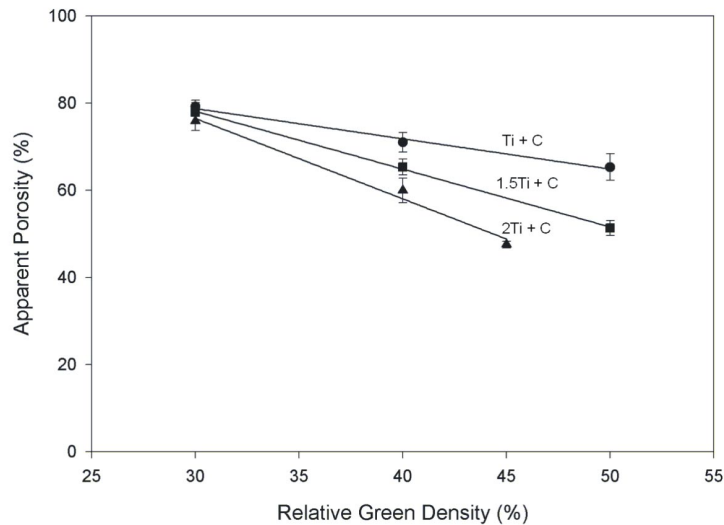
Figure 2. Relative green density vs. apparent porosity for the TiC reactions.

Figure 3. SEM photomicrograph of the reaction 2.5Ti + C

Figure 2 shows how relative green density can affect the apparent porosity of the final sample. When designing an implant, careful considerations involving porosity and distribution of pores are critical. This analysis provides a means of designing a porous FGM implant in which the porosity gradient can be tailored to meet both mechanical property and bone growth requirements.

The SEM photomicrograph shown in Figure 3 exhibits the porous microstructure of these materials. This photomicrograph is for the 2.5Ti + C reaction (30% relative green density) and has a porosity that fits into the range of that in natural bone. There are very fine micro and nano size pores that are not visible in the photomicrograph. A detailed analysis of the composition of the material may result in surface compositions that are conducive to osseointegration with the implant material.

REFERENCES
1.0 F. M. Peters, C. Schiller, M. Siedler, Functionally graded materials of biodegradeable polyesters and bonelike calcium phosphate for bone replacement, Functionally Graded Materials 2000, Ceramic Transactions, 114, (2000) p. 97-107.
2.0 J. J. Moore, An examination of the thermochemistry of combustion synthesis reactions, Processing and Fabrication of Advanced Materials III, The Minerals, Metals & Materials Society, (1994) p. 817-831.
3.0 V. P. Gortcheva, , G. R. Morales, J. J. P. Valdés, et al., Fibrous growth of tricalcium phosphate ceramics, J. of Mat. Sci.: Mat. in Medicine, 8, (1997) p. 297-301.
4.0 Z. A. Munir, J. B. Holt, Combustion synthesis of titanium carbide theory and experiment, J. of Mat. Sci., 21, (1986) 251-259.
5.0 E. K. Storms, The refractory carbides, Academic Press, New York, (1967) p. 3.

Mechanistic Studies of Combustion and Structure Formation during Combustion Synthesis of Advanced Materials: Phase Separation Mechanism for Bio-Alloys

A. Varma, C. Lau and A. Mukasyan

Department of Chemical Engineering
and Center for Molecularly Engineered Materials
University of Notre Dame
Notre Dame, IN 46556

INTRODUCTION. Among all implant materials, Co-Cr-Mo alloys demonstrate perhaps the most useful balance of resistance to corrosion, fatigue and wear, along with strength and biocompatibility [1]. Currently, these widely used alloys are produced by conventional furnace technology. Owing to high melting points of the main alloy elements (e.g. $T_{m.p.}$(Co) ~1768 K), high-temperature furnaces and long process times (several hours) are required. Therefore, attempts to develop more efficient and flexible methods for production of such alloys with superior properties are of great interest.

The synthesis of materials using combustion phenomena is an advanced approach in powder metallurgy [2]. The process is characterized by unique conditions involving extremely fast heating rates (up to 10^6 K/s), high temperatures (up to 3500 K), and short reaction times (on the order of seconds). As a result, combustion synthesis (CS) offers several attractive advantages over conventional metallurgical processing and alloy development technologies. The foremost is that solely the heat of chemical reaction (instead of an external source) supplies the energy for the synthesis. Also, simple equipment, rather than energy-intensive high-temperature furnaces, is sufficient.

This work was devoted to experiments on CS of Co-based alloys by utilizing thermite (metal oxide-reducing metal) reactions, where phase separation subsequently produces materials with tailored compositions and properties. Owing to high reaction exothermicity, the CS process results in a significant increase of temperature (up to 3000 °C), which is higher than melting points of all products. Since the products differ in density, phase separation may be a gravity-driven process: the heavy (metallic phase) settles while the light (slag) phase floats. The goal was to determine if buoyancy is indeed the major mechanism that controls phase segregation.

RESULTS AND DISCUSSION. Fundamental studies of phase separation during CS of Co-based alloys were carried out in both terrestrial and microgravity conditions. The details of the experimental set-up, as well as used procedure, are described elsewhere [cf. 3,4]. Briefly, the samples were placed in the reaction chamber, which was evacuated (approximately 10^3 Pa) and then filled with high-purity argon to 10^5 Pa. An electrically heated tungsten coil was used to initiate the combustion reaction, typically from top of the sample. The combustion front propagation was recorded through a quartz window by using a video camera. The velocity of wave propagation was determined by statistical analysis of the obtained video images (30 frames/s). The temperature-time history of the process was measured by thermocouples (Type C, diameter 0.508 mm, Omega Eng.). Finally, quenching, which involves rapid cooling of the combustion front in massive copper cone-shaped block, was utilized to investigate the mechanisms of microstructural transformation taking place during CS.

While the Co-based alloy used in orthopaedic implants contains other metals such as Cr and Mo [1], for a fundamental study of phase separation, the simpler Co_3O_4-Al system was used in the present work. The following overall reaction occurs in the combustion wave front:

$$3Co_3O_4 + 8Al + xCo + yAl_2O_3 \Rightarrow (4+y)Al_2O_3 + (9+x)Co \qquad (1)$$
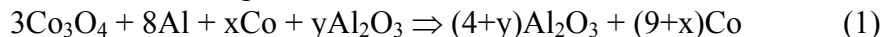
where x and y are coefficients that can be varied to obtain the desired product composition and combustion temperature. Since the metal fraction in melt may be a controlling factor of phase separation process, systems with different ratio of metal and slag were investigated (Table I).

Table I. Characteristics of reaction compositions investigated.

Composition	T_{ad}, K	$T_{m.p.}$, K Al_2O_3	$T_{m.p.}$, K MeO	$T_{m.p.}$, K Me	$T_{m.p.}$, K Al	Metal vol. %
$3Co_3O_4 + 12Co + 8Al \Rightarrow 21Co + 4Al_2O_3$	2690	2327	2123	1768	933	49
$3Co_3O_4 + 8.5Co + 8Al \Rightarrow 17.5Co + 4Al_2O_3$	2966	2327	2123	1768	933	44
$3Co_3O_4 + 3.2Al_2O_3 + 8Al \Rightarrow 9Co + 7.2Al_2O_3$	2677	2327	2123	1768	933	19

Phase Separation. It was shown that the yield, ψ (defined as ratio of the metal product mass to the theoretical metal mass formed from reaction), reaches high values under μg conditions and increases only slightly with gravity (see Table II and also ref. 3). These results suggest that some non-gravity driven phase separation mechanism plays an important role in the CS process of Co-based alloy.

Table II. Average yield (%) of the alloy in different experimental conditions.

Systems	Normal Gravity, 1 g Propagation Direction		Microgravity, 10^{-2} g Propagation Direction	
	Downward	Upward	Downward	Upward
Co (8.5)	83	96	73	86
Co (12)	90	98	73	88

It was also observed that under both gravity and microgravity conditions, after reaction and separation, thin alumina tube formed on the container wall (see Fig.1 for schematic representation). It was also seen that the height of this tube decreases with increase of gravity condition. In fact, under overload conditions (1.7 g), instead of tube an alumina cap forms on top of metal ingot. By making experiments using different container materials, it was shown that alumina tube formed in all cases and that the container material, did not influence the phase separation process (i.e. yield). The following picture of phase separation in the system was thus suggested. The reaction starts at about melting point of Al ($T_{m. p.} = 933$ K), which coats solid metal oxide (Co_3O_4) particles, leading to their dissolution (see next section for details). Further, after reaction when temperature is above melting point of all products, two immiscible liquid phases (Co and Al_2O_3) form (Fig. 2b). In cooling stage, when temperature decreases, Al_2O_3 ($T_{m. p.} = 2327$ K) crystallizes first, while Co ($T_{m. p.} = 1768$ K) remains in liquid form (Fig. 2c). Since at this point, the only solid phase for Al_2O_3 to wet is the container it spreads along its wall (Fig. 2d). From these considerations, it can be concluded that the formation of oxide tube is primarily a characteristic of the system and does not depend strongly on wettability of the container.
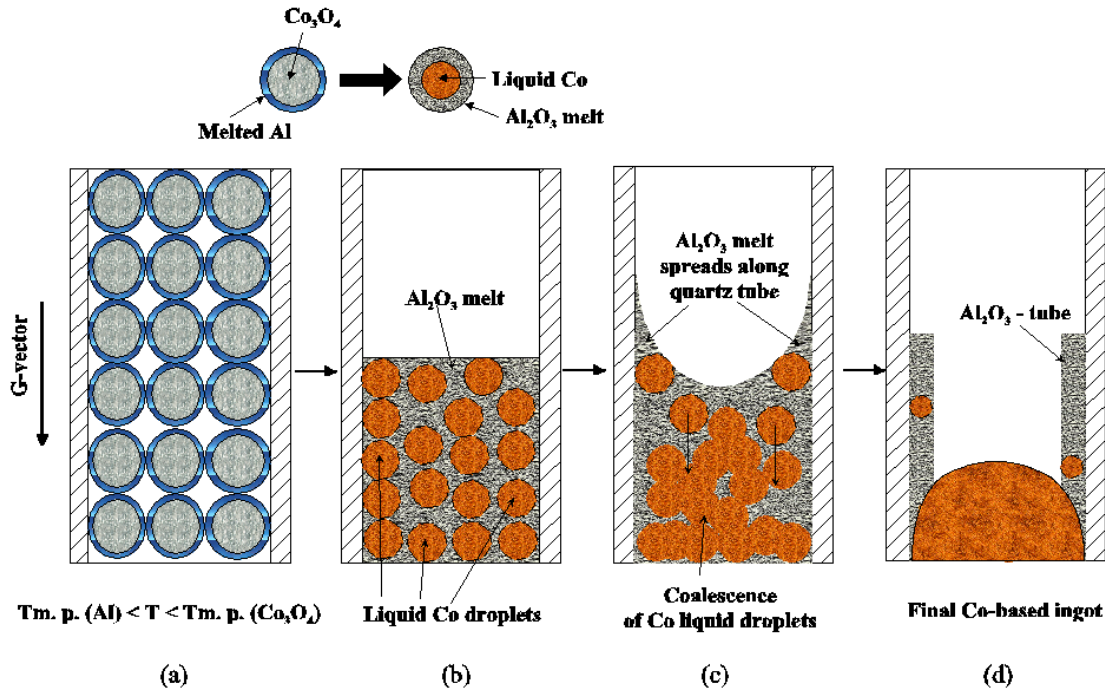
Fig. 1 Schematic representation of structural transformations during combustion in Co-based system.

Mechanism of Reaction and Phase Separation. Investigations of quenched samples reveal that in general, one can identify three characteristic zones: (i) the most dynamic zone of initial products formation; (ii) post-reaction zone of cobalt coalescence; (iii) final product zone. The details of structural transformations in zone (i) are shown in Fig. 2.
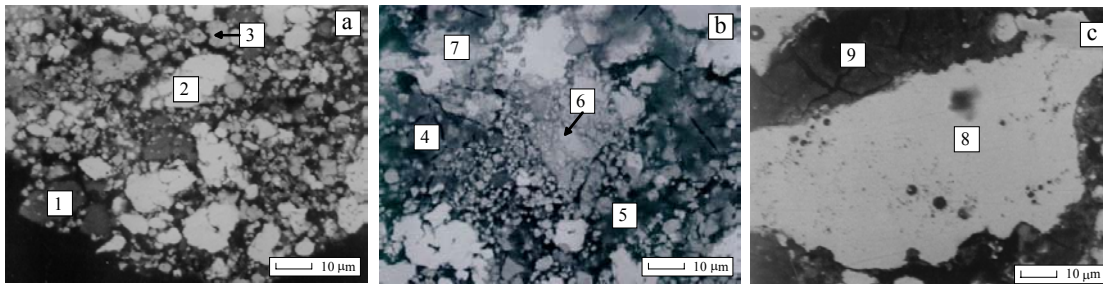
Fig.2 Back-scattered electron images of microstructural transformations in the initial product formation zone: (a) Precursor reactants; (b) Complex oxides and intermetallic compounds; (c) First stage of phase separation. The numbers refer to phases identified in Table III.

It can be seen (Fig. 2a) that initial medium remaining in the cone tip consists of relatively large ($\sim$ 20 μm) Al (phase 1) and Co (phase 2) particles, and finer ($\sim$ 5 μm) Co_3O_4 (phase 3) powder. This is followed by a relatively thin ($\sim$ 300 μm) reaction region, where complex oxides (4, 5) and intermetallic compounds (6, 7) are observed (Fig. 2b). At the end of this region, Co-rich (8) areas surrounded by alumina-rich phases (9) formed rapidly. These observations suggest that reduction of cobalt oxide, as well as metal-metal reactions in the system, occur in this stage due to dissolution of solid Co_3O_4 and Co in liquid aluminum, with formation of various complex phases.

More difficult to understand is the rapid formation of relatively large (~ 100 µm) Co-rich areas (8 in Fig. 2c) surrounded by Al_2O_3 layers (9 in Fig. 2c) at the end of this zone. The above results, along with effective phase separation in microgravity, suggest that the following non-

Table III. Relative intensity of elemental components in combustion zone.

Location	Relative Intensity (%)			Comment
	Al	Co	O	
1	Balance	Trace	Trace	Al
2	Trace	Balance	Trace	Co
3	7.5	72.9	19.6	Co_3O_4
4	23.5	62.1	14.4	Co_xAlO_y
5	14.2	73.7	12.1	Co_xAlO_y
6	44.0	51.2	4.8	$CoAl_x$
7	51.5	46.4	2.1	$CoAl_x$
8	Trace	Balance	Trace	Co
9	76.6	9.6	13.8	Al_2O_3

gravity driven mechanism may be responsible for the observed features. While complex oxides form due to dissolution of Co_3O_4 in liquid aluminum, the process accelerates dramatically at melting point of Co_3O_4 ($T_{m.\ p.} \sim 2100$ K), and at some point concentration of Co in the melt reaches a critical value above which only two immiscible liquids (Co and Al_2O_3) may exist. The latter leads to rapid formation of these liquid phases simultaneously with their separation at the microscopic level. Further segregation of immiscible liquid phases and coalescence of Co agglomerates occurs along an extended (~ 2 cm) post-reaction zone (ii) before reaching the final products region (iii), which involves large areas (~ 5 mm) of Co surrounded by layers of Al_2O_3.

SUMMARY. The obtained results lead to the following general conclusions: (i) non-gravity driven mechanisms play an important role in the phase separation process in such systems [see also 3]. Analysis of microstructural transformations in the quenched samples reveals the true reaction and phase separation mechanisms taking place in the combustion wave. The results show that the segregation process involves two stages: (1) separation of immiscible liquids in the reaction front, and (2) capillary coalescence of liquid metal droplets in solid oxide matrix in the post-reaction zone. These non-gravity driven processes explain the essentially complete phase separation achieved even in microgravity conditions [see also 4]. Based on the general understanding of phase separation mechanism in the investigated CS-systems, a novel technology for synthesis of Co-Mo-Cr bio-alloy has been developed [5].

Acknowledgements

REFERENCES
1. Shetty RH, Ottersberg WH (1995) in: Wise DL, editor. Encyclopedic Handbook of Biomater. and Bioengin., Part B; Applications. New York: Marcel Dekker, pp 509-540
2. Varma A, Mukasyan AS (1998) in: Powder metal technologies and applications, ASM International, Materials Park, Ohio, ASM Handbook, pp.523-540
3. Lau, C., Mukasyan A.S. and A. Varma, *Proc. Comb. Inst.*, 29, (2002).
4. Lau, C., Mukasyan A.S. and A. Varma, *J. Mat. Res.,* 18, 121 (2003).
5. Varma, A., Li, B. and Mukasyan, A., *Adv. Eng. Mater.*, 4, 482 (2002).

A CARBON ARC APPARATUS FOR PRODUCTION OF NANOTUBES IN MICROGRAVITY

J. M. Alford and G.R. Mason
TDA Research, Inc., 12345 W 52nd Ave., Wheat Ridge, CO 80033

D.A. Feikema
NASA Glenn Research Center, Cleveland, OH 44135

ABSTRACT

Although many methods are available for production of single-walled carbon nanotubes (SWNTs), the conventional carbon arc process remains the most popular due to its simplicity and large production rate. However, high temperatures inside the carbon arc generate strong buoyancy driven convection, and it is hypothesized that the non-uniform environment created by this flow will have large effects on the growth and morphology of SWNTs produced by the arc process. Indeed, using normal gravity experiments, Marin *et al*.[1] have demonstrated that changes in the buoyant convection plume produced by altering the arc electrode orientation can be used to change the diameter distribution of the SWNTs produced; an effect they attribute to changes in the temperature of the local nanotube growth environment. While these experiments present convincing evidence that buoyant convection has a strong effect on nanotube growth, normal gravity experiments are severely limited in scope. The ideal way to study the effect of buoyancy on SWNT production is to remove it completely. Toward this goal, a microgravity carbon arc reactor has been designed for use in the NASA Glenn 2.2 and 5 second drop towers. Although simple in principle, conventional carbon arc machines, which generally employ large reaction chambers and require heavy duty welding power supplies capable of supplying kilowatts of power, are not suitable for microgravity experiments. Here we describe a miniature carbon arc machine for SWNT production that fits into a conventional drop rig for use on the NASA Glenn 2.2 and 5 second drop towers, but that has a performance (production rate) that is better than most large ground-based machines.

INTRODUCTION

There is currently a large interest in the synthesis and characterization of carbon nanotubes for many useful applications. Carbon nanotubes were first discovered in 1991 by Iijima[2] who observed the presence of nanometer sized multi-walled carbon nanotubes (MWNTs) on the graphite electrodes used for fullerene production. Addition of a transition metal catalyst was subsequently shown to produce single-walled nanotubes[3] (SWNTs) such as the C_{60} sized nanotube illustrated in Figure 1. Unlike conventional carbon fibers, the SWNT structure is atomically perfect, thus producing defect free fibers that have many unique electronic and physical properties[4]. For example, with a predicted Young's modulus of ~1 Tera-Pascal, SWNTs represent the strongest known type of carbon fiber and form the ideal basis for new composite materials. Calculations show that a carbon nanotube-based cable could have one hundred times the strength of steel while having just one-sixth of the weight. Carbon fiber composites made from nanotubes would save significant weight in spacecraft and aircraft structures. In addition to their mechanical properties, nanotubes also have interesting electronic properties, which are
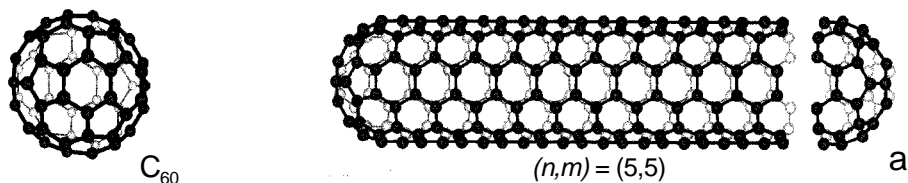
Figure 1. Comparison of C_{60} fullerene and its single-walled nanotube analogue.

dependent upon the tubes morphology. Some tubes have conducting electronic structures and can be envisioned as molecular "quantum" wires, while others are semiconducting and can be used to fabricate the world's smallest "single molecule" transistors. Other promising uses for SWNTs include tips for atomic force microscopy (AFM) and possibly hydrogen storage.

There are currently several methods for the production of single-walled carbon nanotubes, including: the carbon arc[5], laser vaporization of graphite[6], chemical vapor decomposition[7] (CVD), high-pressure disproportionation of CO[8], and flame synthesis[9]. All rely on catalytic growth of the nanotube from either carbon or hydrocarbon vapor in the presence Co/Ni or other transition metal catalysts. As vaporized carbon (or hydrocarbon) and metal catalyst atoms cool, they condense into small nanometer sized clusters that continually collide and grow. When the metal carbide clusters produced from the transition metal catalyst become super-saturated with carbon, the carbon re-crystallizes as nanotubes. The metal particle remains on the head of the growing nanotube and channels the remaining carbon it encounters into it. Studies performed on the vapor plume produced during laser ablation of graphite suggest that nanotube growth can continue as long as the catalyst particle remains saturated with carbon and the temperature remains high enough for carbon to efficiently diffuse through the particle[10]. The formation of a nanotube is undoubtedly a strong function of the time/temperature/concentration history of the growing tube and its precursors, and buoyancy produces an uncontrolled environment that makes estimation and optimization of these critical factors difficult. Microgravity conditions provide a much more controlled environment for measurement, modeling, and optimization of these parameters.

EXPERIMENTAL

The carbon arc method was selected as the basis of our microgravity apparatus because it is simple and provides for a fairly large nanotube production rate. However, several challenges were presented in moving the carbon arc from the production lab to the drop tower. The typical carbon arc apparatus[5, 11] employs large 6-12 mm diameter carbon electrodes and consumes multiple kilowatts of power that is supplied continuously from a large welding power supply. The metal catalyst required to produce SWNTs is introduced by drilling holes in the large electrodes and packing them with metal powder. During operation, the arc gap (which determines the current) is usually adjusted manually while observing the arc through a view port. Substantial innovation was required to adapt this configuration to a drop tower rig while maintaining a useful production rate equivalent to or higher than the ground-based machines.

A schematic of the miniature arc apparatus we developed is shown in Figure 2. The carbon electrodes were downsized to 5 mm and new liquid impregnation method was developed to dope the entire rod with Ni/Y metal catalyst. The arc gap is now continuously adjusted with a spring-loaded electrode. Power for the arc is supplied by a small battery pack that supplies 64 volts and currents in excess of 300 amps. Before producing nanotubes, the reaction chamber is purged of
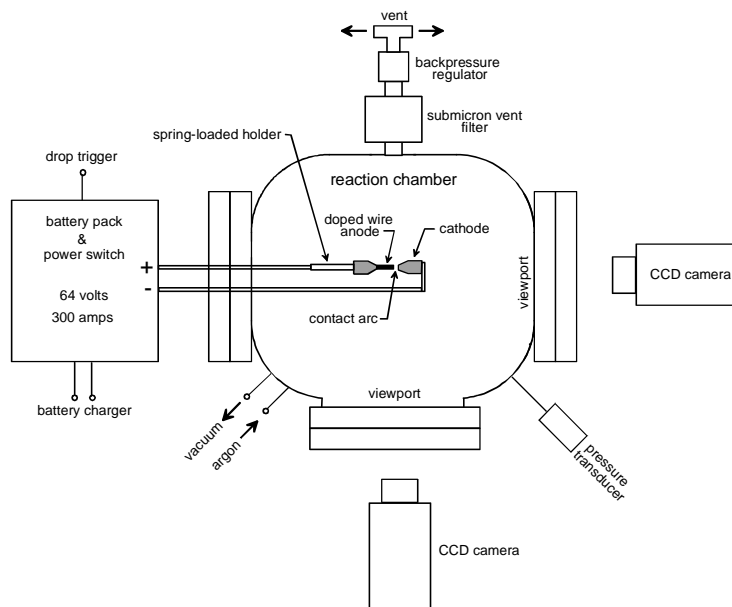
Figure 2. Miniature microgravity carbon arc reactor (chamber dimensions ~20 cm diameter).

air by use of a vacuum. The chamber is then filled with Argon at 600 Torr. The arc vaporizes ~500 mg of carbon during each 2.2 second run, and the resulting SWNTs agglomerate into web like fibers that are easily observed and collected for analysis.

To characterize the performance of the miniature arc, measurements were made of the key electrical parameters such as the arc voltage and current, which determines the carbon vaporization rate and temperature around the arc. Measurements of the voltage and current as well as the instantaneous power and energy deposition for a normal gravity 2-second run are shown on Figure 3. With an arc current of over 300 amps and power of 10kW, this small machine easily outperforms most larger ground based reactors. In addition, as shown by the power and energy curves, the battery pack provides a very stable power source for the duration of the arc, an important factor for providing a uniform nanotube growth environment. When combined with microgravity in the drop tower, this apparatus should provide an ideal environment for studying the formation and growth of carbon nanotubes.

Summary

Although nanotube science has become one of the worlds most rapidly advancing areas of research, very little is known about the processes involved in nanotube synthesis. To study the formation of carbon nanotubes in an environment unhindered by the buoyancy induced flows generated by the high temperatures necessary to vaporize carbon and grow nanotubes, we have designed a miniature carbon arc apparatus that can produce carbon nanotubes under microgravity conditions. Tests in the 2.2 second and 5.18 second drop towers are planned in 2003. We believe that microgravity processing will allow us to better understand the nanotube formation process and eventually allow us to grow nanotubes that are superior to ground-based production.

References

(1) C. Marin, M.D. Serrano, N. Yao and A.G. Ostrogorsky, *Nanotechnology* **13** (2002) 218.

(2) S. Iijima, *Nature* **354** (1991) 56.
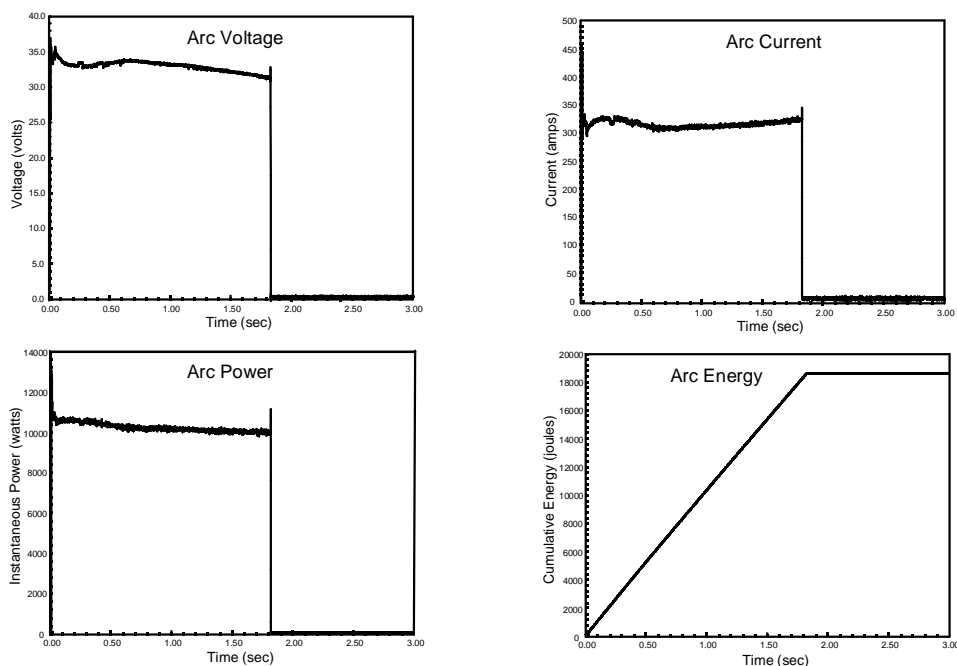
Figure 3. Key electrical parameters for the miniature carbon arc.

(3) (a) S. Iijima and T. Ichihashi, *Nature* **363** (2000) 603. (b) D.S. Bethune, C.H. Kiang, M.S. de Vries, G. Gorman, R. Savoy, J. Vazquez, and R. Beyers, *Nature*, **363** (2000) 605.

(4) The following reviews and references therein provide a good introduction into the current issues in carbon nanotube production, their physical properties, and applications. (a) P. Ajayan, *Chem. Rev*. **99** (1999) 1787. (b) T.W. Ebbeson (Ed.) *Carbon Nanotubes, their Preparation and Properties*, CRC Press, Boca Raton, FL, 1997. (c) R. Satio, M. Dresselhaus, G. Dresselhaus *Physical Properties of Carbon Nanotubes*, Imperial College Press, London, 1998. (d) B.I. Yakobson and R.E. Smalley, *American Scientist* **85**, (1997) 324.

(5) Journet, C., W.K. Maser, P. Bernier, A. Loiseau, M. Lamy de la Chapelle, S. Lefrants, P. Deniard, R. Lee, and J.E. Fischer, *Nature* **388** (1997) 756.

(6) T. Guo, P. Nikoleav, A. Thess, D.T. Colbert, and R.E. Smalley, *Chem. Phys. Lett*. **236** (1995) 419.

(7) J.F. Colomer, C. Stephan, S. Lefrant, G. Van Tendeloo, I. Willems, Z. Konya, A.Fonseca, Ch. Laurent, and J.B. Nagy, *Chem. Phys. Lett*. **317** (2000) 83.

(8) R. Dagani, *Chem. Eng. News* **78** (2000) 78.

(9) (a) R.L. Vander Wal, T.M. Ticich, and V.E. Curtis, *Chem. Phys. Lett*. **323** (2000) 217. (b) M.D. Diener, N. Nichelson, and J.M. Alford, *J. Phys. Chem. B* **104** (2000) 9615.

(10) (a) A.A. Puretzkey, D.B. Geohegan, X. Fan, and S.J. Pennycook, Appl. Phys A. **70** (2000) 153. (b) F. Kokai, K. Takahashi, M. Yudasaka, and S. Iijima, *J. Phys Chem B* **104** (2000) 6777.

(11) (a) Z. Shi, Y. Lian, F.H. Liao, X. Zhou, Z.Gu, Y. Zhang, S. Iijima, H. Li, K.T. Yue, and S. Zhang, *J. Phys. Chem. Solids*. **61** (2000) 1031. (b) Y. Ando, X. Zhao, K. Hirahara, K. Suenaga, S. Bandow, and S. Iijima, *Chem. Phys. Lett*. **323** (2000) 580. (c) A. Huczko, H. Lange, and T. Sogabe, *J. Phys. Chem. A* **104** (2000) 10708.

Flame Synthesis of Single-Walled Carbon Nanotubes and Nanofibers

Randy L. Vander Wal, Gordon M. Berger
NCMR c/o NASA-Glenn
Cleveland, OH 44135
and
Thomas M. Ticich
Chemistry Dept., Centenary College of Louisiana
Shreveport, LA 77134

Introduction

Carbon nanotubes are widely sought for a variety of applications including gas storage, intercalation media, catalyst support and composite reinforcing material [1]. Each of these applications will require large scale quantities of CNTs. A second consideration is that some of these applications may require redispersal of the collected CNTs and attachment to a support structure. If the CNTs could be synthesized directly upon the support to be used in the end application, a tremendous savings in post-synthesis processing could be realized. Therein we have pursued both aerosol and supported catalyst synthesis of CNTs. Given space limitations, only the aerosol portion of the work is outlined here though results from both thrusts will be presented during the talk.

Aerosol methods of SWNT, MWNT or nanofiber synthesis hold promise of large-scale production to supply the tonnage quantities these applications will require. Aerosol methods may potentially permit control of the catalyst particle size, offer continuous processing, provide highest product purity and most importantly, are scaleable. Only via economy of scale will the cost of CNTs be sufficient to realize the large-scale structural and power applications on both earth and in space.

Present aerosol methods for SWNT synthesis include laser ablation of composite metal-graphite targets or thermal decomposition/pyrolysis of a sublimed or vaporized organometallic [2]. Both approaches, conducted within a high temperature furnace, have produced single-walled nanotubes (SWNTs). The former method requires sophisticated hardware and is inherently limited by the energy deposition that can be realized using pulsed laser light. The latter method, using expensive organometallics is difficult to control for SWNT synthesis given a range of gas-particle mixing conditions along variable temperature gradients; multi-walled nanotubes (MWNTs) are a far more likely end products. Both approaches require large energy expenditures and produce CNTs at prohibitive costs, around $500 per gram. Moreover these approaches do not possess demonstrated scalability.

In contrast to these approaches, flame synthesis can be a very energy efficient, low-cost process [3]; a portion of the fuel serves as the heating source while the remainder serves as reactant. Moreover, flame systems are geometrically versatile as illustrated by innumerable boiler and furnace designs. Addressing scalability, flame systems are commercially used for producing megatonnage quantities of carbon black [4]. Although it presents a complex chemically reacting flow, a flame also offers many variables for control, e.g. temperature, chemical environment and residence times [5]. Despite these advantages, there are challenges to scaling flame synthesis as well.

A 1g environment imposes a severe limitation on the timescale available for observing the catalyzed reaction. Buoyancy induced convection limits the entire time period for catalyst particle formation, CNT inception and growth to roughly 100 ms [6]. Therein the synthesis results may reflect kinetic constraints rather than fundamental reactivity differences based on thermodynamics. To achieve flow stability, a chimney or other flow guide is necessary in 1g. This imposes flow

restrictions, accentuates temperature gradients and generally restricts access to the reacting flow. With associated temperature gradients, non-laminar flow, nonuniform temperature and chemical species fields, basic knowledge of CNT inception periods, growth rates and deactivation processes remain unresolved.

Therein fundamental measurements are needed, unencumbered by buoyancy imposed limitations with uniform and well controlled environments of temperature, species concentrations and identities. With such foundational knowledge, practical large scale synthesis can be approached from a rational design perspective and not by Edisonian methods. With this ultimate goal, the objectives of the project of flame synthesis of carbon nanotubes were as follows:
1. To demonstrate flame synthesis of SWNTs and MWNTs.
2. Explore alternative methods of catalyst particle introduction into the flame environment.
3. Investigate the sensitivities to reactive gas environments, e.g. were PAHs involved (or even suitable) for CNT growth.

Results and Discussion

Onset of catalytic reactivity and selectivity based on gas identity

In our previous work pursuing a flame-aerosol approach, various methods of catalyst introduction have been studied; methods such as sublimation of organometallics [7-9], thermal evaporation of pure metals [10] or nebulization of solutions containing metal salts [11, 12] have been tested as a step towards scaling production. Initial work compared flame and high temperature furnace environments in order to identify optimum gas flows and an overall gas composition for SWNT synthesis [10]. Subsequent work made comparisons between two metals, Ni and Fe, and their catalyzed products, SWNTs and nanofibers, using a dual flame configuration [13, 14]. Recently LII has been applied to this system [15]. Using a variety of catalyst systems, we have consistently observed the following results.
Fe reacted in both the CO and CO/C_2H_2-based gas mixtures, producing SWNTs. Fig. 1 shows TEM images of these products at various magnifications. In contrast, Ni was unreactive towards the CO gas mixture. It only reacted with the CO/C_2H_2 gas mixture, producing nanofibers. This is shown in the TEM images of Fig. 2

Ni

Further tests investigated in detail the size effects for Ni catalyst nanoparticles and sensitivities to the reactive gas mixture using the pyrolysis flame configuration. As with Fe, Ni nanoparticles were formed by thermal decomposition of a nebulized Ni nitrate solution entrained into a reactive fuel mixture. Although at the earliest stages of growth, the Ni nanoparticles were sufficiently small to catalyze single-wall nanotubes (SWNTs), only the larger particles appeared catalytically active yielding only nanofibers. Using different reactive gas mixtures consisting of CO or C_2H_2 or their combination, Ni nanoparticles exhibited a high preferential reactivity towards C_2H_2 to form nanofibers.

HRTEM images seen in Fig. 2 reveal that the carbon nanofibers consist of short, undulating carbon lamella forming the nanofiber walls. Where visible, the nanofiber tips are always terminated by a catalyst particle, in intimate association with the nanofiber walls. The structure of the fibers, relative size of the catalyst particles and contact of the carbon lamella with the particle are consistent with the traditional carbon fiber growth mechanism.
Variation of the CO/C_2H_2 ratio alters the nanofiber morphology rather little (though it is different with only C_2H_2 present), instead the relative yield varies dramatically. Ni appears to be relatively unreactive towards CO within the flame environment used here for all particle sizes observed (0.5 - 5 nm). In contrast, Ni is catalytically active towards C_2H_2, but only the larger nanoparticles (4 - 5

nm) exhibit this activity. Both observations are attributed to the nanoparticle physical and electronic structure, and their variation with particle size, as later discussed.

Fe

On the basis of bulk crystal studies, Fe is considered to be more reactive than Ni [16]. Clearly, it achieves an earlier onset of reactivity, as only the very smallest Fe particles catalyze nanotubes, in this case SWNTs. Therein, Fe might be expected to readily react with C_2H_2, particularly since it reacts with CO. One might even predict that CO, as a less reactive carbon source could yet play a similar role in restricting the rate of carbon supply through C_2H_2 dissociative adsorption, as it does with Ni. The difference here is that it would also contribute to the carbon supply.

With CO replaced by a balance of He, the gas mixture containing C_2H_2, as the only carbon source, was tested using Fe. No SWNTs were catalyzed. Only metal catalyst particles were observed. Using the CO/C_2H_2 gas mixture, no definitive increase in SWNT yield was observed. While there may be some synergism between these reactant gases, the absence of an increase in SWNT yield suggests that any synergism is marginal at best. These results demonstrate the selective reactivity of Fe towards CO.

Notably, in either the CO or CO/C_2H_2 gas mixture, Fe does not catalyze MWNTs or nanofibers. Catalysis of either would require larger Fe particles, which are generally not observed in our flame system. If the larger particles that are present were active towards MWNT or nanofiber synthesis, then these products would be expected, given similar temperature and residence time scales to those for Ni. Instead only the smallest Fe nanoparticles, roughly 1 nm in size are catalytically active. They exclusively catalyze SWNTs. The absence of MWNTs or nanofibers despite the presence of suitably sized particles suggests a decline in reactivity with increasing particle size, in contrast to Ni.

Metal Nanoparticles

In a metal nanoparticle, the density of electronic states is finite and the traditional conduction and valence bands are absent due to the small number of constituent atoms [17]. With > 75% of the atoms residing at the surface for a 1 nm particle, the particle properties will largely be determined by the surface atoms. This will be particularly true for those atomic orbitals not participating (contributing electron density) in the free conduction band of the metal, such as the 3d orbitals of the transition metals [16]. If the electronic properties of a metal nanoparticle resembles those of the individual element, given the finite size and high surface area, then based on energetics associated with its outer electron configuration, $[Ar]5s^23d^6$, Fe atoms can achieve a stable half filled d-shell by loss of electron density. Such is the case with donation of electron density to an adsorbate, e.g. CO, which undergoes dissociation primarily by accepting electron density from the catalyst metal. In contrast, acceptance of electron density (by the Fe nanoparticle) might be expected to be energetically unfavorable, given the increase in energy associated with pairing electron density within the d-shell orbitals. Therein, Fe would be expected to be unreactive towards C_2H_2, which undergoes dissociation primarily by donating electron density to the catalyst metal.

The situation for Ni is exactly opposite. Adopting the premise that the individual elemental identity still governs the electronic properties of the surface atoms and hence, their reactivities, it would be energetically favorable for Ni to accept electron density to achieve a more stable, filled d-shell, namely $[Ar]5s^23d^{10}$. Therein, Ni would be expected to be highly reactive towards adsorbates which donate electron density, e.g. C_2H_2. Correspondingly, Ni would be unreactive towards adsorbates that accepted (withdrew) electron density from the metal nanoparticle, e.g. CO.

Admittedly, the size dependent reactivities and selective reactivities towards the different reactive gases required additional study. Undoubtedly, other factors are also integral to these results. Some possibilities include thermal restructuring, adsorbate-enhanced restructuring and electronic interactions between adsorbates mediated by the catalyst particle.   Our previous studies have discussed these effects in other synthetic systems [10, 14]. Further work remains to assess their relative contributions to CNT synthesis within the flame environment.

Acknowledgements

References

1. Calvert, P. "Potential Applications of Carbon Nanotubes" in *Carbon Nanotubes: Preparation and Properties*, (Ebbesen, T. W. Ed.) CRC Press, Boca Raton, Fl (1997), pp. 277-290.
2. P. G. Collins and P. Avouris, Scientific American, Dec. 2000, pp. 38-45.
3. Pratsinis, S. E., "Overview of Material Synthesis by Aerosol Processes", AIChE Symp. Ser., Vol. 85 (#270), (1980) 57.
4. Carbon Black Science and Technology, 2nd ed. J. B. Donnet, R. C. Bansal and M.-J. Wang eds. Marcel Dekker, Inc.1993.
5. Turns, S. R., "An introduction to combustion: Concepts and Applications", McGraw Hill Inc. New York, (1996).
6. Roper, F. G., Comb. and Flame 29:219 (1977).
7. Vander Wal, R. L. and Hall L. J., Combust. and Flame 130:27 (2002).
8. Vander Wal, R. L., Ticich, T. M., and Curtis, V. E., Chem. Phys. Lett. 323:217 (2000);
9. Vander Wal, R. L., Ticich, T. M., and Curtis, V. E., J. Phys. Chem. A104:7209 (2000).
10. Vander Wal, R. L., and Ticich, T. M., J. Phys. Chem. B 105:10249 (2001).
11. Vander Wal, R. L., and Hall, L. J., Chem. Phys. Lett. 349:178 (2001).
12. Vander Wal, R. L., and Ticich, T. M., Chem. Phys. Lett. 336:24 (2001).
13. Vander Wal, R. L., Carbon 40:2101 (2002).
14. Vander Wal, R. L., Comb. and Flame 130:37 (2002).
15. Vander Wal, R. L., Berger, G. M., Ticich, T. M., and Patel, P. D., Appl. Opt. 41:5678 (2002).
16. G. A. Somorjai, C. M. Kim and C. Knight, in "Surface science of catalysis: In situ probes and reaction kinetics", (D. J. Dwyer and F. M. Hoffman, Eds.) American Chemical Society, Washington DC (1992).
17. M. A. El-Sayed, Acc. Chem. Res. 34, 257 (2000).
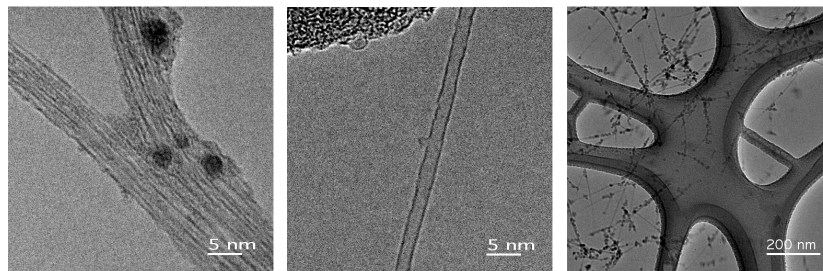
Figure 1. Representative TEM images of Fe-catalyzed SWNTs using a CO gas mixture. Both individual and bundled SWNTs were produced, though bundles were much more prevalent.
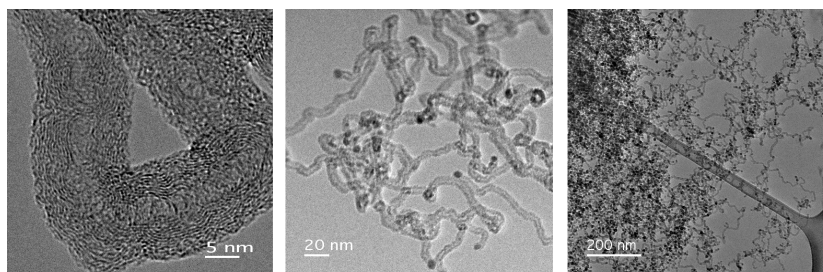
Figure 2. Representative TEM images of Ni-catalyzed nanofibers using a CO/C_2 gas mixture. Catalyst particles are evident at the tips of the nanofibers where exposed in (b). Image c) illustrates the undulation of the graphene segments comprising the nanofiber.

MICROGRAVITY PRODUCTION OF NANOPARTICLES OF NOVEL MATERIALS USING PLASMA SYNTHESIS

A.M. Dato, A.C. Fernandez-Pello, M. Frenklach
Department of Mechanical Engineering, University of California, Berkeley, 94720

INTRODUCTION

Non-oxide materials such as diamond, SiC, SiN, and c-BN, possess a unique combination of useful mechanical, thermal, optical, and electronic properties. These materials are of interest in several industrial applications, such as high temperature load bearings or high speed metal machining. Furthermore, nanoparticulates of these materials have specific application in the fabrication of MEMS based combustion systems, and in the development and growth of nano-systems and nano-structures of these materials. The synthesis of such materials is a great challenge, and research on chemical vapor deposition of these materials is now being carried out throughout the world at an increasing rate. Most of this research has been focused on diamond films. The principal limitation found in these studies is the short length of the reaction zone and small residence time. The best results for the formation of diamond powder were observed at low pressures, at conditions where the reaction zone was stretched.

A research project is currently underway to study the formation in reduced gravity of high quality nanoparticulate of novel materials using plasma synthesis. Particular emphasis will be placed on the production of powders of non-oxide materials like diamond, SiC, SiN, and c-BN. The objective of the study is to investigate the effect of gravity on the plasma synthesis of these materials, and to determine how microgravity synthesis can improve the quality and yield of the produced nanoparticles. Microgravity conditions offer better conditions for the plasma synthesis of non-oxide materials. The controlling mechanisms of the plasma synthesis of high quality nanoparticulate could be better understood in a microgravity environment because of increased uniformity of the reaction zone and the absence of buoyancy effects on the reaction. Also, because of longer residence times and reaction uniformity, higher yields of nanoparticles at a better quality could be produced in microgravity.

In the work we are presenting here, a series of ground-based tests determine the quality and yield of high quality nanoparticulate in normal gravity. Yield and quality of collected nanoparticles were analyzed by means of transmission electron microscopy. The results of these tests will be compared with novel materials produced aboard the KC-135 Parabolic Flight Aircraft in future experiments.

EXPERIMENTAL HARDWARE

Ground-based plasma synthesis experiments were conducted using a microwave plasma reactor operating in diffusion flame mode, as shown in Figure 1. Microwaves are generated via a remote magnetron head capable of a microwave power output of 180W to 1800W at a frequency of 2470MHz. Generated microwaves are passed through a microwave guide into an atmospheric plasma torch. The plasma torch is a chamber-type microwave applicator designed to increase the reaction zone and minimize wall effects. Reactant gases are metered through mass flow controllers and injected into the microwave zone of the plasma torch by means of a ceramic gas feed tube. Argon gas is flowed coaxially in the torch and is used to produce and sustain the plasma in the torch, as well as to isolate the reactants from the reactor walls. Figure 2 shows a top view of the atmospheric plasma torch generating argon plasma. Particles produced in the

atmospheric torch are collected downstream of the reaction zone by means of a particle trap. Recovered particles are analyzed by means of transmission electron microscopy.
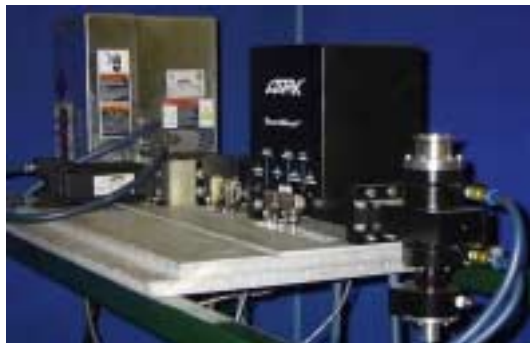
Figure 1. Microwave Plasma Reactor.

Figure 2. Atmospheric Plasma Torch generating Argon plasma.

BACKGROUND

Previous plasma synthesis experiments and their findings will be discussed. Experiments on the production of diamond powder by homogeneous nucleation and subsequent growth in a microwave assisted combustion process have been conducted [1, 2]. The experiments were performed in a tubular flow reactor consisting of a fused silica tube passed vertically through a horizontal microwave transmission guide. Homogeneous nucleation of diamond was observed in dichloromethane-, trichloroethylene-, and acetylene-oxygen mixtures. Pressure was varied in these experiments from 50 to 500 Torr. Most of the diamond particles produced in these experiments were on the order of 10 to 50 nm in diameter. These experiments showed that the diamond nanoparticles produced were generally observed to be larger at lower system pressures. In diffusion flames, higher pressure affects flame thickness through the reaction rate and through transport diffusive and convective effects, which tend to shorten the flame. In the plasma-assisted combustion environment, higher pressures decreased the reaction zone, leading to smaller diameter nanoparticles.

RESULTS & DISCUSSION

The plasma reactor currently being used for normal gravity experiments is designed to operate at low pressures ranging from 50 Torr to atmospheric. Experiments are currently being performed on silicon-carbide powder. Silicon-carbide is formed much easier and in larger yields than diamond powder. Nanoparticles are produced over a range of reaction gas flow rates and microwave forward power. The reactor is currently being operated at atmospheric pressure, with microwaves directed into the atmospheric plasma torch being ranged in power from 180W to 1200W. Collected silicon-carbide particles are currently being analyzed by means of transmission electron microscopy.

FUTURE PLANS

Microgravity plasma synthesis of nanoparticles aboard the KC-135 will be the next step in this project. Results collected in the reduced gravity environment will be compared to the nanoparticles currently being produced in normal gravity. It is expected that nanoparticles will be

produced at a higher yield and higher quality in microgravity because of the increased uniformity of the reaction zone and longer residence times.

REFERENCES

1. M. Frenklach, R. Kematick, D. Huang, K.E. Spear, A.W. Phelps and R. Koba, J. Appl. Phys., **66**, 395 (1989)

2. W. Howard, D. Huang, J. Yuan, M. Frenklach, K.E. Spear, A.W. Phelps and R. Koba, J. Appl. Phys., **68**, 1247 (1990)

COMPUTATIONAL AND EXPERIMENTAL STUDIES OF THREE-DIMENSIONAL FLAME SPREAD OVER LIQUID FUEL POOLS

Jinsheng Cai, Feng Liu, William A. Sirignano
University of California, Irvine, CA 92697-3975

Fletcher J. Miller
National Center for Microgravity Research, MS 110-3, Cleveland, OH 44135-3191

INTRODUCTION

Schiller, Ross, and Sirignano (1996) studied ignition and flame spread above liquid fuels initially below the flashpoint temperature by using a two-dimensional computational fluid dynamics code that solves the coupled equations of both the gas and the liquid phases. Pulsating flame spread was attributed to the establishment of a gas-phase recirculation cell that forms just ahead of the flame leading edge because of the opposing effect of buoyancy-driven flow in the gas phase and the thermocapillary-driven flow in the liquid phase. Schiller and Sirignano (1996) extended the same study to include flame spread with forced opposed flow in the gas phase. A transitional flow velocity was found above which an originally uniform spreading flame pulsates. The same type of gas-phase recirculation cell caused by the combination of forced opposed flow, buoyancy-driven flow, and thermocapillary-driven concurrent flow was responsible for the pulsating flame spread. Ross and Miller (1998) and Miller and Ross (1998) performed experimental work that corroborates the computational findings of Schiller, Ross, and Sirignano (1996) and Schiller and Sirignano (1996).

Cai, Liu, and Sirignano (2002) developed a more comprehensive three-dimensional model and computer code for the flame spread problem. Many improvements in modeling and numerical algorithms were incorporated in the three-dimensional model. Pools of finite width and length were studied in air channels of prescribed height and width. Significant three-dimensional effects around and along the pool edge were observed. The same three-dimensional code is used to study the detailed effects of pool depth, pool width, opposed air flow velocity, and different levels of air oxygen concentration (Cai, Liu, and Sirignano, 2003). Significant three-dimensional effects showing an unsteady wavy flame front for cases of wide pool width are found for the first time in computation, after being noted previously by experimental observers (Ross and Miller, 1999). Regions of uniform and pulsating flame spread are mapped for the flow conditions of pool depth, opposed flow velocity, initial pool temperature, and air oxygen concentration under both normal and microgravity conditions. Details can be found in Cai et al. (2002, 2003). Experimental results recently performed at NASA Glenn of flame spread across a wide, shallow pool as a function of liquid temperature are also presented here.

COMPUTATIONAL RESULTS

Pulsating Spread without Opposed Flow: A recent three-dimensional experimental study by Konishi, Tashtoush, Ito, Narumu, and Saito (2000) presented transient three-dimensional structures of velocity and temperature created by a pulsating flame spread over n-propanol. Computations at similar conditions have been performed in this study under both normal and

zero-gravity. Fig. 1 shows the history of flame position vs. time for different initial pool temperatures at normal and micro gravity levels.
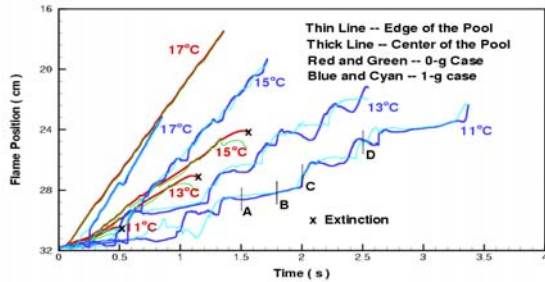
Fig. 1 History of computed flame position vs. time. The symbol x marks extinction
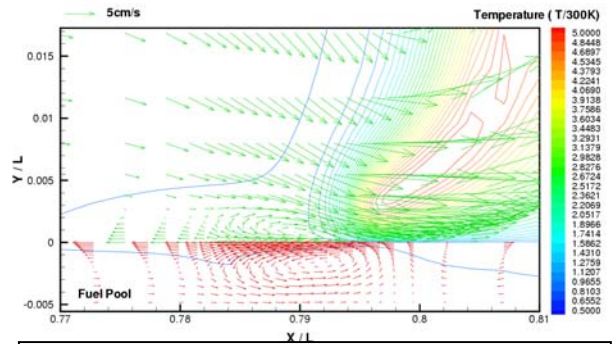
Fig. 2 Velocity vectors and temperature contours at Instant A (side view at center of pool).

Under normal gravity, the flame pulsates at initial pool temperatures of 15 °C or below. The flame spreads faster and the pulsation amplitude decreases while its frequency increases as the initial pool temperature increases. When the initial pool temperature is at 17 °C, the flame essentially propagates at a uniform speed. Under microgravity the flames appear to always propagate at a steady speed without an opposed flow. However, the flames propagate some short distances before they extinguish at later times when the initial pool temperatures are low. When the initial pool temperature reaches 17 °C, the flame spreads at a uniform speed much in the same way as under normal gravity. The temperature and velocity field are examined for the case at 11 °C initial pool temperature under normal gravity at four instants marked as A, B, C, D in Fig. 1. These four instants roughly correspond to the fuel vapor accumulation (Instants A and B), flame jumping (Instant C), and onset of pulsation (Instant D) steps discussed in Konishi et al. (2002), respectively. Fig. 2 shows the side view of velocity vectors and temperature contours at the center of the pool ($z=0$) at Instant A. The almost stationary flame at this instant heats the liquid surface causing significant convective motion of the liquid and the gas due to surface tension. On the other hand, buoyancy draws air towards the flame causing a recirculating zone in the air that can be clearly seen in Fig. 2 (note $L = 30$ cm). Surface tension pulls the liquid on both sides near the maximum temperature point below the flame. Continuity of mass in the liquid then results in a pair of vortices centered around the maximum temperature point. The details of the flow and the flame at other instants are presented in Cai et al. (2003). The computed flow patterns agree well with those observed in the experimental data in Ross and Miller (1996) and Konishi et al. (2002). However, the computed temperature profile above the liquid surface does not indicate the necessity of a pronounced temperature valley in front of the flame for pulsating flame spread as suggested by Konishi et al. (2002). See details in Cai et al (2003).

Influence of Opposed Flow and Other Parameters: A large number of computations have been performed to determine the influences of pool depth, pool width, air oxygen concentration, and opposed flow velocity. Temperature regions of uniform and pulsating flame spread have been determined by varying those different parameters under both normal and zero gravity. Results are presented in Cai et al. (2003).

Wavy Flame Structures for Wider Pools: Cai et al. (2002) studied the detailed flame structure for the 2 cm width pool case and reported significant three-dimensional edge effects as the flame front turns around the corners at the side edge of the pool and trails behind. As the pool width is

increased, the flame front becomes largely a wavy form as can be seen by looking at the contours of the fuel consumption rates at three consecutive time instants for a 6 cm wide pool at 1-g condition shown in Fig. 3. The amplitude of the wavy flame front and the wavelength are large at the low initial fuel temperature end. As the temperature increases, both the amplitude and wavelength decreases and the flame also propagates faster. As
the temperature increases to 18 °C, the flame front becomes completely straight and the flame propagates uniformly. There is a strong correlation between the wavy form of the flame front and the pulsation of the flame spread. The wavy flame front only appears in pulsating spread cases. Similar behavior occurs under microgravity. Two movie clips for the normal and microgravity conditions, respectively, are created and can be seen at http://fliu.eng.uci.edu/Flames/.

Fig. 3 Contours of fuel consumption rate 1mm above the fuel at different time instants for a 6 cm wide pool under 1g.

EXPERIMENTAL TESTS

In most of our previous experiments, the narrow pool width of 20 mm restrained the full development of 3-D effects such as flame wrinkling or corrugation at the leading edge. Additionally, our apparatus did not permit testing with an opposed air flow and a variable pool temperature; either the pool temperature could be varied in quiescent conditions, or the air flow rate could be varied at room temperature. To provide a wider range of data against which to test the numerical model, we undertook further 1g tests as described below. The apparatus was in most respects the same as that described in Ross and Miller (1996), except that the bottom of the flow tunnel was replaced with a new tray insert. This new bottom held a fuel tray 300 mm long x 78 mm wide x 2 mm deep. The flow duct itself remained at 340 mm x 100 mm x 70 mm, with honeycombs and screens at each end to produce an even, laminar flow. The new fuel tray could be temperature controlled via water-cooling channels, and the duct fan could be adjusted to give varying opposed flow velocities to the flame spread. For all the cases reported here, the opposed flow velocity was 45 cm/s, and the fuel was n-propanol.

Figure 4 gives a representative graph of flame position along the tray centerline vs. time as obtained by tracking the flame leading edge (note the time scale starts when the flame first became visible beyond the igniter glow, and the starting position is set to zero). As can be seen, the flame fronts exhibit pulsations as has been well established for n-propanol at these temperatures. Tracking was also performed for the flame front 1.5 cm and 3 cm on one side of the centerline. Generally, all three flame locations tracked very well together, indicating that the
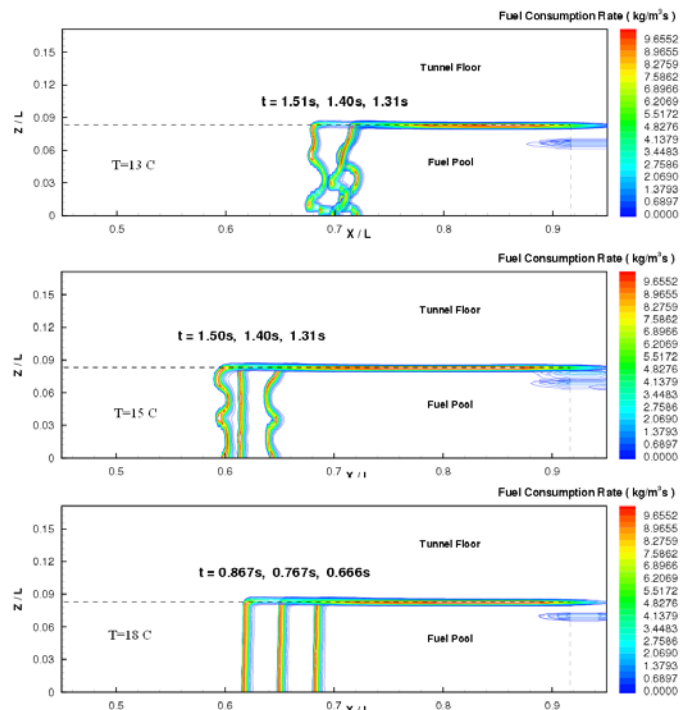
flame, despite being corrugated, moved as a single unit. A sample flame image is given in Fig. 5 to show the non-uniform leading edge.
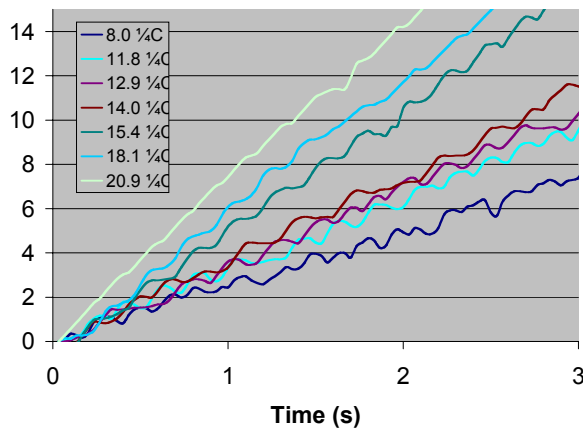
Fig.4. Centerline flame position vs. time for n-propanol pool at 11.8 C.

Fig. 5. The upper portion of the image shows a side view of the flame, while the lower portion shows a top view. Note the nonuniform flame front.

From the data like that shown in Figure 4, the pulsation frequency can be obtained as a function of temperature. Interestingly, over quite a wide temperature range (8-20 °C), the frequency was found to be 4-5 Hz, and to depend only slightly on the pool temperature. Results presented in Cai et al. (2002 and 2003) indicate qualitatively the same behavior of temperature independence when there is an opposed flow velocity and the temperature is above a certain level. This extends the limited temperature range studied in Miller and Ross (1992) where a similar result was reported and the frequency was found to be mainly a function of the pool depth. Although the transition to pulsating spread is very sensitive to pool temperature, once the transition has occurred it apparently is quite robust and seems to be driven more by pool geometry than by the flame (whose speed decreased markedly as the temperature is lowered).

REFERENCES
Cai, J., Liu, F., and Sirignano, W.A. (2003) "Three-dimensional structures of flames over liquid fuel pools," submitted to *Combustion Science and Technology*.
Cai, J., Liu, F., and Sirignano, W.A. (2002), *Combustion Science and Technology*, **174** (5-6):5-34.
Konishi, T., Tashtoush, G., Ito, A., Narumi, A. and Saito, K. (2002), *Proc. Comb. Inst.*, **28**, pp. 2819-2826.
Miller, F.J. and Ross, H.D. (1998), *Proc. Comb. Inst.*, **27**, pp. 2715--2722.
Miller, F. J. and Ross, H. D. (1992), *Proc. Comb. Inst.*, **24**, pp. 1703-1711
Ross H.D. and Miller F. J. (1996), *Proc. Comb. Inst.*, **26**, 1327-1334
Ross, H.D. and Miller, F.J. (1998), *Proc. Comb. Inst.*, **27**, pp. 2723--2729.
Ross, H. D. and Miller, F. J., (1999), *Sixth International Symposium on Fire Safety Science*, pp. 77-94
Schiller, D.N., Ross, H.D., and Sirignano, W.A. (1996), Proc. *Comb. Sci. and Tech.*, **118** (4-6):205--258.
Schiller, D.N. and Sirignano, W.A. (1996), *Proc. Comb. Inst., 26,* pp. 1319--1325.

RADIANT EXTINCTION OF GASEOUS DIFFUSION FLAMES

S. Berhan, M. Chernovsky and A. Atreya
Department of Mechanical Engineering, U of M; Ann Arbor, MI 48109

Howard R. Baum
BFRL, NIST; Gaithersburg, MD 20899

Kurt R. Sacksteder
NASA Glen Research Center; Cleveland, OH 44135

INTRODUCTION

The absence of buoyancy-induced flows in microgravity (μg) and the resulting increase in the reactant residence time significantly alters the fundamentals of many combustion processes. Substantial differences between normal gravity (ng) and μg flames have been reported in experiments on candle flames [1, 2], flame spread over solids [3, 4], droplet combustion [5,6], and others. These differences are more basic than just in the visible flame shape. Longer residence times and higher concentration of combustion products in the flame zone create a thermochemical environment that changes the flame chemistry and the heat and mass transfer processes. Processes such as flame radiation, that are often ignored in ng, become very important and sometimes even controlling. Furthermore, microgravity conditions considerably enhance flame radiation by: (i) the build-up of combustion products in the high-temperature reaction zone which increases the gas radiation, and (ii) longer residence times make conditions appropriate for substantial amounts of soot to form which is also responsible for radiative heat loss. Thus, it is anticipated that radiative heat loss may eventually extinguish the "weak" (low burning rate per unit flame area) μg diffusion flame. Yet, space shuttle experiments on candle flames show that in an infinite ambient atmosphere, the hemispherical candle flame in μg will burn indefinitely [1]. This may be because of the coupling between the fuel production rate and the flame via the heat-feedback mechanism for candle flames, flames over solids and fuel droplet flames. Thus, to focus only on the gas-phase phenomena leading to radiative extinction, aerodynamically stabilized gaseous diffusion flames are examined. This enables independent control of the fuel flow rate to help identify conditions under which radiative extinction occurs. Also, spherical geometry is chosen for the μg experiments and modeling because: (i) It reduces the complexity by making the problem one-dimensional. (ii) The spherical diffusion flame completely encloses the soot which is formed on the fuel rich side of the reaction zone. This increases the importance of flame radiation because now both soot and gaseous combustion products co-exist inside the high temperature spherical diffusion flame. (iii) For small fuel injection velocities, as is usually the case for a pyrolyzing solid, the diffusion flame in μg around the solid naturally develops spherical symmetry. Thus, spherical diffusion flames are of interest to fires in μg and identifying conditions that lead to radiation-induced extinction is important for spacecraft fire safety.

EXPERIMENTAL RESULTS

The experiments were conducted in the 2.2 sec drop tower at the NASA Glenn Research Center. The drop-rig used is described in detail elsewhere [7]. Briefly, it consists of a cylindrical test chamber (0.38m dia.; 0.43m deep) that houses the spherical burner, the hot-wire igniter and the photodiodes and thermocouples used for making radiation and temperature measurements. The spherical burner (19mm dia.) was constructed from a low heat capacity porous ceramic material (93% porosity). Two gas cylinders (150 cc & 500 cc) were charged with various gases up to 45 psig and were used to supply the fuel to the porous spherical burner. Fuel flow rates to the burner were controlled by a calibrated needle valve and a gas solenoid valve was used to open and close the gas line to the burner upon computer command. The test chamber also had a 125mm diameter Lexan

window which enabled the camera to photograph the flame.

Several μg experiments under ambient pressure and oxygen concentration conditions, were conducted with methane (less sooty), ethylene (sooty), and acetylene (very sooty) fuels for flow rates ranging from 3 to 45 cm^3/s. Only a few results are presented here. The data was collected by an onboard computer during the drop and the following measurements were made: (i) *Flame radius* – measured from photographs taken by a color CCD camera (see Figure 1 for three experiments on methane at different flow rates). (ii) *Flame radiation* – measured by photodiodes with different spectral characteristics ranging from UV to IR (See figures 2 & 3 for comparable flow rates of acetylene and methane. Here, the radiation emitted by the flame in different

Figure 2: Acetylene 45 ml/s - Radiation Measurements
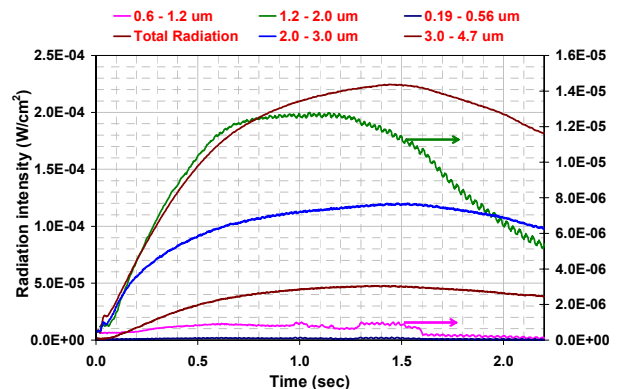
Figure 3: Methane 40 ml/s - Radiation Measurements

Figure 1: Methane Radius Measurements

wavelength intervals is plotted). (iii) *Flame temperature* – measured by five S-type thermocouples and the sphere surface temperature was measured by a K-type thermocouple. The evolution of radial temperature profiles is shown in Figure 4 for an acetylene flame.

Video photographs show that for all fuels (methane, ethylene and acetylene), initially the flame was blue (non-sooty) but becomes very bright yellow (sooty) under μg conditions. Later, as the μg time progresses, the flame grows in size and becomes orange and less luminous and the soot luminosity disappears. For the same fuel flow rate, methane flames eventually become blue (non-sooty) in approximately one second, ethylene flames became blue toward the end of the μg time (i.e. ≈ 2 sec) while acetylene flames remained luminous yellow throughout the 2.2 sec μg time. However, the luminosity of acetylene flames was considerably reduced toward the end of the μg time and would have also become blue given more time. These visual observations are in agreement with the flame radiation measurements shown in Figures 2 & 3 for C_2H_2 & CH_4 respectively. Radiation for CH_4 flames (Fig. 3) gradually increases and then decreases. This is true not just for the visible radiation but also for the infrared radiation containing the major CO_2 and H_2O bands. Clearly, the flame gases are cooling at a rate faster than the combustion heat release. Given sufficient time the flame is expected to extinguish. However, the situation is different for acetylene flames. First, the flame radiation is significantly larger due to soot formation

Figure 4: Evolution of radial temperature profiles - C_2H_2 (Drop 113 - 45 ml/s)

and oxidation in the vicinity of the high temperature reaction zone. This is responsible for the large rise and decrease in the first 0.4 seconds. As time proceeds, the radiation from all wavelengths decreases except radiation from the 2-3μm band which contains the combined CO_2 and H_2O bands. The 3-4.7 band, corresponding to CO_2, however, stays constant but shows a slight peak for t<0.4sec. Since the combined CO_2 & H_2O band dips considerably in this zone, it implies that the increase in radiation is primarily due to soot oxidation. Later, as the distance between the soot shell and the reaction zone increases, only H_2-rich species are burning resulting in an increase in the H_2O band radiation. It would be interesting to calculate the H_2, H_2O and CO_2 CO and OH profiles in this region. Figure 4 provides the radial temperature distribution corresponding to Figure 2. Clearly, the flame temperature continuously falls and we expect even acetylene flame to extinguish given sufficient time.

THEORETICAL RESULTS

To better understand these processes and predict flame radius, radiation and temperature, theoretical models are being developed with chemical kinetics and flame radiation. As a first step, soot formation and oxidation is not included and three types of models are considered: (i) Assuming infinite reaction rate (analytical), (ii) Assuming a single-step reaction mechanism, and (iii) Using a skeletal reaction mechanism from Smooke[10]. Also, emission approximation was made in all cases for modeling the flame radiation. For the simplest case of *constant pressure ideal gas reactions,* we may write the following governing equations for an approximate analysis under conditions of small soot loading:

$$\textit{Mass Conservation}: \frac{\partial \rho}{\partial t} + \frac{1}{r^2}\frac{\partial}{\partial r}(r^2 \rho v) = 0 \tag{1}$$

$$\textit{Conserved Scalar}: \rho\frac{\partial Z}{\partial t} + \rho v\frac{\partial Z}{\partial r} - \frac{1}{r^2}\frac{\partial}{\partial r}\left(r^2 \rho D\frac{\partial Z}{\partial r}\right) = 0 \tag{2}$$

$$\textit{Constant Pressure Ideal gas}: \rho T = \rho_\infty T_\infty \textit{ or } \rho h^s = const. \tag{3}$$

$$\textit{Defining}: \frac{\partial \psi}{\partial t} = -r^2 \rho v ; \frac{\partial \psi}{\partial r} = r^2 \rho ; \Rightarrow \left(\frac{\partial r}{\partial t}\right)_\psi = v \tag{4}$$

Here, the symbols have their usual definitions with ρ = density, T = temperature, v = velocity, Z = Conserved Scalar (mixture fraction variable), h^s = sensible enthalpy and D = diffusion coefficient. Species and energy equations are replaced by a mixture fraction variable 'Z' which is described by a homogeneous equation. The expectation is that this approach may be adequate for calculating the observed expansion rate of the spherical diffusion flames, but it is expected to be inadequate for predicting radiative extinction.

Applying the corresponding initial and boundary conditions for a sphere of radius 'R' blowing fuel gases at a rate $\dot{M}(t)$ we get:

$$\psi(r, t) = \int_{R(t=0)}^{r(t)} r^{*2} \rho (r^*, t) dr^* - \frac{M(t)}{4\pi} \tag{5}$$

Where M(t) is the total fuel mass that has been injected from the sphere in time 't'. For a constant given mass injection rate $\dot{M}(t)$, $M(t) = \dot{M}(t) \times t$. Using $\psi = \psi_o = const$ at $r = r_f$ we obtain in the approximation $Z = Z_C$:

$$r_f(t) = \left(R^3 + \left(\frac{3\dot{V}(\rho_o h_\infty^S + Q \rho_o Y F\infty Z_C)}{4\pi (\rho_o h_\infty^S + \bar{\eta} t)}\right) \times t\right)^{1/3} \tag{6}$$

Where, $\bar{\eta}$ = *Average heat loss rate by radiation per unit volume.* Data correlated according to equation (6) is shown in Figure 5. Clearly, while Equ (6) is approximate, it captures the physics of flame growth. The fact that most of the data falls along a constant value (~1.3) is very encouraging. Furthermore, the numerical calculations with one step reaction mechanism and thin gas radiation also falls along this constant value. Numerical calculations without radiation clearly do not agree with the data. Figures 6 & 7 show calculations with a detailed mechanism. Note how the OH mass fraction and temperature are reduced at extinction.

REFERENCES

1. *Dietrich, D. L., Ross, H. D. and T'ien, J. S.* "Candle Flames in Microgravity," Third Microgravity Combustion Workshop, Cleveland, Ohio, April, 1995.

2. *Ross, H. D., Sotos, R. G. and T'ien, J. S.,* Combustion Science and Technology, Vol. 75, pp.155-160, 1991.

3. *T'ien, J. S., Sacksteder, K. R., Ferkul, P. V. and Grayson, G. D.* "Combustion of Solid Fuels in very Low Speed Oxygen Streams," Second International Microgravity Combustion Workshop," NASA Conference Publication, 1992.

4. *Ferkul, P., V.,* "A Model of Concurrent Flow Flame Spread Over a Thin Solid Fuel," NASA Contractor Report 191111, 1993.

5. *Jackson, G., S., Avedisian, C., T. and Yang, J., C.,* Int. J. Heat Mass Transfer., Vol.35, No. 8, pp. 2017-2033, 1992.

6. *Tsue, M., Segawa, D., Kadota, T. and Yamasaki, H.* Twenty-Sixth (International) Symposium on Combustion, The Combustion Institute, 1996, pp. 1251-1258.

7. *Atreya, A, Agrawal, S., Sacksteder, K., and Baum, H.,* "Observations of Methane and Ethylene Diffusion Flames Stabilized around a Blowing Porous Sphere in :g Conditions," AIAA # 94-0572.

8. *Zhang, C., Atreya, A. and Lee, K.,* Twenty-Fourth (International) Symposium on Combustion, The Combustion Institute, pp. 1049-1057, 1992.

9. *Atreya, A. and Agrawal, S.,* "Effect of Radiative Heat Loss on Diffusion Flames in Quiescent Microgravity Atmosphere," *Combustion & Flame*, p372-382, v115, 1998.

10. *Smooke, M. D.(ed.)* "Reduced Kinetic Mechanisms and Asymptotic Approximations for Methane-Air Flames," Springer-Verlag, 1991.
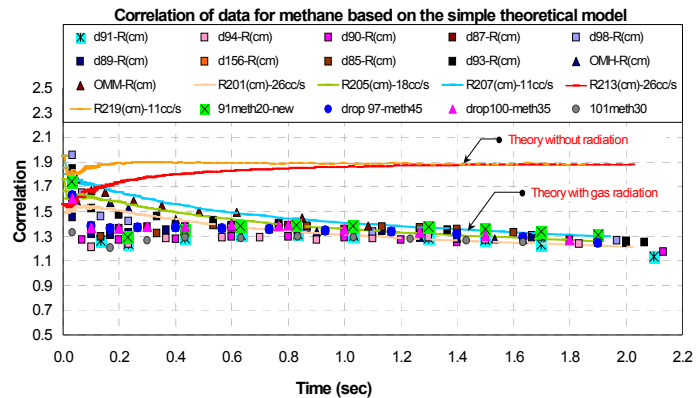
Figure 5
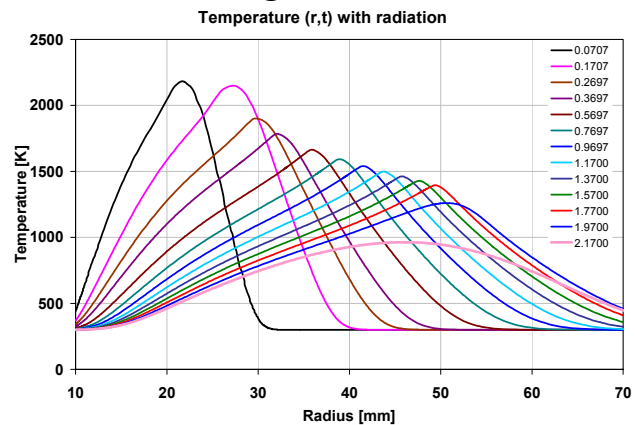
Figure 6: Decrease in the flame temperature due to radiation – Smooke's mechanism [10]
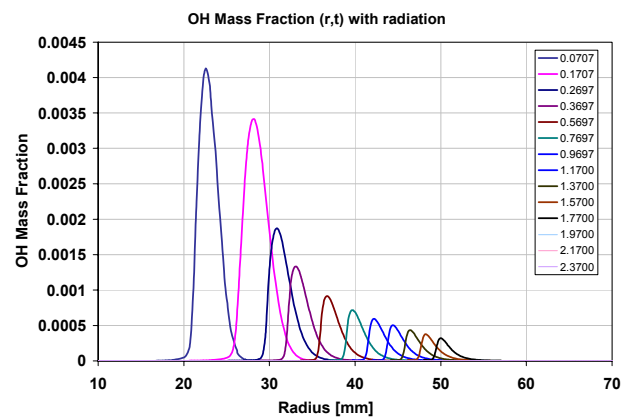
Figure 7: Decrease on OH mass fraction as the flame tends towards extinction.

PARTICLE EFFECTS ON THE EXTINCTION AND IGNITION
OF FLAMES IN NORMAL- AND MICRO-GRAVITY

M.G. ANDAC, F. N. EGOLFOPOULOS & C. S. CAMPBELL
Department of Aerospace & Mechanical Engineering
University of Southern California
Los Angeles, California 90089-1453

INTRODUCTION

Reacting dusty flows have been studied to lesser extent than pure gas phase flows and sprays. Particles can significantly alter the ignition, burning and extinction characteristics of the gas phase due to the dynamic, thermal, and chemical couplings between the phases. The understanding of two-phase flows can be attained in stagnation flow configurations, which have been used to study spray combustion [*e.g.* 1] as well as reacting dusty flows [*e.g.* 2]. The thermal coupling between inert particles and a gas, as well as the effect of gravity, were studied in Ref. 3. It was also shown that the gravity can substantially affect parameters such as the particle velocity, number density, mass flux, and temperature.

In Refs. 4 and 5, the effects of inert particles on the extinction of strained premixed and non-premixed flames were studied both experimentally and numerically at 1-g and μ-g. It was shown that large particles can cool flames more effectively than smaller particles. The effects of flame configuration and particle injection orientation were also addressed. It was shown that it was not possible to obtain a simple and still meaningful scaling that captured all the pertinent physics due to the complexity of the couplings between parameters. Also, the cooling by particles is more profound in the absence of gravity as gravity works to reduce the particle number density in the neighborhood of the flame.

The efforts were recently shifted towards the understanding of the effects of combustible particles on extinction [6], the gas-phase ignition by hot particle injection [7], and the hot gas ignition of flames in the presence of particles that are not hot enough to ignite the gas phase by themselves.

EXPERIMENTAL APPROACH

The experimental configuration includes the use of two counter-flowing jets in 1-g and μ-g. Particles are fed into the flow by using a particle seeder located in the bottom jet. However, the particle pickup is strongly affected by gravitational forces so that the seeder has to be calibrated separately at the lab for 1-g and on board KC-135 for μ-g. Extinction studies were conducted numerically and experimentally with 50-μm combustible glassy-carbon particles. Premixed and non-premixed flame extinction experiments were conducted by varying the particle number density, the equivalence ratio, fuel type, flame configuration, and strain rate.

In all studies, a single flame was established at conditions close to the extinction state, below the gas phase stagnation plane (GSP) by injecting the combustible mixture from the bottom burner with the particles against an air jet. The fuel flow rate was then decreased very slowly, until the flames were extinguished. The final composition was recorded as the extinction

equivalence ratio, ϕ_{ext}, for the prevailing conditions. The strain rates were determined globally. Ignition studies were only performed numerically using 60 and 70-μm Al_2O_3 particles.

NUMERICAL APPROACH

The code was built around a quasi-one-dimensional set of equations for the gas phase similar to the one in [8], by incorporating terms that account for both the dynamic and thermal interactions between the phases. The equations for the particle phase were formulated for a single inert particle, as the number densities are small enough so that particles are unlikely to interact with each other. The code also includes a conservation equation describing the evolution of the particle number density [3]. The solutions are obtained by simultaneously integrating the entire system of equations. The kinetics was described by the GRI 3.0 mechanism [9]. The code is integrated with the CHEMKIN [10] and Transport [11] subroutine libraries.

SUMMARY OF RECENT RESEARCH

The calibration results for carbon particles are shown in Fig. 1 as the variation of injection particle number density, $n_{p.inj}$ with the gas flow rate. It can be observed that for both 1-g and μg, and for both low and high feeder speeds, n_p increases up to a certain flow rate, where it exhibits a local maximum. Above this flow rate, the rate of increase of the amount of particles put in the flow per unit time is smaller than the rate of increase in gas volume flow rate. As might be expected, n_p also increases with the particle feeder speed. The higher the feeder speed, the higher the gas flow rate corresponding to the maximum n_p is reached. More particles are entrained in the flow in μg compared to 1-g at lower flow rates but the amount of particle delivery is the same at higher flow rates regardless of gravity.

Figure 2a depicts the variation of experimentally determined ϕ_{ext} with the global strain rate K_{glb}, in 1-g for CH_4/air flames for injection number density of $n_{p,inj} \approx 0$ and 400 part/cm^3. In both cases ϕ_{ext} increases with K_{glb}, which should be expected as stronger flames are extinguished at larger strain rates. The data reveals that the presence of reacting carbon particles augments the resistance to extinction as weaker flames can be sustained at the same K_{glb}. The results of Fig. 2a also reveal that for high K_{glb}'s the observed difference between the ϕ_{ext}'s obtained with and without particles nearly disappears implying that the particles either do not ignite or even if they do, the ignition occurs well downstream of the gaseous flame so that the effect of the additional heat release has only a small effect on the flame.

Figure 2b depicts similar results for C_3H_8/air flames. Similar to the CH_4 flames, particles appear to resist extinction at the lower K_{glb}'s, but at higher strain rates, the two curves merge and cross each other. Thus, at high strain rates, the particles do not ignite and promote extinction in exactly the same manner as inert particles.

Figure 3 depicts the opposite problem of ignition in the presence of inert particles. It shows the variation of the ignition temperature, T_{ign}, with the injection particle number density, $n_{p,inj}$, for three cases, where 60-μm Al_2O_3 particles are injected at 300 K. In all cases, particles are injected with a 1/3 molar ratio CH_4/N_2 mixture against air. Then, the temperatures of the fuel-side, the air-side or both sides were increased until ignition is achieved.

It is seen that the addition of cold particles into the flowfield significantly affects the ignition temperature for all cases regardless of whether the particles are injected from the hot or cold jet. It is also apparent that much higher temperatures are required for ignition when the air is injected cold compared to other cases. This is solely due to the strong dependence of the ignition process on OH radical generation through the main chain branching reaction $H+O_2 \rightarrow OH+O$. This reaction favors high temperatures and, as the O_2 is only available on the air-side, it will be strongly inhibited by cold air injection.

Looking at the hot air cases, ignition temperatures are smaller if the fuel and particles are initially heated - as would be expected. At first glance it appears that the two curves are parallel, but actually, there is a much weaker effect for the hot-fuel/hot-air case. Note that the two curves are 100 K apart at $n_{p,inj} = 10$ part/cm^3 and 200 K apart at $n_{p,inj} = 1000$ part/cm^3. Figure 4 depicts the gas phase temperature profiles for $n_{p,inj} = 10$ and 1000 part/cm^3 for the two cases right before ignition. For hot fuel, the cold particles cool the gas phase such that the temperatures around GSP are reduced dramatically. Similarly for the cold-fuel case, the location of the rapid temperature rise shifts towards the top burner, again due to the cooling by the particles.

Figure 5 depicts the H radical mass fraction distributions that also serve as markers of the ignition kernels. The results reveal that when the number density is low, the flame tries to ignite very close to the GSP on the air-side, where strain rates are highest. However, the radical pool is larger in magnitude and volume for the case that the temperatures of both jets are increased. The cooling around the GSP shifts the location of the ignition kernels towards the top burner, i.e. to lower strain rate region, but more so for the case for which the temperatures of both jets are increased. Thus, ignition becomes easier for this case compared to the other as $n_{p,inj}$ increases.

Figure 6 depicts the variation of the maximum H mass fraction, $Y_{H,max}$, with $n_{p,inj}$ for cases where premixed twin CH_4/air flames are ignited by hot 70-μm Al_2O_3 particles for three values of the equivalence ratio. The H radical increases rapidly at the ignition point. It is seen that leaner mixtures ignite easier, as indicated by the lower values of $n_{p,inj}$ and $T_{max,ign}$ found as ϕ decreases.

REFERENCES
1. Chen, G. & Gomez, A., *Proc. Combust. Inst.* **24**: 1531-1539 (1992).
2. Gomez, A. & Rosner, D.E., *Combust. Sci. Tech.* **89**: 335-362 (1993).
3. Egolfopoulos, F.N. & Campbell, C.S., *Combust. Flame* **117**: 206-226 (1999).
4. Andac, M.G., Egolfopoulos, F.N., Campbell, C.S. & Lauvergne, R., *Proc. Combust. Inst.* **28**: 2921-2929 (2000).
5. Andac, M.G., Egolfopoulos, F.N. & Campbell, C.S., *Combust. Flame*, **129**:179-191 (2001).
6. Andac, M.G., Egolfopoulos, F.N. & Campbell, C.S., *Proc. Combust. Inst.* **29**, in press.
7. F. N. Egolfopoulos, C.S. Campbell, and M.G. Andac, *Proc. Combust. Inst.* **29**, in press.
8. Bowman, C.T., Frenklach, M., Gardiner, W.R., and Smith, G. 1999 "The GRI 3.0 Chemical Kinetic Mechanism." http://www.me.berkeley.edu/gri_mech/.
9. Kee, R. J., Miller, J. A., Evans, G. H. & Dixon-Lewis, G., *Proc. Combust. Inst.* **22**: 1479-1494 (1988).
10. Kee, R. J., Warnatz, J. & Miller, J. A., Sandia Report SAND83-8209, 1983.
11. Kee, R. J., Rupley, F. M. & Miller, J. A., Sandia Report SAND89-8009, 1989.
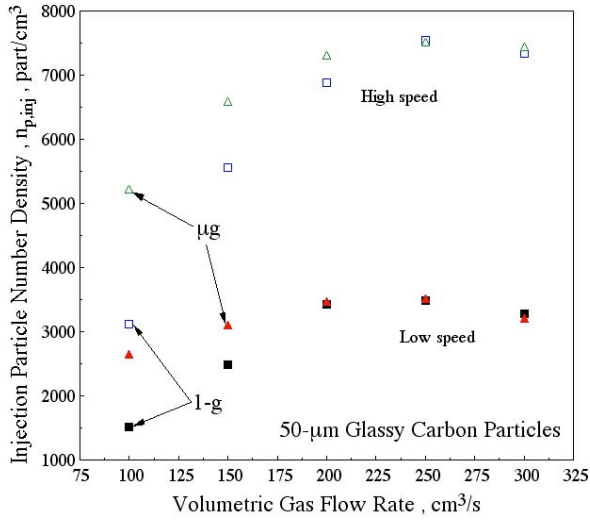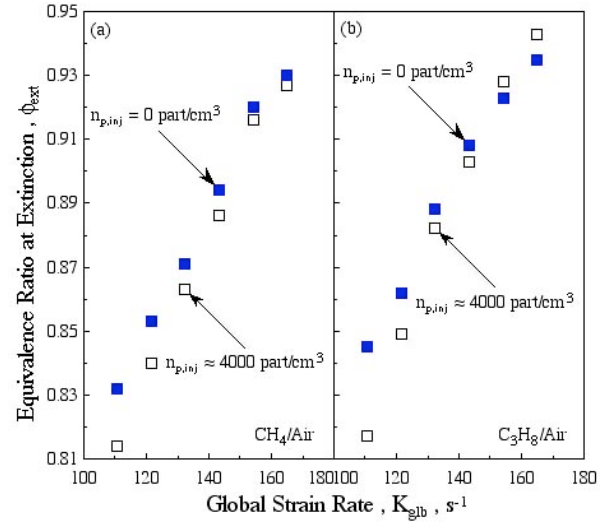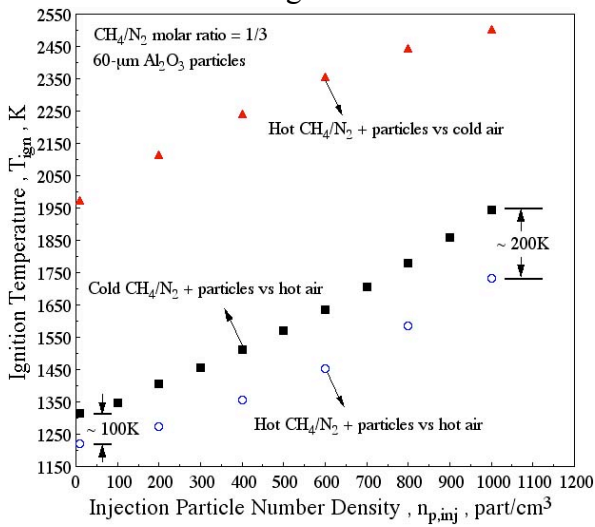
Figure 1

Figure 2

Figure 3
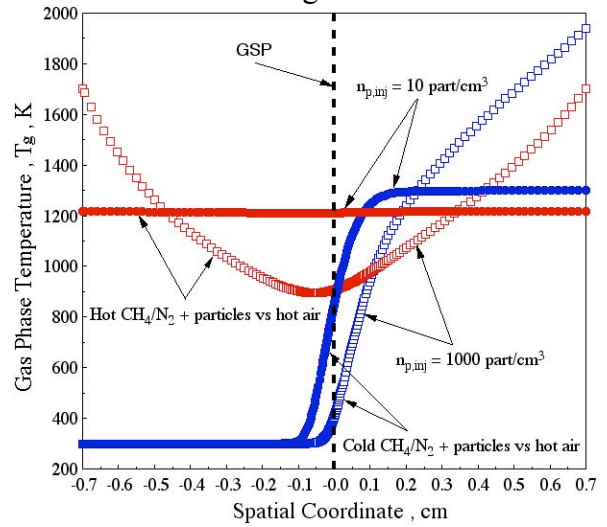
Figure 4
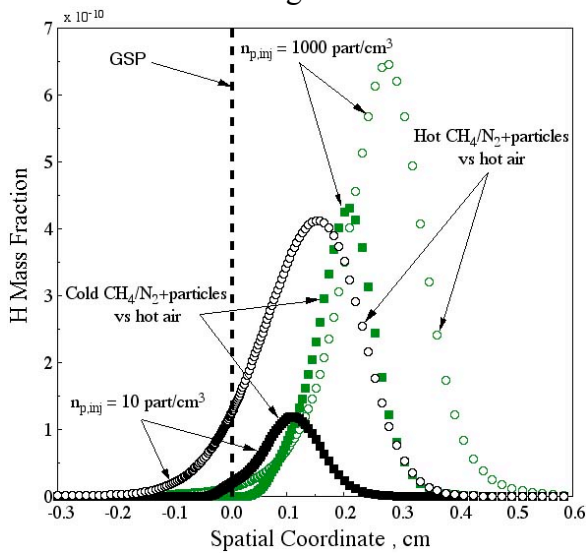
Figure 5
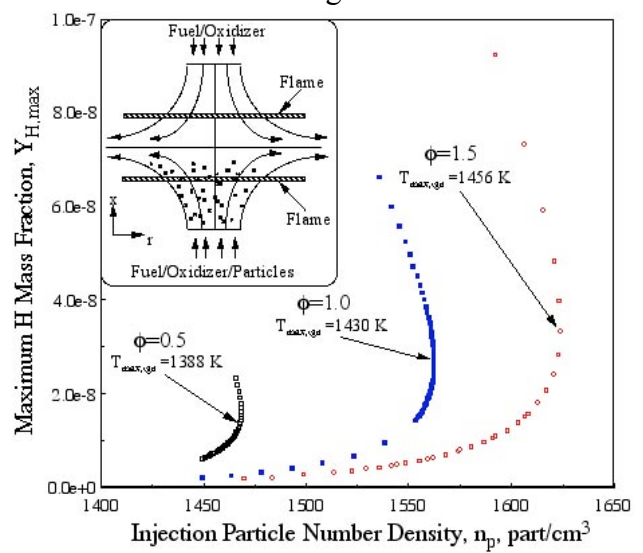
Figure 6

DETAILED DESCRIPTION OF THE STRUCTURE OF A LOW VELOCITY LAMINAR DIFFUSION FLAME IN MICROGRAVITY

Pierre CORDEIRO, Guillaume LEGROS, Sébastien ROUVREAU, Pierre JOULAIN
Laboratoire de Combustion et Détonique – UPR CNRS – ENSMA – Université de Poitiers – BP 40109 – 1 Avenue Clément Ader – 86961 Chasseneuil Futuroscope Cedex – France
José L. TORERO
Department of Fire Protection Engineering - University of Maryland - College Park – MD 20742-303 - USA

Abstract
This paper reports on a detailed experimental study of the velocity fields across a combustion chamber and the associated CH^* and soot extinction measurements performed on the diffusion flame. Experiments were conducted with a gas fuel burner and on board of the Airbus A300. The measurements revealed the detailed three-dimensional nature of the flow and its influence on flame geometry and flame length. Experimental results have been compared with numerical simulations showing good agreement. CH^* measurement have been used to define the reaction zone and incorporate a corrective factor to the soot extinction measurements leading to a more precise mapping of soot concentrations around the flame. Preliminary agreement has been observed for radiation heat losses between radiometer data and the analytical expressions developed using soot concentration evaluations.

Introduction

Motivated by fire safety concerns and the advent of long-term microgravity facilities, a renewed interest in fire propagation at very low Reynolds number has arisen. In spacecraft buoyancy is negligible and the flow is limited to that induced by the ventilation system. In normal gravity, temperature gradients result in natural convective flows that are laminar when scale is small and leading to transition to turbulence as the size of the fuel increases. When gravity is neglected, the problem of a chemically reacting boundary layer flow over a flat-plate resembles the classical combustion problem first described by Emmons [1].

Within this framework is the intent of this study to provide further detail on the characterization of the flow, geometry and location of the flame. However most of the analysis is devoted to the estimation of the flame radiative feedback, transport phenomena essential for the determination of material burning rate and their flammability and extinction limits. The soot volume fraction, required for radiation heat transfer evaluation, is obtained on the basis of attenuation measurements on a micro-gravity diffusion flame. It was found necessary to complement the attenuation measurements with CH^* measurements.

All the experiments were performed during parabolic-flight campaigns and at the Bremen drop tower. The pyrolyzing fuel is modelled by means of an ethylene burner through which airflow leads to boundary layer type conditions. The experimental hardware has been already described elsewhere [2, 3] and will not be presented here.

Structure of the reacting flow: flame location and geometry

The structure of the flame is analysed through spontaneous flame zone emission, either visible flame emission or CH^* radical emission, using high definition CCD cameras and an adequate filter (centred at 532nm for CH^*). For PIV measurements the oxidizing flow is seeded with 5μm zirconium oxide particles, illuminated by a 26mJ mini-YAG laser.

The flow mapping by PIV underlines the perfect laminar character of the incoming stream over the mean velocity range of concern 0.02m/s to 0.2m/s. It also shows that the external flow is accelerated at the vicinity of the flame, in the near downstream of its leading edge,

which leads to the velocity overshoot observed in previous studies but at earth gravity. These observations are very consistent with the numerical results obtained from a computational analysis [4].
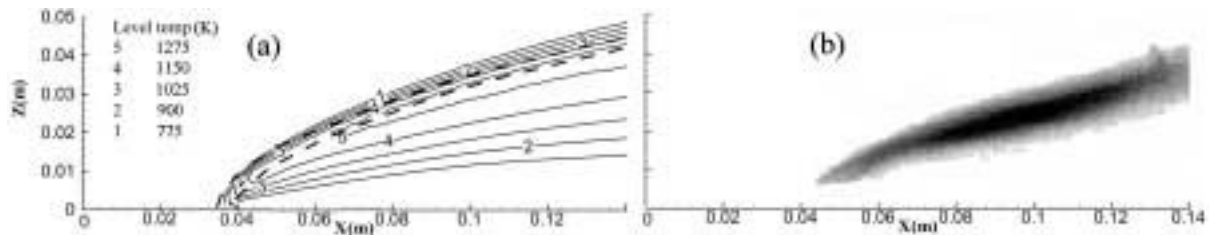
Figure 1(a) Temperature distribution for a reactive flow: the heat release zone is delimited by the grey dashed contour. The fuel injection is set to V_f= 0.003 m/s and the free stream velocity to 0.1 m/s. The origin of the plate is set at X=0, Z=0 and the air flows for Z>0. The leading edge of the porous burner is placed at X=0.04 m. **1(b)** Micro-gravity experiments visible flame. The fuel injection is set to V_f= 0.003 m/s and the free stream velocity is 0.1 m/s (negative image).

A comparison between the high temperature zone and the location of the reaction zone obtained from numerical simulations (Figure 1a) with the location of the visible flame observed in microgravity experiments (Figure 1b) shows a fairly good agreement too.
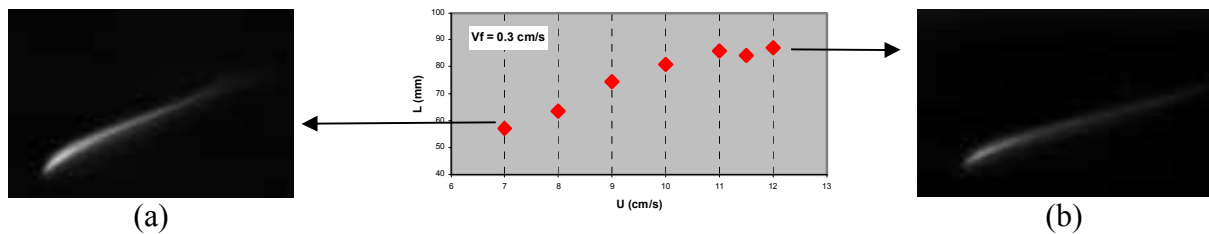
Figure 2 Influence of the mean oxidizer flow velocity U on the mean flame length L for V_f = 0. 003 m/s (fuel injection velocity): a) U = 0.07 m/s   b) U = 0.12 m/s

It appears clearly on figure 2 that U has a great influence on both the flame length and flame stand-off distance. Moreover the flame length is not sensitive to V_f for a given U, but the flame standoff distance is more. Increasing V_f tends to push the flame zone upward, as a consequence of the increase of the blowing ratio. An increase in oxygen mass fraction, 35% of oxygen, leads to a flame zone that appears larger, longer and more luminous. CH^* emissions show that the flame zone enlarges close to the burner and consequently the flame standoff distance decreases.

The data concerning flame length and flame standoff distance are of major importance for the determination of the view factor needed to get the radiative heat feedback from the flame to the surface. However more information is required on the radiative properties of the reacting flow.

Soot layer properties
The characterisation of the soot layer is based both on CH* chemiluminescence's and laser extinction measurements [3]. Concerning CH^* emissions quantitative results can be achieved for premixed flames and while being cautious about extrapolation to diffusion flames some results are of interest. It has been noticed [5, 6] that CH^* chemiluminescence increased when approaching the stoechiometry and even more when pressure decreased towards atmospheric. This provides evidence that for our particular experimental conditions the signal to noise ratio

will be high. Since pressure is atmospheric, the reaction zone is narrow and should be characterized by an equivalence ratio close to stoechiometric. As it has been shown [7] that the volumetric rate of heat release is proportional to the CH^* emission intensity. Thus it is possible to plot relative variations of the local CH^* intensities, in relation with the maximum measured value. The structure of the overall reaction zone was captured by two two-dimensional CH^* chemiluminescence imaging. A side view of the flame provides the emission integrated over the width of the flame y, at different x locations, in the stream direction. A top view of the flame collects the flame emission from the flame surface at different z heights which are assumed to correspond to the flame stand-off distance. The ratio between top and side view emissions is used as a corrective factor for the side view measurements. By analogy this corrective factor is then applied to soot extinction measurement.

The laser extinction measurements were performed to estimate the optical thickness under the flame. According to the literature [8] the error does not exceed 1%. Therefore this study does not account for induced emission. Moreover chopping the laser source allows measuring, somehow, pure extinction, i.e. without flame and sooting spontaneous emission. By subtracting the unbacklighted image to back lighted one, a correct extinction measurement is made. Considering the literature [9] it is possible to get from our measurements, an "equivalent absorbing soot volumetric fraction" and then to calibrate the integration over the soot layer height (z direction). From that the optical thickness for several wavelengths over the thermal radiation spectrum is obtained.
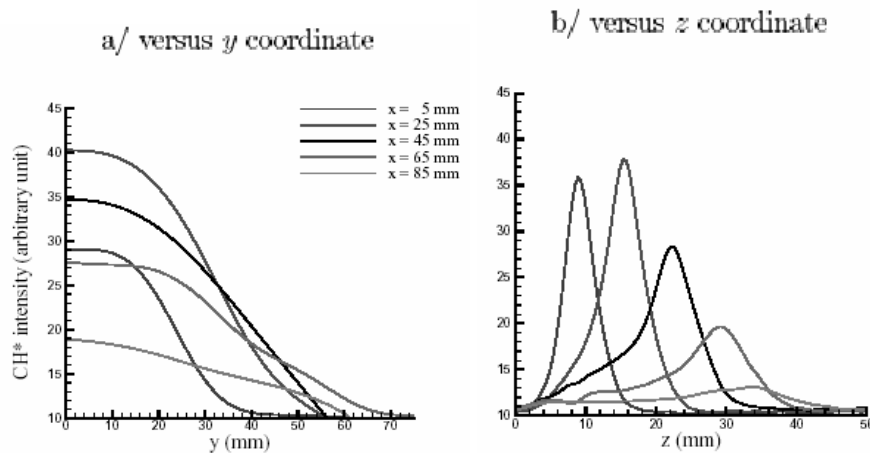
Figure 3 CH^* chemiluminescence intensity cross-sections at different x stream wise coordinate.

From Figure 3a, it can be seen that the reaction zone, small near the leading edge, thickens with the distance downstream. Figure 3b shows that the width of the reaction zone follows the same tendency. On both cross-sections, the maxima occur at the same stage. On Figure 4 the ratio (side view/top view) of the integrated CH^* chemiluminescence intensities is plotted versus stream wise coordinate. The ratio is constant and equal to 0.08 for x between 0.02 and 0.055m. The decay near the trailing edge is related to three-D phenomena.
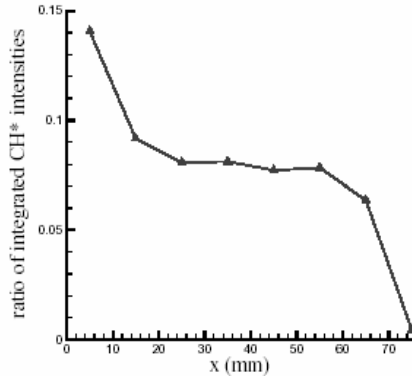
Figure 4 Ratio of the integrated CH* intensity.
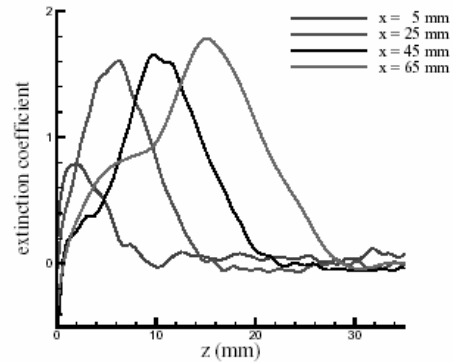
Figure 5 Extinction coefficient at different x and elevation z

Figure 5 exhibits now the cross-section of the effective extinction coefficient. On the range of constant ratio, the extinction characteristics are nearly constant in height and width. This shows that modifications of soot structure are small enough not to change the adsorption coefficient. Accounting for three-dimensional effects by analogy with CH^* chemiluminescence data, the width of soot extinction coefficient was corrected. From our measurements and data from the literature [9] an equivalent absorbing concentration of soot has been obtained. Integration over the soot layer width in the z direction brings an estimation of the optical thickness whose evolution has been computed according to our analysis. Finally it appears that neglecting soot absorption in such a flame will not lead to a significant result. Moreover all the data obtained both on the structure of the reacting flow, including the flame shape and location and on the radiative properties of the system should be very useful in the evaluation of the radiation transport to the surroundings.

References

1. Emmons, H., *Z.Angews Math.Mech.*36, 60, (1956).
2. Vietoris, T., *« Etude de la Combustion quasi stationnaire d'un combustible solide soumis à un écoulement parallèle à sa surface »,* Thèse de Doctorat de l'Université de Poitiers, 30 Juin 1999.
3. Legros, G., Joulain, P., Vantelon, J.-P., Breillat, C., Torero J.L., *« Estimation of a soot layer optical thickness produced by a diffusion flame established in microgravity"* 3rd Mediterranean Combustion Symposium, Marrakech, Marocco, June 8-13, 2003.
4. Rouvreau S., Joulain P., Wang H.Y., Cordeiro P., Torero J.L., "*Numerical Evaluation of Boundary Layer Assumptions Used for the Prediction of the Stand-off Distance of a Laminar Diffusion Flame*", Proceedings of the 29th International Symposium on Combustion, The Combustion Institute, Pittsburgh, 2002. (In Press).
5. Higgins, B., McQuay, ,M.Q., Lacas, F., Candel, S., *Fuel,* 80, 1583-1591, (2001).
6. Berg, P.A., Hill, D.A., Noble, A.R., Smith, G.P., Jeffries, J.B., Crosley, D.R., *Comb. and Flame,* 118, 684-696, (2000).
7. McManus, K., Yip, B., Candel, S., *Exp.Thermal and Fluid Science,* 10, 486-502, (1995).
8. Siegel, R., Hottel, J.R., *Thermal Radiation Heat Transfer,* 2nd Edition, Hemisphere Publishing Co., 1981, p.431.
9. Dalzell, W.H., Sarofim, A.F., *J.Heat Transfer,* 91, 100-104, (1969).

MODELING DEFORMATION OF MELTED POLYMER
ON WIRE INSULATION BURNING IN MICROGRAVITY

M. Uchida and A. Umemura
Department of Aerospace Engineering,
Nagoya University, Furo-cho, Chikusa-ku, Nagoya, 464-8603, Japan

INTRODUCTION

Flame spreading over a flat solid fuel bed of various material have been investigated for the purpose of fire safety. Among them, combustion of the electrical wire insulation is characterized by the existence of the core wire with very large thermal conductivity. In our previous study [1] on an ETFE (Ethylene-Tetrafluorethylene)-insulated Copper wire, it was demonstrated that the copper wire acts as both heating and cooling medium on the burning of wire insulation and the mechanism for the spherical flame formation was proposed as shown in Fig.1. The uncoated, that is the coating being burned out, copper wire inside of the flame receives heat from surrounding hot gas and conducts part of it to the coating to enhance gasification. On the other hand, at the station where the flame touches with the coating surface, the flame extinguishes locally due to heat loss to the copper wire through the coating. The gasification of coating produces strong Stefan flow which tends to reduce the heat flux toward the coating surface through the gas phase.

Microgravity experiments by Fujita et al. [4] have shown that the combustion of Polyethylene-insulated wire has different characteristics from that of ETFE-insulated wire [2,3]. The spheroidal shape of melted coating is formed near the center of the spherical flame due to surface tension and the blue flame is observed at the leading edge of the flame. In the present study, a mathematical model is developed to investigate the effect of melting, gasification and deformation of polymer coating on combustion of Polyethylene-insulated wire in microgravity. Numerical results of the present model contribute to the further understanding of the role of core wire in the formation of spherical flame.

Fig.1 proposed mechanism for formation of spherical flame

FLAME SPREAD MODEL

To develop the thermal pyrolysis model, the following assumptions are introduced.

(1) Phase change of the coating occurs at a certain melting and boiling temperature.
(2) The physical properties of the coating material are constant.
(3) Quasi-steady heat conduction within the coating and the melted polymer occurs only in the radial direction at each station along the wire.
(4) Volume change of the coating occurs only at the instance of phase change.

(5) The lubrication theory can be applied to describe the melted coating flow.
The core wire temperature doesn't change without receiving the large radial heat flux from the coating because thermal conductivity of the core wire is very large. Since the propagation speed of spherical flame is small, the quasi-steady condition for the temperature distribution inside of the coating is valid.

The configuration of melted polymer, core wire temperature and surrounding gas temperature distributions in Fig.2 are assumed for the modeling. We can identify the following four different states.

(1) $z_1 < z < z_2$

At the part where the wire temperature is higher than the boiling point, regardless of the surrounding gas temperature the coating is at the boiling temperature everywhere. This assumption is appropriate, because the surrounding gas temperature is always higher than the boiling point inside of the spherical flame and wire temperature is highest at the uncoated wire part [1]. The coating is assumed to gasify only at the surface and the gasification rate is determined from the thermal inflow from the surrounding gas and the core wire. The shape of melted coating surface is determined by surface tension.

(2) $z_2 < z < z_3$, $z_3 < z < z_4$

At the part where the wire temperature is lower than the boiling point and the surrounding gas temperature is higher than the boiling point, the melted part exists near the surface or the totally melted part appears on condition. At this part, the coating is heated by surrounding hot gas, while it's cooled by core wire. The shape of melting surface is determined according to thermal inflow from the surrounding gas and the core wire. The shape of melted coating surface is determined by the effect of surface tension and volume expansion at the melting surface.

(3) $z_4 < z < z_5$

At the part where the wire temperature is lower than the melting point and the surrounding gas temperature are lower than the boiling point, the coating melt only at the surface. The small gasification rate can be neglected. Surface temperature of the coating is determined from the thermal inflow from the gas and the core wire.

(4) $z_5 < z$

At the part where both wire temperature and surrounding gas temperature are lower than the melting point, the coating is solid. The surface temperature of the coating is determined according to thermal inflow from the gas and the core wire.

Depending on the condition, the melting of coating starts form the wire surface. Such a case is incorporated in the calculation when necessary.
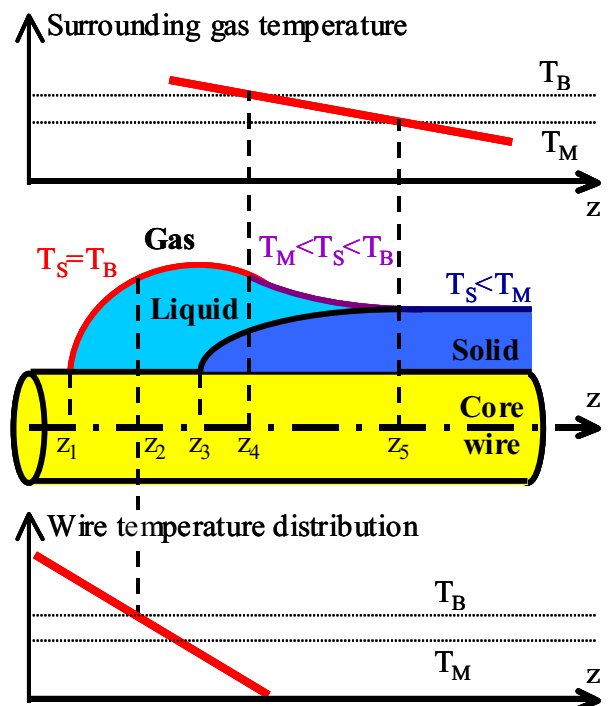
Fig.2 Configuration of melted polymer, core wire temperature and surrounding gas temperature

The core wire temperature is calculated according to a one-dimensional unsteady heat conduction equation with heat loss to the coating (coated part) or surrounding gas (uncoated part). The reactive gas-phase equations in the low mach-number approximation are solved using the transformed coordinates compatible to the coating surface deformation in the SIMPLE method. An Arrhenius type of one-step reaction is applied to describe the combustion of reactive gas. The effects of radiation from the combustion gas and the solid surface radiation loss are neglected, all transport properties are constant and Lewis number is unity in the gas phase. The equation system is made dimensionless using the ambient gas properties and the core wire radius.

RESULTS AND DISCUSSION

Figure 3 shows the temperature (top), fuel mass fraction (middle) and reaction rate (bottom) contours of the flame which propagates steadily from left to right. It is found that the left hand side of the flame is spherical, but the right hand side of the flame is slightly elongated to the forward direction. This is because the gasification of the coating occurs over a rather long range between the coating edge and leading edge of the flame, as can be seen from the fuel mass fraction contour. This point is different from the result of the previous study [1], in which the coating gasification part is restricted to the vicinity of the coating edge. Correspondingly, at leading edge of the flame, the gasified fuel reacts with oxygen near the coating surface. This flame shape change is consistent with experimental observation by Fujita et al. [4].

Figure 4 and Figure 5 show the phase state of coating and temperature distribution along the wire, respectively. It is shown that in the steady flame propagation state, the phase state of the coating is classified into four parts, (1) totally melted part, (2) two melted parts separated by a solid phase part, (3) surface melted part, (4) totally solid phase part. The totally melted part is restricted to the vicinity of coating edge and coating gasification rate is highest at the coating edge. Because thermal inflow from the surrounding gas is small compared to that from the core wire. Inside of the spherical flame, the coating receives heat from the surrounding hot gas, however the part of the coating is cooled by the core wire. Therefore, the separated melted part emerges where the core wire temperature is higher than the

Fig.3 Temperature, fuel mass fraction and reaction rate contours of the flame in the steadily propagating state
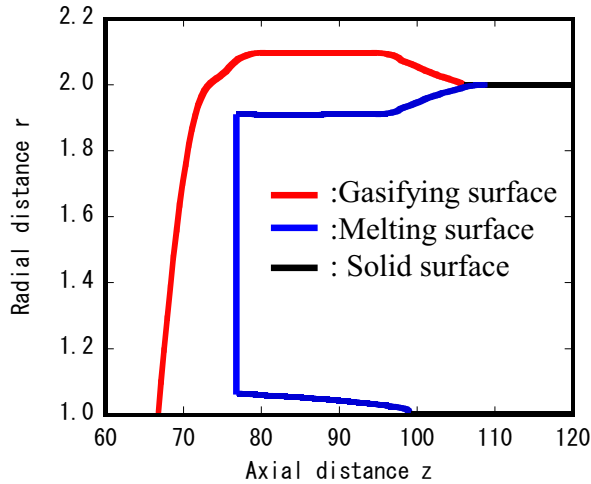
Fig.4 Phase state of coating
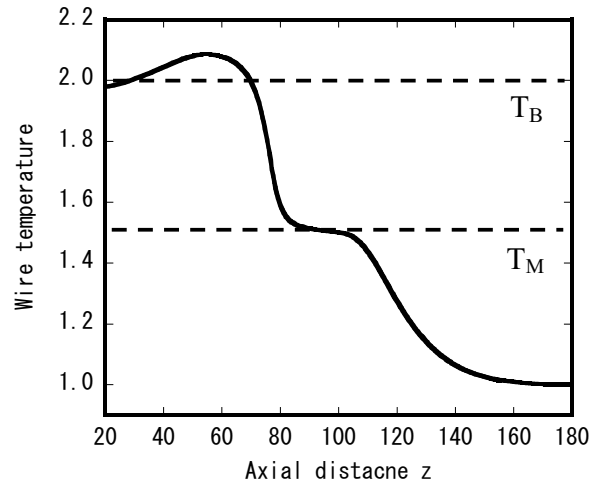
Fig.5 Temperature distribution along wire

melting temperature and the surface melting part emerges where the core wire temperature is lower than the coating temperature. The heat loss to the core wire through the melted/solid coating controls the chemical reaction at the leading edge of the flame. Therefore, the leading edge of the flame cannot self-propagate. These calculation results demonstrate the roles of core wire as both heating and cooling medium. Flame shape is kept nearly spherical, due to the balance between propagation speed of the coating burnout edge which is enhanced by the heat feedback via the core wire and that of the flame front which is limited by the cooling effect of core wire.

SUMMARY

In the present study, the mechanism of Polyethylene-insulated wire burning is examined using the deformable coating pyrolysis model. Though the flame shape and length of coating gasifying region are different from the results of the previous study [1], the roles of core wire as both heating and cooling medium are confirmed. However, the present model needs some improvement because the melted coating shape obtained in the present study differs from that of the experimental results.

REFERENCES
1． Umemura, A., Uchida, M., Hirata, T. and Sato, J., *Proc. Combust. Inst*. 29 (2002), in print.
2． Hirata, T., Sato, J., Iwanami, T., Katano, M. and Imagawa, Y., *Proc. of 35th Japanese Symposium on Combustion*, 1997, pp.82-84.
3． Hirata, T., Sato, J., Iwanami, T., Iwasaki, S., Imagawa, Y. and Ito, K., *Proc. of 36th Japanese Symposium on Combustion*, 1998, pp.480-482.
4． Fujita, O., Nishizawa, K. and Ito, K., *Proc. Combust. Inst*. 29 (2002), in print.

MARS ISRU CO/O$_2$ ROCKET ENGINE DEVELOPMENT AND TESTING

E.E. Rice, D.J. Gramer, C.P. St.Clair, and M.J. Chiaverini
Orbital Technologies Corporation (ORBITEC^{TM})
Madison, WI 53717

INTRODUCTION

This article addresses the current status of a research and development effort in which ORBITEC has undertaken to test new types of ISRU-based propulsion systems for use on Mars. The Martian atmosphere (about 95.5% CO$_2$) provides a readily available supply of carbon dioxide (CO$_2$) to produce both CO and O$_2$, which can be used for rocket engine applications. Hybrid propulsion systems have several safety and operational features that make them attractive for space systems. For Mars ISRU applications, CO gas can be frozen directly to form a solid fuel grain, then burned with liquid oxygen. Alternatively, both CO and O$_2$ gas can be liquefied and burned in a liquid propellant combustion chamber. This article presents the results of a hybrid rocket test program that used storable propellants to simulate SCO/LOX combustion, as well as a discussion of future tests with a vortex combustion, liquid bipropellant CO/O$_2$ thrust chamber.

METHOD OF APPROACH

Previous articles have discussed the testing of a lab-scale cryogenic hybrid rocket that burned solid CO and gaseous oxygen in a classical hybrid rocket configuration, i.e., injection of the oxidizer along the axis of a solid-fuel tube.[1,2] The current work focuses on an alternate hybrid configuration: the vortex end-burning hybrid (VEBH). The end-burning hybrid configuration provides the advantages of a constant fuel surface area and potentially higher regression rates than possible using solid cryogenic fuels in the classical configuration. Since the fuel burning surface area is fixed, the engine mixture ratio can be controlled by varying the oxidizer mass flow rate and/or the combustion chamber diameter (fuel surface area). Classical hybrids have a time-varying mixture ratio because the burning surface area changes with time due to increases in the port diameter. In addition, the swirling nature of the VEBH oxidizer increases the fuel regression rate by a significant degree.

The VEBH shown in Fig. 1 was designed for use with HTPB, a storable, rubber-based hybrid fuel, and gaseous oxygen. The goal of the VEBH testing was to determine the effects of combustion chamber diameter, injected oxygen mass velocity, and separation distance (δ) between the GOX swirl injectors and initial fuel surface location. These results are helpful for the design of the SCO/O$_2$ vortex end burning hybrid. Specific operational characteristics of interest include ignition, regression rate, scaling, burning uniformity, and the internal flow field.

The engine consists of a ring chamber sandwiched between mating top and bottom plates. Gaseous oxygen is tangentially injected through ports at the tail (nozzle) end of the each chamber. The initial distance from the centerline of the injection point to the grain surface was studied at three levels by controlling the initial grain thickness. The number of injection ports was also varied. There are two ring-chambers of each chamber size; one with "small" diameter injection ports, and the other with "large" diameter injection ports. This allows the effects of injector port mass flux to be studied, defined as the oxygen flow rate divided by the injector port area. The oxygen flow rate for each chamber diameter was selected to achieve a chamber port mass flux of 0.132 g/cm^2-s. This is defined as the total oxygen flow rate divided by the cross sectional area of the chamber. The nozzle throat sizes were designed to produce a constant

chamber pressure of approximately 150 psig for all the experiments. An H_2/O_2 torch was used to ignite the solid fuel. Test times were about 5.2 s.
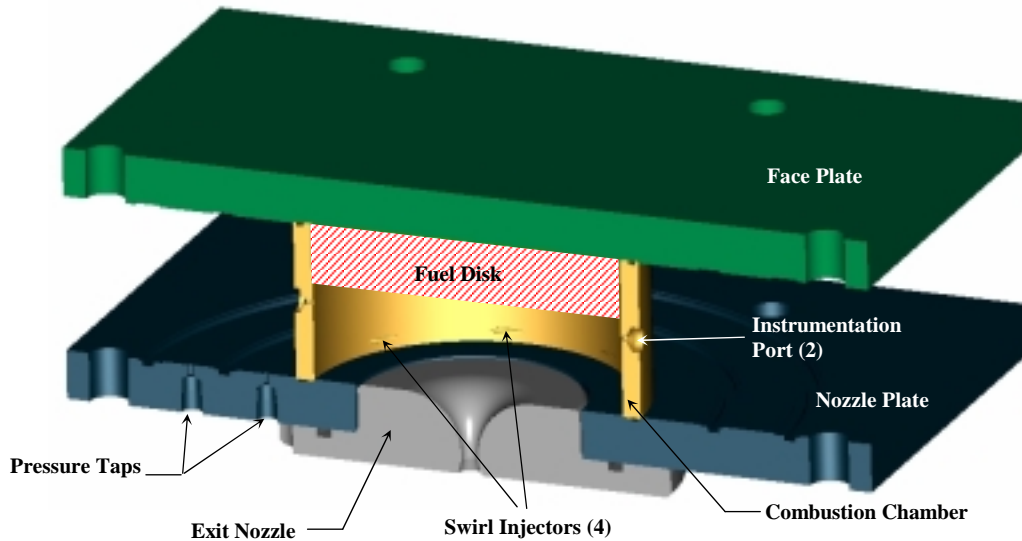
Figure 1. VEBH II with 4-inch Chamber (4 Swirl Injectors)

RESULTS AND DISCUSSION

Figure 2 shows a typical post-firing fuel grain. The swirl pattern is evident. Interestingly, a "counter swirling" pattern of grooves exists near the center of the chamber. These grooves appear to indicate flow opposite that of the swirl GOX injection. One possible explanation for this finding is that the flow is actually spiraling outward from the center of the chamber, rather than inward. In this case, the flow would be spinning in the same direction as the GOX injection. A portion of the oxygen may be spiraling along the bottom of the chamber and up to the head end in the central region where it meets the grain surface and flows back outward. In this case, the flow field might consist of two interwound spirals in the central region of the chamber, with one spinning upwards, and the other spinning down towards the nozzle. This behavior is currently under further investigation. In addition, all of the spent grains had a concave region in their center where there is accelerated regression. The surface of the concave region is textured with shallow pockets.
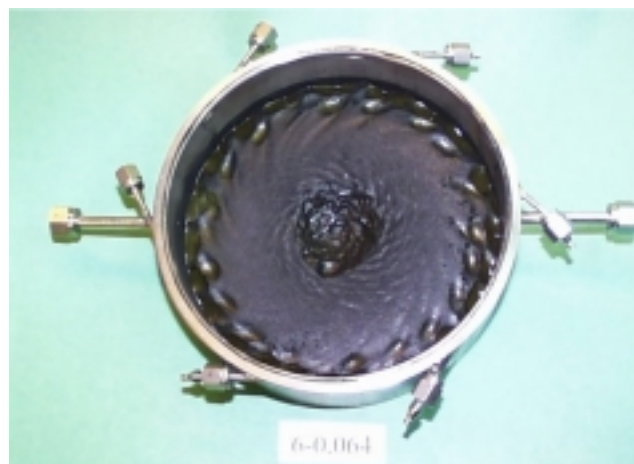
Figure 2. Typical Grain Contour After a Firing

Statistical analysis of the average regression rate response was conducted considering the following independent variables: injector port mass flux, average injection distance, and chamber diameter. The experimental oxidizer mass flux varied by about 10% during the testing. This was accounted for by normalizing the data as follows:

$r_{tran} = r_{exp}/(G_{o,exp})^{0.62}$
Where:

> r_{tran} = *transformed regression rate used for statistical analysis (cm³/g)*
> r_{exp} = *experimental regression rate (cm/s)*
> $G_{o,exp}$ = *experimental oxidizer mass flux (g/cm²-s)*

The motivation for this transformation was to reduce the variability in the regression response caused by differences in mass flux, thereby increasing the sensitivity of the statistical analysis. The exponential relationship between regression rate and mass flux (0.62) was experimentally determined during a previous end burning hybrid test program.

Injector port mass flux and injection distance were found to have a statistically significant effect on the regression rate. Injection distance had about twice the effect of injector port mass flux on the regression rate. The statistical model, shown as Equation 1, predicts a linear relationship between the relevant variables. Note that the regression rate has been un-transformed. No interactions among the independent variables were found to have an effect.

$r = G_o^{0.62}(0.332+3.47E\text{-}3G_{o,p}-0.0224D_{inj})$ -(1)
Where:

> r = *regression rate (cm/s)*
> G_o = *oxidizer mass flux (g/cm²-s)*
> $G_{o,p}$ = *injector port mass flux (g/cm²-s)*
> D_{inj} = *distance from injector to grain surface (cm)*

The optimum mixture ratio for HTPB/GOX is 2.4. As shown in Table 1, the firings were all quite fuel rich. Equation 1 can be used in the future to optimize the design with respect to average mixture ratio.

An important finding of this work is that the chamber diameter was not found to have an effect on the regression rate. Recall that the oxidizer mass flux was designed to be the same for each chamber size/test. This result suggests that the end burning hybrid regression rate scales quite predictably with respect to chamber size, demonstrated here by a factor of four (with respect to port area).

FUTURE WORK

ORBITEC has recently completed design and fabrication of engine hardware to support testing of a vortex combustion cold-wall bipropellant rocket engine with gaseous carbon monoxide and gaseous oxygen. Figure 3 presents a section view of the engine assembly and a top view of the nozzle/vortex injector.

ORBITEC's vortex cold-wall engines operate by establishing a protective layer of cool, unburned propellant between the chamber wall and the combustion zone. This has the primary benefit of shielding most of the chamber wall surfaces from direct contact with hot gases, minimizing the thermal loading and the requirements for active cooling. The basic injection pattern to achieve this effect is illustrated in Figure 3. One of the propellants is injected from the bottom of the engine in a swirling pattern tangent to the chamber wall. This propellant swirls around the wall,

climbing as it goes, until it reaches the top of the chamber. Here, it turns towards the nozzle, entering a downward-swirling co-axial combusting vortex. It also encounters the second propellant, which is injected from the head end. These propellants mix and burn as they swirl down and out of the engine.

Hot fire testing of this engine with CO/GOX is projected to begin shortly after the time of this writing. The preliminary test plan calls for exploring the effects of several variables, including CO ΔP, GOX ΔP, the number of head-end injector ports, the fan angle of the head-end injector ports, the length of the chamber, the propellant mass flow, and the propellant orientation.
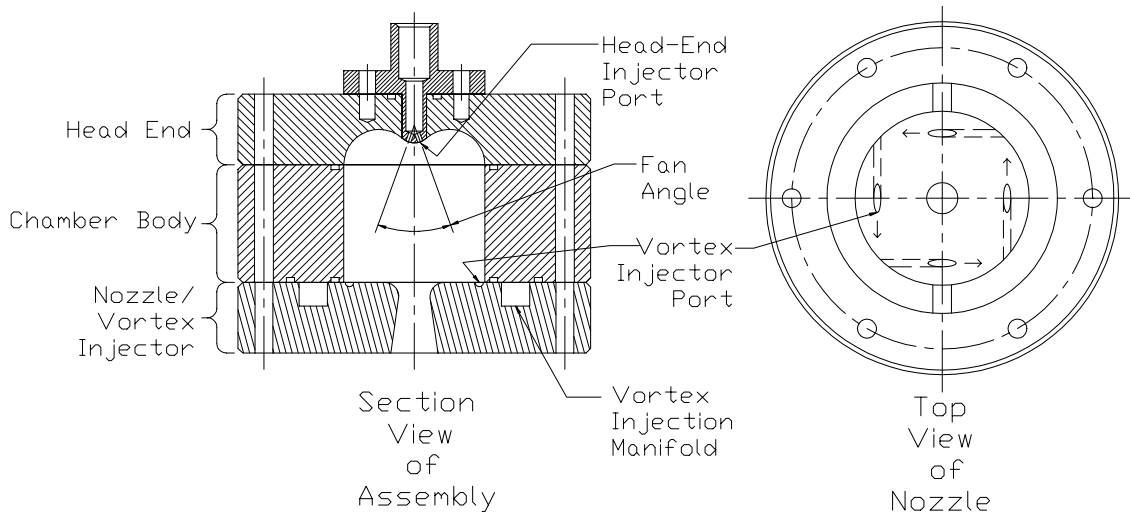
Figure 3. Basic Design of the Carbon Monoxide/GOX Vortex Cold-Wall Engine

REFERENCES

1. Rice, E. E., Chiaverini, M. J., St.Clair, C. P., Knuth, W. H., and Gustafson, R. J., "Mars ISRU CO/O_2 Hybrid Engine Development Status," AIAA 2000-1066, Reno, 2000.

2. Rice, E. E., Chiaverini, M. J., Malecki, M.J., St.Clair, C. P., Knuth, W. H., Gustafson, R. J., and Gramer, D.J., "Status Report on Mars ISRU CO/O_2 Hybrid Engine Development and Testing," presented at the 2001 IMCW, Cleveland, Ohio, May, 2001.

COMPUTATIONAL AND EXPERIMENTAL STUDY OF ENERGETIC MATERIALS IN A COUNTERFLOW MICROGRAVITY ENVIRONMENT

M. D. Smooke
Yale University

T. P. Parr and D. M. Hanson-Parr
Naval Air Warfare Center China Lake

R. A. Yetter
The Pennsylvania State University

ABSTRACT

Counterflow diffusion flames are studied for various fuels flowing against decomposition products from solid AP pellets in order to obtain fundamental understanding of composite propellant flame structure and chemistry. In this paper, we illustrate this approach through a combined experimental and numerical study of a fuel mixture consisting of CO and H_2 flowing against solid AP. For this particular AP-fuel system, the resulting flame zone simulates the flame structure that is expected to exist between reaction products from fine AP crystals and a hydrocarbon binder with the decomposition products from large AP crystals, characteristic of a bimodal AP propellant. As in all our experimental studies, quantitative species and temperature profiles have been measured between the fuel exit and AP surface. Species measured included CN, NH, NO, OH, N_2, O_2, CO_2, H_2, CO, HCl, and H_2O. Temperature was measured using a thermocouple at the exit, spontaneous Raman scattering measurements throughout the flame, OH rotational population distributions, and NO vibrational population distributions. The burning rate of the AP was also measured for this flame's strain rate, given by a separation distance of 5 mm. The measured 12 scalars are compared with predictions from a detailed gas-phase kinetics model consisting of 86 species and 531 reactions. Model predictions are found to be in good agreement with experiment and illustrate the type of kinetic features that may be expected to occur in propellants when AP particle size distributions are varied. Furthermore, the results constitute the continued development of a necessary database and validation of a comprehensive model for studying more complex AP-solid fuel systems in microgravity.

INTRODUCTION

The potential to 1) increase specific impulse, muzzle velocity, and payload mass, as well as 2) assess the safety and reliability of systems containing propellants or explosives that are subjected to normal and abnormal environments, is highly dependent upon the ability to formulate and to model new and existing energetic materials. Systems of this type could be monopropellants or energetic composites comprising oxidizer particles of different sizes, which are randomly imbedded, for example, in a thermoplastic elastomeric binder. The development of advanced propellants employing new nitramines and energetic binders requires a more sophisticated approach than the conventional methods of testing a matrix of ingredients to arrive at a formulation empirically. The latter approach is too costly and time-consuming for the large matrix of nitramine/binder combinations.

In the present research, we have developed a combined experimental and computational program that focuses on the prediction of micro combustion parameters like flame structure, temperature profile, heat release, and species concentrations as well as global parameters such as burn rate and pressure exponent for development of a comprehensive propellant combustion model that may eventually be used for design and optimization of propellant formulations as well as study of their storage and disposal. We are studying propellant ingredient combinations through a systematic approach using a counterflow diffusion flame configuration, which separates the fuel and oxidizer and extends the reaction zones spatially, allowing diagnostics to measure quantitative species and temperature profiles while simplifying the fluid flow of the numerical simulations allowing the program to concentrate on propellant kinetics.

In a typical counterflow diffusion flame experiment two laminar plug flow jets, one of fuel and one of oxidizer, are directed at each other so they impinge in the middle of the domain. Properly designed, this configuration leads to one-dimensional flames that can be modeled with the lower CPU demand of 1D codes. In addition, the experimenter has complete control over many flame parameters including fuel chemistry, fuel thermal properties, flame strain rate, etc. In our case

Figure 1. Experimental Configuration.

the oxidizer side is not a jet but a solid pellet of ammonium perchlorate (AP) (Fig. 1). AP does not normally self deflagrate at pressures below about 200 PSIA (depending on purity), but in the counterflow configuration, AP flames are observed to be self-sustained even at 1 atm, with nearly perfect planar multi-flame structures.

In the current program, we have studied the structure of AP/methane, AP/ethylene, and AP/carbon monoxide and hydrogen flames [1-5]. These flame structures represent the fundamental building blocks of more complex hydrocarbon based binder systems. For example, ethylene is an important decomposition product of HTPB, while methane, carbon monoxide and hydrogen are important sub-mechanisms of ethylene combustion. Furthermore, by selective variations in the fuel composition, we have been able to mimic particular regions of the flame region and the effect of macroscopic variations of the propellant formulation such as the AP particle size. Diagnostics applied to these flames include thermocouple temperature profiles, spatially and spectrally resolved chemiluminescent emission profiles, PLIF (Planar Laser Induced Fluorescence) 2D imaging of CN, NH, NO, OH, OH rotational temperature, and PAH, line of sight absolute calibration of PLIF profiles using UV-visible absorption imaging, planar 2D imaging of soot via LII (Laser Induced incandescence), and 1D profiles of N_2, O_2, CH_4, H_2O, and HCl via point Raman scattering. Utilizing recent developments in hydrocarbon, chlorine, NO_x, N_xH_y, and AP kinetics, a detailed transport, finite rate chemistry system was formulated for the temperature, velocity and species mass fractions of the combined flame system.

AP/(H_2+CO) GASEOUS FUEL DIFFUSION FLAME STUDIES

Most composite propellants based on AP contain a bimodal or trimodal particle size distribution of AP. A typical formulation would contain 85% solids (AP) with 15% binder (e.g., HTPB). The AP would consist of a mixture of coarse and fine AP particles (e.g., 62% 200 μm and 38% 25 μm). In our prior studies, we used methane and ethylene as representatives of the
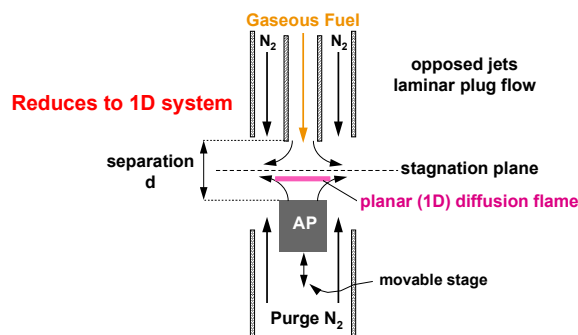
HTPB decomposition gases that would burn with the fine AP. Here, the fuel is a mixture of H_2 and CO in the ratio of 52 to 48 mole percent, respectively. This simulates the chemistry of the combustion products from the binder (HTPB) and fine AP fraction of a composite propellant, which go on to react in a diffusion flame with the large diameter AP fraction. In the formulation example given, the neat AP flame (above large diameter AP crystals) would be 1377K, the fine AP/binder flame would be 1162K, and the final flame between the decomposition products from the large AP and the AP/binder flame products would be 2645K.

Details of the experimental techniques and numerical procedures can be found in our previous

(a)   (b)   (c)   (d)

Figure 2. AP/(H_2+CO) counterflow diffusion flame PLIF images, 5 mm separation between the AP surface and fuel exit. The AP is at the bottom and fuel at the top. (a) OH PLIF. (b) NO PLIF. (c) Close-up view of the AP/(H_2+CO) counterflow diffusion flame and (d) AP/CH_4 counterflow diffusion flame for comparison.

papers. Figures 2a and 2b show representative OH and NO PLIF images. Note the clean image above the OH PLIF due to lack of fuel decomposition products such as PAH and/or soot LII, as was seen for AP/CH_4, and especially AP/C_2H_4 counterflow flames. Color imaging (Fig. 2c) shows two distinct regions for the AP/(H_2+CO) flame. This compares with four colored flame regions in the methane AP case (Fig. 2d). Note also that the AP pellet burns relatively flat and the gas flames are very flat. Both images show the same thin orangish flame near the AP surface and a thicker light blue flame above it (which spatially corresponds to OH radicals in the PLIF image). The bright purple bluish flame above the OH* seen in the methane case is missing for AP/(H_2+CO). The bluish color was chemiluminescence from CN* and NH* radicals which are missing from the hydrogen/carbon monoxide AP flame. There is a top reddish "flame" towards the fuel side for AP/methane, not well shown in the exposure case for Fig. 2d, which correlates with soot volume fraction and is undoubtedly faint black body emission from soot. The AP/(H_2+CO) flame produces no soot.

The experimental temperature profile is shown in Fig. 3. The Stokes/Anti-Stokes Raman results match the OH rotational temperature quite well. Also shown are temperatures obtained from total density (from total Raman Stokes signal); these match the other measurements as well. Temperatures from fitting NO vibrational spectra, shown in Fig. 3, also match. The calculated temperature, NO, OH and NH profiles are shown Fig. 4. In all the plots, the measured scalars are compared with the model predictions. With the exception of NO on the fuel rich side, model

Figure 3. Temperature profile with a 5 mm separation.

predictions and experiment are generally in good agreement. The NO profile predicted in the AP/CH_4 flame distinctively showed the sharp change in slope near 2.8 mm, which is absent from the prediction shown in Fig. 4. However, compared to the experimental data, the model indicates NO to be reduced at a faster rate in the fuel rich regions. Species profiles of CO, H_2, HCl, H_2O, CO_2, N2, and O_2, obtained from spontaneous Raman measurements and compared with

numerical data. Model predictions are in good agreement, with the exception of CO_2, for which the experimental results were lower than the predictions.

SUMMARY

Although these studies have been performed in a 1-g environment, they have provided us with significant experience in the operation of counterflow solid AP – gaseous hydrocarbon flames. The modeling has enabled us to build the foundation chemistry with which to examine systems that are more complex. Our goal has been to study solid oxidizer – solid fuel counterflow systems. Because of melt layer dripping from the solid oxidizer or solid fuel surfaces and the effects of buoyancy on

Figure 4. Comparison of experimental NO, OH and NH species profiles and the temperature with modeling results.

the flame structure, these systems cannot be studied in a 1-g environment. By operating under microgravity conditions, the length scales will be increased and the gravitational forces suppressed on melting binders such that increased resolution of both major and minor species will be possible thus reducing the demands placed on both the computational and diagnostic tools. We have designed and initiated fabrication of a test rig for parabolic flight experiments. Because of significant safety requirements and our initial desire to maximize the number of scalars measured, the design and fabrication of this system has required several modifications.

All of the modeling studies have been conducted with specification of the gas-phase speciation at the AP surface or at the fuel tube exit. We have studied several condensed phase reaction mechanisms for AP decomposition in the literature, and currently, none of these mechanisms is capable of predicting the gas-phase speciation measured at the AP surface. These mechanisms have generally been postulated from empirical evidence. Clearly, significant research, both experimental and theoretical, is required at the molecular level to develop our understanding and knowledge base of condensed phase processes.

REFERENCES

1. Smooke, M. D., Yetter, R.A., Parr, T. and Hanson-Parr, D., Proc. of the 36th JANNAF Combustion Subcommittee Meeting, Cocoa Beach, FL, (1999).
2. Smooke, M.D., Yetter, R.A., Parr, T.P., Hanson-Parr, D.M., Proceedings of the Combustion Institute, 28, The Combustion Institute, pp. 839-846, (2000).
3. Smooke, M.D., Yetter, R.A., Parr, T.P., Hanson-Parr, D.M., Tanoff, M.A., Colket, M.B., and Hall, R.J., Proc. of the Combust. Inst., 28, pp. 2013-2020, (2000).
4. Parr, T. P., Hanson-Parr, D.M., Smooke M.D., and Yetter, R.A., Proceedings of the 37th JANNAF Combustion Subcommittee Meeting, Monterey, CA, (2000).
5. Parr, T., P. Hanson-Parr, D.M., Smooke, M.D. and Yetter, R.A., Proc. of the Combust. Inst., 29, (2002).
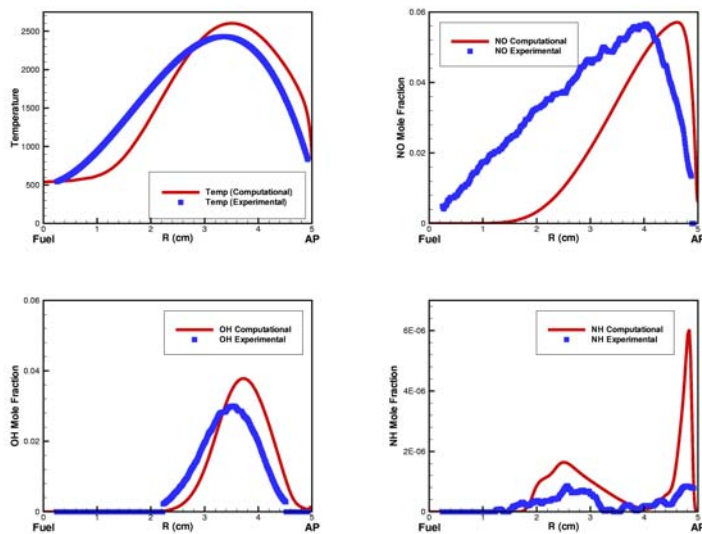
COMBUSTION OF HAN-BASED MONOPROPELLANT DROPLETS IN REDUCED GRAVITY

B. D. Shaw

MAE Department, University of California, Davis, CA 95616

INTRODUCTION

Hydroxylammonium nitrate (HAN) is a major constituent in a class of liquid monopropellants that have many attractive characteristics and which display phenomena that differ significantly from other liquid monopropellants [1]. They are composed primarily of HAN, H_2O and a fuel species. HAN-based propellants have attracted attention as liquid gun propellants (e.g., [1]), and are attractive for NASA spacecraft propulsion applications [2]. Triethanolammonium nitrate (TEAN), methanol and glycine have been investigated as potential fuel species for HAN-based monopropellants for thruster applications [3].

This research is focused upon studying combustion of HAN-based monopropellant droplets. The fuel species considered are TEAN, methanol and glycine, and droplets initially in the mm size range are studied at pressures up to 12 atm. Reduced gravity is employed to enable observations of fundamental combustion behaviors to be made without the complicating effects of buoyant convection. High-pressure normal gravity experiments have previously been performed as a part of this research program [4,5]. The present paper will focus on more recent normal-gravity experiments [6] as well as reduced-gravity experiments [7].

NORMAL GRAVITY EXPERIMENTS

Normal-gravity experiments were performed to investigate the UV spectral absorption characteristics and evaporation characteristics of monopropellant droplets composed of hydroxylammonium nitrate (HAN), methanol and water [6]. Fiber supported droplets initially in the mm size range were investigated, and droplets evaporated in room air with an ambient temperature of about 23 ± 2 °C and a relative humidity of about $44 \pm 4\%$.

Figure 1 shows data for droplet size variations. Droplets generally exhibited two-stage vaporization histories with measurable evaporation rates at early times and essentially no evaporation at long times. Initial evaporation rates were observed to vary significantly with the composition of a droplet, and the presence of methanol significantly increased droplet vaporization rates. Experiments showed that at sufficiently high HAN loadings, vaporization rates could be essentially zero, and theory [6] suggests that this behavior is caused by reductions in vapor pressure as the mass fraction of HAN in the liquid is increased.

Early-time evaporation rate constants were estimated using classical droplet vaporization theory [8]. Here, the evaporation rate constant is the negative of the slope on a plot of d^2/d_0^2 vs. t/d_0^2, where d is the instantaneous droplet diameter, d_0 the initial droplet diameter and t is time. Equation (1), which assumes spherical symmetry, was used to estimate initial evaporation rate constants, $K_{init,0}$, in the absence of buoyant flows. This value is corrected for buoyancy effects using an empirical correlation developed for droplet combustion [9] (Eqs. (2) and (3)).

$$K_{init,0} = 8D(\rho_g/\rho_d)\ln(1 + B_y) = 8\lambda_g/(c_p\rho_d)\ln(1 + B_T) \tag{1}$$
$$K_{init,g} = K_{init,0}(1 + 0.533Gr^{0.52}) \tag{2}$$
$$Gr = (2g\rho_g^2d^3/\mu^2)(T_\infty - T_s)/(T_\infty + T_s) \tag{3}$$

In Eqs. (1) - (3), D is the gas species diffusivity, ρ_g the gas density, ρ_d the liquid density, λ_g the gas thermal conductivity, c_p the specific heat of evaporated species, Gr is a Grashof number, μ is the gas viscosity, T_∞ is the ambient temperature, T_s is the droplet surface temperature, and B_T and B_y are transfer numbers based on temperature and species [6]. Gas and liquid properties were assumed to be constant (though T_s was allowed to vary).

Table 1 shows data from the experiments for initial evaporation rate constants. Also shown are values for $K_{init,0}$ and $K_{init,g}$. The variables Y_H, Y_w and Y_m are the initial mass fractions of HAN, water and methanol in a droplet, respectively. The data in Table 1 show that initial evaporation rate constants depend strongly on the initial droplet composition. In addition, by comparing the theoretical and experimental values for evaporation rate constants, it appears that buoyancy effects are correlated reasonably well by Eqs. (2) and (3).

Liquid	Y_H	Y_w	Y_m	K_{init} (mm^2/s) Experiment	$K_{init,g}$ (mm^2/s) Theory	$K_{init,0}$ (mm^2/s) Theory
A	0.82	0.18	0	-	-	-
B	0.41	0.59	0	0.0011	0.00096	0.00062
C	0	1	0	0.0015	0.0014	0.00087
D	0.656	0.144	0.20	0.0076	0.0067	0.0036
E	0.41	0.09	0.50	0.017	0.010	0.0050
F	0.164	0.036	0.80	0.018	0.017	0.0056
G	0	0	1	0.019	0.012	0.0058

Table 1.   Normal gravity liquid compositions and initial evaporation rate constants. Also shown are theoretical estimates of initial evaporation rate constants.

The experiments also employed 50-micron optical fibers to carry UV light into and out of individual droplets [6], and UV absorption spectra of the liquid between the fibers were measured using a spectrometer coupled to one of the fibers. Representative data for transient UV absorption spectra are shown in Fig. 2. These data show an absorption peak that is consistent with NO_3^- ions [6]. The absorption peak grows with time, indicating that nitrate ion concentrations increase with time. It is also noted that the peak absorbance wavelength shows a blue shift. As discussed elsewhere [6], this shift implies that methanol is preferentially evaporated from droplets. All of the HAN-containing droplets listed in Table 1 were observed to approach steady-state compositions that were essentially methanol-free and which had the same final HAN and water mass fractions of about 0.85 and 0.15, respectively [6].

REDUCED GRAVITY EXPERIMENTS
Experiments were performed to study reduced-gravity combustion characteristics of individual monopropellant droplets composed of HAN, methanol and water [7]. All experiments were performed in air at 0.1 MPa and about 25 °C (future experiments at high pressure are planned). Droplets initially in the mm size range were supported on fibers and were ignited using a hot wire that heated the gas phase near a droplet. Initial HAN loadings varied from zero (initially-pure methanol droplets) to stoichiometric amounts of HAN and methanol. The initial liquid compositions are listed in Table 2. The experiments made use of a NASA drop rig [10].

Burning rates, extinction characteristics and internal bubbling characteristics depended significantly on the initial mass fraction of HAN in a droplet. Figure 3 shows data for droplet sizes (data are not shown for $t/d_0^2 < 0.5$ s/mm^2 because of obscuration from the igniter coil). As with the normal-gravity evaporation experiments, initial burning-rate constants, K_{ave}, defined as the negative of the slope on a plot of d^2/d_0^2 vs. t/d_0^2, vary strongly with the initial droplet composition (Table 2). Increasing Y_H reduced burning rates. In addition, increasing Y_H promoted earlier flame extinction, and droplets could not be ignited when stoichiometric amounts of HAN and methanol were present (mixture 8 in Table 2). These behaviors are likely a result of reduced methanol mass fractions that will occur when the initial HAN mass fraction is increased.

Mixture	Y_H	Y_w	Y_m	K_{ave} (mm^2/s)	Bubbling	Comments
1	0	0	1	0.86	No	Extinction
2	0.0082	0.0018	0.990	---	Yes	Droplet breakup
3	0.041	0.009	0.950	0.55	No	Extinction
4	0.082	0.018	0.900	0.43	No	Extinction
5	0.205	0.045	0.750	---	Yes	Droplet breakup
6	0.310	0.07	0.620	---	Yes	Droplet breakup
7	0.410	0.09	0.500	0.22	Yes (Weak)	Extinction
8	0.694	0.152	0.154	---	No	No ignition

Table 2.   Initial fuel component mass fractions, average burning rate constants, bubbling behaviors and general comments. These data are from reduced gravity experiments.

Internal droplet bubbling was observed in some of the experiments. The occurrence of bubbling varied in a non-monotonic manner with the initial amount of HAN. As noted in Table 2, bubbling occurred for smaller (but nonzero) and larger initial HAN mass fractions, but not for intermediate values. This may be related to formation of associated ions, which will promote ignition of HAN-containing mixtures via the proton transfer reaction $NH_3OH^+ + NO_3^- \rightarrow NH_2OH + HNO_3$. This reaction can be an important initiation step in HAN decomposition [11].

It has been suggested that ion pair levels can peak as a result of nonlinear variations in mean ion activity coefficients [12]. Classical ion association theory with the Debye-Huckel theory for mean ion activity coefficients [13] has been applied to the present HAN-methanol-water mixtures. The results of this analysis suggest that ion pair concentrations can peak at low Y_H values but not at intermediate Y_H values, which is consistent with experimental results that show droplet bubbling at low HAN mass fractions. It is noted that mean ionic activity coefficients are difficult to predict at high HAN loadings, making it difficult to predict ion association levels for higher Y_H values. However, based on data for aqueous HAN mixtures [14,15], it is expected that ion pair (and ion complex) concentrations will approach high values at larger HAN loadings, leading to the increased reactivity that is apparent in the bubbling results obtained with HAN-methanol-water mixtures at higher Y_H values (Table 2).

ACKNOWLEDGEMENTS

REFERENCES

1. N. Klein, Report ARBRL-02471, Ballistic Research Laboratory (1983).
2. R. S. Jankovsky, AIAA Paper 96-2863.
3. E. J. Wucherer and S. Christofferson, AIAA Paper 2000-3872.
4. B. D. Shaw, NASA CP 2001-210826, 257 (2001).
5. M. Farshchi, V. Vaezi and B. D. Shaw, Combust. Sci. Tech. 174, 99 (2002).
6. B. D. Shaw and J. B. Wei, 29th Int'l. Symp. on Comb. (in press).
7. B. D. Shaw and J. B. Wei, paper presented at the 3rd Joint Meeting of the US Sections of the Combustion Institute, Chicago, IL, March 16-19, 2003.
8. F. A. Williams, *Combustion Theory*, 2nd ed., Benjamin Cummings, Menlo Park, CA (1984).
9. C. K. Law and F. A. Williams, Combust. Flame 19, 393 (1972).
10. P. M. Struk, D. L. Dietrich, M. Ikegami, and G. Xu, 29th Int'l. Symp. on Comb. (in press).
11. B. D. Shaw and F. A. Williams, 24th Int'l. Symp. on Comb., 1923 (1992).
12. C. Davies, *Ion Association*, Butterworths, London (1962).
13. J. O'M. Bockris and A. K. N. Reddy, *Modern Electrochemistry: Ionics*, 2nd ed., Plenum Press, New York, (1998).
14. N. Klein, 27th JANNAF Subcommittee Meeting, CPIA Pub. 557, Vol. I, 401 (1990).
15. N. Klein and K. N. Wong, Report BRL-TR-2850, Ballistic Research Laboratory (1987).
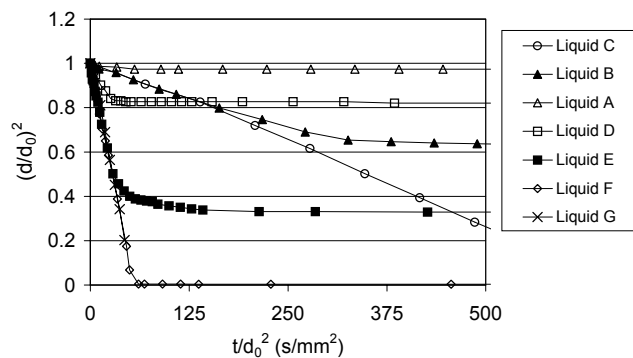
Fig. 1   Size variations for droplets evaporating in normal gravity.
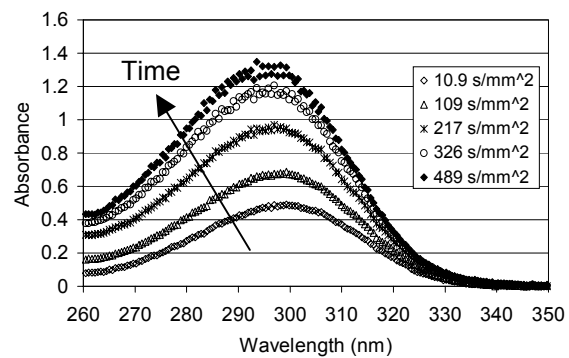
Fig. 2   UV absorbance spectra for droplets evaporating in normal gravity.
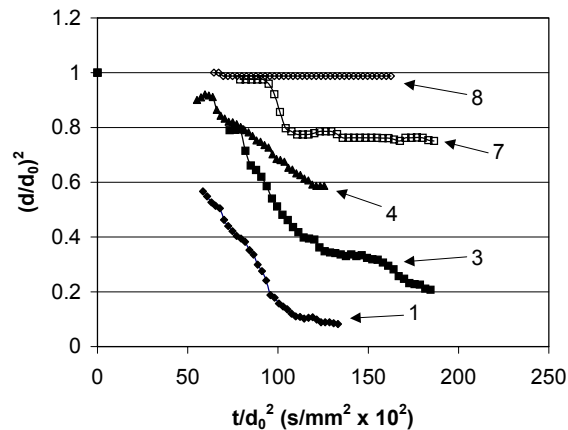
Fig. 3   Size variations for droplets burning in reduced gravity.

PRELIMINARY ASSESSMENT OF THE BURNING DYNAMICS OF JP8 DROPLETS IN MICROGRAVITY

J. H. Bae and C. T. Avedisian

Sibley School of Mechanical and Aerospace Engineering
Cornell University
Ithaca, New York 14853-7501

ABSTRACT

In this report we present new data for fuel droplet combustion in microgravity to examine the influence of ambient gas and fuel composition on flame structure and sooting dynamics for droplets with initial diameters in the range of 0.4mm to 0.5mm. The fuels are JP8 (a kerosene derivative) and nonane. The ambient gas is air and a mixture of 30% oxygen and 70% helium, the latter having been examined for burning under conditions where soot formation is minimal. Some data at elevated pressures are also reported.

The burning process shows a nonlinear D^2 progression which is independent of soot formation as burning in a helium inert showed the same nonlinear trend. Flames were proportionally farther from the droplet surface in helium than they were in air. A nondimensional parameter is presented that consolidates the three 'standoff' distances for the droplet, flame and soot shell diameters within the initial diameter ranges examined.

INTRODUCTION

In an effort to expand the fuel systems that have been studied in microgravity to a fuel which has direct application to terrestrial energy processes, we explored the feasibility of microgravity for studying the burning behavior of the complex fuel system JP8. JP8 is the primary fuel for military aircraft and ground vehicles, and it also serves as the coolant for aircraft and engine subsystems [Edwards and Maurice 2001; Heneghan et al. 1996]. It does not fit the mold for microgravity droplet combustion experimentation because it is highly multicomponent with constituents that have wide ranging boiling points, heats of vaporization and sooting tendencies. On the other hand a single component fuel like n-nonane (C_9H_{20}) is more typical of those selected for microgravity droplet combustion studies (i.e., alcohols, alkanes, and their mixtures [Shaw and Chen 1997; Lee et al. 1996; Avedisian 1997]). Such an 'ideal' fuel provides a useful basis for comparing with JP8, and nonane has a boiling point in the mid-range of JP8.

The experiments utilize droplets in the initial diameter range of 0.4mm to 0.5mm. The ambient gas was air and a mixture of oxygen and helium. The latter was included in order to compare burning of the same fuel under conditions where soot formation would be significantly reduced. Measurements of droplet, flame and soot shell diameters were made and correlated using a nomdimensional parameter that consolidated the measurements.

EXPERIMENT

Spherical droplet flames were created by burning droplets in a quiescent ambient gas environment within microgravity (created by a drop tower) to eliminate buoyancy induced flows. A fiber-supported arrangement was used and calibrated against a free droplet design in microgravity under identical conditions of ignition and fuel type (i.e., nonane) and it gave very good agreement with D^2 progressions from the fiber supported droplets. An instrumentation package which contains a combustion chamber and two cameras inside a drag shield (one for

16mm color or black and white photography using a LOCAM high speed 16mm film camera, and the other for video imaging) was released into freefall to create microgravity. The droplets were then ignited and their burning histories recorded. Quantitative measurements of droplet, flame and soot shell diameters were obtained by transporting images from the 16mm black and white, and color, movie films to a PC and analyzed using a commercial software package (ImagePro). The backlit droplet images were illuminated using either a 16W halogen bulb ('low intensity' backlighting) or a 150 watt bulb ('high intensity' illumination) with the latter being required for the heavily sooting JP8 compared to nonane in order to provide visibility of the droplet. Care was taken to ensure identical backlighting intensities when comparing different conditions for their influence on soot formation.

The fiber support design [Avedisian and Callahan 2000] consisted of two fine SiC fibers 12microns in diameter and crossed at an angle of 120°. By using two crossed fibers and mounting the droplet at the junction of the cross, droplets did not slide along the fiber. Ignition was by two sparks of 0.5ms to 0.8ms duration positioned on opposite sides of the droplet (using four electrodes) and activated 320ms after the package was released. Ignition in a helium inert using our spark ignition system required that the oxygen concentration be increased to 30% (70% He) for the same parameters of ignition energy and duration as in air.

DISCUSSION

Figure 1 shows selected color images of a JP8 droplet burning in microgravity at their peak image intensities. Combustion in air (1a) shows an intense yellow color while in a helium inert (1b) the yellow zone is reduced significantly with the flame structure showing an outer blue zone and a faintly yellow interior. The reduced luminosity indicates less soot formation in helium, most likely due to a lower flame temperature in helium compared to air. At 3atm (1c) in helium soot formation return dominated the luminosity (the influence of pressure on accelerating soot precursor reactions overrides the lower flame temperature in helium). Figure 2 shows selected backlit black and white images of nonane (a) and JP8 (b) droplets at atmospheric pressure. The JP8 droplet is completely obscured in Figure 2b while the nonane droplet and soot shell are still clearly visible in Figure 2a indicating much less soot formation for nonane relative to JP8. Figure 3 shows the evolution of droplet diameter for JP8 in air (3a) and helium (3b). The gap in data for JP8 in air (3a) was caused by the soot shell which became so thick mid-way through burning that the droplet was not visible.

Immediately after ignition, JP8 experienced significant droplet heating as indicated by the relatively constant or increasing droplet diameter (due to swelling) while nonane showed almost no evidence of droplet heating after ignition. This difference is likely due to the lower product of liquid density and specific heat of nonane compared to JP8 [Reid et al. 1987; Coordinating Research Council 1983]. In helium (3b) the JP8 droplet heating period is eliminated, perhaps because of the higher average gas phase thermal conductivity in helium compared to air which would increase gas phase heat transport to the droplet. After the heating period, both nonane and JP8 showed a time dependent burning rate that was evidenced by nonlinear diameter progressions in both air and helium (Figures 3a and 3b). We may then conclude that soot formation is not responsible for nonlinear burning of JP8 because the effect occurred under conditions where soot formation was significantly reduced (i.e., in helium).

The evolution of flame standoff ratio for JP8 in air is compared to JP8 in helium in figure 3c. The flame is proportionally farther from the droplet in helium than in air. There are two influences to consider to explain this trend: helium lowers the flame temperature; and helium weights the average gas thermal conductivity to a higher value. The data show that the JP8 flame position is farther from the droplet in helium compared to that in nitrogen. Therefore, the

increased gas thermal conductivity overrides the reduction of flame temperature. Figure 4 shows the evolution of soot shell standoff ratio. It increases with time and tracks with the flame position. The gap in data after ignition ($t/D_o{}^2 < 0.25$mm^2/s) is caused by the delay period of soot formation where the shell has not yet fully formed.

The three measurements of droplet, flame and soot shell diameters for JP8 and nonane exhibit distinctly different time dependencies as indicated in Figures 3 and 4. We attempted to consolidate these data with a suitable nondimensional parameter. Some guidance for this effort was explored by scaling formulations for the forces acting on soot agglomerates due to Stefan drag, thermophoresis and diffusiophoresis [Jackson et al. 1992; Ben-dor et al. 2003]. One parameter that worked reasonably well was $\dfrac{D_f - D_s}{D_s - D}$ as a function of scaled time, t/t_b where t_b is the total burning time defined as the time for the flame to disappear. Figure 5 shows the result. The number of data involved in this scaling are determined essentially by the number of movie frames where D_s could be reasonably defined. A power-law relationship of the form $\dfrac{D_f - D_s}{D_s - D} = C \cdot \left(\dfrac{t}{t_b} \right)^{-n}$ correlated the measurements with $C \approx 3.47$ and $n \approx 0.43$. The utility of such a correlation for microgravity droplet flames in quiescent conditions is that with knowledge of the droplet and flame position, the soot shell is determined. The correlation appears reasonable for droplets in the diameter range investigated. Using it for droplets outside of the range of initial droplet diameters examined here and for other fuel systems requires further testing.

CONCLUSIONS

The flame structure and influence of ambient gas on combustion of JP8 droplets showed trends similar to those found for a single component fuel except for much more soot formation. The evolution of droplet diameter produced a time dependent burning rate in both helium and air which showed that soot formation was not likely to be responsible for nonlinear burning. The flame was farther from the droplet in helium than that in air, showing the dominance of helium thermal conductivity on increasing the average gas thermal conductivity and heat transfer to the droplet. Extinction of JP8 was not observed for burning in air but was commonly found for burning JP8 in an ambience consisting of 30% oxygen and 70% helium.

The measurements of droplet, soot shell and flame diameter were consolidated onto a single curve using a scaling relationship that will require further investigation for additional fuels and mixtures to establish the generality of the approach. Sooting tendencies were deduced primarily by comparing photographic image intensities. Quantitative methods for measuring soot volume fraction of JP8 and related heavily sooting fuels in microgravity would better establish the influence of parameters on trends of soot formation.

REFERENCES
Avedisian, C.T., in Physical and Chemical Aspects of Combustion, Gordon and Breach Publ., 135-160 (1997).
Avedisian, C.T. and Callahan, B.J., Proc. Combust. Inst. Vol.28: 991-997 (2000).
Ben-dor, G., Elperin, T., and Krasovitov, B., Proc. R. Soc. London A 459: 677-703 (2003).
Coordinating Research Council Report No. 530, Coordinating Research Council, Inc., Atlanta, GA, (1983).
Edwards, T. and Maurice, L.Q., J. Prop. Power, Vol. 17, No. 4: 461-466 (2001).
Heneghan, S.P., Zabarnick, S., Ballal, D.R., and Harrison, W.E., J. Energy Resources. Tech., Vol. 118: 170-179 (1996).

Jackson, G.S., Avedisian, C.T., and Yang, J.C., Int. J. Heat Mass Transfer, Vol. 35, No. 8: 2017-2033 (1992).
Lee, K.L., Jensen, K.A., and Choi, M.Y., Proc. Comb. Inst. Vol. 26: 2397-2404 (1996).
Reid, R.C., Prausnitz, J.M. and Poling, B.E., The properties of gases and liquids, Boston, McGraw Hill: Appendix A (1987).
Shaw, B.D. and Chen, A.G., Microgravity Science and Technology, Vol. X/3: 136-143 (1997).
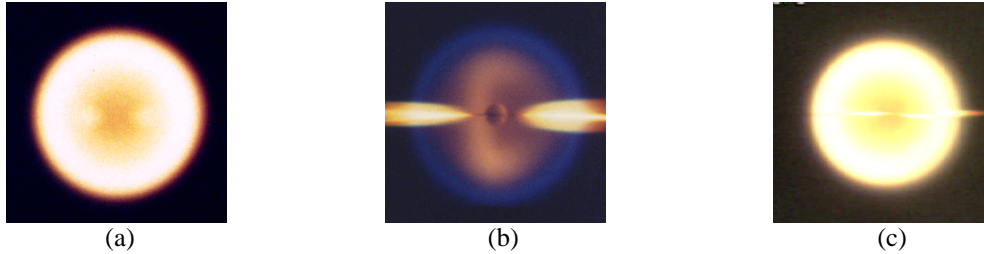
Figure 1: (a) JP8, 1atm in air; (b) JP8, 1atm in 30% O_2/70% He; (c) JP8, 3atm in 30% O_2/70% He
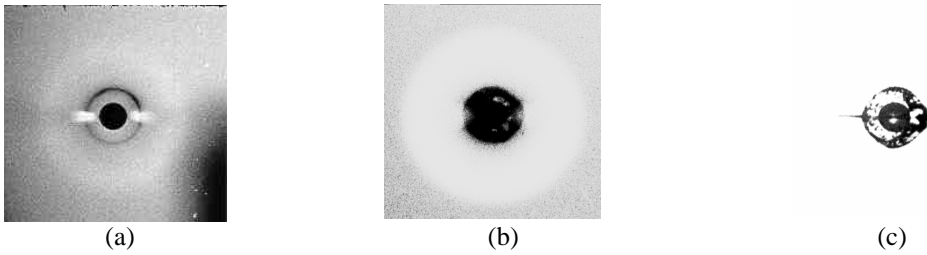
Figure 2: (a) nonane, low intensity; (b) JP8, low intensity; (c) JP8, high intensity
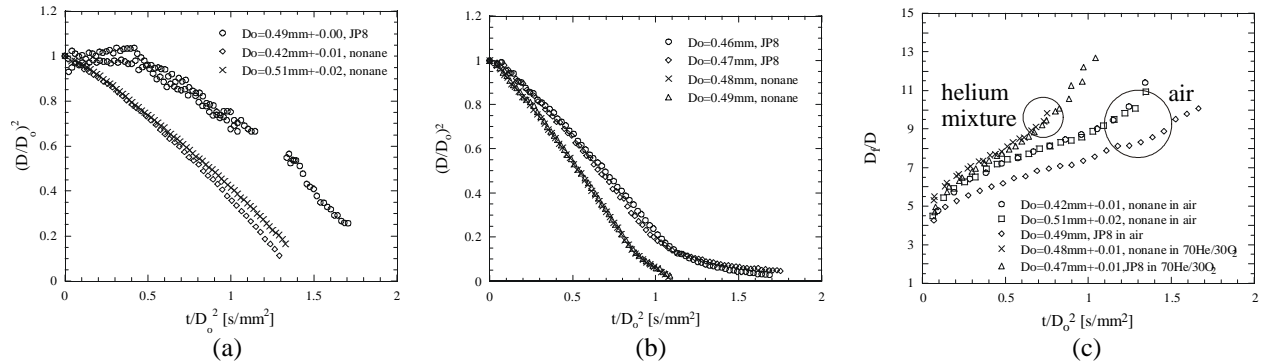
Figure 3: (a) evolution of droplet diameter in air; (b) evolution of droplet diameter in 30% O_2/70% He; (c) flame standoff ratios in air and 30% O_2/70% He
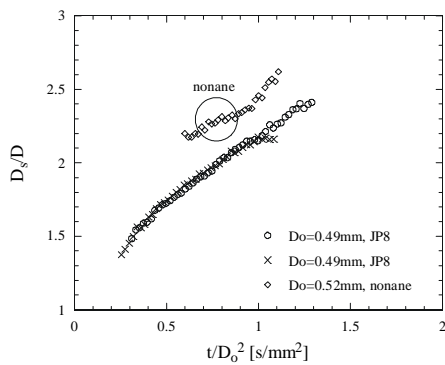
Figure 4: nondimensional soot shell position in air
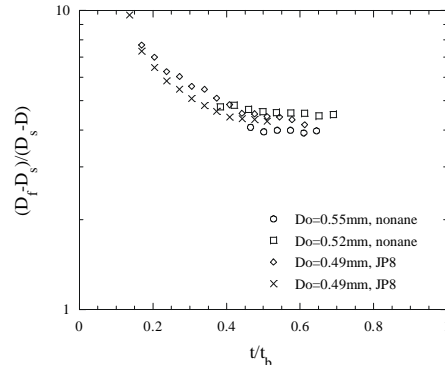
Figure 5: scaling of droplet, flame and soot shell diameters in air

HIGH-PRESSURE TRANSPORT PROPERTIES OF FLUIDS: THEORY AND DATA FROM LEVITATED DROPS AT COMBUSTION-RELEVANT TEMPERATURES

Josette Bellan and Kenneth Harstad
Jet Propulsion Laboratory, California Institute of technology, Pasadena CA 91109

Kenichi Ohsaka
University of Southern California, Los Angeles, CA.

INTRODUCTION

Although the high pressure multicomponent fluid conservation equations have already been derived and approximately validated for binary mixtures by this PI, the validation of the multicomponent theory is hampered by the lack of existing mixing rules for property calculations. Classical gas dynamics theory can provide property mixing-rules at low pressures exclusively. While thermal conductivity and viscosity high-pressure mixing rules have been documented in the literature, there is no such equivalent for the diffusion coefficients and the thermal diffusion factors.

The primary goal of this investigation is to extend the low pressure mixing rule theory to high pressures and validate the new theory with experimental data from levitated single drops. The two properties that will be addressed are the diffusion coefficients and the thermal diffusion factors. To validate/determine the property calculations, ground-based experiments from levitated drops are being conducted.

ACCOMPLISHMENTS

During the last year, progress was made theoretically and experimentally, as follows:

1. Theoretical

The theoretical investigation was devoted both to enlarging the modeling of the high-pressure diffusion coefficients and to developing high-pressure mixing rules.

A. Enlargement of the diffusivity study

Previous high-pressure ($\rho_r \geq O(1)$) data was developed in the form of the function $w_D(\rho_r)$ which modifies known low pressure (kinetic theory) diffusivities. The latter requires values of the empirical normalization factor r_D. Some further data for solvent-aromatic solute (benzene, toluene, naphthalene, cumene) pairs with r_D values that are not known have been examined. Data for the solvent 2,3dimethylbutane [14] show a coincidence of plots of the variable $\omega^{1/4}r_D w_D$ versus ρ_r (Fig. 1); this holds for a generic w_D if $\omega^{1/4}r_D =$ constant, where ω is the solute acentric factor. Other data with CO_2 as the solvent is also available [1-13]. Since r_D for benzene in CO_2 has the value 0.90, the inference is made that $\omega^{1/4}r_D = 0.61$ for aromatics in CO_2. This results in estimates of r_D values of 0.85, 0.82 and 0.81 for toluene, naphthalene and cumene in CO_2, respectively. Using these values, plots of w_D data are shown in Figs. 2-4 together with $w_D =1+ \delta_D$ and $\delta_D = 0.10\rho_r^2$.

B. Multicomponent fluid mixing rules

Generalized transport relations (fluxes in terms of thermodynamic forces) for arbitrary fluid mixtures at all pressures are best determined through the formalism of nonequilibrium

thermodynamics or statistical thermodynamics (fluctuation-dissipation theory). Although the proper forms for these relations are thus found, the transport coefficients themselves (viscosity, thermal conductivity, etc.) are not thereby determined. The coefficients, including their appropriate mixing rules, may be formulated for dilute, low-pressure mixtures through kinetic theory. Thus the conjunction of nonequilibrium thermodynamics and kinetic theory provides a needed starting point to the formulation of generalized mixing rules for fluid mixtures. The 13-moment approach to kinetic theory is utilized for this purpose.
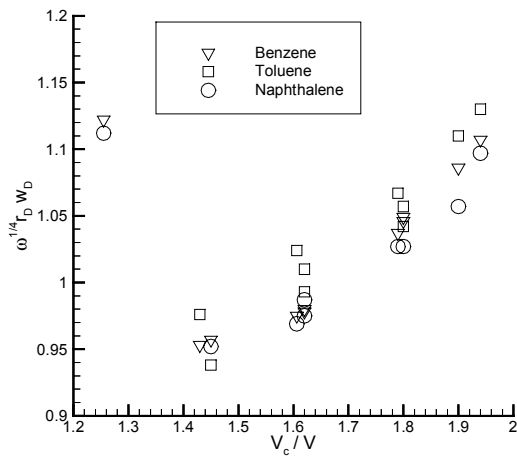
Figure 1 Scaled diffusivities of solutes benzene, toluene and naphtalene in solvent 2,3dimethylbutane.
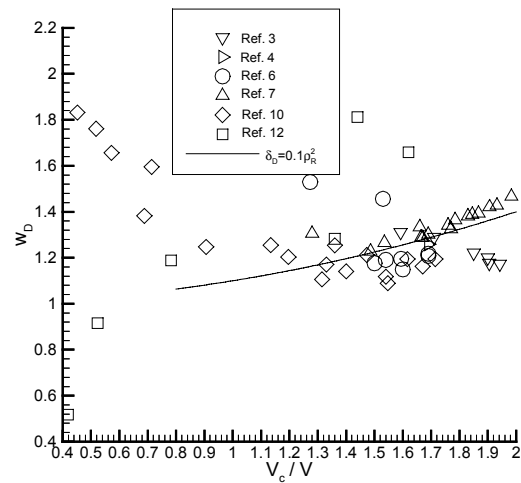
Figure 2 Scaled diffusivity of toluene in CO2: data and correlation.
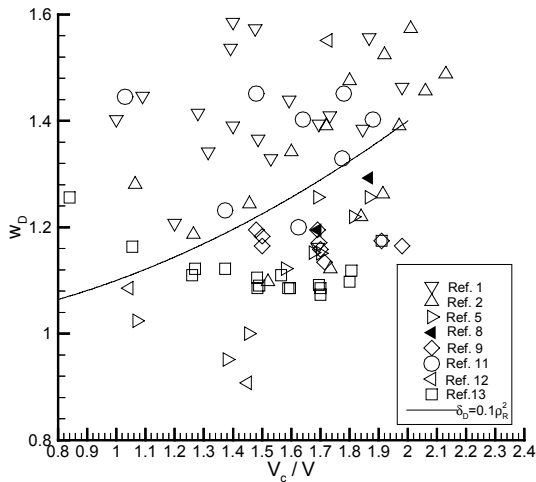
Figure 3 Scaled diffusivity of naphtalene in CO2: data and correlation.
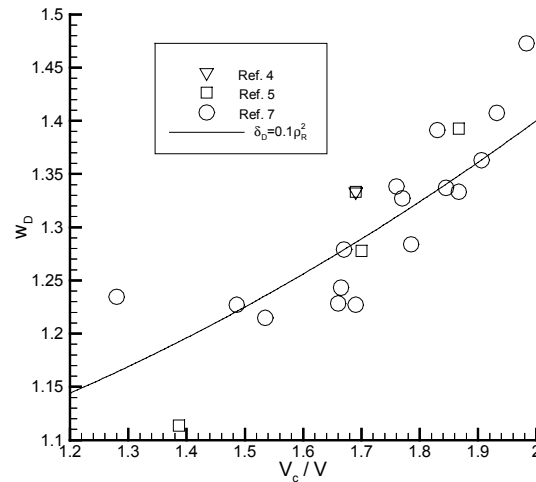
Figure 4 Scaled diffusivity of cumene in CO2: data and correlation.

This approach avoids many of the algebraic complications resulting from the expansions in inverse density (or mean free path) that are prominent in the Chapman-Enskog procedure. Substituting the 13-moment transport formulas into the nonequilibrium thermodynamic forms results in a coupled set of matrix equations that essentially determine the proper mixing rules.

These equations have been studied and manipulated; reduction to a single matrix equation that determines the mixture mass diffusion coefficients in terms of binary diffusion coefficients has been achieved. Then the mixing rules for the mixture thermal diffusion factors (flux cross-couplings) in terms of binary factors and the mixture thermal conductivity are found to be explicit in terms of the resulting mixture mass diffusion coefficients.

[1] M. B. Iomtev and Y. V. Tsekhanskaya, *Zh. Fiz. Khim*. 38 (1964) 896-900
[2] D. M. Lamb, et al, *J. Phys. Chem*. 93 (1989) 5002-5005
[3] T. J. Bruno, *J. Res. Natl. Inst. Stand. Tech*. 94 (1989) 105-112
[4] T. Funazukuri, *J. Chem. Eng. Jpn*. 29 (1996) 191-192
[5] P. R. Sassiat, et al, *Anal. Chem*. 59 (1987) 1164-1170
[6] J. M. H. Levelt-Sengers, et al, *Int. J. Thermophysics* 14 (1993) 893-922
[7] J. J. Suarez, et al, *Chem. Eng. Sci*. 48 (1993) 2419-2427
[8] T. Fuanzukari, et al, *AIChE J*. 38 (1992) 1761-1768
[9] H. H. Lauer, et al, *Anal. Chem*. 55 (1983) 1370-1375
[10] C. C. Lai and C. S. Tan, *Ind. Eng. Chem. Res*. 34 (1995) 674-680
[11] G. Knaff and I. Schlunder, *Chem. Eng. Process*. 21 (1987) 101-105
[12] C. H. Lee and G. D. Holder, *Ind. End. Chem. Res*. 34 (1995) 906-914
[13] A. Akgerman, et al, *Ind. Eng. Chem. Res*. 35 (1996) 911-917
[14] C. K. Sun and S. H. Chen, *AIChE J*. 31 (1985) 1904-1915

2. Experimental

In the previous fiscal year, we built an electrostatic levitation apparatus. A difficult step of the electrostatic levitation is the deployment of a liquid drop. The original device worked well for water drops, but failed to deploy alcohol drops because the good wetting characteristics and small surface tension values of alcohol liquids make the detachment of a drop from the supporting rods difficult. We therefore needed to redesign the drop deployment device to overcome this difficulty. During this fiscal year, we assembled a new device and tested it. With the redesigned device we could levitate both water and ethyl alcohol drops whose diameters were initially approximately 2 mm. The drops could be charged either negatively (excess electrons) or positively (excess ions). We could keep the drops levitated as they gradually evaporated. Figure 5 shows a plot of the diameter squared of an ethyl alcohol drop as a function of the elapsed time. As seen in the figure, evaporation establishes a quasi steady state indicated by the straight line. The figure also shows the applied voltage which decreases as evaporation proceeds. As the diameter of the drop decreases but the charge remains constant, the charge density eventually reaches a limit called the Rayleigh limit. At this limit, some of the charge is discharged from the drop. In the figure, this happened first at around 32 minutes indicated by a kink in the voltage curve. When the drop loses the charge, the voltage must be increased to hold the drop at the same position. This discharge repeated as the drop evaporated further. We also tested the scheme to create a temperature gradient along the levitation axis. The scheme is to heat the top electrode and cool the bottom electrode. After waiting for the chamber to reach a steady state, we measured the temperature using a thermocouple. Figure 6 is a plot of the temperature variation along the levitation axis. The distance is measured from the surface of the bottom electrode. The highest temperature represents the temperature of the top electrode. We actually levitated a water drop, thus confirming that the drop could be levitated in a field where the temperature gradient was present. The drop was initially levitated at 10 mm from the bottom. Figure 7 shows a snapshot of the levitated drop.

We have installed a device which allows us to transport a levitated drop from the initial to final (supercritical temperature) positions. This procedure is necessary to quickly bring the drop in a supercritical state. This operation can be accomplished by moving the position of the drop position monitoring assembly (laser and detector) relative to the electrodes. When the assembly is moved along the axial direction, the levitated drop follows. We performed a demonstration in which a water drop was initially levitated at 10 mm from the bottom and then transported to 5 mm from the top electrode. Figure 8 shows a snapshot of the levitated drop at the final position. A white dot marks the initial position. The wires appear close to the drop, but they actually rest in the retracted position. If this mechanism is used in combination with the levitation field with the temperature gradient, we can quickly expose the levitated drop to different temperatures.
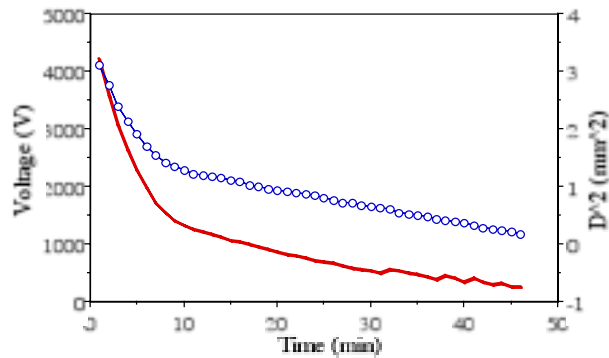
Figure 5 Drop diameter square (circles) and the applied voltage as a function of the elapsed time.
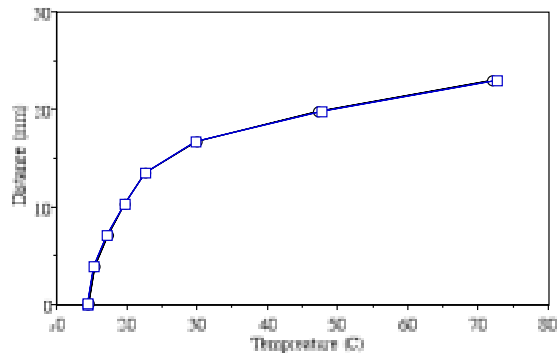
Figure 6 Temperature variation along the levitation axis.
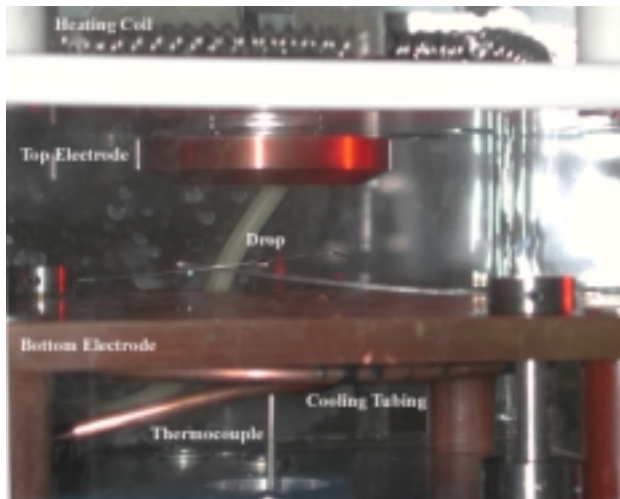
Figure 7 Drop levitated in the field with the temperature gradient.
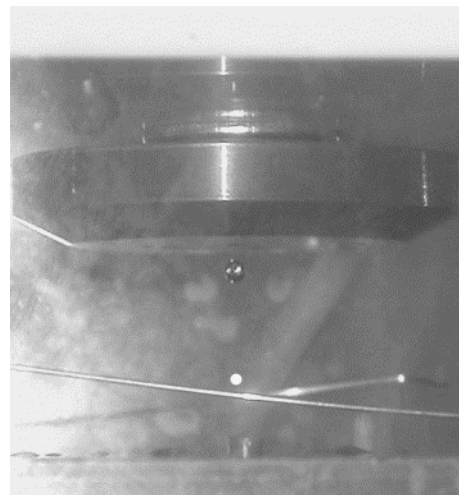
Figure 8 Photo showing a water drop transported to the final position from the initial position (white dot).

SOLID INFLAMMABILITY BOUNDARY AT LOW-SPEED (SIBAL)

J. T'ien[*#], **K. Sacksteder**[+], **P. Ferkul**[#], **R. Pettegrew**[#], **K. Street**[+], **A. Kumar**[*], **K. Tolejko**[*], **J. Kleinhenz**[*], **N.Piltch**[+]

[*]Case Western Reserve University   [+]NASA Glenn Research Center
[#]National Center for Microgravity Research on Fluids and Combustion

This research program is concerned with the effect of low-speed flow on the spreading and extinction processes over solid fuels. The project has passed the Science Concept Review and the experiment is currently scheduled to be performed in the ISS Combustion Integrated Rack. We present an overview of recent and ongoing experimental and theoretical efforts.

(1) <u>Measurement and Evaluation of the Radiative Properties of a Thin Solid Fuel [1]</u>
Surface radiation has a significant role in the combustion of solid fuels. This process contributes not only to the overall heat loss of the system, but also to the interaction between the gaseous flame and the solid fuel. Radiative effects are amplified in microgravity flames because of the decrease of convection. Accurate modeling of combustion systems requires not only the gas-phase but also the surface radiative properties during burning conditions. Effects of heat treatment on spectrally resolved radiative properties of thin solid fuels are described in order to simulate different degrees of pyrolysis and to supplement earlier spectrally resolved data on virgin fuels. An example of spectral absorptance is shown in Fig. 1. The total temperature dependence of total emittance of these solids is evaluated assuming the spectral emission data are independent of temperature. In addition, the total absorptance of the solid is evaluated using simulated gas phase spectra at a specified flame temperature as the incident radiation source. The total emittance and the total absorptance are found to be quite different in value. The two effects, the inequality of emittance and absorptance and the temperature dependence of the total emittance, are manifestations of the non-gray nature of these solids. This has implications for the flame modeling work, which conventionally assumes equal and constant values of emittance and absorptance.

Fig. 1: Specrtally resolved absorptance for unpyrolyzed Kimwipes and Kimwipes subjected to 3 minutes heating in a 300 °C oven (area density reduced by 60%).

(2) <u>Infrared Imaging Diagnostics for Flame Spread over Solid Surfaces [2]</u>
Solid surface temperature measurements are important to solid-fuel flame spreading experiments. The measured variation of surface temperature distributions have been used to deduce flame spread rates and pyrolysis lengths, and are a key link between experimental results and theoretical predictions. Thermocouples or thermocouple arrays have often been used to obtain histories of temperature at discrete locations on the fuel surface, but such measurements are intrusive and may alter the local surface temperature, perhaps sufficiently to quench a weak but otherwise viable flame. Additionally, thermocouple measurements cannot provide the time-

varying two-dimensional temperature distributions that are needed for three-dimensional or transient flame spread studies.

A non-intrusive alternative is to use radiometric infrared imaging of thermal radiation emissions from the burning fuel surface. A narrow band pass filter centered at 3.8 μm is used to reject emissions from CO, CO_2, and H_2O in the flame. Broadband emission from soot cannot be removed entirely by spectral filtering, but an experimental and algebraic method has been developed to estimate its contribution to the imaged radiance. A method has also been developed for determining fuel surface emittance as a function of temperature in the narrow imaging pass band.
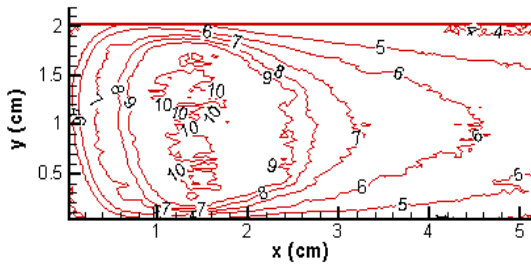
Fig. 2: Surface temperature (non-dimensionalized by 100K) of a downward spreading flame over a 2-cm wide cotton/fiberglass fabric in 11 psia, 25% O_2 atmosphere.

In [2], the application of infrared imaging to the study of flame spreading is illustrated using two distinct fuels in different spreading modes and environments. One fuel is thin cellulose tissue that is normally consumed completely in the flame. The other is a cotton-fiberglass composite from which the cotton is consumed leaving the fiberglass matrix after the flame passage. Surface temperature distributions of a downward spreading flame for the cotton/fiberglass fuel obtained with the infrared imaging method is shown in Fig. 2 using the spectral emittance at 3.8 μm determined in [1].

(3) A Comparison of Extinction Limits and Spreading Rates in Opposed and Concurrent Spreading Flames over Thin Solids [3]

Flame spread phenomena over thin solids are investigated for purely forced opposing and concurrent flows. A two-dimensional opposed-flow flame spread model, with flame radiation, has been formulated and solved numerically. In the first part of this work, flammability limits and spread rates in opposed flow are presented using oxygen percentage, free stream velocity and flow entrance length as parameters. The comparison of the flammability boundaries and spread rate curves for two different entrance lengths exhibits a crossover phenomenon (Fig.3). Shorter entrance length results in higher spread rates and lower oxygen extinction limit in low free-stream flow velocities; but lower spread rates and higher oxygen extinction limit in high free-stream velocities. The entrance length affects the effective flow rate the flame sees at the base region. This affects the radiation loss and gas residence time in an opposing way to cause the crossover. Radiation also affects the energy balance on the solid surface and is in part responsible for solid-fuel non-burnout phenomenon. In the second part of this work, a comparison of flammability limits and flame spreading rates between opposing and concurrent spreading flames are made; both models

Fig. 3: Comparison of extinction boundaries of opposed flow flame spread with concurrent-flow flame spread

contain the same assumptions and properties. While the spread rate in concurrent spread increases linearly with free stream velocity, the spread rate in opposed flow varies with free stream velocity in a non-monotonic manner, with a peak rate at an intermediate free stream velocity. At a given free stream velocity, the limiting oxygen limits are lower for concurrent spread except in the very low free stream velocity regime where spreading flame may be sustainable in opposed mode and not in concurrent mode (Fig.3). The crossover disappears if the two spread modes are compared using relative flow velocities with respect to the flames rather than using free stream velocities with respect to the laboratory as shown in the inset in Fig.3.

(4) A Computational Study on Flame –Solid Radiation Interaction in Flame Spread over Solid-Fuel [4]

A detailed numerical study has been made on the interaction of gas-phase flame radiation with a thin solid fuel in flame spread in quiescent microgravity and in normal gravity environments. The computations are performed using a 2-D opposed flow flame spread model in which gravity, solid total emittance (ε) and total absorptance (α) can be varied as independent parameters. The radiative transfer equation is solved using S-N discrete ordinates method to obtain the gas phase radiation loss to the ambient and heat feed back to the solid. Fig. 4 shows that while flame radiation has only a minor role in downward flame spread in normal gravity (see inset), radiation (gaseous and/or surface) plays an important role in the micro-gravity flames. Both flame-spread rate and low oxygen limit or index (LOI) are sensitive to the radiation parameters. For example, a non-emitting and full absorbing solid ($\varepsilon = 0$, $\alpha = 1$) can spread faster than the adiabatic case (no radiation). The full emitting and absorbing case ($\varepsilon = \alpha = 1$) will spread faster than the adiabatic case in high oxygen environment and slower than the adiabatic case in low oxygen

Fig. 4: Parametric study of flame surface interaction in μ*g* self propagating flame. Inset shows equivalent curves for *1g* flame.

environment and slower than the adiabatic case in low oxygen environment. This reversal phenomenon is due to the shifting relative weight between flame radiation and solid emission. Flame radiation increases at high oxygen environment due to higher flame temperature while surface temperature remains little changed.

A computational experiment [5] has been performed to test the assumption of constant emittance vs. varying emittance as a function of temperature and area density (or degree of pyrolysis). Fig. 5 shows the solid profiles using the variable emittance obtained in [1] while Fig. 6 shows the results assuming a uniform emittance equals to the value of the unpyrolyzed Kimwipes at ambient temperature. There are substantial differences between the two results- one solid burned out with a short pyrolysis length while the other solid does not burn out. These computations have been carried out in two dimensions. Three dimensional calculations for opposed-flow flame spread and extinction in mixed buoyant and forced flow is underway [6].
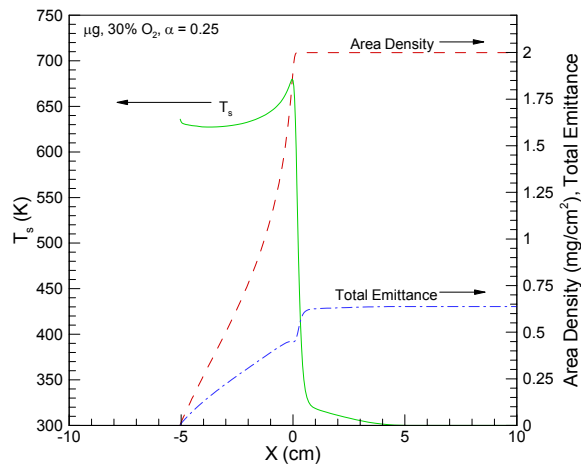
Fig. 5: Total emittance, area density and solid temperature in microgravity at 30% O_2, $\alpha = 0.25$ and variable total emittance
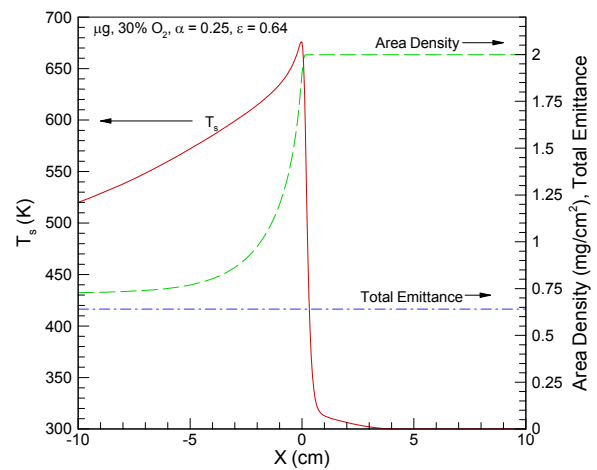
Fig. 6: Total emittance, area density and solid temperature in microgravity at 30% O_2, $\alpha = 0.25$ and $\varepsilon = 0.64$

References:

1. Pettegrew, R., Street, K., Piltch, N., T'ien, J., and Morrison, P.: Measurement and Evaluation of the Radiative Properties of a Thin Solid Fuel, AIAA-2003-0511 (2003).
2. Kleinhenz, J., Feier, I, Pettegrew, R., Sacksteder, K., Ferkul, P., T'ien, J.: Infrared Imaging Diagnostics for Flame Spread over Solid Surfaces, AIAA-2003-0988 (2003).
3. Kumar, A., Shih, H.Y., and T'ien, J.: A Comparison of Extinction Limits and Spreading Rates in Opposed and Concurrent Spreading Flames over Thin Solids, Combust. Flame, Vol. 132/4, pp. 667-677 (2003).
4. Kumar, A., Tolejko, K., and T'ien, J.: A Computational Study on Flame –Solid Radiation Interaction in Flame Spread over Solid-Fuel. Paper C-7-327, Proceedings of the 6th ASME- JSME Thermal Engineering Joint Conference, March 16-20, 2003.
5. Tolejko, K.: A Computational Study on Radiation Effects on Flame Spread over a Thin Fuel in a Quiescent Microgravity Environment. M.S. Thesis, Case Western Reserve University, expected May 2003.
6. Kumar, A.: A Numerical Model Of Opposed Flow Flame Spread Over Thin Fuels. Ph.D. Thesis, Case Western Reserve University, expected August 2003.

Localized Ignition and Subsequent Flame Spread Over Solid Fuels in Microgravity

T. Kashiwagi[1], Y. Nakamura[2], K. Prasad[1], H. Baum[1], S. Olson[3],
O. Fujita[4], K. Nishizawa[4], and K. Ito[4]

[1]Building Fire Research Laboratory, NIST, Gaithersburg, MD 20899 USA
[2]Department of Mechanical Engineering, Nagoya University, Nagoya, Japan
[3]NASA Glenn Research Center, Cleveland, OH 44135, USA
[4]Department of Mechanical Science, Hokkaido University, Sapporo, Japan

Introduction

Localized ignition is initiated by an external radiant source at the middle of a thin solid sheet under external slow flow, simulating fire initiation in a spacecraft with a slow ventilation flow. Ignition behavior, subsequent transition simultaneously to upstream and downstream flame spread, and flame growth behavior are studied theoretically and experimentally. There are **two transition stages** in this study; one is the **first transition** from the onset of the ignition to form an initial anchored flame close to the sample surface, near the ignited area. The **second transition** is the flame growth stage from the anchored flame to a steady fire spread state (i.e. no change in flame size or in heat release rate) or a quasi-steady state, if either exists. Observations of experimental spot ignition characteristics and of the second transition over a thermally thin paper were made to determine the effects of external flow velocity[1]. Both transitions have been studied theoretically to determine the effects of the confinement by a relatively small test chamber[2], of the ignition configuration (ignition across the sample width vs spot ignition)[3], and of the external flow velocity[4] on the two transitions over a thermally thin paper.

This study is currently extending to two new areas; one is to include a thermoplastic sample such poly(methymethacrylate), PMMA, and the other is to determine the effects of sample thickness on the transitions. The recent results of these new studies on the first transition are briefly reported.

Ignition and First Transition over PMMA

Ignition of a PMMA sheet (14 cm long x 10 cm width) was initiated at its middle by a CO_2 laser having a total power of about 28 W at the sample surface. The sheet was mounted in the middle of the test chamber and exposed to a slow external flow of up to 10 cm/s. Therefore, subsequent flame spread from the localized ignition could occur simultaneously upstream and downstream. There are two flames, one on the irradiated surface and the other on the backside surface. Two different sheet thickness of 0.2 mm and 0.4 mm were used. The experiment was conducted in the 10 s drop tower at the Japan Microgravity Center, JAMIC. Ignition of the PMMA sample was observed shortly after the start of the laser irradiation on the irradiated surface but subsequent ignition of the backside surface (non-irradiated side) was significantly delayed. The delay increases with the thicker sample and lower oxygen concentration as shown in Figure 1. Although the number of the experiments is rather limited, the results show that the backside ignition occurs only after the termination of laser irradiation in 21 % oxygen concentration. The

duration of the laser irradiation could have significant effects on the backside ignition. This was demonstrated in the case of the tests with external velocity of 5 cm/s in 21 % oxygen concentration with two different irradiation times. A 6 s duration did not ignite the backside within the available test time of 10 s while a 3 s duration did ignite the backside within 1 s after the termination of irradiation. The behavior of flame during the first transition to backside ignition and subsequent anchored flame is shown in Figure 2. It is curious that it takes several seconds to ignite the backside in 21 % O_2 concentration, even though there is an open hole through the sample by the laser irradiation shortly after the onset of the front side ignition. After the laser termination, the flame becomes very small and moves close to the sample surface and the open hole. Then, backside ignition
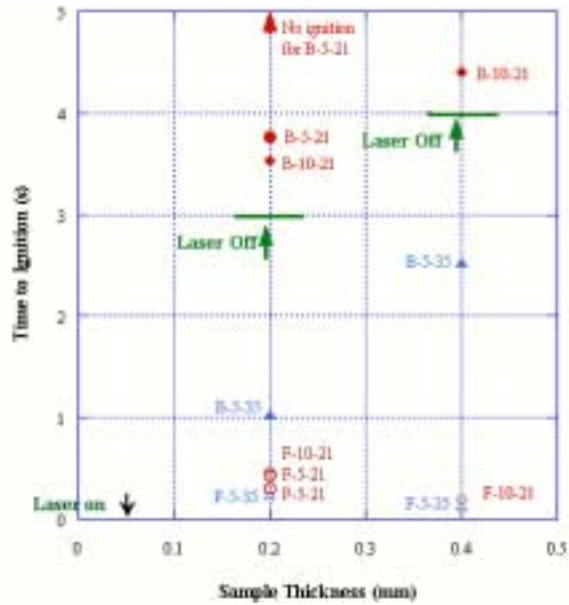
Figure 1. Effects of sample thickness on ignition delay time of PMMA in microgravity. (F-frontside/B-backside)-flow velocity(cm/s)-O_2 concentration.

occurs.

In 35 % O_2 concentration, the flame is brighter than that in 21 % O_2 concentration and backside ignition occurs before the termination of laser irradiation. Similar flame behavior is also observed with paper samples in microgravity. In normal gravity, delayed backside ignition was observed with the PMMA samples in air under the ceiling configuration (upward laser irradiation normal to a downward facing sample surface). This curious behavior of flame during the first transition will be further studied. Our numerical calculation will be used to understand why such long delay occurs for the backside ignition.

Figure 2. Selected edge view video images of flame behavior over 0.2mm thick PMMA sheet in 21 % O_2 at 10 cm/s flow from right to left. Laser irradiation normal to the sample surface from top. (a) 1.13s, (b) 3.16s, (c) 4.01s, and (d) 7.02s.

Ignition behavior of the PMMA sheet by a CO_2 laser in zero gravity and also in normal gravity was numerically calculated. The details of our model and computational scheme can be found in our previous publication[2]. The absorption of the incident laser energy by the degradation products from PMMA is included in our three-dimensional, time-dependent code. The results of ignition delay time (irradiated side) in quiescent normal
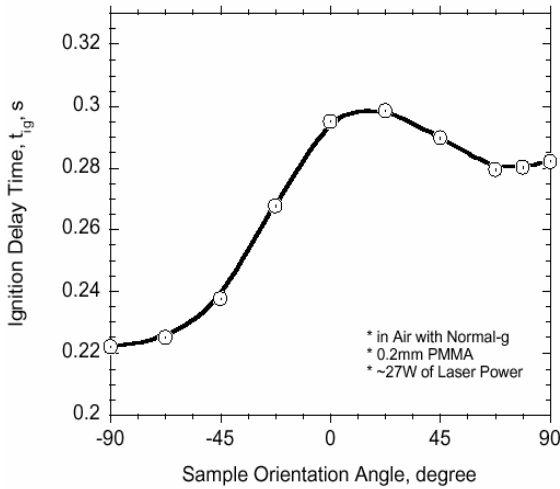
Figure 3. Ignition delay of PMMA (0.2 mm) thick in quiescent normal gravity.

Figure 4. Ignition of PMMA(0.2 mm) in zero gravity.

gravity are shown in Figure 3 as a function of the sample orientation angle. (The sample orientation angle of 0 degree means a vertically mounted configuration and +90 degree means a horizontal upward facing sample.) In this calculation, the laser beam irradiates normal to the sample surface at all angles. The ignition delay time is the shortest at the ceiling configuration (-90 degree) and it increases with an increase in sample orientation angle. However, from about 20 degree to 60 degree ignition delay time tends to decrease with the angle. This decrease is caused by the ignition location moving toward the

Figure 5. Ignition of the front PMMA surface (0.2 mm thick) followed by ignition of the back surface in microgravity.

center of the laser beam. On the other hand, in zero microgravity ignition delay time increases monotonically with an increase in external flow velocity due to blowing away the ignition location from the irradiated area. Ignition behavior on the front (irradiated) surface followed by ignition on the backside surface in zero gravity under an external air flow of 10 cm/s (from right to left) is shown in Figure 5. The calculated results show the

flow from the backside to the front side through an open hole generated by the absorption of the laser beam. This flow is generated by the flame on the front surface and this flow could have significant effects on ignition of the backside surface. We are currently studying in detail the transition behavior from the front surface ignition to the ignition of the backside surface.

Effects of the sample thickness on the transitions.

Our numerical code based on the modified version of the Fire Dynamic Simulation code is being extended to apply to a sample of any thickness, removing the thermally thin limitation. For the above results described of PMMA, thermal conduction in the sample is included but not the transport process of the degradation products in the sample. However, for a paper sample, transport processes of degradation products and oxygen, and a convective flux based on the Darcy's law are included to describe the transport processes in the porous paper sample using a porosity parameter. Preliminary results of the first transition from localized ignition to flame spread are shown in Figure
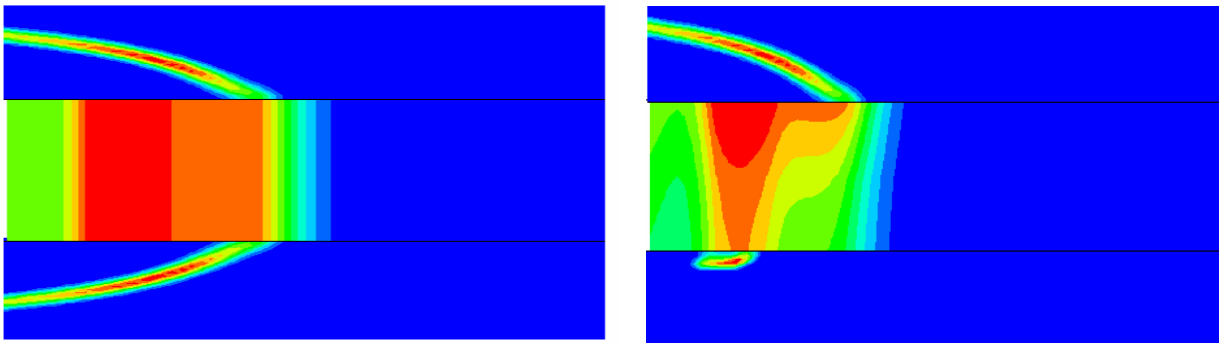
Figure 6. Calculated temperature distribution during the transition from localized ignition to flame spread over a paper based on two case in microgravity, left: thermally thin case and right: general case under external flow of 20 cm/s from right to left. The sample thickness is expanded.

6. For the thermally thin case (includes heat conduction along the sample), flame and subsequent flame spreading appears simultaneously on both sample surfaces. However, for the general case, flame appears at first on the irradiated surface and then on the backside surface with some delay similar to the PMMA case described above. We are currently conducting parametric study to determine under what conditions the species transport processes in the sample become important.

Acknowledgement

[1] Olson, S.L., Kashiwagi, T., Fujita, O., Kikuchi, M., and Ito, K., *Combust. Flame*, **125**:852-864 (2001).

[2] Nakamura, Y., Kashiwagi, T., McGrattan, K.B. and Baum, H.R., *Combust. Flame*, **130**:307-321 (2002).

[3] Mell, W.E. and Kashiwagi, T., *Proc. Combust. Inst.* **27**:2635-2641 (1998).

[4] Prasad, K., Nakamura, Y., Olson, S.L., Fujita, O., Nishizawa, K., Ito, K., and Kashiwagi, T, *Proc. Combust. Inst.* **29**, to appear.

FORCED FORWARD SMOLDERING EXPERIMENTS ABOARD THE SPACE SHUTTLE

A.C. Fernandez-Pello[1], A. Bar-Ilan[1], G. Rein[1], D.L. Urban[2], J.L. Torero[3]
[1]University of California, Berkeley, 94720, ferpello@me.berkeley.edu,
[2]NASA Glenn Research Center, Cleveland, OH 44135
[3]University of Maryland, College Park, MD 20742

INTRODUCTION

Smoldering is a basic combustion problem that presents a fire risk because it is initiated at low temperatures and because the reaction can propagate slowly in the material interior and go undetected for long periods of time [1]. It yields a higher conversion of fuel to toxic compounds than does flaming, and may undergo a transition to flaming. To date there have been a few minor incidents of overheated and charred cables and electrical components reported on Space Shuttle flights [2,3]. With the establishment of the International Space Station, and the planning of a potential manned mission to Mars, there has been an increased interest in the study of smoldering in microgravity.

The Microgravity Smoldering Combustion (MSC) experiment is part of a study of the smolder characteristics of porous combustible materials in a spacecraft environment. The aim of the experiment is to provide a better fundamental understanding of the controlling mechanisms of smoldering combustion under normal- and microgravity conditions. This in turn will aid in the prevention and control of smolder originated fires, both on earth and in spacecrafts. The microgravity smoldering experiments have to be conducted in a space-based facility because smoldering is a very slow process and consequently its study in a microgravity environment requires extended periods of time. The microgravity experiments reported here were conducted aboard the Space Shuttle. The most recent tests were conducted during the STS-105 and STS-108 missions. The results of the forward smolder experiments from these flights are reported here. In forward smolder, the reaction front propagates in the same direction as the oxidizer flow. The heat released by the heterogeneous oxidation reaction is transferred ahead of the reaction heating the unreacted fuel. The resulting increase of the virgin fuel temperature leads to the onset of the smolder reaction, and propagates through the fuel. The MSC data are compared with normal gravity data to determine the effect of gravity on smolder.

EXPERIMENTAL HARDWARE AND PROTOCOL

MSC tests were performed in a 21.7 liter combustion chamber. The fuel sample consists of a polyurethane foam cylinder, 120 mm diameter by 140 mm long. The disc igniter consists of an electrically heated wire between ceramic discs. The oxidizer supply system provides a constant oxidizer mass flow through the foam sample. The fuel sample is instrumented with 10 thermocouples which provide a temperature history of the smolder propagation. In addition to the thermocouples, an ultrasound imaging system (UIS) consisting of 5 ultrasonic transducer pairs fixed along the sample is used to obtain average permeability measurements [4]. The UIS is able to image the location and velocity of the smolder front. The oxidizer used is air. The ignition is achieved by supplying a constant heat flux at the igniter end for 400 s. The overall assembly integrates into a Get Away Special Canister or GAS-CAN, which is flown in the Shuttle cargo bay.

The experiments reported here investigate the dependence of the forward smolder propagation velocity along the foam sample on the air flow. Polyurethane foam was selected as fuel because it is representative of materials commonly used on both earth and space based facilities, its material properties are well known, and it maintains its structural integrity upon smoldering. The forward flow smolder experiments of the STS-105 and STS-108 missions were conducted with a forced oxidizer flow velocity of 3 mm/s and 5 mm/s respectively.

Results

The thermocouples placed along the foam sample are used to calculate propagation velocity of the smolder reaction, as well as to provide information about the intensity of the smolder reaction. The UIS provide permeability data as well as a second method to measure the smolder propagation velocity. This work presents the first ultrasonic data obtained from a microgravity forward smoldering combustion experiment.

For both normal- and microgravity experiments, temperature profiles along the foam centerline are presented in Fig. 1. and permeability histories are presented in Fig. 2.

Figure 1. Thermocouple histories for forced air velocity of (a) 3 mm/s for microgravity, (b) 3 mm/s for normal gravity, (c) 5 mm/s for microgravity and (d) 5 mm/s for normal gravity.
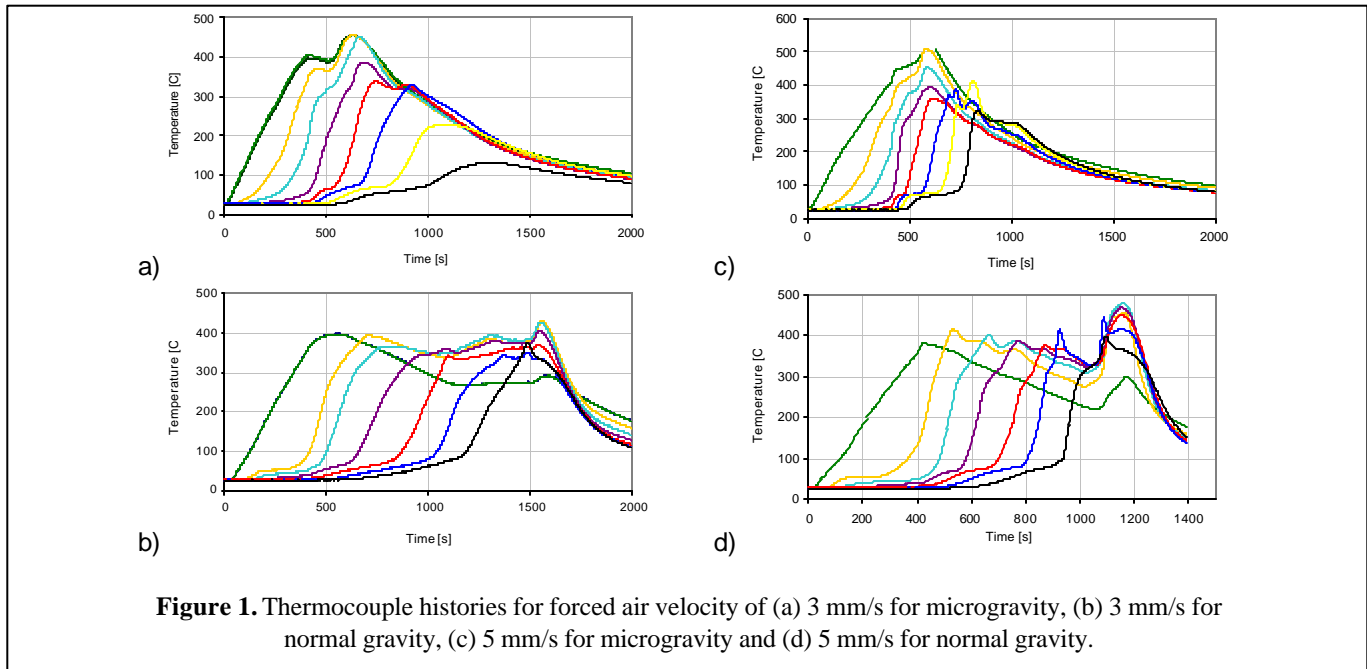
In the 3 mm/s microgravity case, as the foam heats up the thermocouples near the igniter (TC 1 and 2) reach a steady temperature of about 400°C, which is characteristic of foam oxidation. Thermocouple 2 follows the same pattern but does not reach as high of a temperature. This is indicative of upstream consumption of oxygen. This is further evidenced with thermocouple 3 that stabilizes at about 320°C (which is a characteristic temperature for endothermic pyrolysis). As the igniter is turned off a slight decrease in temperature can be perceived at the surface of the foam. But it is followed past 500 s by a sudden generation of heat. Temperatures corresponding to the first 35 mm of the sample (TC 0-3) reach about 450°C, which is typical of char oxidation. A weak re-kindling of the reaction is observed on the temperature traces corresponding to thermocouples 5 and 6 (75 and 95 mm). The temperature traces show a reaction first driven by the igniter and then controlled by energy supply from the char oxidation in the first 35 mm of the foam. Char oxidation consumes the oxygen available and the foam

oxidation fades favoring pyrolysis. Once the char close to the igniter is consumed and the temperature in this region decreases, oxygen flows again and heat generation can be observed once more between 75 and 95 mm. The reaction is not strong enough to progress through the pyrolyzed fuel and eventually extinguishes more than 35 mm away from the sample end. Figure 2(a) shows a dramatic increase in permeability that coincides in location with the regions where the temperature reached the highest value.

Figure 2. UIS permeability histories for forced air velocity of (a) 3 mm/s for microgravity, (b) 3 mm/s for normal gravity, (c) 5 mm/s for microgravity and (d) 5 mm/s for normal gravity.
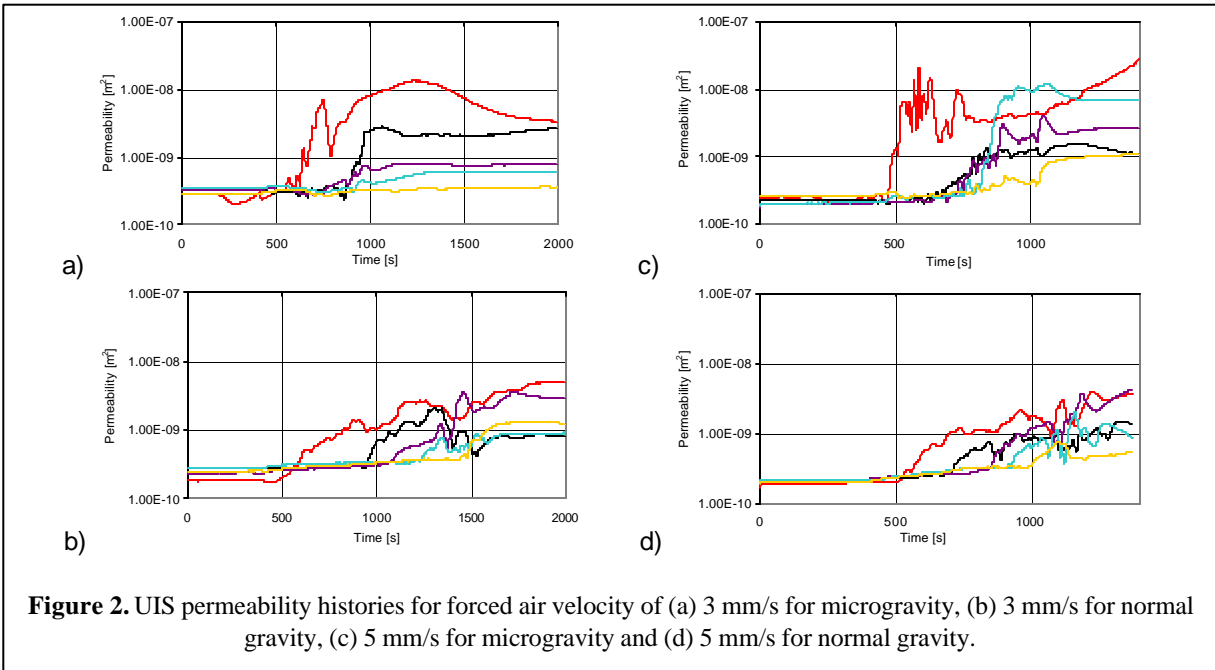
The 3 mm/s normal gravity case in Fig. 1(b) shows a completely different scenario. The temperature increases due to the igniter and the first thermocouples reach the same plateau at approximately 400°C. It is important to note that the temperature increase is slowed down indicating larger losses than in the microgravity case. Once the plateau is reached the temperature immediately begins to decrease. Peak temperatures remain within ranges typical of smoldering. Char oxidation has no significant impact on the temperature traces. After 1000 s the reaction is about 35 mm away from the end of the sample and a gradual increase in the reaction rate throughout the entire foam follows. This effect is related to the decrease in pressure drop through the foam that allows an increase in the total contribution of buoyancy to the supply of oxidizer. An opposed smolder reaction through the char follows (at time greater than 1300 s). A consistent increase in permeability is observed and at each stage of the propagation the change in permeability is smaller. Past 1000 s the increase in permeability continues showing peaks at the locations of the secondary opposed smolder reaction.

Similar to the 3 mm/s microgravity case, the 5 mm/s microgravity case shows a reaction first controlled by the igniter but leading quickly to a strong secondary char oxidation. This secondary char oxidation consumes the oxygen supply, but not completely allowing for a much larger region of secondary char oxidation. Once this secondary char oxidation has consumed the available fuel, the oxygen supply is able to reach further downstream positions. However, the reaction does not extinguish like in the 3 mm/s case, since the supply of oxygen is greater in this case, and stimulates a strong rekindling of the smolder reaction which is able to propagate through to the end of the sample.

Despite the reduced number of experiments, some quantitative data can be obtained. Results for the smolder propagation velocity and smolder reaction temperature from both the normal gravity and microgravity tests are presented in Table 1. The results are divided into regions I, II, and III corresponding to the region influenced by the igniter, the middle region of the sample, and the region dominated by end effects, respectively.

Forced Air Velocity [mm/s]	Smolder Velocity [mm/s]						Smolder Temperature [°C]					
	Region I		Region II		Region III		Region I		Region II		Region III	
	0g	1g	0g	1g	0g	1g	0g	1g	0g	1g	0g	1g
3	0.25	0.19	0.15	0.10	-	0.12	399	396	406	355	-	361
5	0.40	0.24	0.23	0.16	0.25	0.22	398	398	428	387	375	406

Table 1. Smolder propagation velocities and smolder temperatures from normal and microgravity experiments.

A comparison between the temperature profiles in microgravity and in the normal-gravity case shows that the char temperature histories are significantly different between the two cases. In microgravity, the reduced heat losses leads to a hotter char, capable of sustaining a secondary char oxidation reaction but suppressing the smolder reaction through the consumption of the oxygen supply. In the low flow rate microgravity test, the subsequent smolder reaction is extinguished before propagating through the sample, whereas in the high flow rate microgravity test the increased oxygen supply is sufficient to sustain a smolder propagation through the entire sample. The normal-gravity tests display a markedly different behavior. The increased heat losses in normal-gravity force cooling of the char, which allows the forced air flow to pass through the char without significant consumption of the oxygen. This permits the smolder reaction to be sustained and propagate through the sample length at both low and high forced air flow rates.

Concluding Remarks

The present experiments, although limited, are unique in that they provide the only available information about forward smolder combustion in microgravity in sample sizes large enough to allow the self-propagation of the smolder reaction. The experimental results provide further verification about the smolder controlling mechanisms, and data for model verification. Currently the data are being used to verify a numerical model of smolder propagation. Finally, it should be emphasized that since the present conclusions are based on only two microgravity tests, it cannot be generalized until further tests are conducted.

Acknowledgements

References

1. Ohlemiller, T.J., Prog. Eng. & Comb. Sci., 11:277 (1986).
2. Ross, H.D., Natl. Fire Protection Assoc. Meeting, May (1996).
3. Friedman, R., NASA TM-106403 (1994).
4. Tse, S.D, Anthenien, R.A., Fernandez-Pello, A.C., Miyasaka, K., Comb. & Flame 116:120 (1999).

Transport and Chemical Effects on Concurrent and Opposed-Flow Flame Spread at Microgravity

Y. Son, G. Zouein, P. D. Ronney
University of Southern California, Los Angeles, CA 90089-1453

S. Gokoglu
NASA Glenn Research Center, Cleveland OH 44135

INTRODUCTION

Flame spread over flat solid fuel beds is a useful means of understanding more complex two-phase non-premixed spreading flames, such as those that may occur due to accidents in inhabited buildings and orbiting spacecraft. The role of buoyant convection on flame spread is substantial, especially for thermally-thick fuels. With suitable assumptions, deRis [1] showed that the spread rate (S_f) is proportional to the buoyant or forced convection velocity (U) and thus suggests that S_f is indeterminate at μg (since $S_f = U$) unless a forced flow is applied. (In contrast, for thermally thin fuels, the ideal S_f is independent of U [1].) The conventional view [2], as supported by computations and space experiments, is that for quiescent μg conditions, S_f must be unsteady and decreasing until extinction occurs due to radiative losses. However, this view does not consider that radiative transfer to the fuel surface can enhance flame spread. In recent work [3] we have found evidence that radiative transfer from the flame itself can lead to steady flame spread at μg over thick fuel beds. Our current work focuses on refining these experiments and a companion modeling effort toward the goal of a space flight experiment called Radiative Enhancement Effects on Flame Spread (REEFS) planned for the International Space Station (ISS) c. 2007.

OPPOSED FLOW EXPERIMENTS AND MODELING

Microgravity experiments on flame spread over thermally-thick fuels were conducted using foam fuels to obtain low density and thermal conductivity, and thus large spread rate (S_f) over thermally-thick fuels compared to dense fuels such as PMMA. This scheme enabled meaningful results to be obtained even in 2.2 second drop tower experiments. After evaluating numerous candidate materials, we chose open-cell polyphenolic foams primarily because they have lower sooting tendency and negligible melting or dripping tendency compared to other foams such as polystyrene or polyurethane. Experiments were conducted in an apparatus consisting of a 20 liter combustion chamber that was filled with the desired atmosphere by a computer-controlled partial pressure gas mixing system. The samples are ignited by an electrically heated wire than in turn ignited a sheet of nitrocellulose. The flames were imaged using CCD cameras whose signals were connected via fiber-optic cables to ground-based S-VHS video recorders. Both direct video and interferometry were employed. The igniter was controlled and the radiometer data were collected by a microcomputer data acquisition and control system.

Figure 1 shows that for CO_2-diluted atmospheres the steady values of S_f could be higher at μg than 1g, especially at low O_2 concentrations, but for N_2-diluted atmospheres S_f was always higher at 1g than μg. At μg, S_f can actually be higher in CO_2 than N_2 at the same O_2 concentration even though CO_2 has a larger C_P and thus yields lower T_f than N_2 for the same O_2 concentration. Figure 1 also shows that for CO_2 diluent the minimum O_2 concentration supporting combustion is substantially lower at μg than 1g, whereas for N_2 the minimum O_2 concentration is higher at μg. All of these results show that flames in CO_2-diluted atmospheres burn more robustly at μg than 1g whereas the opposite trend is found for N_2. This is likely due to three factors. First, Λ is larger for O_2-CO_2 atmospheres (since both the combustion products and ambient atmosphere contain radiant species, whereas for O_2-N_2 only the combustion products radiate) which increases the heat flux to the fuel bed and thus S_f. Second, without buoyant convection (U = 0), the flame thickness $\delta_g = \alpha_g/(U+S_f)$ is much thicker at μg than at 1g, thus μg flames have more volume and can transfer more radiation to fuel bed. Interferometer images (not shown) confirm that flames are much thicker at μg. This effect is more important for lower O_2 concentrations (thus lower S_f) which explains why the difference between 1g and μg spread rates in O_2-CO_2 atmospheres is larger at lower O_2

concentrations. Third, O_2-CO_2 atmospheres can reabsorb and re-radiate emitted radiation whereas O_2-N_2 atmospheres cannot, thus substantial radiative heat losses that would otherwise occur at µg with thick flames in strongly radiating O_2-CO_2 atmospheres are at least partially suppressed.

Figure 2 shows predicted pressure effects on S_f [3] for O_2-CO_2 atmospheres at µg. Two different assumed values of T_f are shown. All gas properties are evaluated at the average temperature $(T_f + T_\infty)/2$. The model provides reasonable S_f estimates except near the low-pressure extinction limit, where heat losses may dominate, leading to slower than predicted flame spread, and at high pressure where there may be a transition to nearly opaque conditions. The opacity at high pressure causes less radiative transfer thus less fuel bed preheating than predicted by our optically-thin model, which leads to lower S_f than the optically-thin predictions. (Neither of these effects can be predicted by the simple optically-thin, loss-free model developed in [3].)
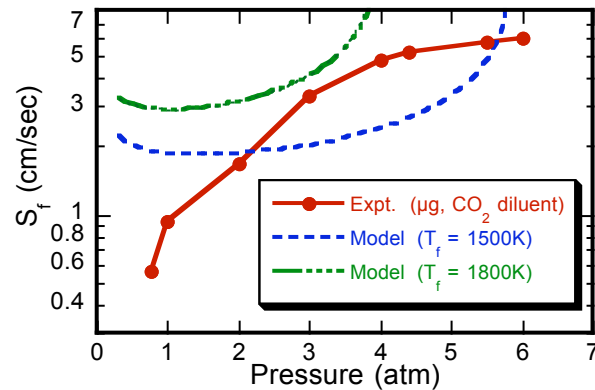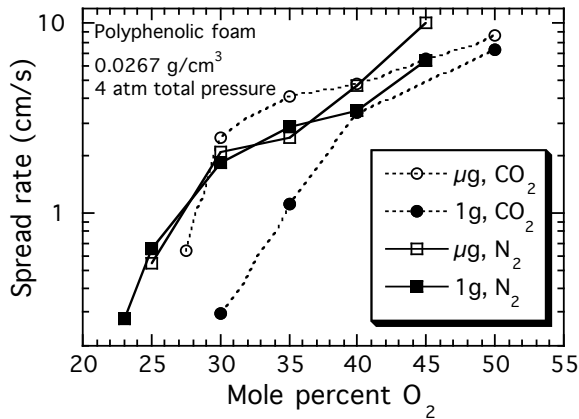
Figure 1. Effect of oxygen concentration on spread rates over thick solid fuel beds at microgravity and earth gravity, polyphenolic foam, density: 0.0267 g/cm^3, 4 atm pressure

Figure 2. Effect of pressure on spread rate over thick solid fuel beds at microgravity for polyphenolic foam, density: 0.0267 g/cm^3, 40%O_2-60%CO_2.

Figures 3a and 3b show the radiative characteristics of flame spread in O_2-CO_2 mixtures at 1g and µg, respectively. Narrow-angle thermopile-type radiometers mounted 10 cm from the fuel bed were used to determine radiative emissions from the flames. Three radiometers were used: (1) a front-side (burning side) radiometer viewing a hole in the fuel bed to measure only the outward gas-phase radiative loss, (2) another front-side radiometer viewing the fuel surface to measure both the outward gas-phase and surface radiative fluxes, thus total radiative loss, (3) a back-side radiometer viewing through the hole to measures the inward gas-phase radiative heat flux, thus the fuel bed heating due to gas-phase radiation. The only case where the back-side radiometer (which measures the gas-phase radiant heat flux to the fuel bed) shows comparable intensity and timing with two front radiometers is for the O_2-CO_2 atmosphere at µg (Fig. 3b). This is likely because only in this case is there substantial emission, absorption and re-emission, which is the only means to obtain substantial radiative flux to the rear-side radiometer. O_2-N_2 atmospheres (not shown) do not show this behavior at all, and even for O_2-CO_2 atmospheres this is seen only at µg (Fig. 3b) where the flame thickness is larger and thus the total radiative flux is greater. Note also that the gas-phase radiative loss ("Front, gas only" curves) at µg is actually lower for O_2-CO_2 than O_2-N_2 atmospheres due to reabsorption by the ambient atmosphere for O_2-CO_2. At 1g, (Fig. 3a) the surface radiation is much larger than gas-phase radiation due to the decreased flame thickness thus decreased volume of radiating gas at 1g. These results confirm our hypotheses concerning radiative transfer effects on µg flame spread, in particular that (1) radiative preheating of the fuel bed by the gas is significant in radiatively-active atmospheres at µg, (2) reabsorption effects can prevent massive heat losses (thus extinction) in radiatively-active atmospheres at µg and (3) these effects are less important at 1g due to substantial U caused by buoyancy which leads to smaller flame thicknesses thus less volume of radiating gas.
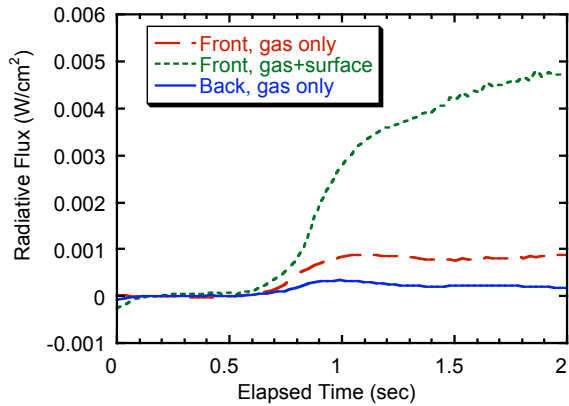
Figure 3. Radiative flux characteristics of flames spreading over polyphenolic foam fuel. (a) 40%% O_2 - 60% CO_2, earth gravity.
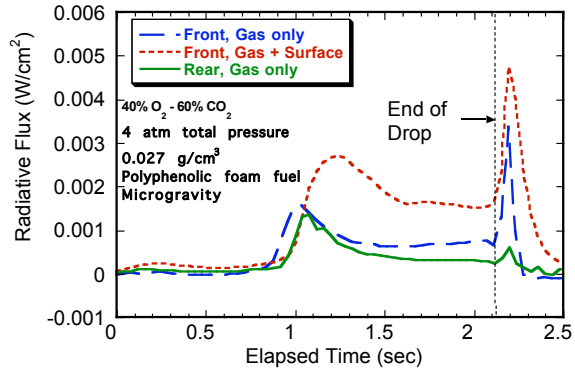
Figure 3. Radiative flux characteristics of flames spreading over polyphenolic foam fuel. (b) 40%% O_2 - 60% CO_2, microgravity.
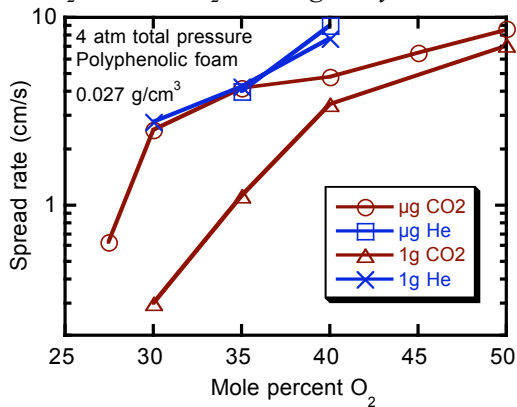
Figure 4. Effect of oxygen concentration on spread rates over thick solid fuel beds at μg and earth gravity – comparison of CO_2 and helium as a fire extinguishing agent.
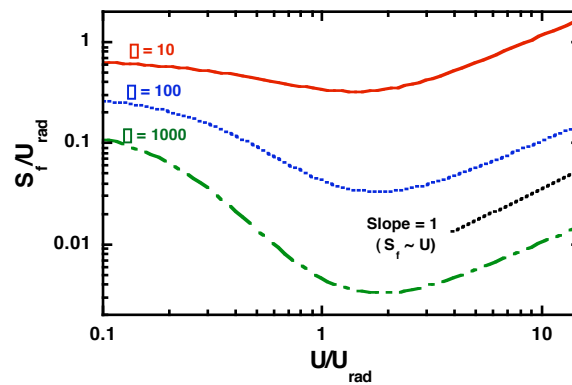
Figure 5. Predicted combined effects of convection and radiation on flame spread rates over thick solid fuel beds

Several tests were conducted using He diluent at 4 atm (Fig. 4). It was found that He- and CO_2-diluted atmospheres exhibit nearly the same S_f, for a given O_2 mole fraction even though CO_2 has a mole-based C_P at 300K that is 1.8 times higher than He, and at 2000K is 3.9 times higher. Also, He has a thermal conductivity (λ_g) 9.4 times higher than CO_2. Both of these factors should lead to higher T_f and S_f in He than in CO_2-diluted atmospheres at the same O_2 concentration. Furthermore, at 1g the minimum O_2 mole fraction supporting combustion was nearly the same (30%) in He and CO_2-diluted atmospheres whereas at μg the minimum O_2 mole fraction was much higher for He (35%) than CO_2 (27%). There are at least three reasons for the observed behavior. First, the Lewis number of O_2 in He is much higher than O_2 in CO_2 (≈ 1.20 vs. ≈ 0.84), which leads to lower spread rates for He [4]. Second, the higher λ_g and α_g of He leads to thicker flames and thus greater radiative loss for the same S_f since the heat loss per unit volume depends only on the radiating combustion products whose concentrations are not significantly different (at fixed ambient O_2 concentration) from O_2-CO_2 atmospheres. Third, unlike CO_2, He is radiatively non-participating and thus no reabsorption or re-emission occurs. Consequently, we conclude that He may be a superior inerting agent at μg on several bases. First, at μg He is more effective than CO_2 on a mole basis (thus pressure times storage volume basis), meaning that the size and weight of storage bottles would be smaller for the same fire-fighting capability. Second, He is much more effective on a mass basis (by about 11x) at μg. Third, He has no physiological activity, unlike CO_2 which affects human respiration. These results are relevant to fire safety in manned spacecraft, particularly the International Space Station that uses CO_2 fire extinguishers.

A model was developed that included the combined effects of convection and radiation on flame spread rates over thick solid fuel beds. Figure 5 shows model predictions in terms of the thick-fuel

flame spread parameter Γ and the opposed forced flow velocity U referenced to a characteristic radiative velocity U_{rad}. It can be seen that there is an intermediate velocity U that minimizes the spread rate. At high U the classical thick-fuel behavior predicted by deRis is observed and at sufficiently low U, the spread rate becomes independent of U (the radiation-dominated regime). Note that in the high-U limit, S_f is proportional to $1/\Gamma$ whereas at low U, the effect of Γ is much weaker.

CONCURRENT FLOW RESULTS AT EARTH GRAVITY

Buoyancy-driven upward flame spread over thermally thick fuels is of great practical importance because it is a paradigm for the main mechanism of fire spread in most building fires. Previously a model for upward flame spread over thermally-thin fuels, including the effects of transverse heat and momentum losses to the sides of the fuel samples and surface radiative losses was developed. Such losses were necessary to yield steady flame lengths and spread rates and with such losses, model predictions were found to agree well with experiments [5]. Recently we conducted analogous experiments using low-density but thermally-thick foam fuels, but instead of steady spread, these tests yielded, for reasons still not clear to us, unsteady behavior due to a "jumping" mode of flame spread. These behaviors were found to occur for a wide range of fuel types, pressures, oxygen mole fractions and sample widths and were found not only near extinction limit but also far from the limit conditions. The spatial and temporal intervals of hopping were very regular for moderately narrow samples, whereas wider samples exhibited an unsteady "walking" or "ratcheting" mode and flames ignited on narrower samples extinguished. For thermally-thin fuels similar behavior was found but only near extinction limits. Figure 6 shows a sequence of images illustrating the "jumping" behavior for a narrow sample. Fig. 7 shows the corresponding temporal history of the leading and trailing edges of the flame. It can be seen that the leading edge progresses at a relatively constant rate as if a "source" of flame length, with the trailing edge pausing then "jumping" to catch up. Current work is focused on determine the mechanism(s) responsible for this unusual behavior.
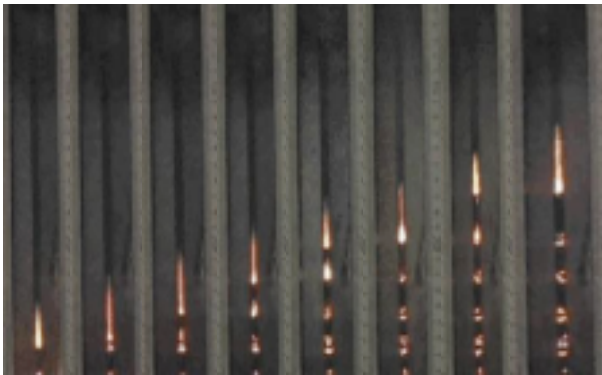
Figure 6. "Jumping" Flame spread, at 45%O_2-CO_2, 1atm, width=10mm, thickness=12mm
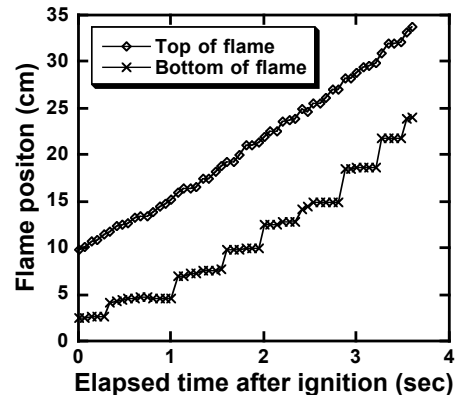
Figure 7. Flame Top and Bottom position as Elapsed time at 45%O_2-CO_2, 1atm, width=10mm, thickness=12mm

REFERENCES

1. deRis, J. N., *Twelfth Symposium (International) on Combustion*, Combustion Institute, Pittsburgh, 1969, p.241.
2. Bhattacharjee, S., West, J., Altenkirch, R. A. *Twenty-Sixth Symposium (International) on Combustion,* Combustion Institute, Pittsburgh, 1996, p. 1477; Altenkirch, R.A., Tang, L., Sacksteder, K., Bhattacharjee, S., Delichatsios, M. A., *Twenty-Seventh Symposium (International) on Combustion,* Combustion Institute, Pittsburgh, 1998, p. 2515.
3. Son, Y., Ronney, P. D., to appear in *Proc. Combust. Inst.*, Vol. 29 (2003).
4. Zhang, Y., Ronney, P. D., Roegner, E., Greenberg, J.B., *Combust. Flame* 90:71 (1992).
5. Honda, L. K., Ronney, P. D., *Proc. Combust. Inst.* 28:2793-2801 (2000).

Low Stretch Solid-Fuel Flame Transient Response to a Step Change in Gravity

Armstrong, J.B., CWRU[+]
Olson*, S.L, NASA GRC
T'ien, J.S., CWRU

Abstract

The effect of a step change in gravity level on the stability of low stretch diffusion flames over a solid fuel is studied both numerically and experimentally. Drop tower experiments have been conducted in NASA Glenn Research Center's 5.2 Zero Gravity Facility. In the experiments burning PMMA cylinders, a dynamic transition is observed when the steadily burning 1g flame is dropped and becomes a 0g flame. To understand the physics behind this dynamic transition, a transient stagnation point model has been developed which includes gas-phase radiation and solid phase coupling to describe this dynamic process. In this paper, the experimental results are compared with the model predictions. Both model and experiment show that the interior of the solid phase does not have time to change significantly in the few seconds of drop time, so the experimental results are pseudo-steady in the gas-phase, but the solid is inherently unsteady over long time scales. The model is also used to examine the importance of fractional heat losses on extinction, which clearly demonstrates that as the feedback from the flame decreases, the importance of the ongoing heat losses becomes greater, and extinction is observed when these losses represent 80% or more of the flame feedback.

Introduction

The stagnation point diffusion flame geometry is ideal for studying the complex coupling between the gas phase flame and the solid fuel. Previous research has utilized this geometry for steady-state flame studies [1-5], adding first surface radiative loss, buoyancy-induced stretch, solid-phase conductive loss, and gas-phase radiative loss. All of these features are included in this work, with the addition of both transient gas and solid phases.

Low stretch diffusion flame experiments (and steady modeling) have been conducted using gaseous burners in drop towers [6], but the coupling between gas and solid is not present in these experiments, so they do not capture important aspects of burning solids. In addition, no discussion of the normal to microgravity flame transition was provided for the "quasi-steady" test conditions which ignited in normal gravity, dropped into microgravity, then changed the fuel flow rate during the drop. Low stretch buoyant flame experiments have been conducted that use large scaling to obtain low stretch in normal gravity[7,8]. The results of those tests show that flame standoff distance grows as flame stretch is reduced, and that the flame temperature reaches a maximum at stretch rates of 6-7 s^{-1}. In addition, the surface energy balance was shown to capture the increasing the fraction of heat feedback from the flame that is lost through radiation and conduction into the solid as stretch rate is reduced until extinction occurs.

Numerical Model

A transient two-phase numerical model with single step finite rate kinetics and temperature-dependent solid-phase properties has been developed to predict the transition behavior seen in drop tower experiments as well as to better understand the gas-solid coupling and time scales to reach steady-state after a change in gas-phase conditions [9] . The unsteady gas phase is modeled using a mixed-convection stagnation point flow below a cylinder[2]. Gas-phase radiation (CO_2 and H_2O only) is accounted for using a two-flux model using a calibrated absorption coefficient[9]. A one-dimensional transient solid model with surface radiative loss and fuel regression is used to describe the solid, with the surface energy balance coupling the two phases. The coupling between the gas-phase and solid-phase models was done in dimensional terms because the step change in stretch rate changes the gas-phase scaling. The physical location of the gas-phase grid is held constant throughout the computation, and the grid spacing definition is converted to account for the change in scaling at the start of the drop. In the computations, a steady normal gravity mixed convection flame is used for the initial conditions. The sample thickness was fixed in each case to be 3.125mm, which is similar to that obtained in the experiments after ignition and stabilization prior to the drop test. The forced flow part of the stretch rate remains fixed throughout the computation, but when the drop occurs, gravity goes to zero, eliminating the buoyancy-driven component of stretch. The flow decays to a purely forced stretch rate, as will be described in the results section.

Experiment Description

Microgravity drop tower experiments were conducted in the 5.18 second Zero Gravity Facility at NASA Glenn Research Center[9]. The experiments were conducted in a droppable wind tunnel[10], that provides air flow from 0-20 cm/s through the 20 cm diameter test section. The sample holder consists of the cast PMMA fuel sample tube, 3.8 cm in diameter, 15 cm long, ~4mm initial wall thickness, mounted hanging from a cross-beam support. A thin kapton tape heater is mounted between the inner wall of the fuel tube and the hollow copper core, which carries cooling water to the apparatus. Between the heater and the cooling water, the backside temperature of the fuel can be adjusted prior to ignition to control in-depth heat loss.

During an experiment, the fuel is heated to a specified temperature ($\approx 150^\circ$C), and then the flow is started. Uniform ignition of the PMMA is achieved, and then the experiment is then dropped. The primary variables in the experiments were the forced stretch rate and the gravity level. The gravity level changed from Earth-normal, or 1g, to 0g during each drop. In normal gravity, the mixed stretch rate was $\approx$ 20 s^{-1}. The forced stretch rate was varied between tests from 3-20 s^{-1}, but the set value was held constant during the drop.

Results
Flame Standoff Distance

When the experiment is dropped, and the gravity step changes from normal gravity to zero gravity, the flame responds rapidly and non-monotically to the change in stretch rate. As shown in Fig. 1, at the drop start, the flame expands away from the fuel surface as the fuel vapor Stefan flow reaches further from the surface before encountering oxygen in the weakening stretch[9]. A maximum standoff distance is reached within a fraction of a second, and then the flame more slowly moves back toward the surface.

Figure 2 shows the measured experimental standoff distance and the model's predicted standoff as a function of time during the drop. In the experiment, the standoff is defined as the distance from the fuel surface to

Figure 1: Sequence of images from drop. Initial 1g steady luminous flame with distinct blue outer flame, followed by sooty, pustular transition flame which evolves during the drop to a smooth blue 0g flame at a stretch rate of 5 s^{-1}. Sequence is side view of burning cylinder.
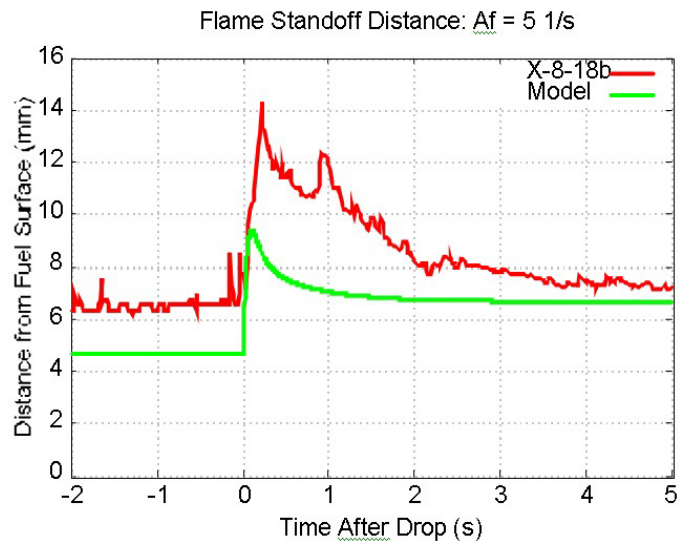
Figure 2: Experimental and computed flame standoff distances for a 1g flame transitioning to a 0g flame at a final stretch rate of 5 s^{-1}. Notice the overshoot in standoff distance at the drop start and the increase in flame standoff distance as stretch rate is reduced.

the outermost visible part of the flame. In the simulations, the standoff distance is defined as the distance from the fuel surface to the location of the maximum flame temperature. Thus it is expected that the predicted standoff is less than the measured standoff distance. As shown in Figure 2, this is indeed the case. The model does a good job of

capturing the transient behavior of the experimental flame, with the overshoot in the standoff distance predicted to occur within the first second of the drop, with a slower recovery to a larger standoff distance at the lower stretch rate in 0g. The experimental time to peak standoff distance appears to be consistent with the gas-phase relaxation time, estimated to be the inverse of the final stretch rate. The model predicts that the time to peak standoff distance is shorter than this estimate by a factor of two. The larger overshoot seen in the experiments is attributed to the vapor jetting from the bubble layer at the surface, which gives the transition flame its pustular appearance[9]. The simple solid-phase model does not include bubble layer effects and uses extrapolated properties at the highest temperatures, which may not be accurate for the molten viscous PMMA[11]. Lastly, the model does not account for the significant soot formation seen in the experiments. There is a second characteristic time noted in this work, which is the relaxation time to steady-state standoff distance under the new low gravity stretch conditions. The model predicts that the standoff distance stabilizes by approximately one second, whereas in the experiments, especially at lower stretch, the flame does not reach a steady standoff in the 5.2 s drop time. This is attributed to the solid-phase response.

Surface Temperature

Figure 3 shows the surface temperature measured in the experiment compared with the predicted surface temperature from the transient model. After the drop, the experiment shows a much longer transient which is still in the process of asymptoting to a lower surface temperature than the theory predicts. The transition to a steady temperature takes much longer than is predicted by the model, which is consistent with the slow transition noted above for the steady-state standoff distance. During a 5.18 s drop tower experiment, a thermal wave will penetrate only $L_{drop} \approx (\alpha t)^{1/2} \approx 0.07$ cm, less than 20% of the way through the sample. For any reasonable change in flame strength, clearly the flame at the end of the drop time will not have reached steady-state. The experimental temperature changes varied from 15-50K, with larger drops in temperature corresponding to lower stretch rate. This change is a significant change in Arrhenius fuel vaporization rate. Since the experimental temperatures remain higher for longer, the fuel vaporization rate will also remain higher for longer, resulting in a slower transition to a stable flame standoff distance.

Surface Energy Balance

The surface energy balance (Eqn. 1) is used to evaluate the coupling between the gas and solid phases during the transition process. The surface energy balance includes conduction from the flame, radiation from the flame zone, in-depth conduction, energy needed to vaporize the fuel, and surface radiation to the environment. The left side represents the net heat flux from the gas to the surface. Each term can be evaluated as a function of time using predicted burning rate data and temperature measurements (gas and solid-phase).
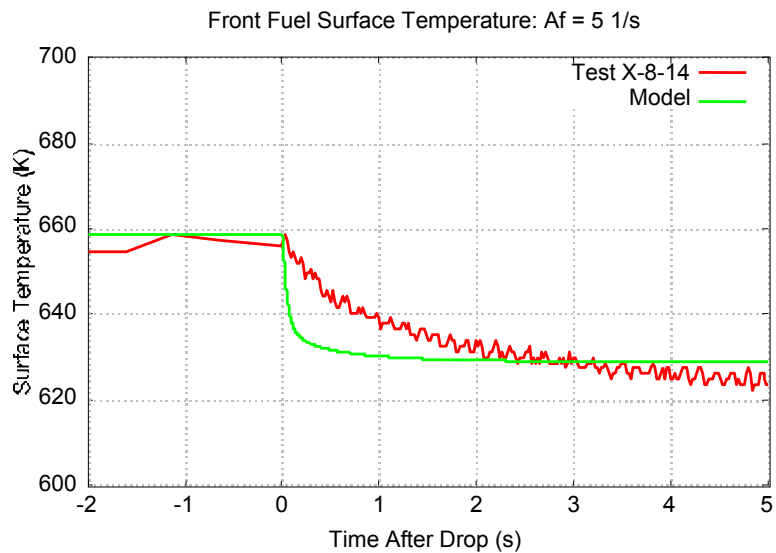
Figure 3: A surface temperature comparison between the experiment and the model. The surface temperature does not overshoot. Rather, the model shows a rapid decay in surface temperature. The experiments show a similar but more gradual decay.

$$\lambda_g \left.\frac{\partial T}{\partial x}\right|_g + q_{rad,g} = \lambda_s \left.\frac{\partial T}{\partial x}\right|_s + \dot{m}L + q_{rad,s} \qquad Eqn(1)$$

The gas conduction to the solid drops dramatically at the start of the drop, due to increase in flame standoff distance. The gas-phase radiation, (CO_2 and H_2O only), increases slightly during the transition but returns to almost the same value after a few seconds. As was shown in Fig. 2, because of the drop in the flame feedback via conduction, the surface temperature drops. Because of this drop, the surface radiation drops slightly. The in-depth conduction loss also drops during transition before rebounding to nearly the same levels, as the in-depth solid

gradients take time to react to the reduced surface temperature. The most dramatic effect of the reduced flame feedback is in the pyrolysis rate. Burning rates are significantly lower at low stretch [7,8].

To determine overall trends, the terms of the surface balance are compared as ratios. The ratio $F_{reutilization}$, is the fraction of gas-to-surface net heat flux used to vaporize more fuel, and the other ratio, F_{loss}, is the fraction of gas-to-surface net heat flux that is lost to the solid interior and radiated from the surface. In this way, $F_{loss}+F_{reutilization}=1$.

These two ratios are plotted as a function of time in Figure 4 for an extinction case and a stable flame case. The model predicts that the surface energy balance changes abruptly after the start of the drop. At a stretch rate of 3 s^{-1}, the flame

Figure 4: Loss and Reutilization Ratios as a function of time during a drop. At a stretch rate of 3 s^{-1}, the flame extinguishes, whereas as 5 s^{-1}, the flame is steady.

extinguishes as the F_{loss} exceeds 0.8. At a stretch rate of 5 s^{-1}, the losses asymptote to a maximum of 0.75 within a few seconds, but hold steady there. In the extinction case, the net heat flux denominator in the ratio becomes too small, whereas the losses reflected in the numerator change only slightly prior to extinction. The primary difference in the two cases is the gas-phase conductive feedback, which is 1.5 W/m^2 for 5 s^{-1}, whereas it is only 1.2 W/m^2 for 3 s^{-1} prior to extinction. Thus extinction is attributable to insufficient heat feedback to the surface under low stretch conditions to compensate for existing heat losses. The model predictions thus agree very well with previous experimental results [7,8] at the 1D flame extinction limits.

Conclusions

The effect of a step change in gravity level on the stability of low stretch diffusion flames over a solid fuel is studied both numerically and experimentally. Both model and experiment show a rapid overshoot in flame standoff distance due to the rapid reduction in stretch rate while fuel blowing changes more slowly. Both model and experiment show that the interior of the solid phase does not have time to change significantly in the few seconds of drop time, so the experimental results are pseudo-steady in the gas-phase, but the solid is inherently unsteady over long time scales. The model is also used to examine the importance of fractional heat losses on extinction, which clearly demonstrates that as the feedback from the flame decreases, the importance of the ongoing heat losses becomes greater, and extinction is observed when these losses represent 80% or more of the flame feedback.

References:
1   T'ien, J.S., Singhal, S.N., Harrold, D.P., and Prahl, J.M.; C&F 33, 55-68, 1978.
2   T'ien, J.S., C&F 65, 31-34, 1986.
3   Foutch, D.W. and T'ien, J.S.; AIAA J.,, V.25, No.7, 972-976, 1987.
4   Yang, C.-T. and T'ien, J.S., , JHT 120, 1055-1063, 1998.
5   Rhatigan, J.L., Bedir, H., and T'ien, J.S.; ", C&F 112, 231-241, 1998.
6   Maruta, K., Yoshida, M., Guo, H., Ju, Y., and Niioka, T. ; C&F 112, 181-187, 1998.
7   Olson, S.L and T'ien, J.S.; *Combustion and Flame*, V. 121, pp. 439-452, 2000.
8   Olson, S.L., Ph.D. Dissertation, CWRU, 1997.
9   Armstrong, J.B., "The Transient Response of a Low-Stretch Solid-Fuel Diffusion Flame to a Sudden Elimination of Gravity", M.S. Thesis, CWRU, Spring, 2002.
10 Olson, S.L.; Comb. Science and Tech., V.76, pp. 233-249, 1991.
11 Olson, S.L., and T'ien, J.S.; Fire and Materials, V. 23, pp. 227-237, 1999.

UPWARD AND DOWNWARD FLAME SPREADING AND EXTINCTION IN PARTIAL GRAVITY ENVIRONMENTS

Kurt R. Sacksteder
NASA Glenn Research Center,

Paul V. Ferkul
National Center for Microgravity Research, and

Ioan I. Feier, Amit Kumar and James S. T'ien
Case Western Reserve University

INTRODUCTION

The premise of this research effort has been to begin exploring the gap in the literature between studies of material flammability and flame spread phenomena in normal-gravity and those conducted in the microgravity environment, with or without forced flows. From a fundamental point of view, flame spreading in upward (concurrent) buoyant flow is considerably different from concurrent forced flow. The flow accelerates throughout the length of the buoyant flame bringing the streamlines and the flame closer to the fuel surface and strengthening the interaction between the flame and fuel. Forced flows are diverted around the flame and away from the fuel surface, except where the flow might be constrained by a finite duct. The differences may be most clearly felt as the atmospheric conditions, viz. pressure or oxygen content, approach the flammability limit. From a more practical point of view, flame spreading and material flammability behavior have not been studied under the partial gravity conditions that are the natural state in space exploration destinations such as the Moon and Mars. This effort constitutes the beginning of the research needed to engineer fire safety provisions for such future missions.

In this program we have performed partial-gravity experiments (from 0.1 to 1 g/g_{Earth}) considering both upward and downward flame spread over thin solid fuels aboard the NASA KC-135 aircraft. In those tests, the atmospheric pressure and the fuel sample width were varied. Steady flame spread rates and approximate extinction boundaries were determined. Flame images were recorded using video cameras and two-dimensional fuel surface temperature distributions were determined using an IR camera. These results are available in [1 – 3], and complement our earlier work in downward spread in partial gravity varying oxygen content [4].

In conjunction with the experiment, three-dimensional models of flame spreading in buoyant flow have been developed. Some of the computed results on upward spreading have been presented in [3]. A derivative three-dimensional model of downward spreading has been developed [5]. It is currently being used to evaluate the standard limiting oxygen index (LOI) measuring device and its potential performance in different gravity levels.

Since radiation plays an important role in flames at low gravity, considerable effort has been spent on flame and surface radiation on spreading flames. A theoretical study using a two-dimensional model with gas-phase radiation compared flame spread in concurrent and opposed flows and clarified a number of questions in low-speed flows. In forced flow, concurrent flame spread rate is approximately proportional to upstream velocity (similar to the gravity dependence

in buoyant case) but opposed flame spread rate is non-monotonic. While at most forced flow velocities, spread rates are generally higher in concurrent flow than in opposed flow, the curves can cross at very low forced velocity. However, the lowest flammable oxygen percentage is always in the concurrent flow case. [6]

In this paper we wish to show a comparison of upward and downward flame spread in partial gravity tests, show some numerical simulation results from opposed flow spreading in mixed convection flow and indicate some conclusions with respect to flame spread behavior in the partial gravity environment.

EXPERIMENTS

Upward and downward flame spreading was observed in reduced-pressure air environments in normal-gravity and in partial-gravity environments using the GIFFTS test apparatus [1-4] with slight modifications. Fuel samples were a thin cellulosic tissue, trade name "Kimwipes." A repeatable pre-test sample-drying procedure was developed using a hot-air gun. Test pressures between 0.2-0.4 atmospheres were established using primary standard, precision mixtures of 21% O_2, balance N_2. Flight tests were performed onboard the NASA KC-135 aircraft providing partial-gravity environments of 0.1, 0.16, and 0.38 g/g_{Earth}. Limited tests were conducted at greater than 1.0 g/g_{Earth}. Chamber pressure and 3-axis accelerations were recorded by the GIFFTS computer. Conventional video and a FSI Inc. Prism DS infra-red camera with a flame filter at 3.8μm (to reject emissions from excited H_2O, CO_2) were used to image the solid surface. The IR camera signal is calibrated to a black body emission; quantitative temperature measurements require the surface emissivity properties within the filter pass band. We have been developing methods for determining surface emittance from a burning surface [7, 8].

Figure 1 shows an example of flame spread rates versus the local gravity level for 2 cm wide Kimwipes burning in air at a reduced pressure of 27.6 kPa. The upward burning spread rate varied linearly with gravity level for all pressure environments and sample widths tested (the inset shows data or 1 cm sample width), which has been predicted in scaling analysis [9]. The primary heat transfer mechanism for upward spread is buoyant convection, which increases with gravity. The measured pyrolysis lengths also increase proportionally with gravity. The three dimensional model predicts nearly linear spread rate dependence on gravity, as shown, for example, by the open symbols in the figure.

The downward spread rate is non-monotonic and peaks near the Martian gravity levels of 0.38 g/g_{Earth}. The reductions from the peak are attributed to finite kinetic effects: a short residence time at high gravity, and
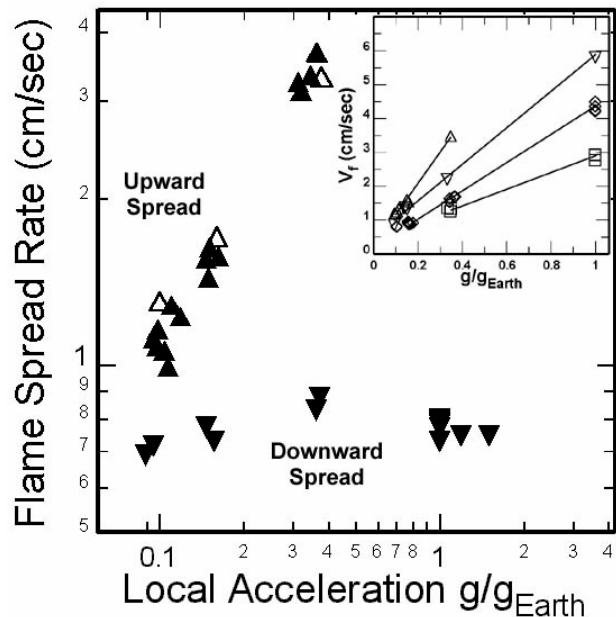
Figure 1. Upward and downward flame spread rates for 2 cm wide samples burned in 27.6 kPa (4.0 psia) air at various gravity levels. Upward pointing symbols indicate upward spread; downward pointing symbols, downward spread. Open symbols indicate results of numerical simulations of flame spread. The inset shows results for 1 cm wide samples.

radiative loss at low gravity. This spread rate behavior is qualitatively similar to composite observations of forced flow spreading. Here a single fuel, test apparatus and testing environment provide an unambiguous demonstration of the behavior.

Within the gravity levels tested, the upward spread rates are everywhere larger than the downward rates. If the upward and downward spread rates were extrapolated to lower gravity levels, a merging or crossover would occur. While this possibility has not been confirmed by experiment, the forced flow analog has been predicted [6].

Figure 2 shows flammability boundaries for flame spreading upward or downward over 2 cm wide Kimwipes burning in air. Elevated gravity levels (>1g/g_{Earth}) were obtained by testing during the aircraft pull-up maneuver. The downward spreading boundary is U-shaped showing the dual extinction limits (insufficient residence time in high g, radiative loss in low g) now predicted by several diffusion flame models.

Figure 2. Flammability boundaries for upward and downward spreading flames over 2 cm wide samples. Open and closed symbols indicate flammable and non-flammable conditions respectively. Crosses indicate observed extinctions occurring well after ignition. Downward pointing symbols indicate downward spread, upward pointing indicates upward spread.

The upward spreading case has a wider flammable domain that the downward case. In the upward case, tests at elevated gravity were not feasible in the current apparatus because of size limitations. The flammable domain shrinks as the sample width is reduced from 2 cm to 1 cm as expected. For both the concurrent flow (upward spread) and opposed flow (downward spread) cases, the stabilization of the flame, and therefore the flammability of the material, is established at the base of the flame where it first encounters the fresh oxidizer flow. In the upward case the flame is stabilized where the fuel burnout occurs while in the downward case the flame is stabilized where the fuel is preheated to the pyrolysis temperature. Differing thermal demands on the flame stabilization zone lead to different limiting conditions.

THREE-DIMENSIONAL MODELING OF DOWNWARD SPREADING FLAMES

In additional to the 3-D model of steady upward spreading flames, 3-D downward spread in a mixed forced and buoyant flow was recently simulated numerically for a flow in a duct that resembles the standard limiting oxygen index (LOI) apparatus [5]. In this study, the limiting oxygen mole fractions were determined as functions of sample width, tunnel width, sample holder configuration, forced velocity and gravity level. A cotton fiberglass composite fuel was simulated. The detailed flame structure and the flow field in the duct were resolved. Fig. 3 shows a computed LOI as a function of forced flow velocity at normal and zero gravity. The normal gravity boundary is monotonic with respect to the forced velocity while the LOI at zero gravity is non-monotonic and has a minimum around 5 cm/s. The LOI at normal gravity are higher than those at zero gravity for the range of forced velocity computed.
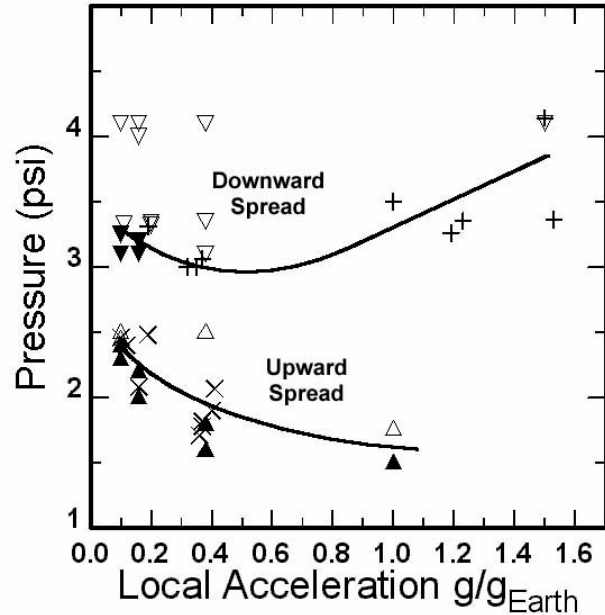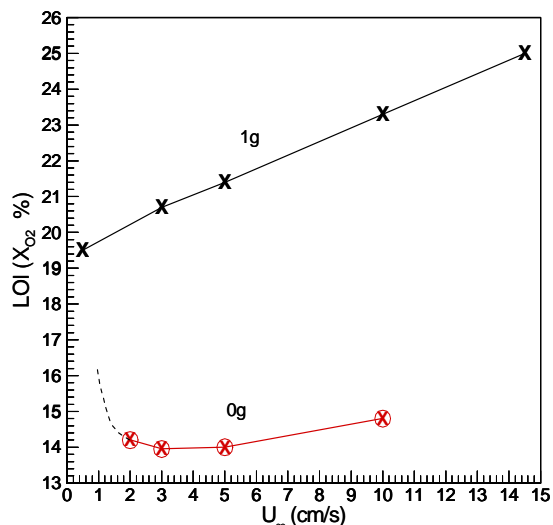
Figure 3. Limiting Oxygen Index (LOI) prediction for cotton/ fiberglass fuel in a mixed-convection environment, computed using a three dimensional model with as-yet uncalibrated kinetic constants. Fuel samples are 5 cm wide by 15 cm long burning in a vertical flow tunnel with a 10cm by 10cm cross section and 50 cm length. The flame location is fixed at the middle of the tunnel. A uniform forced flow is introduced from the tunnel bottom. The upper end of the tunnel is open to 21% air. The sample has inert side stripes 6 mm wide on each side. The symbols are the computed LOI. The last point in the 1g data (i.e. at 0.5 cm/s) is affected by the flow entrained from the atmosphere at the top of the tunnel. The dotted line in the zero-gravity result is what we expect from future computations at lower velocities (based on 2-D results).

CONCLUSIONS

This exploratory study of flame spreading and material flammability in partial gravity environments provides some practical results that require further study. Upward flame spread rates are proportional to gravity level, the downward case is non-monotonic. Over the partial gravity range accessible to testing, flames spread more quickly in the upward than the downward direction, and the flammable domain of upward spreading is wider than for downward spreading.

REFERENCES

1. Feier, I.I., Shih, H.-Y., Sacksteder, K.R. Sacksteder and T'ien, J.S., "Upward Flame Spread over Thin Solids in Partial Gravity," presented to the 39th AIAA Aerospace Sciences Meeting, Reno, January 2001, AIAA 2001-0466, (2001).
2. Feier, I. I., "Experimental Upward Flame Spread over Thin Solids in Partial Gravity," Masters Thesis, Case Western Reserve University, May 2001.
3. Feier, I.I., Shih, H.-Y., Sacksteder, K.R. Sacksteder and T'ien, J.S., *Proc. Combust. Inst.* **29**, in press, (2002).
4. Sacksteder, K.R., and T'ien, J.S., *Proc. Combust. Inst.* **25**: 1685 (1994).
5. Kumar, A., "A Numerical Study of Opposed-flow Flame Spread over a Solid Fuel," Ph.D. Thesis, Case Western Reserve University, expected August 2003.
6. Kumar, A., Shih, H.Y. and T'ien, J.S.: A Comparison of Extinction Limits and Spreading Rates in Opposed and Concurrent Spreading Flames Over Thin Solids, *Combust. and Flame*, **132**: 667-677 (2003).
7. Kleinhenz, J.E., Feier, I.I., Pettegrew, R.D., Sacksteder, K.R., Ferkul, P.V. and T'ien J.S., "Infrared Imaging Diagnostics for Flame Spread over Solid Surfaces," presented to the 41st AIAA Aerospace Sciences Meeting, Reno, January, 2003, AIAA-2003-0988 (2003).
8. Pettegrew, R., Street, K., Piltch, N., T'ien, J. and Morrison, P., "Measurement and Evaluation of the Radiative Properties of a Thin Solid Fuel," presented to the 41st AIAA Aerospace Sciences Meeting, Reno, January, 2003, AIAA-2003-0511 (2003).
9. Honda, L.K. and Ronney, P. D., "," *Proc. Combust. Inst.* **28**: 2793-2801, (2000).

ANALYSIS OF MSL-1 MEASUREMENTS
OF HEPTANE DROPLET COMBUSTION

Malissa Ackerman and Forman Williams
Center for Energy Research, Mechanical and Aerospace Eng., Univ. of California, San Diego

Introduction

A droplet combustion experiment (DCE) was performed on the MSL-1 mission of the Space Shuttle Columbia. There were two flights of this mission—STS-83 in April of 1997 and STS-94 in July of 1997. The reflight occurred because a fuel-cell power problem onboard the shuttle forced an early termination of the first flight; this was the only shuttle mission to be flown twice. DCE data were obtained during both flights. A fiber-supported droplet combustion (FSDC) experiment also was run on STS-94. This smaller "glovebox" experiment, which investigated the combustion of fiber-supported droplets in Spacelab cabin air, had previously flown on the first United States Microgravity Laboratory (USML-1) mission of STS-73, but successful measurements with heptane as the fuel in this experiment were first obtained on STS-94. Although heptane droplet combustion in convective flow also was studied on STS-94, only data without forced convection are considered here. The objective of the present paper is to analyze the results on heptane droplet combustion in quiescent atmospheres.

Data Analysis

A PC-based image-analysis system [1] was used to measure droplet and flame diameters as functions of time. Reduction of some of the data from STS-83 was reported previously [2]. In the present work, two approaches to reducing flame-diameter and droplet-diameter data were employed. One involved graphically exhibiting raw data extracted from the image-analysis system, and the other involved smoothing with a second-degree Loess smoother [3] in the statistical software package S-Plus. Full details of the data analysis, these reduction techniques and various characteristics of the resulting procedures that dictated selection of the methods adopted will be available elsewhere [4] and can be obtained now by contacting the authors.

Results

Results are reported in full elsewhere [4]; there were 34 DCE tests in helium-oxygen atmospheres and 4 in air, 2 fiber-supported. Figure 1 shows raw data on droplet diameters for the 15 FSDC tests, while for comparison Fig. 2 shows smoothed data on both droplet and flame diameters for the DCE tests in one particular atmosphere. Here solid curves are for the flames and dashed curves for the droplets, error bars indicate maximum scatter, a large dot signifies flame extinction and D means that the image drifted out of the field of view. Figure 2 clearly shows diffusive extinction for the small droplets and radiative extinction for the larger droplets. Results are discussed first in terms of extinction diameters and next in terms of burning rates.

Extinction Diameters

When diffusive extinction occurs, droplet diameters at extinction are very small, usually too small to be measured and quite possibly often zero. For seven DCE experiments it was found that diameters at extinction are too small to be measured, that is, less than a limit of resolution between about 0.05 mm and 0.5 mm, depending on the experiment. Only three experiments have measurable droplet extinction diameters for diffusive extinction, two of which are shown in Fig. 3, the third being similar but in a different atmosphere. On the other hand, for radiative extinction, the droplet extinction diameters are much more readily determined. Four such

Figure 1: Raw data for the fifteen FSDC tests analyzed

Figure 2: Smoothed graph for 1.00 bar, 25 % oxygen

Figure 3: Droplet diameter at extinction

Figure 4: Final flame diameter
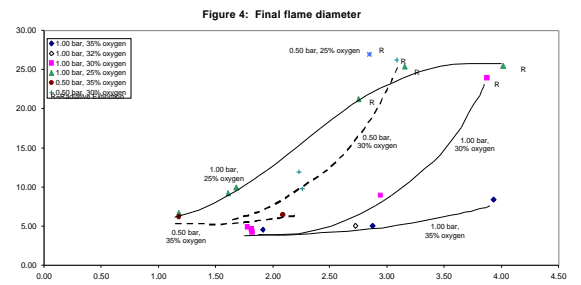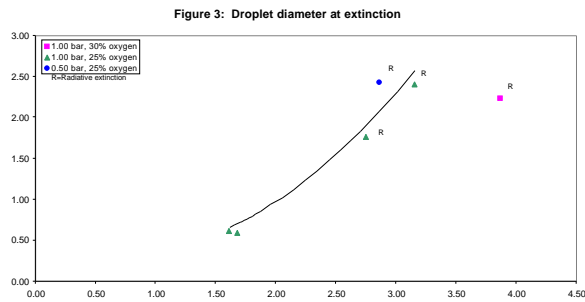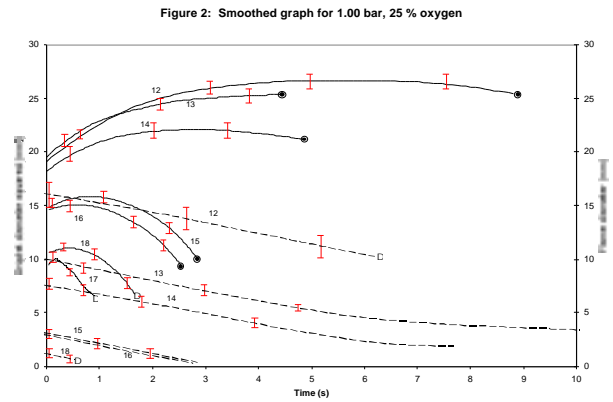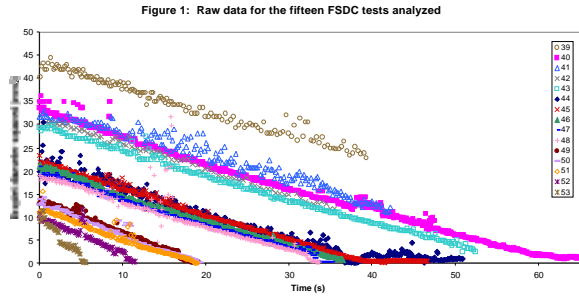
droplet diameters at extinction were obtained and are also plotted in Fig. 3, identified by the symbol R.

From the data in Fig. 3 for 1.00 bar and 25% oxygen, through which the curve is drawn, it is seen that in this atmosphere the droplet extinction diameter increases with increasing initial droplet diameter. This trend is consistent with theoretical estimates for radiative extinction. For diffusive extinction with the flame in the quasisteady region, if the liquid fuel remains pure then the droplet diameter at extinction theoretically is independent of the initial droplet diameter [5]; the available data are insufficient to test this prediction. Although no significant functional dependences for diffusive extinction could be measured, trends were obtained for radiative extinction. The point at 1.00 bar and 30% oxygen in Fig. 3 suggests a decrease in the droplet radiative extinction diameter with increasing oxygen concentration at a given pressure and initial droplet diameter, while that at 0.50 bar and 25% oxygen indicates an increase in the droplet radiative extinction diameter with decreasing pressure at a given oxygen mole fraction and initial droplet diameter. Both of these trends are expected from the dependence of the reaction rate on pressure and oxygen concentration.

In contrast to droplet diameters at extinction, substantial data were acquired on flame diameters at extinction in helium-oxygen atmospheres. Indications are that flames always extinguish at flame diameters large enough to be measured. Since fewer theoretical predictions have been made of these flame extinction diameters (final flame diameters), additional theoretical work is needed for making comparisons with the present experimental results, which are partially plotted in Fig. 4 and discussed elsewhere [4] (because of insufficient space here).

It is of interest to exhibit graphically the boundary between radiative and diffusive extinction, in a plane of oxygen mole fraction and initial droplet diameter for different pressures, as determined by these experiments. Figure 5 is such a plot, with the open symbols corresponding

Figure 5: Boudary between radiant and diffusive extinction

Figure 6: Burning rate comparison
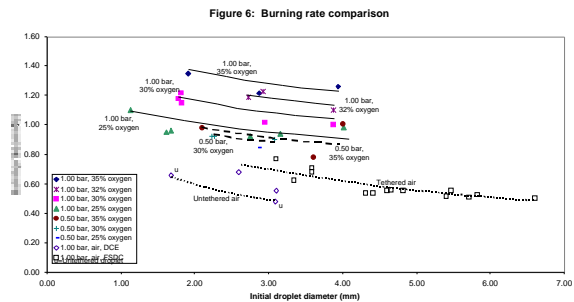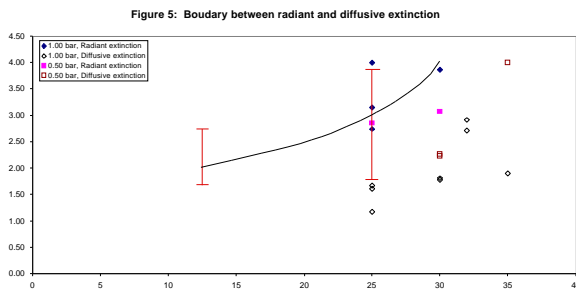
to observations of diffusive extinction and the closed symbols correspond to radiative extinction. Figure 5 shows that, although there is considerable uncertainty about exactly where the boundary lies, the general direction and curvature of the boundary between the two regimes seems well defined. The error bars indicate the range of uncertainty of the boundary location at 1.00 bar; data are insufficient to distinguish differences in boundary locations at 1.00 bar and 0.50 bar.

Burning Rates

A summary graph of burning-rate constants as functions of initial droplet diameter is shown as Fig. 6. In this figure the solid curves pertain to helium-oxygen atmospheres at 1.00 bar, the dashed curves to helium-oxygen atmospheres at 0.50 bar and the dotted curves to air. The general trend of a decrease in the burning-rate constant with increasing initial droplet diameter is evident in all of this data. Some specific data points, particularly the triangular points representing 1.00 bar and 25% oxygen and the circles representing 0.50 bar and 35% oxygen, suggest the existence of a minimum burning-rate constant at a particular initial droplet diameter, but in view of the general trends of most of the data, it seems likely that these minima are only apparent and are the result of run-to-run variability, although their existence cannot entirely be ruled out. The decreasing of the burning-rate constant with increasing initial droplet diameter is consistent with previous work [6], where the change was attributed to the formation of larger quantities of soot.

Figure 6 clearly shows that the burning-rate constant decreases with increasing dilution, as expected. It seems noteworthy that the extent of this increase is much greater at 1.00 bar (solid curves) than at 0.50 bar (dashed curves). At 0.50 bar the results for 35% and 30% oxygen are very close together, and even the single point available at this pressure for 25% oxygen is quite close to these. Although there would be greater confidence in the conclusion that the dilution effect is small at 0.50 bar if more data were available at that pressure, there seems to be sufficient data to motivate seeking possible theoretical reasons for the small effect. The results in Fig. 6 for air clearly show the increase in the burning-rate constant caused by the fiber support (tether). The two untethered droplets definitely exhibited lower burning-rate constants, and the FSDC tether appears to increase the burning rate more than the DCE tether, which was made of a different material, suggesting that the enhancement may be associated with heat conduction along the fiber from the flame. The burning-rate constants for air are substantially lower than those for helium-oxygen mixtures because of the high thermal conductivity of helium.

Conclusions

The tests performed during MSL-1 led to the first documented radiant extinction in n-heptane droplet combustion. Tests performed at 1.00 bar showed that diffusive extinction occurs for droplets smaller than 4.1 mm burning in a 35% oxygen environment with helium as the inert. Diffusive extinction also occurs for droplets under 3.2 mm in a 30% environment and 1.7 mm in

25% oxygen. The 20% oxygen environment was shown to be unable to support the combustion of droplets larger than 0.9 mm in initial diameter. At 1.00 bar radiant extinction was observed for droplets over 3.9 mm in the 30% environment and 2.8 mm in the 25% and 20% environment. No tests at 35% in 1.00 bar exhibited radiant extinction (the largest droplet was 4.1 mm). For the half-bar tests radiant extinction was observed during two tests: 3.1 mm initial droplet diameter in a 30% oxygen environment and 2.9 mm initial droplet diameter in the 25% oxygen environment. The quarter-bar tests showed radiant extinction at 35% oxygen with an initial droplet diameter of 2.6 mm and diffusive extinction at 50% oxygen with an initial droplet diameter of about 1.5 mm.   These results can be viewed graphically in Fig. 5 with an approximate radiant extinction limit drawn.

All of the droplets exhibited the classic linear decrease in time of the square of their diameter. This behavior occurred independent of the more complex flame behavior. Flames were generally found to grow and then shrink for tests that underwent diffusive extinction, and grow to a maximum diameter, occasionally shrinking slightly, in cases of radiant extinction. Some exceptions were found to this flame behavior, but all occurred during the 1.00 bar 20% oxygen tests, and they were assumed to result from combustion of the accumulated vapors only. In several environments the curves of the square of the droplet diameter as a function of time exhibited a curvature wherein the burning-rate constant decreased over time. The lower oxygen environments, as well as the lower pressures, did not exhibit this curvature.

Finite final flame diameters were measured in all tests that stayed within the view of the flame-imaging camera. The final flame diameters appear to be dependent on initial droplet diameter, especially in cases of radiative extinction. Additionally, several of these droplets in the richer oxygen environments have immeasurably small to zero final droplet diameters, while in other atmospheres the droplet still exists when the flame extinguishes.

Burning rates vary with initial droplet diameter, pressure and oxygen content. The burning-rate constant decreases with increasing initial droplet diameter. Additionally, the pressure and oxygen percentage have the predicted effect on burning-rate constants—decreasing the pressure or the oxygen mole fraction increases the burning rate. More study of the influences of the initial droplet diameter is desirable because the cause of the decrease is not well understood. Further quantitative study of radiant extinction also needs to be done, as does examination of final droplet and flame diameters with diffusive extinction.

Acknowledgment

References

1. Klimek, R.B., Wright, T.W., and Sielken, R.S., "Color Image Processing and Object Tracking System", NASA TM-107144, 1996.
2. Nayagam, V., Haggard, J.B., Jr., Colantonio, R.O., Marchese, A.J., Dryer, F.L., Zhang, B.L. and Williams, F.A., *AIAA Journal*, 36, 1369-1378 (1998).
3. Cleveland, W.S., *Journal of the American Statistical Association*, 74, 829-836 (1979).
4. Ackerman, M., et al, "A Treatment of Measurement of Helptane Droplet Combusiton Aboard MSL-1", NASA TP, in preparation, 2003.
5. Card, J.M., and Williams, F.A., *Combustion and Flame*, 93, 375-390 (1993).
6. Avedisian, C.T., "Soot Formation in Spherically Symmetric Droplet Combustion", Physical and Chemical Aspects of Combustion, Gordon and Breach, 1997, pp. 148-160.

Recent Advances in Science Support for Isolated Droplet Combustion Experiments

F. L. Dryer, A. Kazakov, B.D. Urban and K. Kroenlein
Mechanical and Aerospace Engineering, Princeton University, Princeton, NJ 08544-5263

INTRODUCTION

In a joint program involving Prof. F.A. Williams of the University of California, San Diego and Dr. V. Nayagam of the National Center for Microgravity Research, the combustion characteristics of isolated liquid fuel droplets of n-heptane, n-decane, methanol, methanol-water, ethanol and ethanol-water having initial diameters between about 1 mm and 6 mm continues to be investigated. The objectives of the work are to improve fundamental knowledge of droplet combustion dynamics for pure fuels and fuel-water mixtures through microgravity experiments and theoretical analyses. The Princeton contributions support the engineering design, data analysis, and data interpretation requirements for the study of initially single component, spherically symmetric, isolated droplet combustion studies through experiments and numerical modeling. UCSD contributions are described in a companion communication in this conference. The Princeton effort also addresses the analyses of Fiber Supported Droplet Combustion (FSDC) experiments conducted with the above fuels and collaborative work with others who are investigating droplet combustion in the presence of steady convection. A thorough interpretation of droplet burning behavior for n-heptane and n-decane over a relatively wide range of conditions also involves the influences of sooting on the combustion behavior, and this particular aspect on isolated burning of droplets is under consideration in a collaborative program underway with Drexel University (M.Y. Choi and collaborators). This collaboration is addressed in another communication at this conference.

The one-dimensional, time-dependent, numerical modeling approach that we have continued to evolve for analyzing isolated, quiescent droplet combustion data has been further applied to investigate several facets of isolated droplet burning of simple alcohols, n-heptane, and n-decane. Some of the new results are described below.

LIQUID DENSITY EFFECTS ON ETHANOL DROPLET COMBUSTION

In a recent paper, we quantitatively evaluated the effects of thermal expansion and solution density variations on liquid drop diameter over the burning history of ethanol and ethanol water droplets [1]. We treated the liquid mass and thermal transport via "effective" empirical transport corrections (as we previously have done), and additionally considered a radial convective liquid flow velocity component in the governing equations to assess the importance of variations in the local liquid-phase density.

We found that the effects of liquid phase density changes are primarily confined to the initial droplet heat-up period where an increase in droplet diameter due to thermal expansion results in large negative contributions to the observed rate of droplet diameter change. After the initial heat-up period is over, the contribution becomes much less important than that from the actual liquid gasification rate, becoming mildly competitive again near the condition of extinction. At extinction, the gasification rate ceases while an increase in liquid water content and subsequent cooling both result in droplet contraction. The observed difference in drop diameters between cases with and without consideration of liquid density changes is within about 6 %.

Since the effects associated with liquid density changes are confined to a very short initial period in the overall droplet gasification history, they can be essentially compensated for by shifting the gasification rate curve. In other words, when plotted against the "extent of burning" coordinate, $1-(d/d_0)^2$, the gasification rate curves match within about 2 % during most of the burning history. The integrated total water mass fraction histories in the liquid phase agree well within the uncertainty with which this parameter can be determined experimentally.

The analyses show that the liquid phase density terms in the governing equations do not affect significantly the model results for ethanol droplet combustion. By ignoring these terms, the numerical stiffness of the computations can be significantly reduced. Once robust droplet burning is established, there is very little "memory" of the initial transient heat-up period (as long as the applied ignition energy does not overdrive the process) in the subsequent computational predictions. All microgravity droplet combustion experiments involve some asymmetry initially, due to ignition. However, these results support the assumption that experimental burning histories can still be compared with uni-dimensional model results by matching the parts of the curves subsequent to the initial heat up period. Nearly all investigators that have performed microgravity experiments in droptowers and on space platforms have employed this assumption. It should be stressed that results may be different for pure droplet vaporization, but certainly the terms in question can be neglected in the analysis of microgravity experiments in which relative gas phase and droplet velocities are small and one is interested in burning rate, flame structure and extinction in the robust phases of burning.

TWO-STAGE IGNITION OF n-HEPTANE DROPLETS

Several microgravity studies on the thermal ignition behavior of n-heptane droplets have appeared, one of the more recent being that of Schnaubelt et al.[2]. Data typically have been generated by exposing a droplet that was initially at room temperature to a high ambient temperature within a surrounding "oven". Two-stage type ignition processes have been observed, with complex kinetics suggested as the principal source of the behavior. With the exception of the above work, numerical modeling of the experiments has not utilized reaction mechanisms that included low-temperature, intermediate-temperature, and high-temperature kinetics in significant detail. We used our numerical model with the kinetics of Peters et al. [3] to investigate the two-stage ignition character of an n-heptane droplet immersed in a hot oxidizing environment.

Figure 1 depicts the calculated thermal ignition and gasification rate as functions of time for a 0.7mm n-heptane droplet instantaneously immersed in air with different far-field gas temperatures from 600-950 K. At far-field temperatures higher than 950 K, a short period of droplet heating and gasification leads to flaming ignition and the establishment of a high temperature diffusion flame surrounding the droplet. The gasification rate of the droplet increases very rapidly due to heat conducted to the droplet surface. The vapor formed diffuses away from the surface into

Figure 1 Thermal ignition and combustion of a 0.7 mm diameter n-heptane droplet in atmospheric pressure air at different far field (ambient) temperatures.
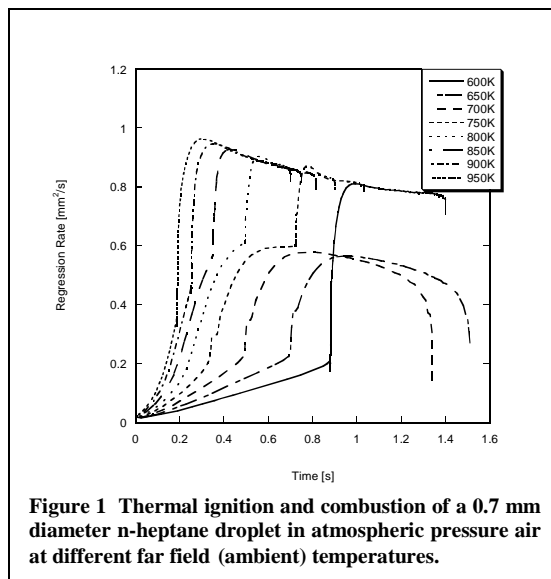
the surrounding hot gases and begins to react with oxygen, producing localized heating of the mixture. The localized chemical heat release leads to the occurrence of a flaming ignition. Little local heat release is needed to drive the local region into explosively fast, chain branched (high temperature) kinetic behavior within the fuel vapor surrounding the droplet (where oxygen is also present). The exact region where this occurs is a complex function of temperature, local equivalence ratio and time. The region of ignition leads to propagation of reaction through the remaining stratified pre-mixed layer of fuel species and oxidizer and a sharp increase in gasification rate due to the accompanying rapid heat release. This transitions into the typical diffusive flame structure observed to be surrounding a burning droplet. Subsequently, a burning rate above 0.8 mm^2/s is achieved. This burning rate is consistent with the combustion of the same size n-heptane droplet and far-field temperature, but established by the ignition processes used to emulate spark ignition (as in our previous calculations).

For lower far-field ambient temperatures in air, the period of gasification prior to establishing a high temperature diffusion flame structure becomes longer. The droplet is consumed initially with a slower increase in gasification rate with time. As chemical heat release builds in the gas phase from the vaporized n-heptane diffusing into the surrounding hot oxidizer, the regression rate increases due to increases in the local gas temperatures nears the drop surface. This characteristic persists at ambient temperatures between 950 K down to ones approaching 800 K. Note that the 800 K case shows an abrupt change in the gasification rate at about 0.35 seconds, a short time span over which the gasification rate increases very little with time, followed by a period in which the gasification rate again increases rapidly to that found for established diffusive burning. This behavior occurs because the portion of the fuel-vapor/air mixture with conditions that lie in the intermediate and high temperature kinetic regimes at higher ambient far field temperatures now partially lie within a temperature range characteristic of negative temperature coefficient (NTC) behavior and the chemical heat release rate available to modify the temperature profile is reduced. Sufficient heat release eventually exists to drive the region to temperatures characteristic of the high temperature regime (explosively fast chemistry), and the remaining system is driven to flaming ignition and a diffusion flame structure the same as that achieved for initially higher far field temperatures.

The same droplet in ambient air at temperatures from 800 K to approaching 600 K behave differently that those with either higher or lower far field temperature conditions. As the far field temperature drops, the characteristic period of the plateau region increases and the heat release that can occur is lessened to an extent that overall, none of the reacting environment can be driven into explosively fast chemical kinetic behavior before the droplet has been entirely consumed. As regions are driven to conditions within the parameter space characterized by NTC kinetic behavior, the destruction of n-heptane in those regions and heat release rate become very slow. Some the vaporized fuel in these regions is not consumed over the lifetime of the drop, even though it is mixed with oxidizer. Thus, although the droplet gasifies completely, a substantial fraction of the n-heptane vapor formed escapes to the ambient.

Interestingly, when the far-field temperature is reduced below 650K to 600 K, the slowing of the gasification rate disappears, and the system is driven to explosively fast kinetic behavior and the same diffusive flame structure found for the high temperature far field conditions again. In these cases, large regions of the reaction layer surrounding the droplet are at conditions characteristic of low temperature oxidation kinetics, and the accompanying heat release is so

rapid and large that conditions are driven through those characterizing NTC behavior and to explosively fast kinetic behavior.

A similar parametric study is shown in Fig. 2 for a larger 1.4 mm diameter n-heptane droplet over the same range of initial conditions. The size of the droplet affects the period of droplet heating, its gasification rate during the initial phases of gasification, the thickness of the layer of fuel-vapor/oxidizer/intermediate reaction species surrounding the drop, and its volume relative to the mass of liquid. In addition the time scale of relevance (gasification time of the drop) also changes. As a result the coupling with low, NTC, intermediate, and high temperature reaction kinetics lead to a different ignition and burning behavior. Now, no conditions are evidenced that eventually reach flaming combustion conditions. However, it is clear from

Figure 2 Thermal ignition and combustion of a 1.4 mm diameter n-heptane droplet in atmospheric pressure air at different far field (ambient) temperatures.

inspection of these curves that, between 700 and 800K, there remains a period over which some of the regions surrounding the droplet exhibit NTC kinetic behavior, slowing the rate of gasification by reducing the rate of gas phase chemical heat addition.

Further calculations are presently underway using a minimized mechanism [4] derived from the large detailed n-heptane oxidation mechanism published by Curran et al. [5].

REFERENCES

1. A. Kazakov, J.D. Conley and F.L. Dryer, "Detailed Modeling of an Isolated Ethanol Droplet Combustion under Microgravity Conditions", *Combust. Flame*, (2003). In Press

2. S. Schnaubelt, O. Mariui, T. Coordes, C. Eigenbrod, and H.J. Rath, *Proc. Comb. Ins.*, 28, 953 (2000).

3. N. Peters, G. Paczko, K. Seiser, and R. Seshadri, *Combust Flame*, 38, 159 (2002).

4. J. Conley, A. Kazakov, and F.L. Dryer, "Experimental and Numerical Observations on n-heptane oxidation: Mechanism Comparisons and Minimization", presented at the Joint Spring Sectional Meeting of the Combustion Institute, Chicago, IL, March 2003.

5. H. J. Curran, P. Gaffuri, W. J. Pitz, and C.K. Westbrook, *Combust. Flame*, 114, 149 (1998).

Experiments and Model Development for the Investigation of Sooting and Radiation Effects in Microgravity Droplet Combustion

Ahmet Yozgatligil and **Mun Young Choi**
Department of Mechanical Engineering and Mechanics
Drexel University, Philadelphia, PA 19104

Frederick L. Dryer and Andrei Kazakov
Mechanical and Aerospace Engineering
Princeton University, Princeton, NJ 08544

Ritsu Dobashi
Department of Chemical Systems Engineering
University of Tokyo
Tokyo, Japan

INTRODUCTION

The spherically-symmetric burning of an isolated droplet is a dynamic problem that involves the coupling of chemical reactions, multi-phase flow (liquid, gas, particulate) with phase change. To this end, microgravity droplet combustion serves as an ideal platform for advancing the understanding the diffusion flame physics of liquid hydrocarbon fuels and additives that are typically used in internal combustion engines and gas turbines. Due to the complex and incomplete understanding of soot processes in the combustion of large molecular weight hydrocarbon droplets, theoretical/computational formulations have historically neglected sooting behavior. Testbed experiments in microgravity using droplet flames, used a mildly sooting fuel, n-heptane, and employed parameter adjustment techniques to minimize sooting for comparisons with and validations of numerical models. None of the experimental techniques, however, were entirely successful and sooting remains a critical component in the analysis of droplet combustion, commensurate with its importance in the burning of conventional fuels. *A thorough interpretation of droplet burning behavior cannot be accomplished without examining and incorporating the influences of sooting and radiation.* Concurrently, isolated droplet combustion studies offer an opportunity to investigate sooting phenomena on the dynamics of diffusion flames, and over parameter ranges not available in quasi-steady experiments such as annular jet diffusion flames. The current state of numerical modeling approaches for droplet combustion and diagnostics permits consideration of the transient nature of the sooting and radiation at a level of detail that is computationally prohibitive and experimental intractable for multi-dimensional configurations. Experimental measurements and numerical model development can provide a comprehensive test of their influence on the burning rate, flame structure, flame extinction, and soot aerosol properties. Thus, this problem is a logical extension of non-sooting droplet combustion experiments and numerical modeling efforts that have been previously conducted.

This study involves flight experiments (for droplets between 1.5 to 5 mm) and supportive ground-based experiments, with concurrent numerical model development and validation. The experiments involve two fuels: n-heptane, and ethanol. The diagnostic measurements include

light extinction for soot volume fraction, two-wavelength pyrometry and thin-filament pyrometry for temperature, spectral detection for OH chemiluminescence, broadband radiometry for flame emission, and thermophoretic sampling with subsequent transmission electron microscopy for soot aerosol property calculations.

ETHANOL EXPERIMENTS

Ethanol droplet combustion has been extensively studied by researchers using reduced-buoyancy techniques. In a classical investigation, Godsave [1953] analyzed the burning behavior of suspended ethanol droplet combustion. Kumagai and coworkers [Okajima and Kumagai, 1975; Hara and Kumagai, 1991] studied ethanol combustion using droptower facilities to measure burning rates and flame diameters of ethanol for various initial droplet diameters and investigate the importance of relative velocity of moving droplets. Lee and Law [1992] studied combustion of small, freely-falling methanol and ethanol droplets in which they reported droplet burning histories and time resolved bulk liquid-phase water mass fractions. Ethanol was also one of the primary fuels studied aboard the STS-94/MSL-1 Shuttle mission in the Fiber-Supported Droplet Combustion-2 (FSDC-2) program [Colantonio et al., 1998]. In those studies, the burning rate, flame diameter measurements, and extinction behavior for droplets ranging from 2.5 to 6 mm were measured and analyzed. In all of the studies mentioned above, experiments were performed for ethanol droplets burning in atmospheric pressure. Consequently, there were no observations of sooting in those experiments.

Soot formation in ethanol droplet combustion was first observed by Yap [1984] in his experiments using freely-falling droplets in a high-pressure drop-tube. In 2001, Urban et al. [2001] observed the formation of a sootshell for ethanol droplets burning in pressures of 2 atm in the NASA 2.2 sec. droptower. However, soot concentrations were not measured in these experiments due to a lack of appropriate diagnostic equipment.

In this work, we describe new experiments on the burning characteristics of isolated ethanol droplets and the environmental conditions leading to soot formation and luminous radiation. Experiments were performed by varying the pressure from 1 to 2.2 atm, the oxygen concentrations from 21% to 50%, and the initial diameters from 1mm to 2.5 mm. Experiments were performed at both the NASA Glenn 2.2 sec. drop tower and the JAMIC 10 sec. dropshaft.

Figure 1 displays the backlit images of ethanol droplets of 1.7 mm diameter burning in air at pressures ranging from 1.0 to 2.2 atm. The lack of the presence of a sootshell is clearly observed in the 1.0 and 1.5 atm experiments with slight attenuation caused by small concentrations of soot in the 2.2 atm experiment. In an effort to increase the likelihood of forming soot in ethanol experiments, ambient pressure and the oxygen concentration were varied in conjunction. Figure 2 displays the laser-backlit images of ethanol droplets burning in various oxygen concentrations in nitrogen at 2.2 atm. At 21% and 25% O_2 in N_2, there is no luminosity exhibited in the flame view and the attenuation of the laser beam in the backlit view was lacking. As the oxygen concentration is increased to 30% O_2 in N_2, the formation of a distinct sootshell and a luminous flame are observed. Another interesting behavior was noted in which the sooting propensity appears to decrease at 40 % O_2 in N_2 case compared to the 30% O_2 in N_2 case. Additional experiments and analysis are required to investigate this interesting behavior. From the experiments shown in figure 2, the maximum soot volume fraction, $f_{v,max}$, was measured the using tomographic inversion technique. These measurements clearly bear out the interpretation

from the visual observation – at 21% O_2 in N_2, there is no measurable soot concentration, while at 30% O_2 in N_2, the maximum soot volume fraction is approximately 13 ppm. These experiments clearly demonstrate the strong dependence of sooting behavior of ethanol droplets on ambient pressure and oxygen concentration.

DROPLET COMBUSTION COMPUTATIONAL MODEL DEVELOPMENT

In this project, the numerical computation of droplet combustion is performed using a moving finite-element chemically reacting flow model. The model simulates the transient, spherically symmetric combustion of a liquid droplet in an infinite oxidizing medium by solving the conservation equations of mass, species, and energy in both liquid and gas phases. The model includes detailed description of gas-phase chemical kinetics and transport. Radiative heat transfer is described using a Planck-mean absorption formulation for both the gas phase (non-luminous) and soot.

Recently, many improvements to the model have been made that include:

a. The code structure was entirely rewritten to improve speed, stability, expandability, and to simplify its future maintenance.
b. Numerical improvements include the use of hardware-optimized linear algebra subroutines, modern iterative solvers (GMRES-based), dynamic memory management.
c. Liquid phase thermal contraction/expansion is implemented (via supplied liquid-phase equation of state).
d. The transport sub-models were custom-coded for efficiency; calculation of transport coefficients is now (optionally) based on multicomponent formulation (as opposed to prior mixture-averaged formulae) with inclusion of thermal diffusion terms for light species (previously not available). The latter was shown to have a significant effect on soot predictions in counterflow diffusion flames.
e. Chemical reaction terms are computed with the fast custom package that can be produced from any CHEMKIN-formatted reaction mechanism; this approach offers drastic speed improvements over the use of standard CHEMKIN libraries.
f. The basic framework for *generic* soot model was implemented and coupled with the main components (the source terms for nucleation, coagulation, and surface growth/oxidation, and the transport terms for molecular and thermal diffusion) via third-order method of moments.

REFERENCES

1. Colantonio, R.O., Dietrich, D.L., Haggard, J.B., Jr., Nayagam, V., Dryer, F.L., Shaw, B.D., and Williams, F.A. NASA L+1 Conference Proceedings, Marshall Space Flight Center,Huntsville, AL. (1998).
2. Godsave, G.A.E. *Proc. Combust. Inst.* 4:818 (1953).
3. Hara, H. and Kumagai, S. *Proc. Combust. Inst.* 23:1605 (1991).
4. Lee, A., and Law, C. K.*, Combust. Sci. Technol.* 86: 253 (1992).
5. Okajima, S. and Kumagai, S. *Proc. Combust. Inst.* 15:401 (1975).
6. Urban, B.D., Ernst, L.F., Kroenlein, K., Kazakov, A., Dryer, F.L., Yozgatligil, A., Shor, L., Choi, M.Y., Manzello, S.M., Lee, K.O., and Dobashi, R., "Initial Observations of Soot

Formation During Ethanol Droplet Combustion at Elevated Pressures", Microgravity Sci. Technol., submitted (2003).

7. Yap, L.T. Ph.D. Dissertation, Princeton University, Mechanical & Aerospace Engineering (1984).

ACKNOWLEDGMENTS

FIGURES
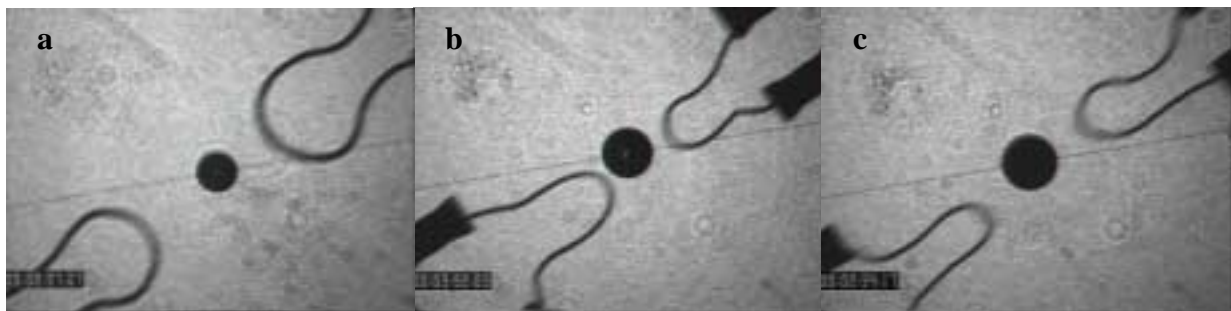
Fig. 1 Ethanol droplets burning at 21 % oxygen in nitrogen and elevated pressure a) 1 atm; b) 1.5 atm; c) 2.2 atm
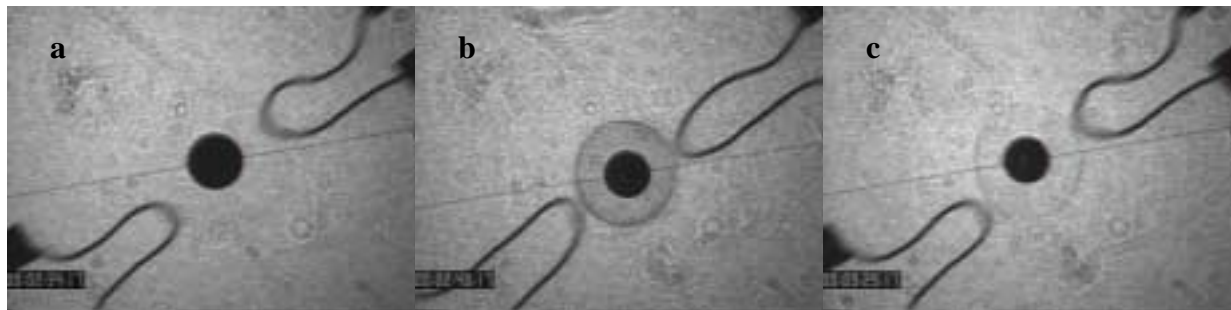
Fig 2 Ethanol droplets burning at elevated pressure and enhanced oxygen concentration a) 2.2 atm 21% O_2; b) 2.2 atm 30% O_2; c) 2.2 atm 40% O_2

DROPLET COMBUSTION IN A SLOW CONVECTIVE FLOW

V. Nayagam[1], M.C.Hicks[2], M.Ackerman[3], J.B. Haggard, Jr.[2], F.A. Williams[3]
[1]National Center for Microgravity Research, [2]NASA Glenn research Center
21000 Brookpark Rd., Cleveland OH, 44135
[3]Center for Energy Research, University of California at San Diego, La Jolla, CA 92093

INTRODUCTION

The influences of slow convective flow on droplet combustion, particularly in the low Reynolds number regime, have received very little attention in the past. Most studies in the literature are semi-empirical in nature and they were motivated by spray combustion applications in the moderate to high Reynolds number regime. None of the limited number of fundamental theoretical studies applicable to low Reynolds numbers have been verified by rigorous experimental data. Moreover, many unsteady phenomena associated with fluid-dynamic unsteadiness, such as impulsive starting or stopping of a burning droplet, or flow acceleration/deceleration effects, have not been investigated despite their importance in practical applications. In this study we investigate the effects of slow convection on droplet burning dynamics both experimentally and theoretically. The experimental portion of the study involves both ground-based experiments in the drop towers and future flight experiments on board the International Space Station. Heptane and methanol are used as test fuels, and this choice complements the quiescent-environment studies of the Droplet Combustion Experiment (DCE). An analytical model that employs the method of matched asymptotic expansions and uses the ratio of the convective velocity far from the droplet to the Stefan velocity at its surface as the small parameter for expansion ε has also been developed as a part of this investigation. Results from the ground-based experiments and comparison with the analytical model are presented in this report.

EXPERIMENTS

Three separate experimental configurations were examined to generate slow convective flows past a burning droplet in microgravity in preparation for the flight experiment. The first configuration, used in the 2.2 Second Drop-Tower Facility employed a "flow tunnel" powered by a pressurized gas bottle to establish a uniform flow field around a droplet suspended at the end of a fiber. Initial droplet diameters for these tests were approximately 1.0 mm to 1.5 mm. The second test configuration, designed for use in the Zero-Gravity Facility (ZGF, the larger drop tower providing up to 5 seconds of microgravity), utilized a translating mechanism to move the droplet at very precise velocities through a quiescent medium to generate a uniform flow field. The velocities for this system ranged from 0 cm/s to 3 cm/s and initial droplet diameters were nominally 2.3 mm. The third test configuration was designed to fly on the KC-135 aircraft, which provides around 20 seconds of microgravity, and it employed a flow-tunnel concept similar to the 2.2 second tower. However, rather than using pressurized bottles of gas with a sonic orifice, a fan was used to generate the required flows. In this test configuration only two flow velocities were used (i.e., 5 cm/s and 10 cm/s) and the initial droplet diameters were considerably larger at approximately 3 mm.

Tests were run for both n-heptane and methanol in the first two test configurations and for only n-heptane in the KC-135 experiments. Two wide-band radiometers (i.e., 0.6 μm to 40 μm) were used in each experimental configuration in the drop towers to obtain measurements of the gas phase radiative losses. A single wide-band radiometer was used in the KC-135 experimental rig. All radiometers were calibrated against a blackbody source at distances equal to the distance from the droplet support fiber employed in the experimental rigs. The backlit images of the droplet as well as the color images of the flames were obtained during these experiments. Further details of the experiments can be found in [1].

ANALYSIS

An idealized model for droplet vaporization or combustion in the Burke-Schumann reaction-sheet approximation is analyzed in terms of a Peclet number based on the Stefan velocity, taken to be of order unity, for Lewis numbers of unity and for small values of a parameter ε, defined as the ratio of the convective velocity far from the droplet to the Stefan velocity at its surface. Asymptotic solutions for the velocity, pressure and mixture-fraction fields are obtained through second order in ε. All earlier studies (see, e.g., [2-4]) treated the Reynolds number of convection as the small parameter. The present analysis is different in principle because a different small parameter is selected, namely the ratio, ε, of the convection velocity of the gas at infinity to the velocity of the gas at the droplet surface without nonspherical convection. The mathematical development therefore is different and precludes addressing the limit of a nonvaporizing droplet. This selection was made with a view towards the problem intended to be studied. Despite this difference, the resulting expansions contain all the elements in most of the earlier analyses, some of which explicitly refer to a "large radial velocity" and become equivalent mathematically to the present development with appropriate restrictions. The present expansions thus retain essentially the same range of applicability as earlier analyses, and the resulting alternative development given here can help to clarify possible differences associated with different expansion procedures. The results of this analysis are employed to calculate the effects of convection on the burning rate and on the flame shape. Qualitative comparisons with experiment help to identify the strengths and limitations of this model. The reader is referred to an earlier paper [5] for a more detailed discussion of the formulation used in this analysis.

RESULTS AND DISCUSSION

The burning-rate constant, K, the slope of the graph of the square of the droplet diameter as a function of time, was determined for each test run for which ε is smaller than one. Figure 1 shows the comparison between the experimental measurements and the predictions of the current asymptotic analysis, where $(K/K_0 - 1)$ is plotted against the square root of Reynolds number based on droplet radius ($Re = U_\infty R / \nu_\infty$). Here U_∞ is the imposed flow velocity, R is the droplet radius, ν_∞ is the kinematic viscosity, and K_o is the burning rate constant when there is no flow. A K_0 value of 0.75 mm^2/s was employed in Fig. 1, although a somewhat higher value (probably 0.8 mm^2/s, within experimental accuracy) would be more appropriate, as suggested theoretically and by the data point at Re=0 in the figure. Also, in calculating the Reynolds number the kinematic viscosity was taken to be that of air at a mean temperature of 850K, although a somewhat higher mean temperature (perhaps as high as 1200K) may be more appropriate, which would move the data points in the figure to smaller values of Re. Since the present theory does not account for

variable properties, it is essential in comparisons to make an adjustment of this type; if the theoretical formula is used with ν_∞ evaluated at the ambient temperature of about 300K, then the slope of the theoretical line is much too steep. In view of the uncertainties in K_0 and in the manner of evaluating mean properties, it is best to anticipate differences between theory and experiment on the order of a factor of two and to consider the agreement that is seen here as being only qualitative.

The flame shape predictions from the analytical results show good agreement with experiment. Experimental flame measurements appear to be somewhat narrower and longer than predicted, as illustrated in Figure 2 for a particular test. This general trend, observed for most of the comparisons with experiment, may be due to the increase in flame length through finite-rate chemistry downstream as well as variable properties, which are not addressed in the simplified analytical model. The comparisons clearly indicate that, even after optimizing the selection of the value of the diffusion coefficient, flame-shape differences between theory and experiment of at least 20% should be anticipated.

Figure 3 shows the instantaneous radiative heat loss, Q_{rad}, plotted against the instantaneous droplet diameter for n-heptane droplets burning in air with ambient flow velocities ranging from 0 cm/s to 10 cm/s. Average initial droplet diameters were 1.25 mm for the 2 second tower, 2.31 mm for the ZGF, and 3.3 mm for the KC-135. The aggregate plot, showing all results on the same droplet scale, indicate that once the flame transient passes there is an expected convergence in radiative heat loss. It is apparent that tests performed in the ZGF never extended beyond the flame transient where flame expansion relative to the droplet diameter reached a maximum. This is due to the relatively large initial droplet diameters used in these tests and the commensurately short burn time allowed in this facility (i.e., data begins approximately 3 seconds after 0-g ignition and steady velocity was reached). The considerably smaller droplets used in the 2 second tower, coupled with the fact that the drop occurred after ignition, allowed these tests to proceed beyond the flame-expansion period. When results from these tests are plotted separately on a larger scale an interesting observation can be made concerning the relationship between radiative heat losses and flow velocity. Preliminary results indicate that radiative losses tend to decrease as the flow velocity is increased. One possible explanation is that the flame shape becomes increasingly distorted into an ellipsoidal shape with increased flow. The distorted flame shape results in a smaller radiating volume and this, coupled with an increase in convective losses as hot gases are swept downstream, causes a decrease in radiative output from the gas phase. Additionally, decreases in soot radiation resulting from shorter soot residence times due to increased convective effects, also contribute to the observed decrease in radiative output. Recently, we have carried out several experiments with accelerating and decelerating droplets and the results will be presented elsewhere. Some preliminary results can be found in [1].

CONCLUDING REMARKS

Predicted qualitative trends from the asymptotic analysis are supported by experiment. The prediction that the burning rate increases linearly with Reynolds number for small Reynolds numbers is consistent with experiment. The predicted general elongation of the flame in the flow direction and its narrowing transversely are consistent with experiment, but these variations appear to be somewhat more pronounced experimentally, likely because of effects of variable properties and finite-rate chemistry, especially of soot. It may thus be concluded that qualitative

trends may be obtained from the theory, but refinements (introducing greater complexity) are needed for improved quantitative predictions. Experimental results from each of the test configurations show that radiative heat losses from the gas phase contribute to a substantial portion of the overall heat loss mechanism. Additional tests are currently underway to investigate the unsteady effects during convective droplet burning.

REFERENCES

1. Hicks, M.C., Kaib, N., Easton, J., Nayagam, V., *Third Joint Meeting of the U.S. Sections of the Combustion Institute,* The Combustion Institute, Pittsburgh, PA, 2003.

2. Wichman, I. S., Baum, H. R. in: C.T. Avedisian, V.A. Arpaci (eds), <u>Heat Transfer in Microgravity</u>, HTD series 269, ASME, New York, 1993, p 111.

3. Fendell, F. E., Sprankle, M. L., Dodson, D. S., *J. Fluid Mechanics* 26 (1966) 267-280.

4. Gogos, G.., Ayyaswamy, P. S., *Combustion and Flame*, 74 (2) (1988) 111-129.

5. Ackerman, M., Nayagam, V., Williams, F.A., *Third Joint Meeting of the U.S. Sections of the Combustion Institute,* The Combustion Institute, Pittsburgh, PA, 2003.
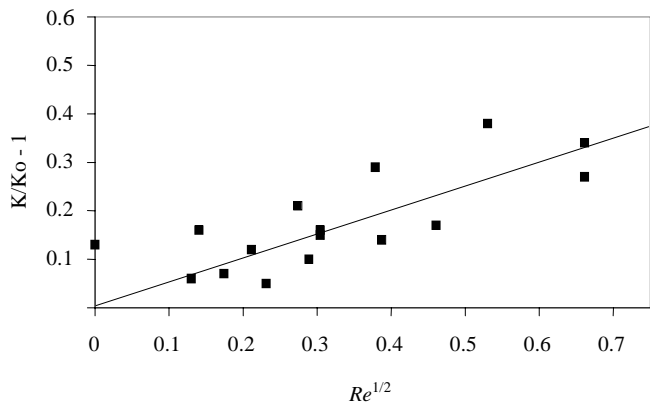
Figure 1. Burning-rate constant vs $Re^{1/2}$ number according to the present theory (line) compared with experimental data (points).
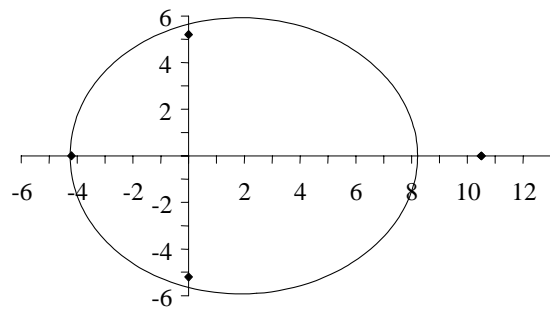
Figure 2. Flame shape for an initial droplet diameter of 1.5 mm, an imposed flow speed of 4 cm/s. The solid line is calculated using the theory while the points represent experimental values.
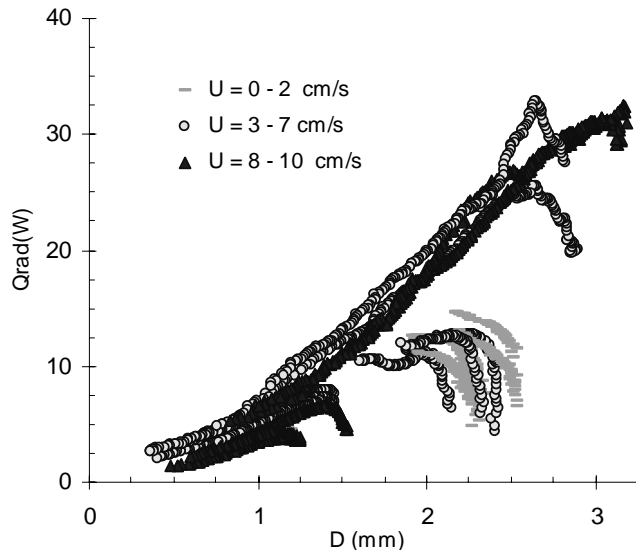
Figure 3. Total radiative flame emission as a function of droplet diameter for various flow velocities during n-heptane burning in air at atmospheric pressure.

Combustion of Moving Droplets and of Droplets Suspended within a Convective Environment: Transient Numerical Results

George Gogos and Daniel N. Pope
Department of Mechanical Engineering
University of Nebraska-Lincoln
Lincoln, NE 68588-0656

Numerical Model

The problem considered is that of a single-component liquid fuel (n-heptane) droplet undergoing evaporation and combustion in a hot, convective, low pressure, zero-gravity environment of infinite expanse. For a moving droplet, the relative velocity (U_∞) between the droplet and freestream is subject to change due to the influence of the drag force on the droplet. For a suspended droplet, the relative velocity is kept constant.

The governing equations for the gas-phase and the liquid-phase consist of the unsteady, axisymmetric equations of mass, momentum, species (gas-phase only) and energy conservation. Interfacial conservation equations are employed to couple the two phases. Variable properties are used in the gas- and liquid-phase. Multicomponent diffusion in the gas-phase is accounted for by solving the Stefan-Maxwell equations for the species diffusion velocities. A one-step overall reaction is used to model the combustion [1].

The governing equations are discretized using the finite volume and SIMPLEC methods. A colocated grid is adopted. Hyperbolic tangent stretching functions are used to concentrate grid points near the fore and aft lines of symmetry and at the droplet surface in both the gas- and liquid-phase. The discretization equations are solved using the ADI method with the TDMA used on each line of the two alternating directions. Iterations are performed within each time-step until convergence is achieved. The grid spacing, size of the computational domain and time-step were tested to ensure that all solutions are independent of these parameters. A detailed discussion of the numerical model is given in [2,3].

Results and Discussion

The numerical model was used to investigate the combustion of a n-heptane droplet with an initial diameter (d_0) of 500 μm. Two cases were studied: a) a moving droplet, and b) a suspended droplet within a convective environment. The results presented here are for an ambient temperature (T_∞) of 1000 K, an ambient pressure (P_∞) of 1 atm, an initial droplet temperature (T_0) of 297 K and initial Reynolds numbers (Re_0) of 8, 10 and 50.

Table 1 compares the lifetimes of both moving and suspended n-heptane droplets for the Reynolds numbers considered. The table contains interesting results that need to be explained. For example, the lifetime of a moving droplet with $Re_0 = 50$ is longer than the lifetimes of moving droplets with initial Reynolds numbers of 8 and 10. Furthermore, for the same initial Reynolds number, the suspended droplet burns out faster than its moving droplet counterpart in two cases ($Re_0 = 8, 50$), while for $Re_0 = 10$, the result is opposite. In the remainder of this section, the results presented in Table 1 will be discussed in more detail.

Figure 1 shows the time history of the dimensionless droplet diameter squared ($d/d_0)^2$, Reynolds number, Damköhler number and evaporation constant (K) for a suspended and a moving droplet with $Re_0 = 8$. The suspended and moving droplet developed envelope flames at approximately the same time ($t = 30$ ms). Considering the droplet lifetimes (231 and 240 ms),

this happened at a very early stage. Once the envelope flame formed, it remained for both droplets until the end of their lifetimes. Thus during most of the droplet lifetime, both the suspended and the moving droplet experience the same flame configuration. This implies that the two droplets will exhibit similar burning behavior and thus similar lifetimes. Figure 1(a) shows that to be true. The droplets in both cases have very similar diameter squared time histories.

	$Re_0 = 8$	Suspended	$t_d = 231\ ms$
$P_\infty = 1\ atm$		Moving	$t_d = 240\ ms$
$T_\infty = 1000\ K$	$Re_0 = 10$	Suspended	$t_d = 335\ ms$
$T_0 = 297\ K$		Moving	$t_d = 243\ ms$
$d_0 = 0.5\ mm$	$Re_0 = 50$	Suspended	$t_d = 250\ ms$
		Moving	$t_d = 316\ ms$

Table 1: n-heptane droplet lifetimes for suspended and moving droplets.

Figure 1(b) shows the time history of the instantaneous Reynolds number (*Re*) for both cases. Both Reynolds numbers decrease monotonically with time however, they decrease at different rates. The Reynolds number is defined as $Re = d(t)U_\infty(t)/v_\infty$, where $d(t)$ and $U_\infty(t)$ are the instantaneous droplet diameter and freestream velocity. The freestream velocity remains constant for the suspended droplet. As a result, the Reynolds number changes only with the droplet diameter. However, for the moving droplet, the droplet diameter decreases, and the droplet velocity decreases due to drag. Thus the Reynolds number for the moving droplet decreases faster than that for the suspended droplet.

The higher Reynolds number associated with the suspended droplet implies a stronger convection. This results in a higher evaporation constant for the suspended droplet than for the moving droplet as shown in Figure 1(d). At the beginning of the droplet lifetime, the evaporation constants for the two cases are very close and both increase rapidly due to the high temperature environment. A difference between the evaporation constants appears at about one tenth of the lifetime due to the difference in the convective strength for the two cases. At the relatively low initial Reynolds number of 8, the difference in the evaporation constants between the suspended droplet and the moving droplet remains small during the entire droplet lifetime. As a result, the droplet lifetimes for the two cases are very close.

Figure 1(c) compares the instantaneous Damköhler numbers for the two cases. Here, Damköhler number is defined as:

$$Da = \frac{R(t)}{U_\infty(t)} A\rho_\infty^{a+b-1} W_f^{1-a} \left(\frac{1}{W_o}\right)^b \exp\left(-\frac{E_a}{R_u T_\infty}\right)$$

where W_o and W_f are molecular weights for the fuel and oxygen, and a, b, A, and E_a are constants. The Damköhler number is proportional to the ratio of droplet diameter to instantaneous freestream velocity. This ratio is the characteristic convective time-scale. Thus, *Da* is proportional to $d(t)/U_\infty(t) = t_{conv}$. Figure 1(c) shows that the Damköhler number for the suspended droplet decreases with time, while for the moving droplet case it increases slowly with time. The former result is expected since for the suspended case, U_∞ is constant while the droplet diameter decreases. This results in a monotonic decrease in *Da*. For the moving droplet case, both $d(t)$ and $U_\infty(t)$ decrease. The resulting trend in Damköhler number is not obvious. For $Re_0 = 8$, it seems that the droplet velocity decreases slightly faster than the droplet diameter.

For $Re_0 = 50$, both droplets ignite in the wake areas far downstream. After ignition, for the

moving droplet case, the flame moves toward the droplet slowly, and finally forms an envelope flame (at approximately $t = 270$ ms) near the end of its lifetime. For the suspended droplet, no envelope flame is developed throughout its lifetime, and the wake flame remains at approximately the same location for most of the droplet's lifetime. At $t = 237$ ms the wake flame trailing the suspended droplet extinguishes. Thus, a pure evaporation process dominates in both cases. In the absence of envelope flames, the difference in Reynolds number histories between the two cases (Re is smaller for the moving droplet due to its deceleration) is the only cause for their different lifetimes shown in Table 1.

The combustion behavior for the two cases at $Re_0 = 10$ is quite different from the cases discussed above. Although the Reynolds number for the suspended droplet is again higher than that for the moving droplet throughout the droplet lifetime, the lifetime of the suspended droplet is approximately 40% longer than that of the moving droplet. The big difference in droplet lifetimes, is caused by the difference in flame configurations. The moving droplet develops an envelope flame at an early stage ($t = 40$ ms) of its lifetime. In contrast, the suspended droplet exhibits a transition flame (the flame partially surrounds the droplet) during most of the droplet lifetime. As a result, the front of the droplet is exposed to the ambient temperature, leading to a longer lifetime for the suspended droplet.

The results presented above for the three different Reynolds numbers seem to suggest that a moving droplet tends to develop an envelope flame at some stage during its lifetime, whereas a suspended droplet develops an envelope flame only at low initial Reynolds numbers. The flame configurations present in a burning droplet are a function not only of the Reynolds number, but of the Damköhler number as well.

For all three initial Reynolds numbers, the Damköhler number for suspended droplets always decreases with time, while Da for moving droplets always increases with time. The Reynolds number decreases with time for both moving and suspended droplets. Figure 2 shows the quasi-steady solutions for flame configurations as a function of Da and Re for a n-heptane droplet with a diameter of 500 μm. The quasi-steady solutions were obtained using a previously developed code [3] that was modified to include the current multicomponent diffusion formulation and kinetics parameters. The x's correspond to the quasi-steady solutions and the dash-dot lines on the figure indicate the predicted boundaries between the different flame configurations. Note that these flame configuration boundaries are for a fixed diameter as compared to the decreasing diameter present in the unsteady problem. Since both Da and Re scale with diameter, we would expect the flame configuration boundaries to move down and to the left on the figure for decreasing diameter.

Figure 2 also shows the actual paths of the moving (indicated with 'M') and suspended (indicated with 'S') droplets in the $Da - Re$ plane. When $Re_0 = 8$, an envelope flame forms for both the moving and suspended droplet very early in the droplet lifetime. For $Re_0 = 10$, both droplets ignite to form a transition flame near the start of the droplet lifetime. The decrease in the droplet diameter coincides with the aforementioned shift (to the left and down) in the configuration boundary between an envelope and a transition flame. The increasing Damköhler number present for the moving droplet case causes a rapid change from a transition to an envelope flame while the decreasing Damköhler number for the suspended droplet results in a transition flame configuration throughout the droplet lifetime. One can also see from the figure that in the $Re_0 = 50$ the moving droplet may eventually form an envelope flame whereas the suspended droplet may not form an envelope flame.
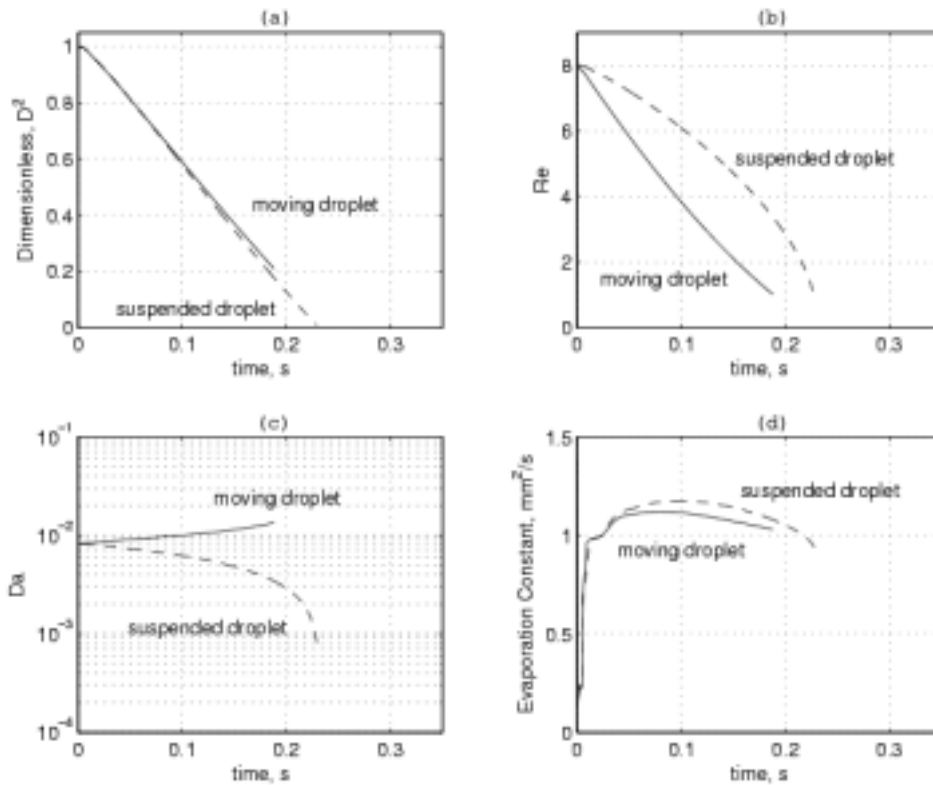
Figure 1: Comparison between moving droplet and suspended droplet combustion for Re_0 = 8 ($d_0 = 500\ \mu m$ and $T_\infty = 1000\ K$).
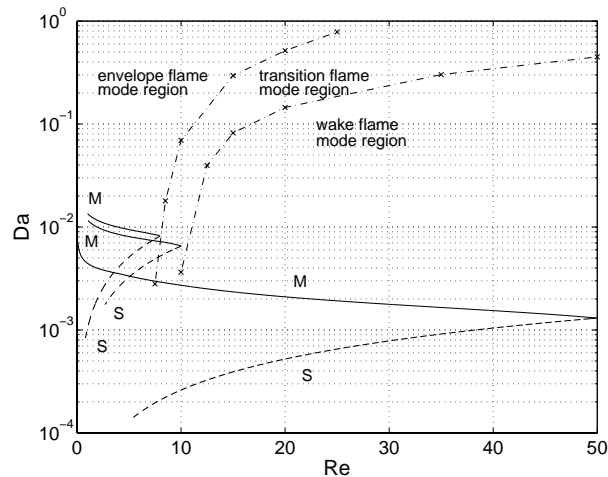
Figure 2: Flame configurations in the Damköhler vs. Reynolds number plane: $d = 500\ \mu m$.

Acknowledgements

References

1. Westbrook, C. K. and Dryer, F. L., *Comb. Sci. and Tech.*, 27:31 (1981).
2. Lu, K., *M.S. thesis*, Mechanical Engineering, University of Nebraska-Lincoln, 2002.
3. Pope, D. N., *Ph.D. thesis*, Mechanical Engineering, University of Nebraska-Lincoln, 2001.

BI-COMPONENT DROPLET COMBUSTION IN REDUCED GRAVITY

B. D. Shaw
MAE Department, University of California, Davis, CA 95616

INTRODUCTION

This research deals with reduced-gravity combustion of bi-component droplets initially in the mm size range or larger. The primary objectives of the research are to study the effects of droplet internal flows, thermal and solutal Marangoni stresses, and species volatility differences on liquid species transport and overall combustion phenomena (e.g., gas-phase unsteadiness, burning rates, sooting, radiation, and extinction). The research program utilizes a reduced-gravity environment so that buoyancy effects are rendered negligible. Use of large droplets also facilitates visualization of droplet internal flows, which is important for this research.

In the experiments, droplets composed of low- and high-volatility species are burned. The low-volatility components are initially present in small amounts. As combustion of a droplet proceeds, the liquid surface mass fraction of the low-volatility component will increase with time, resulting in a sudden and temporary decrease in droplet burning rates as the droplet rapidly heats to temperatures close to the boiling point of the low-volatility component. This decrease in burning rates causes a sudden and temporary contraction of the flame. The decrease in burning rates and the flame contraction can be observed experimentally. Measurements of burning rates as well as the onset time for flame contraction allow effective liquid-phase species diffusivities to be calculated, e.g., using asymptotic theory [1]. It is planned that droplet internal flows will be visualized in flight and ground-based experiments. In this way, effective liquid species diffusivities can be related to droplet internal flow characteristics.

This program is a continuation of extensive ground based experimental and theoretical research on bi-component droplet combustion that has been ongoing for several years. The focal point of this program is a flight experiment (Bi-Component Droplet Combustion Experiment, BCDCE). This flight experiment is under development. However, supporting ground-based studies have been performed. This ground-based research is summarized below.

REDUCED GRAVITY EXPERIMENTS

Data have been obtained on droplet combustion behaviors in environments with various diluents. The diluents were selected to have significant variations in molecular weight, allowing investigation of variations in properties such as binary species diffusion coefficients on combustion behaviors such as transient flame diameters. The droplets were composed of either decane or decane-hexadecane mixtures. Experiments were performed at 0.1 MPa with ambient oxygen mole fractions, X_{O_2}, of 0.21 and 0.5.

Data for normalized droplet diameters and flame standoff ratios are shown in Fig. 1 for $X_{O_2} = 0.21$. Here, Y is the initial hexadecane mass fraction, d_0 is the initial droplet diameter, d is the instantaneous droplet diameter, d_f is the instantaneous flame diameter, and K_{ave} is an average burning rate constant (i.e., the negative of the slope on a plot of d^2/d_0^2 vs. t/d_0^2). Figure 1(a) shows that changing the inert species in the environment has a significant effect on K_{ave}. Helium produces the largest burning rate while burning rates for Xe and N_2 are about the same.

Flame unsteadiness is also influenced by the inert species. From Fig. 1(b), it is evident that using Xe as an inert species promotes quasisteady flame standoff ratios, while N_2 and He promote flame unsteadiness with He producing the least steady flames. To interpret this behavior, we will consider an effective O_2 diffusivity, D_{O_2}, between the environment and the

flame zone. Since droplets exist for only a finite time, quasisteady flame behaviors will be promoted when D_{O_2} values are increased. If it is assumed that $D_{O_2} = D_{IO_2}$, where D_{IO_2} is the binary species diffusion coefficient for the inert species and O_2, it is found that D_{O_2} increases as the inert molecular weight decreases, which should promote stronger flame unsteadiness for Xe relative to He (and N_2). However, this trend does not agree with the experimental results and it is likely that other phenomena influence flame unsteadiness

Other factors that can influence flame unsteadiness are Soret transport and differences between binary species diffusion coefficients [2,3]. Aharon and Shaw [2] provided theory to estimate these effects on transport of O_2 to droplet flames. When this theory is applied to environments containing O_2 with He, N_2 or Xe, it is found that D_{O_2} values are largest for Xe and smallest for He, with Soret effects being as important as differences in binary diffusion coefficients. Thus, stronger flame unsteadiness is predicted for He, with Xe predicted to exhibit the most quasisteady flames (N_2 is in between). These predictions agree with the present experimental results, suggesting that Soret transport and differences between binary species diffusion coefficients were important in the present experiments.

NUMERICAL MODELING OF PROPANOL-GLYCEROL DROPLET COMBUSTION

A one-dimensional computational model was developed to simulate reduced-gravity combustion of propanol-glycerol droplets. This model provides an intermediate step between asymptotic models and a 3-d code that is being developed as part of this research. The new code employs an implicit finite difference formulation with variable gridding. It allows for variable liquid properties, nonideal liquid effects, absorption of water, liquid radial velocity fields (from liquid density changes) and droplet swelling. The code has been used to model previous experimental results on combustion of propanol-glycerol droplets [4].

The code solves the liquid-phase conservation equations for temperature and mass fraction profiles within a droplet. The continuity equation is integrated to determine liquid radial velocities. Properties vary spatially and temporally and boundary conditions are evaluated using second order difference equations. Liquid properties and activity coefficients are evaluated using correlations and the UNIFAC method [5-7]. The gas phase is treated as quasisteady, allowing analytical results to be used for gas-phase profiles and droplet-flame standoff ratios [2,8]. The assumption of a quasisteady gas phase is consistent with experimental results that show quasisteady flame standoff ratios for these droplets [4].

Figure 2(a) shows experimental results for droplet size variations, with numerical results superimposed as solid lines. The calculations sought to provide a good match between experimental and theoretical results on burning rates so that the onset of flame contraction predicted by the model could be compared with experimental results. This was accomplished by adjusting the gas-phase thermal conductivity by relatively small amounts. Initial droplet swelling from droplet density changes is evident in the computational and experimental results. The swelling in the experiments was slightly larger than predicted by the computations, though the predicted swelling is essentially within the uncertainty of the measurements. In Fig. 2, E is an enhancement factor by which liquid thermal conductivity and species diffusivity were increased during a particular calculation. This factor was introduced to allow effects of internal circulation to be modeled. The value E = 1 predicted flame contraction much earlier than the experiments, while E = 10 provided a much closer prediction (Fig. 2(a)).

Figure 2(b) shows experimental flame size data as well as computational predictions of flame sizes. Agreement between calculations and experiment is reasonable, both qualitatively as well as quantitatively, when the value E = 10 is used. The E values required to match theory and

experiment typically ranged from 8 to 10, which are larger that what would be expected to apply to droplets with Hills-type vortex flows [9]. As a result, the droplets may have contained more than one vortex or perhaps chaotic flows may have been present, which can cause larger increases in effective diffusivities [10].

NUMERICAL MODELING OF FIBER-SUPPORTED DROPLETS

A computer code is being developed to simulate 3-d vaporization of droplets that are attached to thin fibers. This code, which is being developed in collaboration with Prof. H. A. Dwyer of UC Davis, includes multi-component liquids as well as Marangoni flows from temperature gradients and liquid concentration gradients. The present status of the code is as follows. Fully validated: gas and liquid fluid mechanics and heat transfer; mesh generation and interaction between the fiber, gas and liquid phases; gas phase chemical reactions; variable properties; interface forces. Partially validated: mass transfer between gas and liquid phases; multi-component liquid properties; thermal surface tension forces. Continuing development: concentration driven surface tension forces; adaptive mesh generation for resolution of flame structure; resolution of ignition processes. The code has been run for various validation cases.

Figure 3 shows representative results for a nonreacting fiber-supported droplet in a hot environment. In this case, the fiber diameter is 1/20 of the droplet diameter. Flows were observed to form within the droplet as a result of thermal Marangoni effects (see the dark streamlines in the droplet). The fiber and the droplet are cooler than the environment, and the location of the fiber on either side of the droplet can be seen by the thermal boundary layer over the fiber length (green coloring in Fig. 3(a)). For validation, this case was run with a cross flow, yielding temperature variations in Fig. 3(b).

ACKNOWLEDGEMENTS

REFERENCES

1. I. Aharon and B. D. Shaw, Combust. Flame 113, 507 (1998).
2. I. Aharon and B. D. Shaw, Micrograv. Sci. Tech. X/2, 75 (1997).
3. D. E. Rosner, R. S. Israel and B. La Mantia, Combust. Flame 123, 547 (2000).
4. V. Dee and B. D. Shaw, AIAA paper 2001-0468 (2001).
5. S. I. Sandler, *Chemical and Engineering Thermodynamics* (2nd ed), John Wiley & Sons, New York (1989).
6. R. H. Perry, *Perry's Chemical Engineers' Handbook* (7th ed.), McGraw-Hill, New York (1997).
7. R. C. Reid, J. M. Prausnitz and B. E. Poling, *The Properties of Gases and Liquids* (4th ed), McGraw-Hill, New York, (1987).
8. B. D. Shaw, Combust. Flame 81, 277 (1990).
9. J.-P. Delplanque, R. H. Rangel and W. A. Sirignano, *Progress in Astronautics and Aeronautics* 132, 164 (1991).
10. M. D. Dryden and H. Brenner, J. Fluid Mech. 379, 319 (1999).
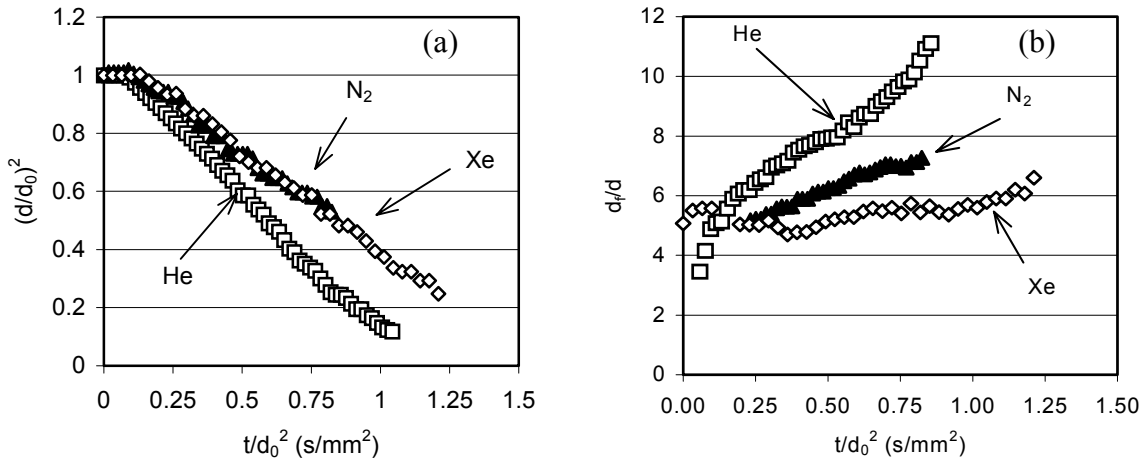
Figure 1.   Data for a decane-hexadecane droplet (Y = 0.2): (a) normalized droplet diameters; and (b) flame standoff ratios. Ambient inert species are noted on the figures.
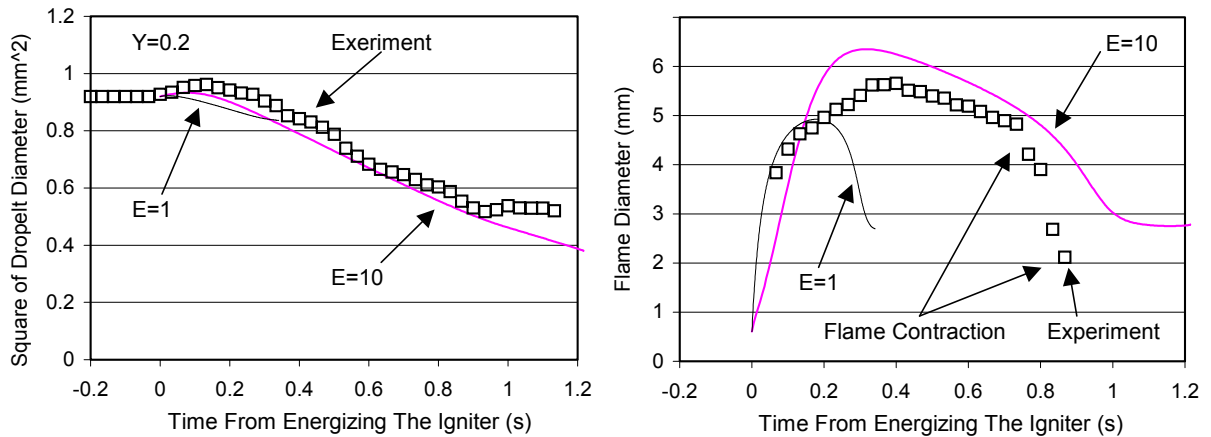
Figure 2   Histories for (a) droplet and (b) flame sizes (Y = 0.2). The symbols are from the experiments and the lines are from the computational model.
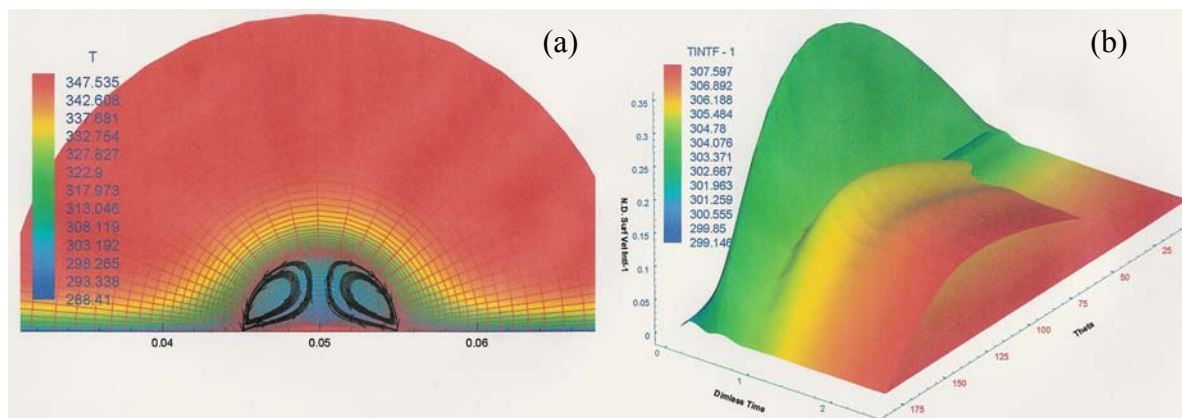
Figure 3   Numerical simulation of a droplet on a fiber: (a) grid, streamlines and temperature profiles; and (b) transient surface temperature development on a symmetry line.

COMBUSTION OF METALS IN REDUCED GRAVITY AND EXTRATERRESTRIAL ENVIRONMENTS

A. Abbud-Madrid, A. Modak and M.C. Branch
Mechanical Engineering Department
University of Colorado
Boulder, Colorado

The recent focus of this research project has been to model the combustion of isolated metal droplets and, in particular, to couple the existing theories and formulations of phenomena such as condensation, reaction kinetics, radiation, and surface reactions to formulate a more complete combustion model. A fully transient, one-dimensional (spherical symmetry) numerical model that uses detailed chemical kinetics, multi-component molecular transport mechanisms, condensation kinetics, and gas phase radiation heat transfer was developed. A coagulation model was used to simulate the particulate formation of MgO. The model was used to simulate the combustion of an Mg droplet in pure O_2 and CO_2. Methanol droplet combustion is considered as a test case for the solution method for both quasi-steady and fully transient simulations. Although some important processes unique to methanol combustion, such as water absorption at the surface, are not included in the model, the results are in sufficient agreement with the published data.

Since the major part of the heat released in combustion of Mg, and in combustion of metals in general, is due to the condensation of the metal oxide, it is very important to capture the condensation processes correctly. Using the modified nucleation theory, an Arrhenius type rate expression is derived to calculate the condensation rate of MgO. This expression can be easily included in the CHEMKIN reaction mechanism format. Although very little property data is available for MgO, the condensation rate expression derived using the existing data is able to capture the condensation of MgO. An appropriate choice of the reference temperature to calculate the rate coefficients allows the model to correctly predict the subsequent heat release and hence the flame temperature.

Quasi-Steady Model. Before simulating the transient phenomena, quasi-steady simulations are performed. The model correctly predicts the combustion parameters of methanol droplet combustion, used here as a test case. The flame temperature predicted by the quasi-steady simulator in both Mg/O_2 and Mg/CO_2 is very close to the vaporization-dissociation temperature and the melting point of MgO, respectively. However, the predicted high flame temperature in the Mg/O_2 case suggests the formation of MgO(l) in the flame and this formation is not captured in the present modeling effort due to the lack of the rate expression for the liquid-solid transition. The relatively small difference between the enthalpies of formation of MgO(l) and MgO(s) compared to the total heat released thus results in slight over-prediction of the flame temperature when only MgO(s) is included.

The predicted quasi-steady surface temperature, 1352 K for combustion in O_2 and 1317 K in CO_2, for a 1-mm diameter Mg droplet burning in both O_2 and CO_2 is close to the Mg boiling point at 1 atm (1366 K). Surface temperature being lower in the case of CO_2 is a direct result of the lower adiabatic flame temperature of the Mg/CO_2 system. The temperature profile near the surface shows a very sharp gradient due to the high enthalpy of vaporization of Mg. The

reaction of Mg with CO occurs very close to the surface and hence there is a step change in the temperature profile near the surface. The reaction with CO may very well be a surface reaction. For a given droplet diameter, the burning rate in O_2 is almost twice as fast as that in CO_2 for pressures above 1 atm. This ratio decreases with decreasing pressure.

The condensed phase oxide is treated as a gas-phase species with low diffusivity by arbitrarily assigning to it a high value of Lennard-Jones collision diameter in the transport property input data. The higher the value of the collision diameter, the higher is the accumulation of the oxide and greater is the hindrance to transport. The burning rate decreases with an increase in the collision diameter with a corresponding slight increase in the flame temperature, the flame standoff ratio, and the surface temperature for a given droplet diameter. The burning rate decreases with decreasing droplet diameter in both O_2 and CO_2 at a given ambient pressure. The extinction diameter is approximately equal to 30 micron in O_2 and 100 micron in CO_2 at 1 atm pressure. The burning rate in both O_2 and CO_2 increases with increasing ambient pressure. The increase in the flame temperature for a given diameter of Mg droplet is higher in O_2 than that in CO_2 for a given increase in pressure. The difference in the boiling point and the quasi-steady surface temperature of the Mg droplet of a given diameter decreases in O_2 and increases in CO_2 with increasing ambient pressure. The low-pressure extinction limit is found to be approximately equal to 0.05 atm for O_2 and 0.1 atm for CO_2.

Fully-Transient Model. Before beginning the transient simulations of Mg combustion, transient methanol droplet combustion was simulated with good agreement to published data. The ignition process is modeled as a spark ignition source near the droplet. The required initial temperature of Mg droplet to undergo burning is 1100 K in O_2 and 1200 K in CO_2 at 1 atm pressure. These values are close to the ignition temperatures published in the literature. The surface temperature approaches the temperature predicted by the quasi-steady simulations and is almost constant throughout the droplet interior. The predicted extinction diameter is 50 micron for a 1-mm diameter Mg droplet burning in O_2 and the total burning time is 1.24 s. Inclusion of gas phase radiation decreases the gasification rate and consequently predicts higher burning time. For large droplets, the radiation loss increases the extinction diameter.

Although some molecular oxygen leaks through the reaction zone and reaches the droplet surface, its mole fraction at the surface is very small. The surface reaction rate being proportional to the square root of O_2 partial pressure at the surface is thus insignificant compared to the rate of evaporation and hence the combustion rate of Mg in vapor phase. The surface reactions are thus dominant only during the initial heating of the droplet. The surface oxide coating, however, may play an important role in the experimentally observed jetting and fragmentation.

The predicted extinction diameter is 60 micron for a 1-mm diameter Mg droplet burning in CO_2 and the total burning time is 2.52 s. As observed in the quasi-steady simulation, the Mg-CO reaction occurs very close to the surface and is responsible for the initial heat release. Along with a higher initial droplet temperature, the model predicts that a higher ignition temperature is required for combustion of Mg droplet in CO_2 than that in O_2. These both trends agree with the fact that combustion of Mg in CO_2 is a less energetic process than that in O_2.

The predicted burning rate constant is 1.14 s/mm^2 for the Mg/O_2 system and 2.52 s/mm^2 for the Mg/CO_2 system. The total burning time decreases with increasing pressure in both O_2 and

CO_2 for a given diameter Mg droplet, however, the decrease is quite small in CO_2. This is due to the smaller increase in the flame temperature (heat evolved) with increasing pressure in CO_2.

The predicted total burning times are almost twice as long as those observed in microgravity. However, the model is unable to simulate the jetting, fragmentation, and explosions observed in microgravity and thus the predicted burning times can be considered as the "quiet limit". Also important to note is that a strong ignition source is used in the experiments and the burning times are measured from the onset of a visible flame unlike the total burning time predicted by the model. However, the effect of this factor will certainly be less than that of the violent combustion observed in microgravity.

Simulation of an initially cooler droplet (surface temperature = 950 K) placed in a hotter O_2 environment (ambient temperature 1000 K) predicts the ignition temperature as 1090 K. The predicted burning time with the above initial conditions for a 1-mm diameter droplet at 1 atm pressure is 1.2 s.

The coagulation model predicts that MgO particles of about 0.03-micron and 0.2-micron diameter are present at the quasi-steady flame location in O_2 and CO_2 respectively. The higher particle diameter in CO_2 is a direct consequence of the lower flame temperature. Far away from the droplet surface (more than 100 times the droplet radius), particle size increases to about 3 microns. No quasi-steady solution is obtained when the thermophoretic velocity is included in the analysis. This result suggests that the particle accumulation observed in the experiments is a transient phenomenon and this may be responsible for the observed time-dependent explosions. From the present results it appears that the coupling of the coagulation model with the transient model is required to capture this process.

It should be noted that the combustion parameters obtained in both, quasi-steady and transient simulations of Mg particle combustion are affected by the approximations used in the condensation modeling and the reaction mechanism. The uncertainty in the reaction rate parameters is a major limitation of the results obtained here. Although the condensation rate expression and the kinetic mechanisms used in this work give the results in agreement with those observed (and expected), these rates are only approximate. The number of parameters is thus too large compared to the available experimental data. On the experimental part, data such as MgO properties, kinetics rate parameters, measured temperature and species profiles, and surface regression rate are required whereas future model development should focus on exact simulation of the experimental ignition conditions, and treatment for the oxide accumulation on the surface.

Rocket Motor Simulator. Future missions to Mars may use a rocket motor with Mg/CO_2 propellant for propulsion in the Martian environment. As an example of a practical application of the results of this study, a simulator was developed for the analysis of a future Mg/CO_2 rocket motor. This simulator can be used to predict the performance of the rocket motor and most importantly, when coupled with the coagulation module, it can predict the location of condensation and coagulation of the condensed phase MgO in the rocket nozzle. The simulation of MgO coagulation can help map the parameter space to explore the feasibility of an Mg/CO_2 rocket.

References

1. Abhijit Modak, "Detailed Numerical Simulation of Isolated Droplet/Particle Combustion with Applications to Combustion of Metals," Ph.D. Thesis, University of Colorado, Boulder, Colorado, March 24, 2003.

2. A. Modak, A. Abbud-Madrid, M.C. Branch and J.W. Daily, "Combustion of Mg with CO_2 and CO at Low Gravity," Journal of Propulsion and Power, 17, pp. 2561-2570, 2001.
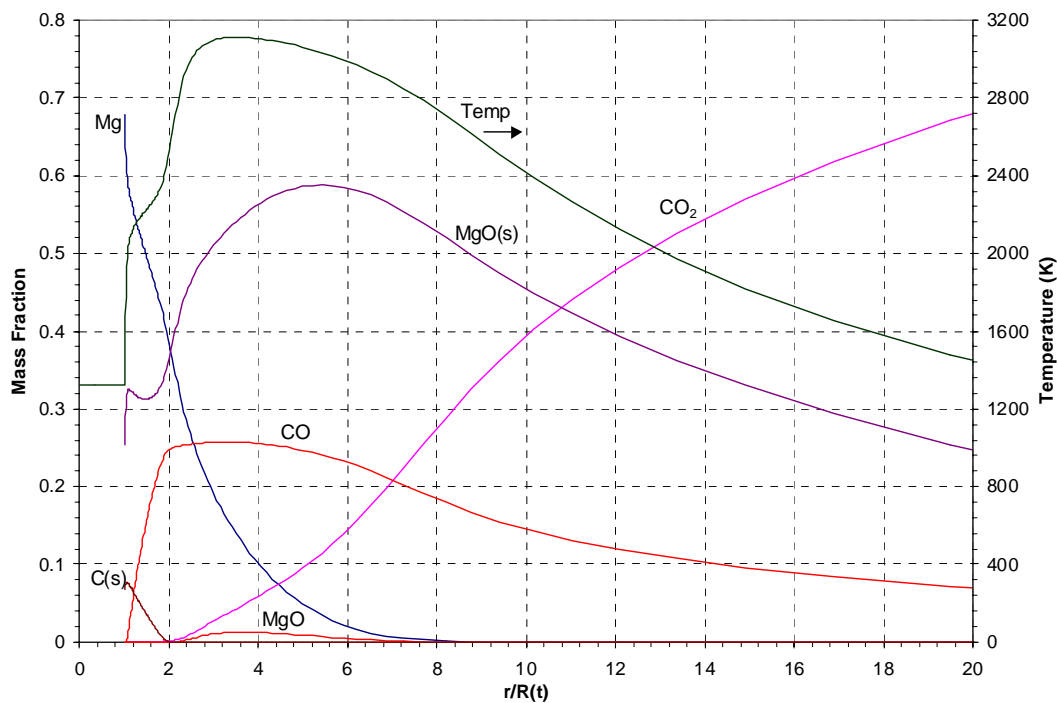
Figure 1. Species concentration and temperature profiles calculated during combustion of Mg in CO_2.

QUENCHING COMBUSTIBLE DUST MIXTURES USING ELECTRIC PARTICULATE SUSPENSIONS (EPS): A NEW TESTING METHOD FOR MICROGRAVITY

Gerald M. Colver, Nathanael Greene, David Shoemaker, Hua Xu
Department of Mechanical Engineering
Iowa State University, Ames, IA. 50011

Abstract   The Electric Particulate Suspension (EPS) is a combustion ignition system being developed at Iowa State University for evaluating quenching effects of powders in microgravity (quenching distance, ignition energy, flammability limits). Because of the high cloud uniformity possible and its simplicity, the EPS method has potential for 'benchmark' design of quenching flames that would provide NASA and the scientific community with a new fire standard. Microgravity is expected to increase suspension uniformity even further and extend combustion testing to higher concentrations (rich fuel limit) than is possible at normal gravity. Two new combustion parameters are being investigated with this new method: (1) the particle velocity distribution and (2) particle-oxidant slip velocity. Both walls and (inert) particles can be tested as quenching media. The EPS method supports combustion modeling by providing accurate measurement of flame-quenching distance as a parameter in laminar flame theory as it closely relates to characteristic flame thickness and flame structure. Because of its design simplicity, EPS is suitable for testing on the International Space Station (ISS). Laser scans showing stratification effects at 1-g have been studied for different materials, aluminum, glass, and copper. PTV/PIV and a leak hole sampling rig give particle velocity distribution with particle slip velocity evaluated using LDA. Sample quenching and ignition energy curves are given for aluminum powder. Testing is planned for the KC-135 and NASA's two second drop tower. Only 1-g ground-based data have been reported to date.

EPS Design An electric particulate suspension (EPS) utilizes a high voltage electric field to disperse a powder of semi-insulating or conductive material in a cloud of (oppositely) charged particles. The resulting steady state suspension is subsequently ignited by a spark discharge from a stationary (or moving) needle electrode, Fig.1.[1] Particle motion in the direction of the electric field is confined between two parallel plate electrodes with diffusive motion in the horizontal direction confined by a Pyrex cylindrical retainer. High voltage capacitors provide the necessary energy for the spark.   Wall quenching tests involve adjusting the height distance between the parallel plate electrodes and testing for flame propagation following the spark. Quenching by inert powders is accomplished by suspending various amounts of copper or glass particles with a combustible powder or gas mixture and igniting the mixture. Acoustic vibration is utilized to aid the suspension of cohesive particle such as coal dust or other fine particles (Fig. 1).[1] The centered spark kernel produces a cylindrically outward propagating flame. Fig. 3 shows a photograph of quench (batch) test of aluminum powder 25-35 μm using the system in Fig. 2.

Powder quenching   Powder (wall) quenching studies carried out to date at 1-g include the measurement of quenching and ignition energy curves for aluminum powder and coal dust in various admixtures of oxygen, nitrogen, and carbon dioxide at ambient conditions of temperature and pressure.[2] Example quenching and ignition curves for coal dust and aluminum powder are shown in Figs. 3 and 4 respectively, using the setup of Fig. 1. Aluminum powder 25-30 μm in

concentrations of 150-3300 g/m^3 was tested in admixtures of oxygen, nitrogen, and carbon dioxide (mole ratio 0.21). These data are then curve fit as in Fig. 4. Flammability curves have been developed for lean to stoichiometric powder mixtures at 1-g. For cohesive particles, 17.5 µm spherical aluminum and 16.7 µm Illinois No. 6 coal, quenching tests are carried out with acoustic assist in Fig. 1. Test results indicate that both the quenching distance and lean flammability limit increase with particle size while the quenching distance of coal is observed to decrease with increasing volatile content.
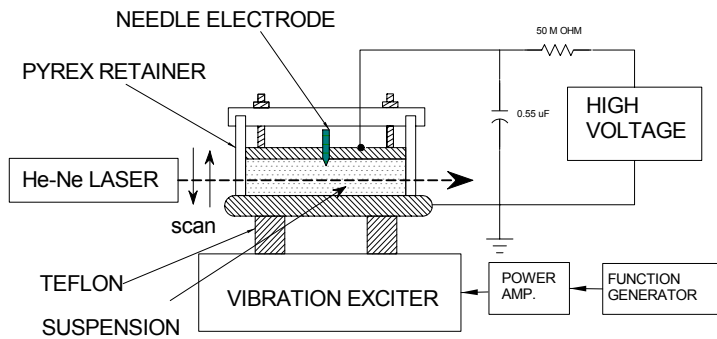
Fig. 1 Batch feed (closed) system with Pyrex cylinder walls: tests of quenching distance, ignition energy, flammability limits.
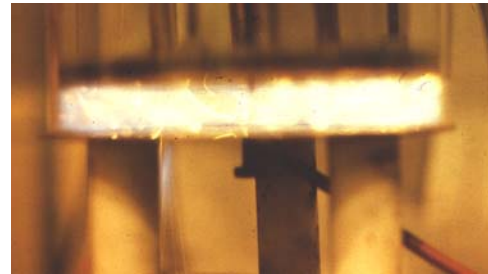
Fig. 2 EPS method: Ignition of 17.5 µm (avg) spherical aluminum powder.
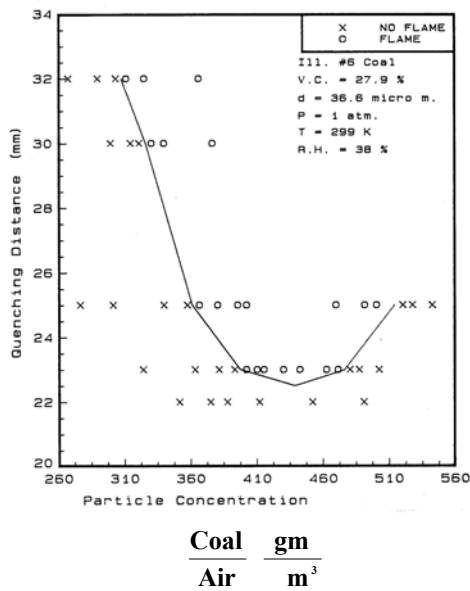
Fig. 3 Quenching distance (mm) vs fuel-air ratio 36.6µm Illinois #6 coal.
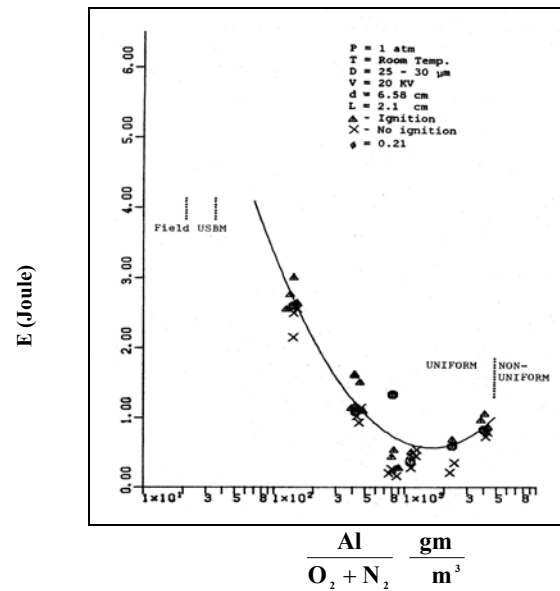
Fig. 4 Spark ignition energy (J) vs. fuel-air ratio, 27.5 µm aluminum.

Fig. 5 shows the ignition of a propane-air mixture using copper particles as quenching media. Streaks of particles are apparent following ignition from the spark between the high voltage electrodes. Once breakdown occurs, the suspension collapses with the field. However, the motion of the particles persists over times needed for passage of the flame front, usually ms. The problem of suspension collapse is expected to be reduced in microgravity.

Spark ignition energy The EPS experiment in Fig 5 is used to investigate spark ignition energy and quenching of propane-air mixtures in the presence of copper particles. This particular EPS system utilizes a high speed moving electrode (~10 m/s) to trigger the spark so as to preserve the uniformity of the suspension prior to breakdown.[3] For copper particles the parameter Nd^2 (N = particle number density, d= particle diameter) is found to be important for gas ignition (Fig. 5). The quenching effect of particles in Fig. 6 for propane-air mixtures shows that a greater ignition energy is needed for either higher values of particle concentration N or particle diameter D (E_{io} is the energy to ignite a particle free propane-air mixture for the same fuel-air ratio).

Fig. 5 EPS method: Quenching mixtures of propane air with 96 μm copper particles.
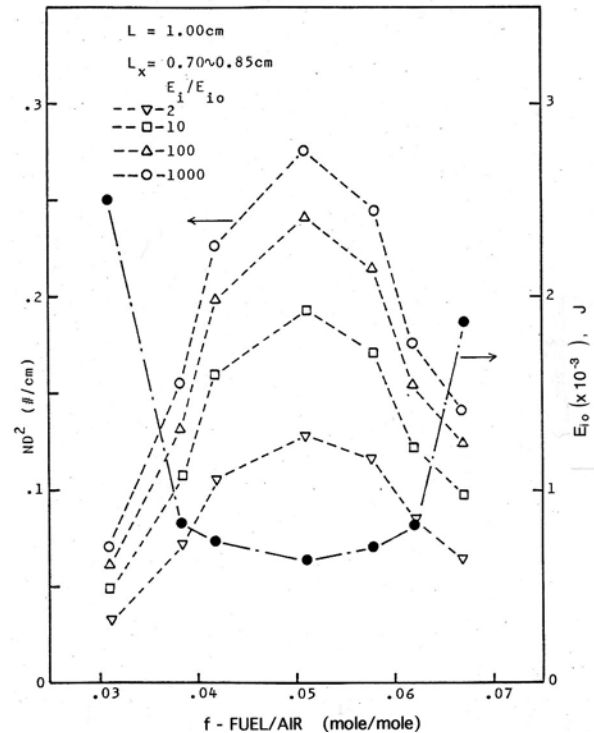
Fig. 6 Ignition energy and ND^2 parameter for quenching copper-propane-air mixtures.

Particle velocity distribution & particle-oxidant slip velocity The Particle Velocity Distribution (PVD) associated with randomized motion from particle-particle and particle-wall collisions is being investigated in this study. Particles are leaked from a 1.61 mm hole located in the top of an EPS test section and their velocity vectors determined by the height attained. Particle Tracking Velocimetry (PTV/PIV, LaVision Flowmaster System) has also been utilized to compute particle velocities between successive pulses. A laser sheet is formed by imaging the beam with a cylinder lens that is directed just above the EPS leak hole. A second combustion variable, the **particle-oxidant slip velocity,** can be computed or measured using LDA and studied with the electric field. The slip velocity can affect heat and mass transfer in flames for large particles and high temperatures. For example, increasing the particle Reynolds number from 1 to 10 doubles both Sherwood and Nusselt numbers for a spherical particle.

Stratification of dust clouds at 1-g Particle forces resulting from gravity induce stratification in the cloud similar to the decrease in gas density observed with elevation in normal atmosphere. Microgravity is expected to extend the range of combustion testing to near E = 0 values while also reducing cloud stratification. Figs. 7 show an automated X-Y laser scanning facility for measuring particle concentration. At 1-g, laser attenuation scans show that gravitational stratification occurs in particle concentration of copper spheres with height (Fig. 7 top right). The test data were collected at different values of electric field strength and a large electrode separation distance (3.9 cm) to bring out the stratification effect. The completely automated data acquisition system (LabView) samples the power meter at 10-80 readings per "window" with a

tolerance up to ±0.01 cm (each data point in Fig. 7-top right). The user can specify multiple scans of the motorized system and automatic reversals (up-down traverses).
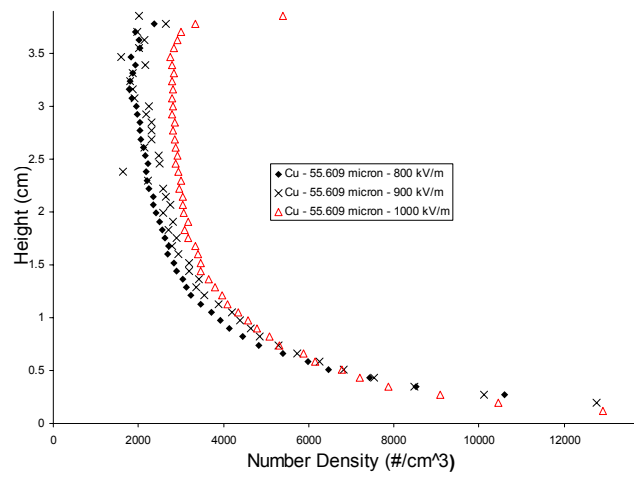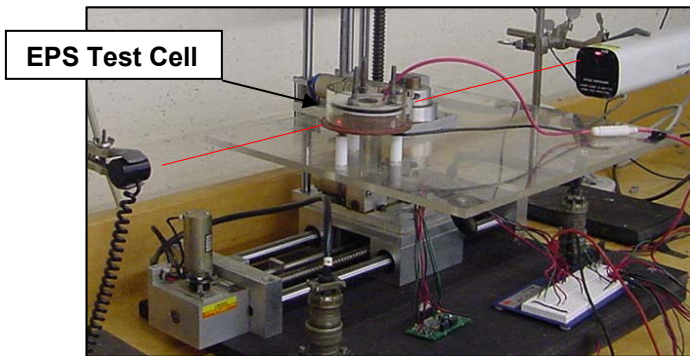
Figs. 7 (**top**) EPS X-Y automated scan rig for measuring of particle concentration by laser attenuation; (**top-right**) Effect of electric field strength brings out stratification at 1-g and large electrode separations (3.9 cm) using 55.6 µm copper powder (60 readings per data point at ±0.01 cm); (**right**) Size distribution for 55.6 µm copper powder compared to log-normal distribution.
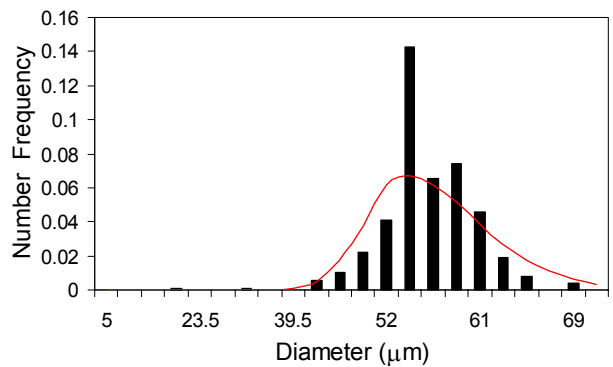
Summary and Limitations using EPS The EPS combustion test method can produce steady-state clouds of high uniformity while providing alternative methods for measuring particle concentration. Reduced gravity (microgravity) is expected to further reduce cloud stratification and electric field requirements while extending the concentration range of powders. Spark breakdown at 1-g limits present fields between 2-5 kV/cm, as determined by gravitational forces, and the highest values of 6-20 kV/cm where sparkover can occur. For cohesive particles (< 5 µm) acoustic excitation can be helpful in the EPS method for breaking up the particle clusters.

References 1. Colver, G. M., C. Eimers, and N. Greene, "Quenching of Combustible Dust Mixtures Using Electric Particulate Suspension (EPS): Review of a New Testing Method for Microgravity," paper AIAA 2003-705, 41st AIAA Aerospace Sciences Meeting and Exhibit, Reno, Jan. 6-9, 2003 (on CD).
2. Colver, G. M., S. W. Kim, and Tae-U Yu, "An Electronic Method for Testing Spark Breakdown, Ignition, and Quenching of Powder," J. of Electrostatics, V. 37, 1996, pp. 151-172.
3. Yu, Tae-U and Colver, G. M. , "Spark Breakdown of Particulate Clouds: A New Testing Device'" IEEE Trans. Ind. Appl., V. 1A-23, No 1, Jan./Feb. 1987, pp. 127-133.

EFFECT OF LOW EXTERNAL FLOW ON FLAME SPREADING
OVER ETFE INSULATED WIRE UNDER MICROGRAVITY

Katsuhiro Nishizawa, Osamu Fujita, Kenichi Ito
Dept. of Mechanical Science, Hokkaido University, Kita-13 Nishi-8, kita-ku, Sapporo, 060-8628,
Japan

Masao Kikuchi
National Space Development Agency of Japan, 2-1-1, Sengen, Tsukuba, Ibaraki, 305-8505,
Japan

Sandra L. Olson
NASA Glenn Research Center, Cleveland, OH, 44135, USA

Takashi Kashiwagi
National Institute of Standards and Technology, Gaithersburg, MD, 20899, USA

1. INTRODUCTION

Fire safety is one of the most important issues for manned space missions. A likely cause of fires in spacecraft is wire insulation combustion in electrical system. Regarding the wire insulation combustion it important to know the effect of low external flow on the combustion because of the presence of ventilation flow in spacecraft. Although, there are many researches on flame spreading over solid material at low external flows under microgravity [1,2], research dealing with wire insulation is very limited. An example of wire insulation combustion in microgravity is the Space Shuttle experiments carried out by Greenberg et al [3]. However, the number of experiments was very limited. Therefore, the effect of low flow velocity is still not clear. The authors have reported results on flame spreading over ETFE (ethylene-tetrafluoroetylene) insulated wire in a quiescent atmosphere in microgravity by 10 seconds drop tower [4]. The authors also performed experiments of polyethylene insulated nichrom wire combustion in low flow velocity under microgravity [5]. The results suggested that flame spread rate had maximum value in low flow velocity condition. Another interesting issue is the effect of dilution gas, especially CO_2, which is used for fire extinguisher in ISS. There are some researches working on dilution gas effect on flame spreading over solid material in quiescent atmosphere in microgravity [4,6]. However the research with low external flow is limited and, of course, the research discussing a relation of the appearance of maximum wire flammability in low flow velocity region with different dilution gas cannot be found yet. The present paper, therefore, investigates the effect of opposed flow with different dilution gas on flame spreading over ETFE insulated wire and change in the presence of the maximum flammability depending on the dilution gas type is discussed within the limit of microgravity time given by ground-based facility.

Generally, solid combustion has longer time scale than other phase fuel, especially with thick sample and/or low oxygen concentration and it is difficult to obtain reliable data in short time microgravity test. Therefore, the present work is limited to high oxygen concentration cases with thin fuel. To attain general understanding of wire insulation combustion, the test with long-term microgravity is essential. This subject is selected as a candidate of ISS flight test at IAO2000

(Effect of Material Properties on Wire Flammability in Weak Ventilation of Spacecraft (FireWIRE)) and the research is now under definition stage.

2. EXPERIMENTAL

The experiments were performed at the Japan Microgravity Center (JAMIC) 10s dropshaft and NASA's KC-135 aircraft. The detail of the setup for KC-135 test is described in Ref. [7].

Figure 1 shows the combustion chamber with flow duct used for JAMIC test. The combustion chamber is a rectangular airtight vessel, and a flow duct is installed in the chamber. The chamber has an air suction fan at the left end of the duct. The flow velocity in the duct is controlled in the range 0 to 30cm/s.

A sample wire, which is fixed to the sample holder with igniter, is installed in the center of the flow duct

Fig.1 Out line of combustion chamber

parallel to the external flow. Flame spreads opposed to the external flow (from left to right in Fig.1). ETFE (ethylene- tetrafluoroethylene copolymer) insulated copper wire was used as a test sample. The sample use in the experiments is 0.32mm inner core and 0.15mm insulation thickness (AWG28). Experiments were performed with different O_2 concentrations, external flow velocities and dilution gas, N_2 and CO_2.

3. EXPERIMENTAL RESULTS AND DISCUSSION
3.1 OBSERVATION OF FLAME

Figure 2 shows photographs of spreading flame at different flow velocity in 35% O_2 with CO_2 dilution. It shows that the flame is luminous with blue flame region at the front of the flame in all external flow velocity. At 0cm/s, the trailing edge of flame becomes wide in comparison with the leading edge. When external flow is given, flame shape as seen in Fig.2 (b), (c) and (d), is cylindrical with almost same diameter along the wire.

Another interesting phenomenon is unsteady flame spreading with CO_2 dilution at low flow velocity, 0 and 2cm/s. Figure 3 shows the typical sequential photos of spreading flame at 2cm/s with CO_2 dilution. The time interval of each photo is approximately 0.2s. A most ordinal flame shape is the one as shown in Fig. 3 (a). Then, at the

(a) 0cm/s   (b) 2cm/s

(c) 5cm/s   (d) 10cm/s
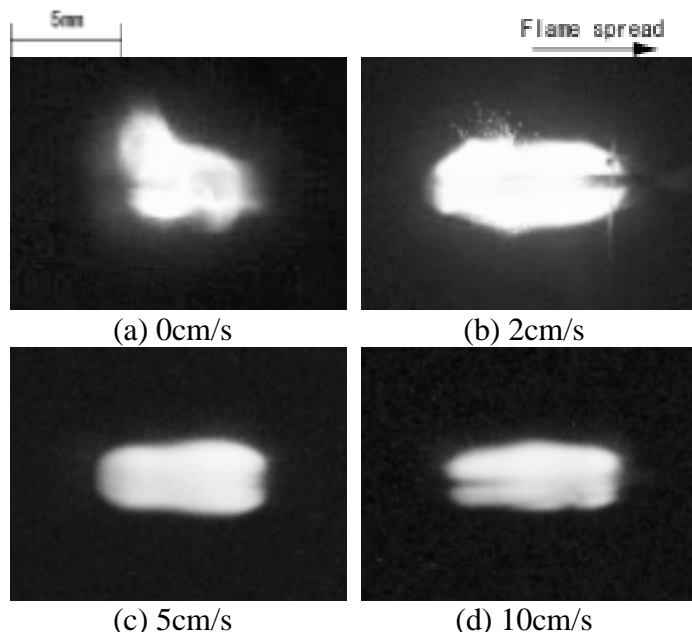
Fig.2 Photographs of spreading flames over ETFE insulated wire under different external air flow with CO_2 dilution (O_2=35%)

flame front blue flame propagates fast as shown in Fig.3(b), (c). After that, another luminous flame grows at the front of spreading blue flame front as see in Fig.3 (d). This secondary luminous flame is small at first but increases in size with time as shown in Fig. 3(e), (f). Then, the primary luminous flame quenches and secondary flame spreads. This unsteady phenomenon is unique phenomena observed in low external flow condition with CO_2 dilution. One of the possibility reasons of the unsteady phenomenon is reabsorption effect of CO_2 gas. In low flow velocity, preheat length is strongly affected by reabsorption [8]. The preheat

(a)   (b)

(c)   (d)

(e)   (f)

Fig.3 Sequential photographs of spreading flames in low velocity flow with CO_2 dilution (V_e=2.1cm/s)

length becomes longer with time by CO_2 reabsorption when flow velocity is low. Then, heat transfer to unburned fuel at the preheat zone increases. When total heat supply to the unburned region reaches critical amount, suddenly flame spreads fast and the preheat length decrease again.

3.2 FLAME SPREAD RATE

Flame spread rate is determined based on the motion picture taken by digital video camera. Fig.4 shows plots of flame spread rate as a function of flow velocity for different oxygen concentrations with N_2 dilution. The flame spread rate generally increases with increase in ambient oxygen concentration, irrespective of flow velocity. Another interesting feature with N_2 dilution is the trend to show a maximum flame spread rate at a certain flow velocity, around
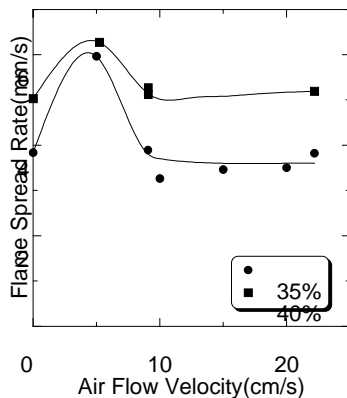
Fig.4 Flame spread rate as a function of external air flow velocity (N_2 dilution)
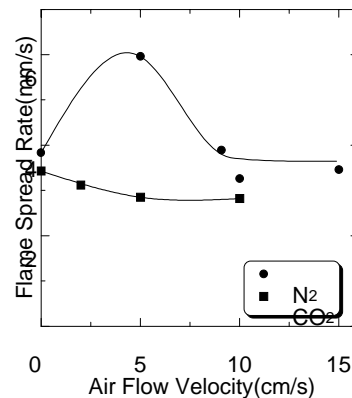
Fig.5 Flame spread rate with different dilution gas (O_2=35%)

5cm/s, in low flow velocity region. This trend qualitatively agrees with the case of polyethylene insulated wire [5]. This is one of the feature of wire insulation combustion, which is explained as an geometrical effect in Ref.[5].

Figure 5 shows the flame spread rate change as a function of external flow velocity with different dilution gas. The flame spread rate with N_2 is faster than that with CO_2 at 35% O_2, irrespective of flow velocity. The trend of flame spread rate is different between N_2 and CO_2. With N_2, flame spread rate tends to have maximum value as mentioned baove. On the other hand, CO_2 dilution case resulted in the highest flame spread rate at V_e=0cm/s and decrease monotonically with increase in flow velocity. Then, it reaches almost constant spread rate over a certain flow velocity. Therefore, the flame spread rate has no maximum value in low flow velocity region with CO_2 case. One of the reasons of the difference is reabsorption effect of CO_2 gas. With CO_2, radiation heat from the flame is reabsorbed in preheat region [8] and flame temperature decrese is not large, while N_2 dilution leads to large temperature decrease causing decrease in flame spread rate. In high flow velocity region the reabsorption effect is not important and the trend becomes similar to N_2 dilution case.

4. SUMMARY

(1) The dependence of flame spread rate on flow velocity was examined with drop tower and aircraft. Specially, flame spread rate with N_2 and CO_2 was compared. Flame spread rate was 2-6mm/s even if oxygen concentration was 35% or higher. Therefore, it is difficult to obtain data with low O_2 concentration or thick sample in ground-based facility. Long term microgravity test such as ISS is expected.

(2) Flame spread rate with N_2 has maximum value in low flow velocity region, while with CO_2 flame spread rate increases monotonically with decrease in flow velocity. One of the explanations of the difference is effects of sample geometry and reabsorption of CO_2 gas.

(3) Unsteady flame spread phenomenon was observed with CO_2 dilution. This phenomenon is explained by CO2 reabsorption effect, which is to be investigated in the next step.

REFERENCES

[1] S. L. Olson, Combust. Sci. Technol, 76, 233, (1991)

[2] T. Kashiwagi et al., Proc. Combust. Inst., 26, 1345, (1996)

[3] P. S. Greenberg et al., 3rd International Microgravity Combustion Workshop, 25, (1995) / K.R Sacksteder, P.S.Greenberg, and J.S.T'ien, Proc. of the 3rd Joint Metting of U.S.Sections of the Combustion Institute.

[4] M. Kikuchi et al., Proc. Combust. Inst., 27, 2507, (1998)

[5] O. Fujita et al., Combust. Inst., 29, (2002) (in print)

[6] L. K. Honda et al., Combust. Sci. Technol., 133, 267, (1998)

[7] O. Fujita et al., 6th International Microgravity Combustion Workshop, (2001)

[8] O. Fujita et al., Proc. Combust. Inst., 28, 2905, (2000)

Cellular Instabilities and Self-Acceleration of Expanding Spherical Flames

C. K. Law
Department of Mechanical and Aerospace Engineering
Princeton University, Princeton, NJ 08544, USA

O. C. Kwon
School of Mechanical Engineering
Sungkyunkwan University, Suwon, Kyunggi-do, Korea

Introduction

In the present investigation we aim to provide experimental information on and thereby understanding of the generation and propagation of spark-ignited, outwardly propagating cellular flames, with three major focuses. The first is to unambiguously demonstrate the influence of the four most important parameters in inducing hydrodynamic and diffusional-thermal cellularities, namely thermal expansion, flame thickness, non-unity Lewis number, and global activation energy. The second is to investigate the critical state for the onset of cellularity for the stretch-affected, expanding flame [1-4]. The third is to identify and consequently quantify the phenomena of self-acceleration and possibly auto-turbulization of cellular flames [5, 6]. Due to space limitation the effects of activation energy and the critical state for the onset of cellularity will not be discussed herein. Details can be found in Ref. 7.

Experiments were conducted using C_3H_8-air and H_2-O_2-N_2 mixtures for their opposite influences of nonequidiffusivity. The additional system parameters varied were the chamber pressure (p) and the mixture composition including the equivalence ratio (ϕ). From a sequence of the flame images we can assess the propensity of cell formation, and determine the instantaneous flame radius (R), the flame propagation rate, the global stretch rate experienced by the flame, the critical flame radius at which cells start to grow, and the average cell size.

Effects of Instability Parameters

The hydrodynamic theory of Darrieus [8] and Landau [9] shows that, in the limit of an infinitely thin flame propagating with a constant velocity, the flame is unstable to disturbances of all wavelengths. The growth rate is proportional to the density jump across the flame, increasing with increasing σ. Thus σ is probably the most sensitive parameter controlling the onset of hydrodynamic instability.

Next to σ, the flame thickness δ_T is also expected to have a strong influence on the hydrodynamic instability, for two reasons. First, it measures the influence of curvature which, being positive for the expanding flame, has a stabilizing effect on the cellular development. The thinner the flame, the weaker is the influence of curvature and consequently the stronger is the destabilizing propensity. The second influence is that it controls the intensity of the baroclinic torque developed over a slightly wrinkled flame surface, which depends on the density gradient across the flame and the pressure gradient along the flame [10]. Since the density gradient increases with decreasing flame thickness, development of the hydrodynamic instability is correspondingly enhanced due to the increased intensity of the induced baroclinic torque.

For the development of the diffusional-thermal instability, an appropriate parameter representing the effect of nonequidiffusion is the flame Lewis number, *Le* [11]. It is well established and understood theoretically that unstretched flames are diffusionally unstable (stable) for *Le*'s that are smaller (greater) than a value slightly less than unity.

The last parameter of importance, especially for the present outwardly expanding flame, is the Karlovitz number, which is the nondimensional stretch rate and is defined as $Ka = (2/R)(dR/dt)/(s_u^o/\delta_T)$, where s_u^o is unstretched laminar burning velocity and t is time. It was theoretically shown for the stagnation flame [12] and the expanding flame [1, 2] that the associated positive stretch tends to be stabilizing. Conceptually, cells cannot form if their growth rate is smaller than that of flame expansion. Since the expanding flame suffers the strongest stretch during the initial phase of its propagation when its radius is small, the tendency for cell development is expected to increase as the flame propagates outward. The influence of stretch also shifts the critical Le, at which the flame response reverses, to a smaller value than that of the unstretched flame.

We now present in sequence the influence of δ_T, σ, and Le on the propensity of cell development, with the comparison conducted at the same or similar Karlovitz numbers.

Flame Thickness Effects: Figure 1 shows the burning sequences of almost diffusionally neutral, stoichiometric propane-air flames in 2, 5, and 10 *atm.* The corresponding flame thicknesses are $\delta_T = 0.17$, 0.10, and 0.062 *mm*. The sequence at 2 *atm.* shows that the flame surface remains smooth, with the presence of only a large ridge throughout the observation period. At 5 *atm.* a few large cracks, formed as a consequence of the disturbance caused by the spark discharge, persist down to $Ka = 0.05$. However, when Ka is reduced to 0.03, small cells of an average size of 3.6 *mm* emerge. The sequence at 10 *atm.* shows that the cracks first grow in a self-similar manner up to $Ka = 0.08$. Then further cracking through branching is developed, as seen for $Ka = 0.05$. Eventually the average cell size is reduced to 1.1 *mm* at $Ka = 0.03$. The above flame morphology readily substantiates the concept that positive stretch and a thicker flame tend to delay the onset and development of hydrodynamic cells, and that as the flame becomes thinner not only it is destabilized earlier (i.e. for larger values of Ka), but the cell size is also smaller.

Thermal Expansion Effects: Figure 2(a) shows the burning sequences of two diffusionally stable flames that have different values of σ but nearly the same values for other parameters: namely a $\phi = 0.9$, $p = 10$ *atm.*, propane-air flame with $\sigma = 7.7$, $\delta_T = 0.068$ *mm*, and $Le = 1.6$, and a $\phi = 3.0$, $p = 5$ *atm.*, hydrogen-air flame with $\sigma = 5.9$, $\delta_T = 0.059$ *mm,* and $Le = 1.7$. Since the former has a larger expansion ratio, it is more unstable, as shown.

Nonequidiffusive Effects: For this demonstration, we compare in Fig. 2(b) the burning sequences of two $p = 5$ *atm.*, $\sigma = 7.7$, propane-air flames at $\phi = 0.9$ ($Le = 1.6$, $\delta_T = 0.10$ *mm*) and 1.5 ($Le = 0.95$, $\delta_T = 0.21$ *mm*), such that the former is diffusionally stable while the latter unstable. Considering that the former has a smaller δ_T and hence is hydrodynamically more unstable, the fact that the latter actually exhibits a more prominent instability pattern illustrates the powerful destabilizing influence imposed by the diffusional-thermal instability mechanism. The absence of any cells for the diffusionally stable flame, even at $Ka = 0.10$, and the presence of the (large) hydrodynamic cells for the diffusionally unstable flame at $Ka = 0.32$, possibly triggered by the diffusional-thermal instability, are particularly worth noting.

Self-Acceleration of Cellular Flames

A series of crucial questions can be asked about the propagation rate of the expanding flame. First, after development of the cells, will the wrinkled flame propagate faster than the original smooth flame? Second, if it is faster, will it accelerate? Third, if it accelerates, will the acceleration be constant? Stated alternatively, by determining the flame radius history $R(t) \sim t^\alpha$,

and hence the propagation velocity $dR(t)/dt \sim t^{(\alpha-1)}$, affirmative answers to the above three questions would require α assuming a constant value greater than unity. Furthermore, a constant α would imply that the flame propagation and morphology have a fractal character, and that if the fractal dimension is close to that of turbulent flame propagation, the self-acceleration process of the wrinkled flame propagation can be considered as one of auto-turbulization [5, 6, 13].

Figure 3 plots $R(t)$ for three highly unstable flames of H_2-15%O_2-N_2 mixtures of $\phi = 0.5$, 1.0, and 1.5, at 15 *atm*. The corresponding *Le* are 0.40, 0.94, and 1.65. The data were subsequently fitted according to $R(t) = R_o + At^{\alpha}$, where R_o is the virtual origin, representing the effect of the initial period of steady propagation. The fitting yields $R = 0.0013+1.90t^{1.26}$ for $\phi = 0.5$; $R = -0.0015+41.53t^{1.36}$ for $\phi = 1.0$; and $R = -0.0032+26.04t^{1.23}$ for $\phi = 1.5$, where R is in *m* and t in sec. The correlation of the data in the numerical fitting is accurate to 99.9%. The inset shows the corresponding $R(t)$-R_o in logarithm coordinates, demonstrating the linearity of the fitting and hence the constancy of α.

The above fitting shows that all the three flames are self-accelerating. The acceleration exponents determined for the three cases are 1.26, 1.36, and 1.23, which do not show any particular pattern in relation to any of the flame parameters. Indeed, the three values are purposely shown as typical values since at the present state it is difficult to pin down a precise number, if indeed there exists a precise number. However, they are smaller than the value of 1.5 reported in Ref. [5], but are basically within the range of 1.25 to 1.5 mentioned in a subsequent publication [14]. Thus by using the relation $\alpha = 1/(1-d)$ [6], where d is the fractal excess, our results basically yield d in the range of 0.20 to 0.25, implying a fractal dimension, $(2+d)$, of 2.20 to 2.25.

Summary

From high-speed imaging of outwardly propagating propane-air and hydrogen-oxygen-nitrogen flames under elevated pressures, it was demonstrated that hydrodynamic instability is greatly enhanced with increasing pressure and hence decreasing flame thickness. The cellular flames were found to be self-accelerating, including those that are diffusionally unstable, with fractal dimensions between 2.20 and 2.25.

References

1. Istratov, A.G., and Librovich, V.B., Acta Astronautica 14: 453 (1969).
2. Bechtold, J.K., and Matalon, M., Combust. Flame 67: 77 (1987).
3. Bradley, D., Cresswell, T.M., and Puttock, J.S., Combust. Flame 124: 551 (2001).
4. Kwon, O.C., and Faeth, G.M., *Combust. Flame* 124: 590 (2001).
5. Gostintsev, Yu.A., Istratov, A.G., and Shulenin, Yu.V., *Combust. Expl. Shock Waves* 24: 563 (1989).
6. Bychkov, V.V., and Liberman, M.A., *Physics Reports* 325: 115 (2000).
7. Kwon, O.C., Rozenchan, G. and Law, C.K., *Proc. Combust. Inst.,* 29, (2002), in press.
8. Darrieus, G., *La Technique Moderne* 30: 18 (1938).
9. Landau, L.D., *Acta Physicochem* 19: 77 (1944).
10. Pan, K.L., Qian, J., and Law, C.K., *Proc. Combust. Inst.,* 29, (2002), in press.
11. Sivashinsky, G.I., *Ann. Rev. Fluid Mech.* 15: 179 (1983).
12. Sivashinsky, G.I., Law, C.K., and Joulin, G., *Combus. Sci. Tech.* 28: 155 (1982).
13. Filyand, L., Sivashinsky, G.I., and Frankel, M.L., *Physica D* 72: 110 (1994).
14. Gostintsev, Yu.A., Istratov, A.G., Kidin, N.I., and Fortov, V.E., *High Temp.* 37: 282 (1999).

C$_3$H$_8$-air: ϕ = 1.0

2 atm	5 atm	10 atm
7 ms (Ka = 0.14)	5 (0.14)	3 (0.14)
9.5 (0.11)	7 (0.11)	4.5 (0.11)
11.5 (0.08)	9 (0.08)	6.5 (0.08)
19 (0.05)	17 (0.05)	12.5 (0.05)
27 (0.03)	25.5 (0.03)	17 (0.03)
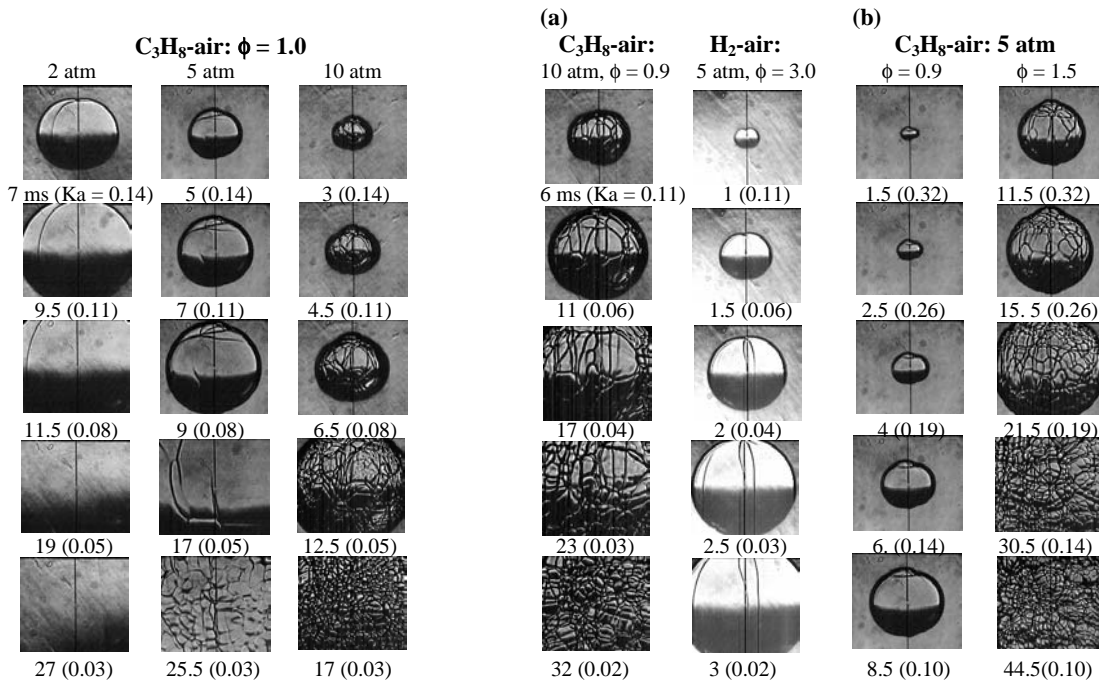
Figure 1. Schlieren photographs of stoichiometric C$_3$H$_8$-air flames at 2, 5, and 10 atm.

(a)

C$_3$H$_8$-air:	H$_2$-air:
10 atm, ϕ = 0.9	5 atm, ϕ = 3.0
6 ms (Ka = 0.11)	1 (0.11)
11 (0.06)	1.5 (0.06)
17 (0.04)	2 (0.04)
23 (0.03)	2.5 (0.03)
32 (0.02)	3 (0.02)

(b)

C$_3$H$_8$-air: 5 atm

ϕ = 0.9	ϕ = 1.5
1.5 (0.32)	11.5 (0.32)
2.5 (0.26)	15. 5 (0.26)
4 (0.19)	21.5 (0.19)
6 (0.14)	30.5 (0.14)
8.5 (0.10)	44.5 (0.10)

Figure 2. Schlieren photographs of (a) C$_3$H$_8$-air flames of ϕ = 0.9 at 10 atm. and H$_2$-air flames of ϕ = 3.0 at 5 atm., and (b) C$_3$H$_8$-air flames of ϕ = 0.9 and 1.5 at 5 atm.
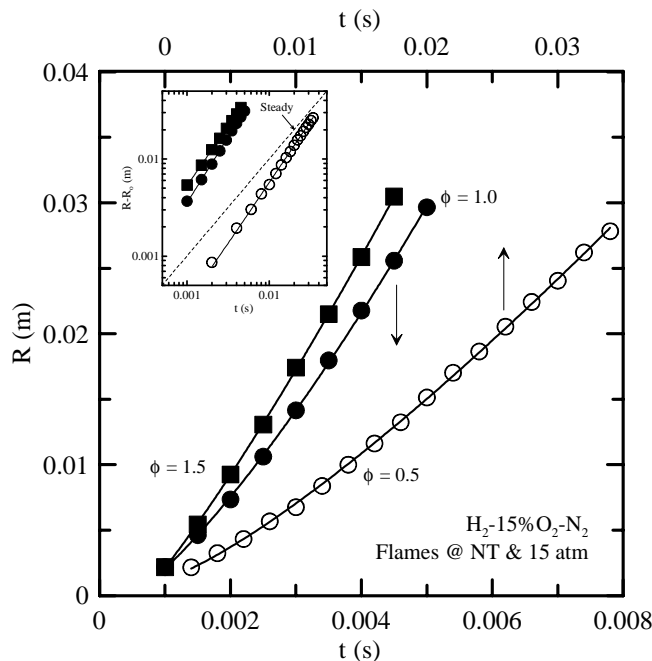
Figure 3. Flame radii as a function of time for H$_2$-15%O$_2$-N$_2$ flames of ϕ = 0.5, 1.0, and 1.5 at 15 atm. Symbols represent experimental data, and lines represent fittings. The insert shows the corresponding flame radii subtracted by the respective virtual origins in logarithm coordinates.

QUANTITATIVE STUDIES ON THE PROPAGATION AND EXTINCTION OF NEAR-LIMIT PREMIXED FLAMES UNDER NORMAL AND MICROGRAVITY

Y. DONG, G.R. SPEDDING & F.N. EGOLFOPOULOS
Department of Aerospace & Mechanical Engineering
University of Southern California
Los Angeles, California 90089-1453

and

F.J. MILLER
National Center for Microgravity Research
21000 Brookpark Rd
Cleveland, OH 44135-3191

INTRODUCTION

Near-limit flames cannot be studied under normal-gravity conditions, as the induced buoyant flow does not allow for their stabilization. Such flames are of significant fundamental interest as they are particularly sensitive to chain-mechanism competitions, thermal radiation, and unsteadiness [*e.g.* 1]. Furthermore, the dynamics of such flames are of interest in terms of fire safety in reduced gravity environments such as the space station and space vehicles. This point has been realized and indeed the extinction limits of such flames have been measured in drop towers [2, 3]. Those measurements have been independently conducted in counterflow configurations in which symmetric premixed flames were stabilized and subsequently extinguished. The determination of the extinction limits was based, however, on global strain rates, as detailed fluid mechanics diagnostics were not available on drop towers. While global strain rates do demonstrate qualitatively the effect of fluid mechanics on the flame response, the details of the flow-field at the flame vicinity can also have a first order effect on the flame dynamics especially for near-limit concentrations. More specifically, the very low velocities that are involved may result in rather thick boundary layers so that assumptions such as top-hat velocity profiles at the nozzle exit could be incorrect. Furthermore, the local strain rate just before the flame can be noticeably different compared to the value derived based on global description.

OBJECTIVES

The main objective of this research is to introduce accurate fluid mechanics measurements diagnostics in the 2.2-s drop tower for the determination of the detailed flow-field at the states of extinction. These results are important as they can then be compared with confidence with detailed numerical simulations so that important insight is provided into near-limit phenomena that are controlled by not well-understood kinetics and thermal radiation processes. Past qualitative studies did enhance our general understanding on the subject. However, quantitative studies are essential for the validation of existing models that subsequently be used to describe near-limit phenomena that can initiate catastrophic events in micro- and/or reduced gravity environments.

EXPERIMENT APPROACH

As part of this research, a new Digital Particle Image Velocimetry (DPIV) system has been developed appropriate for the GRC 2.2-s Drop Tower. A schematic of the system is shown in

Fig.1. A dual head Nd-YAG laser with beam conditioning optics is focused into a quartz fiber optic cable with a 1 mm diameter core. The laser operates at 532 nm and each head has a repetition rate of up to 30 Hz, a pulse length of 5 ns, and theoretical pulse energy of up to 30 mJ (both the pulse rate and energy are user selectable). On the rig end of the fiber we measured a pulse energy of 13 mJ/pulse without having the laser on its highest capacity, which provided plenty of energy for particle illumination. The wide beam divergence from the fiber requires some trial and error with lenses to get a light sheet that is both thin and illuminates the region of interest. We settled on a bi-convex spherical lens with a focal length of 88.3 mm, followed by a plano-convex cylindrical lens of focal length 150 mm to form the light sheet. Given the space limitation of the rig, a L-shaped light path is used. In order to decrease the laser scattering, the test section is almost fully closed using aluminum sheet with black paper cover.
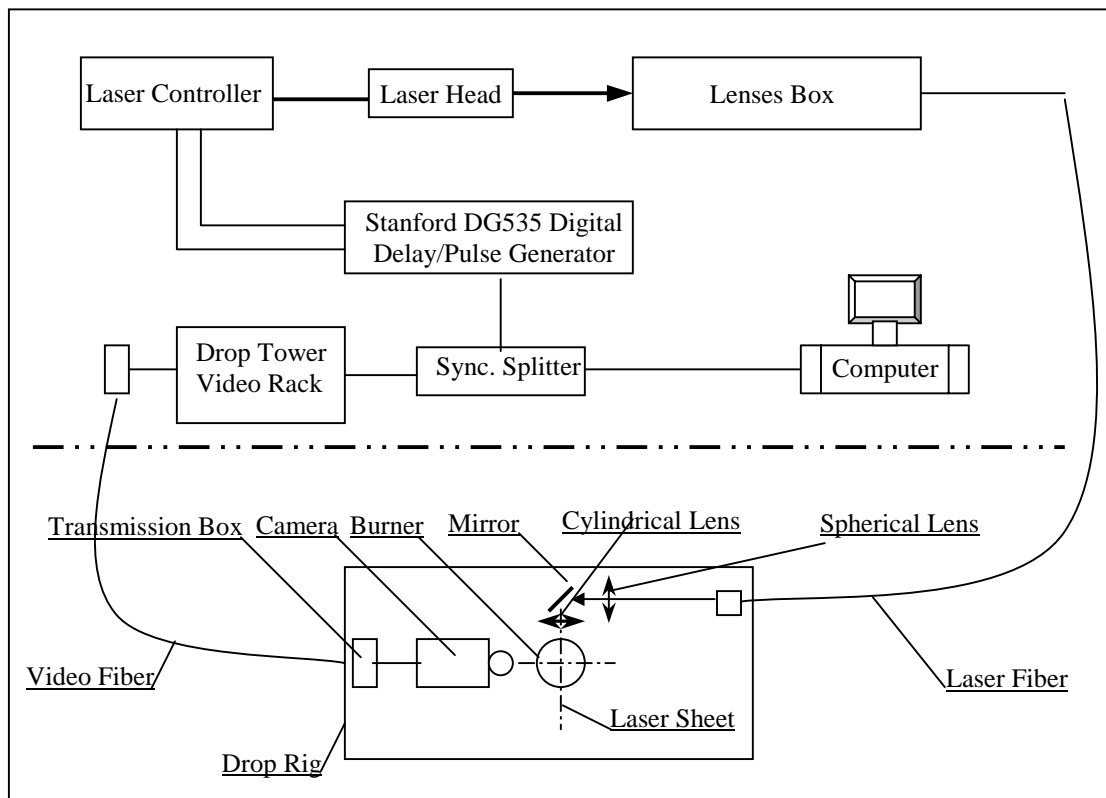
Fig.1 Schematic of 2.2s Drop Tower PIV System

The plane of the light sheet was aligned with a special jig to be along the burner centerline perpendicular to the optical axis of the camera. A Pulnix TM 9701 progressive scan CCD camera was used to record the PIV images and the video signal was sent to the top of Drop Tower via the video fiber. Once there, the signal was split by an odd field pulse delay box, with the video signal going to a Matrox frame-grabber, and the sync signal going to a digital delay/pulse generator, which in turn controlled the laser.

Similarly to our previous studies [3], the counterflow configuration is used for the flame stabilization. It consists of two burners equipped with 30 mm contoured-shaped nozzles that are separated by 50 mm. The seed particles used are 5 μm Al_2O_3, which are introduced into the lower burner and carried out by the flow. A 5 mm extension tube is used with the camera lens to

get the 200 pixels/cm resolution. An optical filter with a pass band from 460 nm to 540 nm is mounted in the front of the camera lens to minimize the luminous emission from the flames.

The Correlation Image Velocimetry (CIV) post-processing software is used to calculate displacement fields from each image pair. CIV has the useful property that the search distances for performing correlations is decoupled from the search box size itself. This allows displacements and vector densities to be tuned independently to the appropriate flow characteristics.

SUMARY OF RESEARCH

The performance of nozzles that have been designed by using 5th polynomial contraction contour [4,5] was assessed experimentally. Figures 2a and 2b depict DPIV results from 1g tests. This kind of burner produces uniform velocity in the center area of the burner (Fig.2a). The thickness of the boundary layer decreases as the Reynolds number increases (Fig.2b). The existence of a boundary layer results in exit velocities at the centerline of the burner that are higher than the average velocity based on the flow rate. The exit velocity at the centerline can be 1.8 times more than the average velocity at low Reynolds number, when the velocity distribution is parabolic and no uniform area exists.
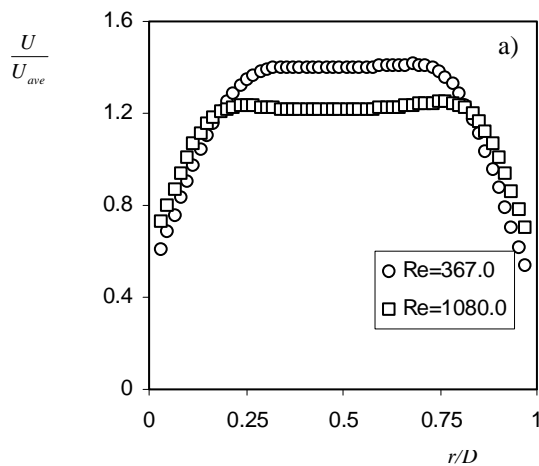
Fig.2a Comparison of exit velocity distributions at different Reynolds number
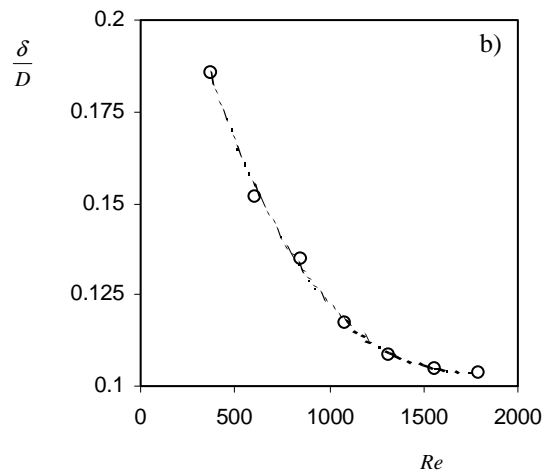
Fig.2b Variation of thickness of boundary layer against Reynolds number

The flame structures at low strain rates at 1g were investigated. Figure 3a depicts an example, where the minimum velocity measured just before the dilatation zone $S_{uref} = 18.1$ cm/s at $x = 2.5$ cm, and for strain rate $K \equiv (-du/dx)_{max} = 26.01/s$ at $x = 2.25$ cm. It is interesting to note that, for this weakly strained flame, the velocity distribution from nearly uniform around the burner exit gradually evolves to a non-uniform curvature around the flame (Fig. 3b). This phenomenon was also reported in a previous investigation [6].

Figure 4a is an example image from a cold flow microgravity test, and the corresponding vector map is shown in Fig. 4b. The weak point in the system remains the particle seeder, which is not always consistent. In order to avoid that problem, a nebulizer (a liquid particle generator) is introduced into the system. We use the nebulizer in 1g to produce 0.5 μm silicone oil droplet to trace the flow. The silicone oil does not have any observable effect on flames [7]. Two needle valves were used to adjust the ratio of the flow rate passing/not passing through the

nebulizer and subsequently control the seeding density. Test results demonstrate that silicone oil droplets work well.
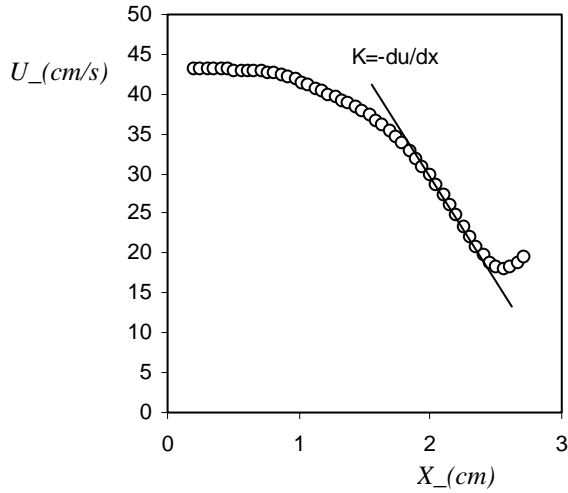
Fig.3a U(x) at the centerline of the jet from bottom burner, D=3.0cm, L=5.0cm, Φ(CH4/Air)=0.66
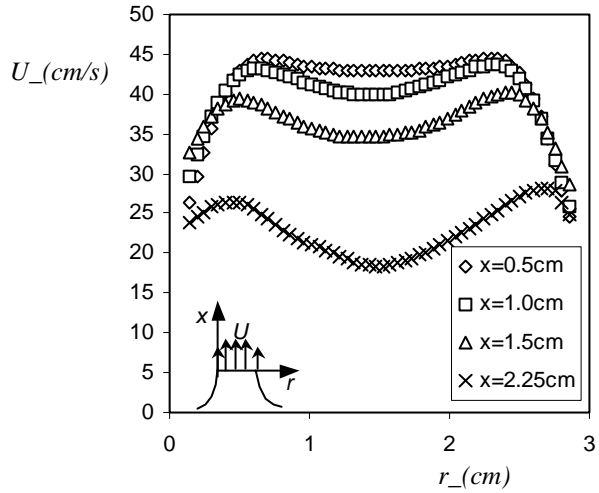
Fig.3b Evolution of velocity distribution along streamwise, D=3.0cm, L=5.0cm, Φ (CH4/Air)=0.66
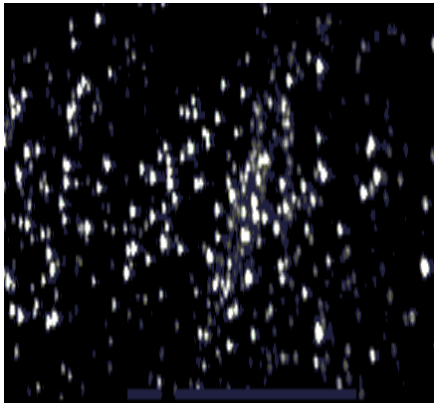
Fig.4a DPIV image from microgravity test
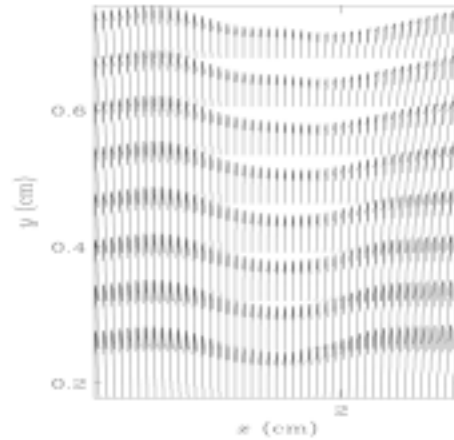
Fig.4b Calculated vector map for left image

REFERENCES

1. Egolfopoulos, F.N., *Proc. Combust. Inst.* **25**: 1375-1381 (1994).
2. Maruta, K., Yoshida, M., Ju, Y., and Niioka, T., *Combust. Inst.* **26**: 1283-1289(1996).
3. Zhang, H. and Egolfopoulos, F.N., *Combust. Inst.* **28**: 1875-1882 (2000).
4. Chmielewski, G.E., *J. Aircraft,* **11**: 435-438 (1974).
5. Tan-atichat, J., Nagib, H., and Drubka, R., Effects of Axisymmetric Contractions on Turbulence of Various Scales, *NASA CR*-165136, 1980.
6. Vagelopoulos, C.M., and Egolfopoulos, F.N., *Combust. Inst.* **27**: 513-519(1998).
7. Ueda, T., Yahagi, Y., and Mizomoto, M., *Transaction JSME* **B57-541**: 3255(1991).

GRAVITATIONAL INFLUENCES ON FLAME PROPAGATION THROUGH NON-UNIFORM, PREMIXED GAS SYSTEMS

Fletcher J. Miller and John Easton, National Center for Microgravity Research, MS 110-3, Cleveland, OH, 44135-3191, fletcher@grc.nasa.gov
Anthony Marchese and Fred Hovermann, Rowan University, Glassboro, NJ, 08028-1701

INTRODUCTION

Flame propagation through non-uniformly premixed (or layered) gases has importance both in useful combustion systems and in unintentional fires. As summarized recently [1] and in previous Microgravity Workshop papers [2-4], *non-uniform* premixed gas combustion receives scant attention compared to the more usual limiting cases of diffusion or *uniformly* premixed flames, especially regarding the role gravity plays. This paper summarizes our recent findings on gravitational effects on layered combustion along a floor, in which the fuel concentration gradient exists normal to the direction of flame spread. In an effort to understand the mechanism by which the flames spread faster in microgravity (and much faster, in laboratory coordinates, than the laminar burning velocity for uniform mixtures)[1], we have begun making pressure measurements across the spreading flame front that are described here. Earlier researchers, testing in 1g, claimed that hydrostatic pressure differences could account for the rapid spread rates [5]. Additionally, we present the development of a new apparatus to study flame spread in free (i.e., far from walls), non-homogeneous fuel layers formed in a flow tunnel behind an airfoil that has been tested in normal gravity.

EXPERIMENTAL APPARATUS FOR FLOOR LAYER STUDIES

The experimental rig, described more fully in earlier papers [1-4], consists of a porous bronze fuel holder 76 cm long by 10 cm wide by 3.2 mm deep, inside a thermally controlled tray that is covered by a stainless steel lid and Lexan gallery. The gallery has a 10 cm square cross section, and for the tests reported here had a closed top and ignition end, while the end opposite the igniter was open. The lid over the fuel holder retracts automatically, and after a predetermined time for fuel vapor to diffuse and form a stratified, flammable boundary layer along the floor, a flame is ignited at one end and spreads to the opposite end of the gallery. We use the same rig for the microgravity experiments in the NASA Glenn 2.2s Drop Tower, with ignition and flame spread after release. Two Cohu model 2200 color cameras image the flame spread from the top and side, each covering half of the gallery, which allows position vs. time data to be obtained.

As mentioned above, in an effort to understand the effects of gravity on the flow field, a microphone was added to the experiment drop rig to measure pressure before, during, and after flame ignition and spread. The microphone is a Brüel & Kjær model 4136 microphone (with a model 2670 preamplifier), installed 36 cm from the igniter and 1.7 cm above the fuel frit, with the microphone face parallel to the gallery side wall. The microphone face extends 0.7 cm from the sidewall. A laptop computer with a National Instruments model AI-16-E data acquisition card collected and recorded the microphone signals at 1000 Hz. The data acquisition software also activated a light emitting diode (LED) in the camera field of view at the start of data collection, allowing for correlation of the pressure and flame location data.

NUMERICAL MODEL FOR FLOOR LAYER STUDIES

The model used in this work was originally developed for studying flame spread across sub-flash liquids, primarily 1-propanol and 1-butanol [6]. The numerical model uses the SIMPLE algorithm [7] and a hybrid-differencing scheme to solve the gas-phase continuity, species,

energy, x-y momentum equations and the liquid phase energy and x-y momentum equations. To simulate the experiments, the model initially runs for a specified time period (e.g. 60 seconds) without introducing the ignition source. During this period, a time step of 5 ms is used. This allows the fuel to vaporize at the pool surface and diffuse into the gas phase, setting up initial conditions consistent with the experiments. The output from the non-reacting case becomes an input to the reacting case. Reference [8] contains a diagram and further description of the model, and changes we made to the code are detailed in [4].

NEW APPARATUS AND MODEL FOR FREE LAYERS

A major new initiative in this project has been the development of an apparatus to study flame spread through non-uniform free layers. By free layers, we mean those far from the influence of walls, which can impose heat and momentum loss to the flow field and flame. The details of the apparatus and model are given in [9,10]; here only a summary is given. To obtain a free layer of vaporized liquid fuel in air, the fuel is allowed to flow into a porous airfoil-shaped fuel dispenser in a slow convective flow inside a flow duct (Fig. 1). The fuel evaporates due to heating of the airfoil and forms a non-uniform flammable mixture in the laminar wake of the airfoil that extends the length of the flow duct. The convective flows of interest here are in the range of 10-40 cm/s, and the fuel used for the tests was ethanol. A side view video camera images the flame after it is ignited by a hot wire igniter.

RESULTS

Figure 2 shows the flame velocity as a function of diffusion time, as determined from the video record for 1-propanol at 27 °C, 31 °C, and 35 °C in both normal and microgravity. Also shown on the graph are the results for the numerical model. Both the model and the experiment show that the flame spreads faster in microgravity, with increasing initial temperature, and, to a slight degree, with increasing diffusion time (i.e., layer thickness). Of these, the gravitational influence is the most notable. See [1] for a discussion of possible reasons. That the model and the experiment do not agree quantitatively stems from the use of single step kinetics; no one set could be found that agreed at all temperatures.

In Figures 3 and 4 we present side view images of the flames in 1g and μg, respectively. Modeling results of reaction rate contours are also shown for the 1g flame in Fig. 3. The images and numerical computations reveal a double flame structure in 1g, with a premixed upper branch and a lower diffusion flame along the surface consisting of excess air that is unreacted after passing through the lean premixed flame and fuel vapor that evaporates from the surface. There appears to be a hint of a third branch near the surface that is quenched. The initial lean limit height is also labeled (note that the flame exceeds that height once it is spreading), and the flame height, H_f [1]. A representative μg flame is shown in Figure 4. Due to the rig design, we cannot image completely to the surface, so it is not possible to determine if there is a diffusion flame or not. The premixed flame, however, shows a much higher flame height for the same initial conditions. This increased height provides more flame surface area for burning and likely contributes to the flame spreading faster in μg.

To determine if the flame spread and shape are affected by hydrostatic pressure, we began pressure measurements as described above. Figure 5 presents the pressure measured by the microphone as a function of time for flame spread with a 20 second diffusion time, 35 °C initial temperature, in normal gravity. The red line in the figure indicates the time of flame ignition in the video record, and the green line indicates the time when the flame passed the microphone position in the video record. The microphone detects the ignition transients, which decay after time, and then shows the flame passing the microphone, apparently without a change in the pressure response. There is a sinusoidal change in the pressure toward the end of the test, in this case almost 0.4 seconds after ignition. The pressure rose approximately 4 Pa above the

background level, fell to 4 Pa below the background level, and then returned to the background reading. As Figure 5 shows, the microphone responds to ignition, but does not appear to respond to the flame front as it passes the microphone. The sinusoidal peak already described may arise from the flame reaching the end of the gallery. These experiments do not show the pressure response of the flame passing a microphone seen in [5]. One reason may be that the gallery walls in the current experiment have rubber strips along the bottom to prevent the escape of fuel vapor. These strips may not contain the pressure pulse from the propagating flame front. Future tests will determine the pressure profile in the flame spread experiments.

A free layer flame obtained with the new apparatus is shown in Fig.6. In this case, ethanol was used as the fuel and the opposed airflow velocity was 25 cm/s. The experiment is described more fully in [9,10]. The flame exhibits a triple like structure, with two branches on either side of the centerline, and a dim trailing flame. We did not measure the fuel concentration in this flow, so we are unable to say with certainty the conditions, but based on the cold flow modeling and measured fuel flow rate, the conditions should be on the lean side of stoichiometric. Thus, it is not a classic triple flame that spans rich to lean conditions. There is an ongoing effort as part of this project to make fuel concentration measurements [11]. The measured flame spread rate for this flame was 148 cm/s, not accounting for the 25 cm/s opposed free stream flow.

CONCLUSIONS

Tests reported here and in earlier papers conclusively show an affect of gravity on flame spread in nonuniform mixtures, with the flames spreading faster in the absence of gravity. The flame height is also higher in microgravity, consistent with faster flame spread. To test the hypothesis that pressure may be a factor, we began making pressure measurements across the flame front. Tests to date are inconclusive. A new apparatus for studying these flames away from the effect of walls has been developed and initial tests show the same high spread rates as for floor layers.

ACKNOWLEDGEMENTS

REFERENCES

[1]   F. J. Miller, J. W. Easton, A. J. Marchese, and H. D. Ross, "Gravitational Effects on Flame Spread Through Non-Homogeneous Gas Layers," *Proc .of the Comb. Inst.*, Vol.29, 2003 (to appear)

[2]   F. J. Miller, E. B. White, and H. D. Ross, "Gravitational Influences on Flame Propagation Through Non-Uniform Premixed Gas Systems," NASA CP-10194, 343-348, 1997.

[3]   F. J. Miller, J. Easton, H. D. Ross, and A. Marchese, "Gravitational Influences on Flame Propagation Through Non-Uniform Premixed Gas Systems," NASA/CP-1999-208917, 57-60, 1999.

[4]   F. J. Miller, J. Easton, A. Marchese, H. D. Ross, D. Perry, and M. Kulis, NASA/CP-2001-210826, 321-324 2001

[5]   M. Kaptein and C. E. Hermance, "Horizontal Propagation of Laminar Flames Through Vertically Diffusing Mixtures Above a Ground Plane," 16th Symposium (Int'l) on Combustion, 1295-1305, 1976.

[6]   D. N. Schiller, H. D. Ross, and W. A. Sirignano, "Computational Analysis of Flame Spread Across Alcohol Pools," *Combust. Sci. Technol.*, vol. 118, pp. 205, 1996.

[7]   S. V. Patankar, *Numerical Heat Transfer and Fluid Flow*, Hemisphere Publishing Corporation, NY, 1980.

[8]   F. J. Miller, J. Easton, A. Marchese, and H. D. Ross, "Flame Spread Through Non-Homogeneous Gas Layers," presented at the Western States Section of the Combustion Institute Spring 2000 Meeting, Golden, CO, March 2000. Paper number 13-4

[9]   F. Hovermann, "Flame Spread Through a Free Stratified Fuel/Air Mixture: an Experimental and Numerical Study," Master's Thesis, Rowan University, Dept. of Mech. Eng., 2003

[10] F. Hovermann, A. J. Marchese, and F. J. Miller, "Initial Results of Flame Spread Through a Free Stratified Layer," 3rd Joint Meeting of the US Sections of the Combustion Institute, Chicago, IL, March 16-19, 2003

[11] M. Kulis, D. Perry, F. J. Miller and N. D Piltch, "A Diode Laser Diagnostic for Fuel Vapor Measurements in Microgravity Flame Spread," this Workshop.
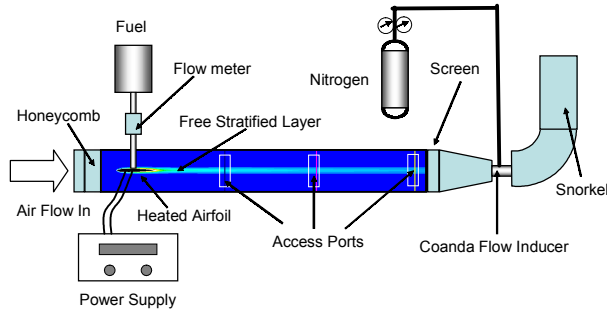
Figure 1. New apparatus for creating free layers of fuel/air mixtures.
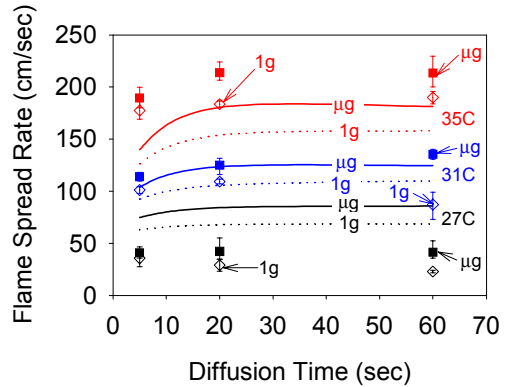
Figure 2 Flame spread rate vs. diffusion time for 1-propanol. Solid line is the model result.
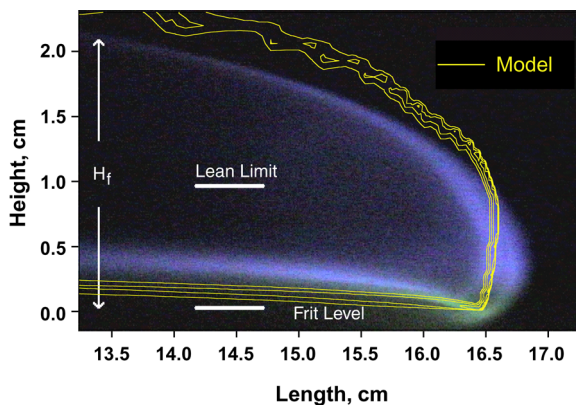
Figure 3. Side view of a 1g flame over 1-propanol at 27 °C in initially quiescent conditions.
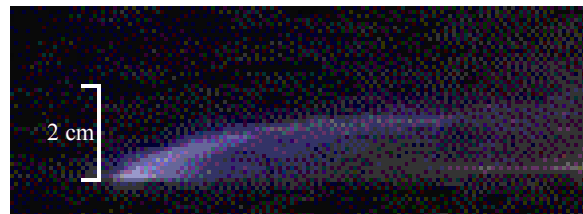
Figure 4. Side view of a μg flame over 1-propanol at 27 °C. The bottom 2 cm of the flame are cropped by the side wall. Total flame height is approximately 3 cm.
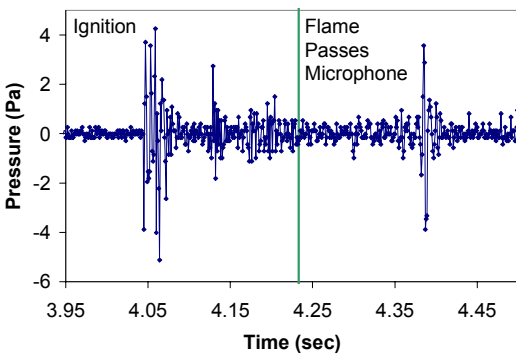
Figure 5 Pressure vs. time for flame spread over 1-propanol at 35 °C.
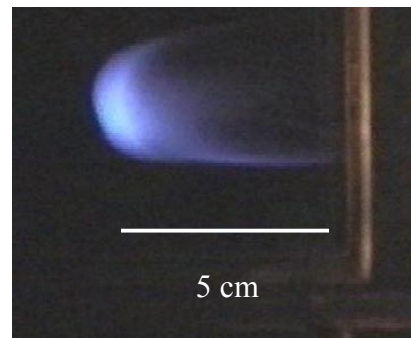
Figure 6 Side view of free layer ethanol flame.

Cool Flames in Propane-Oxygen Premixtures at Low and Intermediate Temperatures at Reduced-Gravity

Howard Pearlman[†], Michael Foster, Devrez Karabacak
Drexel University, Dept. of Mechanical Engineering and Mechanics, Philadelphia, PA 19104

INTRODUCTION

The Cool Flame Experiment aims to address the role of diffusive transport on the structure and the stability of gas-phase, non-isothermal, hydrocarbon oxidation reactions, cool flames and auto-ignition fronts in an unstirred, static reactor. These reactions cannot be studied on Earth where natural convection due to self-heating during the course of slow reaction dominates diffusive transport and produces spatio-temporal variations in the thermal and thus species concentration profiles (Griffiths, et al., 1971; Melvin, 1969). On Earth, reactions with associated Rayleigh numbers (Ra) less than the critical Ra for onset of convection (Ra_{cr}~600; Tyler, 1966; Fine, et al., 1970; Barnard and Harwood, 1974) cannot be achieved in laboratory-scale vessels for conditions representative of nearly all low-temperature reactions. In fact, the Ra at 1g ranges from 10^4-10^5 (or larger), while at reduced-gravity, these values can be reduced two to six orders of magnitude (below Ra_{cr}), depending on the reduced-gravity test facility.

Currently, laboratory (1g) and NASA's KC-135 reduced-gravity (μg) aircraft studies are being conducted in parallel with the development of a detailed chemical kinetic model that includes thermal and species diffusion. Select experiments have also been conducted at partial gravity (Martian, $0.3g_{earth}$) aboard the KC-135 aircraft. This paper discusses these preliminary results for propane-oxygen premixtures in the low to intermediate temperature range (310-350^oC) at reduced-gravity.

GROUND-BASED COOL FLAME AND AUTO-IGNITION STUDIES

<u>Laboratory Studies in a Mallard-LeChatlier Static, Unstirred Reactor</u>: A classic Mallard-LeChatlier apparatus (Mallard, 1880) was developed and used to conduct 1g and reduced-gravity experiments. A schematic of the hardware is shown in figure 1. It consists of a furnace, a fused-silica spherical vessel of given diameter (i.d.=10.2cm) and a gas delivery system. The furnace employs resistive heating elements in the rear and top panels, an internal mixing fan to circulate the hot air, three parallel 7.5cm diameter (0.32cm thick, 1.2cm separation distance) quartz windows on both the top and side walls of the furnace for viewing and a gas feedthrough built into the door. The temperature uniformity within the furnace is $\pm 10^oC$ throughout its operating range (20-600^oC), measured at random spatial locations using 0.51mm diameter wire, unsheathed, type-K thermocouples. The vessel pressure is recorded at 100Hz using a Setra 0-25psia Model 204 transducer (accuracy:$\pm$0.028psia=$\pm$1.4Torr) situated at the vessel inlet, on the cold side of the oven door. Two intensified, ultraviolet and visible-sensitive cameras operating at maximum gain (~10^{-6} fc minimum sensitivity) and full exposure, record the integrated light intensity at 30 frames/s.

[†] Corresponding Author
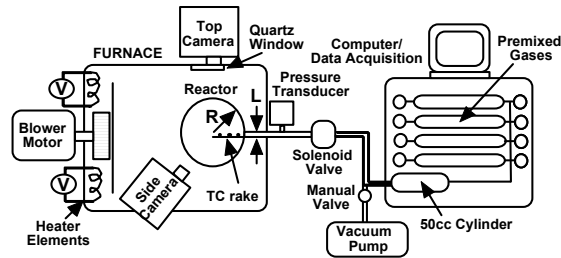
Fig. 1: Schematic of static, unstirred reactor, furnace and gas delivery system

Representative experimental results obtained at 1g for different initial pressures at two different vessel temperatures (a: T=310°C, b: T=320°C) are shown in figures 2a and 2b, respectively. At low pressures, steady, dark (non-visible) reaction is observed with induction periods on the order of minutes. As the pressure increases at fixed temperature, multiple cool flames occur. Further pressure increase results in a decrease in the first induction period. At sufficiently high initial pressures, two-stage ignition (a cool flame preceding a hot ignition) occurs. These and similar results at different temperatures (in the range of 300-400°C) are being used to compile detailed ignition diagrams.
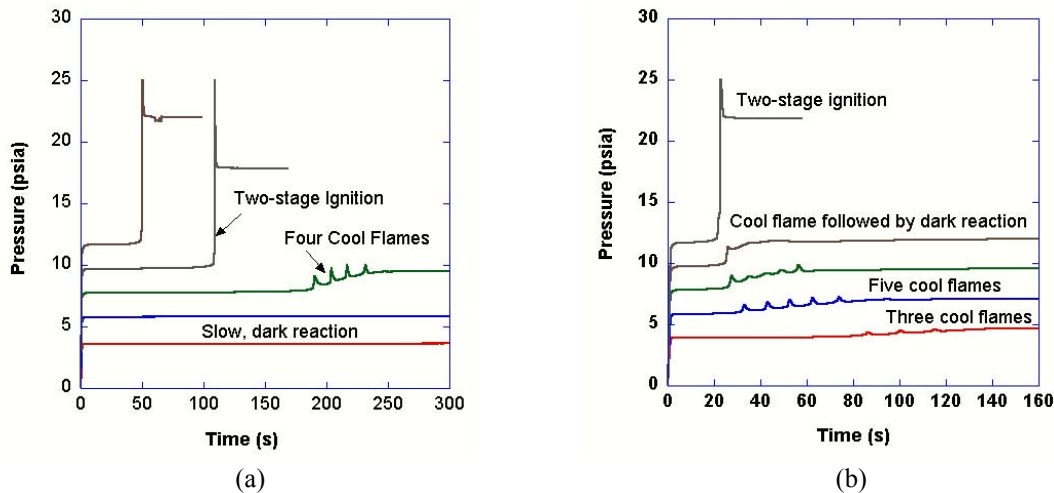
Fig. 2: Pressure histories at 1g at (a) T=310°C, (b) T=320°C for five experiments at different initial pressures. Mixture composition is $C_3H_8:O_2$ (1:1).

KC-135 Aircraft Reduced-Gravity and Martian-Gravity Results: Representative cool flame results obtained during KC-135 parabolic maneuvers at reduced-gravity using propane-oxygen mixtures at T=320°C are shown in figures 3a and 3b for pressures less than (and equal) to 7.7psia. At 7.7psia, one cool flame is observed with an induction period of 15s, followed by a steady, non-visible reaction that continues throughout the remainder of the available test time. Beyond 20s, the g-level is time-dependent and varies from 10^{-2}g to 1.8g (see lower curve in fig. 3b). This transitional period induces buoyant mixing in the vessel and a complicated pressure history. At lower initial pressures, experiments conducted at 3.9psia and 6.2psia show little evidence of reaction during the available reduced-gravity test time, while reaction in the subsequent "pull-up"/transitional g period following the reduced-gravity period is observed. Figure 3b shows a plot of the pressure history associated with the experiment conducted at 3.9psia along with the vertical-component of the acceleration. These results clearly demonstrate the need for additional reduced-gravity test time.
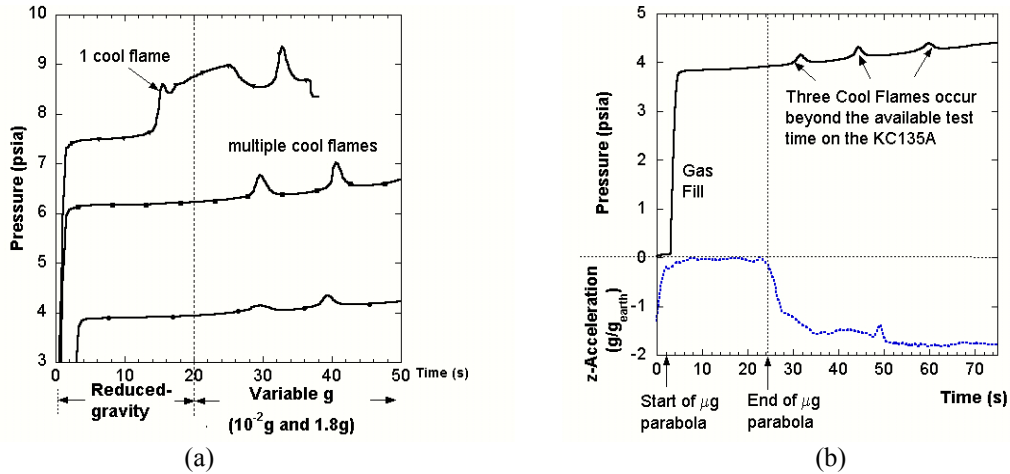
Fig. 3: Cool flames in C_3H_8:O_2 (1:1) mixture at different initial pressure at T=320°C and μg;
Reaction continues beyond the available reduced-gravity test time.

As mentioned, select experiments were also conducted at 0.3g_{earth} (Martian-g) to study the effect of "weak" convection/mixing without changing any physical parameters or the mixture composition (i.e., the Ra can be changed by varying g). The pressure histories obtained at 1g and μg and those obtained at 0.3g and 1g are plotted in figures 4a and 4b for nearly identical initial pressures (ranged from 7.5 to 7.8pia), fixed temperature (320°C) and fixed mixture composition.

At 1g, five sequential cool flames are observed. The first cool flame follows an induction period of approximately 27s. At 0.3g, two sequential cool flames are visually observed and the first induction period shortens to 15s. In contrast, only a single cool flame is observed at μg followed by a monotonic pressure increase until the end of the available 20s test time at which time the pressure gradient remains positive. The vertical-components of acceleration associated with these three tests are also shown in the lower half of figures 4a and 4b.
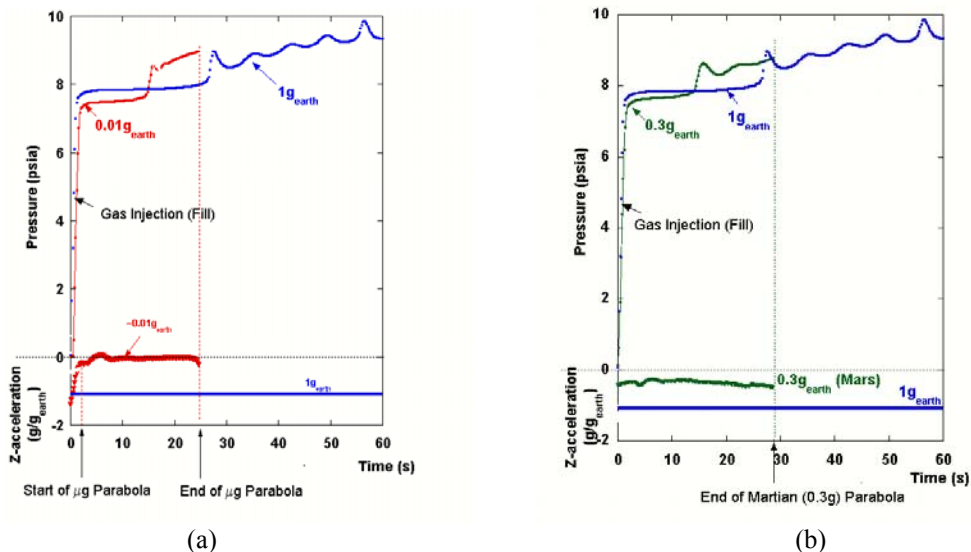
Fig. 4: (a) Comparison of pressure histories obtained at reduced-gravity (KC-135 aircraft) and 1g and (b) Martian gravity versus 1g for nearly identical initial pressures at T=320°C. The 1g data is the same in both (a) and (b). Mixture composition is C_3H_8:O_2 (1:1). The vertical component of acceleration is shown in the lower portion of the plot (negative value indicates downward acceleration).

<u>Imaging Cool Flames in Propane-Oxygen and Propane-Air Premixtures:</u> For the propane-oxygen and propane-air experiments reported herein, the overall intensity of the integrated ultraviolet and visible emission (integrated over the spectral sensitivity of the intensified camera) is significantly lower than that observed in earlier experiments with butane-oxygen reported by Pearlman (1999).   At maximum camera gain (10^{-6} fc), very few propane-oxygen and only one propane-air cool flame(s) have been imaged at reduced-gravity. Some of the clearest images obtained from the KC-135 testing at a: μg, b: 0.3g, and c: 1g in the propane-oxygen system are shown in figure 5. In all sequences shown, the temperature is fixed at $320^{\circ}C$.

| (a) | (b) | (c) |
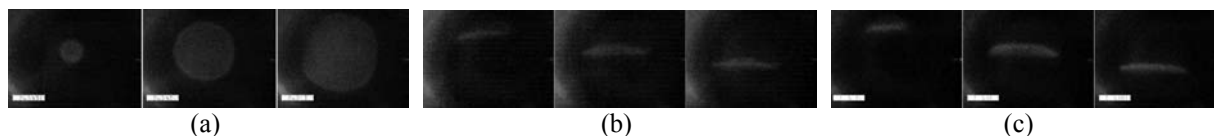
Fig. 5: Representative cool flame images in C_3H_8:O_2 at $320^{\circ}C$, 10.2cm i.d. quartz vessel at (a) μg ~10^{-2}g (12.0 psia), (b) 0.3g (7.6psia), and (c) 1g (7.8psia). Time lapse between sequential images in 1/3s.
Images have been enhanced for clarity.

CONCLUSIONS

Preliminary experimental results have been obtained for a propane:oxygen system at 1g, μg, and 0.3g. Multiple cool flames have been observed at 1g and 0.3g, yet only a single cool flame has been observed at μg within the available test time. Reaction is observed to continue beyond the 20s available on the KC-135 aircraft. Qualitatively, the frequency of oscillation is observed to decrease as g-level decreases (second and subsequent induction periods decrease with a decrease in g-level). Cool flames at 0.3g appear qualitatively similar to those at 1g, yet those at μg are radially (presumably spherically) symmetric. Ignition diagrams will be developed using this and subsequent reduced-gravity data. Additional work is needed to quantify the role of g-jitter (gravitational fluctuations) on the spatio-temporal structure and evolution of reduced-gravity cool flames. Numerical models will be tuned based on these results and used to predict the behavior of cool flames beyond the available 20s in ground-based facilities. These results will guide the planned space-flight experiment.

ACKNOWLEDGMENTS

REFERENCES

1. Barnard, J.A. and Harwood, B.A. (1974) Combustion and Flame **22** 35-42.
2. Fine, D.H., Gray, P. and MacKinven, R. (1970) Royal Society of London **A316** 223-240.
3. Griffiths, J.F., Gray, B.F., and P. Gray (1971) 13th Symposium (Int.) on Comb., 239-248.
4. Mallard, E. and LeChatelier, H.L. (1880) C.R. Acad. Sci. Paris **91** 825.
5. Melvin, A. (1969) Combustion and Flame **13** 438-9.
6. Pearlman, H. (1999) Combustion and Flame **121** (1-2) 390-3.
7. Tyler, B.J. (1966) Combustion and Flame **10** 90-91.

STUDIES OF PREMIXED LAMINAR AND TURBULENT FLAMES AT MICROGRAVITY

O. C. Kwon, M. Abid, J. Porres, J. B. Liu, P. D. Ronney
University of Southern California, Los Angeles, CA 90089-1453

P. M. Struk, K. J. Weiland
NASA Glenn Research Center, Cleveland, OH 44135

INTRODUCTION

Several topics relating to premixed flame behavior at reduced gravity have been studied. These topics include: (1) flame balls; (2) flame structure and stability at low Lewis number; (3) experimental simulation of buoyancy effects in premixed flames using aqueous autocatalytic reactions; and (4) premixed flame propagation in Hele-Shaw cells. Because of space limitations, only topic (1) is discussed here, emphasizing results from experiments on the recent STS-107 Space Shuttle mission, along with numerical modeling efforts.

STRUCTURE OF FLAME BALLS AT LOW LEWIS-NUMBER (SOFBALL) EXPERIMENT

The objective of the SOFBALL space flight experiment was to study weakly burning flames in hydrogen-oxygen-inert and methane-oxygen-inert mixtures in a configuration called "flame balls" that were originally predicted by Zeldovich in 1944 but not seen experimentally until over 40 years later in short-duration drop tower experiments [1]. Because flame balls are steady, convection-free, spherically symmetric and occur in fuels with simple chemistry, they represent the simplest possible interaction of chemistry and transport in flames. In this sense flame balls bear a similar relationship to combustion research that the fruit fly does to genetics research.

On STS-107 a total of 39 tests were performed in 15 different mixtures, resulting in a total of 55 flame balls, of which 33 were named by the crew. Most tests (by design) produced only 1 flame ball, though one test intentionally designed to produce a large number of flame balls resulted in 9 balls. The total burn time for all flames was 6 $\frac{1}{4}$ hours. Since flame balls are extremely sensitive to gravitational acceleration, all tests were conducted during orbiter free drift periods. The quality of the microgravity was found to be excellent, averaging less than 1 micro-g for most tests. Over half of the science data was downlinked during the mission, resulting in minimal loss of science despite the loss of Columbia and its crew. Among the accomplishments of the experiment were

- The weakest flames ever burned, either in space or on the ground. The weakest flame balls produced about 0.5 watts of thermal power. By comparison a birthday candle produces about 50 watts of thermal power.
- The leanest flames ever burned, either in space or on the ground. The leanest hydrogen-air test points contained 3.2 mole percent H_2 in air (equivalence ratio < 0.079).
- The longest-lived flame ever burned in space (81 minutes)

Several totally new results were found, including

- Oscillating flame balls that were predicted theoretically [2] but heretofore never observed experimentally (Fig. 1). It is not been established whether the mechanism outlined in [2] is responsible for the observed oscillations.
- For some tests, particularly in methane-oxygen-sulfur hexafluoride mixtures, flame ball drift not related to gravitational disturbances nor interactions with other balls or walls. This was a completely unexpected and as yet unexplained result.

Several issues not resolved during the previous space flight experiments on STS-83 and STS-94 in 1997 [3] were addressed by experiments on STS-107:

- *Can flame balls last much longer than the 500 sec maximum test time on STS-83 and STS-94 if free drift (no thruster firings) can be maintained for the entire test*? Answer: not usually - some type of flame ball motion, not related to microgravity disturbances, causes flame balls to drift to walls within ≈ 1500 seconds. The only exception to this was the

very last test in which 9 flame balls formed initially (Fig. 2) and extinguished one by one until only one (name "Kelly" by the crew) remained. Unexpectedly, Kelly survived 81 minutes, seemingly immune to drift, until it was intentionally extinguished due to operational limitations (it was still burning at the time). The mechanism responsible for the drift of isolated flame balls has not yet been identified, though some mechanisms have been proposed [4]. The shorter-than-expected test times on most tests meant enough time for multiple reburns of each mixture within the flight timeline.

- *Can oscillating flame balls be observed in long-duration, free-drift conditions*? Answer: Probably, but it is still necessary to determine if flame ball motion rather than inherent oscillations of stationary flame balls may have caused the observed oscillations).
- *Are higher Lewis number flame balls (e.g. H_2-O_2-He-CO_2, Le ≈ 0.8) more likely to oscillate, as predicted theoretically* [2]? Answer: No. These flames were extremely stable (Fig. 3).
- Do the flame balls using methane (CH_4-O_2-SF_6 mixtures) behave differently from those in hydrogen fuel (*e.g.* H_2-O_2-SF_6 mixtures)? Answer: Yes. They frequently drifted in corkscrew patterns, though again the mechanism responsible for this drift is not clear.
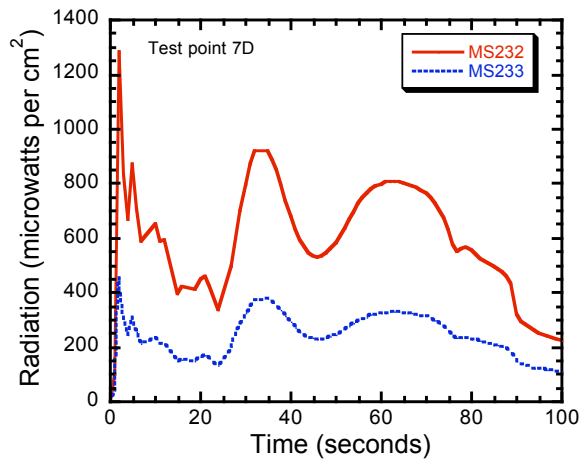
Figure 1. *Signals from two different radiometers showing flame ball oscillations. Mixture: 9.9% CH_4 – 19.8% O_2 – 70.3% SF_6 at 1 atm. This test produced 1 flame ball.*
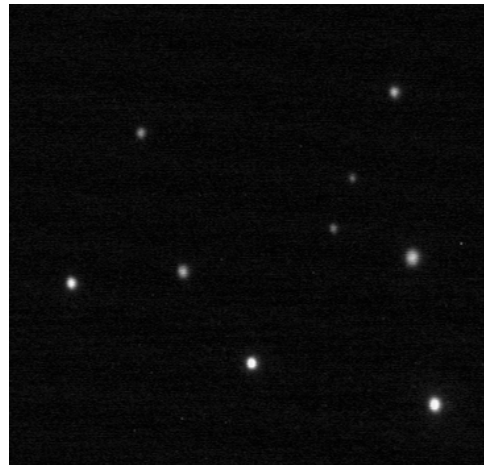
Figure 2. *Image of flame balls in a 7.5% CH_4 – 15% O_2 – 77.5% SF_6 mixture at 3 atm.*

NUMERICAL MODELING OF FLAME BALLS

Despite their simplicity, flame balls present a number of interesting challenges to the computationalist. In particular, prior computations comparing results obtained assuming optically thin vs. optically opaque (no transmission) CO_2 radiation suggest that reabsorption of emitted radiation is probably a dominant effect in flame ball mixtures diluted with CO_2. Consequently, an investigation of the effects of reabsorption of emitted radiation on flame balls was conducted using a numerical code [5] with detailed chemical, transport, and radiative emission-absorption models. A Statistical Narrow Band – Discrete Ordinates method was used to model radiative transport [6]. The boundary conditions were ambient temperature and composition at the outer boundary with a blackbody wall. Zero gradient and zero radiative flux conditions were enforced at r = 0.

The predicted flame radius (r^*), which is defined at the location of maximum volumetric heat release, and total radiative heat loss are plotted as a function of fuel-equivalence ratio (ϕ), for H_2-air mixtures with and without reabsorption in Fig. 4. Consistent with theory [7], for this stable solution branch r^* increases with fuel concentration for both cases with and without reabsorption. It is observed that reabsorption of emitted radiation leads to larger flame ball sizes and extinction limits shifted toward weaker fuel concentrations than calculations using optically-thin radiation models. In addition, it is noteworthy that the total radiative loss is actually greater with

reabsorption. Figure 4 also shows comparisons between the numerical predictions and the space experimental results. The agreement between model and experiment is better with regard to flame radius, but worse with respect to radiative loss, when reabsorption (i.e. optically-thick radiation) effects are considered.

Figure 5 shows the predicted flame radius and total radiative heat loss as a function of fuel concentration for H_2-O_2-CO_2 mixtures with and without reabsorption, along with the space experimental results. In this case much stronger reabsorption effects can be anticipated because the diluent gas itself is strongly emitting/absorbing. In fact, the net radiative loss with reabsorption was only about 1/1000 that that would occur with the same temperature and species concentration profiles were the mixture optically thin. Similar to the H_2-air mixtures (Fig. 4), Fig. 5 shows that the agreement between model and experiment is better with regard to flame radius when reabsorption effects are considered, although the agreement is somewhat worse than that for the H_2-air mixtures. In addition, when reabsorption effects are considered, comparison with the experiments is more favorable with respect to the total heat loss, which is different from the case of the H_2-air mixtures.
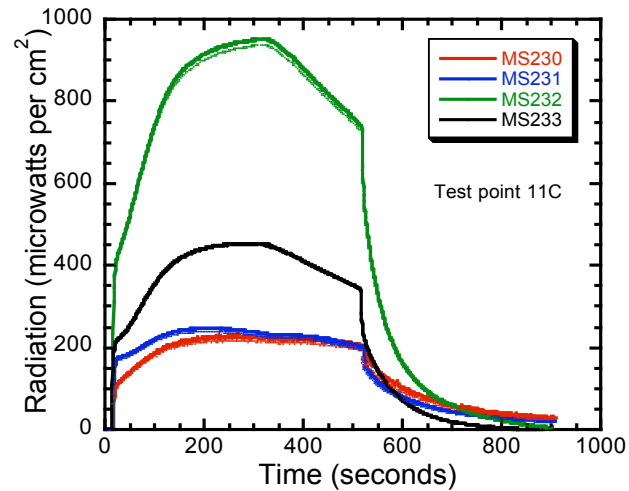
Figure 3. Signals from two different radiometers showing flame ball oscillations. Mixture: 9.9% CH_4 − 19.8% O_2 − 70.3% SF_6 at 1 atm. This test produced 1 flame ball.
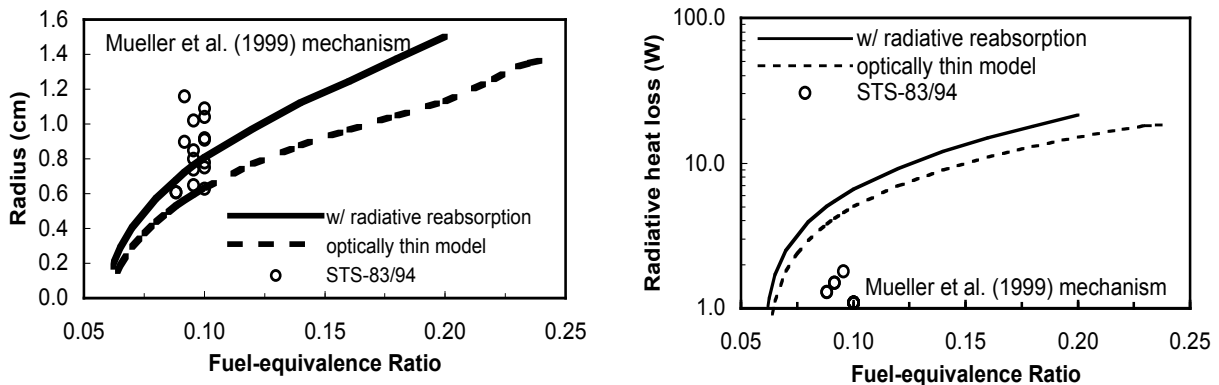
Figure 4. Predicted (lines) and measured (symbols) flame ball radius (left) and total heat loss (right) as a function of fuel-equivalence ratio for steady H_2-air flame balls at 1 atm. Predictions based on the Mueller et al. (1999) mechanism and with Soret effects. Measurements from Space Shuttle missions STS-83 and STS-94.

Figure 6 (left) shows the predictions of flame ball radius as a function of fuel-equivalence ratio for the H_2-air mixtures, using the GRI mechanism [8], with and without the Soret effect. As shown in the figure, the Soret effect is found to be significant; in particular, for the near-extinction limit conditions the predicted values of r^* with the Soret effect almost double those of r^* without the effect. This observation was somewhat expected because it has an effect similar to increasing the fuel concentration or decreasing the effective Lewis number. In order to evaluate the effect of different reaction mechanisms, the predictions of flame ball radius as a function of fuel-equivalence ratio for the H_2-air mixtures are shown in Fig. 6 (right). For this comparison, the

Soret effect was included for both the cases. Considering the comparison of the predictions with the space experimental results in Fig. 1, although the Mueller *et al.* [9] mechanism provides a slightly better prediction with respect to flame radius, it does not with respect to total heat loss.
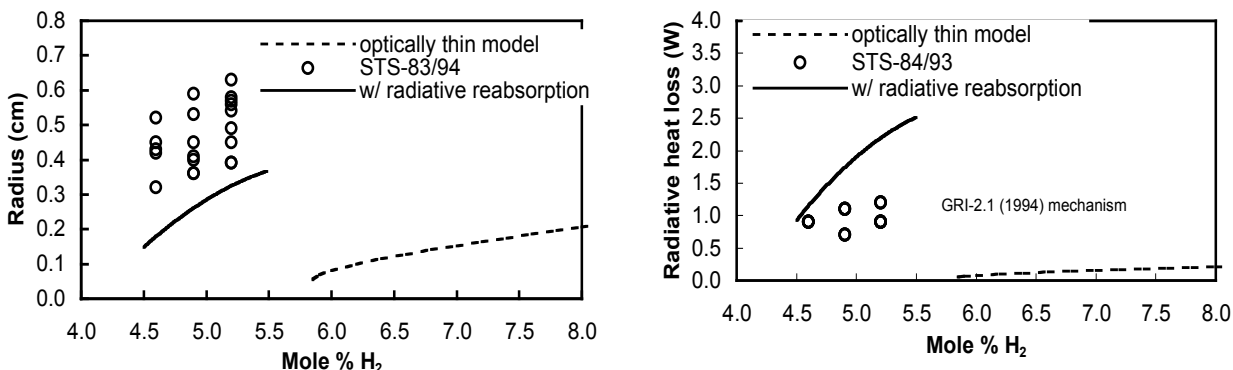
Figure 5. Predicted (lines) and measured (symbol) flame ball radius (left) and total heat loss (right) as a function of fuel concentration (%) for steady H_2-O_2-CO_2 flame balls of $\phi = 0.25$ at 1 atm. Measurements from Space Shuttle missions STS-83 and STS-94.
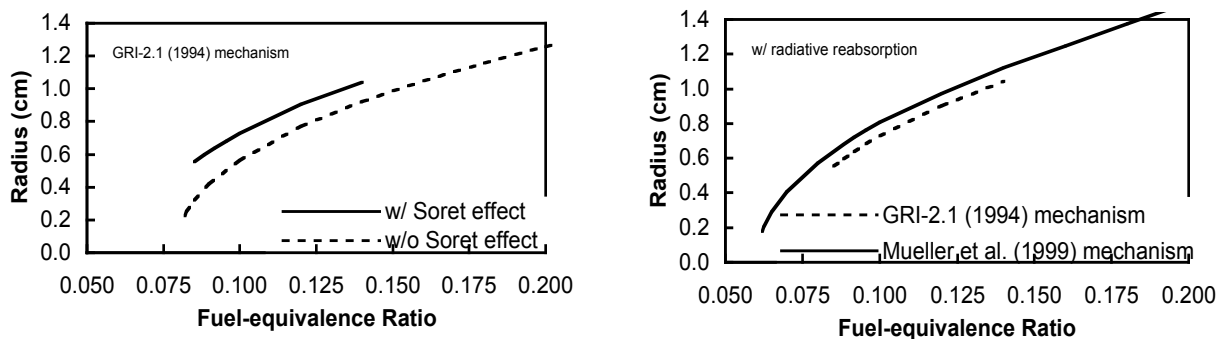
Figure 6. Left: predicted flame ball radius as a function of fuel-equivalence ratio for steady H_2-air flame balls at 1 atm, with and without Soret effects. Right: predicted flame ball radius as a function of fuel-equivalence ratio for steady H_2-air flame balls at 1 atm, with radiative reabsorption and Soret effects, comparing the Mueller et al. (1999) and GRI (Frenklach et al., 1994) mechanisms.

REFERENCES

1. Ronney, P. D., <u>Combustion and Flame</u>, Vol. 82, 1990, pp. 1-14.
2. Buckmaster, J. D., Joulin, G. and Ronney, P. D., <u>Combustion and Flame</u>, Vol. 79, 1990, pp. 381-392; *Ibid.*, <u>Combustion and Flame</u>, Vol. 84, 1991, pp. 411-422.
3. Ronney, P. D., Wu, M. S., Pearlman, H. G. and Weiland, K. J., <u>AIAA Journal</u>, Vol. 36, 1998, pp. 1361-1368.
4. Drift papers
5. Rogg, B., <u>RUN-1DL: The Cambridge Universal Flamelet Computer Code</u>, 1993.
6. Liu. F., Gulder, O. L., Smallwood, G. J. and Ju, Y., <u>International Journal of Heat and Mass Transfer</u>, Vol. 41, 1998, pp. 2227-2236.
7. Buckmaster, J. D. and Smooke, M., <u>Combustion and Flame</u>, Vol. 94, 1993, pp. 113-124.
8. Frenklach, M., *et al.*, "An Optimized Kinetics Model for Natural Gas Combustion," <u>25th Symposium (International) on Combustion</u>, Poster 26, Session 3, 1994.
9. Mueller, M. A., Kim, T. J., Yetter, R. A. and Dryer, F. L., <u>International Journal of Chemical Kinetics</u> Vol. 31, 1999, pp. 113-125.

EXTINCTION CRITERIA FOR OPPOSED-FLOW FLAME SPREAD IN A MICROGRAVITY ENVIRONMENT

SUBRATA BHATTACHARJEE
CHRIS PAOLINI
San Diego State University, San Diego, California

and

KAZUNORI WAKAI
SHUHEI TAKAHASHI
Gifu University, Gifu, Japan

INTRODUCTION: A simplified analysis is presented to extend a previous work [1] on flame extinction in a quiescent microgravity environment to a more likely situation of a mild opposing flow. The energy balance equation, that includes surface re-radiation, is solved to yield a closed form spread rate expression in terms of its thermal limit, and a radiation number that can be evaluated from the known parameters of the problem. Based on this spread rate expression, extinction criterions for a flame over solid fuels, both thin and thick, have been developed that are qualitatively verified with experiments conducted at the MGLAB [2] in Japan. Flammability maps with oxygen level, opposing flow velocity and fuel thickness as independent variables are extracted from the theory that explains the well-established trends in the existing experimental data [3].

Thermal Regime: An energy balance for the solid phase control volume of Fig. 1 can be written as.

$$\lambda_g \frac{\left(T_f - T_v\right)}{L_g} L_g - \varepsilon\sigma\left(T_v^4 - T_\infty^4\right)L_g \sim V_f \rho_s c_s \tau_h \left(T_v - T_\infty\right) \tag{1}$$

where, T_f and T_v are characteristic flame and vaporization temperature, τ_h is the thickness of the heated layer, and $L_g = \alpha_g / \left(V_f + V_g\right)$ is the gas-phase length scale. For thin fuels in the thermal limit, $\tau_h = \tau$ and $\varepsilon = 0$ produces the de Ris solution $V_{f,\text{th,thn}} \sim \left(\lambda_g / \rho_s c_s \tau\right)F$, where $F \equiv \left(T_f - T_v\right)/\left(T_v - T_\infty\right)$. Using $V_{f,\text{th,thn}}$ to non-dimensionalize V_f , $\eta_f \equiv V_f / V_{f,\text{th,thn}}$ Eq. (1) can be expressed in non-dimensional form as follows.

$$\left(\eta_f^2 + \eta_f\eta_g\right)\frac{\tau_h}{\tau} - \left(\eta_f + \eta_g\right) + \Re_0 \sim 0 \text{; where, } \Re_0 \equiv \frac{1}{F^2}\frac{\rho_s c_s}{\rho_g c_g}\frac{\varepsilon\sigma\tau}{\lambda_g}\left(\frac{T_v^4 - T_\infty^4}{T_v - T_\infty}\right), \eta_g \equiv \frac{V_g}{V_{f,\text{th,thn}}} \tag{2}$$

The thermal thin limit $\eta_{f,\text{th,thin}} \sim 1$ is recovered when $\Re_0 = 0$ and $\tau_h = \tau$. To obtain a more general solution τ_h / τ for a thick fuel can be scaled as

$$\frac{\tau_h}{\tau} \sim \frac{\sqrt{\alpha_s t_{\text{res,s}}}}{\tau} \sim \sqrt{\frac{\alpha_s L_g}{\tau^2 V_f}} \sim \frac{\Omega}{F}\frac{1}{\sqrt{\eta_f\left(\eta_f + \eta_g\right)}} \quad \text{where, } \Omega \equiv \sqrt{\frac{\lambda_s \rho_s c_s}{\lambda_g \rho_g c_g}} \quad . \tag{3}$$

Substituting this into Eq. (2) and still ignoring radiation, we obtain the thermal limit for semi-infinite fuel beds.

$$\eta_{f,\text{th,thick}} \sim \frac{F^2}{\Omega^2}\eta_g\left(1 - \frac{F^2}{\Omega^2}\right)^{-1} \sim \frac{F^2}{\Omega^2}\eta_g \text{ if } \tau \geq \tau_h; \text{ or, } \tau \geq \frac{\lambda_s}{\rho_g c_g V_g F}; \text{ or, } \eta_g \geq \frac{\Omega^2}{F^2} \tag{4}$$

The simplification above is achieved because for both PMMA and cellulose it can be shown that $F < \Omega$. Equation (4) also provides a criterion for transition between the thin and the thick limit for $\eta_g \gg 1$. Prediction from Eq. (4)

is plotted in Fig. 2 showing the transition from the thin to the thick limit in the thermal regime. Not much data in the thick-thin transitional region is available to verify this simple transition criterion.

Radiative Regime: The energy balance equation, Eq. (2), is solved in both the thick and thin limit producing

Thin Limit: $\eta_{f,\text{thin}} \sim \dfrac{1-\eta_g}{2} + \dfrac{1}{2}\sqrt{\left(1+\eta_g\right)^2 - 4\Re_0}$; **Thick Limit:** $\eta_{f,\text{thick}} \sim \dfrac{F^2}{\Omega^2}\eta_g\left(1-\dfrac{\Re_0}{\eta_g}\right)^2$; (5)

These results are plotted in Figs. 3 and 4 for several values of the radiation parameter $\Re_0$. A number of important features of the radiative effects on flame spread rates are revealed by these plots. When $\Re_0 > 0$, the slope of the spread rate curves decreases with opposing velocity for thin fuels while this trend is completely reversed for thick fuels. The MGLAB data [2] for flame spread over thin PMMA, shown in Fig 5, support this predicted trend for thin fuels. The DARTFIRE experiments [4] for flame spread over thick PMMA lends supports to the trends predicted by Fig. 4.

Obvioulsy, for $\Re_0 = 0$ and/or $\eta_g \to \infty$, the thermal limits are recovered with $\eta_{f,\text{thin}} = 1$ and $\eta_{f,\text{thick}}$ being proportional to η_g. To establish a criterion for the transition between the thermal and radiative regimes, we simplify Eq. (5) assuming $\eta_g \gg 1$. If the spread rate is non-dimensionalized by the corresponding thermal limit, Eq. **Error! Reference source not found.** for both the thick and thin limit can be shown to approach the same form.

Thin and Thick Fuels: For $\eta_g \gg 1$, $\quad \eta_f' \equiv \dfrac{V_f}{V_{f,\text{thermal}}} \sim \left(1-\dfrac{\Re_0}{\eta_g}\right)^2 \sim 1-2\Re_V$; where, $\Re_V \equiv \dfrac{\Re_0}{\eta_g}$ (6)

A single parameter $\Re_V$, therefore, controls the radiative effects on the spread rate for both thermally thin and thick fuels. η_f' from Eq. (6) is plotted in Fig. 6 against versus $1/\Re_V$, so that the abscissa is proportional to V_g. Superposed on this figure are experimental spread rates from MGLAB experiments, only part of which were previously reported [2]. Although the spread of the data around the prediction of Eq. (6) is substantial, the onset of radiative effects seems to be well correlated by the analytical prediction.

Extinction Criteria: The spread rate expressions of Eq. (5) can be used to establish criterion for flame extinguishment. As can be seen from Figs. 3 and 4, there are two types of extinction behavior. For $\eta_g \geq 1$, in both the thin and thick limit, steady flame cannot be sustained provided $\eta_g > \Re_0$, a criterion that is independent of fuel thickness. For $\eta_g < 1$, the thick fuel criterion remains unaltered. However for thin fuels, the spread rate assumes complex values, an indication of extinguishment, when $\eta_g < 2\sqrt{\Re_0}-1$. For flame spread over PMMA, these criteria are combined in the flammability map of Fig. 7. Note that for a critical thickness can be calculated from the relation $\eta_g = \Re_0 = 1$, beyond which extinction is independent of fuel thickness, thereby, defining a radiatively thick fuel.

Conclusion

In this article we present a simplified analysis to develop for the first time a closed-form expression for the spread rate and extinction criterion for flame spread over condensed fuels in a mild opposing-flow microgravity environment. The results presented are supported by experiments on thin PMMA conducted in the MGLAB.

REFERENCES: [1] Bhattacharjee, S., Takahashi, Wakai, K., A., *Prediction of a Critical Fuel Thickness for Flame Extinction in a Quiescent Microgravity Environment,* Combustion and Flame, to appear, 2003

[2] Takahashi, S., Kondou, M., Wakai, K., A., Bhattacharjee, S., Proceedings of the Combustion Institute, Vol 29, 2002.)

[3] Olson, S.L., Ferkul, P.V., and T'ien, J.S., Proceedings of the Combustion Institute, 22:1213, (1988)

[4] Altenkirch, R.A, Olson, S., and, Bhattacharjee, S., "Diffusive and Radiative Transport in Fires", NASA Contract NCC3-221 (1993-1998)
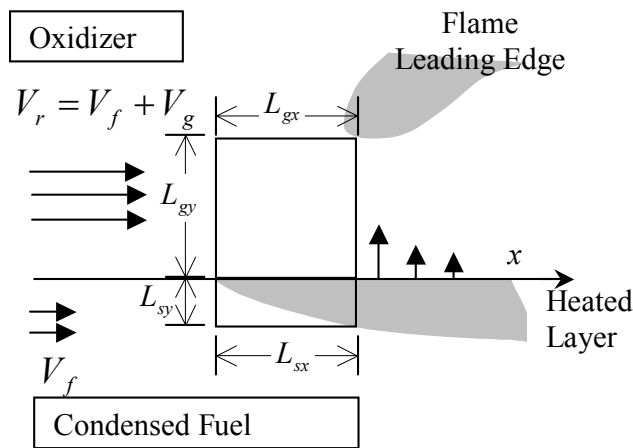
Fig. 1 Control volumes at the flame leading edge in the gas and the solid phases.
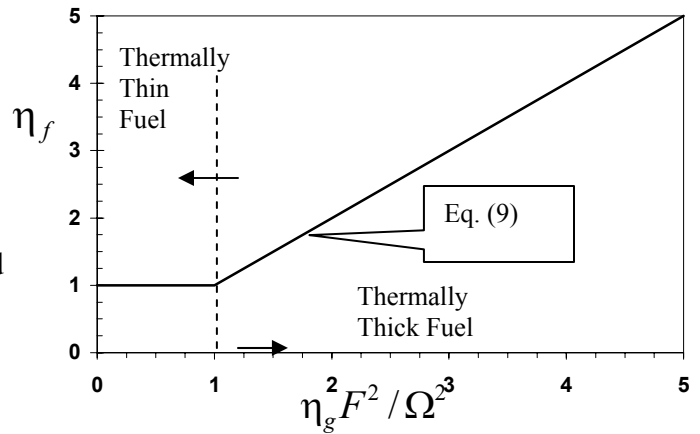
Fig. 2. Non-dimensional spread rate in the thermal regime.
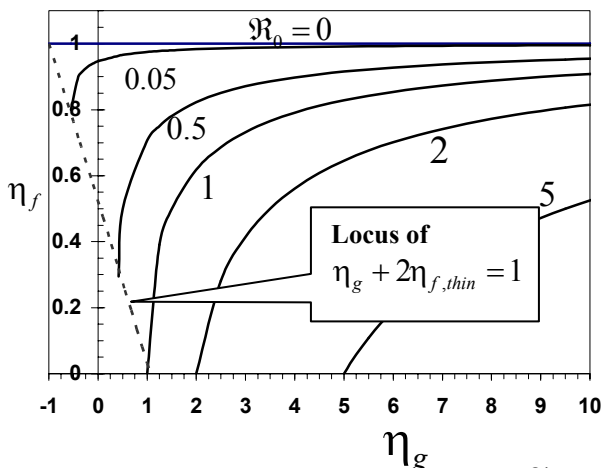
Fig. 3. Spread rate as a function of η_g and $\mathfrak{R}_0$ as predicted by Eq. (7). Opposed-flow flame spread extends down to $\eta_g = -1$.
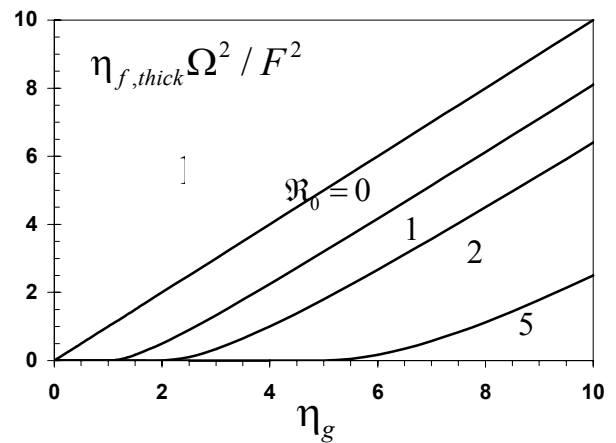
Fig. 4. Spread rate for thick fuel as a function of η_g and $\mathfrak{R}_0$ as predicted by Eq. (7). The spread rate is zero (extinction) for $\eta_g < \mathfrak{R}_0$.
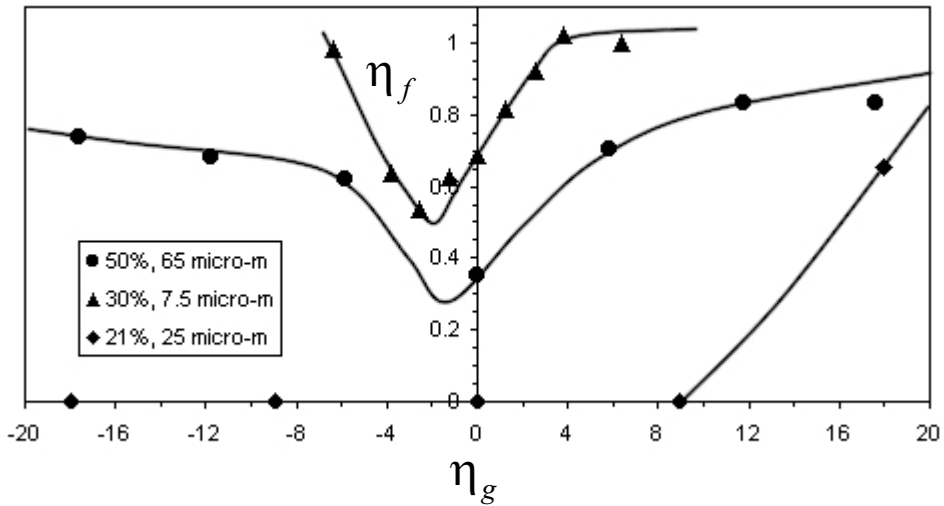
Fig. 5. Non-dimensional experimental spread rate [9] as a function of η_g for different oxygen mole fractions and fuel half-thickness. Note that in this plot the highest experimental spread rate is used to normalize V_f and V_g instead of the theoretical thermal limit.

Fig. 7. Flammability map for PMMA fuel at various half-thickness at 1 atm. Radiative extinction happens on the left side of each curve.

Fig. 6. Prediction of the non-dimensional spread rate η_f plotted as a function of inverse of $\mathfrak{R}_{0,thin}$ from Eq. (10). The prediction is compared with the spread rate data from the MGLAB experiments.

MATERIAL PROPERTIES GOVERNING CO-CURRENT FLAME SPREAD: THE EFFECT OF AIR ENTRAINMENT

Mickael Coutin, Ali S. Rangwala, Jose L. Torero
Department of Fire Protection Engineering, The University of Maryland
College Park, MD20742, USA
Steven G. Buckley
Department of Mechanical Engineering, The University of Maryland
College Park, MD20742, USA

ABSTRACT

A study on the effects of lateral air entrainment on an upward spreading flame has been conducted. The fuel is a flat PMMA plate of constant length and thickness but variable width. Video images and surface temperatures have allowed establishing the progression of the pyrolyis front and on the flame stand-off distance. These measurements have been incorporated into a theoretical formulation to establish characteristic mass transfer numbers ("B" numbers). The mass transfer number is deemed as a material related parameter that could be used to assess the potential of a material to sustain co-current flame spread. The experimental results show that the theoretical formulation fails to describe heat exchange between the flame and the surface. The discrepancies seem to be associated to lateral air entrainment that lifts the flame off the surface and leads to an over estimation of the local mass transfer number. Particle Image Velocimetry (PIV) measurements are in the process of being acquired. These measurements are intended to provide insight on the effect of air entrainment on the flame stand-off distance. A brief description of the methodology to be followed is presented here.

INTRODUCTION

The necessary flammability requirements for all materials to be used in space vehicles (NASA specifications) are given by the: "Flammability, Odor, Offgassing, and Compatibility Requirements and Test Procedures for Materials in Environments that Support Combustion" document [1]. This document specifies two tests that need to be performed before a material is qualified to be used in a space vehicle, the "Upward Flame Propagation Test" (Test 1) and the "Heat and Visible Smoke Release Rates Test" (Test 2). These two tests are expected to properly assess the flammability of a material in micro-gravity conditions. These two test methods attempt to provide a worst case scenario (Test 1) and a measure of the heat release (Test 2), and consequently, the "damage potential" of a fire. A detailed description of these test methods is provided in NASA-NHB 8060.1 [1] and an extensive list of the materials that have been tested is provided in the "Materials Selection List for Space Hardware Systems" [2].

The present study will address Test 1 and Test 2 in normal and micro-gravity to provide sound theoretical and experimental information that will serve to validate these methodologies and to help translate the results from normal-gravity to micro-gravity. The use of appropriate diagnostic techniques will help to accomplish these objectives.

Three fundamental parameters will be extracted as a combination of the results of Test 1 and Test 2 (B_A, B_R, B_C). These parameters can be incorporated into fire growth models and used to bound the growth of a fire in micro-gravity due to co-current flame spread. Following this methodology the results are not only a "worst case scenario," but a realistic representation of fire growth (through B_R), bounded by a "worst case scenario" (B_A) and a best case scenario (B_C).

For risk assessment this information is essential. More details on the theory behind these mass transfer numbers are provided in reference [3].

DESCRIPTION OF THE EXPERIMENTAL FACILITY

The experimental facility consists of a vertical sample of PMMA (0.45 m x 0.05 m (0.1 m and 0.15 m) x 0.012 m) mounted on an insulation board and covered with a metal plate (Figure 1). Tests were conducted with different arrangements for the edges to guarantee the most repeatable results. The sample was placed under a hood and ignition was induced with an electrically heated Kanthal wire. Five thermocouples were drilled from the back of the sample and melted on to the surface. Five thermocouples were placed at the back end of the sample between the fuel and the insulation. All thermocouples were spaced to provide a progression of the pyrolysis front and an estimate of the thermal thickness of the material. Two CCD cameras were used to obtain a frontal and a side view of the flame. Based on the characteristic times scales for propagation it was estimated that an average of all images covering a 10 second period was adequate to obtain an average stand-off distance and flame shape. Experiments were conducted with all three widths of the sample at least 5 times.
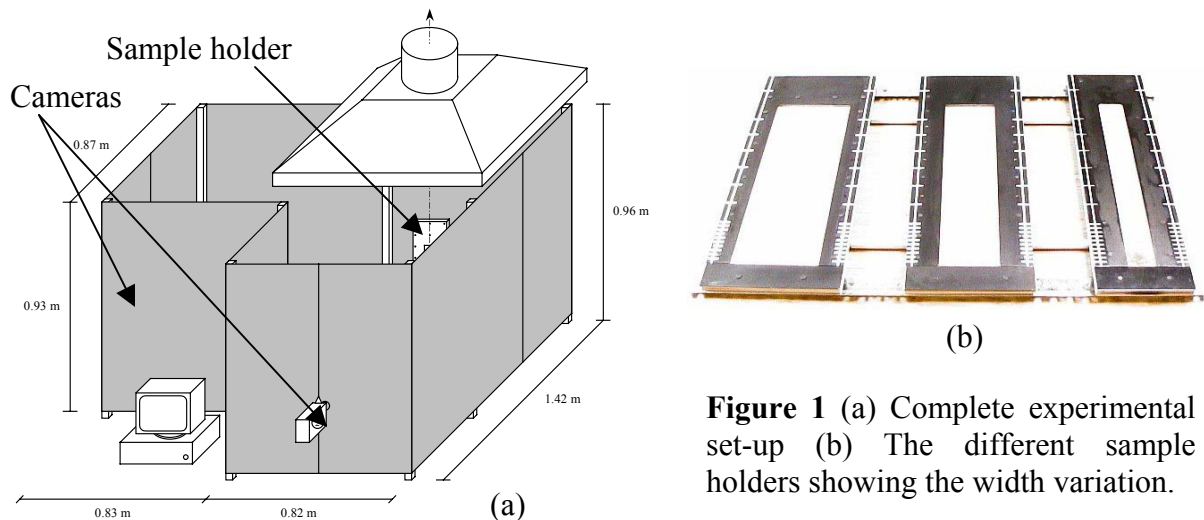
Figure 1 (a) Complete experimental set-up (b) The different sample holders showing the width variation.

A PIV optical setup has been completed, including the optics to form the laser sheet and the image acquisition. The light sheet is placed perpendicular (and parallel) to the fuel surface and velocity measurements will be obtained at the edge of the flames. The location of the Laser sheet will be varied systematically to obtain a clear idea of the three-dimensional features of the flow. Several smoke generation techniques have been considered, including seeding with TiO_2 particles, the use of a fog generator, and finally, the use of incense sticks. The TiO_2 was rejected due to potential toxicity of the particles and the observed tendency of the particles to agglomerate. Attempts with a fog generator produced too much smoke, with the result that white particles settled throughout the laboratory. Currently incense sticks, which produce a light white smoke, are being tested.

EXPERIMENTAL RESULTS

The progression of the pyrolysis front and the flame length was obtained from the thermocouple measurements and the video recordings. Figure 2 shows a characteristic set of data for a sample 0.05 m wide. As it can be seen the propagation rate and flame length seem to increase as a linear function of time. Other tests show similar relationships. It was noted that for

all cases studied the ratio between the flame pyrolysis lengths remains constant, $L_F / L_P \approx 1.4$ with little scatter ($\sigma < 0.2$). It is important to note that a single test provides a significant amount of data points, since the ratio can be evaluated at each stage of propagation. This ratio is much lower than earlier values reported by Orloff et al. (1974) who established L_F/L_P of the order of four. The reason for this is most likely consumption of fuel by lateral entrainment of air. The ratio L_F/L_P remained approximately the same for all sample width. This might indicate that lateral entrainment is not the cause for the flame length reduction but frontal views of the flame showed clearly that entrainment is dependent on the width and thus increases with this dimension. This compensates for the increased distance from the edges to the plane of symmetry.
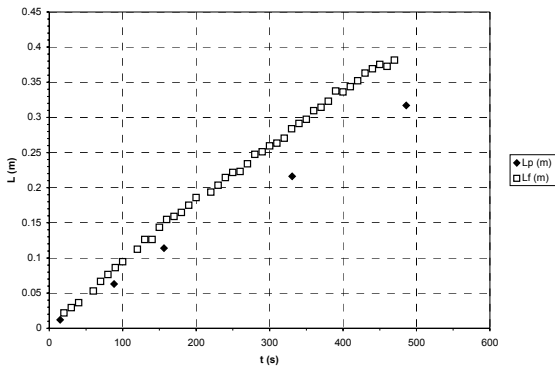
Figure 2 Progression of the flame length (L_F) and Pyrolysis length (L_P) as a function of time.
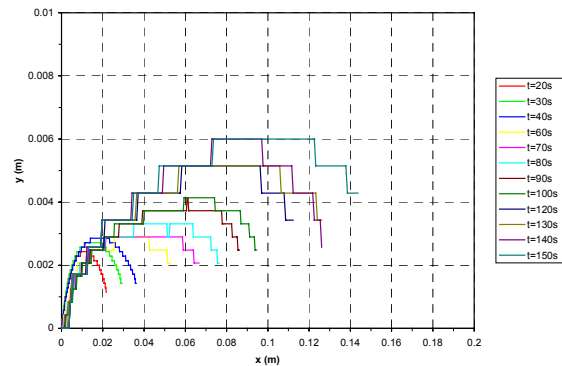
Figure 3 Stand-off distance as a function of time and distance down stream from the leading edge.

Figure 3 shows the evolution of the stand-off distance with the stream wise coordinate "x." As it can be seen as the flame length increases the stand-off distance increases. This is counter intuitive since an increase in flame length results in an increase in the characteristic length scale inducing natural convection and thus a thinner boundary layer (i.e. stand-off distance) should be expected. Fundamental theoretical studies of this type of flames will indicate that given a two-dimensional problem the stream wise length scales can be transformed by the following expression $\eta = (Gr_{L_F}^{1/4} / L_F \sqrt{2}) \int_0^y \frac{\rho}{\rho_\infty} dy$ where the Grashoff number is given by:

$$Gr_x = \frac{gL_F^3 (T_w - T_\infty)}{\nu_\infty^2 T_\infty}$$, thus the flame length is the dominant parameter controlling natural convection [5].

Although the discrepancies with two-dimensional theory have been noted, it is useful to establish the theoretical stand-off distance as a function of the mass transfer number ("B" number). The analysis is the same as that reported by Annamalai and Sibulkin [5] and Pagni and Shih [6] so it will not be repeated here. Figure 4 shows the theoretical predictions for different values of the "B" number. Realistic mass transfer numbers for PMMA have been reported to be approximately 3 [6]. As can be observed from Figure 4, the stand-off distance increases with the mass transfer number. By matching the experimental stand-off distance with the theoretical predictions [3] the evolution of an empirical "B" number can be estimated. A set of these values has been presented in Figure 5. According to the theory, the stream wise coordinate should scale

with LP, thus all data should collapse to a single curve. This has been shown to be valid in micro-gravity by Torero et al. [3]. This is clearly not the case in normal gravity. Furthermore, the predicted values of the "B" number are much larger than those expected. An experimental over prediction of the stand-off distance will result in a significant increase in the mass transfer number. This again points towards lateral entrainment. Lateral entrainment lifts the flame away from the surface leading to much larger stand-off distances than those predicted by two dimensional theory. One final point to be made, the maximum value of the "B" number (i.e. stand-off distance) is achieved at the pyrolysis length, the reduction occurring downstream indicates the elimination of the fuel production for $x>L_P$. The "B" numbers presented in Figure 5 are thus only valid for $x/L_P<1$, values downstream are only presented for illustration.
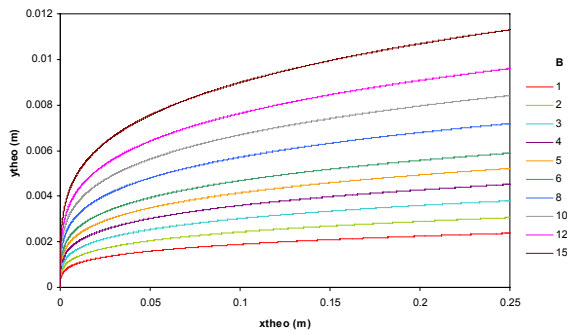
Figure 4 Evolution of the theoretical stand-off distance with the "B" number.
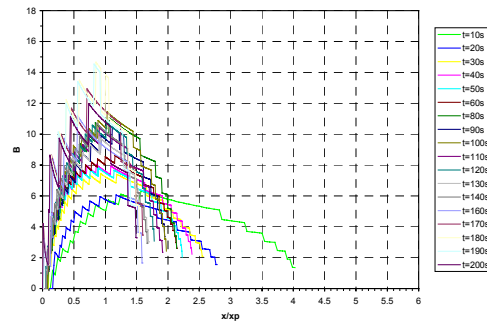
Figure 3 Evolution of the empirical "B" number as a function of the normalized distance and time.

CONCLUSIONS

A series of upward burning experiments have been conducted and have shown the importance of lateral entrainment in the establishment of the mass transfer number from flame stand-off distances. In micro-gravity gas expansion eliminates air entrainment and a two dimensional treatment is adequate. In normal gravity the lateral flow moves towards the plane of symmetry making impossible a two-dimensional treatment. Evaluation of these entrained flows using PIV and a numerical solution of the quasi-steady diffusion flames are the current tasks of this program.

REFERENCES

1. "Flammability, Odor, Offgassing, and Compatibility Requirements and Test Procedures for Materials in Environments that Support Combustion" NASA-NHB 8060.1, 1981.
2. "Materials Selection List for Space Hardware Systems" MSFC-HDBK-527-REV F, September 30, 1988.
3. Torero, J.L., Vietoris, T., Legros, G., Joulain, P. "Estimation of a Total Mass Transfer Number from Stand-off Distance of a Spreading Flame," *Combustion Science and Technology*, **174** (11-12), pp.187-203, 2002.
4. Orloff, L., De Ris, J. and Markstein, G.H. "Upward Turbulent Fire Spread and Burning of Fuel Surface," *Fifteenth Symposium (International) on Combustion, The Combustion Institute*, 183-192, 1974.
5. Annamalai and Sibulkin, "Spread over Combustible Surfaces for Laminar Flow Systems, Combustion Science and Technology, v.19, pp.167-183, 1979.
6. Pagni P. J. and T. M. Shih, T.M., "Excess Pyrolyzate," *Sixteenth Symposium (International) on Combustion*, The Combustion Institute, pp.1329, 1978.

PILOTED IGNITION OF POLYPROPYLENE/GLASS COMPOSITES IN A FORCED AIR FLOW

A.C. Fernandez-Pello[1], D. Rich[1], C. Lautenberger[1], A. Stefanovich[1], S. Metha[1],
J.Torero[2], Z. Yuan[3], H. Ross[3]
[1]University of California, Berkeley, 94720, ferpello@me.berkeley.edu, [3]N
[2]The University of Edinburgh, Edinburgh EH9 3JL, J.Torero@ed.ac.uk
[3]NASA Glenn Research Center, Cleveland, OH 44135

INTRODUCTION

The Forced Ignition and Spread Test (FIST) is being used to study the flammability characteristics of combustible materials in forced convective flows [1]. The FIST methodology is based on the ASTM E-1321, Lateral Ignition and Flame Spread Test (LIFT) [2,3] which is used to determine the ignition and flame spread characteristics of materials, and to produce "Flammability Diagrams" of materials. The LIFT apparatus, however, relies on natural convection to bring air to the combustion zone and the fuel vapor to the pilot flame, and thus cannot describe conditions where the oxidizer flow velocity may change. The FIST on the other hand, by relying on a forced flow as the dominant transport mechanism, can be used to examine variable oxidizer flow characteristics, such as velocity, oxygen concentration, and turbulence intensity, and consequently has a wider applicability. Particularly important is its ability to determine the flammability characteristics of materials used in spacecraft since in the absence of gravity the only flow present is that forced by the HVAC of the space facility [4].

In this paper, we report work on the use of the FIST approach on the piloted ignition of a blended polypropylene fiberglass (PP/GL) composite material exposed to an external radiant flux in a forced convective flow of air. The effect of glass concentration under varying external radiant fluxes is examined and compared qualitatively with theoretical predictions of the ignition process. The results are used to infer the effect of glass content on the fire safety characteristics of composites.

EXPERIMENTAL HARDWARE AND PROTOCOL

The general configuration of the problem investigated by the FIST methodology is shown in Figure 1. It consists of a duct where a flow of oxidizer gas of prescribed oxygen concentration and velocity is forced along its longitudinal direction. A rectangular slab of fuel is embedded flush in a plate of insulating material that forms one wall of the duct. The exposed surface is impulsively subjected to an external heat flux of known intensity and approximately uniform distribution using an IR strip heater placed opposite the fuel. Ignition of fuel pyrolysates is forced with an electrically heated wire placed at the sample end. Ignition delay is defined as the time lapse from the instant that the fuel is exposed to the external radiant flux to the onset of flaming. A sudden rise in surface temperature is used to determine ignition, corroborated by visual and video observation.
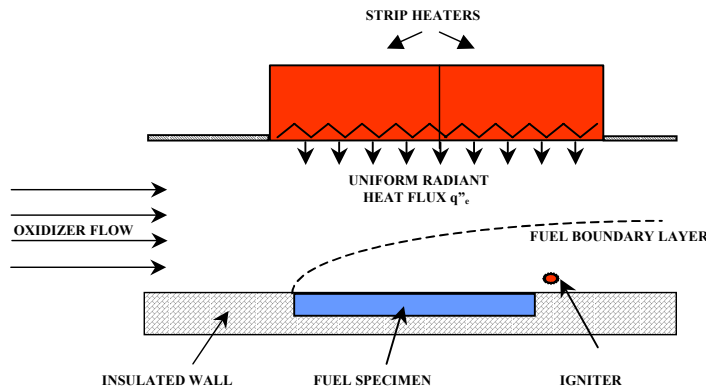
Figure 1. FIST apparatus

BACKGROUND

In the LIFT methodology, the analytical solution to the transient heating of a semi-infinite solid by a constant surface heat flux is used to determine the ignition time, by calculating the time necessary for the solid surface to attain an "ignition" temperature (T_{ig}). To obtain an analytical solution to the surface temperature (T_S), the convective heat transfer coefficient is averaged and assumed constant, and surface re-radiation is treated by means of a linear approximation at an average surface temperature. Assuming that the ignition temperature is constant, for large values of the external radiant flux, the following expression is obtained for the ignition delay time (t_{ig}) as a function of the external radiant flux

$$\frac{1}{\sqrt{t_{ig}}} = \frac{2}{\sqrt{\pi}} \frac{\alpha}{\sqrt{k\rho C}} \frac{\dot{q}_e''}{(T_{ig} - T_\infty)} \tag{1}$$

Where the α is the material absorptivity, $\dot{q}_e''$ the external radiant flux, T_∞ the ambient temperature, k the thermal conductivity, ρ the density and C the specific heat of the solid. The product $k\rho C$ is often referred to as the "thermal inertia" of the solid. The methodology followed by the LIFT standard [2,3] can be used to qualitatively analyze the effect of glass content on the ignition characteristics of the composite. The values for $k\rho C$ from the literature [5,6] confirm that the thermal inertia of the composite increases as the percentage of glass is increased, and thus from Eq. (1) it is predicted that, for a given radiant flux and ignition temperature, the ignition delay should increase.

The glass addition has two main effects on the physics governing the material ignition delay. One is the increase in the density of the composite, which for a given external heat flux would require a longer period to reach a certain surface temperature. The other effect is the increase in thermal conductivity k, which favors the in-depth penetration of the thermal wave, and consequently also requires a longer period of time to reach a certain surface temperature for a given external heat flux. Both effects contribute to increased ignition times and critical heat fluxes for ignition.

RESULTS

In Figure 2 surface temperature histories for PP/GL with glass percentages of 0%, 20%, 30%, and 40%, at a constant heat flux of 20.0 kW/m^2 and an air velocity of 1m/s are presented. The results show that the glass percentage moderately affects the surface temperature profile, but that as the percentage of glass is increased both the surface temperature at which ignition occurs and the ignition delay increase. As explained

previously, these results are due primarily to the increase of the thermal inertia of the composite as the glass content is increased.
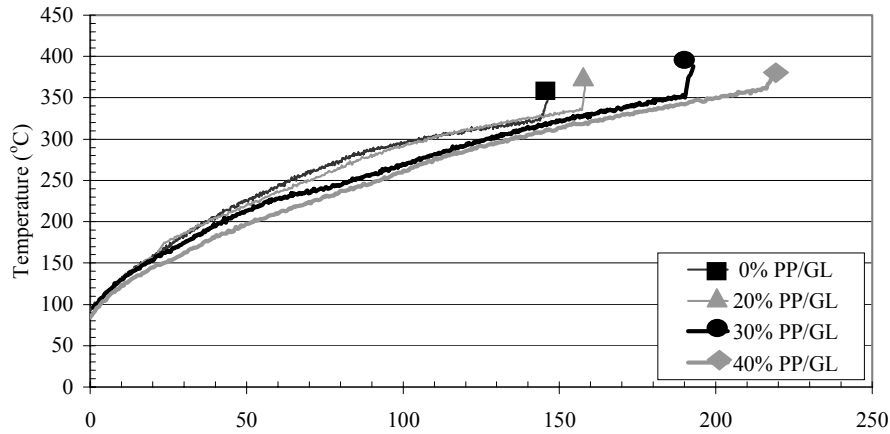
Figure 2. Surface temperature histories for different glass concentrations at a radiant flux of 20 kW/m^2 and air velocity of 1 m/s.

Figure 2 shows that ignition delay and critical heat flux for ignition (asymptotic value of the heat flux for large ignition times) are functions of the glass concentration in the composite, increasing as the glass concentration is increased. Three to four tests are conducted for each data point but error bars have been removed for clarity of presentation.
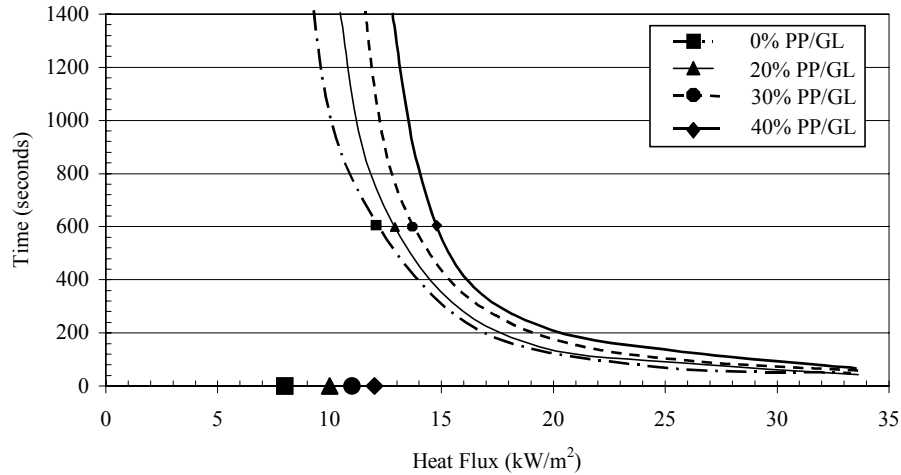
Figure 3. Ignition delay graph for PP/GL of different fiberglass percentages and air velocity of 1 m/s.

Correlation of the ignition delay data of Fig. 3 with Eq. (1) can be used to experimentally determine the kρC of the composite. It is found that calculated value of kρC qualitatively agrees with the values obtained from the literature, although there is quantitative disagreement due to fuel pyrolysis effects that are not included in Eq. (1).

The critical heat flux for ignition obtained from Figure 3 can be used to produce ignition/ no ignition diagrams (Figure 4), where a "no ignition" region can be defined

based on the fiberglass content of the composite under a given external heat flux. This has important fire safety implications.
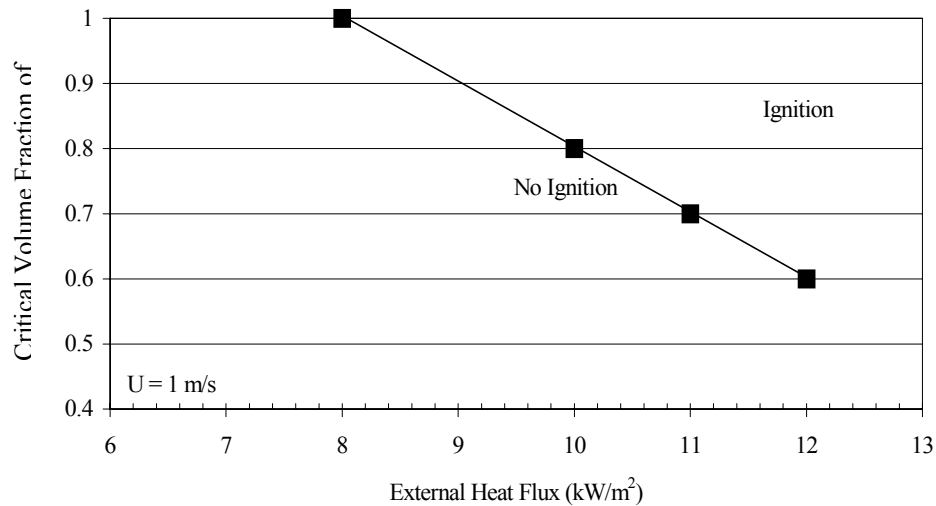
Figure 4. Critical PP volume fraction for ignition.

CONCLUDING REMARKS

It has been shown that the glass volume fraction of a composite material affects its ignition characteristics, particularly near the critical heat flux range. Whereas the use of fire-retardant matrix materials is usually the primary means for improving fire safety in composites, the present research suggests that fire safety may also be enhanced by using composites with high glass concentrations.

ACKNOWLEDGMENTS

REFERENCES

1. Cordova, J.L., Torero, J.L., Walther, D., Fernandez-Pello, A.C., "Oxidizer Flow Effects on the Flammability of Solid Combustibles," *Combustion Science and Technology,* **164**: 253. (2001).
2. Quintiere, J.G., "A Simplified Theory for Generalizing Results from a Radiant Panel Rate of Flame Spread Apparatus," *Fire and Materials*, **5**: 52. (1981).
3. ASTM E 1321-93, "Standard Test Method for Determining Material Ignition and Flame Spread Properties," *Annual Book of ASTM Standards*, 04.07. (1996).
4. Roslon, M., Olenick, S.,Walther, D., Torero, J.L., Fernandez-Pello, A.C. and Ross, H.D. "Microgravity Ignition Delay of Solid Fuels in Low Velocity Flows" *AIAA Journal* **39**: 2336 (2001).
5. Maier, C., Calafut, T. "Polypropylene. The Definitive User's Guide and Databook, Plastics Design Library", Norwich, NY, (1998).
6. Lubin, G., "Handbook of Composites", New York, Van Nostrand Reinhold, (1981).

An Earth-Based Equivalent Low Stretch Apparatus
to Assess Material Flammability for Microgravity & Extraterrestrial Fire-Safety Applications

S.L. Olson*,
NASA Glenn Research Center, Cleveland, OH 44135
H. Beeson, and J.P. Haas,
NASA White Sands Test Facility, Las Cruces, NM

Abstract

The objective of this project is to modify the standard oxygen consumption (cone) calorimeter (described in ASTM E 1354 and NASA STD 6001 Test 2) to provide a reproducible bench-scale test environment that simulates the buoyant or ventilation flow that would be generated by or around a burning surface in a spacecraft or extraterrestrial gravity level. This apparatus will allow us to conduct normal gravity experiments that accurately and quantitatively evaluate a material's flammability characteristics in the real-use environment of spacecraft or extra-terrestrial gravitational acceleration. The Equivalent Low Stretch Apparatus (ELSA) uses an inverted cone geometry with the sample burning in a ceiling fire configuration that provides a reproducible bench-scale test environment that simulates the buoyant or ventilation flow that would be generated by a flame in a spacecraft or extraterrestrial gravity level. Prototype unit testing results are presented in this paper. Ignition delay times and regression rates for PMMA are presented over a range of radiant heat flux levels and equivalent stretch rates which demonstrate the ability of ELSA to simulate key features of microgravity and extraterrestrial fire behavior.

Introduction

NASA's current method of material screening determines fire resistance under conditions representing a worst-case for normal gravity flammability - the Upward Flame Propagation Test (Test 1[1]). The applicability of Test 1 to fires in microgravity and extraterrestrial environments, however, is uncertain because the relationship between this buoyancy-dominated test and actual extraterrestrial fire hazards is not fully understood. Flames in micro-gravity are known to preferentially spread upwind [2], not downwind as in the normal gravity upward flammability screening Test 1. At low flow velocities, the concurrent (Test 1 configuration) flame spread was not viable over vertical solid cylinders, while the stagnation point flame at the bottom end of the cylinder (low stretch flame) was viable [3,4]. In addition, the maximum flammability in the upwind spread configuration is known to be at lower imposed flows and lower oxygen concentrations than in normal gravity [5].

Theoretical predictions by Foutch and T'ien (1987)[6] indicate that it should be possible to understand a material's burning characteristics in the low stretch environment of spacecraft (non-buoyant, but with some movement induced by fans and crew disturbances) by understanding its burning characteristics in an equivalent Earth-based stretch environment (induced by normal gravity buoyancy). Experimental results [7] demonstrate the transition from a robust flame at stretch rates of 10-20 s^{-1} to a quenched flame at very low stretch (1-2 s^{-1}) in air where the stretch rate is purely buoyant. In these tests, sample radius of curvature was the primary variable controlling the stretch rate, but this is not convenient for standardized testing.

Experiment Setup

The ELSA apparatus, shown conceptually in Figure 1, uses a mass-flow controlled forced-air flow issuing from a 7.5 cm diameter nozzle into the cone to augment the low buoyant stretch. Stretch rates have been varied in a prototype facility from purely buoyant (estimated ~ 3.5 s^{-1} for the 28 cm sample plate) to 33.5 s^{-1} with forced convection. Cone heat flux has been varied from 10-25 kW/m^2. Samples are mounted 2.5 cm above the cone, which is the same distance as the normal cone configuration.

The samples used are 2.4 cm thick PMMA, cut to the standard cone test sample size of 10 cm x 10 cm exposed surface area, but also have
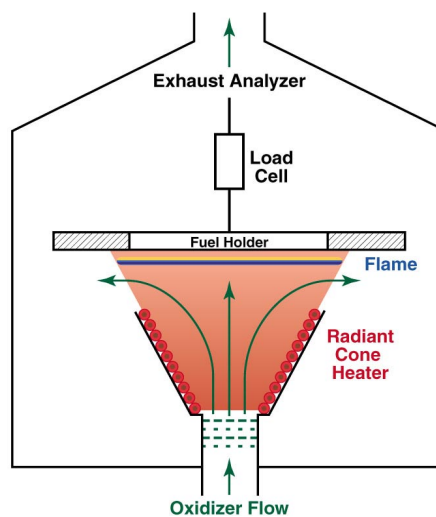
Figure 1: Concept of ELSA apparatus, showing fuel sample suspended above radiant cone heater and oxidizer flow jet. The enclosure reflects the WSTF Controlled Atmosphere Cone Calorimeter facility[1].

---

* Dr. Sandra L. Olson, Sandra.olson@grc.nasa.gov

a 2.5 cm lip around the opening to prevent the sample from falling through the opening. The holder is 0.2 cm thick stainless steel, 28cm wide.

The test procedure first establishes the cone heat flux using a heat flux gauge. The low velocity flow is established and then the sample moved into position to expose it to this environment. It should be noted that the net heat flux increases due to the addition of convective flow. The pilot (hot source or spark) was positioned to the side of the sample, very near the surface of the plate to ignite the vapors once a flammable mixture is obtained. Thermocouples on the surface of the sample record the surface temperature, video cameras record the ignition and flame behavior. The air mass flow rate, radiant flux and cone temperature are recorded as well.

Once burning is established, the flame reaches a "pseudo-steady state" in approximately 10 seconds. Because the sample is of intermediate thickness, the interior continues to heat up throughout the test time, so true steady state is never obtained.

Equivalent stretch rates can be determined as a function of gravity, imposed flow, and geometry. For purely buoyant flow, the equivalent stretch rate is $a_b = [(\rho_e - \rho^*)/\rho_e] [g/R]^{1/2}$ [6,7], where the density difference from the average flame temperature to ambient is used, g is gravity, and R is the radius of curvature of the sample. For purely forced flow, the equivalent stretch rate is characterized by either $a_f = 2U_\infty/R$ for a cylinder[6], or $a_f = U_{jet}/d_{jet}$ for a jet impinging on a planar surface[8]. U is the velocity of the ambient stream or the jet, R is the radius of curvature of the cylinder, and d is the diameter of the jet. A generalized expression for stretch rate which captures mixed convection includes both buoyant and forced stretch is defined[6] as $a_{equivalent} = a_f(1 + a_b^2/a_f^2)^{1/2}$.

The contributions of the buoyant stretch on the equivalent stretch rate were evaluated by correlating regression rate data for flat disks of various radii[9] and cylindrical samples with reported stretch rates [7]. The correlation, shown in Figure 2, allows us to determine the inherent buoyant stretch for ELSA to be ~3.5 s-1 by matching the regression rates for cylinders and flat disks. Note that this correlation worked even through the range of radii where Rayleigh-Taylor instabilities were found at larger radii (>8cm)[9].

Results and Discussion
Ignition
The samples are radiantly ignited with the assistance of a gas-phase pilot (a hot source or spark) to ignite the vapors. Ignition of the sample was recorded on video, and the time to ignition determined for each test condition.
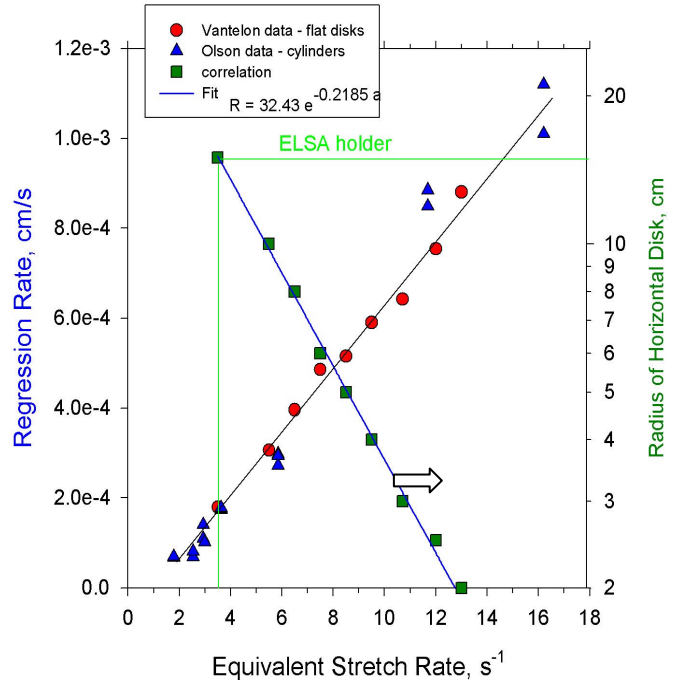
Figure 2: Linear correlation of flat disk radius with equivalent buoyant stretch[7,9]. Regression rates for cylinders and flat disks were correlated, and the equivalent stretch rate for the 14 cm radius ELSA holder determined from the linear relation found between radius of the disk and equivalent stretch rate.
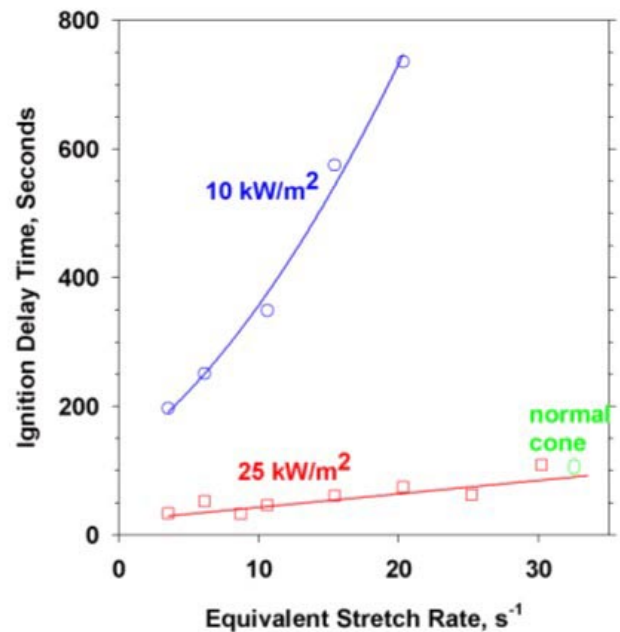
Figure 3 Ignition delay times as a function of equivalent stretch rate.

Ignition delay times were measured at 10 kW/m^2 and 25 kW/m^2 flux levels, as shown in Figure 3. For a fixed radiant flux, ignition delay times are shown to decrease with decreasing stretch rate. The difference between a normal cone ignition delay time and ignition delay times at very low stretch is a factor of three, demonstrating that ignition delay times determined from normal cone tests significantly *overestimate* the ignition delay times of materials in microgravity or in low stretch extraterrestrial environments. In addition, at the 10 kW/m^2 flux level, the ignition delay time at low stretch approaches the value of the normal cone at 25 kW/m^2, indicating the sensitivity of low stretch flames to even weak levels of external flux.

Surface temperature was also recorded during tests. Figure 4 shows surface temperature rising as a power law relation once the sample is exposed to the cone heat flux, as would be expected for a slab with constant heat flux at the surface. Ignition is noted by a sudden jump in temperature in each test. The ignition temperature is defined as the temperature at which this jump starts. The surface temperatures at ignition decreased with increasing stretch, and were lower at lower imposed flux levels, and the slope is similar for both flux levels, reflecting the effect of the additional convective heat transfer on ignition.

Figure 4: Surface temperature histories as a function of stretch rate for 10 kW/m^2 cone heat flux.

Cellular Instabilities

Due to the flat sample geometry, at low forced stretch rates, Rayleigh-Taylor instabilities were observed beneath the sample. These instabilities were not observed for curved samples[7]. The instabilities in these tests were notably worse at higher flux levels, where fuel vaporization rates are quite vigorous.

Figure 5 shows the decrease in the cellular instabilities with increasing stretch. The nominal transition from cellular planar occurs at ~ 8 s^{-1}.

While the cellular instability is clearly gravity dependent, its development occurs well after ignition. Thus ignition delay time and ignition temperature data is not affected by this instability. The pseudo-steady-state flame shape is dominated by this instability. It is less clear whether average burning rates are significantly affected, as will be discussed below.

Surface Regression

After ignition, samples were allowed to burn for a period of time in order to obtain information about the average burning rates of the material. For all stretch rates, the samples were found to regress uniformly across the exposed area, which indicates that the Rayleigh-Taylor cells do not affect the fuel surface regression locally. It is less clear if the cellular flow field significantly affects the burning rate in a global sense. Due to the enhanced convection, the burning rates could be higher than they would be without the cellular flow. On the other hand,

Figure 5: Rayleigh-Taylor instabilities are observed at stretch rates less than ~8 s^{-1}. These instabilities are due to the flat samples used in these experiments as well as the augmented heat flux levels. At low stretch rates, the cells are very large, and extend into the cone.

they could be lower because of the larger average standoff distance between the flame and the fuel surface.

Average regression rates, shown in Figure 6, were obtained by weighing the samples before and after the test and dividing the mass loss by the test time, exposed area and density (=1.19 g/cc, A=100 cm^2). Regression rates increase with heat flux and stretch rate, but regression rates are much more sensitive to heat flux at the low stretch rates. A modest increase in heat flux of 25 kW/m^2 increases the burning rates *by an order of magnitude* at the lower stretch rates. These trends are reasonable for low stretch flames, which have been shown to be very sensitive to the ratio of heat loss to heat generated via combustion[7].

Even at 10 kW/m^2, the cone heater offsets the surface radiative loss, which is significant relative to the weak heat generation rates[7]. Thus, low stretch flames with these losses offset may find themselves vaporizing much more fuel than there is oxygen available with which to react. The products of combustion from such flames will be more toxic (CO, soot, THC, etc.) in addition to posing a significant risk of buildup to explosive levels in a confined space.
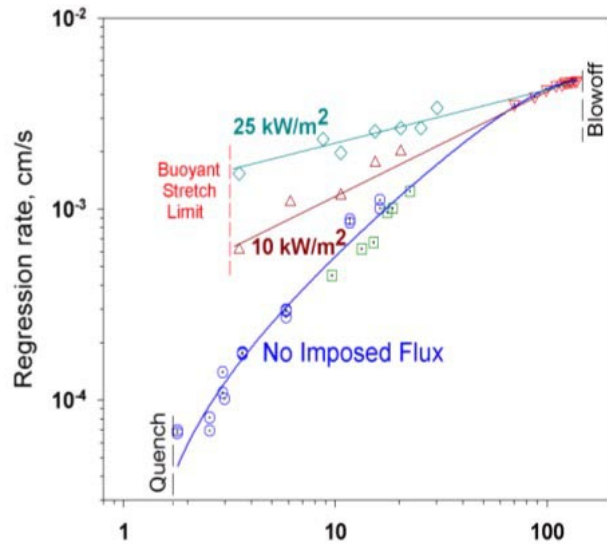
Figure 6 : PMMA regression rates for three levels of imposed heat flux from radiant cone heater, plotted as a function of equivalent stretch rate. Data: ◇, △ this work, ○[7], □[10], ▽[8].

Conclusions

The Equivalent Low Stretch Apparatus (ELSA) uses an inverted cone geometry with the sample burning in a ceiling fire configuration that allows for low stretch stagnation flow. Ignition delay times and regression rate data have been measured in a prototype unit.

For a fixed radiant flux, ignition delay times for PMMA are shown to decrease by a factor of three at low stretch, demonstrating that ignition delay times determined from normal cone tests significantly underestimate the risk in microgravity.

Regression rates for PMMA increase with heat flux and stretch rate, but regression rates are much more sensitive to heat flux at the low stretch rates, where a modest increase in heat flux of 25 kW/m^2 increases the burning rates by an order of magnitude.

These results demonstrate the ability of ELSA to simulate key features of low stretch materials flammability behavior. ELSA provides a new tool to assess microgravity and extraterrestrial fire hazards.

Acknowledgements

References

1) NASA-STD-6001, 1998.
2) McGrattan, K.B., Kashiwagi, T., Baum, H.R., and Olson, S.L.; *Combustion and Flame (C&F)*, V. 106, pp.377-391, 1996.
3) Halli, Y., and T'ien, J.S., NBS-GCR-86-507, Feb. 1986.
4) Ivanov, A.V, et. al, NASA Contract NAS3-97160 final report, Russian Space Agency, Keldysh Research Center, Moscow 1999, also NASA CP-1999-208917, pp. 47-50.
5) Olson, S.L., *Comb. Sci.& Tech.* V. 76, pp.233-249, 1991.
6)Foutch, D.W.,& T'ien, J.S., *AIAA J.*,V.25, No.7,pp.972-6, 1987.
7) Olson, S.L and T'ien, J.S.;*C.&F*,V.121,pp.439-452, 2000.
8) T'ien, J.S., Singhal, S.N., Harrold, D.P., and Prahl, J.M.; *Combustion and Flame*, Vol. 33, pp.55-68, 1978.
9) Vantelon, J.P., Himdi, A., and Gaboraiud, F.; *Combust. Sci. and Tech*., V54, pp. 145-158, 1987.
10) Ohtani, H., Akita, K., and Hirano, T., *Combustion and Flame*, Vol. 53, pp. 33-40, 1983.

Flame-Vortex Studies to Quantify Markstein Numbers Needed to Model Flame Extinction Limits

James F. Driscoll[1], and Douglas A. Feikema[2]

[1]University of Michigan, Ann Arbor MI 48109
[2]NASA Glenn Research Center, Cleveland OH 44135

This has quantified a database of Markstein numbers [1-3] for unsteady flames; future work will quantify a database of flame extinction limits for unsteady conditions. Unsteady extinction limits have not been documented previously; both a stretch rate and a residence time must be measured, since extinction requires that the stretch rate be sufficiently large for a sufficiently long residence time. Ma was measured for an inwardly-propagating flame (IPF) that is negatively-stretched under microgravity conditions. Computations also were performed using RUN-1DL to explain the measurements. The Markstein number of an inwardly-propagating flame, for both the microgravity experiment and the computations, is significantly larger than that of an outwardy-propagating flame. The computed profiles of the various species within the flame suggest reasons. Computed hydrogen concentrations build up ahead of the IPF but not the OPF. Understanding was gained by running the computations for both simplified and full-chemistry conditions.

The drop tower experiment in Fig. 1 [4-6] was used to create a flat propane-air flame which interacts with a vortex, causing the flame to wrap around the vortex. The distorted flame surface eventually pinches off from the main surface, creating a pocket of reactants surrounded by an inwardly propagating spherical flame. An electrical connection is broken which signals the beginning of the drop; after a 500 ms wait time, exhaust ports are opened to prevent pressure buildup and the flame is ignited using a spark. After 200 ms the speaker is pulsed and the pocket formation occurs 300 – 400 ms later. Final pocket burnup occurs in another 150 ms, so the entire process takes less than 1.2 seconds. Flame speeds were measured by recording shadowgraph images of pocket at 500 frames/second using a Kodak RO digital camera. Figure 2 shows the digitized image of the flame boundary at five different times. For the IPF the velocity of the gas ($\mathbf{u}$) inside the pocket is zero due to symmetry, so the stretch rate of an IPF is $K = S_u / R_c$.

Numerical Simulations. To explain the experimental findings, numerical simulations of both inwardly and outwardly propagating spherical flames (with complex chemistry) were generated using the RUN-1DL code [7], which includes 16 species and 46 reactions.

Figures 2 and 3 show some results of the microgravity IPF experiment, for which the propane-air equivalence ratio was 0.54. The slope of the curve in Fig. 3 is –Ma. Figures 4 and 5 show some numerical results for complex propane-air chemistry. The Markstein number is 11.5, which is within the range of values that were measured in the microgravity experiment. The Ma of the computed IPF is larger than that of the corresponding OPF. A difference between the IPF and OPF is that there is a buildup of hydrogen molecules ahead of the IPF that is caused by stretch, but no such buildup occurs for the OPF.

Conclusions

1. Markstein numbers of a inwardly-propagating flame were measured in microgravity using a unique experiment. This flame is of interest because it is subjected to negative stretch rates, and because curvature effect alone are present; the complications associated with strain are absent. The measured values of Ma for the IPF are significantly larger than previous measurements reported for the OPF case.

2. Computed Ma were obtained using the RUN-1DL code and complex chemistry. Results agreed with the experiment. Computed Ma for the IPF were significantly larger than computed for the OPF case, in agreement with the measurements.

3. When the heat release is artificially removed from the computations, both IPF and OPF cases are subjected to curvature effects alone, and strain effects are absent; the resulting computed Markstein numbers are identical. This indicates that the Markstein numbers associated with strain and curvature differ. The difference between Ma of IPFs and OPFs does not appear to be due to radicals and intermediate species.

4. The profiles of certain species concentrations, such as hydrogen molecules, has a significantly different shape for the IPF case than for an OPF. This is due to the boundary conditions for the IPF at the origin, which differ from those of the OPF.

References
1. Sun, C.J., Sung, C.J., He, L.,Law, C.K., *Combust. Flame* 118:108-128 (1999).
2. Kwon, S., Tseng, L.K., and Faeth, G.M., *Combust. Flame* 90:230-246 (1992).
3. Tseng, L.K., Ismail, M.A., and Faeth, G.M., *Combust. Flame* 95: 410-426 (1993).
4. Ibarreta, A. and Driscoll, J.F., *Proc. Combust. Inst*. 28: 1783-1791 (2000).
5. Ibarreta, A., Driscoll, J.F., Feikema, D. *Proc. Combust. Inst*. 29 (2002).
6. Sinibaldi, J., Mueller, C., and Driscoll, J., *Proc. Combust. Inst*. 27: 827-832 (1998).
7. Rogg, B. and Wang, W., *RUN-1DL* - Ruhr-Universitat Bochum, 1997.
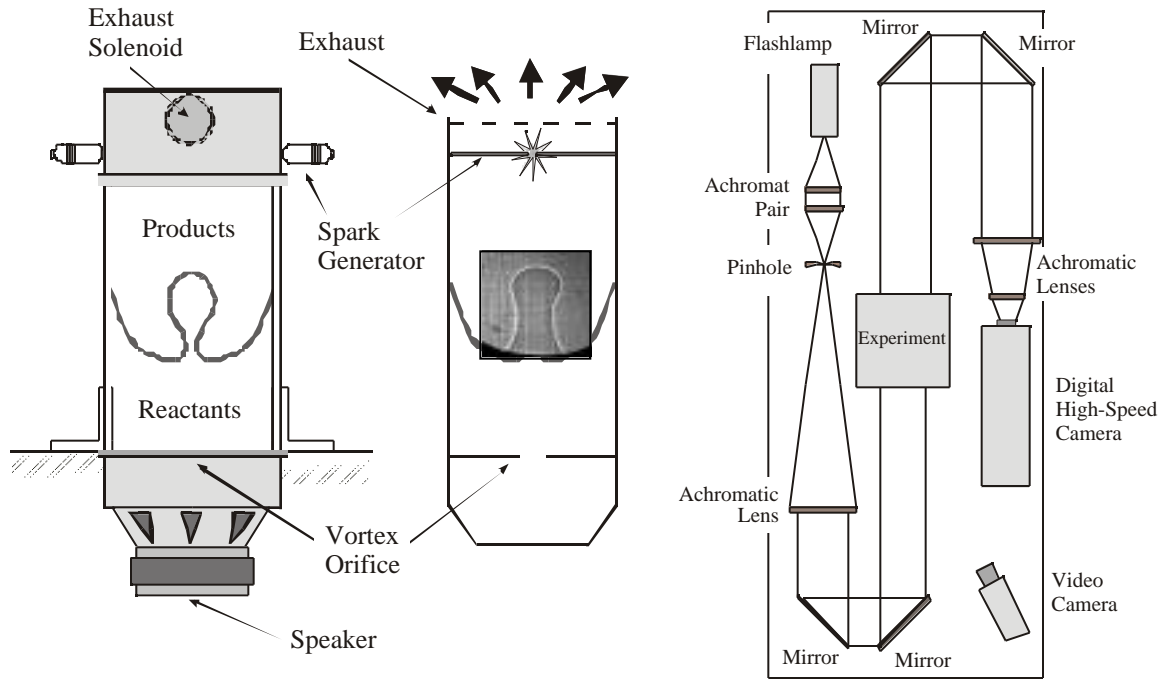
Figure 1. Michigan Microgravity Experiment to Create Unsteady Stretched Flames
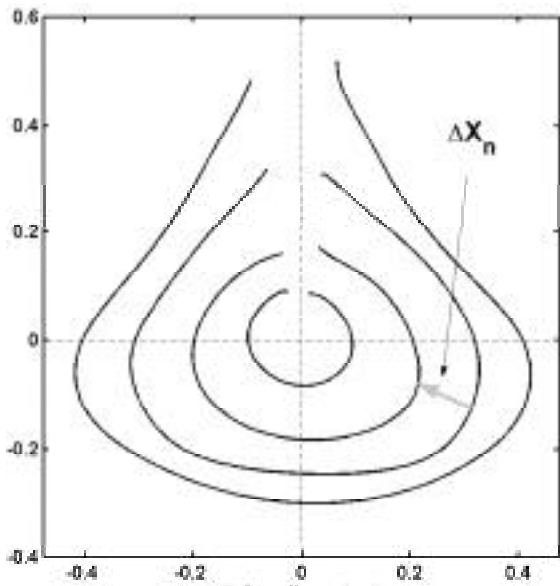
Fig. 2. Shadowgraph of Flame Positions
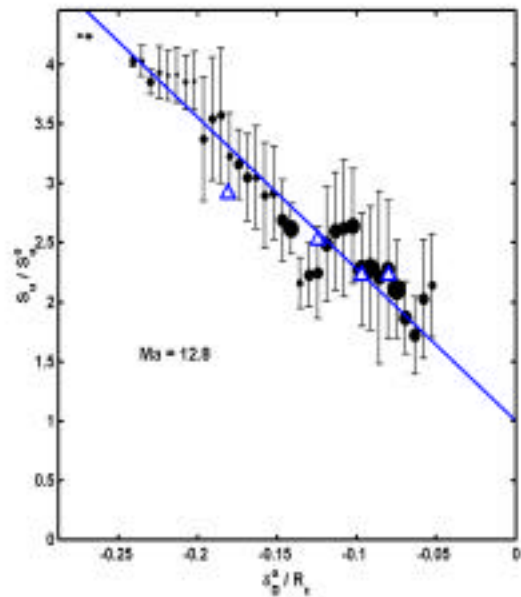
Fig. 3. Flame Speeds to Determine Ma
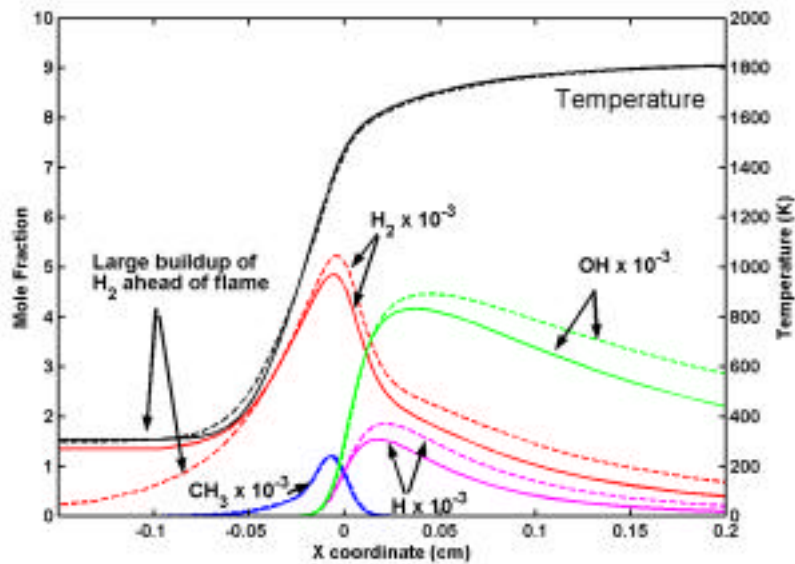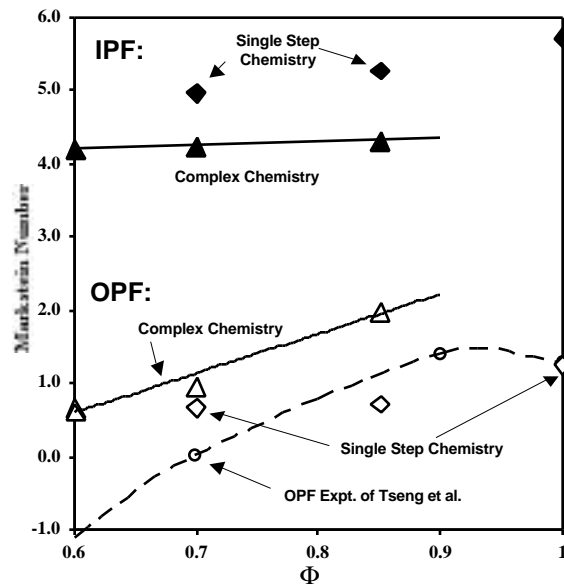
Figures 4 and 5. Computed and Measured Markstein Numbers Showing that Inward and Outward Propagating Flames (Negatively and Positively Stretched Flames) Have Different Ma. Computations show that H2 builds up ahead of IPFs but not OPFs.

FIELD EFFECTS OF BUOYANCY ON
LEAN PREMIXED TURBULENT FLAMES

R. K. Cheng, M. R. Johnson
Lawrence Berkeley National Laboratory, Berkeley, CA.

P. S. Greenberg & M. P. Wernet
NASA John H. Glenn Research Center at Lewis Field, Cleveland, OH

INTRODUCTION

The study of field effects of buoyancy on premixed turbulent flames is directed towards the advancement of turbulent combustion theory and the development of cleaner combustion technologies. Turbulent combustion is considered the most important unsolved problem in combustion science and laboratory studies of turbulence flame processes are vital to theoretical development. Although buoyancy is dominant in laboratory flames, most combustion models are not yet capable to consider buoyancy effects. This inconsistency has impeded the validation of theories and numerical simulations with experiments. Conversely, the understanding of buoyancy effects is far too limited to help develop buoyant flame models.

Our research is also relevant to combustion technology because lean premixed combustion is a proven method to reduce the formation of oxides of nitrogen (NO_x). In industrial lean premixed combustion systems, their operating conditions make them susceptible to buoyancy thus affecting heat distribution, emissions, stability, flashback and blowoff. But little knowledge is available to guide combustion engineers as to how to avoid or overcome these problems.

Our hypothesis is that through its influence on the mean pressure field, buoyancy has direct and indirect effects on local flame/turbulence interactions. Although buoyancy acts on the hot products in the farfield the effect is also felt in the nearfield region upstream of the flame. These changes also influence the generation and dissipation of turbulent kinetic energy inside the flame brush and throughout the flowifield. Moreover, the plume of an open flame is unstable [1] and the periodic fluctuations make additional contributions to flame front dynamics in the farfield. Therefore, processes such as flame wrinkling, flow acceleration due to heat release and flame-generated vorticity are all affected. Other global flame properties (e.g. flame stabilization limits and flame speed) may all be coupled to buoyancy. This problem poses major challenges to combustion modeling due to its need for a computation domain extending into the farfield and full specifications of upstream, wall and downstream boundary conditions.

OBJECTIVE

The overall objective of our flight experiments planned for the Combustion Integrated Rack (CIR) onboard the International Space Station is to quantify the global flowfield and local flame/turbulence interactions of μg flames. Buoyancy is omnipresence in terrestrial experiments. Removing buoyancy through prolong reduced gravity is the only means to obtain statistically stable and accurate benchmark μg data to characterize complex flame/turbulence interactions. Buoyancy contributions to these process will be elucidated by comparing with extensive terrestrial studies flames subjected to normal (+1g) and reversed (-1g) gravity. The flight experiments will be focussed on determining the effect of buoyancy on three aspects of turbulent flames: (1) the mean

characteristics of the scalar and velocity fields; (2) local turbulence/flame coupling processes, determined by the conditioned velocity statistics and expressed in terms of the reaction rate and turbulent transport; and (3) combined effects of buoyancy and thermal/diffusive instabilities.

EXPERIMENTAL CONFIGURATION, DIAGNOSTICS & ANALYSIS

The experimental configuration selected for the flight experiments is an axi-symmetric Cone-stabilized LEAN (CLEAN) flame. (Figure 1). This flowfield is amenable to numerical modeling and theoretical analysis. In many respects, this flowfield is similar to that generated by rod-stabilized V-flame [2] but without the influences of flame edge effects. The burner has an exit diameter of 17 mm with a turbulence generating plate placed at about 20 mm upstream of the exit. The bluff body stabilized is cone shaped and supported by a stem anchored at the burner's central axis.

The same methodology, data acquisition and data analysis methods we have developed for laboratory flames will be used ultimately for the flight experiments. The emphasis is to obtain statistically stable sets of detailed velocity and scalar data for the analysis of conditional statistics and turbulence transport processes. We plan to measure the scalar field by a Planar Imaging of Flame Fronts (PIFF) method (i.e., planar laser induced fluorescence of OH [2] or Mie scattering from oil aerosol). Particle image velocimetry (PIV) is the preferred method to measure mean and RMS velocities. The data will be analyzed to obtain mean properties as well as detailed flame structures and turbulence transports.

Figure 1 Schematics of the Clean Flame burner and flow supply

GROUND-BASED LABORATORY EXPERIMENTS

In preparation for the flight experiments, we have conducted a series of laboratory investigations to determine that the CIR system and its support fulfill all the scientific requirements of the experiments. These studies have helped to determine the appropriate sizes of the burner and the stabilizer, and to optimize the design of the ignition and exhaust systems.

We have also developed a Particle Imaging Velocimetry (PIV) system to investigate the flowfields of CLEAN flames subjected to +1g and −1g. The system consists of a New Wave Solo PIV laser which produces double 120 mJ pulses at 532 nm and a Kodak Megaplus ES 4.0 digital frame-straddling camera with 2048 by 2048 pixel resolution. The optics were arranged to capture a 6 by 6 cm field of view (30.27 μm per pixel resolution). The flow was seeded with 0.3 μm Al_2O_3

particles. Data acquisition (PIVACQ) and analysis (PIVPROG) were performed using software developed by one of the authors (MPW).

Twelve sets of PIV data have been obtained thus far. They consist of three laminar and three turbulent CH_4/air flames with equivalence ratios, ϕ = 0.7, 0.8 and 0.9 in +1g and −1g. The mean flow velocity U for all the experiments were 3 m/s. For the turbulent flames, turbulence produced by the grid is slightly anisotropic with u' = 0.44 m/s and v' = 0.3 m/s.
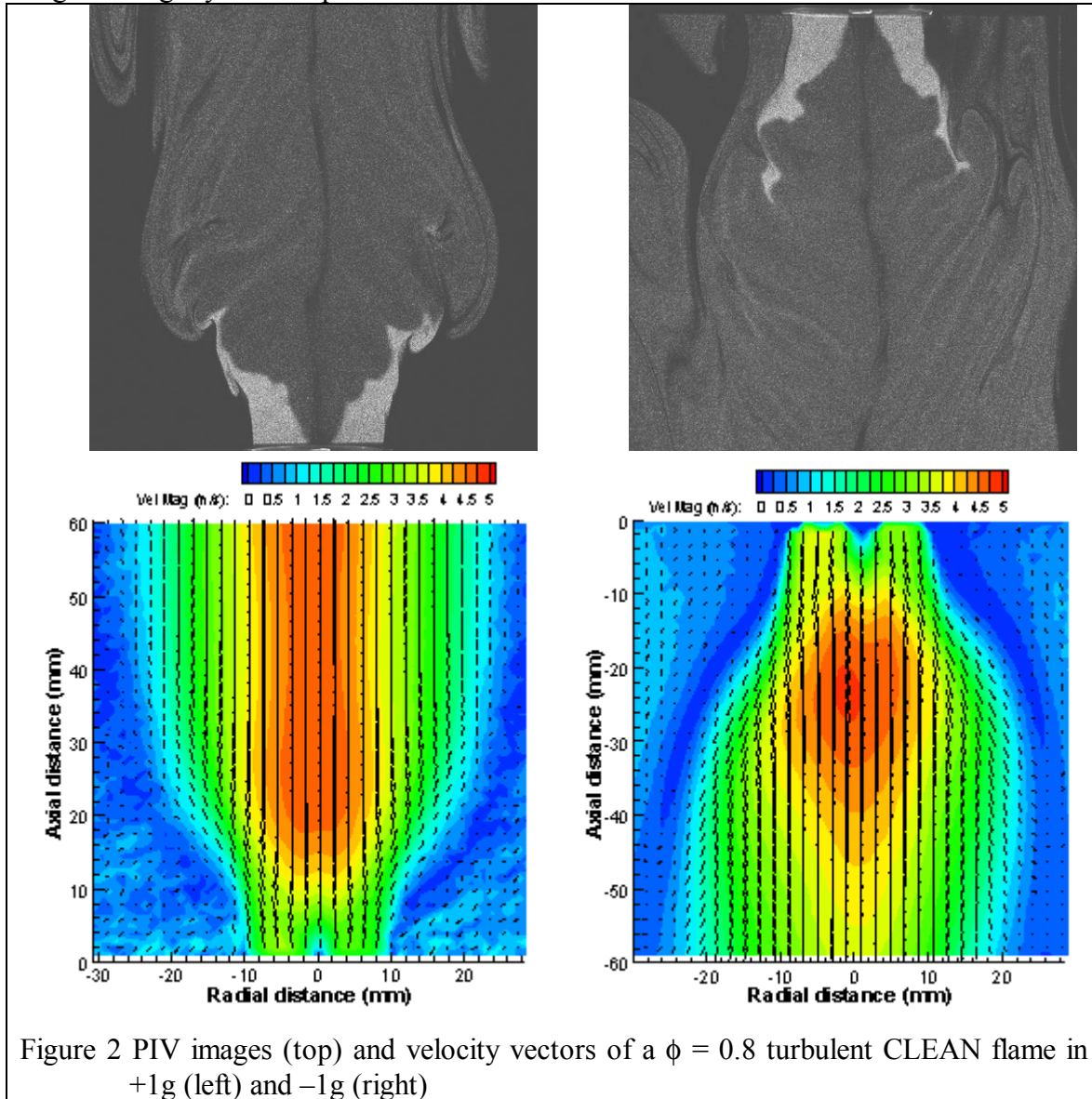
Figure 2 PIV images (top) and velocity vectors of a ϕ = 0.8 turbulent CLEAN flame in +1g (left) and −1g (right)

Figure 2 compares the raw image and velocity vectors measured in a ϕ = 0.8 turbulent flames subjected to +1g and −1g. Also shown in the background are contours of the velocity magnitude $|U| = (U^2+V^2)^{1/2}$. Due to high contract bewteen the Mie scattering intensities in the reactants and the products regions, the wrinkled flame fronts are clearly discernable on the raw images. Therefore, PIV may be the only diagnostics needed for the flight experiments because the essential scalar information can be deduced from the analysis of the flame wrinkle geometry. The velocity contours also shows that in +1g, buoyancy forces coupled with flame generated flow

acceleration help to maintain a high velocity region along the centerline. In contract, buoyancy forces acting against the heat release effects cause the flow to decelerate in –1g.
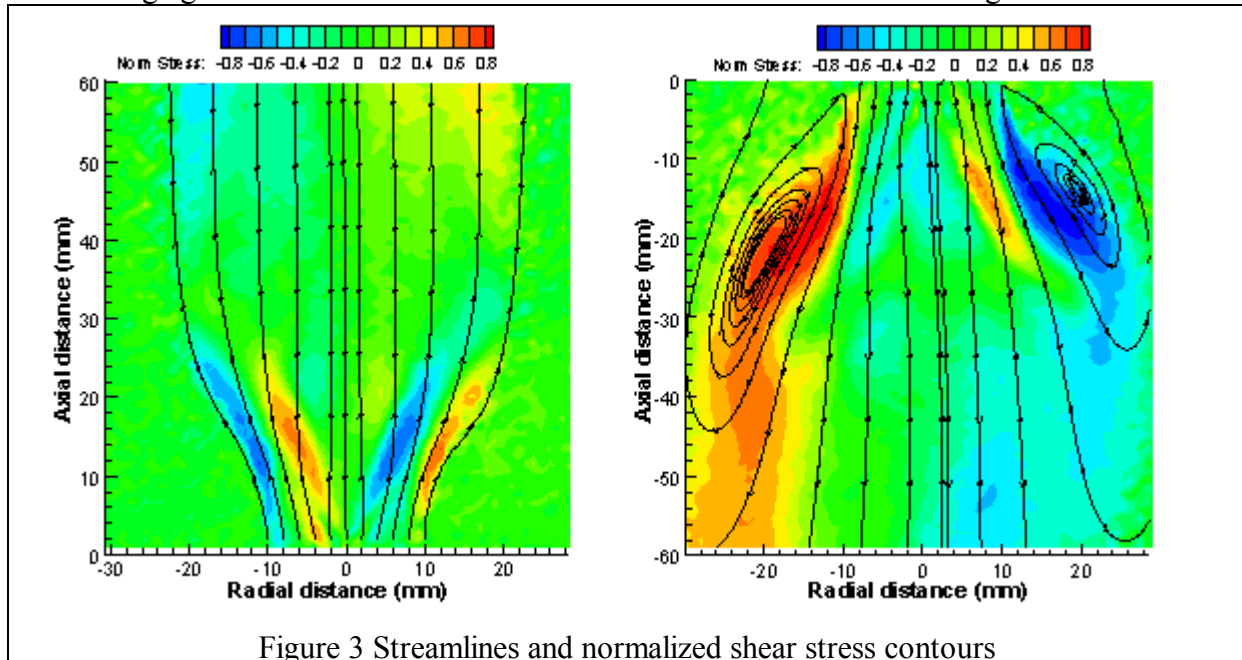
Figure 3 Streamlines and normalized shear stress contours

Other differences between the flowfields of +1g and –1g flames are shown in Figure 3. In –1g, the streamlines clearly trace regions of strong flow recirculation outside the flame, and the farfield region has a divergent trend. The normalized shear stress contours in the background show that the recirculation zones of the –1g flame are marked by high shear regions that are substantially broader than those found in the +1g flame. The two smaller shear regions closer to the centerline of both +1g and –1g flames are generated by the wrinkled flames. Though this shear stress is artificial due to intermittent contributions from the velocities in the reactants and the products [3], differences in the stress levels in the +1g and –1g flames are indicators of changes in the flame generated flow dynamics. Further analysis of the PIV data to obtained conditioned velocities will help to quantify these changes to give better insights.

PLANNED PARABOLIC FLIGHT EXPERIMENTS

To continue with the development of the flight experiments, we plan to conduct PIV measurements on board parabolic flights. The experience will guide the development of a PIV system for CIR and to address issues concerning chamber venting and seeding requirements. Though the duration of the parabola are not sufficient to allow the CLEAN flames to reach steady state the PIV data provide preliminary results on the flowfield of μg CLEAN flames.

REFERENCE
[1] Kostiuk, L.W. and Cheng, R.K., *Combustion and Flame* 103:27 (1995).
[2] Cheng, R.K. and Bedat, B., *Combustion and Flame* 116:360 (1999).
[3] Cheng, R.K., *Combustion Science and Technology* 41:109 (1984).

FLAME-GENERATED VORTICITY PRODUCTION IN PREMIXED FLAME-VORTEX INTERACTIONS

G. Patnaik and K. Kailasanath
Laboratory for Computational Physics and Fluid Dynamics
Naval Research Laboratory, Washington DC 20375

INTRODUCTION

Theoretical analysis, experimental observations, and numerical simulations have all indicated that flame-vortex interactions play an important role in the propagation and extinguishment of turbulent flames in microgravity [1]. Most studies of flame-vortex interactions ignore the effects of gravity and experiments are usually conducted in Earth gravity. Recently, Sinibaldi et al. [2] and Driscoll and coworkers [3] have reported the results of drop-tower experiments that show that for some vortex strengths, the reduction in gravity can significantly alter the structure of the flame produced by the flame-vortex interaction. These studies found that the flame is much more wrinkled in microgravity conditions, attributable to the lack of the stabilizing effect of buoyancy.

In order to examine flame-generated vorticity (FGV), it is customary to look at the production and loss terms in the vorticity equation, that is, perform a vorticity budget. We will focus our attention on those terms that can increase or decrease the total vorticity in a region containing the flame. Terms that merely redistribute vorticity, such as convective terms, do not change the total vorticity and thus do not contribute to FGV. Only two terms in the vorticity equation can create vorticity where none was originally present before; these are the viscous term and the baroclinic torque term. The stretch term, cannot create new vorticity, but can amplify or attenuate the total vorticity.

The baroclinic production term is perhaps the most interesting and has been studied in detail (see for example Refs. 4-7). It has been presumed that the misalignment of the density gradient and the pressure gradient is a major cause of FGV. The density gradient across the flame is very large, and so any small misalignment of the gradients will produce FGV. In flame-vortex interactions, the flame is highly curved and the gradients get misaligned. In order to extract the effect of gravity, it is customary to separate the pressure into a hydrostatic pressure and a dynamic pressure. The baroclinic torque can be then separated into two parts: one due to the dynamic pressure and the other due to the gravity-induced hydrostatic pressure. The role of the latter term will determine the effect of gravity.

In this study, we use detailed time-dependent, multi-dimensional numerical simulations to investigate the relative importance of the processes leading to FGV in flame-vortex interactions in normal gravity and microgravity and to determine if the production of vorticity in flames in gravity is the same as that in zero gravity except for the contribution of the gravity term. The numerical simulations will be performed using the computational model developed at NRL, FLAME3D. FLAME3D is a parallel, multi-dimensional (either two- or three-dimensional) flame model based on FLIC2D [8], which has been used extensively to study the structure and stability of premixed hydrogen and methane flames.

OUR PREVIOUS WORK

In our previous work, we examined the effect of gravity on the flame-vortex interaction in lean methane-air flames [9]. All our simulations indicated that buoyancy controls the flame shape after the flame-vortex interaction. Gravity has the strongest effect on weak vortices with small Froude numbers. Figure 1 shows qualitative comparison of numerical and experimental results [3] for a downward propagating flame interacting with an intermediate strength vortex.
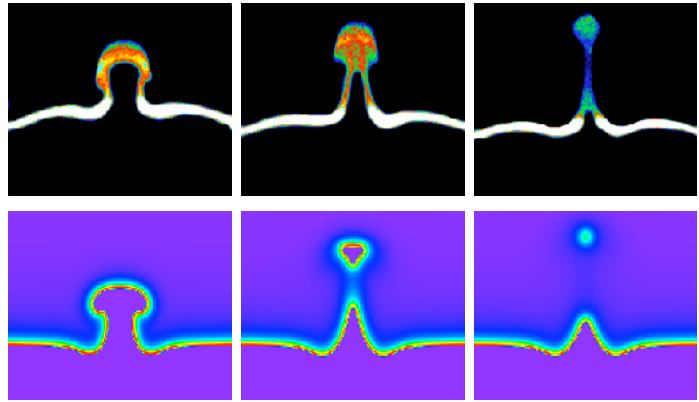
Figure 1. Experimental from U. Michigan (above) and numerical (below) comparison of OH concentration.

VORTICITY EQUATION

The vorticity equation is derived from the conservative form of the fully compressible, variable viscosity Navier-Stokes equation including the gravity source term. In our simulations, the axisymmetric form of the Navier-Stokes equation is used; thus only the θ-component of the vorticity is nonzero. The θ-component of the vorticity equation (after simplification) becomes:

$$\frac{D\omega}{Dt} + \omega(\nabla \cdot \mathbf{V}) = \underbrace{\nabla \times \frac{\mathbf{F}_v}{\rho}}_{viscous} + \underbrace{\frac{1}{\rho^2}[\nabla\rho \times \nabla P]}_{baroclinic} + \underbrace{\frac{\omega v_r}{r}}_{stretch},$$

where ω is the θ-component of the vorticity, $\mathbf{V}$ is the velocity, ρ is the density, $\mathbf{F}_v$ is the viscous force. Note that gravity does not appear explicitly anywhere. In order to extract the effect of gravity, it is customary to separate the pressure into a hydrostatic pressure and a dynamic pressure $P = p_H + p_D$, where the hydrostatic pressure, is given by: $p_H = \int_0^z \rho g dz$. With this decomposition, the baroclinic torque term can be written (after simplification) as:

$$\frac{1}{\rho^2}[\nabla\rho \times \nabla P] = \underbrace{\frac{1}{\rho^2}[\nabla\rho \times \nabla p_D]}_{dynamic} - \underbrace{\frac{g}{\rho}\frac{\partial\rho}{\partial r}}_{hydrostatic}.$$

The first of these terms is the baroclinic torque due to the dynamic pressure and the second is the torque due to the gravity-induced hydrostatic pressure.

An alternate approach [5,6] that has been taken is to assume that the hydrostatic pressure is given by: $p_H = \int_0^z \rho_A g dz$. This leads to a gravity term of the form: $-\frac{g\rho_A}{\rho^2}\frac{\partial\rho}{\partial r}$. This approach assumes that the density is basically perturbed around the constant ambient value ρ_A. This assumption is quite good for non-reactive flows, but it is incorrect for our flame-vortex simulations with large burned and unburned regions of greatly differing density. We will stick to the earlier form that does not make such an assumption.

RESULTS AND DISCUSSION

We will examine the total production of vorticity within a large control volume that fully contains the initial vortex and regions downstream into which the vorticity may be convected. We will look at the vorticity production by an "intermediate" strength vortex (peak initial vorticity 600 s-1, see Ref. 8 for details). The flame vortex interaction during upward flame propagation and propagation in zero gravity is qualitatively quite similar to downward propagation for "intermediate" strength vortices. We will examine the influence of gravity on the vorticity enhancing terms. The results show the production rate of vorticity integrated over the entire control volume versus time for the terms of interest.

Total Production of Vorticity

Figure 2 Total vorticity production.

Figure 2 shows the overall production of vorticity. The production rate remains mostly positive while the flame is being distorted by the vortex. Once the flame bubble created by the vortex is consumed and flame is no longer greatly distorted, the production rate becomes negative and total vorticity is destroyed. The curve for zero gravity propagation usually lies between the upward and downward propagation curves as might have been expected.

Figure 3 shows the partition of the baroclinic production of vorticity into the hydrostatic component induced by gravity and the dynamic component. The hydrostatic components of the baroclinic torque in the upward and downward cases are essentially similar except for sign up to the point of bubble consumption. The dynamic components in all three cases exhibit the same features, but they are not identical. If the effect of gravity were limited only to the hydrostatic term, we would expect the dynamic component to be the same in all cases. Since this is not so, it is clear that gravity also affects the dynamic component indirectly.

Baroclinic Production of Vorticity Dynamic and Hydrostatic Components

Figure 3. Hydrostatic (gravity) and dynamic components of the baroclinic production term.

Figure 4 shows the contribution to FGV from the viscous term. This contribution, though smaller than from the other terms is far from negligible. Thus, the usual assumption that has been made that this term can be neglected [4] or is identically zero [5-7] is not valid.

Vorticity is greatly enhanced by stretch while the flame is greatly distorted by the vortex. The vorticity enhancement by stretch varies by a factor of three in upward, downward, and zero-

gravity cases, indicating that gravity is significantly affecting this term, indirectly via the flame shape.

CONCLUSIONS

It is incorrect to presume that gravity's effect is fully explained just by the gravity term; the role of gravity is far more complex. All terms involved with vorticity enhancement are greatly dependent on the flame shape. Though the flame shape is quite similar in upward, downward, and zero gravity propagation, it is the subtle differences that cause the effect of gravity to be felt in the other terms as well. Thus it does not appear possible to isolate the effect of gravity on FGV to the one term in which it explicitly appears.

Figure 4. Viscous term.

Several assumptions made about the vorticity production terms have been examined. The common assumption that the viscous term does not contribute to FGV was shown to be incorrect.

References

1. Marble F., Growth of a Diffusion Flame in the Field of a Vortex, in *Recent Advances in Aerospace Science*, C. Bruno and C. Casci, Editors. 1985, Plenum, NY. pp. 395-413.
2. Sinibaldi, J., Driscoll, J., Mueller, C., and Tulkki, A., Flame-Vortex Interactions: Effects of Buoyancy from Microgravity Imaging Studies, AIAA Paper No. 97-0669, AIAA, 1997.
3. Driscoll, J., Private Communication, 1997.
4. Mueller, C. J. and Driscoll, J. F., *Combust. Flame* 112:342-358 (1998).
5. Ghoniem, A. F., Lakkis, I., and Soteriou, M., in *Proceedings of the 26th Symposium (International) on Combustion*, The Combustion Institute, Pittsburgh, PA, 1996, pp. 1531-1539.
6. Jiang, X. and Luo, K. H., *Theoret. Comput. Fluid Dynamics* 14:55-74 (2000).
7. Louch, D. and Bray, K., in *Proceedings of the 27th Symposium (International) on Combustion,* The Combustion Institute, Pittsburgh, PA, 1998, pp. 801 - 810.
8. Patnaik, G., Laskey, K., Kailasanath, K., Oran, E., and Brun, T., FLIC — A detailed, Two-Dimensional Flame Model, Memorandum Report No. 6555, NRL, Washington, DC, 1989.
9. Patnaik, G. and Kailasanath, K., Role of Gravity in Premixed Methane-Air Flame-Vortex Interactions, AIAA Paper No. 98-0742, AIAA, 1998.
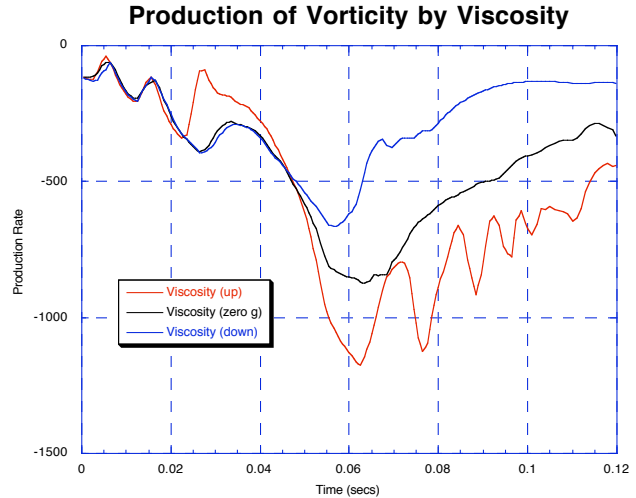
ELIMINATION OF GRAVITY INFLUENCE
ON FLAME PROPAGATION VIA ENHANCEMENT OF THE
SAFFMAN-TAYLOR INSTABILITY

R. C. Aldredge
Department of Mechanical and Aeronautical Engineering
University of California, Davis, CA 95616-5294, USA

INTRODUCTION

In this analytical work the influence of the Saffman-Taylor instability [1] on flame propagation is formulated for computational investigation. Specifically, it is of interest to examine the influence of this instability as a potential means of eliminating the effect of gravitational acceleration on the development of thermoacoustic instability. Earlier experimental investigations of thermoacoustic instability [2-6] employed tubes of large circular or annular cross-section, such that neither heat loss nor viscosity at the burner walls was of significant importance in influencing flame behavior. However, it has been demonstrated recently [7] that flames propagating between closely spaced walls, may be subject to long-wavelength wrinkling associated with the Saffman-Taylor instability, known to be relevant when a less-viscous fluid pushes a more-viscous fluid through a porous medium or between two closely spaced walls.

FORMULATION

Conservation equations governing the interaction between a flame and the dynamics of the flow through which it propagates have been formulated for conditions under which the activation energy characterizing the overall chemical reaction is large and the flame thickness and characteristic chemical time are much smaller than the length and time scales characterizing temporal and spatial variations of the flow field, respectively [8]. These equations have been solved analytically for freely propagating flames with weak curvature and flow-field strain to provide jump conditions for the flow field across the flame and an evolution equation governing the motion of the flame [9-12]. Recently, the formulation has been extended to account for the presence of acoustic waves in the flow that may influence flame dynamics and result in thermoacoustic instabilities [4, 13, 14]. This formulation does not take into account, however, influences of heat loss or viscosity at the burner walls, either of which could be important if the walls confining flame propagation are sufficiently close. In the present work the formulation of Searby and Rochwerger [14] is employed to account for the presence of acoustic waves, but with the addition of a term in the momentum conservation equation accounting for the effect of viscosity at the burner walls, following the phenomenological approach of Joulin and Sivashinsky [7]. The following equations are assumed to govern fluctuations of the velocity and pressure field ($\underline{u}$, p), assumed to be small.

$$
\left.
\begin{aligned}
&\boldsymbol{r}\frac{\partial \underline{u}}{\partial t}+\frac{\partial \underline{u}}{\partial x}=-\nabla p+\left(\nabla \boldsymbol{a}\right)\frac{d\overline{P}}{dx}+\boldsymbol{e}\Pr s\left(\nabla^2 \underline{u}-f\underline{u}\right)\\
&\frac{d\overline{P}}{dx}=-\boldsymbol{r}\mathrm{R_i}-\boldsymbol{e}\Pr\left(s/\boldsymbol{r}\right)f\\
&\nabla^2 p=\left(\nabla^2 \boldsymbol{a}\right)\frac{d\overline{P}}{dx}
\end{aligned}
\right\}
\tag{1}
$$

The independent spatial variables appearing in Eq. (1) are measured in units of the tube diameter, annulus width or flat-plate separation distance d, while time is measured in units of d/U_L; where U_L is the laminar burning speed for the given reactive mixture. Like the independent spatial

variables, the dependent flame-surface perturbation a about the location of the mean flame-surface plane is also measured in units of d while velocity, pressure and density r are measured in units of U_L, $r_u U_L^2$ and r_u, respectively; where r_u is the density of the cold reactant flow. Other parameters appearing in the equation are the Prandtl and Richardson numbers defined as $\mathrm{Pr} \equiv n/a$ and $\mathrm{R_i} \equiv gd/U_L^2$, where n and a are the kinematic viscosity and thermal diffusivity of the mixture, respectively; and the ratios e and s of the flame thickness to d and of the thermal conductivity of the mixture to its value in the cold reactant flow, respectively. The parameter f is a constant friction factor accounting for the effect of viscosity at the inner walls of the tube or annulus within which, or flat plates between which, the flame propagates and is determined by the profile of the mean velocity across the flow cross-section. Note that the independent spatial variable x is measured normal to the reaction zone of the flame, having been introduced through a transformation from laboratory coordinates to a coordinate system that moves with the flame locally [8].

The motion of the flame, considered as an interface separating the cold reactants from the hot products, is dictated by its advection by the flow and its local rate of propagation into the reactants, as determined by thermodynamic and transport properties of the flow and local flow-field strain and flame-surface curvature. Small local perturbations about the mean reaction-zone location of a quasi-planar, weakly stretched flame (with small flow-field strain and flame-surface curvature) are predicted [8-10, 12, 15-18] to obey a linear evolution equation when the overall chemical activation energy is assumed to be large; namely,

$$\frac{\partial a}{\partial t} = u_{(x=0^-)} + e\left[\nabla^2 a - \left(\partial u/\partial x\right)_{(x=0^-)}\right], \tag{2}$$

where the velocity fluctuation along the direction of mean flame propagation u and its gradient $\partial u/\partial x$ are evaluated in the reactant flow just upstream of the flame, as denoted. Eqs. (1) and (2) comprise a closed set of five equations to be solved for the five flame and flow-field perturbation variables $(a, p, \underline{u})$. Since the flow-field equations are valid only in the incompressible regions on either side of the flame, jump conditions on the flow variables must be satisfied at the moving flame front to ensure continuity of the flow across the flame. The jump conditions are obtained in the same manner as that leading to Eq. (2), through integration of the full set of conservation equations, including those for energy and reactant species, across the reaction and preheat zones of the flame using asymptotic expansions that exploit large chemical activation energies and the disparity between the thicknesses of the reactant and preheat zones and between the overall flame thickness and the length scales over which order-unity variations of the hydrodynamic reactant and product flow occur.

Evaluation of linear stability proceeds with the assumption of harmonic flow-field and flame-surface fluctuations $(\underline{u}, p, a)$ according to $e^{\Omega t + i\underline{k}\cdot\underline{y}}$, where $\underline{k}$ is the wavenumber vector characterizing fluctuations in the transverse coordinate plane, measured in units of d^{-1}, and Ω represents the growth rate (real part) and frequency of fluctuations (imaginary part) measured in units of U_L/d. Calculation of the fluctuation amplitudes by solution of Eqs. (1) and (2), subject to the jump conditions across the flame, results in a dispersion relation which governs whether the fluctuation amplitudes will grow in time or be attenuated by stabilizing influences. The dispersion relation, which takes the form

$$A(k)\Omega^2 + B(k)\Omega - C(k) = 0, \tag{3}$$

where A, B and C are functions of the magnitude k of the wavenumber vector characterizing fluctuations in the transverse coordinate plane and the thermodynamic and transport properties of the reactant and product flows, has been derived in earlier studies of the stability of freely propagating wrinkled flames with weak curvature and flow-field strain [9-12]. Recently, corrections to the functions A, B and C valid through order e^2 to account for the effect of viscosity at the

burner walls has been provided by Joulin and Sivashinsky [7]. However, in this recent work second-order influences on flame stability associated with flame stretch were neglected. In the present work, the recent corrections have been incorporated into the earlier formulation to provide the following forms of the functions *A, B* and *C* that account for influences of both viscous damping of the mean flow that could give rise to the Saffman-Taylor instability as well as flame-stretch, which may provide attenuation of small-scale flame-surface wrinkles.

$$
\left.
\begin{aligned}
A &= (s+1) + ek(s-1)\left(Ma - \tfrac{s}{s-1}J\right) \\
B &= 2eks\left[1 + eks(Ma-J)\right] + e^2\Pr f\left(s^{3/2} + s\right) \\
C &= (ek)^2 s(s-1)\left[1 + (2\Pr-1)h - ek\left(c_b + \tfrac{3s-1}{s-1}Ma - \tfrac{2s}{s-1}J\right)\right] \\
&\quad - ek(s-1)\left\{\left[1 - ek\left(Ma - \tfrac{s}{s-1}J\right)\right]\mathrm{R_i} - e^2\Pr f s\left(\tfrac{s^{3/2}-1}{s-1}\right)\right\}
\end{aligned}
\right\}
\tag{4}
$$

The new parameters introduced in Eq. (4) are defined as follows,

$$
\left.
\begin{aligned}
h &\equiv \int_0^1 \left[c_b - c(q)\right]dq \\
J &\equiv (s-1)\int_0^1 \frac{c(q)}{1+(s-1)q}\,dq \\
Ma &\equiv \tfrac{s}{s-1}J - \tfrac{1}{2}l_e\int_0^1 \frac{c(q)\ln(q)}{1+(s-1)q}\,dq \\
l_e &\equiv b(Le-1), \quad b \equiv \tfrac{E}{RT_b}\left(\tfrac{s-1}{s}\right)
\end{aligned}
\right\},
\tag{5}
$$

where q denotes the ratio of the departure of the temperature from that of the reactants $(T - T_u)$ to the temperature difference across the flame $(T_b - T_u)$, c is the ratio of the thermal conductivity to the specific heat normalized by the same ratio evaluated in the cold reactant mixture, and Le is the Lewis number defined as the ratio of the thermal diffusivity to the mass diffusivity of the limiting reactant, where one reactant is considered to be present in excess. The Zel'dovich number b is defined as the ratio of the activation energy E to the product of the gas constant R and burnt-gas temperature T_b, normalized by a measure of the temperature difference across the flame, and is assumed to be large. The parameter s is simply the ratio of the temperature of the burnt gases to that of the cold reactant flow. The dispersion relation as defined in Eq. (3) indicates that flow-field and flame-surface perturbations will be unstable and grow exponentially in amplitude when the sign of last term of the equation, $C(k)$, is positive. Otherwise, the growth rate Ω has no positive real part and such perturbations will be attenuated as a result of stabilizing influences. The new terms in the dispersion relation accounting for possible influence of the Saffman-Taylor instability appear as second-order corrections to coefficients A and B involving the product of the friction factor f and the Prandtl number. Note in particular that although the effect of gravitational acceleration acting along the mean propagation direction, exhibited through the Richardson number $\mathrm{R_i}$, is stabilizing in that the value of $C(k)$ decreases with increasing $\mathrm{R_i}$, the new second-order viscous term counteracts the influence of this stabilizing effect and may cause $C(k)$ to become positive when the tube diameter, annulus width or flat-plate separation distance d is sufficiently small.

The problem of linear stability can be posed alternatively, in terms of the same coefficients *A, B* and *C*, by considering the dispersion relation as the characteristic equation associated with a second-order evolution equation governing a linear oscillator. Specifically, the second-order, linear ordinary differential equation

$$A(k)\frac{\partial^2 \boldsymbol{a}}{\partial t^2} + B(k)\frac{\partial \boldsymbol{a}}{\partial t} - C(k)\boldsymbol{a} = 0 \tag{6}$$

has solutions of the form $\exp(\Omega t)$, with the growth rate Ω satisfying the dispersion relation given in Eq. (3) resulting from solution of the set of Eqs. (1) and (2) and application of the flow-field jump conditions at the flame front. Analysis of Eq. (6) can be fruitful, therefore, in obtaining predictions of the stability of flame-surface perturbations once the coefficients A, B and C have been determined in the manner described above. Eq. (6) serves also as a point of departure for consideration of the influence of acoustic flow-field fluctuations on flame stability, following Searby and Rochwerger [14] and Bychkov [13], through the introduction an oscillating acceleration field as an additional term in the function $C(k)$. Specifically, replacing R_i in this function with $R_i - U_a \boldsymbol{w} \cos(\boldsymbol{w}t)$, where U_a and $\boldsymbol{w}$ are the amplitude and frequency of axial acoustic velocity fluctuations present in the flow measured in units of U_L and U_L/d, respectively, results in the following modified form of Eq. (6).

$$\left. \begin{array}{l} A(k)\dfrac{\partial^2 \boldsymbol{a}}{\partial t^2} + B(k)\dfrac{\partial \boldsymbol{a}}{\partial t} - \left[C(k) - D(k)U_a \boldsymbol{w} \cos(\boldsymbol{w}t) \right]\boldsymbol{a} = 0 \\[3mm] D(k) \equiv \boldsymbol{e}k\left(\boldsymbol{s} - 1\right)\left[1 - \boldsymbol{e}k\left(Ma - \frac{\boldsymbol{s}}{\boldsymbol{s}-1}J \right) \right] \end{array} \right\} \tag{7}$$

Analysis of Eq. (7) allows the calculation of stability diagrams predicting acoustic-velocity amplitudes and wavenumbers for which flame propagation is unstable [13, 14]. The stability diagrams are obtained in the same manner as that described in detail by Bychkov [13]. However, predictions made with the modified formulation presented herein account for the importance of the Saffman-Taylor instability, associated with the disparity between the viscosities of the reactant and product flows, when the tube diameter, annulus width or flat-plate separation distance d is sufficiently small.

REFERENCES

1. Saffman, P. G. and Taylor, G. I., *Proceedings of the Royal Society of London A* 245:312 (1958).
2. Clanet, C., Searby, G. and Clavin, P., *Journal of Fluid Mechanics* 385:157 (1999).
3. Clanet, C. and Searby, G., *Physical Review Letters* 80:3867 (1998).
4. Aldredge, R. C. and Killingsworth, N. J., *Combustion and Flame* submitted (2003).
5. Vaezi, V. and Aldredge, R. C., *Combustion and Flame* V121:356 (2000).
6. Searby, G., *Combustion Science and Technology* 81:221 (1992).
7. Joulin, G. and Sivashinsky, G. I., *Combustion Science and Technology* 98:11 (1994).
8. Williams, F. A., *Combustion Theory*. Addison-Wesley, Reading, MA, 1985.
9. Pelce, P. and Clavin, P., *Journal of Fluid Mechanics* 124:219 (1982).
10. Sivashinsky, G. I., *Acta Astronautica* 4:1177 (1977).
11. Matalon, M. and Matkowsky, B. J., *Journal of Fluid Mechanics* 124:239 (1982).
12. Clavin, P. and Garcia-Ybarra, P., *Journal de Mecanique Appliquee* 2:245 (1983).
13. Bychkov, V., *Physics of Fluids* 11:3168 (1999).
14. Searby, G. and Rochwerger, D., *Journal of Fluid Mechanics* 231:529 (1991).
15. Markstein, G. H., in *Nonsteady Flame Propagation* (Markstein, G. H., Ed.), The MacMillan Company, New York, 1964.
16. Aldredge, R. C. and Williams, F. A., *Journal of Fluid Mechanics* V228:487 (1991).
17. Joulin, G. and Clavin, P., *Combustion and Flame* 35:139 (1979).
18. Clavin, P. and Williams, F. A., *Journal of Fluid Mechanics* 116:251 (1982).

HYPERSPECTRAL INFRARED IMAGING OF FLAMES

W.T. Rawlins, D.B. Oakes, S.D. Wehe, D.X. Hammer, W.J. Marinelli, and M.G. Allen
Physical Sciences Inc., 20 New England Business Center, Andover, MA 01810-1077

INTRODUCTION

Investigations of the dynamics of flame spread over combustible surfaces in microgravity are critical to spacecraft fire safety, as well as to the understanding of fundamental fire phenomena. In the absence of gravity-induced buoyancy and forced convection, heat transfer between the flame gases and the fuel surface is dominated by conductive and radiative mechanisms. The detailed understanding of these mechanisms requires direct observations of the spatial propagation and radiative fluxes of key flame product species such as CO_2 and H_2O. We describe a method and instrument to perform such measurements non-intrusively by observing spatially resolved, spectrally scanned infrared emission images from flame-produced molecular species including CO_2, H_2O, and CO. The species-specific rovibrational band structures of the spectra enable discrimination between gas phase, particulate, and hot surface contributions to the observed emission, as well as determinations of path-integrated species concentrations and temperatures.

The instrument, named AIRIS (Adaptive Infrared Imaging Spectroradiometer), is a computer-controlled, rapidly scanning Fabry-Perot etalon, coupled to an infrared camera and an optical collection system, which is capable of imaging flame radiance spectra in the infrared. The device combines the imaging capability of an infrared camera with the fast spectral scanning capability of a Fabry-Perot etalon, at medium spectral resolutions in the infrared. Through rapid stepping of the etalon through a series of pre-programmed wavelengths, a series of images of the scene at each wavelength is produced over a short (<1 second) time frame, resulting in a hyperspectral "cube" of spectral radiance as a function of height, width, and wavelength.

During the currently funded project, we are using the AIRIS instrument in laboratory flame measurements to characterize its performance, to develop the necessary data analysis tools, and to examine its potential for microgravity investigations of flame spread phenomena over solid fuels. Ultimately, the AIRIS instrument can use four mirror sets to operate over the spectral ranges 2.5 to 3.3 µm, 3.7 to 5.0 µm, 5.0 to 6.5 µm, and 8 to 11 µm, encompassing the spectral features of H_2O, CO_2, CO, NO, hydrocarbons, and fuel surface emissions. The present work focuses on spectrally scanning imaging measurements in the 2.6 to 2.9 and 3.7 to 5.0 µm regions.

INSTRUMENT DESCRIPTION

The AIRIS Fabry-Perot filter is interfaced to an infrared focal plane array (FPA) camera/dewar system obtained on loan from NASA/GRC. The fully assembled instrument is shown in Figure 1. The AIRIS filter consists of a high-finesse, low-order Fabry-Perot interferometer, using a pair of high-reflectivity mirrors which are coated for the spectral regions of interest. In this work, we have used mirror sets coated for the 3.7 to 5.0 µm and 2.0 to 3.0 µm spectral regions. The mirrors are driven at high precision (~4 nm) by a set of three inchworm motors controlled by a four-point capacitance micrometer circuit which measures the mirror spacing and parallelism. The instrument includes a computer system and a data acquisition
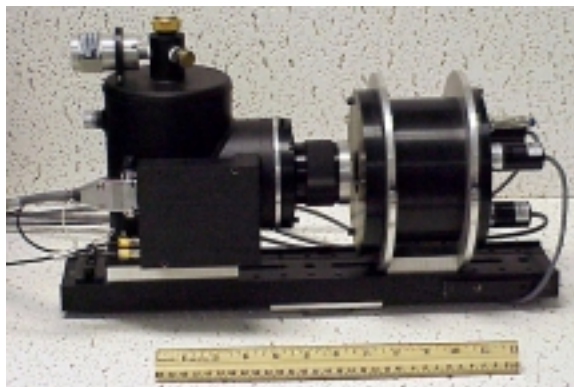
Figure 1. Photograph of the AIRIS instrument, consisting of scanning Fabry-Perot filter, collection lens, and InSb camera/dewar system.

board. The computer, camera controls, and inchworm motor controls are housed in an instrument rack modified for aircraft use as recommended by NASA/GRC. The NASA/GRC camera is an Amber 4128C InSb focal plane array, 128 x 128 (6.4 mm x 6.4 mm), with a 50 μm pitch. The FPA is integral with a liquid nitrogen dewar which is specially designed for microgravity measurements on the KC-135. We have developed a data acquisition interface for this camera using an Imaging Technologies Inc. (ITI) framegrabber board and custom software.

The mid-wavelength optical collection system consists of a 50 mm DIOP multi-element lens, positioned to give 1/10 magnification of the object plane. This results in a field of view 6.4 cm x 6.4 cm (0.5 mm x 0.5 mm per pixel) at the object plane, which is 55 cm from the lens. The AIRIS filter is 18 cm long and 15 cm o.d. with a 36 mm clear aperture, and is positioned immediately in front of the lens. A cold bandpass filter mounted on the FPA restricts the spectral range to 3.7 to 5.0 μm, eliminating higher-order radiation transmitted by the AIRIS filter. The entire assembly of camera, lens, and filter is mounted on an optical rail 46 cm (18 in.) long. The observed spatial resolution near 4 μm is limited by diffraction, and is intermediate between 0.5 and 1 mm. The observed depth of field is ~4 cm. For second-order operation of the Fabry-Perot filter between 3.7 and 5 μm (i.e. mirror spacing = wavelength), the observed free spectral range is 1.48 μm, the spectral resolution is 0.043 μm (FWHM), and the finesse is 34, all of which agree well with predicted values. Typical spectral scanning rates for the fully automated system are 10 to 50 wavelengths/s.

Flame measurements using the 2 to 3 μm mirror set employed a free spectral range of 0.26 μm in 10th order, a finesse of 26, and a spectral resolution of 0.01 μm. An order-sorting bandpass filter restricted the instrument response to 2.65 to 2.90 μm, in keeping with the free spectral range for 10th order. The short-wavelength measurements also employed a Cincinnati Electronics liquid-nitrogen-cooled InSb camera (120 vertical x 160 horizontal pixels, each 50 μm square) with a 4 μm short-pass cold filter inside the dewar, a 1/25 zoom lens, and manually triggered image acquisition at each wavelength.

LABORATORY FLAME MEASUREMENTS

We have observed spectral images of the exhaust plume above a laboratory quasi-premixed flame generated by a flat flame, Hentgen-style burner. The measurements were made at heights greater than 10 cm above the burner surface, i.e. well above the active flame zone. The flame is surrounded and stabilized by an annular flow of nitrogen. Previous temperature, OH PLIF, and LII imaging measurements on this burner indicate flame diameters of 2 to 3 cm at heights up to 4 cm above the burner surface. For the exhaust-stream IR imaging measurements, a circular 1/8-in. thick aluminum plate, with a central hole 2.5 in. (6.35 cm) in diameter, was placed over the flame at a height 10 cm above the burner surface. This plate was used to define the bottom

edge of the imager's field of view. The AIRIS imager was positioned to view the flame exhaust stream from the top of the plate to a height some 6 to 10 cm above the plate.

Example spectral images in the 3.7 to 5.0 µm range are shown in Figure 2. These images show the exhaust stream above a stoichiometric CH_4/air flame at three wavelengths probing the blue edge, center, and red edge of the $CO_2(\nu_3)$ band near 4.3 µm. The camera's 6.4 x 6.4 cm field of view is indicated on the figure. The bright regions near the bases of the images are reflections from the flame on the walls of the aluminum housing which shrouds the flame up to 10 cm HAB. The diameter of the hot exhaust stream ranges from ~1.4 cm near the bottom of the image to ~1.1 cm near the top of the image. Figure 3 shows two spectral distributions obtained from the 128 x 128 images for single pixels on the stream centerline: one near the top of the image (horizontal and vertical pixel coordinates (59,1), 16 cm HAB), and one near the brightest part of the exhaust stream ((59,80), 12 cm HAB). Both spectra show the characteristic $CO_2(\nu_3)$ band, however the differing spectral widths signify differences in temperature, and the differing intensities signify different CO_2 concentra-

Figure 2. Spectrally resolved images of the exhaust stream of a stoichiometric CH_4/air flame at 4.20, 4.35, and 4.45 µm. The exhaust stream is observed at heights of 10 to 16 cm above the burner surface. The 6.4 x 6.4 cm field of view is indicated on the center frame.

Figure 3. Single-pixel AIRIS spectra from the flame exhaust stream of Figure 2, for the stream centerline at heights of 12 and 16 cm above the burner surface.

tions. Spectral band shape analysis (accounting for effects of optical thickness and room air absorption near the band center) gives apparent temperatures of 1150 K for the centerline at the top of the image (16 cm HAB), and 1250 K for the lower height (12 cm HAB). Temperatures as low as 600 K can be observed at the edges of the exhaust stream.

Spectral imaging measurements near 2.8 µm can be used to diagnose both CO_2 and H_2O simultaneously. The principle is illustrated in Figure 4, which shows spectra for $H_2O(\nu_3)$ and $CO_2(\nu_1+\nu_3)$ radiances observed with a Fourier transform spectrometer in a stoichiometric C_2H_4/air flame. The figure also shows the fundamental band shapes and strengths of the two bands, plotted against the right-hand axis, and a computed fit to the observed spectrum. Both of these bands are optically thin for flame dimensions of a few cm, and they are not significantly affected by room air absorption in the optical path. Example infrared images of flame exhaust streams at 2.70 µm (0.01 µm FWHM) are shown in Figures 5 and 6. As in Figure 2, the
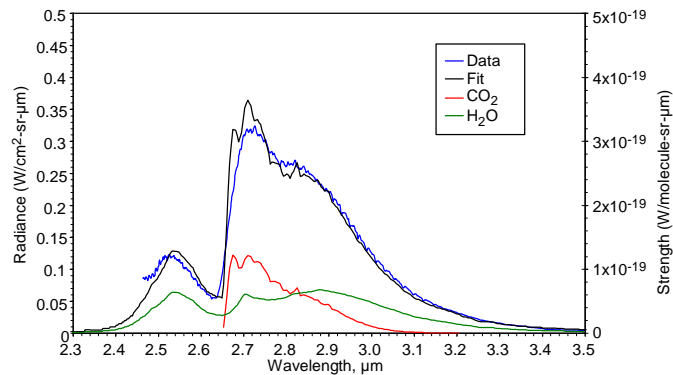
Figure 4. Comparison of observed C_2H_4/air flame spectrum and computed spectrum for $H_2O(\nu_3)$ and $CO_2(\nu_1+\nu_3)$ emission at 2000 K. Individual species band strengths are plotted against the right-hand ordinate. The spectral fit was computed for equal H_2O and CO_2 column densities of 2 x 10^{18} molecules/cm^2.

horizontally extended feature at the base of the image is the top of the housing around the flame, and is located at 10 cm HAB. The top of the frame is located at 21 cm HAB. The image in Figure 5 shows radiance from $H_2O(\nu_3)$ produced in a fuel-lean H_2/air flame. The emission from the hot exhaust vapor shows a maximum at ~13 cm HAB, and extends up to ~16 cm HAB. In contrast, the image in Figure 6 shows emission from both $H_2O(\nu_3)$ and $CO_2(\nu_1+\nu_3)$, produced by the addition of CO to a fuel-lean H_2/air flame. In this case, the observable infrared emission extends to at least 21 cm HAB, owing to additional heat release from CO oxidation. In each case, the diameter of the hot exhaust stream is 1.6 to 1.8 cm at the height of maximum intensity (12 to 13 cm HAB). Spectral analysis of images from 2.64 to 2.90 μm is in progress.
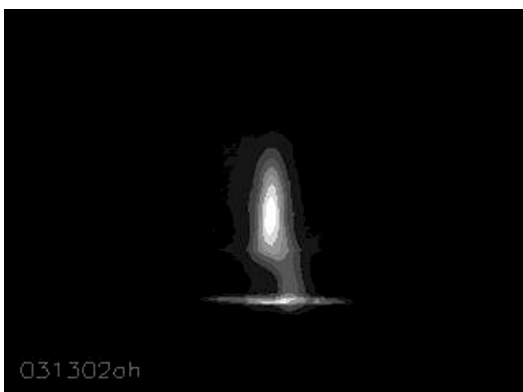
Figure 5. AIRIS image of $H_2O(\nu_3)$ emission at 2.70 μm, in the exhaust stream of a H_2/air flame, 10 to 21 cm above the burner surface.

Figure 6. AIRIS image of $H_2O(\nu_3)$ and $CO_2(\nu_1+\nu_3)$ emission at 2.70 μm, in the exhaust stream of a H_2/CO/air flame, 10 to 21 cm above the burner surface.

SUMMARY

This paper describes and demonstrates a hyperspectral infrared imaging spectrometer for quantitative infrared emission spectroscopy and imaging of flames. We plan to apply this non-intrusive measurement method to investigations of flame spread over solid surfaces in microgravity and reduced gravity environments. The hyperspectral infrared imaging technique is also applicable to other microgravity combustion experiments, such as diffusion and premixed flame structure, soot formation, and droplet combustion investigations.

FAN BEAM EMISSION TOMOGRAPHY FOR LAMINAR FIRES

Yudaya Sivathanu and Jongmook Lim
En'Urga Inc., West Lafayette, IN 47906

Douglas Feikema
NASA Glenn Research Center, Cleveland, OH 44135

Introduction

Obtaining information on the instantaneous structure of turbulent and transient flames is important in a wide variety of applications such as fire safety, pollution reduction, flame spread studies, and model validation. Durao et al. (1992) has reviewed the different methods of obtaining structure information in reacting flows. These include Tunable Laser Absorption Spectroscopy (Hanson et al., 1980), Fourier Transform Infrared Spectroscopy (Best et al., 1991), and Emission Spectroscopy (Sivathanu and Gore, 1991) to mention a few.

Diagnostics with high power lasers are difficult to implement in microgravity environment. Absorption spectroscopy using either tunable laser diodes (Hanson et al., 1980) or FTIR (Best et al., 1991) can be used with deconvolution to obtain local gas species concentrations, soot volume fractions and temperatures in laminar flames. However, absorption spectroscopy requires a source, with corresponding alignment problems. The advantages of absorption spectroscopy are that it can be utilized even in low temperature flows, and is ideally suited to measure gas species concentrations (Zhang and Cheng, 1986).

Most flames emit significant radiation signatures that are used in various applications such as fire detection (Sivathanu and Tseng, 1996), light-off detection (Vaidya et al., 1982), flame diagnostics (Choi et al., 1995), etc. Radiation signatures can be utilized to maximum advantage for determining structural information in turbulent flows (Sivathanu and Faeth, 1990, Sivathanu and Gore, 1991, Sivathanu et al., 1991). Emission spectroscopy is most advantageous in the infrared regions of the spectra, principally because these emission lines arise from transitions in the fundamental bands of stable species such as CO_2 and H_2O.

Based on the above, the objective of this work was to develop a fan beam emission tomography system to obtain the local scalar properties such as temperature and mole fractions of major gas species from path integrated multi-wavelength infrared radiation measurements.

Experimental and Theoretical Method

Tomographic reconstruction of local scalar properties is based on the deconvolution of a finite number of two-dimensional path-integrated multi-wavelength radiation measurements that would be acquired by a mid-infrared spectrometer with a scanner (Spectraline Inc., Model ES100). For an axisymmetrical flame, the experimental arrangement is illustrated in Fig. 1. For each ring, unique scalars (temperature, mole fraction of CO_2 and H_2O) are defined. In the Fig.1, gas temperature, mole fraction of CO_2 and H_2O are denoted as T_i, X_{i1} and X_{i2}, respectively.

The spectral radiation intensity emitted from a homogeneous path is represented as

$$I_\lambda = I_{b\lambda}(1 - \tau_\lambda) \tag{1}$$
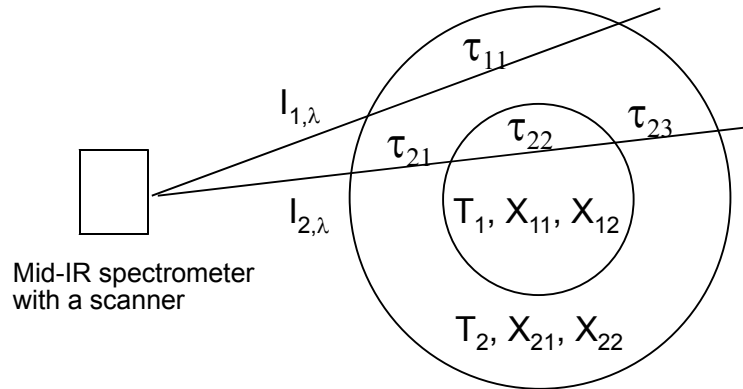
Figure 1. Schematic of Fan Beam Emission Tomography.

where $I_{b\lambda}$ is the Planck function (dependent on the gas temperature), and τ_λ is the spectral transmittance of the homogeneous path. For a given temperature and mole fractions of CO_2 and H_2O, the spectral transmittance (τ_λ) along the optical path can be calculated using a narrow band radiation model, RADCAL (Grosshandler, 1993). For the two representative homogeneous rings shown in Fig. 1, the measured path-integrated intensities are:

$$I_{1,\lambda} = I_{1,b\lambda}(1 - \tau_{11}) \tag{2}$$

$$I_{2,\lambda} = I_{1,b\lambda}\left[(1 - \tau_{23}) \cdot \tau_{22} \cdot \tau_{21} + (1 - \tau_{21})\right] + I_{2,b\lambda}(1 - \tau_{22}) \cdot \tau_{21}. \tag{3}$$

These two path-integrated intensities are calculated at several mid-infrared wavelengths. The iterative deconvolution algorithm used to obtain the local scalars from the path-integrated intensities involves two steps: (1) Calculation of the local spectral radiation intensities for all homogeneous rings, given the value of the transmittances for all segments in the optical path, and (2) Estimation of the gas temperature and mole fractions of CO_2 and H_2O from the local spectral intensities within each homogeneous ring.

A linearized MLE inversion method is used to find the three scalars in the homogeneous gas path. The estimated local temperatures and mole fractions are used to calculate the transmittances for all segments in the domain. These transmittances are then used in Step 1. This two-step process is repeated until convergence is achieved. At the first iteration, local intensities are found only considering emission and neglecting self-absorption by intervening gaseous components.

Results and Discussion

The performance of the inversion algorithm was evaluated using a synthetic dataset. The synthetic dataset consists of a 13 point radial profile of gas temperatures and mole fractions of CO_2 and H_2O. The radial profile is representative of measurements obtained in a laminar ethylene diffusion flame by Santoro et al. (1987). The major difference between the measurements (Santoro et al., 1987) and the synthetic data set is that soot is absent in synthetic data set. The path-integrated radiation intensities at 140 wavelengths (2.2-4.8 μm) are computed for 25 view angles using the RADCAL database. The diameter of the flame is 2 cm.

The synthetic and deconvoluted path-integrated intensities, at the point of convergence, for the center of the flame are shown in Fig. 2. The temperatures and gas concentrations obtained from the deconvolution algorithm and the synthetic data are shown in Fig. 3. The lines represent the synthetic data and the symbols represent the deconvoluted results.
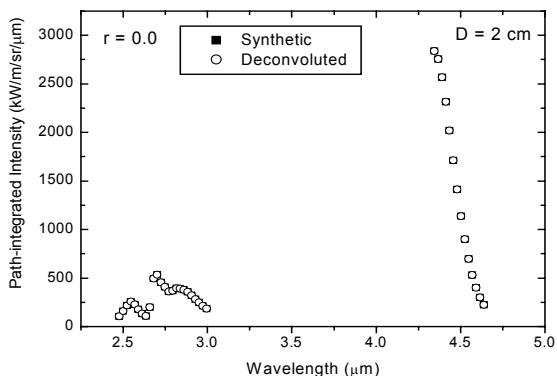
Figure 2: Synthetic and deconvoluted path integrated intensities at the center.
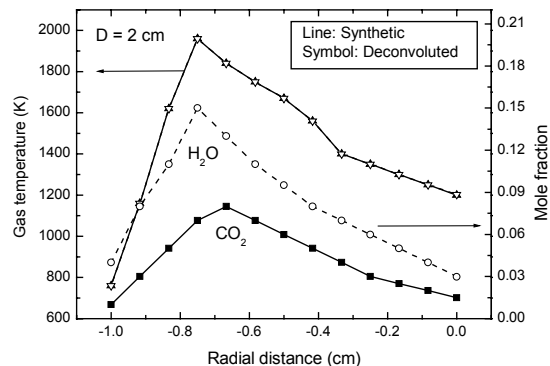
Figure 3: Synthetic and deconvoluted scalars at x/d = 2.0.

At the point of convergence, the spectral radiation intensities obtained from deconvolution are within 0.1% of those obtained from the synthetic data. This indicates that the deconvolution algorithm provides scalars that can match the spectral radiation intensities provided by the synthetic data set very closely. Since radiation intensities at 25 view angles were used in the deconvolution algorithm, it is possible to obtain temperatures and gas species concentrations for 13 rings. For all 13 rings, the deconvoluted scalars are within 0.1% of the synthetic data. In general, it is more difficult to obtain the scalar property at the center accurately, since the volume of gas emitting radiation is the lowest in the innermost ring. However, the results obtained are accurate to within 0.1%, even for the innermost ring.

The sensitivity of the algorithm to random noise in the intensities and wavelength was examined using the synthetic data. A random 1% noise was added to the synthetic spectral radiation intensities, and then deconvoluted using the algorithm. At the outer rings, the inversion error for the gas temperatures is less than 1 %. However, the inversion error increases toward the center of the flame. At the center of the flame, the error is approximately 20 %. The higher error at the center could be attributed to two reasons. The area of the center ring is approximately one tenth of the outermost ring, so the contribution of the center ring to the overall path-integrated intensities is much lower than those of outer rings. Therefore, any error in the path-integrated spectral radiation intensities could lead to high deconvolution errors at the center of the flame. The second reason for the higher deviation is that the temperature of the center ring is lower than the peak temperature. Therefore, noise contribution to the local intensity of center ring is higher since the random noise 1 % is defined for peak intensities. The error in deconvoluted temperatures due to a 10 nm noise in the specified wavelength is less than 2%.

The deconvolution algorithm was then applied to spectral radiation intensity data measured from a methane/air diffusion flame. The flame was stabilized on a Santoro burner, with a methane flow rate at 7.4 cc/s and a air flow rate at 1100 cc/s. The temperatures and gas concentrations obtained from the deconvolution are shown in Figs. 4 and 5 respectively.
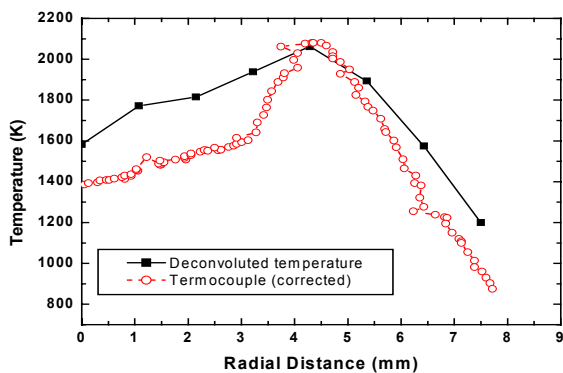
Figure 4. Temperatures obtained using fan beam emission tomography
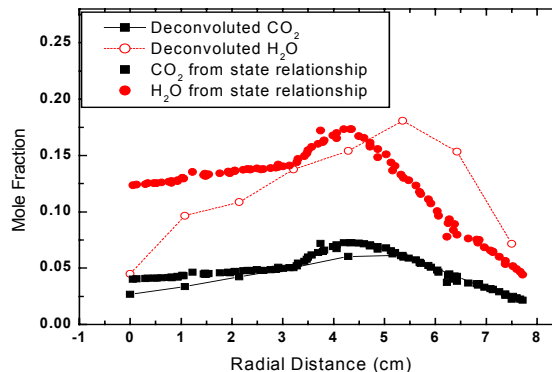
Figure 5. Gas concentrations obtained using fan beam emission tomography

The results obtained from fan beam emission tomography are in reasonable agreement with temperatures obtained from thermocouple data and gas concentrations inferred from state relationships. However, the lack of spatial resolution results in higher estimated temperatures, and consequently lower gas concentrations at the center of the flame.

Conclusions

A tomographic algorithm was developed to estimate local scalars from the multi-wavelength path-integrated spectral radiation intensities. The algorithm was evaluated using a synthetic data set. The deconvolution algorithm successfully recovers the temperature and gas concentrations within 0.1 % for a laboratory flame. The deconvolution algorithm was less successful with experimental data due to the lack of spatial resolution for the measurements.

Acknowledgement:

References

Best, P. E., Chien, P. L., Carangelo, R. M., Solomon, P. R., Danchak, M. and Ilovici, I 1991, Combust. Flame, vol. 85, pp. 309-318.

Choi, M. Y., Hamins, A., Mullholland, G. W., and Kashiwagi, T., 1995, Combust. Flame, vol. 99, pp. 174-186

Durao, D. F. G., Heitor, M. V., Whitelaw, J. H., and Witze, P. O., 1992, *Combustion Flow Diagnostics,* Kluwer Academic Publishers, Netherlands.

Grosshandler, W. L., 1993, *http://fire.nist.gov/bfrlpubs/ fire93/ art096.html.*

Hanson, R. K., Varghese, P. L., Schoenung, S. N., and Falcone, F. K., 1980, *Laser Probes for Combustion Chemistry*, ACS-Symposium Series, vol. 134, pp. 413-426.

Santoro, R. J., Semerjian, Yeh, T. T., Horvath, J. J., and Semerjian, H.G., 1987, Combust. Sci. Tech. 53, 89.

Sivathanu, Y. R., and Gore, J. P., 1991, Combust. Sci. & Tech., vol. 80, pp. 1-21

Sivathanu, Y. R., and Tseng, L. K., 1998, Fire Safety Journal, vol. 29, pp. 301-315.

Sivathanu, Y. R., and Faeth, G. M., 1990, Combust. Flame, vol. 81, pp. 150-165.

Sivathanu, Y. R., Gore, J. P., and Dollinar, J., 1991, Combust. Sci. Tech., vol. 76, pp. 45-66.

Vardi, Y., and Lee, D., 1993, J. R. Statist. Soc. B, vol. 55, pp. 569-612.

Vaidya, D. B., Horvath, J. J., and Green, A. E. S., 1982, Applied Optics, vol. 21, p. 3357.

Zhang, J. Q., and Cheng, J. S., 1986, Combust. Flame, vol. 65, pp. 163-176.

QUANTITATIVE SPECIES MEASUREMENTS
IN MICROGRAVITY COMBUSTION FLAMES

Shin-Juh Chen, Jeffrey S. Pilgrim and Joel A. Silver
Southwest Sciences, Inc.

Nancy D. Piltch
NASA Glenn Research Center

INTRODUCTION

The capability of models and theories to accurately predict and describe the behavior of low gravity flames can only be verified by quantitative measurements. Although video imaging, simple temperature measurements, and velocimetry methods have provided useful information in many cases, there is still a need for quantitative species measurements. Over the past decade, we have been developing high sensitivity optical absorption techniques [1-3] to permit *in situ*, non-intrusive, absolute concentration measurements for both major and minor flames species using diode lasers [4, 5]. This work has helped to establish wavelength modulation spectroscopy (WMS) as an important method for species detection within the restrictions of microgravity-based measurements.

More recently, in collaboration with Prof. Dahm at the University of Michigan, a new methodology combining computed flame libraries with a single experimental measurement has allowed us to determine the concentration profiles for all species in a flame. This method, termed ITAC (*I*terative *T*emperature with *A*ssumed *C*hemistry) was demonstrated for a simple laminar non-premixed methane-air flame at both 1-g [6] and at 0-g in a vortex ring flame [7]. In this paper, we report additional normal and microgravity experiments which further confirm the usefulness of this approach.

We also present the development of a new type of laser. This is an external cavity diode laser (ECDL) which has the unique capability of high frequency modulation as well as a very wide tuning range. This will permit the detection of multiple species with one laser while using WMS detection.

EXPERIMENTAL

The drop tower apparatus has been described previously [7, 8]. In brief, a diode laser beam is repetitively rastered across a flame region of interest at 10-20 Hz, with a data collected at a spatial resolution of $0.5 - 1.0$ mm. Second harmonic ($2f$) WMS spectra are recorded and analyzed to obtain temporal and spatial species profiles. In this work, an 1854 nm diode laser was used to detect water vapor using both direct and WMS absorption. The results described here are based primarily on the direct measurements, since the absorbances are sufficiently high (up to 8%) and the more sensitive (but more complicated) WMS analysis was not required. The microgravity measurements were made using the NASA GRC 2.2-sec drop tower. The only difference, from an experimental standpoint, from earlier work is that the Wolfhart-Parker (one dimensional, non-premixed) burner

was modified so as to make the flame twice as long (8-cm) and half as wide so as to maintain the same total gas flow, but improve the absorption path. The spatial resolution was narrowed from 1.0 to 0.5 mm to accommodate this change.

ECDL

Diode lasers have become increasingly important for optical detection of gases. However, a drawback of using diode lasers for gas sensing applications is that they operate over a very limited wavelength range. Typically, only one species can be detected with a given laser. One way in which to expand the output wavelength range of a diode laser is to use an external cavity configuration. A Fabry-Perot (multi-mode) diode laser is combined with a grating and return mirror to create a resonator which, through feedback, couples with the gain region of the diode. The properties of these lasers are that they typically exhibit wider coarse tuning ranges than a simple diode laser, but still show single mode (*i.e.,* single frequency) output. With such a configuration, multiple species detection is possible. However, external cavity diode lasers (ECDLs), in general, cannot be wavelength modulated more than a few kHz (limited by mechanical tuning of an optical element to vary wavelength; diode current tuning no longer is effective). This inability to provide rapid wavelength modulation at higher frequencies results in only limited achievable sensitivity.

The ECDL developed in this research relies on a novel cavity design (Patent Pending) that overcomes the low modulation frequency limitations of present external cavity lasers. This ECDL is wavelength modulated with diode injection current, just like a regular diode laser. Furthermore, in contrast to present external cavity laser designs, the design is simple, inexpensive to implement and rugged. Our design combines the stability and tunability of an ECDL with the wavelength agility of a diode laser. The wide availability of Fabry-Perot diode lasers permits the construction of an ECDL at almost any wavelength from 680 nm to 2.3 μm, with a tuning range exceeding 25 nm (50 times that of a diode laser). As a result, strong absorption bands of virtually all major and minor flame species of interest are now accessible.

RESULTS

Flame Species Measurements – 1g

In a previous paper [6], we presented a comparison of ITAC-derived methane profiles in the non-premixed flame compared with directly measured profiles (using the observed methane absorbance coupled with thermocouple readings). In Fig. 1, we add the ITAC-derived methane profile using only the thermocouple measurements as input to the ITAC computation. While the center

Figure 1 - Methane profile in non-premixed flame.

concentrations is in good agreement with the other approaches, the wings are wider. The discrepancy may be due to how the separation between the noisy baselines in the spectra and

methane absorption spectra are defined, as well as the sensitive dependence of the absorption cross section on temperature for the specific absorption line used. We do not believe that radiative heat loss effects are the source, since preliminary calculations for this flame show them to be relatively weak [10]. The estimated accuracy of the thermocouple measurements in the region of interest is ± 50° C. We are currently analyzing the water vapor measurements to clarify this issue and expand the results to both the rich and lean sides of the flame.

Flame Species Measurements – 0g

The use of the Wolfhard-Parker burner for micro-gravity studies is relatively new. As shown in Fig. 2, the transition from normal to zero gravity is striking. The flame front (dark regions in the photos) expands

Figure 2 - Photographs of the Wolfhard-Parker flame during transition from normal to zero gravity.

and greatly diminishes in height as gravity is reduced. As a result, this should make the observation of intermediates such as OH and C_2H_2 easier to observe. Direct absorption measurements of water vapor across this flame were made at zero gravity. At this time, the results are still undergoing analysis and will be presented at the Workshop.

External Cavity Diode Laser Development

Broadband optical sources are useful for performing survey spectroscopy of unique samples and combinations of samples. This type of survey is indispensable when determining interferences between a gas to be detected and other contaminant gases present in a sample. These surveys are typically done with an FTIR or equivalent direct absorption-based instruments. However, these instruments are bulky and prohibitively expensive.

An additional feature of our ECDL laser is that it can be configured to simultaneously put out wavelengths over a wide spectral band, where direct absorption survey spectra can be obtained with a scanning monochromator. The ECDL causes the longitudinal mode spacing to narrow such that a typical monochromator can not resolve them. Thus, to the monochromator, the ECDL appears as a white light source. However, the ECDL retains the excellent spatial propagation properties of a laser. An illustration of this feature is the recording of the entire 1.53 μm band of acetylene in Fig. 3.
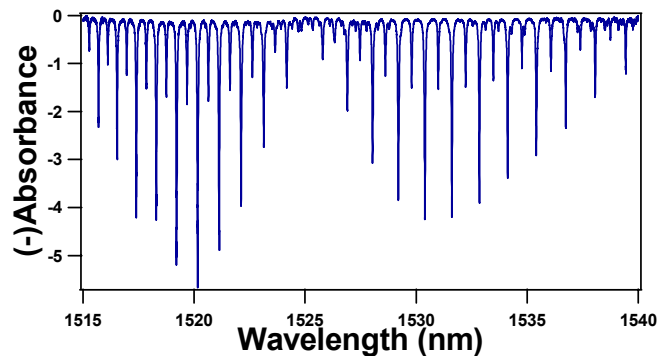
Figure 3 - Broadband ECDL spectrum of acetylene.

For WMS detection, the laser must be capable of high frequency (> 10 kHz) tuning over wavelength ranges commensurate with the absorption line width. DFB lasers tune continuously with injection current; in that manner it could be considered to be an analog tuning device. The ECDL, on the other hand, tunes in discrete jumps. There is a continuing change in the laser power within one jump, but the wavelength is static to first order. This manner of tuning is more digital in nature. It should be emphasized that continuously tunable lasers are often operated with modulation waveforms that, in effect, cause discrete tuning behavior. An example of such a discrete modulation waveform is the square or modified square waveform. Thus, there is no inherent drawback with a digitally tuned laser. An example of a $2f$ (10 kHz) spectrum is shown for HCN in Fig. 4.
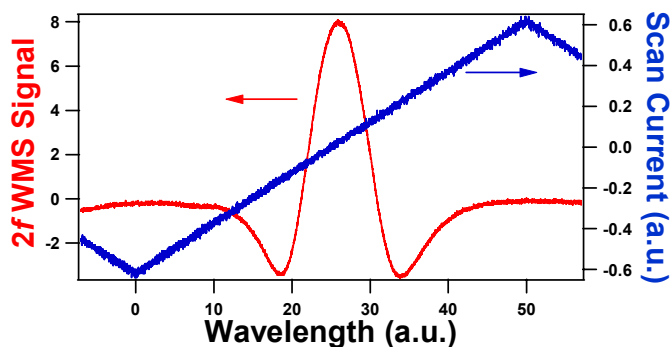
Figure 4 - $2f$ WMS absorption spectrum of HCN at 1545 nm.

With the stand-alone WMS technique, noise equivalent absorbances of 1×10^{-4} have been obtained. This is about an order of magnitude lower performance than for typical WMS implementations. An electronic spectrum analyzer was used to determine the limiting noise source in the 1535 nm ECDL. The limiting noise source was not an etalon, as is usually the case, but second harmonic distortion. This is not uncommon with Fabry-Perot diode lasers and is also present in distributed feedback devices. Since second harmonic distortion is a feature of the laser output and not due to the optical set-up, it can be suppressed by incorporation of a 'noise canceller' dual beam subtraction after the design of Haller and Hobbs [9].

ACKNOWLEDGMENT

REFERENCES

[1] Silver, J.A., Appl. Opt. 31: 707 (1992).
[2] Bomse, D.S., Stanton, A.C.*, et al.*, Appl. Opt. 31: 718 (1992).
[3] Kluczynski, P. and Axner, O., Appl. Opt. 38: 5803 (1999).
[4] Silver, J.A., Kane, D.J.*, et al.*, App. Opt. 34: 2787 (1995).
[5] Silver, J.A. and Kane, D.J., Measurement Sci Technol. 10: 845 (1999).
[6] Chen, S.-J., Silver, J.A.*, et al.*, Proc. Combust. Institute, 29: (in press) (2002).
[7] Dahm, W.J.A., Chen, S.-J.*, et al.*, Proc. Comb. Inst., 29: (in press) (2002).
[8] Silver, J.A., Wood, W.R.*, et al.*, 6th International Microgravity Combustion Workshop, 61 (2001).
[9] Haller, K.L. and Hobbs, P.C.D., Proc. SPIE, 1435: **298** (1991).
[10] Mullin, J. A., University of Michigan (private communication, 2003).

OSCILLATORY EXTINCTION OF SPHERICAL DIFFUSION FLAMES

C. K. Law, S. W. Yoo, and E. W. Christiansen

Department of Mechanical and Aerospace Engineering
Princeton University, Princeton, NJ 08544

INTRODUCTION

Since extinction has been observed in an oscillatory manner in $Le>1$ premixed flames [1], it is not unreasonable to expect that extinction could occur in an unsteady manner for diffusion flames. Indeed, near-limit oscillations have been observed experimentally under microgravity conditions for both candle flames [2] and droplet flames [3]. Furthermore, the analysis of Cheatham and Matalon [4] on the unsteady behavior of diffusion flames with heat loss, identified an oscillatory regime which could be triggered by either a sufficiently large Lewis number (even without heat loss) or an appreciable heat loss (even for $Le=1$).

In light of these recent understanding, the present investigation aims to provide a well-controlled experiment that can unambiguously demonstrate the oscillation of diffusion flames near both the transport- and radiation-induced limits. That is, since candle and jet flames are stabilized through flame segments that are fundamentally premixed in nature, and since premixed flames are prone to oscillate, there is the possibility that the observed oscillation of these bulk diffusion flames could be triggered and sustained by the oscillation of the premixed flame segments. Concerning the observed oscillatory droplet extinction, it is well-known that gas-phase oscillation in heterogeneous burning can be induced by and is thereby coupled with condensed-phase unsteadiness. Consequently, a convincing experiment on diffusion flame oscillation must exclude any ingredients of premixed flames and other sources that may either oscillate themselves or promote the oscillation of the diffusion flame. The present experiment on burner-generated spherical flames with a constant reactant supply endeavored to accomplish this goal. The results are further compared with those from computational simulation for further understanding and quantification of the flame dynamics and extinction.

SPECIFICATION OF EXPERIMENT AND COMPUTATION

An inverse flame configuration was employed with the oxidizer being ejected from a porous sphere burner (20μm pore-diameter, 1.27cm sphere diameter) into a low-density fuel environment comprising of He and H_2 at a pressure of 0.096atm to effectively minimize buoyancy. Various inert gasses (N_2, CO_2, He) were used to dilute the oxidizer in order to change the Lewis number and radiative properties of the mixture so that both the transport-induced and radiative-induced limit could be achieved. A Xybion IMC-201 intensified multi-spectral video camera with a UV-transmissive lens was adopted for visualization. The excited CO_2 (CO_2*) chemiluminescence was used as a marker for detecting the CO_2-diluted flames, whereas OH* due to transition $^2\Sigma^+ \rightarrow {}^2\Pi$, observable at 305.4nm, was used for the N_2-diluted flames. The radiometer was placed 14 cm from the center of the burner to detect emission changes in the flame before extinction.

Extinction was triggered by gradually decreasing the H_2 mole fraction in the ambient. Four oxidizer mixtures, hereafter referred to as cases (a), (b), (c) and (d), diluted with different

combinations of CO_2, N_2, and/or He flow rates were selected to modify the transport and radiative properties of the mixture. Table 1 lists their respective mixture composition and mass flow rates.

The spherically symmetric unsteady diffusion flame was simulated using a modified version of the code developed by Ref. [5] where terms representing unsteadiness, radiation, heat loss, and boundary conditions for non-premixed burning were added. The flame was assumed to be optically thin with CO_2, CO, and H_2O as radiating species, with respective emission/absorption coefficients obtained from Ju et al. [6]. The mass flow rate m, the burner temperature T_s (432K), the oxidizer and ambient fuel compositions, and the chamber pressure p were selected to simulate the experiment. The size of the computational domain was selected to be the effective radial distance (24.8cm) from the burner surface to the chamber wall. The boundary condition at the end of the computational domain on temperature was the chamber wall temperature measured in the experiment (T_∞=305K). The H_2/O_2 reaction mechanism used was that of Mueller *et al*. [7]. To simulate the effect of adding CO_2 as diluent, Mueller's mechanism was augmented with 9 additional elementary reactions, describing the oxidation of CO and the formation/consumption of HCO from the moist CO mechanism of Kim *et. al.* [8]. Helium was also added to the mechanism simply by assuming the same third body efficiencies as argon.

EXPERIMENTAL AND COMPUTATIONAL RESULTS

In general, as the ambient H_2 mole fraction was decreased, the flame luminosity became weaker and the flame size increased. Furthermore, the occurrence of flame oscillation in terms of luminosity and flame size was not visually discernable. The experimentally determined ambient H_2 mole fractions at flame extinction are listed in Table 1. Although all cases appeared to extinguish without pulsating visibly in terms of the flame size, the recorded emission data for cases (a) and (b) revealed that the flames pulsate at 2.1 and 2.3Hz, shown in Fig. 1, prior to extinction, as was predicted in Ref [9]. For cases (c) and (d), no oscillation was observed as shown in Fig. 2.

The steady-state response of spherically symmetric diffusion flames was computationally simulated for the experimental cases (a) through (d). In general the maximum flame temperature decreased while its location increased as the ambient fuel concentration was decreased. When the maximum flame temperature and the fuel molar concentration were plotted, a typical extinction flame response curve was obtained. Whether the observed extinction limit is transport-induced, for which T_{max} increases with increasing m, or radiation-induced, for which T_{max} decreases with increasing m, may be determined by perturbing the mass flow rate from the burner, as discussed in Ref. [9]. For the four mixtures investigated here, this interrogation reveals that cases (a) and (b) are at the radiation-induced limit, while cases (c) and (d) are at the transport-induced limit.

The unsteady simulations were carried out in order to determine the stability of the steady-state solutions. To do so, a steady-state temperature profile of the near-limit flames was perturbed and the ensuing transient response was noted. The perturbation either damped out and relaxed back to steady-state or triggered a growing oscillatory response resulting in extinction.

Figure 3 shows the maximum temperature versus time for the oxidizer mixture given in case (a). For the 32.20% H_2, the perturbed flame relaxes back to the steady-state solution. However, when the H_2 mole fraction is reduced to 32.19%, oscillatory instability develops and the flame eventually extinguishes after quite a number of cycles. The oscillation grows even faster for 32.18%. Similar behavior was observed for case (b) except that the onset of oscillation was

28.09%. Figure 4 shows the maximum temperature versus time for cases (c) and (d). For case (c), pulsating extinction was not observed computationally; instead the perturbed flame at an ambient H_2 mole fraction of 8.024% would extinguish without any oscillations. For case (d), pulsating extinction was observed at H_2 = 7.727%, while H_2 = 7.728% is stable, although only one cycle of oscillation is observed before extinction. This also verifies that increase in *Le* in the oxidizer does make the flame pulsate before extinction.

The experimental and computational results are compared in Table 1. It is seen that for oxidizer mixtures with CO_2 (cases (a) and (b)) the computational results over-predict the H_2 mole fraction at extinction by a substantial amount, while the opposite holds for cases (c) and (d). This is mainly due to the two heat transfer mechanisms that were neglected in the computations: (1) heat loss to the rod support and burner, which would promote extinction at higher H_2 mole fractions, (2) radiation reabsorption, which would strengthen the flame. Hence the CO_2-diluted flames were experimentally observed to extinguish at lower fuel concentrations due to the dominance of reabsorption over heat loss to the support, while for cases (c) and (d), flames were observed to extinguish at higher fuel concentrations. Despite the disagreement on the hydrogen concentration at extinction, the experimentally observed frequencies at the onset of oscillation do agree quite well with the calculations, hence providing at least partial support to the notion that the same mechanism is responsible for both the computationally and experimentally observed oscillations. While pulsating extinction was observed computationally for case (d), pulsations were not observed experimentally. However, close inspection of the computationally observed pulsating extinction reveals that the flame extinguishes after only one cycle of oscillation, and the amplitude of oscillation is about 2K (compared to 10K for cases (a) and (b)), suggesting that these oscillations might prove difficult to be observed experimentally.

ACKNOWLEDGEMENTS

REFERENCES

1. Law, C. K., and Sung, C. J., *Prog. Energy Combust. Sci.* 26, 459-505 (2000).
2. Dietrich, D.L., Ross, H.D., and T'ien, J.S., AIAA 94-0429 (1994).
3. Nayagam, V. and Williams, F.A., *Seventh International Conference on Numerical Combustion*, York, England, (1998).
4. Cheatham, S. and Matalon, M., Proc. *Combust. Inst.* 26:1063-1070 (1996).
5. Kee, R.J., Grcar, J.F., Smooke, M.D., and Miller, J.A., Sandia Report, SAND 85-8240, 1985.
6. Ju, Y., Guo, H., Liu, F., and Maruta, K., *J. Fluid Mech.* 379:165-190 (1999).
7. Mueller, M. A., Kim, T.J., Yetter, R.A., and Dryer, F.L., *Int. J. Chem. Kinet.*, 31: 113-125 (1999).
8. Kim, T. J., Yetter, R. A. and Dryer, F. L., *Proc. Combust. Inst.*, 25: 759-766 (1994).
9. Christiansen, E.W., Tse, S.D., and Law, C.K., AIAA 2001-1084 (2001).

Table 1 Comparison of experimental and numerical results, where Leo is the oxidizer Lewis number and Le_F the fuel Lewis number (*No pulsation observed)

	Case (a)		Case (b)		Case (c)		Case (d)	
	Comp.	Exp.	Comp.	Exp.	Comp.	Exp.	Comp.	Exp.
Mixture Composition	87.15% CO_2 / 12.85% O_2		70.95% CO_2 / 16.20% He / 12.85% O_2		87.15% N2 / 12.85% O_2		70.95% N_2 / 16.20% He / 12.85% O_2	
Mass Flowrate (mg/s)	59		59		39		39	
%H_2 at Extinction	32.19	19.1	28.09	20.3	8.024*	15.9*	7.727	17.0*
Le_F	0.91	1	0.94	0.99	1.08	1.02	1.08	1.014
Le_O	0.82	0.82	1.19	1.19	1.14	1.14	1.47	1.47
Frequency (Hz)	2.3	2.1	2.3	2.3	n/a	n/a	0.1	n/a
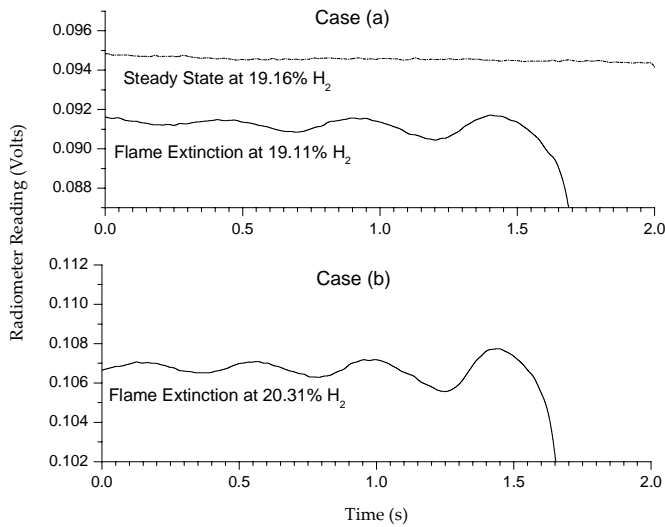
Figure 1 The radiometer voltage readings respect to time near flame extinction for cases (a) and (b). For figure/case (a), steady state flame emission readings are also plotted at hydrogen molar fraction of 19.16%.
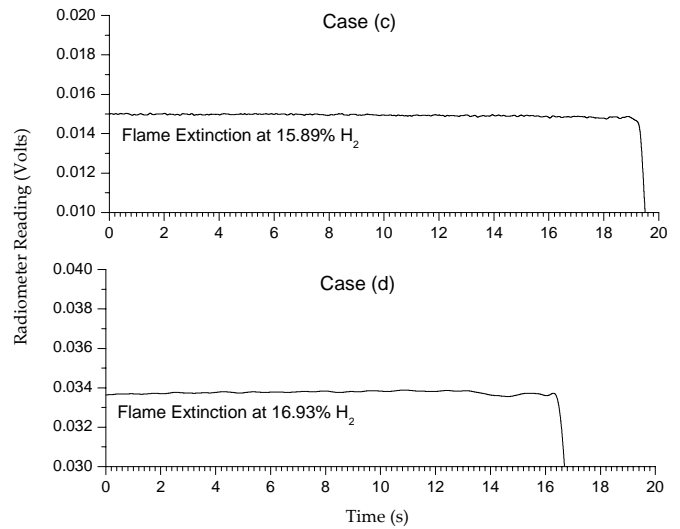
Figure 2 The radiometer voltage readings respect to time near flame extinction for cases (c) and (d).
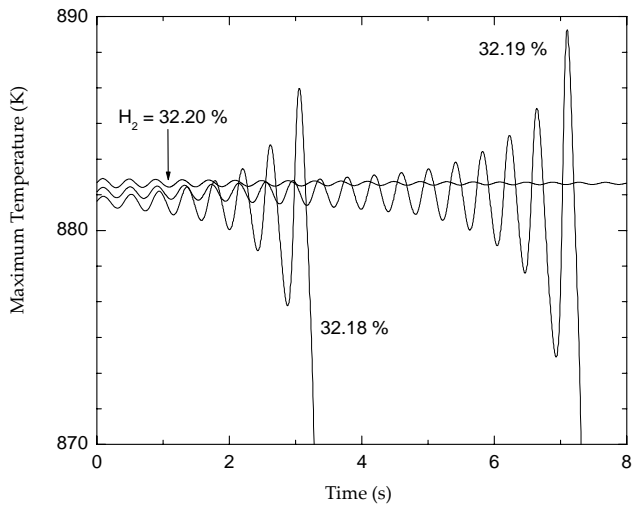
Figure 3 Temporal response of the maximum temperature for case (a), with H_2 = 32.20, 32.19 and 32.18%.
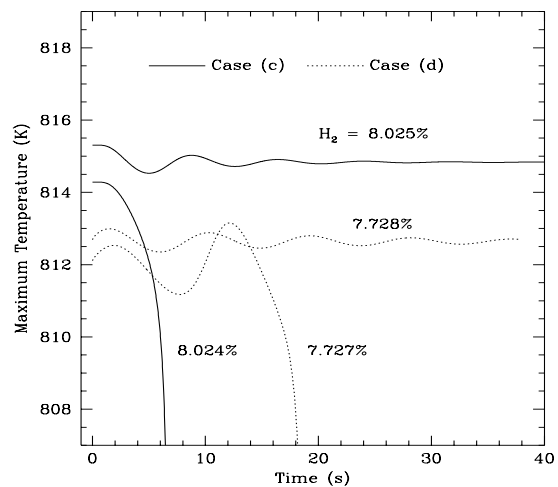
Figure 4 Temporal response of the maximum temperature for case (c), with H_2 = 8.025 and 8.024%, and case (d), with H_2 = 7.728 and 7.727%.

A ROLE OF THE REACTION KERNEL IN PROPAGATION AND STABILIZATION OF EDGE DIFFUSION FLAMES OF C_1-C_3 HYDROCARBONS

Fumiaki Takahashi

National Center for Microgravity Research on Fluids and Combustion, Cleveland, OH 44135

Viswanath R. Katta

Innovative Scientific Solutions, Inc., Dayton, OH 45440

INTRODUCTION

Diffusion flame stabilization is of essential importance in both Earth-bound combustion systems and spacecraft fire safety. Local extinction, re-ignition, and propagation processes may occur as a result of interactions between the flame zone and vortices or fire-extinguishing agents. By using a computational fluid dynamics code [1] with a detailed chemistry model for methane combustion, the authors have revealed [2-5] the chemical kinetic structure of the stabilizing region of both jet and flat-plate diffusion flames, predicted the flame stability limit, and proposed diffusion flame attachment and detachment mechanisms in normal and microgravity. Because of the unique geometry of the edge of diffusion flames, radical back-diffusion against the oxygen-rich entrainment dramatically enhanced chain reactions, thus forming a peak reactivity spot, i.e., *reaction kernel*, responsible for flame holding. The new results have been obtained for the edge diffusion flame propagation and attached flame structure using various C_1-C_3 hydrocarbons.

EXPERIMENT

Global observations of flames were made in the NASA Glenn 2.2-Second Drop Tower using a circular fuel tube (2.87 mm i.d. × 330 mm length) in a vented combustion chamber (255 mm i.d., × 533 mm length). A fuel jet was ignited at ~10 mm above the jet exit using a heated Nichrome wire immediately after dropping the rig for microgravity tests.

COMPUTATION

The time-dependent two-dimensional numerical code, developed by Katta et al. [1], is described elsewhere [3]. The C_3-chemistry model [6, 7] (33 species and 112 steps) includes C_1- or C_2-chemistry portions previously used [2-5]. A radiation model [8] based on an optically thin-media assumption and Plank's mean absorption coefficients was used for CO_2, H_2O, CH_4, and CO. The computational domain of 60 × 50 mm in the axial (z) × radial (r) directions is represented by a mesh of up to 601 × 201 with clustered grid lines near the jet exit with a minimum spacing of 0.05 mm. The inner diameter and lip thickness of the fuel tube are d = 3 mm and 0.5 mm, respectively. The fuel tube exit plane is placed 10 mm downstream from the inflow boundary in the open computational domain. Table 1 shows the test conditions. The fuel jet velocity of each fuel is determined based on the stoichiometric fuel requirement per unit volume of oxygen as same as that of methane (Case 1) studied previously [5]. The ambient air velocity is negligibly small (U_a = 0.001 m/s).

Table 1 Test conditions

Case	Fuel	U_j (m/s)	Gravity
1	Methane	0.1200	$0g$
2	Ethane	0.0686	$0g$
3	Ethylene	0.0800	$0g$
4	Acetylene	0.0960	$0g$
5	Propane	0.0480	$0g$
6	Ethane	0.0686	$1g$

RESULTS AND DISCUSSION

Figure 1 shows examples of video images of methane, ethane and propane flames in still air in microgravity at elapse times after ignition of $t = 2$ s. Spherical blue flames of nearly equal size were formed with the flame base approx. 3–4 mm below the jet exit and approx. 3–4 mm away from the burner wall. The weak methane flame has a larger quenched space. Soot formed initially at ignition disappeared completely for methane, almost diminished for ethane, but remained for propane. Each flame expanded slowly for the entire drop period ($t = \sim 2$ s).

Figure 2 shows the calculated temperature fields in ethane flames in 0g and 1g. In each case, the cold fuel jet issued for 0.3 s prior to ignition. The fuel jet was ignited at a centerline location where the stoichiometric mixture was formed. The edge of the flame propagated through the fuel-air mixing layer. Figure 3 shows the flame displacement velocity vector (v_f) and its angle (θ_f) with respect to the horizon determined from the temperature field images for various fuels in 0g. Table 2 summarizes the average displacement velocities ($|\bar{v}_f|$) and the stoichiometric laminar flame speed (S_L) data in the literature [9]. There is an excellent correlation between these quantities as $|\bar{v}_f| = 0.9475 S_L$ with $R = 0.99797$. This result is important because the computations were conducted using the identical detailed chemistry model for various fuels without adjusting chemical kinetic parameters and the propagating edge diffusion flame possessed the reaction
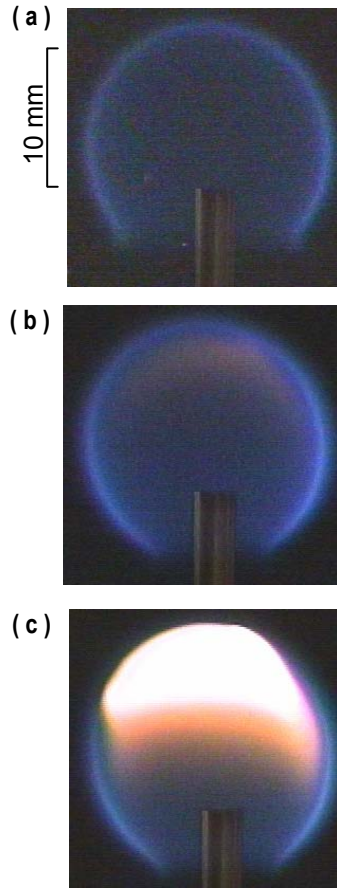
Fig. 1 Video images of (a) CH$_4$, (b) C$_2$H$_6$, and (c) C$_3$H$_8$ flames in µg. $t = 2$ s. .
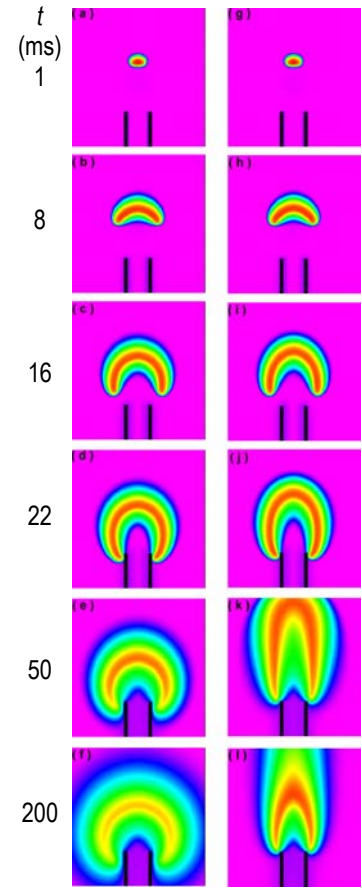
0g (Case 2)   1g (Case 6)
Fig. 2 Calculated temperature field in ethane flames.
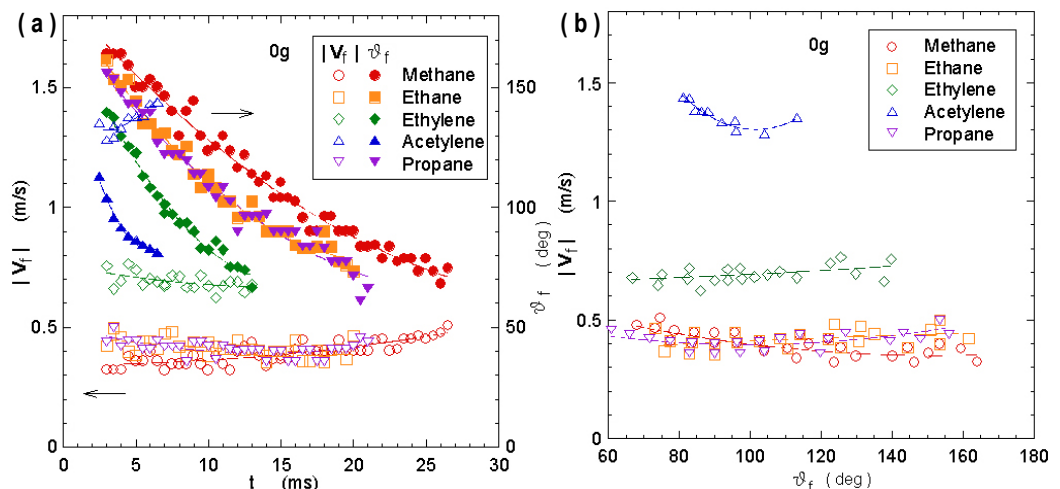
Fig. 3 Calculated flame displacement velocity and angle in the 0g flames (Cases 1-5).

kernel structure capable of consuming the reactants as fast as a stoichiometric premixed flame.

Figure 4 shows the structure of an ethane flame in $0g$ at the

Table 2   Flame displacement velocity

Fuel	$|\bar{v}_f|$ (cm/s)	S_L (cm/s)
Methane	39.3 ($0g$)	43.4
Ethane	41.4 ($0g$)	44.5
	40.7 ($1g$)	
Ethylene	69.1 ($0g$)	68.0
Acetylene	136.2 ($0g$)	144
Propane	41.0 ($0g$)	45.6

elapse time after ignition of 16 ms (see Fig. 1c), including the velocity vectors (v), molar flux vectors of the H atom ($\mathbf{M}_H$), isotherms (T), total heat-release rate ($\dot{q}$, 20, 100, and 300 J/cm³s), and equivalence ratio (ϕ). The heat-release rate shows a peak reactivity spot (i.e., the reaction kernel) at the flame base. The $\dot{q}$, $|v|$, and T at the reaction kernel were 378 J/cm³s, 0.0065 m/s, and 1436 K, respectively.

Figure 5 shows the variations of the species mole fractions (X_i), temperature, species formation rate ($\hat{\omega}_i$), and heat-release rate across the reaction kernel. The overall structure resembled to that of the $1g$ stationary methane flame with the standoff distance of several mm [4]. Besides the features of the radial diffusion-flame-like processes, the premixed combustion processes occurred at the center of the reaction kernel in the direction of the flame propagation. The reaction zone in the propagating flame broadened radially as a result of the thicker flammable mixture layer (~1.2 mm) formed in 0.3 s of the fuel-air mixing time, compared to the stationary flame (0.6-0.8 mm [4, 5]) with a short residence time (~0.01 s order) of the fluid particles over the standoff distance (4-9 mm) in a coflowing air (~0.7 m/s). For the C_2/C_3-fuels, the C_2-route in the oxidation process dominated over the C_1 route, and the C_2 exthothermic reactions, CHCO + O → CO + CO + H (R59) and C_2H_2 + O → CH_2 + CO (R60) exceeded the C_1 reaction, CH_3 + O → CH_2O + H (R46), in contributing to the total heat-release rate.

Figures 6 and 7 show the structure of an attached ethane flame (Case 2) at t =0.76 s ($\dot{q}$: 30, 10, and 15 J/cm3s.). The flame shpe, including the quenched space, matched the observation (Fig. 1b). The trend of the flame structure resembled to that of a methane flame [5], except that the C_2H_2 concentration in the high-temperature zone was an order of magnitude

Fig. 4   Calculated propagating ethane flame structure in $0g$ (Case 2). $t = 16$ ms.

Fig. 5   Calculated flame structure across the reaction kernel (Case 2). $t = 16$ ms, $z = 1.58$ mm.

higher than that of the initial fuel. As a result, the fuel fragments burning near the peak temperature were C_2H_2 and H_2, and CO was oxidized on the air side where radical-scavenging hydrocarbons disappeared.

CONCLUSIONS

Computations of C_1-C_3 hydrocarbon jet flames using a detailed chemistry model have determined the edge diffusion flame displacement velocity after ignition in $1g$ and $0g$ environments. The calculated flame displacement velocity through the flammable mixture layer almost reached the stoichiometric laminar flame velocity for each fuel. The reaction kernel, which broadened radially facing the flammable mixture layer possesses a hybrid structure of diffusion and premixed flames in the lateral and longitudinal directions, respectively, with respect to the direction of the flame propagation. The structure of the reaction kernel in the attached flames of C_2 and C_3 hydrocarbons resembles to that of methane except for the high acetylene concentration in the peak-temperature region and the dominant C_2-route oxidation pathway.

ACKNOWLEDGMENT

REFERENCES

1. Katta, V. R., Goss, L. P., and Roquemore, W. M., *AIAA J.* 32:84 (1994).
2. Takahashi, F. and Katta, V. R., *Proc. Combust. Inst.* 27:675 (1998).
3. Takahashi, F. and Katta, V. R., *Combust. Sci. Technol.* 155:243 (2000).
4. Takahashi, F. and Katta, V. R., *Proc. Combust. Inst.* 28:2071 (2000).
5. Takahashi, F. and Katta, V. R., *Proc. Combust. Inst.* 29: in press (2002).
6. Peters, N., in *Reduced Kinetic Mechanisms for Applications in Combustion Systems* (N. Peters and B. Rogg, Eds.), Springer-Verlag, Berlin, 1993, pp. 3-14.
7. Warnatz, J., in *Combustion Chemistry*, Springer-Verlag, New York, 1984, p. 197-360.
8. Annon., International Workshop on Measurement and Computation of Turbulent Nonpremixed Flames, http://www.ca.sandia.gov /TNF/radiation.html, 2001.
9. Glassman, I., *Combustion,* 3rd ed., Academic Press, San Diego, 1996.

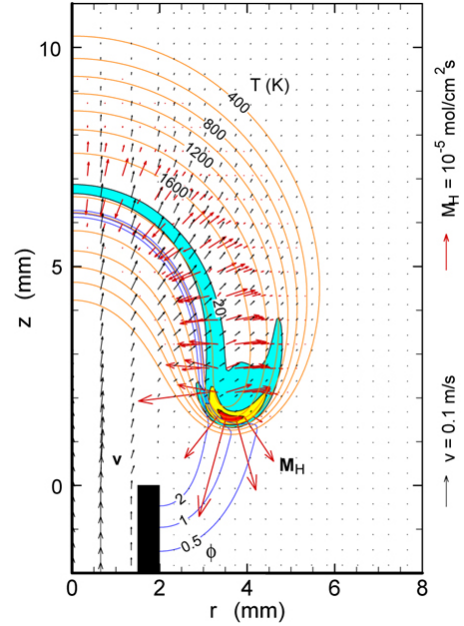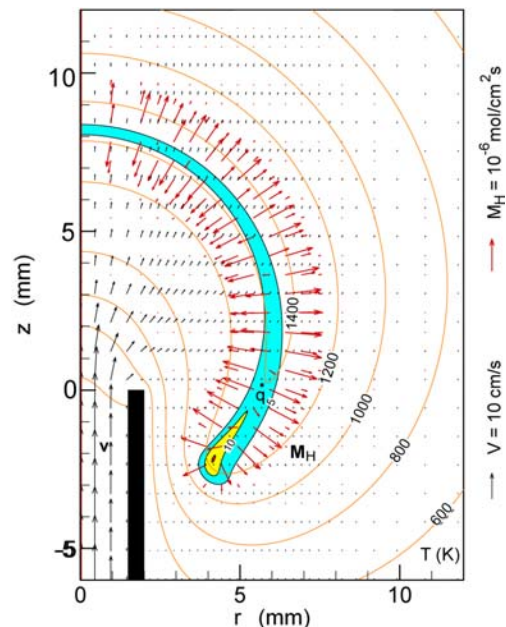**Fig. 6   Calculated attached ethane flame structure in $0g$ (Case 2). $t = 0.76$ s.**
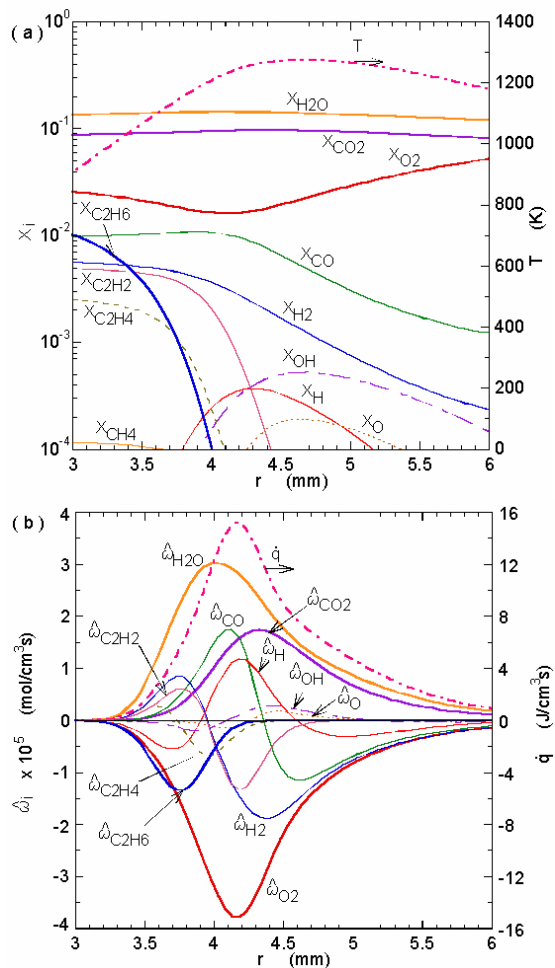
Fig. 7   Calculated flame structure across the reaction kernel (Case 2). $t = 0.76$ s, $z = -2.93$ mm.

GRAVITY EFFECTS OBSERVED IN PARTIALLY PREMIXED FLAMES

Ishwar K. Puri, Suresh K. Aggarwal, Andrew J. Lock, Ranjan Ganguly,
University of Illinois at Chicago, Chicago, Illinois

Uday Hegde,
National Aeronautics and Space Administration, Cleveland, Ohio

INTRODUCTION

Partially premixed flames (PPFs) contain a rich premixed fuel–air mixture in a pocket or stream, and, for complete combustion to occur, they require the transport of oxidizer from an appropriately oxidizer–rich (or fuel–lean) mixture that is present in another pocket or stream. Partial oxidation reactions occur in fuel–rich portions of the mixture and any remaining unburned fuel and/or intermediate species are consumed in the oxidizer–rich portions. Partial premixing, therefore, represents that condition when the equivalence ratio (φ) in one portion of the flowfield is greater than unity, and in another section its value is less than unity. In general, for combustion to occur efficiently, the global equivalence ratio is in the range fuel–lean to stoichiometric. These flames can be established by design by placing a fuel-rich mixture in contact with a fuel-lean mixture, but they also occur otherwise in many practical systems, which include nonpremixed lifted flames, turbulent nonpremixed combustion, spray flames, and unwanted fires. Other practical applications of PPFs are reported elsewhere [1, 2].

Partially premixed flames contain multiple reaction zones [3, 4, 5, 6] that have either a premixed-like structure or a transport-limited nonpremixed flame characteristics in which mixing and entrainment effects are significant. A rich premixed reaction zone is established on the fuel rich side, a lean premixed zone on the fuel lean side, with a nonpremixed zone in between these two in the case of triple flames. Double flames are established when a fuel rich mixture burns in air and have two reaction zones, rich premixed and nonpremixed.

Heat release from a flame causes flow dilatation and accelerates the gas across the flamefront. In normal gravity, free convection accelerates the heated gas due to buoyancy, which leads to air entrainment into the flame it its ambient is air rich. For low Froude numbers ($Fr=\upsilon/(gl)^{1/2}$, where υ denotes the fuel stream velocity, l the characteristic length scale and g the gravitational acceleration) flames, gravity effects on a flame can dominate the effects of other physical phenomena, e.g., radiative heat transfer and diffusive transport.

Although extensive experimental studies have been conducted on premixed and nonpremixed flames under microgravity [7, 8], there is a absence of previous experimental work on burner stabilized PPFs in this regard. Previous numerical studies by our group [9, 10] employing a detailed numerical model [11, 12, 13] showed gravity effects to be significant on the PPF structure. We report on the results of microgravity experiments conducted on two-dimensional (established on a Wolfhard-Parker slot burner) and axisymmetric flames (on a coannular burner) that were investigated in a self-contained multipurpose rig [9,14,15]. Thermocouple and radiometer data were also used to characterize the thermal transport in the flame.

RESULTS

Direct imaging techniques were used to characterize the reaction zone topology. The heat
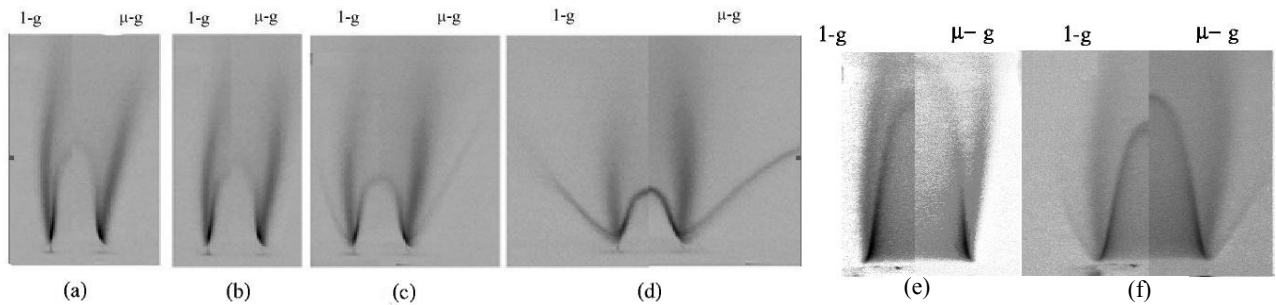
Figure 1: Direct images of the double ((a), (b) and (e)) and triple ((c) and (f))flames at 1-g and μ-g on the slot burner ((a)—(d)) and coannular burner ((e) and (f)). Conditions: (a) ϕ_{in} = 2.38, ϕ_{out} = 0, V_{in} = 21.2 cm/s, V_{out} = **32.3 cm/s; (b)** ϕ_{in} = 1.68, ϕ_{out} = 0, **(c)** ϕ_{in} = 1.68, ϕ_{out} = 0.36;**and (d)** ϕ_{in} = 1.68, ϕ_{out} = 0.5; **for (b), (c) and (d),** V_{in} = **15.9 cm/s, V_{out} = 25.8 cm/s, (e)** ϕ_{in} = 1.8, ϕ_{out} = 0, **(f)** ϕ_{in} = 1.8, ϕ_{out} = 0.36; **for (e), and (f), V_{in} = V_{out} = 30 cm/s.**

release regions of the flames were characterized with the color band associated with C_2^* chemilluminescense that was digitally isolated [14]. These images allowed us to observe the multiple reaction zones. Figure 1 presents images of double and triple flames established on both a slot burner (Figure 1 (a) – (d)) and a coannular burner (Figure 1 (e),(f)) at 1-g (left) and μ-g (right) conditions. All of these burner-stabilized microgravity flames were observed to reach a visually steady structure within 200ms of rig release from 1-g.

Figure 1(a) and (b) depict double flames with nearly identical momentum ratios between the inner and outer flows. In both cases, the outer nonpremixed reaction zone weakens towards the tip, moves outward significantly, and widens slightly in μ-g. The inner premixed reaction zone is similarly influenced by the gravity change, although to a smaller extent. The spreading and weakening of the outer reaction zones in μ-g is a result of the lower oxidizer entrainment [9, 10]. The outer nonpremixed flame depends more on advective oxidizer entrainment for larger values of φ_{in}. This advection is largely dependent on buoyancy, and, therefore, the effect of microgravity on the outer nonpremixed flame increases with increasing values of φ_{in}. This observation has been corroborated through other investigations [9, 16]. The flames established on a coannular burner, are shown in Figure 1 (d). These behave similarly to those established on a slot burner. The global effects of gravity are similar, although there are some specific configuration-dependent effects (e.g. the inner premixed flame of the axisymmetric burner elongates more in μ-g than the one of the slot burner). Figure 1 (b),(c), and (e),(f) present flame images for which the value of φ_{in} is maintained constant and that of φ_{out} is increased. The addition of the third reaction zone, and the increase in φ_{out} were observed to reduce gravity related effects on the two inner reaction zones.

Thermocouple measurements were taken at 50Hz and corrected for radiation losses. The processed data for a characteristic flame is presented in Figure 2. It presents the temperature at a specific spatial location for a double flame as it transitions from 1-g to μ-g. The high temperature region lies in the nonpremixed reaction zone, which slightly differs from previous numerical simulations [9, 10]. These differences may arise due to the model approximations or thermocouple measurement errors and will be further investigated, e.g., with more accurate nonintrusive measurement techniques. As evident from the direct images, the reaction region spreads out over a larger volume in μ-g, leading to a reduction in local heat release rate. Moreover, radiative heat transfer from the flame increases under microgravity. Consequently, the average flame temperature is observed to drop by ~17% in μ-g. Numerical predictions by our group, which included an optically thin thermal radiation model, also predicted similar temperature drop [17].
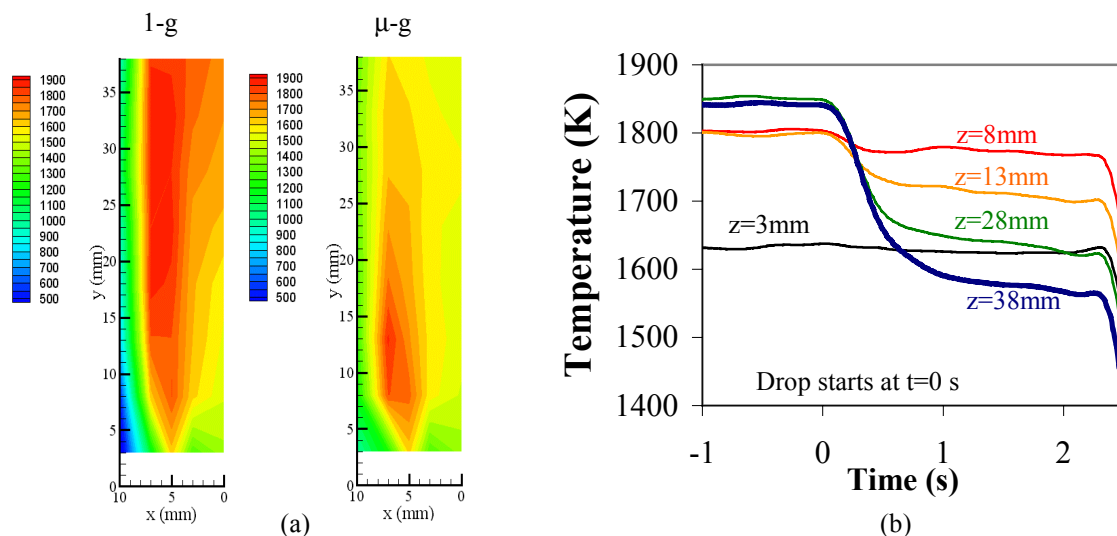
Figure 2: Temperature (a)contours and (b)transient of a double flame: ϕ_{in}=1.8, ϕ_{out}=0; V_{in}=V_{out}=30cm/s

Figure 2 (b) presents the transient response of the thermocouples for a single lateral position along a slot burner flame. Transients with two different time scales are observed as the rig is dropped. A phenomenological analysis [14] illustrates the phenomena responsible for these different responses. The first transient diminishes within the first 200 ms occurs due to the sudden change in the advection associated the flame. The second transient that persists until the end of the drop is attributed to the diffusive transport. Although the flame temperature is lower under microgravity, the total radiative heat loss from the flame increases due to the larger flame volume. Figure 3 presents data obtained from a radiation pyrometer that retains the entire axisymmetric flame in its field of view at both 1-g and µ-g. Although the time constant of the air-cooled pyrometer is too large to obtain quantitative transient data, the qualitative trend clearly shows an increase in radiative heat transfer form the flame under microgravity.
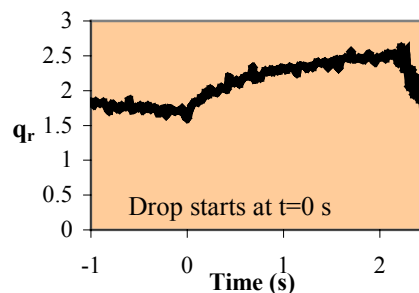
Figure 3: Radiation flux transient.

Lifted flames were observed for very rich φ_{in} and a correspondingly high reactant stream velocity. Figure 4 presents an image of a nitrogen diluted lifted double flame under 1-g and µ-g. In general, the flames were observed to oscillate in 1-g, but became steady at µ-g. The flames moved closer to the burner during the transition to µ-g during the experiment.

CONCLUSIONS AND FUTURE WORK

Herein, some of the first experimental observations of burner-stabilized, methane-air microgravity partially premixed flames are presented. Digital color, black and white, and C_2^* imaging reveals that buoyancy changes the structure of double and triple flames in a similar manner. Buoyancy induced entrainment influences regions away from the flame centerline so that the outermost flame regions are most affected by it. Gravity effects on the rich premixed and nonpremixed zones of a triple flame are less than that for a double flame. Temperature measurements corroborated this finding by showing similar structural effects on the temperature profiles. The temperature data obtained during a show changes in the advective flow during a small initial transient period. A longer transient period is also observed that is related to changes

1-g   μ-g
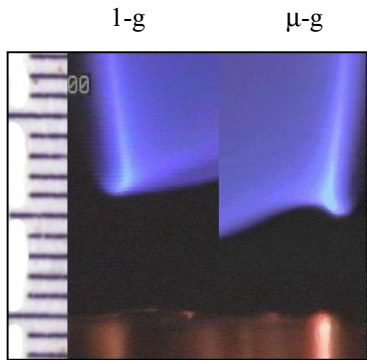
Figure 4: Lifted N$_2$-diluted flame; ϕ_{in} = 3.0, N$_2$=40%, ϕ_{out} = 0; V$_{in}$ = 30 cm/s, V$_{out}$ = 30 cm/s.

(b)

(a)
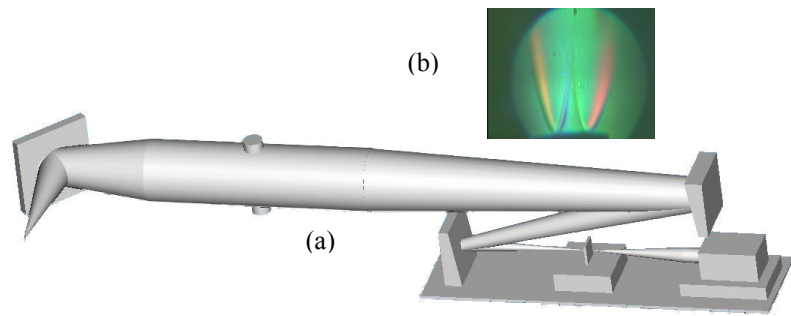
Figure 5: (a)The proposed RSD setup, and (b)image of a 1-g double f lame

in the diffusive flux, which suggests that longer μ-g times are necessary for a better understanding of microgravity effects on these flames. The average and peak temperatures of the flame were observed to decrease in μ-g due to drop in local heat release in μ-g and an increase in radiative loss. The increased radiative loss with a decreased temperature is a result of the flame radiating over a larger volume in μ-g. Nonintrusive temperature measurements involving rainbow schlieren deflectometry (RSD – Figure 5:planned setup) and holographic interferometry (DHI) have been proposed for future work.

ACKNOWLEDGEMENT

REFERNCES

1 Smooke, M. D., Seshadri, K., and Puri, I. K., *Proc. Combust. Inst.* 22: 1555-1563 (1988).

2 Peters, N., *Proc. Combust. Inst.* 20: 353-360 (1984).

3 Seshadri, K., Puri, I., and Peters, N., *Combust. Flame* 61:237-249 (1985).

4 Law, C. K., Li, T. X., Chung, S. H., Kim, J. S., and Zhu, D. L., *Combust. Sci. Tech.* 64: 199-232 (1989).

5 Shu, Z., Aggarwal, S. K., Katta, V. R., and Puri, I. K., *Combust. Flame* 111: 276-295 (1997).

6 Shu, Z., Aggarwal, S. K., Katta, V. R., and Puri, I. K., *Combust. Flame* 111: 296-311 (1997).

7 Lin K.C., Faeth G.M., Sunderland P.B., Urban D.L. and Yuan Z.G., *Combust. Flame* 116: 415-431 (1999).

8 Takahashi, F., and Katta, V.R., *Proc. Combust. Inst.* 28: 2071-2078 (2000).

9 Shu, Z, Choi, C. W., Aggarwal, S. K., Katta, V. R., and Puri, I.K., *Combust. Flame* 118: 91-107 (1999).

10 Azzoni, R., Ratti, S., Puri, I. K., and Aggarwal, S. K., *Phys. Fluids*, 11: 3449-40 (1999).

11 Shu, Z., Katta, V.R., Puri, I.K., and Aggarwal, S.K., *Combust. Sci. Tech.* 157: 185-211 (2000).

12 Katta, V. R., Goss, L. P., and Roquemore, W. M., *Combust. Flame* 96: 60-74, (1994).

13 Aggarwal, S. K., Park, T. W., and Katta, V. R., *Combust. Sci. Tech.* 113: 429-438 (1996).

14 Choi, C. W., Ganguly, R., Lock, A. J., Puri, I. K., Aggarwal, S. K., Hegde, U., *AIAA 41st Aerospace Science Meeting and Exhibit, Jan 6-9, 2003, Reno, Nevada*, Paper No. AIAA-2003-0811

15 Lock, A.J., Choi, C. W., Ganguly, R., Puri, I.K., Aggarwal, S.K., Hegde, U., *Proceedings of the Third Joint Meeting of the U.S. Sections of The Combustion Institute*, March 16-19, 2003, Paper No. A19

16 Bennett, B. A. V., McEnally, C. S., Pfefferle, L. D., and Smoke, M.D., *Combust. Flame* 123: 522-546 (2000).

17 Qin, X., Aggarwal, S.K., Puri, I.K., and Katta, V.R., *AIAA 41st Aerospace Science Meeting and Exhibit, Jan 6-9, 2003, Reno, Nevada*, Paper No. AIAA-2003-1018

Numerical Simulation and Experimental Investigation of the Lift-off and Blowout of Enclosed Laminar Flames

Rajasekhar Venuturumilli, Yong Zhang and Lea-Der Chen
Department of Mechanical and Industrial Engineering, and
National Advanced Driving Simulator
The University of Iowa
Iowa City, IA 52242

INTRODUCTION

Enclosed flames are found in many industrial applications such as power plants, gas-turbine combustors and jet engine afterburners. A better understanding of the burner stability limits can lead to development of combustion systems that extend the lean and rich limits of combustor operations. This paper reports a fundamental study of the stability limits of co-flow laminar jet diffusion flames. A numerical study was conducted that used an adaptive mesh refinement scheme in the calculation. Experiments were conducted in two test rigs with two different fuels and diluted with three inert species. The numerical stability limits were compared with microgravity experimental data. Additional normal-gravity experimental results were also presented.

NUMERICAL

An adaptive mesh refinement (AMR) is used to replace the single-grid numerical scheme of Sheu and Chen (1996). Based on user-defined criteria, the AMR forms successive fine grids on a base coarse grid in a sequential order, e.g., see Berger and Oliger (1984), Almgren et al. (1998) and Pember et al. (1998). A finite volume is used to discretize the computational domain into a staggered, non-uniform grid mesh. A semi-implicit fractional step time marching scheme is used to solve the transport equations of mass, momentum, energy and species. The major assumptions are axisymmetric, low Mach-number laminar flow, Newtonian fluid, negligible viscous dissipation and no radiative heat loss. A four-step reduced mechanism is used to model the methane oxidation. The reduced mechanism is based on an extended Peters mechanism (Sheu, 1996) that incorporates a fifty-step starting mechanism and considers seventeen species. The mechanism invokes steady-state approximations for ten species, i.e., O, OH, C, CH, CH_2, CH_3, CHO, CH_2O, HO_2 and H_2O_2, and solves seven reactive species, i.e., CH_4, H, H_2, H_2O, CO, CO_2 and O_2. A more detailed description of the numerical scheme is given in Venuturumilli and Chen (2003).

EXPERIMENTAL

Two test rigs were used to determine the stability limits of enclosed laminar flames. The laminar flamed were fueled by methane or ethane with diluent gases of N_2, He or Ar. The dilution was used to yield the same fuel mass fractions as the baseline case of CH_4/N_2 (50% by volume). The fuel mixtures have the same stoichiometric mixture fraction values. One of the test rigs is the NASA's ELF rig. The ELF has an inner cross-section of 90 mm by 90 mm and an axial length of 150 mm. A fuel tube of 1.6 mm in diameter is used. The second test rig is the

NASA's MAGIC rig, which has an inner cross-section of 100 mm by 100 mm and an axial length of 400 mm. A 12-mm fuel tube is used.

RESULTS AND DISCUSSION

Numerical. The AMR code was validated by comparing the results with published calculations of an axisymmetric, Burke-Schumann diffusion flame (Sheu and Chen, 1996). The AMR code is also used to calculate the stability limits of an experimental flame. The experimental flame was the ELF Glovebox Investigation, on-board of the NASA STS-87/USMP-4 Space Shuttle Mission. A single-grid was used in earlier efforts to calculate the ELF stability limits. The grid resolutions that we had attempted, however, were not adequate; the calculations resulted in unacceptable numerical diffusion errors that falsely stabilized the flame at high fuel jet velocity conditions. Further "static" grid refinements of the flow field were not pursued as computational efforts were already excessive for the grid resolutions examined. Instead, the current AMR code was developed and used. Comparison of the single-grid and AMR calculations was summarized in Fig. 1. As can been seen in Fig. 1, the AMR code yielded converged results without the false stabilization effects. The stability limits calculated by the AMR were compared, in qualitative agreement, with the experimental results.

The AMR code was also used to study the structures of the laminar flames at the attached, lifted and near-blowout conditions. The contours of the local heat release rates are plotted in Fig. 2 for the fuel jet velocity at 0.2 m/s and air flow velocities of 0.1 (attached), 0.3 (lifted), or 0.6 (near blowout) m/s. The heat release rates in the mixture fraction space are shown in Fig. 3. The hear release rates reach their maximum near the stoichiometric locations for the attached and lifted flames. For the near blowout conditions, the maximum, however, occurs on the lean side in the mixture fraction space. The maximum values for all three cases are nearly the same. For the flame stabilized slightly above the burner exit (fuel at 0.2 m/s and air at 0.3 m/s), there is a second local maximum on the lean side as shown in Fig. 4. The corresponding scalar dissipation rates are shown in Fig. 5. The profiles of the scalar dissipations rates are qualitatively similar to those of the heat release rates, cf. Figs. 4 and 5. The peak heat release rates and scalar dissipation rates are not located at the stoichiometric surface for the near blowout conditions. They are located at the lean side of the stoichiometric location. Although Fig. 2 showed a "triple-flame" like picture near the flame base (or the edge flame), no apparent triple flame characteristics are observed when the results are plotted in the mixture fraction space.

Experimental. The stability results shown in Fig. 6 included the results of the baseline case (CH_4/N_2), and the mixtures of CH_4/Ar and C_2H_6/N_2. These mixtures had the same fuel mass fractions as the baseline case; the respective fuel mole fractions were 0.59 and 0.37. A CH_4/He mixture (with the fuel mass fraction same as the baseline case) was also used. However, a stable, lifted flame was not observed for this CH_4/He mixture. Over the conditions examined, the CH_4/Ar flame was more stable than the CH_4/N_2 flame. The C_2H_6/N_2 flame was more stable than the CH_4/Ar flame. The difference of the coflowing air velocities between the CH_4/Ar and CH_4/N_2 flames at lifted and blowout conditions was 0.18 m/s. The standard deviation was 0.004 m/s. It is noted that the fuel mixtures in Fig. 6 have the same stoichiometric mixture fraction values. The binary diffusion coefficients (D) of fuel or inert species (for diffusion into the mixture), however, are different. The adiabatic flame temperatures calculated using the NASA equilibrium code, McBride et al. (1993), are 1810K, 2124 K, 2180 K and 2152 K for the

mixtures of CH4/He, CH4/N2, CH4/Ar and C2H6/N2, respectively. The substantially lower adiabatic flame temperature of the CH4/He-air flame probably is an important factor that may have led to the blowout of the flame once it lifted from the burner. The calculated adiabatic flame temperatures and reported maximum laminar burning velocities of CH4- and C2H6-air flames are similar. The C2H6/N2 flame requires higher coflowing air velocities to reach the liftoff and blowout conditions at given fuel jet velocities. It is noted that C2H6 species has a lower binary diffusion coefficient than CH4. The stability limits of CH4/Ar, CH4/N2 and CH4/He mixtures are also in qualitative agreement with the trend of $D_{Ar}<D_{N2}<D_{He}$, where D is the binary diffusion coefficient. These observations suggest that species diffusion might also be an important factor in the stability limits of co-flow laminar diffusion flames.

The stability limits of CH4/N2 diffusion flames in ELF and MAGIC test rigs are summarized in Fig. 6. The test results showed that there was a distinct transition from a lifted flame to the blowout when tests were conducted using the ELF rig in normal gravity. However, this transition was not observed when the experiments were conducted in the MAGIC rig. The distinct transition from a lifted flame to the blowout condition was in agreement with Papanikolaou and Wierzba (1996), in which a critical coflowing air velocity of 0.3 m/s was reported for a burner diameter of 1.5 mm, and no stable lifted flames were observed when the coflowing air velocity was increased beyond this critical value. The coflowing air velocities of ELF liftoff conditions are lower than the critical velocity of 0.3 m/s, and stable lifted flames are observed. The burner diameter used in the MAGIC rig (12 mm) is larger than the maximum diameter (2 mm) used by Papanikolaou and Wierzba (1996). Direct comparison with their results was not made in current study. Further study is needed to gain additional insight on the effects of the fuel jet nozzle size, diluent gases and transport properties on the stability limits.

REFERENCES
Almgren, A. S., Bell, J. B., Collela, P., Howell, L. H. and Welcome, M. L., , J. Comput. Phys., 142 (1): 1-46 (1998).
Berger, M. J., and Oliger, J.. J. of Comput. Phys., 53 (3): 484-512 (1984).
McBride, B. J., Gordon, S. and Reno, M. A., NASA Technical Memorandum 4513, (1993).
Papanikolaou and Wierzba (1996), ASME J. Energy Res. Tech., 118 (2): 134-139 (1996).
Pember, R. B., Howell, L. H., Bell, J. B., Colella, P., Crutchfield, W. Y., Fiveland, W. A. and Jessee, J. P., Combust. Sci. and Tech., Vol. 140, pp. 123-168 (1998).
Sheu, J.-C. and Chen, L.-D., AIAA J., Vol. 34, No. 10, pp. 2090-2098 (1996).
Sheu, J.C., "Numerical Simulation of Burke-Schumann Diffusion Flame Using Finite-Rate Chemical Kinetics," Ph. D. Dissertation, The University of Iowa, Iowa City, Iowa (1996).
Venuturumilli, R. and Chen, L.-D., AIAA Paper No. 2003-0807, AIAA (2003).
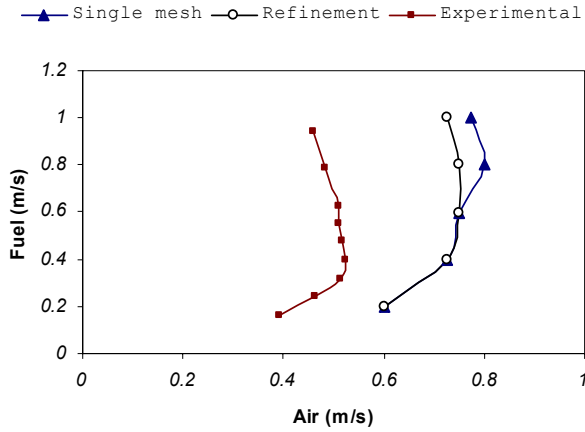
Figure 1. Comparison with experimental data of blowout conditions in 0g.
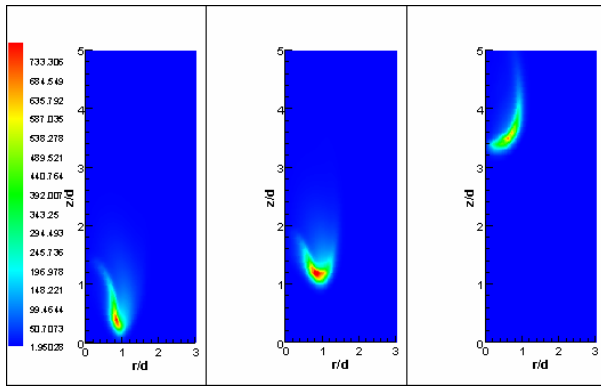
Figure 2. Heat release rate contours, fuel at 0.2 m/s and air at 0.1 m/s, 0.3 m/s or 0.6 m/s.
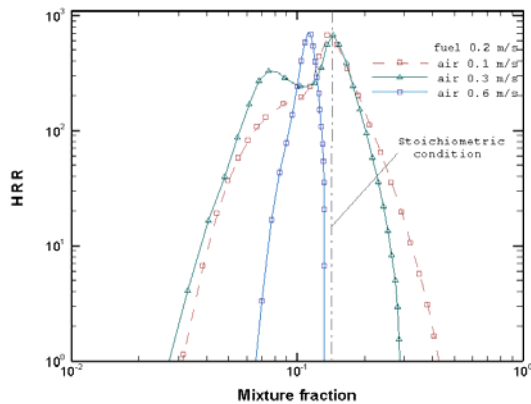
Figure 3. The heat release rates of attached (air at 0.1 m/s), lifted (air at 0.3 m/s) and near blowout (air at 0.6 m/s) flames.
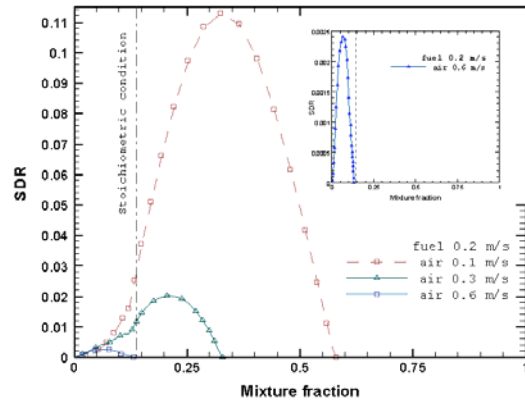
Figure 4. The heat release of attached (air at 0.1 m/s) and lifted (air at 0.3 m/s) flames.
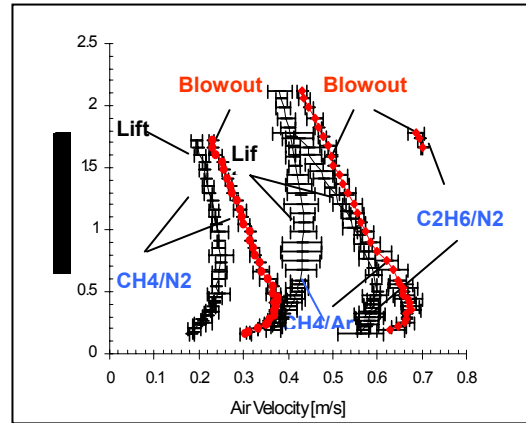
Figure 5. Summary of ELF stability results.
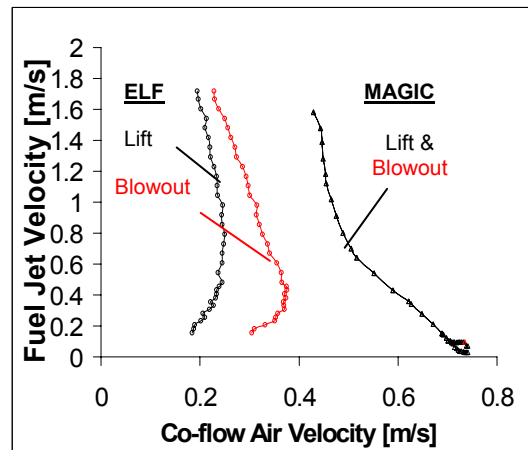
Figure 6. Summary of ELF and MAGIC CH4/N2 stability results.

MODELING CANDLE FLAME BEHAVIOR IN VARIABLE GRAVITY

A. Alsairafi, J.S. T'ien
Case Western Reserve University

S.T. Lee
National Taiwan University

D.L. Dietrich and H.D. Ross
NASA John H. Glenn Research Center

Introduction

The burning of a candle, as typical non-propagating diffusion flame, has been used by a number of researchers to study the effects of electric fields on flame, spontaneous flame oscillation and flickering phenomena, and flame extinction [1- 3]. In normal gravity, the heat released from combustion creates buoyant convection that draws oxygen into the flame. The strength of the buoyant flow depends on the gravitational level and it is expected that the flame shape, size and candle burning rate will vary with gravity. Experimentally, there exist studies of candle burning in enhanced gravity (i.e. higher than normal earth gravity, g_e) [4], and in microgravity in drop towers and space-based facilities [5-7]. There are, however, no reported experimental data on candle burning in partial gravity ($g < g_e$).

In a previous numerical model of the candle flame [7], buoyant forces were neglected. The treatment of momentum equation was simplified using a potential flow approximation. Although the predicted flame characteristics agreed well with the experimental results, the model cannot be extended to cases with buoyant flows. In addition, because of the use of potential flow, no-slip boundary condition is not satisfied on the wick surface. So there is some uncertainty on the accuracy of the predicted flow field.

In the present modeling effort, the full Navier-Stokes momentum equations with body force term is included. This enables us to study the effect of gravity on candle flames (with zero gravity as the limiting case). In addition, we consider radiation effects in more detail by solving the radiation transfer equation. In the previous study, flame radiation is treated as a simple loss term in the energy equation [7]. Emphasis of the present model is on the gas-phase processes. Therefore, the detailed heat and mass transfer phenomena inside the porous wick are not treated. Instead, it is assumed that *a thin layer of liquid fuel coated the entire wick surface* during the burning process. This is the limiting case that the mass transfer process in the wick is much faster than the evaporation process at the wick surface.

Model Formulation

The theoretical model considers a vertical candle with a 1*mm* wick diameter, an exposed wick length of 5*mm* and candle length (from candle base to wick tip) of 25*mm* burning in an infinite, air ambient (1 atm pressure). For most of the computation performed, the wick diameter will be 1*mm*. The main assumptions of the mathematical model are as follows. The flow is steady, laminar and axisymmetric (cylindrical coordinates). The gas-phase model assumes a single-step, second-order overall Arrhenius reaction, variable specific heats and thermal conductivity, constant Lewis number for each species (but different for each species), and ideal gas behavior. Full Navier-Stokes equations along with the conservation equation of mass, energy and species

are solved. Flame radiation from CO_2 and H_2O is accounted for through the radiative divergence term in the energy equation. The radiative transfer equation is solved by the discrete ordinates method (DOM). For the application of DOM, the physical domain is assumed as a right cylindrical shaped enclosure containing an absorbing-emitting, non-scattering medium with mean absorption coefficients that vary from location to location. The mean absorption coefficient κ is $\kappa = 0.4[X_{CO_2}K_{P,CO_2} + X_{H_2O}K_{P,H_2O}]$ where the Planck mean absorption coefficients $K_{p,i}$ as a function of local temperature are taken from [9]. The multiplication factor 0.4 is used because of the non-optically thin nature of the flame [10]. The reason of this modification factor is that CO_2 and H_2O are not thin enough in the flame and self absorption in the spectral bands can be substantial. In other words, the use of the Planck Mean absorption coefficient would over-predict the gas radiation heat fluxes if not modified. The activation energy and the pre-exponential factor of the combustion reaction are selected such that the oxygen concentration at extinction for a candle with a $1mm$ wick diameter is 0.17 (mole fraction). This results in values of $30 kcal\ mole^{-1}$ and $3x10^{12} cm^3\ g^{-1}\ s^{-1}$, for the activation energy and the pre-exponential factor, respectively. For the boundary conditions, the entire wick is assumed to be coated with liquid fuel at boiling temperature 620K). The candle surface is assumed to be an inert solid with a prescribed temperature distribution. Complete details of the model and solution procedure are available elsewhere [8], along with complete listing of the results and discussion.

Results and Discussions

Effect of gravity

Figure 1 shows the influence of gravity (up to $5g_e$) on candle flame shape and size. The reaction rate contour of $w_f=5x10^{-5}g\ cm^{-3}\ s^{-1}$ represents the boundary of the visible flame. The flame length increases as the gravity level increases from $0g_e$ to $3g_e$, decreases from $3g_e$ to $60g_e$ and blows off at higher gravity levels. The stand-off distance (the distance from the line of symmetry to the maximum width of flame) decreases with increasing gravity level. Figure 1 also shows that there is a sudden downstream retreat of the flame base position from $3g_e$ to $5g_e$. At $10g_e$ and above (not shown in Fig. 1), the flame base is downstream of the flat wick top surface. In this model we have assumed that the liquid fuel is coated over the entire wick surface including the top. The solutions for $10g_e$ and above show that the fuel vapors that support the flame come entirely form the wick top surface. In other words, above $10g_e$ the candle flame is a wake flame.

If the top surface of the wick is made inert, the model predicts that the flame blows off at $6g_e$, instead of at approximately $60g_e$. Villermaux and co-workers [10] gave a blow-off limit of approximately $7g_e$. It seems very possible that no liquid wax reaches the wick tip in the experiments. In normal candle burning, the wick adjusts its length by the self-trimming process. If the wick is too long, it is unable to draw enough liquid to the top portion. The lack of evaporative cooling in this dry portion increases its temperature and burns off the excess length. The result of this process is that for a self-trimmed candle, the wick length is where the wick tip fails to have enough liquid fuel. Also, in increasingly high gravity levels the gravitational force on the liquid in the wick becomes more significant [4]. It is reasonable to believe therefore that the inert wick top results are applicable and the numerical model and existing experimental data are in good agreement.

Figure 2 shows the total wax burning rate and maximum flame temperature as a function of gravity level. The burning rate increases with gravity and reaches a maximum at $3g_e$. At higher gravity levels, the flame retreats (Fig. 1), and the burning rate drops quickly (Fig. 2).
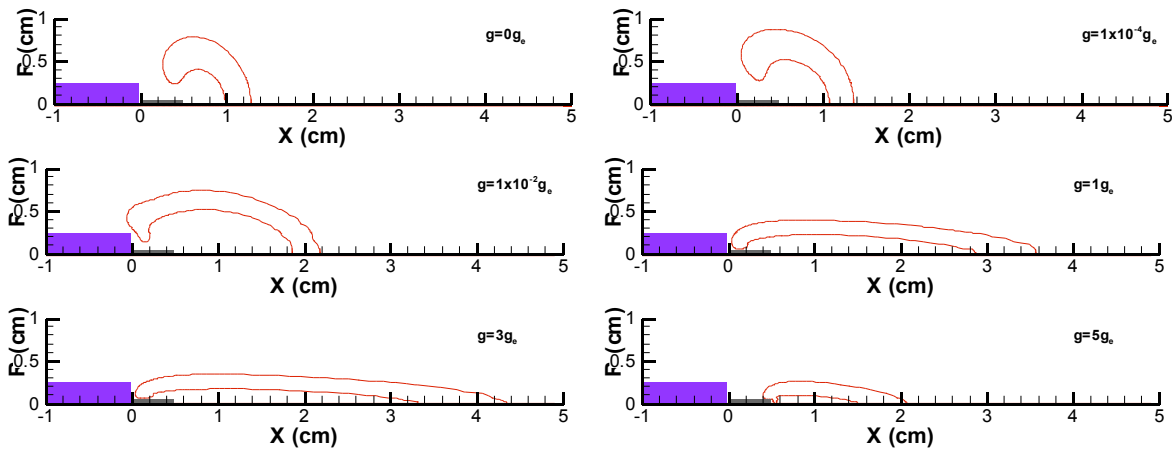
Figure 1: Fuel reaction rate contours at various gravity levels (each contour has a value of $5 \times 10^{-5} g\ cm^{-3}\ s^{-1}$).

At high g_e's, the maximum temperature is close to the adiabatic temperature, but it decreases as g decreases and reaches 1130K at zero g_e. The low flame temperatures at the reduced gravity levels suggest the influence of heat losses (radiation and conduction).

Comparison of Flame Structure Between $0g_e$ and $1g_e$ Flames

Figure 1 shows that there is a large difference between candle flame shapes at high and low gravity levels. The shape difference is a manifestation of the different transport processes important in these flames. Figure 3 presents the fuel vapor reaction rate contours and the temperature contours for (a) $0g_e$ and (b) $1g_e$. At $0g_e$, both the reaction rate and the temperature contours are hemispheric shaped with a thermal-diffusive length about $6mm$. The model predicts a steady flame diameter, D, and flame height, H, of $14.9mm$ and $9.45mm$, respectively, which compares quite well with the experimental values of $14.5mm$ and $11.2mm$ [7]. At $1g_e$, the flame is elongated and narrow. The flame base stabilization zone, located at the wick base, is small compared with the wick length. The thermal-diffusional distance is of the order of $1mm$.
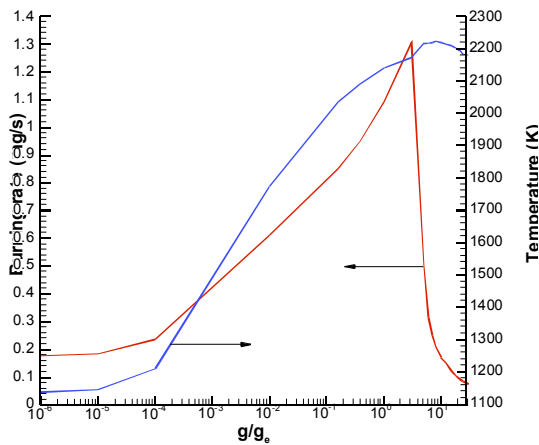
Figure 2: Candle burning rate and maximum gas temperature at various gravity levels.

Effect of Radiation

Radiative heat loss has been attributed to the occurrence of low-stretch one-dimensional diffusion flame extinction [11] and has also been suggested to contribute to the observation of blue colored microgravity candle flame [7]. In $0g_e$ candle flame, the ratio of radiation loss/heat generation is 37.6% and the ratio of conduction loss/heat generation is 29%. We performed computations to determine the relative contributions of the different types of radiation sources (gas vs. surface). The three computations were: (1) with flame and surface radiation (flame temperature 1130.5K), (2) without flame but

with surface radiation and (1435.8K) (3) without both flame and surface radiation (1452.2K). From this, we can deduce that surface radiative loss is not important and radiative and conductive losses are both important. Furthermore, there is substantial unburnt fuel vapor leaking through the quenched base that contributes to the low flame temperature. We note in computing the heat generation rate, the total evaporation rate has been used.

The small loss from surface radiation seems surprising since in other solid burning problems with similar surface temperatures [12] it is a major contributor to total heat loss. The difference is that in the microgravity candle flame, the total surface area of the wick is small so the majority of radiative loss comes from the gas phase. The conductive loss in this example is even bigger than the radiative loss. The exact amount of radiative and conductive losses will depend on the wick (or flame) diameter and the surface temperature boundary conditions but suffice to say that both types of losses are important in the candle low burning rate regime.

(a)   (b)
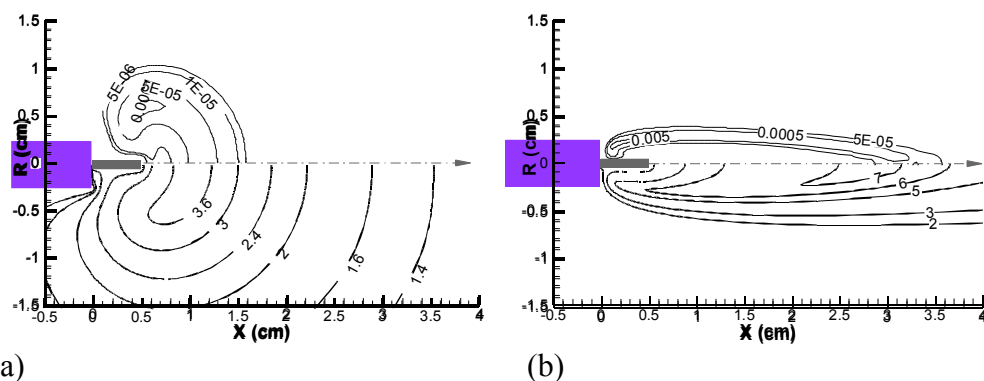
Figure 3: Flame temperature (lower half, normalized by 300K) and fuel vapor reaction rate (upper half) contours for 1mm diameter candle (a) microgravity ($0g_e$) and (b) normal gravity ($1g_e$).

References

1. Lawton, J.; Weinberg, F. J. *Electric Aspects of Combustion*, Clarenton, Oxford, 336-340, 1969
2. Chan, W. A.; T'ien, J. S. *Combust. Sci. and Tech.*, **18:** 139-143, (1978).
3. Buckmaster, J.; Peters, N. 21st *Symposium (International) on Combustion*, 1829-1836, (1986).
4. Villermaux, E.; Durox, D. *Combust. Sci. and Tech.*, **84:** 279-294, (1992).
5. Ross, H. D.; Sotos, R. G.; T'ien, J. S. *Combust. Sci. and Tech.*, **75**: 155-160, (1991).
6. Dietrich, D. L.; Ross, H. D.; T'ien, J. S. *AIAA-94-0429*, 32nd Aerospace Science Meeting and Exhibit, Reno, Nevada, (1994).
7. Dietrich, D. L.; Ross, H. D.; Shu, Y.; Chang, P.; T'ien, J. S. *Combust. Sci. and Tech.*, **156:** 1-24, (2000).
8. Alsairafi, A. A. "A Computational Study on the Gravity Effect on Wick-Stabilized Diffusion Flames," *Ph.D. Thesis*, Case Western Reserve University, Expected May, (2003).
9. Abu-Romia, M. M.; Tien, C. L. *J. Heat Transfer*, **89C:** 321-327, (1967).
10. Bedir, H.; T'ien, J. S.; Lee, H. S. *Combustion Theory Modeling,* **1:** 395-404, (1997).
11. T'ien, J. S. *Combust. Flame*, **65:** 31-34, (1986).
12. Rhatigan, J. L., Bedir. H. and T'ien, J. S. *Combust. Flame*, **112:** 231-241, (1998).

Characteristics of Gaseous Diffusion Flames With High Temperature Combustion Air in Microgravity

M. Ghaderi and A. K. Gupta

University of Maryland, Department of Mechanical Engineering, College Park, MD

Abstract

The characteristics of gaseous diffusion flames have been obtained using high temperature combustion air under microgravity conditions. The time resolved flame images under free fall microgravity conditions were obtained from the video images obtained. The tests results reported here were conducted using propane as the fuel and about 1000°C combustion air. The burner included a 0.686 mm diameter central fuel jet injected into the surrounding high temperature combustion air. The fuel jet exit Reynolds number was 63. Several measurements were taken at different air preheats and fuel jet exit Reynolds number. The resulting hybrid color flame was found to be blue at the base of the flame followed by a yellow color flame. The length and width of flame during the entire free fall conditions has been examined. Also the relative flame length and width for blue and yellow portion of the flame has been examined under microgravity conditions. The results show that the flame length decreases and width increases with high air preheats in microgravity condition. In microgravity conditions the flame length is larger with normal temperature combustion air than high temperature air.

Introduction

Study of laminar diffusion flames has important role to understand and utilize their thermal and chemical behavior in practical combustion systems. The flame length and width is an important property of laminar flames. No previous data are available on the effect of combustion air preheat in microgravity conditions. Combustion with high temperature air is a relatively new concept and has many practical benefits [1,2]. Some of the benefits of using high temperature air for combustion that have been demonstrated include (i) energy savings of about 30%, (ii) pollution reduction, including NO_x and CO_2, by about 30%, (iii) 25% reduction in the size of the equipment, and (iv) far uniform thermal field in the combustion zone. In this study we provide information on the behavior of flames formed with high temperature combustion air in microgravity.

Experimental

The experiments were conducted using a 1 sec drop tower facility. The experimental burner consisted of a 0.686 mm diameter fuel jet that was centrally located in a 12.7 mm diameter air jet. The combustion air could be preheated up to about 1100°C using electrical heating. The experiment test rig consisted of burner, voltage regulator, electrical air preheater, combustion chamber, color CCD camera, digital camcorder, and gas cylinders for fuel, combustion air and burner cooling, see Figure 1. The flame images were captured using a CCD camera in the emission mode at a framing rate of 30 frames per second and then recorded onto a digital camcorder. Experiments were conducted under microgravity conditions at normal pressure and normal oxygen concentration air using propane as the fuel at a flow rate 0.02 SCFH. The flame photographs, recorded with the color CCD camera and camcorder, were analyzed to determine the flame shape (length and width) and color.

Results and Discussion

The results are presented at two air preheat temperatures of 900°C and 1000°C. A sequence of diffusion flame photographs using propane as the fuel in microgravity conditions for experiments # 3 and 4 are shown in Fig. 2. In this paper results from two specific experiments with combustion air preheats at 900°C (for expt. # 3) and 1000°C (for expt. # 4) are reported to provide the effect of air preheat temperature on flame size, shape and color (hybrid) under microgravity and normal gravity conditions. The time sequence photos of flame during drop were recorded onto the video camera at a speed of 30 frames/s. The results show that in both cases the flames are of hybrid color consisting of initial blue color flame followed by a yellow color flame downstream of the burner. The length of the yellow color flame is higher at higher air preheat temperature (compare flame photos from experiments # 4 with # 3). The yellow portion of the flame with experiments # 4 (having higher air preheat temperature) is higher. A close examination of the entire flame length (blue and yellow portion) shows that the length of flame in experiment # 4 is shorter as compared to flames produced in experiment # 3.

The flames photographs were further analyzed with respect to the total length and width as well as the length and width of the blue and yellow portion of the flames during the entire time duration in the microgravity environment. The results for the total length and width are shown in Fig. 3. The results show shorter flame at higher air preheats temperatures (compare flame lengths in Fig. 3 for experiments # 3 and 4 at t = 0 to about t = 0.1 sec). Immediately after the onset of drop (very low microgravity conditions) the flame length for experiment # 4 (with high air preheats) is smaller. This suggests that higher temperature air reduces the flame length in microgravity. Our results obtained at 1-g conditions also showed that the flame length decreases with increase in air preheats [2] using normal O_2 concentration in air. In contrast the flame width increases with increase in air preheats under microgravity conditions (compare flame width from t =0 to about t = 0.1 for the two cases). At the onset of microgravity the flame with high air preheat temperature experiences a rapid increase in flame width (experiment # 4) as compared to low temperature air case (experiment # 3). The rate of increase of flame width is higher with higher air preheats at t =0.1 to about t = 0.2. After t = 0.2 sec both flames reach the maximum width due to lower gravity field. The change in gravity with time during the drop was calculated by balancing the force on the entire drop package (i.e., drag and gravity = mass x acceleration). At higher residence times (t) under microgravity conditions the flame length increases because of the drag and hence a higher gravity values as compared to that obtained at the onset of drop. This suggests that under microgravity conditions the flames are smaller and wider with increase in air preheats.

A comparison of the blue and yellow portion of the flame for the two experiments is shown in Figure 4. At higher air preheats the yellow portion of the flame becomes higher and the blue portion of the flame becomes smaller. Hotter flames (with higher air preheats) affect both the length and width in microgravity. The initial trend observed for the entire flame length and width applies to both flames with even greater differences in blue portion of the flame length at the two airs preheat. Global features on the change in flame length and width as affected by gravity and air preheat temperature are summarized in Figure 5. They show that high air preheats further widens the flame width and reduces the flame length in microgravity conditions.

Conclusions

Flame length decreases and the width increases under microgravity conditions. At higher air preheat temperatures the flame length decreases under microgravity conditions. Under

microgravity conditions at high air preheat temperature, the flame width is even wider as compared to normal temperature air and normal gravity conditions. The flame luminosity as measured by the yellow color of the flame increases with increase in air preheats temperature under microgravity conditions. The data obtained provides useful information for model validation and model development.

Acknowledgments

References

1. Tsuji, H., Gupta, A. K., Hasegawa, T., Katsuki, M., Kishimoto, K., and Morita, M.: High Temperature Air Combustion: From Energy Conservation to Pollution Reduction, CRC Press, 2003, pp. 401.
2. Gupta, A. K.: Flame Characteristics and Challenges with High Temperature Air Combustion, Invited Lecture, Proc. 2nd International Seminar on High Temperature Combustion in Industrial Furnaces, Stockholm, Sweden, January 17-18, 2000.

Fig. 1. A photograph of the experimental facility.

T=0.000 sec   T= 0.033 sec   T=0.066 sec   T=0.166 sec

T=0.000 sec   T=0.033 sec   T=0.066 sec   T=0.133 sec
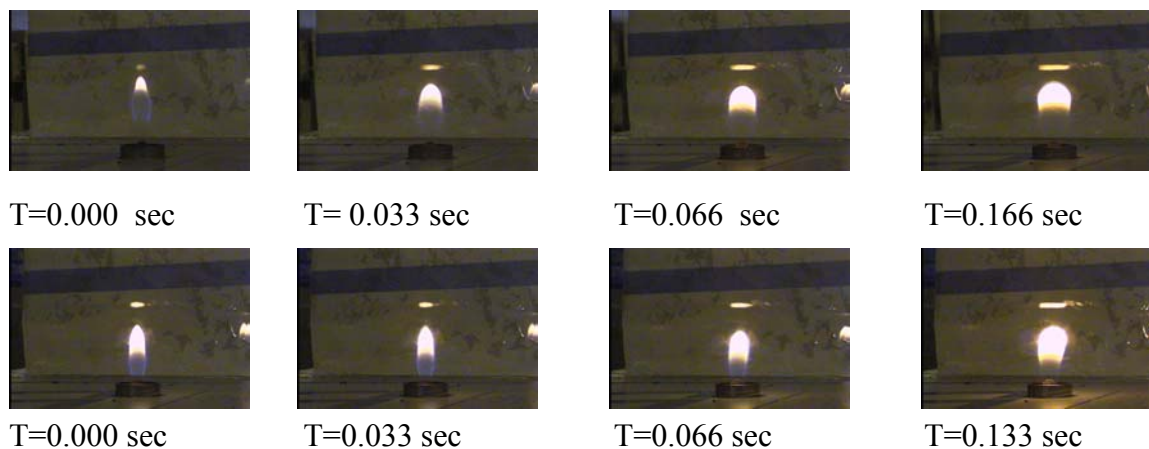
Fig. 2. Flame photos with 900°C (upper row, expt. # 3) and 1000°C (lower row, expt. #4) air preheat temperature.
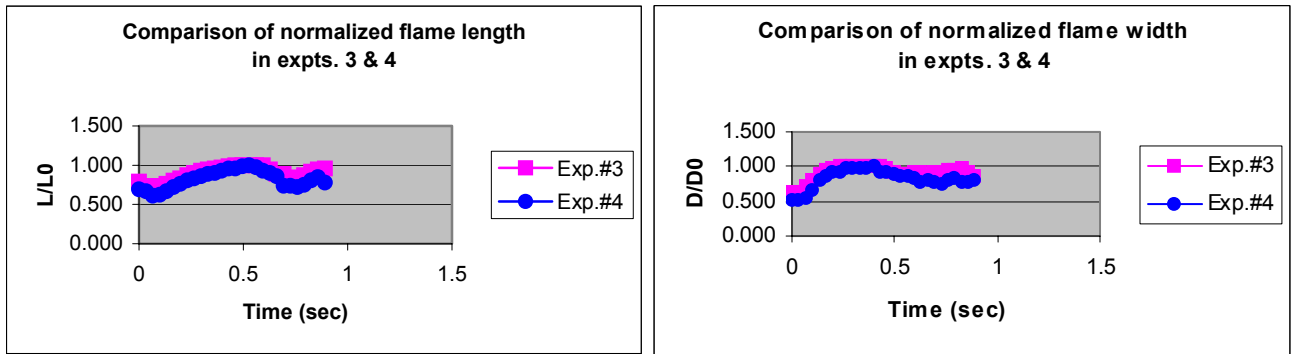
Fig. 3. Change in normalized flame length (left) and width (right) during the experiments.
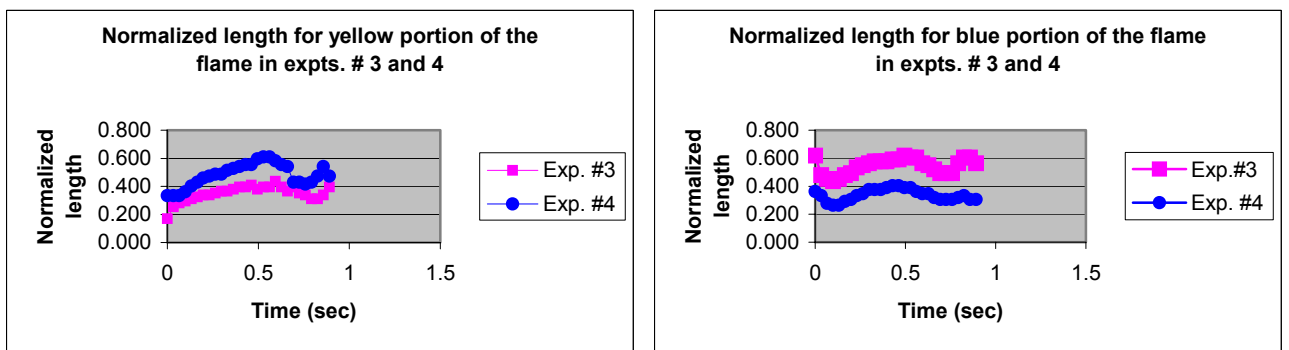
Fig. 4. Change in normalized yellow (left) and blue (right) portion of the flame length.

Gravity	Normal Temp. Air	High Temp. Air
1-g	Flame shape	Decreased flame length
μ-g	Small and wider flame	Smaller and even wider flame

Fig. 5. A schematic representation of the effect of air preheats temperature and microgravity on the global flame shapes.

"SMOKE:" CHARACTERIZATION OF SMOKE PARTICULATE FOR SPACECRAFT FIRE DETECTION

David L. Urban
NASA Glenn Research Center, Cleveland OH
George W. Mulholland, Jiann Yang, Thomas G. Cleary
National Institute for Standards and Technology, Gaithersburg, MD
Zeng-guang Yuan
National Center for Microgravity Research in Fluids and Combustion, Cleveland, OH

INTRODUCTION

The "Smoke" experiment is a flight definition investigation that seeks to increase our understanding of spacecraft fire detection through measurements of particulate size distributions of preignition smokes from typical spacecraft materials. Owing to the catastrophic risk posed by even a very small fire in a spacecraft, the design goal for spacecraft fire detection is to detect the fire as quickly as possible, preferably in the preignition phase before a real flaming fire has developed. Consequently the target smoke for detection is typically not soot (typical of established hydrocarbon fires) but instead, pyrolysis products, and recondensed polymer particles. At the same time, false alarms are extremely costly as the crew and the ground team must respond quickly to every alarm. The U.S. Space Shuttle (STS: Space Transportation System) and the International Space Station (ISS) both use smoke detection as the primary means of fire detection. These two systems were designed in the absence of any data concerning low-gravity smoke particle (and background dust) size distributions. The STS system uses an ionization detector coupled with a sampling pump and the ISS system is a forward light scattering detector operating in the near IR. These two systems have significantly different sensitivities with the ionization detector being most sensitive (on a mass concentration basis) to smaller particulate and the light scattering detector being most sensitive to particulate that is larger than 1 micron. Since any smoke detection system has inherent size sensitivity characteristics, proper design of future smoke detection systems will require an understanding of the background and alarm particle size distributions that can be expected in a space environment.

Prior studies of spacecraft aerosol particulate include (Urban et al. 1997 and Liu et al. 1991). Urban et al. (1997) measured the STS and ISS detector response to various smoke particulate sources. In general the size of the smoke particulate was found to be larger in low gravity and the apparent size of the particles in smokes where the particulate was primarily liquid drops was found to increase to the point that the STS detector was essentially unable to detect the smoke. Liu et al. (1991) measured the mass concentration and particle size distribution of the cabin air on one shuttle flight. Two particle size distributions were measured and were found to have the mass median particle size greater than 100 microns. This is to be compared with their values of about 1 μm to 3 μm for ambient aerosols. The large difference results from the larger particles rapidly settling out at 1 g. The mass concentration of the particulate was found to be approximately 55 μg/m^3 in the shuttle, versus 11 μg/m^3 for 1-g ambient conditions.

The ideal approach would be to obtain complete particle size distributions for all of the smokes of interest. Unfortunately, the instruments that provide data of this type (classifiers or

impactors) are unsuited for spaceflight experiments either because they are too large or cannot provide real time measurements. The Smoke experiment seeks to work around this problem by measuring three moments of the particle size distribution using instruments that are adaptable to space experimentation. This paper discusses progress toward development of the flight experiment. Progress in the moment method is described below in the first section of this paper. This is followed by the results of detailed characterization of the ISS and STS smoke detectors. Design of the space experiment and generalization of the results requires understanding of the smoke growth process. To develop a predictive understanding of the aerosol growth process, a model is being developed by extending the NIST FDS (Fire Dynamics Simulator) program to model the smoke particle growth process. This work is discussed in the final section below.

MOMENT METHOD DEVELOPMENT

As discussed in more detail by Cleary et al (2001), 5 test smokes were studied using instruments capable of measuring the zeroth, first and third moments. Specifically, the zeroth moment was measured using a condensation particle counter (CPC), the first moment by a measuring ionization counter (MIC) and the third moment by a taper element oscillating microbalance (TEOM). Similar instruments are planned for the smoke experiment for the zeroth and third moments and the third moment will be measured using a light scattering measurement. Figure 1 presents the size distributions for these smokes (determined using a cascade impactor). The slope of the points on the plot increase with the geometric standard deviation. The slopes are very similar with the toast having the lowest slope and therefore the narrowest size distribution. Assuming a log-normal size distribution, the three moments can be used to calculate the geometric standard deviation and the diameter of average mass (Hinds 1999). Assuming unit density spherical particles, the Hatch-Choate relationships can be used to estimate the Mass Median Aerodynamic Diameter (MMAD) which can be compared to the MMAD determined from the impactor data. The results of this comparison can be seen in Table 1. The comparison is very good for the Cotton Wick, Wood and Corn Oil and reasonably close for the polyurethane smoke. In the case of the toast, there was no solution because the count mean diameter was larger than the diameter of average mass which suggests a problem with the measurement system since the moment average should increase with the moment (for the same distribution). In general these results suggest that the moment method can be used to develop a summary description of the particle size distribution.

SMOKE DETECTOR CHARACTERIZATION

To characterize the comparative performance of the STS and ISS detectors, the detectors were exposed to Monodisperse dioctyl phthalate (DOP) aerosols generated using the procedure discussed by Mulholland and Liu (1980). The system is able to develop mono-disperse aerosols with sizes ranging from 0.056 to 1.34 μm although the number concentration decreases strongly with particle size. The results are presented in figures 2-4. The response of the two detector types is consistent with their design. The STS ionization detector is most affected by changes in the number concentration but also shows increasing sensitivity as the particle size increases. The ISS light scattering device, which basically responds to mass concentration, is very strongly affected by the particle size for particle sizes less than 1 μm. Thus, it is able to detect the largest particles even though the number concentration is low.

AEROSOL DYNAMICS MODELING

The modeling effort is based on the NIST Fire Dynamics Simulator (FDS, version 2), which is a CFD code with LES (large eddy simulation) and DNS (direct numerical simulation) options. The code was modified to include homogeneous nucleation and growth to model aerosol dynamics that includes two-phase, momentum, heat and mass transfer. The computational procedure can be briefly summarized as follows. The velocity, temperature, and concentration fields are first determined using DNS mode of the modified code. The saturation ratio field is then computed. Homogeneous nucleation (in this case, condensation) occurs when a critical saturation ratio is reached. Nucleation is modeled using classical homogeneous nucleation theory. The aerosol diameter at nucleation is then calculated, and condensation growth follows and is assumed to be diffusion-limited. Coagulation and agglomeration are not considered in the model. The flow fields are then corrected for interfacial momentum, heat and mass transfer. Droplet number density, size distribution, and the moments are then computed in each grid cell.

Figures 5 and 6 show graphical representations of the results from a simulation. The computational domain, which simulates a flow duct, is 0.2 m in length with a cross section of 0.028 m by 0.028 m. The solid block in the figures simulates an aerosol generator with dibutyl phthalate (DBT) vapor being ejected from four sides (except the two ends). The generator is located 0.05 m downstream from the inlet. A vapor mass flux of 8.55×10^{-4} kg/s m^2 at 200 °C was used in the simulation. The inlet air velocity was set at 0.05 m/s and 25 °C. The calculations were performed using zero gravity and an ambient temperature of 25 °C. In this particular case, 31 x 31 x 700 grids were used in the simulation to ensure convergence. These results are very promising and our current main effort focuses on the validation and improvement of the aerosol dynamics model.

REFERENCES

Cleary, T.G., Weinert, D.W. and Mulholland, G.W. 2003. "Moment Method for Obtaining Particle Size Measures of Test Smokes," NISTIR, in press.

Hinds, W.C., 1999. *Particle Technology*, Wiley-Interscience, New York.

Liu, B.Y.H., Rubow, K.L., McMurray, P.H., Kotz, T.J., and Russo, D. 1991. "Airborne Particulate Matter and Spacecraft Internal Environments", SAE paper 911476, 21st Conference on Environmental Systems, San Francisco, CA, July 15-18.

Mulholland, G.W. and Liu, B.Y.H, 1980. "Response of Smoke Detectors to Monodisperse Aerosols, Journal of Research of the National Bureau of Standards, V 85, p 223- 238.

Urban, D. L., D. W. Griffin and M.Y. Gard, 1997, Proceedings of the USML-2 and USMP-3 Joint Launch plus 1 Year Conference, National Academy of Science, Washington D.C. February.

Table 1. Comparison of Mass Median Aerodynamic Diameter predicted from moment measurements with that from impactor data

Smoke	Mean D_{30} (µm)	Mean σ_g	Predicted MMAD (µm)	Impactor MMAD (µm)	σ_g
Cotton Wick	0.24	1.4	0.28	0.31	1.7
PU foam	1.0	1.6	1.4	2.0	1.6
Wood	0.53	2.25	1.4	1.5	1.9
Corn Oil	0.50	2.5	1.8	1.6	2.2
Toast	0.32	invalid	invalid	0.43	1.6
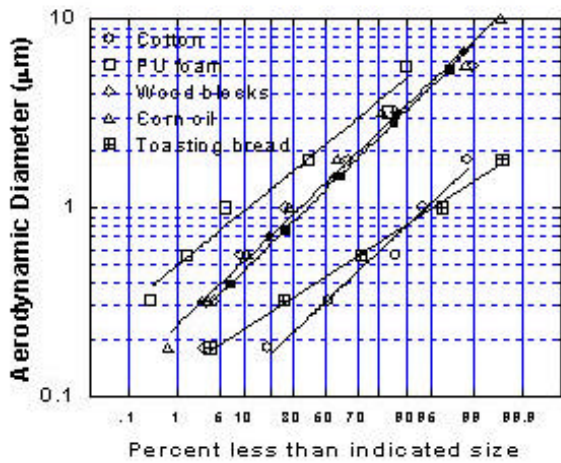
Figure 1.   Temperature profile at the mid-plane at 2 s.
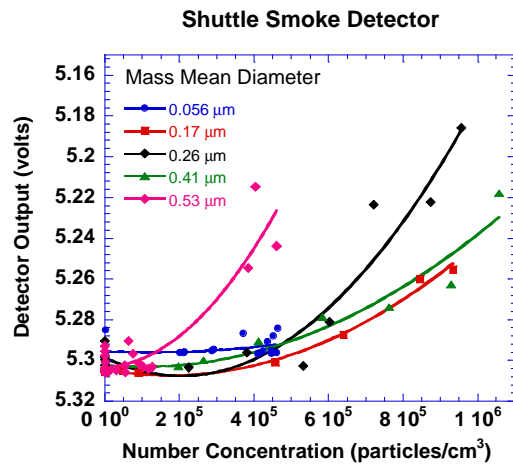
Figure 2.   STS detector output versus number concentration.
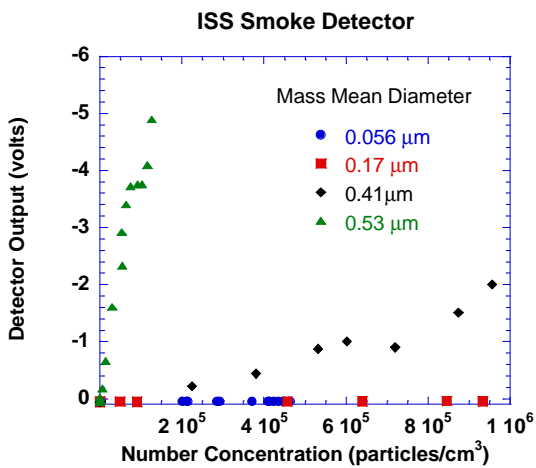
Figure 3.   ISS detector output versus number concentration for droplets from 0.056 to 0.53 µm.
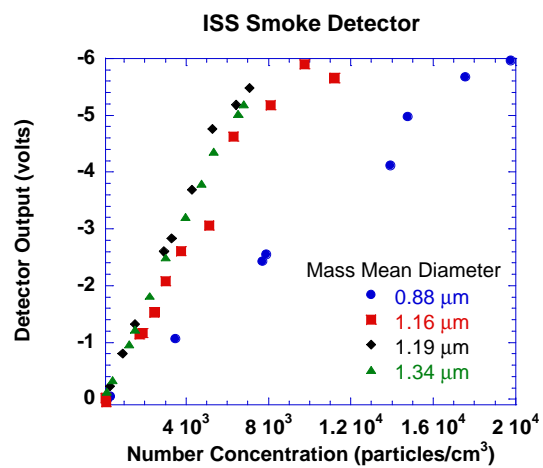
Figure 4.   ISS detector output versus number concentration for droplets from 0.88 to 1.34 µm.
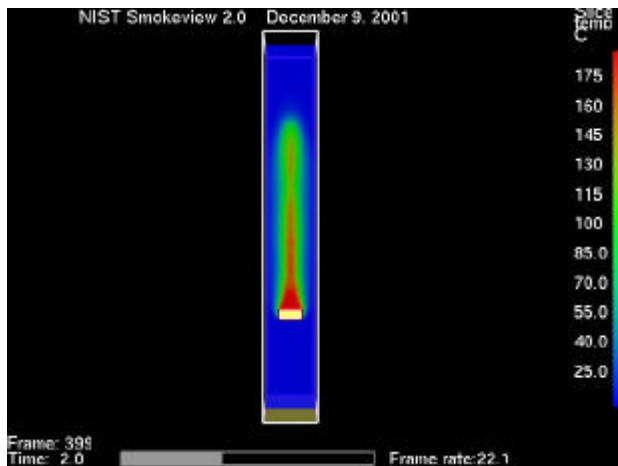
Figure 5.   Temperature profile at the mid-plane at 2 s.
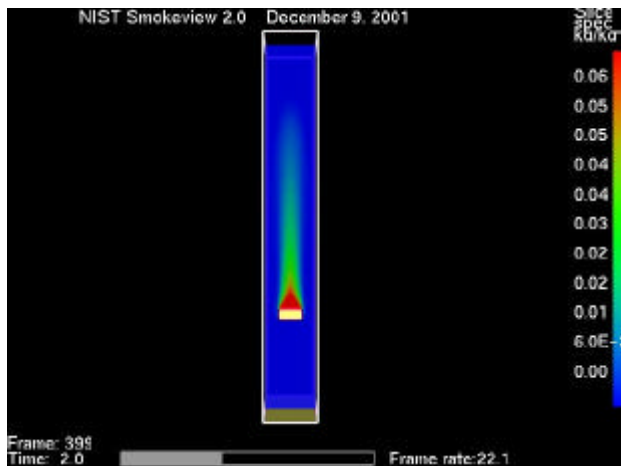
Figure 6. Mass fraction profile of DBT vapor at the mid-plane at 2 s

SUPPRESSION AND STRUCTURE OF LOW STRAIN RATE NONPREMIXED FLAMES

Anthony Hamins, Matthew Bundy, Woe Chul Park[1], Ki Yong Lee[2] & Jennifer Logue
National Institute of Standards and Technology

Gaithersburg, Maryland 20899-8663

The agent concentration required to achieve suppression of low strain rate nonpremixed flames is an important fire safety consideration. In a microgravity environment such as a space platform, unwanted fires will likely occur in near quiescent conditions where strain rates are very low. Diffusion flames typically become more robust as the strain rate is decreased. When designing a fire suppression system for worst-case conditions, low strain rates should be considered

The first comprehensive extinction measurements of very low strain non-premixed flames in microgravity were reported by Maruta *et al.* [1]. The extinction of methane-air flames with N_2 added to the fuel stream was investigated using the JAMIC 10 s drop tower. The minimum methane concentration required to sustain combustion was measured to decrease as the strain rate decreased until a critical value was observed. As the global strain rate was further reduced, the required methane concentration increased. This behavior was denoted as a "turning point" and was attributed to the enhanced importance of radiative losses at low strain rates. In terms of fire safety, a critical agent concentration assuring suppression under all flow conditions represents a fundamental limit for nonpremixed flames.

The objective of this study is to investigate the impact of radiative emission, flame strain, agent addition, and buoyancy on the structure and extinction of low strain rate nonpremixed flames through measurements and comparison with flame simulations. The suppression effectiveness of a suppressant (N_2) added to the fuel stream of low strain rate methane-air diffusion flames was measured. Flame temperature measurements were attained in the high temperature region of the flame ($T > 1200$ K) by measurement of thin filament emission intensity. The time varying temperature was measured and simulated as the flame made the transition from normal to microgravity conditions and as the flame extinguished.

EXPERIMENTAL METHOD

Flame suppression and the temperature field in low-strain diluted methane/air non-premixed flames were measured in microgravity using a counterflow flame configuration. Experiments were performed at the NASA Glenn research facility using the 2.2 s drop. A 15 mm diameter stainless steel counterflow burner was enclosed in a 25 L cylindrical chamber. The duct separation distance was 15 mm. The burner ducts were designed to have minimal dead volume as glass beads and a series of fine mesh steel screens were used to impose a near plug-flow velocity profile at the burner exit.

To control each of the reactant gas flows, a fast response time (~10 ms) pressure controller was used in series with a critical flow orifice. The total system response time was equal to the flow control response time plus the residence flow time from the mixing tee to the flame zone, estimated as 0.0665 s to 0.6397 s for strain rates of 50 s^{-1} and 7 s^{-1}, respectively. The

Permanent addresses: 1. Dept of Safety Engineering, Pukyong National University, Pusan, Republic of Korea 608-739; 2. School of Mechanical Engineering, Andong National University, Andong, Republic of Korea 760-749.

flow of dry air and methane were calibrated using a dry cell primary flow meter. A 0.25 mm diameter, 7 cm long coiled resistance igniter wire (Pt + 30% Rh) positioned between the fuel and oxidizer ducts was used to ignite the flame. A rotary brushless torque actuator was used to control the position of the ignition wire.

Extinction measurements were performed by incrementally increasing the agent flow, while maintaining a constant global strain rate (a_g), accomplished by simultaneously reducing the air or fuel flow. The value of a_g in the axisymmetric counterflow configuration is defined as:

$$a_g = (-2V_O/L) \cdot (1 + [(V_F/V_O) \cdot (\rho_F/\rho_O)^{1/2}]) \tag{1}$$

where V and ρ denote the velocity and density of the reactant streams at the boundaries, L is the duct separation distance, and the subscripts O and F represent the oxidizer and fuel streams, respectively. The standard uncertainty in agent extinction concentration was 2 % based on repeat measurements.

Measurement of the visible emission intensity from a 13 µm SiC filament placed along the burner centerline allowed the determination of flame temperatures for T>1200 K. Radiation emitted by the filament was recorded using a digital CCD camera with a close-up lens. Spatial resolution of the image was 0.07 mm/pixel. The camera exposure was adjusted to prevent image saturatation (over-exposure) at the maximum flame temperature. The intensity measurements were calibrated using Oppdff [3]. The uncertainty is 50 K based on repeat measurements.

NUMERICAL METHODOLOGY

Two flame codes were utilized. The structure and extinction of methane-air flames with N_2 addition were investigated using a one-dimensional numerical simulation that employs detailed models of molecular transport and chemistry, but ignores buoyancy [2,3]. A term for the radiative heat loss rate was added to the energy equation in the one-dimensional flame code. Radiative losses were modeled with a narrowband spectral model [4]. A transient two-dimensional (axisymmetric) solution to the Navier-Stokes equations including buoyancy using either a mixture fraction approach or one-step chemistry based on the NIST Fire Dynamic Simulator (FDS) was developed [5]. The effects of global strain rate and buoyancy were investigated and results were compared to the one-dimensional Oppdif flame code at 0-g.

RESULTS AND DISCUSSION

Figure 1 shows extinction measurements performed for stain rates of 7 s^{-1} through 50 s^{-1}, confirming the "turning point" behavior observed previously by Maruta and coworkers [1] and confirming the viability of these 2 s duration extinction measurements. The maximum nitrogen volume fraction in the fuel stream, $C_{a,ext}$, needed for extinction was found to be 0.855 ± 0.016 at a strain rate of 15 s^{-1}, consistent with the results of Maruta. These values are different from analogous measurements performed in normal gravity [6], implying that the local oxidizer-side strain rate differs in normal and microgravity for small a_g. On-going Particle Imaging Velocimetry (PIV) measurements are quantifying these differences.

Figure 2 compares a photograph of a 12 s^{-1} near-extinction methane/air diffusion flame in normal gravity (fuel = 20% CH_4 + 80 % N_2) with the FDS simulation. The flame curvature in 1g is captured by the simulation. Figure 3 compares drop measurements to FDS simulations of the position of the maximum flame temperature as a function of time after microgravity occurs for constant flow conditions, a_g=20 1/s and the fuel = 82 % N_2 + 18 % CH_4. There is general agreement between the model and the measurements within measurement uncertainty. Figure 4 shows agreement between the simulated (Oppdif and FDS) and measured (filament and

thermocouple) temperature profiles in normal and microgravity. Figure 5 shows consistent trends between the calculated (Oppdif) and measured peak flame temperatures in near-extinction methane/air diffusion flames in microgravity. As the strain rate decreases, the peak flame temperature decreases until low peak temperatures are observed (< 1400 K), rather unusual for a flamelet.

REFERENCES

1. Maruta, K., Yoshida, M., Guo, H., Ju, Y., & Niioka, T, *Combust. Flame*, 112:181 (1998).

2. Bowman, C. T., Hanson, R. K., Davidson, D. F., Gardiner, Jr., W. C., Lissianski, V., Smith, G. P., Golden, D. M., Frenklach, M., & Goldenberg, M., "GRI-MECH 2.11", URL: http://www.me.berkeley.edu/gri-mech/, 1995.

3. Lutz, A., Kee, R. J., Grcar, J., & Rupley, F. M., "A Fortran Program Computing Opposed Flow Diffusion Flames", SAND96-8243, Sandia National Labs, Livermore (1997).

4. Grosshandler, W.L., RADCAL: NIST Technical Note 1402, National Institute of Standards and Technology, Gaithersburg, Maryland, 1993.

5. McGrattan, K. B., Baum, H. R., Rehm, R. G., Hamins, A., Forney, G. P., Floyd, J. E., and Hostikka, S., "Fire Dynamics Simulator Technical Reference Guide," National Institute of Standards and Technology, Gaithersburg, MD (2001).

6. Bundy, M., Hamins, A., & Lee, K.Y., *Combust. Flame*, to appear (2003).
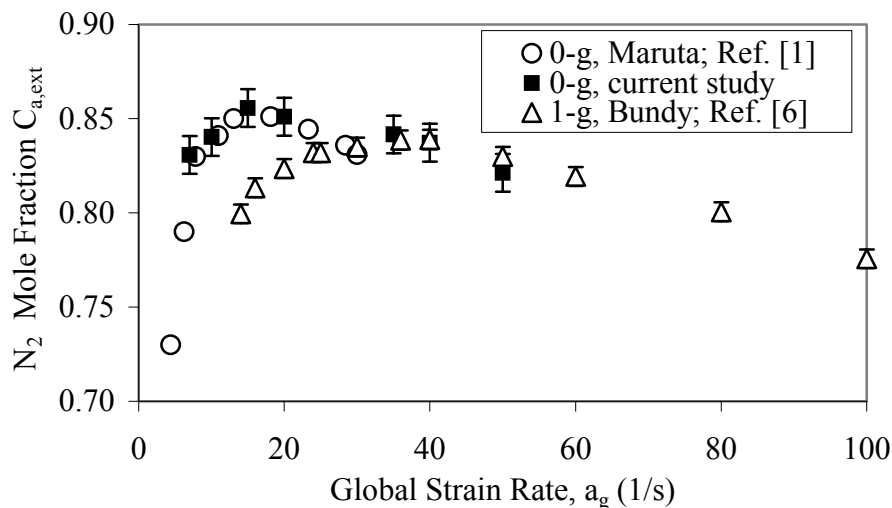
Figure 1. Critical mole fraction of N_2 in the fuel stream required to extinguish a methane/air diffusion flame in normal and microgravity. The results of Maruta et al. [1] are also shown. Flammable region is below the data points.
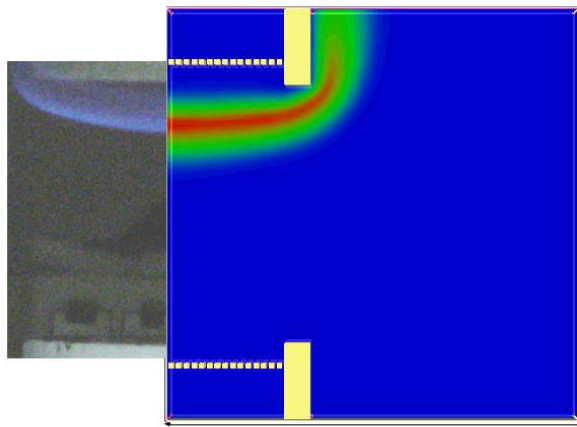
Figure 2. Photograph and simulation of a 12 s^{-1} diluted methane/air diffusion flame in normal gravity. (Fuel =20%CH$_4$ + 80 % N$_2$)
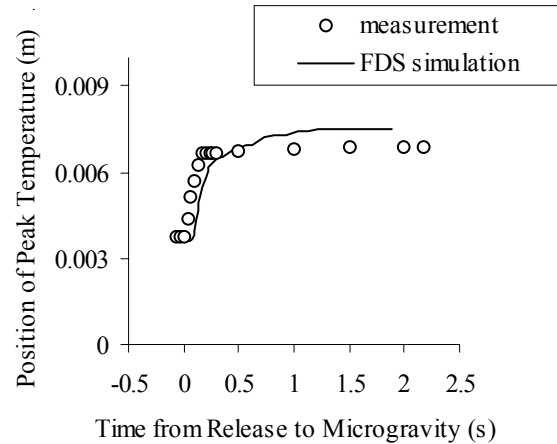
Figure 3. The measured and calculated (FDS) position of the peak flame temperature as a function of time after microgravity occurs. a_g=20 s^{-1}, 18% CH$_4$
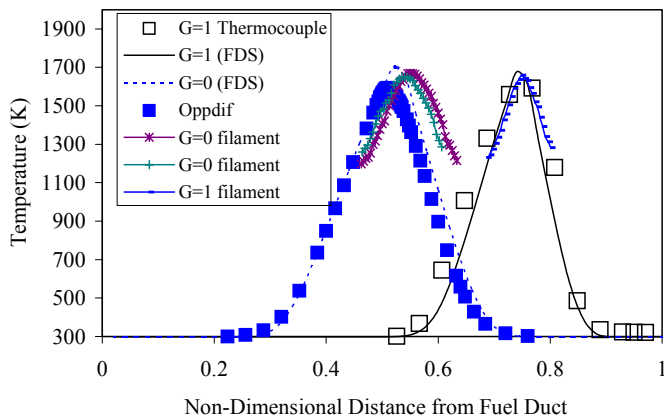
Figure 4. Comparison of the calculated (FDS and Oppdif) and measured (SiC filament intensity and thermocouple) flame temperatures in diluted methane/air diffusion flames in normal and microgravity with a_g=20 s^{-1} and the fuel composed of ~20 % CH$_4$ + 80 % N$_2$.
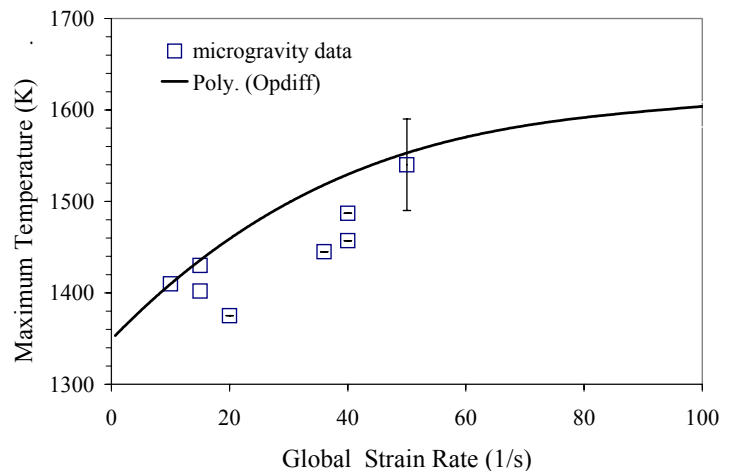
Figure 5. Comparison of the calculated (Oppdif) and measured peak flame temperature in near-extinction methane/air diffusion flames in microgravity. Conditions were extremely near extinction, such that the agent concentration was > 99.4 % of that required for extinction, corresponding to the conditions shown in Fig. 1.

EXPERIMENTAL AND NUMERICAL EVALUATION OF GASEOUS AGENTS FOR SUPPRESSING CUP-BURNER FLAMES IN LOW-GRAVITY

Fumiaki Takahashi
National Center for Microgravity Research on Fluids and Combustion

Gregory T. Linteris
Fire Research Division, National Institute of Standards and Technology

Viswanath R. Katta
Innovative Scientific Solutions Inc.

INTRODUCTION

Longer duration missions to the moon, to Mars, and on the International Space Station (ISS) increase the likelihood of accidental fires. NASA's fire safety program for human-crewed space flight is based largely on removing ignition sources and controlling the flammability of the material on-board. There is ongoing research to improve the flammability characterization of materials in low gravity; however, very little research has been conducted on fire suppression in the low-gravity environment. Although the existing suppression systems aboard the Space Shuttle (halon 1301, CF_3Br) and the ISS (CO_2 or water-based form) may continue to be used, alternative effective agents or techniques are desirable for long-duration missions.

The goal of the present investigation is to: (1) understand the physical and chemical processes of fire suppression in various gravity and O_2 levels simulating spacecraft, Mars, and moon missions; (2) provide rigorous testing of analytical models, which include detailed combustion-suppression chemistry and radiation sub-models, so that the model can be used to interpret (and predict) the suppression behavior in low gravity; and (3) provide basic research results useful for advances in space fire safety technology, including new fire-extinguishing agents and approaches.

APPROACH

In order to achieve these objectives we have embarked upon a comprehensive program involving experiments and numerical modeling of the extinction of diffusion flames with added suppressants. The experiments involve both a 1*g* testing (for baseline data and for model validation) and low-*g* testing program (in drop towers and the KC-135 aircraft). The numerical modeling uses a time-dependent 2-D direct numerical simulation with full chemistry (UNICORN) for simulating either the low-*g* or 1*g* flames, and interpreting the effect of gravity on the extinction process with and without a variety of agents (of types which act both physically and chemically). The configuration selected is a cup burner (a co-flow diffusion flame with a 2.8 cm diameter fuel source, either a liquid pool or a low-velocity gas jet, inside an 8.5 cm diameter chimney with oxidizer flowing at ~10 cm/s. The cup burner is a common metric for suppression agent performance in fire safety engineering and a large database is available for comparison to extinction in 1*g*. A low-*g* cup-burner test rig, equipped with a particle image velocimeter and a Mach-Zehnder interferometer, is nearly complete. For supporting development and validation of the kinetics, experiments and modeling are also performed for premixed Bunsen-type flames and counterflow diffusion flames.

RESULTS AND DISCUSSION

In a 1*g* laboratory, the combustion and extinction characteristics of the cup burner, including the extinction conditions, flame shape, time-dependent flame tip and base locations, and flicker frequency, have been measured for various fuels, including methanol, methane, heptane, and trioxane. For the liquid or solid fuels, the variation of the fuel mass loss rate with addition of inhibitor have also been measured. The fundamental kinetic work necessary for other parts of the project have been determined [1,2].

Carbon dioxide used on the ISS is relatively inefficient and requires high concentrations (15-20 vol.%) when injected into air. Therefore, the deployment and dispersion of the agent to achieve the critical concentration everywhere inside a cluttered compartment such as instrumentation racks require careful system design considerations. One approach for reducing the critical agent concentration and, thus the total amount of agent is to combine inert agents with effective chemical compounds. In this case, the overall reaction rate is lowered in part through the lower temperature caused by the inert and in part through radical recombination by the added catalytic agent. Figure 1 shows the variation of the fuel consumption rate in a methanol cup-burner flame with addition of CO_2, CF_3Br, or their blend. The result demonstrates that by blending 2.2% of CF_3Br, the critical CO_2 concentration required for suppression dropped to 1/3 of that of CO_2 alone. Figure 2 presents the effect of some very active chemical agents in cup-burner flames [3,4].

Figure 1   Methanol consumption rate (and extinction condition) in a cup burner with CO_2, CF_3Br, or their blend, added to the air stream.

Although only a few hundred ppm of super-effective agents rapidly reduced the critical CO_2 concentration at suppression, material condensation prohibited further blending [4]. By using data from our experiments as well as those in the literature, the performance benefit (volume based, compared to CO_2), as shown in Figure 3, has been compiled to compare the effectiveness of various agents, ranging from inert up to highly chemically active, in a variety of flames, including cup-burner (Cup), counterflow diffusion (CF, 10 s^{-1}, 20 s^{-1}, 30 s^{-1} strain rate), and premixed flames (Pre, 10%, 30%, 45% laminar flame speed reduction). Some super-effective

Figure 2 CO_2 volume fraction at extinction in a cup burner with added catalytic inhibitors.

agents are orders of magnitude more efficient.

Numerical simulations have been performed to investigate the flame structure of methane-air flames with added CO_2 [5-8], CF_3H, and $Fe(CO)_5$ [4]. Figure 4 shows the temperature contours for flames in 1g with a CO_2 volume fraction of 0.05 and 0.145 (the suppression limit). The computation has revealed that the suppression of cup-burner flames occurs via a blowoff process (in which the flame base drifts downstream) rather than the global extinction phenomenon typical of counterflow diffusion flames.

Figure 5 shows the structure of the flames in 0g for $X_{CO_2} = 0$ and $X_{CO_2} = 0191$ (the suppression limit) [6,8]. The calculations for the zero-gravity flames show:
- the flame flicker (~ 10 Hz at 1g) is eliminated for gravity levels below 0.5 g.
- with lower gravity, flame diameter increases, the tip opens, and the edge of the flame base becomes vertical.
- the flame tip opening is calculated to be due to radiative losses, which become more important at lower gravity as the lack of convective mixing reduces the local reaction rate.
- The extinction process (a gradual edge blow-off with increasing CO_2 volume fraction in the air) is similar in 0g to that in 1g.
- the extinction condition for CO_2 addition is about 32 % higher in 0g than in 1g.
- at the extinction CO_2 volume fraction, elimination of the radiation losses creates a stable flame.

Figure 3 Performance comparison for a several agents assessed with a variety of flame metrics.
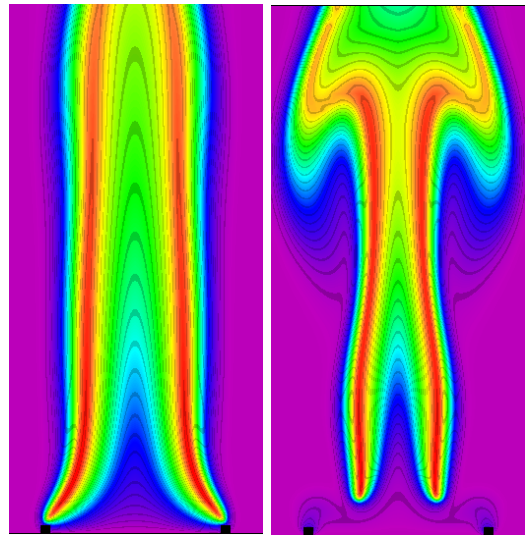
Figure 4 Calculated temperature contours in a 1g cup-burner methane flame with X_{CO_2} = 0.05 (left) and 0.145 (right) in the air stream.

The calculations were used to examine the importance of radiation transport in the 0g flames. Figure 6 shows the variation of the heat-release rate and radiative heat loss across the flame at 20 mm above the burner. As the gravity force was reduced, the radiative heat loss maintained a same level, while the heat-release rate decreased significantly due to diffusion-limited reactant fluxes into the flame zone. As a result, the net heat release decreased, thus leading to extinction in the downstream locations. Figure 7 shows the variation of the temperature and axial velocity with height up the flame, calculated with and without the influence of radiation. The figure

clearly indicates the decreased temperature in the 0g flames, which is not so dramatic in the 1g flames.

FUTURE PLANS

Experiments for flame shape and extinction will be conducted in low-g for comparison with the modeling results and 1g experimental results. The model will be used for more detailed examination of both the present 1g results and the 0g results (to be obtained). Further 1g results will be obtained for a wider variety of inhibitors.

REFERENCES

1. Linteris, G. T., Knyazev, V., and Babushok, V., *Halon Options Technical Working Conference*, Albuquerque, NM, 2001, pp. pp.72-82.
2. Linteris, G. T., Knyazev, K., and Babushok, V., *Combustion and Flame* 129:221 (2002).
3. Linteris, G. T., *Science, Technology, and Standards for Sire Suppression Systems, NRIFD*, Tokyo, Japan, July 2002.
4. Linteris, G. T., Katta, V. R., and Takahashi, F., submitted to *Combustion and Flame,* 2003.
5. Katta, V. R., Takahashi, F., and Linteris, G. T., *Fire Safety Science: Proc. of the Seventh Int. Symp.*, Int. Assoc. for Fire Safety Science, 2002, in press.
6. Katta, V. R., Takahashi, F., and Linteris, G. T., *41st Aerospace Sciences Meeting and Exhibit,* AIAA Paper No. 2003-1150, Reno, NV, 2003.
7. Katta, V. R., Takahashi, F., and Linteris, G. T., *Proc. of the Third Joint Meeting of the U.S. Sections of the Combustion Institute*, Chicago, IL, 2003.
8. Katta, V. R., Takahashi, F., and Linteris, G. T., submitted to *Combustion and Flame,* 2003.
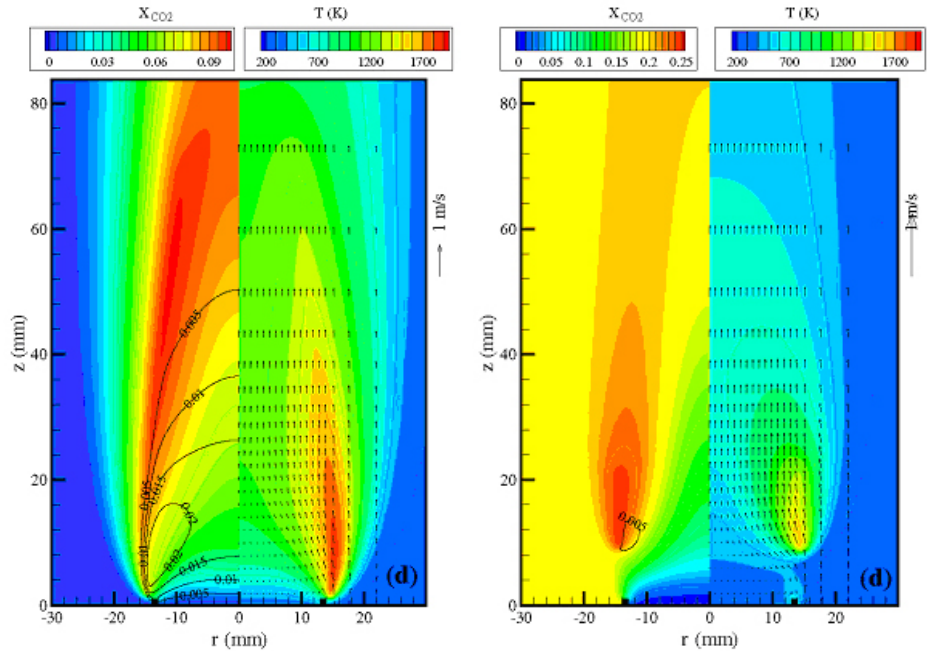
Figure 5 Calculated velocity, temperature (right), CO2, and H2 mole fractions (left) in 0g flames. (a) X_{CO_2} = 0, (b) X_{CO_2} = 0.191.
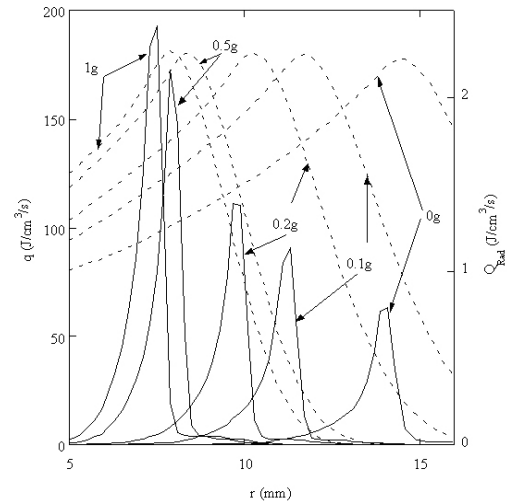
Figure 6 Heat-release rate (solid) and radiative heat loss (dashed) at 20 mm above the burner.
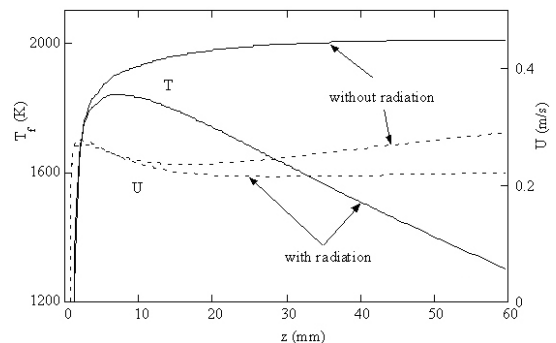
Figure 7 Variation of temperature and axial velocity with height along 0g flame.

THE WATER-MIST FIRE SUPPRESSION EXPERIMENT (*Mist*): PRELIMINARY RESULTS FROM THE STS-107 MISSION

Angel Abbud-Madrid, J. Thomas McKinnon, Francine Amon
Center for Commercial Applications of Combustion in Space
Colorado School of Mines
Golden, CO 80401

Suleyman Gokoglu
NASA Glenn Research Center
Cleveland, Ohio 44135

INTRODUCTION

The deficiency in replacing the chemical fire-suppression agents banned by the Montreal Protocol has lead to an increasing interest in fine water mists as fire suppressants since mists pose no adverse environmental or health issues and they offer the promise of meeting the requirements of protecting both water- and weight-sensitive areas due to the low requirements for total water flow. Unfortunately, there is to date no widely accepted interpretation of the critical concentration of droplets or the optimum droplet size required to suppress a flame, or more importantly, of the fundamental mechanisms involved in flame extinguishment by a water mist.

One of the main obstacles to obtaining such understanding is the difficulty of providing a simple, well-characterized experimental setup for the flame front/water mist interaction. A weightless environment provides an ideal place to study this interaction by eliminating the distorting effects of gravity on the prolonged suspension of a uniform concentration of droplets and on the complex flow patterns induced by natural convection between the flame front and the water droplets. In order to take advantage of this environment, the Water-Mist Fire Suppression experiment (*Mist*) was flown on the STS-107 mission of the Space Shuttle on January, 2003. It consisted of a series of microgravity tests that explored the effect of uniformly distributed clouds of polydisperse water mists on the speed and shape of propagating propane-air premixed flames. The results from these tests will be used to assess the feasibility of using water mists on the new generation of fire suppressants on Earth as well as on spacecraft.

DESCRIPTION OF THE *Mist* EXPERIMENT

Figure 1 shows a three-dimensional model of the *Mist* flight apparatus with the main components of the experiment. A mixture of propane (C_3H_8) and air is loaded in a transparent cylindrical tube of 6.3-cm diameter and 49.5-cm length. The two gases are introduced in the tube from separate tanks through a static mixer using mass flow controllers. A polydisperse water mist generated by an ultrasonic atomizer is introduced in one half of the tube separated by an iris from the dry region. A light extinction system consisting of three diode lasers shining radially through the tube into three photodiode detectors is used to obtain droplet concentration data in different parts of the wet section. After the mist injection, the iris opens and the mixture is ignited in the dry section while keeping the valve at that end of the tube open for an isobaric combustion process. In order to measure the fire suppression ability of a given water-mist

droplet size and water concentration, the propagation velocity of the premixed flame is measured by a video camera and by an array of 16 photodiodes installed along the tube. The *Mist* experiment was designed, fabricated, assembled, and tested at the Center for Commercial Applications of Combustion in Space (CCACS) at the Colorado School of Mines and later tested and integrated to the Combustion Module-2 (CM-2) at the NASA Glenn Research Center.
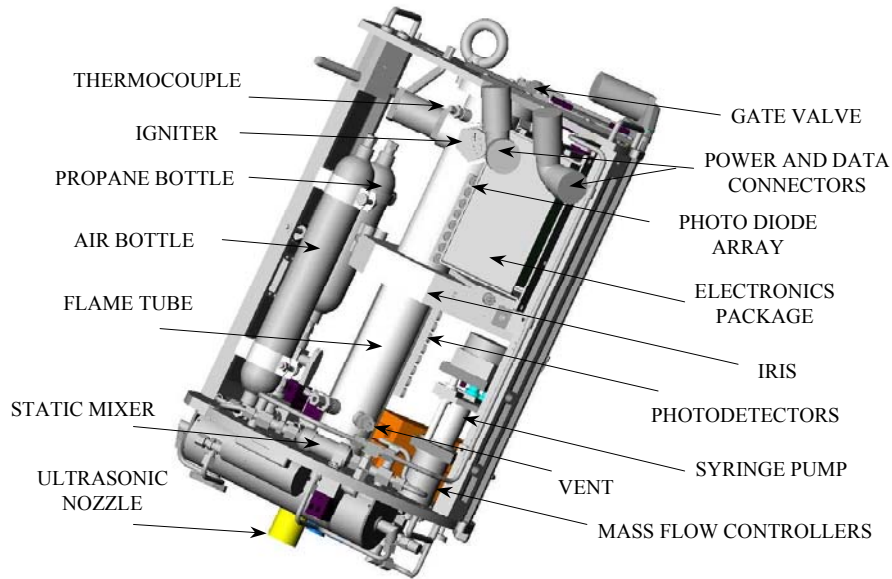
Figure 1. The *Mist* experiment flight unit.
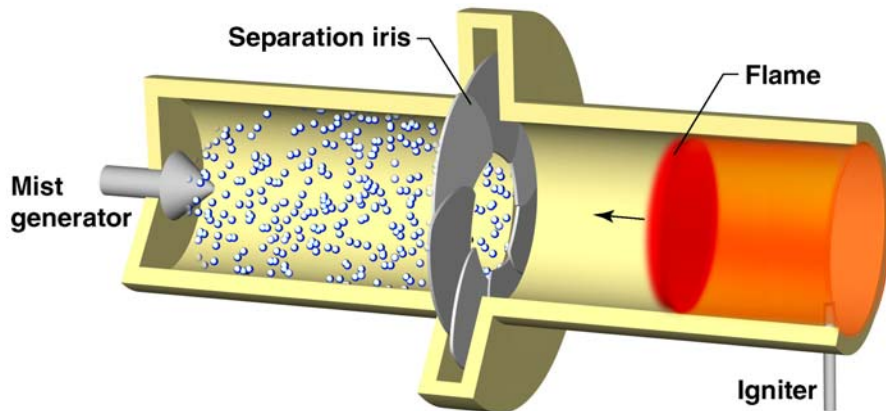
Figure 2. Configuration used in the microgravity tests and in the numerical model.

In this investigation, a computational model has been developed that uses a hybrid Eulerian-Lagrangian formulation to simulate the two-phase, flame/mist interaction. Currently, the model is capable of simulating the free propagation of planar, premixed laminar flames of various stoichiometries and their interaction with monodisperse water droplets as shown in Fig. 2. Gas-phase chemical kinetics, thermodynamic, and transport properties are handled by the PREMIX software [1] and are used in the Eulerian representation of the propagating flame. Various chemical databases are used for the fuel-air reaction mechanisms. This formulation is

then coupled with droplet source terms from Lagrangian equations of mass, momentum, energy, and particle flux fraction. The interaction between the two phases is modeled using an imaginary gas packet that follows the droplet. This algorithm facilitates a stable coupling between the phases, yet permits solving the gas-phase equations and droplet equations separately.

EXPERIMENTAL AND NUMERICAL RESULTS

Numerical simulations have been conducted with both CH_4-air and C_3H_8-air flames. The first simulations consist of two freely propagating, stoichiometric flames–one wet (at 100% relative humidity) and the other dry. In the case of CH_4-air flames, due to the thermal, physical, and chemical effects of the steam, the burning velocity for the wet case is about 34 cm/s, which is considerably lower than the dry flame speed of about 39 cm/s. After establishing the two base cases mentioned above, different droplet sizes and concentrations are introduced in the wet-gas mixture case. These simulations show that larger droplets penetrate further into the post-flame region than smaller droplets which undergo rapid vaporization. Near the end of the droplet lifetime, the vaporization rate accelerates due to the rapidly increasing surface-area-to-volume ratio. Also, as more condensed water is added into the gas mixture, the maximum and post-flame temperatures are reduced. Consequently, the burning velocities are also reduced with increasing water-mass loading. At some point, the amount of water mist is sufficient to extinguish the flame. Figure 3 shows the effect of water concentration and droplet size on the burning velocity of CH_4-air flames. As clearly seen in the plot, very fine mists should be more efficient fire suppressants than larger droplets, although there appears to be a limit around 10 μm droplets.

During the STS-107 mission, 32 tests were conducted with four different stoichiometries (ϕ=0.6, 0.7, 1.0, and 1.3), various water concentrations ranging from water mass fractions of 0 up to 0.40, and with two different droplet size distributions with 20 and 30 μm mean droplet sizes. A mist behavior characterization study was also performed that showed a consistent generation and suspension of an extremely uniform and quiescent cloud of droplets for several minutes as a result of the low microgravity levels (with negligible jitter or oscillations) experienced in the Space Shuttle. Preliminary results show that the leanest propane-air flames exhibit progressively lower burning velocities with increasing water loadings and decreasing droplet size (as predicted by the model) with final extinction at the highest water concentrations. Stoichiometric and rich flames show additional flame distortion and cellular break up as the flames traverse the misted section of the tube. Pulsating flames were also observed for lean mixtures under certain water loadings. It is important to point out that none of these observations have been possible on the ground or on the KC-135 airplane due to the inability to form a uniform cloud of droplets prior to the passage of the flame. Thus, the jitter-free environment of the Space Shuttle was absolutely essential to conduct a controlled study of the effect of water mist on propagating premixed flames.

CONCLUSIONS

An investigation of the effect of water mists on premixed flame propagation has been conducted onboard the Space Shuttle to take advantage of the prolonged microgravity environment to study the effect of uniformly distributed clouds of polydisperse water mists on the speed and shape of propagating propane-air premixed flames. The suspension of a quiescent and uniform water mist cloud was confirmed during the microgravity tests. Preliminary results

show good agreement with trends obtained by the numerical predictions of a computational model that uses a hybrid Eulerian-Lagrangian formulation to simulate the two-phase, flame/mist interaction. Effective flame suppression is observed at progressively higher water loadings and smaller water droplet sizes. Other unusual flame behavior, such as flame front breakup and pulsating flames, is still under investigation. The promising results from the microgravity tests will be used to assess the feasibility of using water mists as fire suppressants on Earth and on spacecraft.
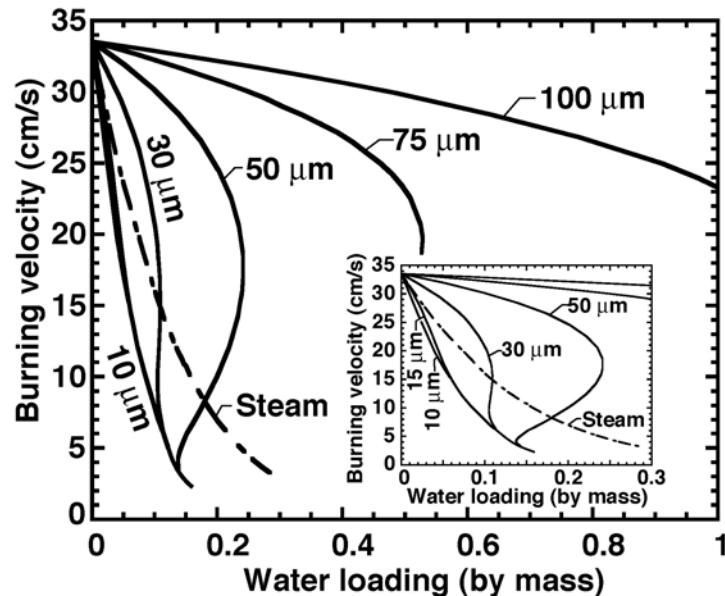
Figure 3. Effect of droplet diameter at various mass fractions of water on the flame speed of a planar, stoichiometric CH_4-air premixed flame obtained by numerical simulation (from [2]).

ACKNOWLEDGMENTS

REFERENCES

1. Kee, R.J., Grcar, J.F., Miller, A., and Meeks, E., "PREMIX: A Fortran Program for Modeling Steady Laminar One-Dimensional Premixed Flames," Sandia National Laboratories, 1998.

2. W. Yang and R.J. Kee, "The Effect of Monodispersed Water Mists on the Structure, Burning Velocity, and Extinction Behavior of Freely Propagating, Stoichiometric, Premixed, Methane-Air Flames," *Combustion and Flame*, in press.

BUOYANCY EFFECTS IN FULLY-MODULATED,
TURBULENT DIFFUSION FLAMES

J.C. Hermanson
University of Washington, Seattle, WA 98195

H. Johari and E. Ghaem-Maghami
Worcester Polytechnic Institute, Worcester MA 01609

D.P. Stocker, U. G. Hegde, and K.L. Page
NASA Glenn Research Center, Cleveland, OH 44135

INTRODUCTION

Pulsed combustion appears to have the potential to provide for rapid fuel/air mixing, compact and economical combustors, and reduced exhaust emissions. The objective of this experiment (PuFF, for Pulsed-Fully Flames) is to increase the fundamental understanding of the fuel/air mixing and combustion behavior of pulsed, turbulent diffusion flames by conducting experiments in microgravity. In this research the fuel jet is fully-modulated (i.e., completely shut off between pulses) by an externally controlled valve system. This gives rise to drastic modification of the combustion and flow characteristics of flames,[1-2] leading to enhanced fuel/air mixing compared to acoustically excited or partially-modulated jets. Normal-gravity experiments suggest that the fully-modulated technique also has the potential for producing turbulent jet flames significantly more compact than steady flames with no increase in exhaust emissions. The technique also simplifies the combustion process by avoiding the acoustic forcing generally present in pulsed combustors. Fundamental issues addressed in this experiment include the impact of buoyancy on the structure and flame length, temperatures, radiation, and emissions of fully-modulated flames.

EXPERIMENTAL APPROACH

Experiments are conducted both in the laboratory at WPI and in the GRC 2.2s Drop Tower. The combustor configuration consists of a single fuel nozzle with diameter $d = 2$ mm centered in a combustor 20×20 cm in cross section and 67 cm in height. The gaseous fuel jet flow (ethylene or a 50/50 ethylene/nitrogen mixture by volume) is fully-modulated by a fast-response solenoid valve actuated in an on-off (rectangular wave) fashion for injection times ranging from $\tau = 4$ to $\tau = 300$ ms. The mean fuel velocity during injection, U_{jet}, gives a nominal Reynolds number of 5,000. A slow oxidizer co-flow with velocity of approximately 10 cm/s (air for laboratory experiments; an oxygen/nitrogen mixture of either 21% or 30% O_2 by volume for the Drop Tower rig) is provided to properly ventilate the flame.[3] An electrically heated wire loop of 0.24 mm diameter situated at the nozzle exit serves as a continuous ignition source.

Three types of diagnostic techniques are employed in the experiments. Video imaging is used to study the turbulent structure and flame length of the pulsed flames. Temperatures and radiant emissions are determined using fine-wire thermocouples and thermopile radiometers. Finally, the concentrations of stable gas species (CO, CO_2, O_2, NO_x, and unburned hydrocarbons) in the post-flame region are measured by gas sampling and standard emissions instruments. The emissions measurements are performed in the laboratory only; the thermal measurements and video imaging are performed both in the laboratory experiments and in Drop Tower tests.

SELECTED EXPERIMENTAL RESULTS

Structure and flame length

The fully-modulated flames can be roughly divided into two categories: (i) injection time sufficiently short to result in a compact, puff-like structure, and (ii) injection interval longer, resulting in elongated flame structures. The parameter $P \equiv (U_{jet}\tau/d)^{1/3}$ can be employed to distinguish between the two cases.[1] Generally, puff-like behavior is seen for values of P less than approximately $P = 8$ for ethylene/air flames. For $P > 11$, elongated flames similar to steady jet flames but with a distinct cap are created.[1,3] Typical images of steady, elongated, and puff-like ethylene/air diffusion flames in microgravity are presented in Fig. 1.

The flame lengths of fully-modulated (f-m) diffusion flames can be substantially less that those of steady turbulent jet flames, as shown in Fig. 2. In all cases shown the duty cycle was sufficiently low to give isolated, non-interacting flame structures. The flame length for compact, puff-like structures appears to scale reasonably well with the parameter[2] $P(1+\psi)^{1/3}$, where ψ is the stoichiometric air/fuel ratio, up to values consistent with $P \approx 8$. For sufficiently high P, the mean flame length approaches that of the corresponding steady flame. The flame length interestingly does not appear to be highly sensitive to the action of buoyancy for all P. This is consistent with the results of Ichideria *et al.*[4] for piloted flames, but differs from the significant increase in length reported by Hegde *et al.*[5] in microgravity for unpiloted flames stabilized by reduced nozzle clearance.

The flame length in fully-modulated diffusion flames can also be significantly impacted by the duty cycle, as shown in Fig. 3. In general, increasing the duty cycle causes the discrete fuel puffs to give way to more closely-packed, interacting flame structures, which lead in turn to a longer flame length. This is to be expected since for the case of high duty cycles each flame structure has to "compete" with its neighbors for the same air, decreasing the rate of air entrainment. The greatest fractional increase in flame length appears to be for the shortest injection time, as seen previously in normal gravity[1]. This suggests a substantially lower impact of neighboring structures on the rate of entrainment and mixing for elongated flames than for their puff-like counterparts. For microgravity conditions the increase in flame length with increasing duty cycle can significantly exceed that seen in normal gravity.

The celerity for flame puffs near burn-out, taken from the slope of the puff trajectory versus time, is generally less in microgravity than in normal gravity. This is consistent with the longer time to burn-out observed for microgravity flame puffs. These two effects appear to be offsetting, with the result that the flame length of isolated, compact puffs is insensitive to buoyancy.

The combination of increasing flame puff size and decreasing puff celerity with downstream distance serves to change the separation between puffs, effectively increasing the duty cycle locally. The amount by which the duty cycle near the flame tip exceeds the injection duty cycle is greater in microgravity than in normal gravity due to the lower celerity in the former case, suggesting that the change in flame length with increasing injection duty cycle would be correspondingly greater in microgravity. This is in qualitative agreement with the experiments.

Varying the duty cycle allows for the systematic examination of the interaction and merging of the large structures, especially for the case of slowed flame motion in microgravity. An example of a microgravity flame at a duty cycle sufficiently high to result in significant structure-structure interaction is shown in Fig. 4, where the merging of discrete flame structures is shown.

<u>Thermal characteristics</u>

Buoyancy appears to have a strong effect on the thermal characteristics of fully-modulated turbulent diffusion flames.[6] The cycle-averaged centerline temperatures are generally higher in the microgravity flames than in normal gravity, especially at the flame tip where the difference was as much as 200 K. This is shown in Fig. 5 for $P = 12$ and $\alpha = 0.5$. The flame is 50/50 ethylene/nitrogen in 21/29 oxygen/nitrogen ($\psi = 7.1$). It can be seen that centerline temperature is higher in microgravity than in normal gravity throughout the length of the flame. The cycle-averaged thermal radiation appears to be more strongly influenced by gravity than the temperature, and can be as much as 60% greater in microgravity than in normal gravity.

Elevated values of temperature and radiation intensity are also found for other values of P. The peak values of cycle-averaged centerline temperature are roughly 80 K greater in microgravity for all values of P. The peak radiation was about 30% to 60% greater in microgravity than normal gravity. The peak temperature appears to decrease, then to become roughly constant as P is increased, with the transition occurring at $P \approx 8$ (a similar value as that for the transition in flame length mentioned previously). By contrast, the radiation increases with P, and appears to level off at sufficiently high P in a similar fashion to the flame length.

<u>Emissions</u>

Time-averaged emissions were measured on the combustor centerline downstream of the visible flame tip in normal gravity[7]. The time-averaged CO emission index (g CO/kg fuel) for fully-modulated flames is shown as a function of the injection duty cycle in Fig. 6. The highest emission indices of CO were found for compact, isolated puffs and were roughly an order of magnitude higher than emissions from elongated flames. The amount of CO for compact puffs decreased substantially as the duty cycle (and the flame length and residence time). The emission indices of CO for all fully-modulated flames approached the low, steady-flame values (dashed line) for a duty cycle of approximately 0.35, while flame length in some cases was significantly shorter than that of the steady flame. The emissions of unburned hydrocarbons follow similar trends to those of CO. The trends in NO_x for fully-modulated flames have not yet been established. Further, all of the preceding results were acquired in the laboratory in normal gravity; the emissions levels of flames in microgravity have not yet been investigated.

ACKNOWLEDGEMENTS

REFERENCES

[1] Hermanson, J.C., Dugnani, R., and Johari, H., *Comb. Sci. Tech.* **155**, 203-225, 2000.
[2] Johari, H. and Motevalli, V., *Comb. Sci. Tech.* **94** (1-6), 229-245, 1993.
[3] Hermanson, J.C., Usowicz, J., Johari, H., and Sangras, R., *AIAA Journal* **40** (7), 2002.
[4] Idicheria, C.A., Boxx, I.G., and Clemens, N.T., *AIAA 2001-0628*, Reno, NV, Jan. 2001.
[5] Hegde, U., Zhou, L., and Bahadori, M.Y., *Comb. Sci. Tech.* 102, 95-113, 1994.
[6] Page, K.L., Stocker, D.P, Hegde, U.G., Hermanson, J.C. and Johari, H., *Third Joint Meeting of the U.S. Sections of The Combustion Institute*, Chicago, IL, March, 2003.
[7] Johari, H., Ghaem-Maghami, E., and Hermanson, J.C., AIAA *03-1015*, Reno, NV, Jan. 2003.
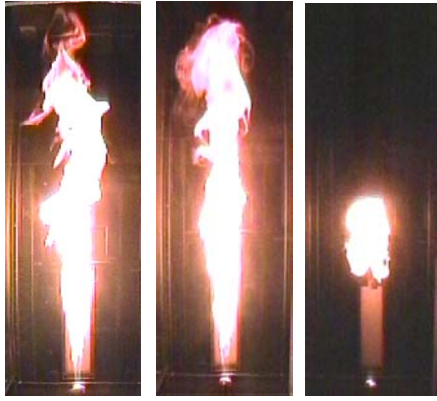
Fig. 1 Turbulent ethylene/(30% O_2 in N_2) diffusion flames in microgravity. Left, steady flame, middle, f-m flame with $\tau = 300$ ms, $P = 15$, right, $\tau = 40$ ms, $P = 7.7$.
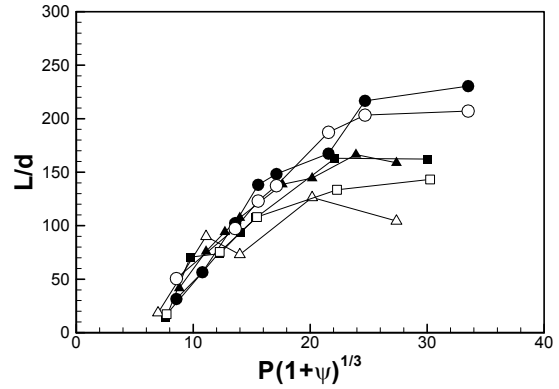
Fig. 2 Normalized flame length for f-m flames. Solid symbols, microgravity; open symbols, normal gravity. $\bigcirc$, $\bullet$ $\psi = 10$; $\blacksquare$, $\square$ $\psi = 7.1$, $\triangle$, $\blacktriangle$ $\psi = 5$.
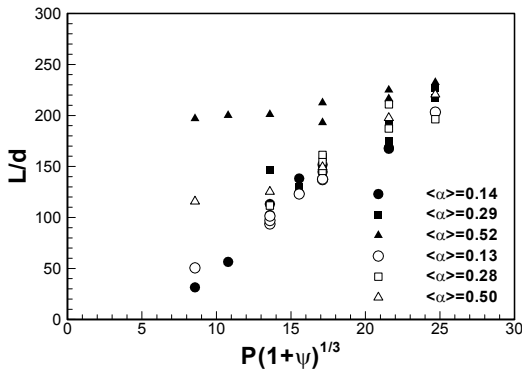
Fig. 3 Effect of injection duty cycle on normalized flame length for f-m flames for $\psi = 10$. Solid symbols, microgravity; open symbols, normal gravity.

Fig. 4 Sequence of f-m flames in microgravity showing the merging of large-scale turbulent structures. $P = 7.6$, $\alpha = 0.5$.
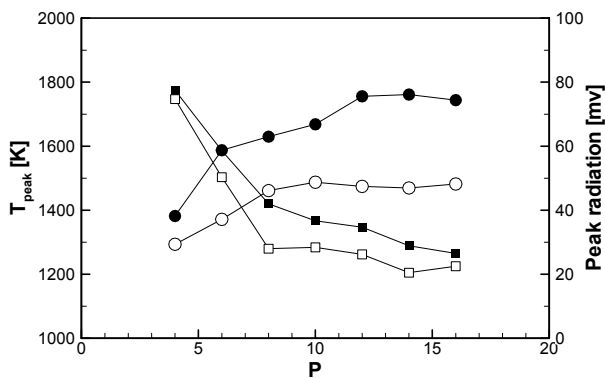
Fig. 5 Mean centerline temperatures and radiation for a $P = 8$ f-m flame. Solid symbols, microgravity; open symbols, normal gravity. $\bigcirc$, $\bullet$ radiation; $\blacksquare$, $\square$ temperature.
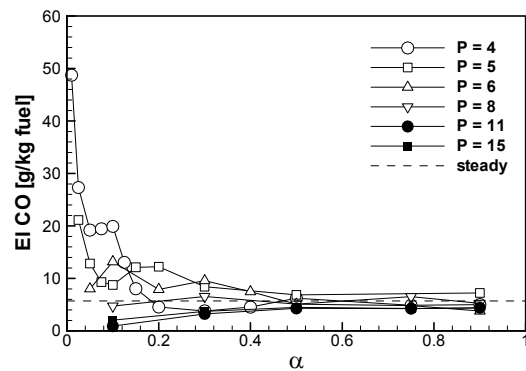
Fig. 6 CO emission index for f-m flames in normal gravity.

CHARACTERISTICS OF TURBULENT NONPREMIXED JET-FLAMES AND JET-FLAMES IN CROSSFLOW IN NORMAL- AND LOW-GRAVITY

N. T. Clemens, I.G. Boxx, C.A. Idicheria

Department of Aerospace Engineering and Engineering Mechanics, The University of Texas at Austin, Austin, TX 78712-1085

INTRODUCTION

It is well known that buoyancy has a major influence on the flow structure of turbulent nonpremixed jet flames. For example, previous studies have shown that transitional and turbulent jet flames exhibit flame lengths that are as much as a factor of two longer in microgravity than in normal gravity.[1-2] The objective of this study is to extend these previous studies by investigating both mean and fluctuating characteristics of turbulent nonpremixed jet flames under three different gravity levels (1 g, 20 mg and 100 μg). This work is described in more detail elsewhere.[3-5]

In addition, we have recently initiated a new study into the effects of buoyancy on turbulent nonpremixed jet flames in cross-flow (JFICF). Buoyancy has been observed to play a key role in determining the centerline trajectories of such flames.[6] The objective of this study is to use the low-gravity environment to study the effects of buoyancy on the turbulent characteristics of JFICF. This work is described in more detail in Ref. 7.

EXPERIMENTAL APPARATUS/CONDITIONS

The low-gravity experiments were conducted in the University of Texas 1.25 second drop tower and the NASA GRC 2.2 second drop tower. Figure 1 shows a solid model of the drop-rig used in both towers. The drop-rig uses an aluminum frame (38"×16"×36") that is covered on each side with 0.08" aluminum sheet-metal. In the jet-flame experiments the jet issued into the quiescent air in the interior of the drop rig. The fuel jet was delivered from a 1.75 mm (inner diameter) stainless steel tube, with a 25.4 mm diameter concentric, premixed, methane-air flat-flame pilot. Fuel for the jet was stored in two onboard, 18.3 in^3 stainless steel pressure vessels. The flow rate was controlled with line pressure regulators upstream of choked micro-metering valves.

The JFICF experiments used the same basic drop rig, but the rig was equipped with a blow-through cross-flow section (8"×8"×24") as shown in Fig. 1. A round jet of ethylene issues from a 1/8" diameter circular orifice mounted flush with one wall of the test section. The cross-flow is driven by two DC-powered axial, in-line blowers. The cross-flow velocity can be set to 0.94 m/s or 1.32 m/s by using one or two blowers, respectively.

For both flow configurations, the flame luminosity was imaged using a Pulnix TM-6710 progressive scan CCD camera, capable of operating at 235 fps or 350 fps at resolutions of 512×230 pixels and 512×146 pixels, respectively. The camera was electronically shuttered, with the exposure time depending on flame luminosity (1/235 to 1/2000 seconds), and the field of view was typically 405mm in the streamwise direction. The drop-rig was controlled by an onboard computer (CyberResearch Inc). Three different jet fuels were studied in the jet flame experiments: propane, ethylene and methane. These experiments were conducted over Reynolds numbers (based on jet-exit conditions) ranging from 2000 to 10500. The Becker & Yamazaki[8] "buoyancy parameter" $\xi_L=Ri_s^{1/3}L_f/D_s$ (where $Ri_s=gD_s/U_s^2$ is the source Richardson number based on the source diameter $D_s=D(\rho_o/\rho_\infty)^{1/2}$, and source velocity $U_s=U_o$, L_f is the average visible flame length, ρ_o is the jet fluid density and ρ_∞ is the ambient density) for these flames ranged from 0.22 in microgravity up to 12 in

normal gravity. In all JFICF cases the fuel was ethylene. The momentum flux ratio ($r = \sqrt{(\rho_j u_j^2 / \rho_{cf} u_{cf}^2}$), where the subscripts refer to the jet and cross-flow conditions, respectively) ranged from 6 to 10, and Reynolds numbers ranged between 3000 and 5000. Two cases were chosen so as to compare two JFICF of identical momentum flux ratio but different jet exit Reynolds numbers. Two other cases were chosen so as to maintain a constant jet-exit Reynolds number at two different momentum flux ratios.

RESULTS AND DISCUSSION

Jet Flames -- The RMS fluctuations of flame luminosity were computed from the instantaneous luminosity images. Figure 2 shows RMS images for ethylene and propane flames at a range of Reynolds numbers and where the buoyancy has been quantified with ξ_L. This figure shows that flames with similar ξ_L have similar fluctuations, which indicates that ξ_L does an excellent job of quantifying the level of buoyancy. Large fluctuations are present near the flame tip in the large ξ_L (buoyant) flames, whereas small ξ_L flames exhibit the largest fluctuations off centerline near the regions of high shear. These results further suggest that the structure of the large-scale turbulence reaches its momentum-driven asymptotic state for values of ξ_L less than about 2-3.

Figure 3a shows the variation of the normalized mean visible flame length for each of the jet flame cases studied. It is evident from the figure that the flame lengths are essentially the same under the different gravity levels at the highest Reynolds numbers. For comparison, Fig. 3a also shows the data of Hegde et al.[1,2] for propane flames under normal and microgravity. It is clear that we do not observe the large differences in flame lengths with g-level that were observed in their studies. To provide some validation of our 1g data, Fig. 3b shows the current 1g data plotted with those of Becker and Yamazaki[8] and Mungal et al.[9] It can be seen that our data are in excellent agreement with these previous 1g studies.

Volume rendering of jet flame image sequences was used to investigate the large-scale structure characteristics. In this technique, 3-D isocontours (x,y,t) of the jet flame edge are generated from the luminosity images, allowing comparisons of such features as large-scale structure evolution and propagation velocity (celerity). Figure 4 shows a plot of the ratio of celerity to jet exit velocity, U_s/U_o (%), against the buoyancy parameter, ξ_L. The normal gravity flames (i.e. those with high ξ_L values) are associated with higher celerity. This suggests that celerity is in fact buoyancy dependent, contrary to the findings of Mungal et al.[9], who found the celerity to be 12 ± 2% of the jet exit velocity irrespective of ξ_L and fuel type. For $\xi_L < 4$, the celerity appears to become independent of the gravity level and fuel type. In this regime, there is reasonable agreement with the findings of Mungal et al.[9]

Jet Flames in Crossflow -- Figure 5 shows typical time-sequence luminosity images of the JFICF under normal- and low-gravity conditions. In the JFICF image sequences, we observe that the jet shear-layer vortices tend to be wider and slower to roll up in low-gravity than in normal-gravity. Jet flames exhibit a similar broadening in low-gravity. The deeper penetration of unburned air into the JFICF in normal-gravity than in low-gravity seen in these images was characteristic of all JFICF cases run. Volume rendering and frame-by-frame analysis revealed a greater degree of spatial and temporal uniformity and coherence in the shear-layer vortex behavior in low-gravity compared to those in normal-gravity.

Figure 6 shows the centerline trajectories for the JFICFs, plotted in log-log scale. We specify the centerline as the midpoint of each line in a threshholded, ensemble average of 600 instantaneous luminosity images. Using linear regression analysis, we fit each trajectory to a power-law formula of the form $z/rd = A(x/rd)^n$, where z is the coordinate in the direction of the jet and x is the coordinate

in the direction of the cross-flow. The trajectories are based on data limited to x/rd > 2 due to the low luminosity of the near-field region. In all eight cases, the exponent of the power-law ranged from 0.18 to 0.21. This is in reasonable agreement with the correlation of Huang and Chang[10] for the far-field trajectory of a propane JFICF. In no case did the non-buoyant JFICF follow the 0.33 power scaling characteristic of non-reacting jets in cross-flow. This plot also illustrates a systematic departure from power-law scaling in the far-field in every normal-gravity JFICF case, a trend not seen in any of the low-gravity JFICF cases. We conclude this departure from power-law scaling is due to buoyancy-induced acceleration of the hot combustion products in the far-field region.

ACKNOWLEDGEMENTS

REFERENCES

1. Hegde, U., Zhou, L., Bahadori, M. Y., *Combust. Sci. Technol.* 102:95-100 (1994).
2. Hegde, U., Yuan, Z.G., Stocker, D.P. and Bahadori, M.Y., *Proc. of Fifth International Microgravity Combustion Workshop*, pp. 259-262 (1999).
3. Idicheria, C.A., Boxx, I. G., Clemens, N.T. AIAA Paper 2001-0628 (2001).
4. Clemens, N.T., Idicheria, C.A. and Boxx, I.G., Proc. of Sixth International Microgravity Combustion Workshop, pp. 133-136 (2001).
5. Idicheria, C. A., Boxx, I. G., Clemens, N. T., Proceedings of the Third Joint Meeting of the U.S. Sections of the Combustion Institute (2003).
6. Kuppu Rao, V. and Brzustowski, T. A., *Combust. Sci. Technol.* 27: 229-239 (1982).
7. Boxx, I. G., Idicheria, C. A., Clemens, N.T. AIAA Paper 2003-1151 (2003)
8. Becker, H. A. and Yamazaki, S., *Combust. Flame* 33: 123-149 (1978).
9. Mungal, M.G., Karasso, P.S. and Lozano, A., *Combust. Sci. Technol.* 76:165-185 (1991).
10. Huang, R. F. and Chang, J. M., *Combust. Flame* 98: 267-278 (1994).
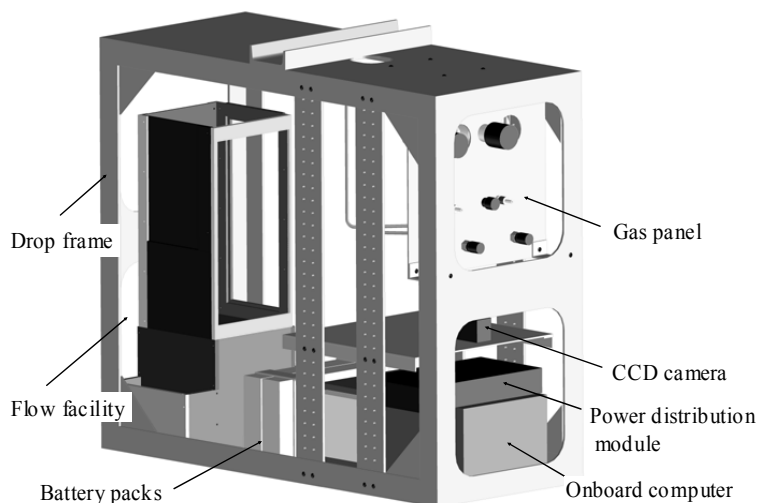
Figure 1. Schematic of the turbulent nonpremixed jet-flame drop rig.
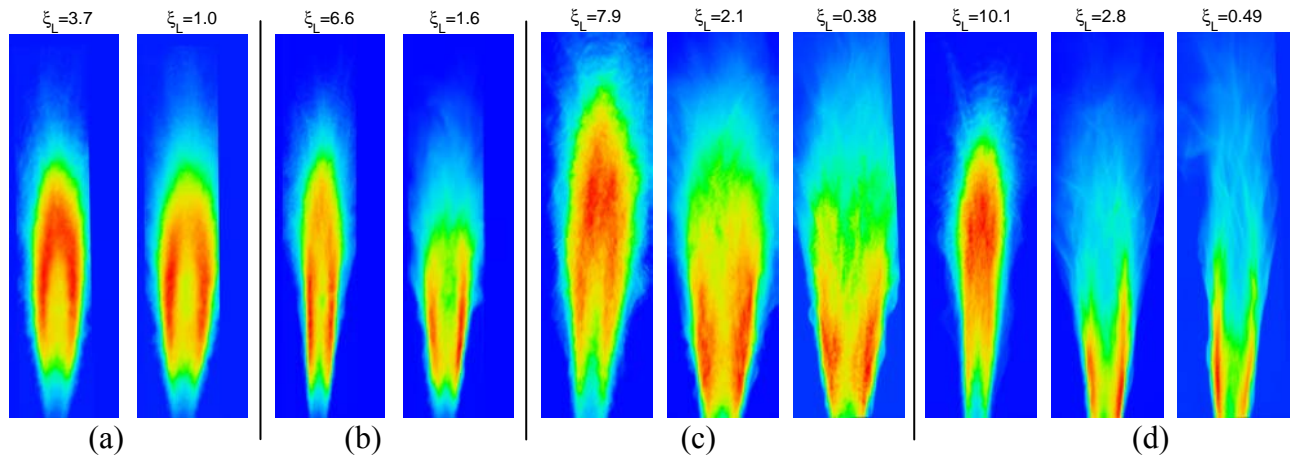
Figure 2. Sample RMS luminosity images: (a) Ethylene Re_D=10,500, 43<x/D<279, (b) Ethylene Re_D=5000, 43<x/D<279, (c) Propane Re_D=8500, 76<x/D<308, and (d) Propane Re_D=5000, 76<x/D<308.
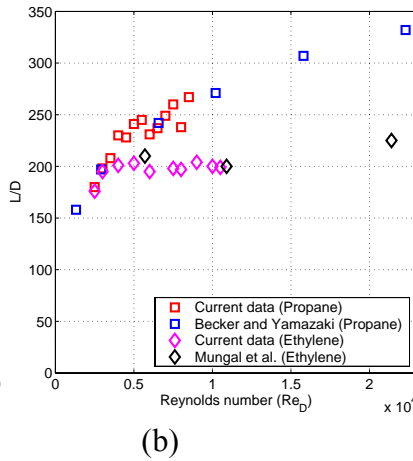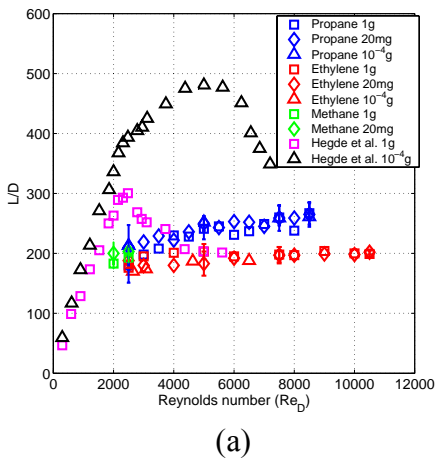
Figure 3. Flame length data. (a) 1g and low-g. (b) 1g only.
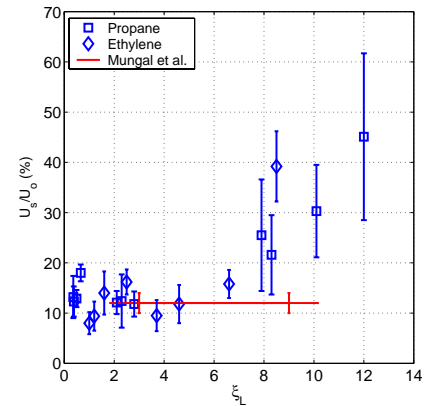
Figure 4. Jet flame structure celerity.
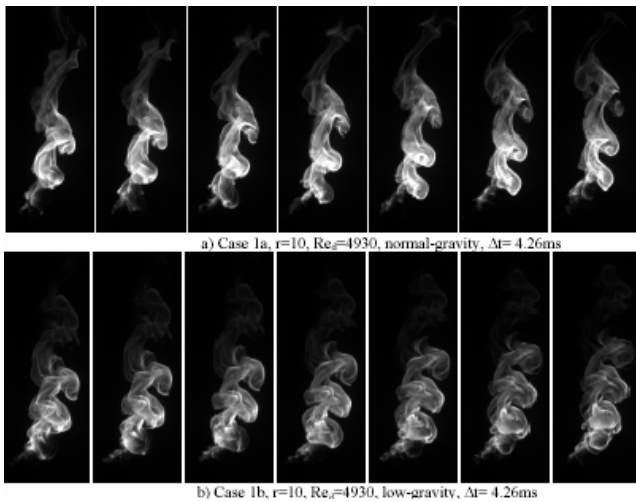
Figure 5. JFICF – Instantaneous time-sequenced images for JFICF with Re_d=4930, r=10. (a) 1g, (b) low-g.
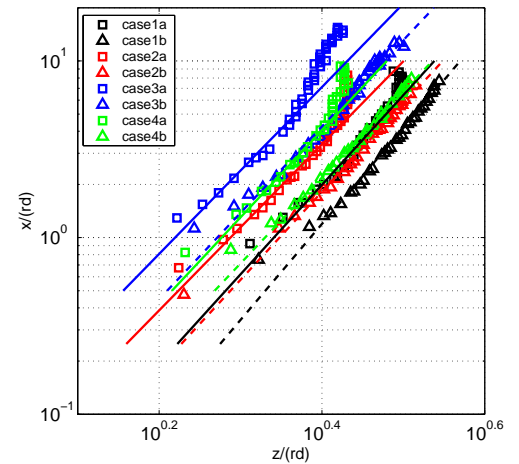
Figure 6. JFICF centerline trajectories. (Square symbols 1g, triangles low-g)

LARGE EDDY SIMULATION OF GRAVITATIONAL EFFECTS IN TRANSITIONAL AND TURBULENT GAS-JET DIFFUSION FLAMES

Farhad A. Jaberi, Department of Mechanical Engineering, Michigan State University,
East Lansing, MI 48824.
Peyman Givi, Department of Mechanical Engineering, University of Pittsburgh,
Pittsburgh, PA 15261.

INTRODUCTION

The influence of gravity on the spatial and the compositional structures of transitional and turbulent hydrocarbon diffusion flames are studied via large eddy simulation (LES) and direct numerical simulation (DNS) of round and planar jets. The subgrid-scale (SGS) closures in LES are based on the filtered mass density function (FMDF) methodology [1-3]. The FMDF represents the joint probability density function (PDF) of the SGS scalars, and is obtained by solving its transport equation. The fundamental advantage of LES/FMDF is that it accounts for the effects of chemical reaction and buoyancy exactly. The methodology is employed for capturing some of the fundamental influences of gravity in equilibrium flames via realistic chemical kinetic schemes. Some preliminary investigation of the gravity effects in non-equilibrium flames is also conducted, but with idealized chemical kinetics models.

APPROACH

The primary objective of this work is to develop and implement the LES/FMDF methodology for understanding of gravity effects in turbulent gas-jet diffusion flames. In addition, some DNS is also conducted for validation of some of our findings and for assessment of some of the modeling assumptions made in the LES procedure. In DNS, the coupled set of Navier-Stokes, energy, and scalar transport equations are solved together with the equation of state, a one-step kinetics model for the chemistry and constitutive relations for the molecular viscosity, diffusivity and conductivity. In LES/FMDF, the scalar field, $\phi \equiv \phi_\alpha$, $\alpha = 1, 2, \ldots, N_s + 1$ (mass fractions and enthalpy) is obtained from the joint scalar FMDF [1],

$$F_L(\boldsymbol{\psi}, \mathbf{x}; , t) \equiv \int_{-\infty}^{+\infty} \rho(\mathbf{x}', t)\zeta\left[\boldsymbol{\psi}, \boldsymbol{\phi}(\mathbf{x}', t)\right] H(\mathbf{x}' - \mathbf{x})d\mathbf{x}', \tag{1}$$

where H denotes the filter function, and ζ is the "fine-grained" density [4]. The final form of the FMDF transport equation is

$$\frac{\partial F_L}{\partial t} + \frac{\partial[\langle u_i \rangle_L F_L]}{\partial x_i} = \frac{\partial}{\partial x_i}\left[\langle \rho \rangle_\ell(\langle D \rangle_L + D_t)\frac{\partial(F_L/\langle \rho \rangle_\ell)}{\partial x_i}\right] + \frac{\partial}{\partial \psi_\alpha}\left[\Omega_m(\psi_\alpha - \langle \phi_\alpha \rangle_L)F_L\right] - \frac{\partial[\widehat{S}_\alpha F_L]}{\partial \psi_\alpha} \tag{2}$$

where, $\langle f(\mathbf{x}, t) \rangle_\ell$ and $\langle f(\mathbf{x}, t) \rangle_L = \langle \rho f \rangle_\ell / \langle \rho \rangle_\ell$ represent the filtered, and the Favre-filtered values of the transport variable $f(\mathbf{x}, t)$. In Eqs. (1) and (2), S_α, u_i, ρ, $\boldsymbol{\psi}$, and Ω_m, denote the production rate of species α, the ith component of the velocity vector, the density, the "composition space" of scalar ϕ, and the SGS mixing frequency, respectively. The molecular diffusivity coefficient, and the SGS diffusivity coefficient are denoted by D, and

D_t, respectively. The last term on the right hand-side (RHS) of Eq. (2) represents the effects of chemical reaction and is in a closed form. The first two terms on RHS represent the effects of SGS mixing and SGS convection, respectively and are closed via models similar to those used in conventional PDF methods [4].

Equation (2) is solved by the "Lagrangian Monte Carlo" procedure in which the FMDF is represented by an ensemble of computational elements. These elements are transported in the "physical space" by the combined actions of large scale convection and diffusion (molecular and subgrid). In addition, transport in the "composition space" occurs due to chemical reaction and SGS mixing. In doing so, the notional particles evolve via a "stochastic process," described by the set of stochastic differential equations (SDEs) [1]. These are coupled with the hydrodynamic solver which is via a "compact parameter" finite difference scheme.

Combustion is modeled via two chemistry models: (1) an equilibrium model via realistic kinetics, (2) a finite rate, single-step model for non-equilibrium flames. In (1), the LES/FMDF is employed in conjunction with equilibrium methane-oxidation model. This model is enacted via "flamelet" simulations; which consider a laminar counterflow (opposed jet) flame configuration. The full methane oxidation mechanism of the Gas Research Institute (GRI) accounting for 53 species and 325 elementary reactions is employed. At low strain rates, the flame is close to equilibrium. Thus, the thermo-chemical variables are determined completely by the "mixture fraction." This flamelet library is coupled with our LES/FMDF solver in which transport of the mixture fraction is considered. In (2), methane oxidation is modeled via a finite-rate, single-step global kinetics model.

RESULTS AND DISCUSSIONS

The (few) sample results presented in this section pertain only to the effects of gravity on the overall flow structure in gas jet diffusion flames. LES is conducted of three-dimensional (3D) round jet flames involving methane combustion under zero- and normal-gravity conditions. In the latter, the gravity vector is aligned opposite to the direction of the axial jet flow. The effect of gravity on the evolution of the jet flame is shown in Fig. 1, where the contour plots of the instantaneous filtered values of CO_2 mass fraction are considered. As expected, the flow is initially 2D (axisymmetric), and then becomes strongly 3D with significant small scales. In the absence of gravity, turbulence levels decrease due to damping of flow instabilities by exothermicity. In the presence of gravity, however, the buoyancy induced instabilities lead to increased turbulence, particularly at small scales. The combustion generated density variations and buoyancy induced instabilities lead to deformation of large-scale organized structures. This is known as "flickering" [5] and results in increase of hydrodynamic mixing.

The enhanced mixing discussed above does not always yield increased combustion. Analysis of the compositional structure of the non-equilibrium flame in zero- and normal-gravity indicates that in the absence of gravity, the peak temperature is close to adiabatic and the rate of reactant conversion is significant. However, in the presence of gravity the flame experiences local extinction due to large straining caused by enhanced small scale structures.

Some of the physical features captured by LES/FMDF are verified by DNS of 3D planar jet
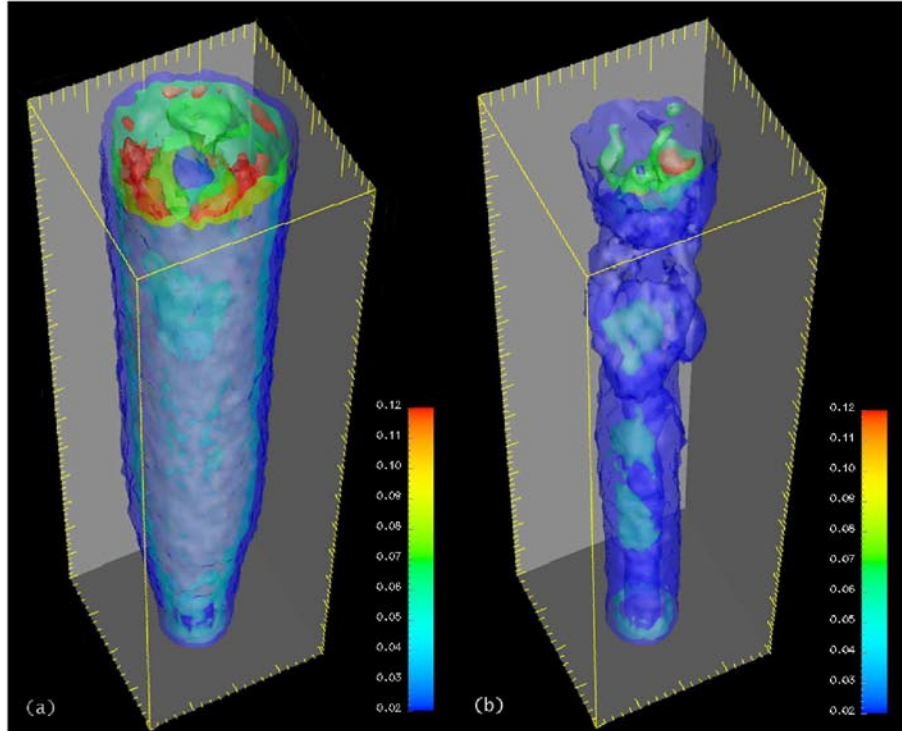
Figure 1: Contour plots of the instantaneous, filtered values of the mass fraction of CO_2 in an upward methane round jet flame under non-equilibrium condition, as predicted by LES-FMDF. (a) Zero gravity, (b) Normal gravity.

flames. These simulations are based on an idealized single-step irreversible chemical kinetics model in which the range of parameters such as the Reynolds and Damkohler number are smaller than those considered in LES. Obviously, a quantitative comparison between DNS and LES results is not possible. Figure 2 shows the contour plots of the vorticity. Similar to that captured by LES, the flow is initially dominated by large scale 2D vortical structures and then becomes strongly 3D with significant small scales. The effect of reaction is consistent with that obtained by LES as discussed above. All of the LES and DNS results are analyzed statistically. These will be presented at the workshop. In all cases, it is observed that gravity enhances turbulence, and thus promotes mixing. In some cases, this enhanced mixing leads to a larger rate of reactant conversion. This is always true in equilibrium flames, but not always true in non-equilibrium flames. In the latter, the enhanced strain field may yield local flame extinction and reduction in reactant conversion.

WORK IN PROGRESS

Our current work is focused on analysis of non-equilibrium diffusion flames with realistic chemical kinetics. In future work, we plan to develop and implement the joint velocity-scalar FMDF methodology for LES of diffusion flames. This would have the advantage of closing the effects of SGS convection [6].
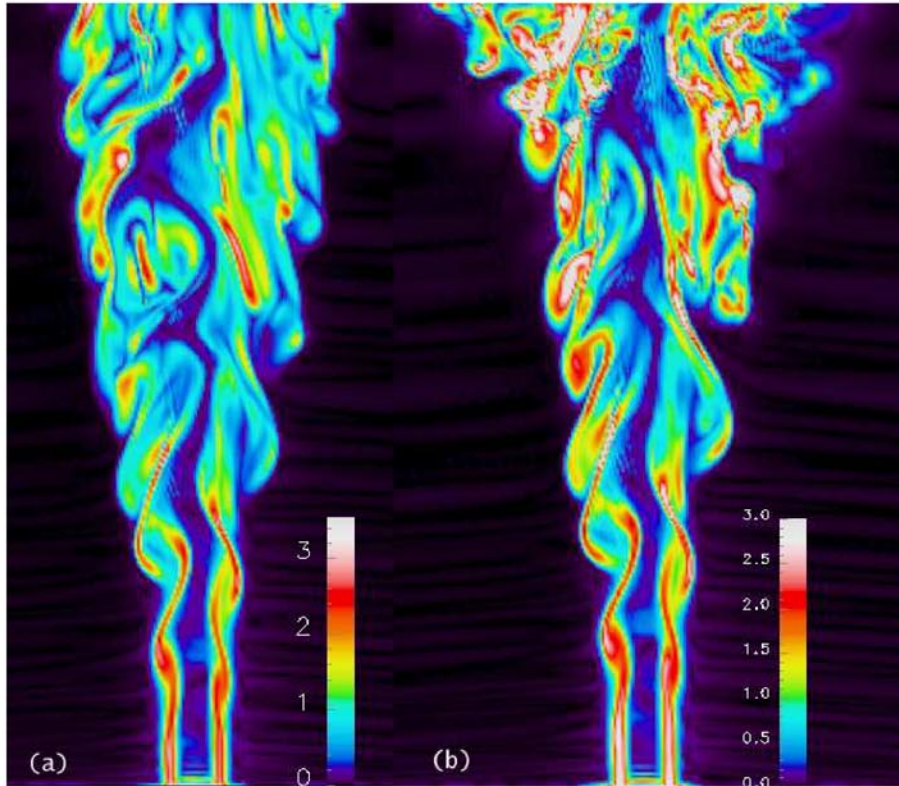
Figure 2: Contour plots of the instantaneous vorticity magnitude in an upward reacting, 3D planar jet flame as obtained by DNS. (a) Zero gravity, (b) Normal gravity.

ACKNOWLEDGMENT

REFERENCES

[1] Jaberi, F.A. Colucci, P.J. , James, S. , Givi, P. , and Pope, S.B. *J. Fluid Mech.* , **401**, pp. 85-121 (1999).

[2] James, S. and Jaberi, F.A. , *Combust. Flame*, **123**, pp. 465-487 (2000).

[3] Givi, P. *DNS/LES-Progress and Challenges*, pp. 81-92, Greyden Press (2001).

[4] Pope, S.B. , Turbulent Flows Cambridge University Press, Cambridge, UK (2000).

[5] Bahadori, M.Y. Zhou, L. , Stocker, D.P. , and Hegde, U. *AIAA Journal*, **39**, pp. 1200-1208 (2001).

[6] Gicquel, L.Y.M. , Givi, P. , Jaberi, F.A. and Pope, S.B. *Phys. Fluids*, **14**(3), pp. 1196-1213 (2002).

Effects of Buoyancy and Forcing on
Transitioning and Turbulent Lifted Flames

George Kosály, John C. Kramlich, James J. Riley, and Joseph W. Nichols

Department of Mechanical Engineering

University of Washington

Seattle, Washington

Introduction

The objectives of this paper are two-fold. First, a numerical scheme for the simulation of a buoyant, reacting jet is presented with special attention given to boundary conditions. In the absence of coflow, a jet flame is particularly sensitive to boundary conditions enforced upon the computational domain. However, careful consideration of proper boundary conditions can minimize their effect upon the overall simulation.

Second, results of some preliminary simulations are presented over a range of Froude and Damköhler numbers. This range was chosen so as to produce lifted flames in both normal gravity and microgravity environments.

Numerical Method

A low Mach number approximation [1] is applied to the Navier-Stokes equations and the resulting system is solved numerically using a predictor-corrector method similar to that described by Najm et al. [2]. This predictor-corrector scheme handles large density ratios necessary to study buoyancy effects. A one-step, reversible, Arrhenius-type reaction is used to model the chemistry. Also, the numerical method is adapted for numerical solution on a variable spaced, staggered, cylindrical mesh, with a computational domain as shown in Figure 1. For more details about this numerical method, please refer to [3].

Boundary Conditions
Inlet

The inlet condition corresponds to a jet issuing from a small orifice in a wall. The velocity is specified at all points using a "top-hat" profile constructed from a tanh function as suggested by Michalke [4].

Lateral

As a jet flow develops, it entrains ambient fluid from its surroundings. In the absence of coflow, a closed lateral boundary condition encourages recirculation by preventing entrainment across the lateral boundary. Recirculation of heat and species can have a significant effect upon a reacting system. In order to allow entrainment across the lateral boundary, a modification of the traction-free boundary condition discussed by Boersma et al. [5] is
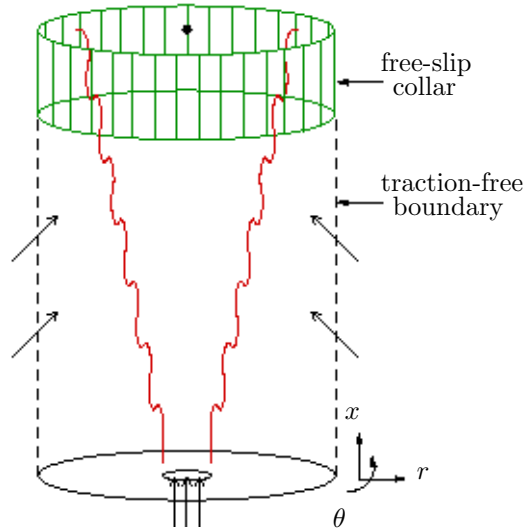
Figure 1. Diagram of the computational domain with a traction-free lateral boundary condition and a free-slip collar around the outlet.

employed. This condition specifies that

$$\boldsymbol{\tau} \cdot \hat{\boldsymbol{n}} = \boldsymbol{0}, \tag{1}$$

where $\hat{\boldsymbol{n}}$ is the unit outward normal vector at the lateral boundary. The left hand side of (1) is proportional to the force due to viscosity exerted on a small surface element of the boundary.

Outlet

At the outlet of the domain a convective boundary condition was employed of the form:

$$\frac{\partial \rho \boldsymbol{u}}{\partial t} + U_{max} \frac{\partial \rho \boldsymbol{u}}{\partial x} = 0 \tag{2}$$

The convective speed U_{max} was chosen to be the maximum measured velocity in the plane of the outlet [6]. This choice was found to be representative of the small central portion of the domain containing the jet with which the simulation is primarily concerned. Therefore, it exerts the least amount of unphysical influence upon the region of interest.

Mass Conservation

Mass conservation was preserved by correcting ρu_x at the outlet. The amount of excess mass flux j across the outlet was determined by a control volume analysis of the form:

$$j = \int \int \int \frac{\partial \rho}{\partial t} dV + \int \int \rho \boldsymbol{u} \cdot \boldsymbol{n} dS \tag{3}$$

The outlet mass flux was corrected by uniformly subtracting j/A from ρu_x, where A is the cross sectional area of the outlet.

Free-slip Collar

Physically, the outlet mass flux correction is equivalent to introducing a uniform pressure gradient in the x direction across the entire outlet, so that Eqn. (2) can be written:

$$\frac{\partial \rho \boldsymbol{u}}{\partial t} + U_{max}\frac{\partial \rho \boldsymbol{u}}{\partial x} + \frac{\partial p_c}{\partial x} = 0 \qquad (4)$$

Note that the addition of a corrective pressure gradient is not consistent with the traction free boundary condition at the edge of the domain. It was found that the introduction of a free-slip "collar" around the outlet (see Figure 1) significantly improves numerical stability by decoupling the convective outflow and the lateral traction-free boundary conditions.

Results and Discussion

Sixteen axisymmetric simulations were performed with Damköhler numbers varying in increments of 100.0 from 600.0 to 900.0 and inverse Froude number varying in increments of 0.1 from 0.0 (non-buoyant) to 0.3 (highly buoyant). A mesh of 256 by 512 grid points was used with spatial resolution such that in the region of the flame $\Delta r \approx 0.03$ and $\Delta x \approx 0.04$. A time step of $\Delta t = 0.002$ was used. Initially, the flame was piloted by the introduction of a region of high temperature at the edge of the nozzle. Then, at non-dimensional time 16.0, the pilot was turned off, allowing the flame to lift.

Figure 2 shows contours of density of four resulting lifted flames taken at time $t = 192.0$ corresponding to the four different Froude numbers tested and a Damköhler number of 800.0. It is immediately apparent that in the case of $Fr = 3.33$, the flow is much more complicated than in the non-buoyant case. Although the flow is unforced at the inlet, the buoyant cases develop an instability in the convection layer at the outer edge of the flame. Note that in this region, the baroclinic torque has the same sign as the vorticity generation due to viscous shear. The initial source of this instability may be numerical noise associated with roundoff as well as rather high frequency, small fluctuations in pressure at the outflow boundary.

Although the non-buoyant momentum-dominated jet is expected to be unstable, it is evident from Figure 2 that the instability is not manifested. Although there is always numerical noise associated with computations performed on a discrete computer, this noise is very low level (on the order of 10^{-6} for single precision arithmetic) compared to the main flow, so that these instabilities are not triggered. However, the instabilities generated by buoyancy seem to be very sensitive to low level excitation. Bahadori et al. [7] note that even slightly buoyant flames, with Froude numbers in excess of 40.0, show significant differences from non-buoyant flames. This seems reasonable in light of the fact that in a laboratory setting low-level noise is usually several orders of magnitude greater than that introduced by a computer simulation. Also, the fact that the flow is constrained to be axisymmetric in the computer simulations may help stabilize the flow for moderate Froude numbers where unstable flow is observed experimentally. Buoyant instabilities are often highly three dimensional and this may play a key role in the transition to turbulence for lifted flames.

Conclusions

From numerical experiments, it was found that a convective outflow boundary condition with a choice of U_{max} for the convective wind speed, and a traction-free lateral boundary
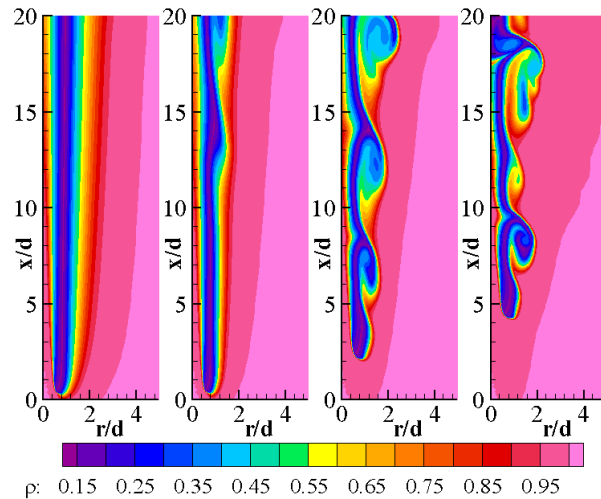
Figure 2. Density field of lifted flames at time 192 with Damköhler number 800. From left to right, the Froude number in each plot is ∞, 10.0, 5.0, and 3.33 respectively.

condition yielded the best performance for the jet flow. The addition of a free-slip collar around the outlet provided the decoupling necessary for these conditions to function together.

It was also observed that the effects of buoyancy tend to destabilize the jet flow. However, for moderate Froude numbers, the computer simulated flames appeared to be weakly unstable whereas corresponding flames in the laboratory exhibited stronger instabilities.

Acknowledgments

References

1. P. A. McMurtry, Direct numerical simulations of a reacting mixing layer with chemical heat release, Ph.D. thesis, University of Washington (1987).
2. H. N. Najm, P. S. Wyckoff, O. M. Knio, A semi-implicit numerical scheme for reacting flow. i. stiff chemistry, *Journal of Computational Physics* **143** (1998) 381–402.
3. J. W. Nichols, J. J. Riley, Effects of buoyancy and forcing on transitioning and turbulent lifted flames, in: *Proceedings of the Third Joint Meeting of the U.S. Sections of the Combustion Institute*, The Combustion Institute, Chicago, 2003.
4. A. Michalke, Survey on jet instability theory, *Progress in Aerospace Sciences* **21** (1984) 159–199.
5. B. J. Boersma, G. Brethouwer, F. T. M. Nieuwstadt, A numerical investigation on the effect of the inflow conditions on the self-similar region of a round jet, *Physics of Fluids* **10** (4) (1998) 899–909.
6. C. D. Pierce, P. Moin, Progress-variable approach for large-eddy simulation of turbulent combustion, Tech. rep., Stanford University (2001).
7. U. Hegde, L. Zhou, M. Y. Bahadori, The transition to turbulence of microgravity gas jet diffusion flames, *Combustion Science and Technology* **102** (1994) 95–113.

CO$_2$ Suppression of PMMA Flames in Low-Gravity

G. A. Ruff[1], M. Hicks[1], W. Mell[2], R. Pettegrew[3], and A. Malcom[3]
[1]NASA Glenn Research Center, MS 77-5, 21000 Brookpark Road, Cleveland, OH 44135
[2]University of Utah, 50 South Campus Drive, Salt Lake City, UT 84112
[3]National Center for Microgravity Research, 21000 Brookpark Road Cleveland, OH 44135

INTRODUCTION

Even though much has been learned about the effects of microgravity on material flammability, flame spread, and suppressant effectiveness, uncertainties remain regarding some of the practical aspects of fire protection in spacecraft. The experiments and simulations underway in this project are aimed directly at testing, understanding and improving NASA's existing policies and practices toward fire safety in spacecraft and extraterrestrial habitats. Specifically, the objectives of this research are:

1. Determine systematically the conditions that will ignite onboard flammable materials upon passage of an initial premixed gas, firebrand, or aerosol flame over these materials.
2. Test the effect of firebrands and configuration spacing.
3. Determine the effectiveness of the flow of CO$_2$ extinguisher or other extinguishing agents.

Experimental and computational investigations are planned to achieve each of the three objectives above. Even though progress has been made in all of the areas, the majority of data has been collected for objective (3). Current results from these investigations are discussed below.

EXPERIMENTAL INVESTIGATION

Determining the effectiveness of a flow of CO$_2$ to extinguish a fire and whether secondary fires can occur when oxygen is re-introduced after initial extinguishment is the objective of the first set of experiments conducted in this investigation in the Spacecraft Fire Safety Facility (SFSF), a test facility designed for operation on NASA's low gravity aircraft. To examine the effectiveness of CO$_2$ to extinguish fires, an oxidizer flow is established over a hollow cylinder (tube) of PMMA (polymethyl methacrylate) 25 mm long and 19 mm in diameter. The inner diameter of the tube is 9.5 mm. A cartridge heater in the center of the tube pre-heats the sample to 100 deg C to help ensure a uniform and repeatable ignition. Thermocouples are located on the external surface of the inserted cartridge heater and on the external surface of the PMMA test sample at the downstream stagnation point to monitor these temperatures.

Flame extinguishment at flow velocities between 0 and 10 cm/s and 1 atm pressure were investigated. To begin a test, the oxidizer flow is established at the desired velocity. As the aircraft exits a parabola, the igniter is energized until a sustained flame is observed on the PMMA. The igniter is then turned off and the flame becomes well-established through the remainder of the 2-g pull-up. During the microgravity period, the flame is observed to determine if it extinguishes because of the low flow rate. If the flame is sustained through this first microgravity period, it is allowed to burn through a second 2-g pull-up, during which it increases in intensity. At the end of the pull-up, the flow is quickly switched from oxidizer to a suppressant mixture (either a mixture of CO$_2$/air or He/air) so that the suppressant reaches the sample after the first few seconds of low gravity. The flame is then observed to determine if it (i) extinguishes during the low-gravity period,

(ii) continuously decreases in intensity during low gravity but does not extinguish, or (iii) maintains a fairly stable intensity and does not extinguish within the low gravity period (approximately 20 sec).

Tests have been conducted for oxidizer mixtures of 21% O_2/79% N_2 (standard air) and 25% O_2/75% N_2 (rich air). Suppressant mixtures having 12.5%, 25%, and 50% CO_2 with the balance being either standard or rich air, depending on the oxidizer, have been evaluated. Data has also been obtained with He replacing CO_2 in the suppressant at similar concentrations. To date, tests have been conducted on 26 flights and a total of 142 data points have been obtained. A series of ground tests have also been conducted so that 0-g and 1-g behavior can be compared.

Experimental Results

Figure 1 shows the PMMA surface temperature at the rear stagnation point as a function of mass flow rate of oxygen (%O_2 in flow x ρUA). The open symbols show conditions that self-extinguished. The closed symbols show conditions where the suppressant was applied with the solid circles indicating flames that were extinguished. The conditions represented by triangles did not extinguish within the 20 seconds of low-gravity. For O_2 flow rates below about 0.7 g/s (velocities below 5 cm/s for standard air) and surface temperatures below approximately 270 deg C, the flames extinguished within 20 sec with no addition of suppressant. Increasing either the flow velocity or the surface temperature allowed the flame to be sustained through the low-gravity period. This result is similar to that obtained by Goldmeer [1] who showed that increasing the sample temperature made the flame more difficult to extinguish. On this plot, there is no discernable boundary between flames that were extinguished by suppressant and those that were not. This is likely the result of the influence of a number of parameters such a g-jitter, sample pre-heat, flame shape, and duration of suppressant flow. The effect of these parameters will be the focus of future work.

Figure 2 shows the time-to-extinguish as a function of flow velocity for an oxidizer of rich air and the suppressant 25% CO_2/75% rich air. The time to extinguish plotted in the figure is the time from when suppressant reached the sample to extinguishment. The images show end views of the PMMA sample in flowing oxidizer after the flames became stable in low-gravity. At 1 cm/s, the flame extinguished within 4 sec, primarily because of the weak flame. The time to extinguish increased at 2 cm/s but was then observed to decrease with increasing velocity. At the higher velocities, the flame did not wrap completely around the cylinder but was open in the wake region. The luminosity and thickness of the flame increased with velocity, as did the width of the wake region where the flame was absent. These results show the interdependence of the flow velocity and subsequent flame intensity and structure on the suppression behavior. Additional tests are being conducted using lower CO_2 concentrations to elucidate the role of velocity and flame development on the time to extinguish.

THEORETICAL INVESTIGATION

Due of the limited duration of low gravity on the aircraft and the difficulty in quantifying the effect of g-jitter on suppression near the extinction boundary, a modeling effort is supporting the experimental program. A modified version of the Fire Dynamics Simulator (FDS) computer code [2,3] was used to conduct two-dimensional simulations of ignition and flame spread along (perpendicular to the axis) a PMMA cylinder. Prior to beginning calculations, the finite volume radiation solver in the FDS code was modified so that gas-phase radiation was properly accounted for when the finite rate chemistry model is invoked. This radiation solver determines the radiation flux on the surface of the PMMA and the divergence of the radiation flux in the gas. The ideal gases were assumed to be gray and non-sooting. Absorption coefficients for H_2O and CO_2 were determined using RadCal [4].

Following the work of previous researchers, the chemical reaction of MMA vapor generated by PMMA pyrolysis was modeled using a one-step overall chemical reaction ($F + O_2 \rightarrow CO_2 + H_2O$) and second-order Arrehnius kinetics [5,6]. Kinetic constants were obtained from Seshandri and Williams [7]. The specific heats of the gaseous species were assumed constant and equal; molecular transport coefficients were temperature-dependent [4]. In-depth heat transfer at each surface point on PMMA solid was modeled using a one-dimensional conduction equation. The net heat flux at each surface point was comprised of convective flux, incident radiation flux, re-radiation from the hot surface, and heat loss due to PMMA vaporization. The degradation of the PMMA solid and resulting mass flux of fuel gas was modeled assuming constant density, negligible surface regression, and first order kinetics [4].

The two-dimensional simulations assumed a symmetry plane oriented parallel to the imposed flow through the axis of the cylinder. Gas phase ignition occurred by placing a "hot wire" in the symmetry plane just upwind of the solid. Experimentally measured values of the incoming flow velocities and composition, igniter duration, acceleration disturbance, and the initial temperature of the PMMA were used. Most simulations used a uniform grid with 1 mm grid cell dimensions in a 4.5 cm x 10 cm domain.

Model Results

A number of experimental cases have been simulated and, in general, the trends observed in the experiments were reproduced. Interestingly, the simulation has also mirrored the sensitivity of the environmental conditions on the effect of suppressant just as in the experiment. For example, a test condition having an oxidizer of standard air at 8.5 cm/s and suppressant mixture of 12.5% CO_2 at 9.3 cm/s was simulated. A plot of the net surface heat flux from simulations with and without incident radiation flux is shown on Fig. 3a while the associated acceleration history is shown in Fig. 3b. It can be seen that up to the onset of reduced gravity ($t < 325$ s), the net flux is larger when gas-phase radiation incident on the PMMA is included. Although the contribution of incident radiant flux does not appear to be significant, relative to the net flux, it raises the PMMA surface temperature enough (i.e., preheats the PMMA) to ensure pyrolysis throughout the duration of reduced gravity and suppressant. When the gray-gas model was applied, the flame sustained because of the higher surface temperatures. It extinguished when the surface temperature was lower.

SUMMARY AND FUTURE WORK

A significant amount of data has been obtained and is being analyzed to extract the details about the effect of CO_2 and He suppressants in low gravity. The simulations have proven useful in identifying the effect of various parameters that are difficult to isolate in the experiment. Meanwhile, the preparations are underway to conduct the experiments to achieve objectives (1) and (2), as previously identified.

Acknowledgements

References

1. Goldmeer, J. S., T'ien, J. S. and Urban, D. L., 1999, "Combustion and extinction of PMMA cylinders during depressurization in low-gravity," Fire Safety Journal, Vol. 32, pp. 61-88.

2. McGrattan, K.B. and Baum, H.R. and Rehm, R.G. and Hamins, A. and Forney, G.P. and Floyd, J.E. and Hostikka, S. and Prasad, K., "Fire Dynamics Simulator, Technical Reference Guide," National Institute of Standards and Technology (NIST), 2002, NISTIR 6782, 2002 Ed., http://fire.nist.gov/bfrlpubs/

3. Mell, W.E., McGrattan, K.B., Baum, H.R., "g-jitter Effects on Spherical Diffusion Flames," to be submitted to Microgravity Science and Technology.

4. Grosshandler, W. 1993, "A narrow band model for radiation calculations in a combustion environment," NIST Technical Note (TN 1402).

5. Altenkirch, R.A., Tang, L., Sacksteder, K., Bhattachrjee, S., and Delichatsios, M.A., 1998, "Inherently unsteady flame spread to extinction over thick fuels in microgravity," Proceedings of the Combustion Institute, Vol. 27, pp. 2515-2524.

6. Yang, C.T. and T'ien, J.S., 1998, "Numerical simulation of combustion and extinction of a solid cylinder in low-Cspeed cross flow," J. Heat Transfer, Vol. 120, pp. 1055-1063.

7. Seshandri, K. and Williams, F.A., 1978, "Structure and extinction of counterflow diffusion flames above condensed fuels: Comparison between Polymethyl Methacrylate and its liquid monomer, both burning in nitrogen-air mixtures," J. of Polymer Science: Polymer Chemistry Ed., Vol. 16, pp. 1755-1778.
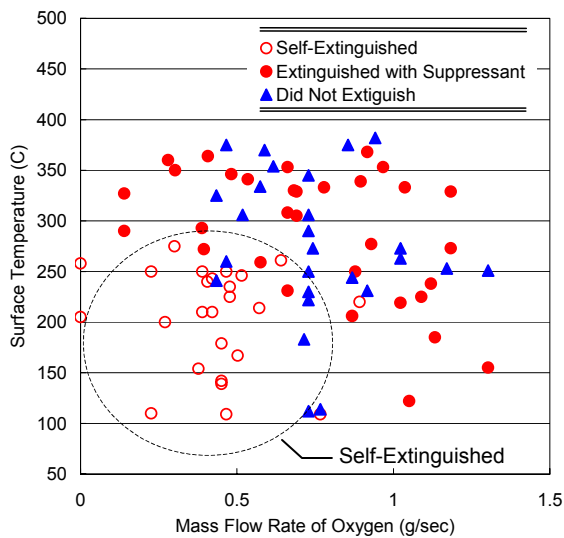
Figure 1. Low-gravity sustained flammability map
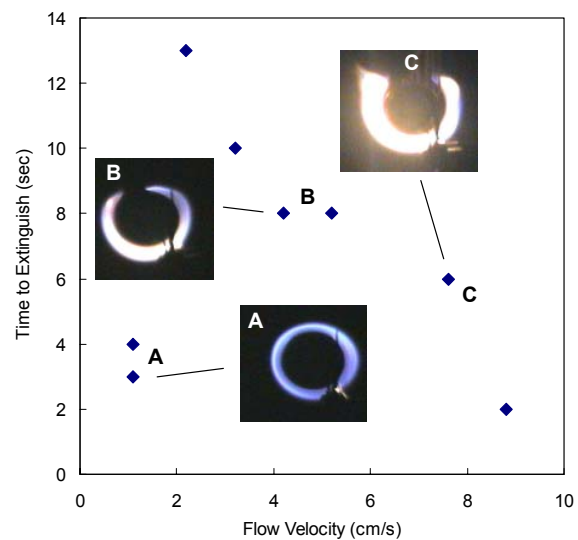
Figure 2. Time to extinguish for 25% CO_2/75% rich air mixture

a. Net heat flux

b. Acceleration
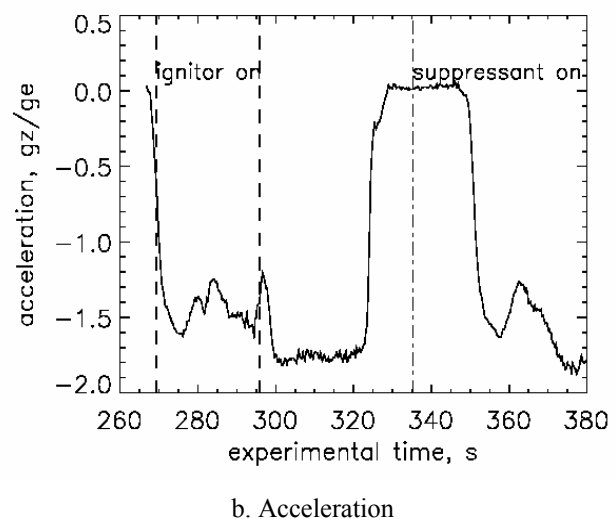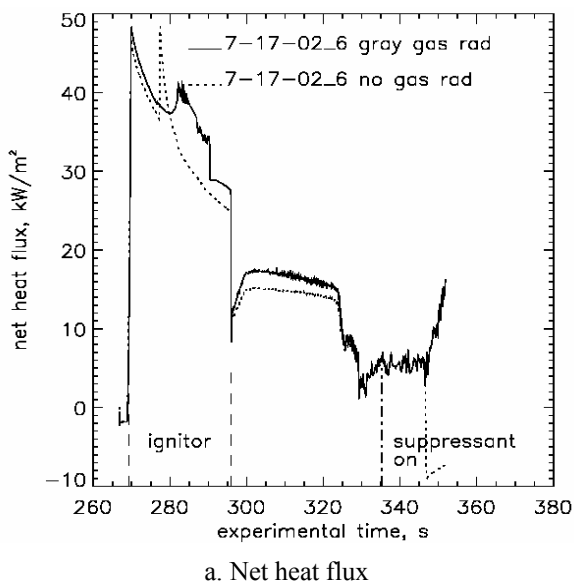
Figure 3. Effect of gas radiation model on suppression

EFFECTS OF ELECTRIC FIELD ON HYDROCARBON-FUELED FLAMES

Z.-G. Yuan and U. Hegde
National Center for Microgravity Research, Cleveland, OH

INTRODUCTION

It has been observed that flames are susceptible to electric fields that are much weaker than the breakdown field strength of the flame gases.[1-6] When an external electric field is imposed on a flame, the ions generated in the flame reaction zone drift in the direction of the electric forces exerted on them. The moving ions collide with the neutral species and change the velocity distribution in the affected region. This is often referred to as ionic wind effect. In addition, the removal of ions from the flame reaction zone can alter the chemical reaction pathway of the flame. On the other hand, the presence of space charges carried by moving ions affects the electric field distribution. As a result, the flame often changes its shape, location and color once an external electric field is applied. The interplay between the flame movement and the change of electric field makes it difficult to determine the flame location for a given configuration of electrodes and fuel source. In normal gravity, the buoyancy-induced flow often complicates the problem and hinders detailed study of the interaction between the flame and the electric field.

In this work, the microgravity environment established at the 2.2 Second Drop Tower at the NASA Glenn Research Center is utilized to effectively remove the buoyant acceleration. The interaction between the flame and the electric field is studied in a one-dimensional domain. A specially designed electrode makes flame current measurements possible; thus, the mobility of ions, ion density, and ionic wind effect can be evaluated.

EXPERIMENTS

Figure 1 shows the test section of the experiment apparatus. Fuel gas is issued from a porous brass spherical burner with a diameter of 12.7 mm, which also serves as the inner electrode. A 1.6 mm OD stainless steel tube provides fuel passage and electric connection to the burner. It is insulated with a 2.3 mm ID thin-wall ceramic tube, which prevents any electric current from leaking to the surrounding gases. The outer electrode is a Buckyball-shaped Faraday cage with an inner diameter of 70 mm.[7] The two electrodes are arranged concentrically to establish spherical equipotential surfaces in between, except the local region of the thin stainless fuel tube where the electric field deviates from spherical symmetry. The outer electrode is made of a nylon wire frame coated with a thin layer of copper. A group of wire members at the top of the Buckyball that covers a solid angle of 1.6 Sr is electrically separated from the rest of the ball so that the current through this part can be measured independently. An adjustable high-voltage DC source provides desired voltages and polarity between the two electrodes. The fuel system consists of a fuel bottle, a pressure regulator, a mass flow meter and a solenoid valve to provide constant fuel flow during the drop. During a test run, the flame is ignited at normal gravity. As soon as the ignition is confirmed, the drop rig is released and the high-voltage is turned on. The current value is logged by an onboard computer and the flame images are acquired with a CCD camera. The output signal of the camera is sent to a ground device via a fiber-optic cable for recording. Three types of fuels were tested: ethylene, methane and propane. The applied voltage covered two ranges: from -0.6 kV to -2.0 kV and from +0.8 kV to +2.0 kV with a 0.2 kV increment between two neighboring test points. Flames with no applied voltage were also tested for comparison. A fixed fuel flow rate for each fuel was selected for adequate

flame size. Since flames of the three different fuels behave similarly, only the test results with ethylene fuel at a flow rate of 2.3 mg/s burning in the atmospheric pressure will be discussed below.

RESULTS AND DISCUSSIONS

Figure 2 shows flame images of sixteen tests, acquired 1.8 seconds into free fall. The magnitude and polarity of the applied voltage marked on each image represent the voltage of the outer electrode vs. that of the inner electrode. For most cases, the top portion of the flame is quite spherical. For negative applied voltages, as the magnitude of the voltage increases, the flame size decreases monotonically, while the intensity of the flame increases. The blue color of the flames indicates low or no soot inside the flame. For positive applied voltages, the size of the flame slightly decreases as the voltage increases. The flames are much dimmer than the negative voltage cases. Various intensities of the orange/red color in the flame seem to indicate that the soot content decreases at low positive voltages and then increases at high positive voltages. Figure 3 shows the average flame radius as a function of time. With zero applied voltage, the flame radius increases during the entire course of 2.2 second free fall. For +2.0 kV applied voltage, the flame radius also increases during the drop, but at a lower rate than the zero voltage case. The flame radius of the -2.0 kV case essentially remains constant. The observed flame behavior suggests that the flame reaches a quasi-steady state quicker in the presence of an electric field.

The current magnitude averaged over elapsed time from 1.6 seconds through 1.8 seconds vs. applied voltage for 14 tests is plotted in Fig. 4. The magnitude of the current increases with the magnitude of the applied voltage as expected, i.e., the increased voltage strips more ions from the reaction zone. The relationship between the voltage and current does not follow Ohm's law because the conduction of electricity through gases is fundamentally different from that through metals. In gases, the conduction of electricity is carried out by moving ions, thus the net charge density must not be zero. As a result, the current density is proportional to the electric field multiplied by the divergence of the electric field. Therefore, the relation between the current and the field becomes nonlinear. In addition, the flame radius varies with applied voltage. The location of the flame, as the source of ions, also affects the current.

It is known that the flame reaction zone of the present tests is thin in comparison with the distance between the two electrodes and the apparent resistivity in it is low because of the co-existence of positive and negative ions. Thus, the voltage drop across the two electrodes mostly takes place in the two electrode spaces, (i.e., the spaces between the flame and electrodes). In each electrode space, the charge carrier is unipolar. There is neither charge generation, nor charge recombination in an electrode space. By integrating Gauss's theorem of electrostatics and the equation of conservation of electric charges, an equation relating the total voltage, total current, the mobilities in the two electrode spaces, and the flame radius can be obtained.[7] Applying the resulting equation to the experimental data, we obtain (a) for negative applied voltages, the mobilities are 45.9 cm^2/s/v and 2.2 cm^2/s/v for negative and positive ions, respectively, and (b) for positive applied voltages, the mobilities are 0.44 cm^2/s/v and 10.3 cm^2/s/v for negative and positive ions, respectively. It is noticed that in either case the mobility of negative ions is much lower than that of electrons (the mobility of electrons is more than 1000 cm^2/s/v),[8,9] indicating that electrons are captured by neutral species soon after leaving the flame reaction zone. The distribution of the charge density, $\sigma(r)$, for the two cases of +2.0 kV and -2.0 kV was evaluated and plotted in Fig. 5, based on the obtained mobility data. It can be seen that the charge density is very low compared with the gas density (e.g., at standard conditions, there

are 2.69×10^{19} molecules per cubic centimeter). Therefore, only a very small amount of ions are removed from the flame gas.

To evaluate the impact of the moving ions on the velocity distribution of gases, the Navier-Stokes equations must be invoked, in which the effect of the electric field is represented by a body force term. In a one-dimensional spherically symmetric case, this body force is proportional to the total current and inversely proportional to the ion mobility, i.e., $f = I/(4\pi Kr^2)$.[7] By defining a variable, F(r), such that dF/dr = -f, F(r) can then be lumped into the pressure gradient term in the momentum equation[7] and viewed as an apparent pressure: $F(r) = \dfrac{I}{4\pi} \left(\dfrac{1}{K_o r_o} - \dfrac{1}{Kr} \right)$.

Figure 6 shows the distribution of the apparent pressure, F(r), based on the data obtained from the +2.0 kV case and the -2.0 kV case. Note that the electric field-induced body force is always in the same direction as that of the moving ions, thus it is inward (i.e., compressive) in the inner electrode space and outward (i.e., expansive) in the outer electrode space. As a result, the field-induced pressure becomes positive in the inner electrode space and negative in the outer electrode space. For a one-dimensional case, the conservation of mass relates a change of the velocity distribution to a change of the density distribution. Since the apparent pressure, F(r), is about six orders of magnitude lower than the ambient pressure in which the drop tests were conducted, the density change caused by the apparent pressure is negligible and so is the velocity change. Therefore, the ionic wind effect is negligible in the current test conditions.

CONCLUSIONS

The electric current through a spherical flame region has been measured successfully using the present experiment apparatus. The current data were used to estimate the mobilities of ions in electrode spaces. The values of the mobilities suggest that soon after leaving the flame reaction region, the electrons attach themselves to neutral molecules or radicals. The ion number densities in electrode spaces are also calculated, indicating very low ion concentration in the gases. The ionic wind effect in a spherically symmetric system can be studied as an apparent pressure term and is found to be negligible. Many flames do not reach quasi-steady state during the drop test so that longer microgravity time is needed.

ACKNOWLEDGMENT

REFERENCES
1. Calcote, H. F., *Proc. Combust. Inst.* 9:622(1963).
2. Lawton, J., and Weinberg, F. J., *Electrical Aspects of Combustion,* Clarendon Press, Oxford, 1969.
3. Carleton, F. B. and Weinberg, F. J., *Nature* 330:635 (1987).
4. Saito, M., Arai, T., and Arai, M., *Combust. Flame* 119:356 (1999).
5. Yuan, Z. -G., Hegde, U., and Faeth, G. M., *Combust. Flame* 124:712 (2001).
6. Yuan, Z. -G., Hegde, U., and Faeth, G. M., AIAA paper No. 2002-1075, 40th Aerospace Science Meeting & Exhibit, 14-17 Jan. 2002, Reno, Nevada, USA.
7. Yuan, Z. -G., Hegde, U., AIAA paper No. 2003-0812, 41st Aerospace Science Meeting & Exhibit, 6-9 Jan. 2003, Reno, Nevada, USA.
8. Heinsohn, R. J., Wulfhorst, D. E., and Becker, P. M., Combust. Flame 11:288 (1967).
9. Mayo, P. J., and Weinberg, F. J., Proc. Roy. Soc. Lond. A. 319, 351 (1970).
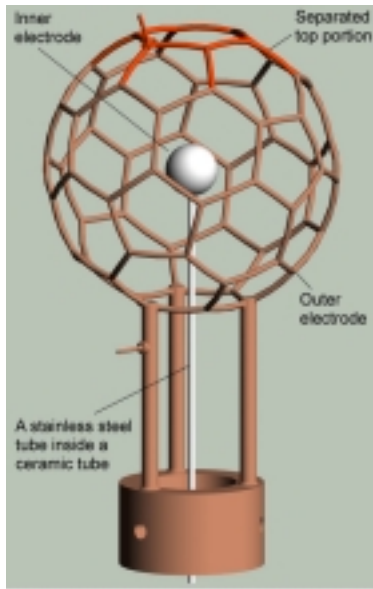
Figure 1. The test section of the experiment apparatus. The red top portion of the outer electrode is electrically separated from the rest of the electrode.

Figure 2. Ethylene/air diffusion flames in sixteen drop tests. The dark lines in each image are out-of-focus elements of the Buckyball. For most cases, the top portion of the flame is quite spherical.

Figure 3. The flame radius vs. time. For both zero and +2.0kV cases, the flame radius increases with time, but more rapidly in the zero voltage case. For the -2.0 kV case, the flame radius is significantly smaller than the zero voltage case and essentially remains unchanged.
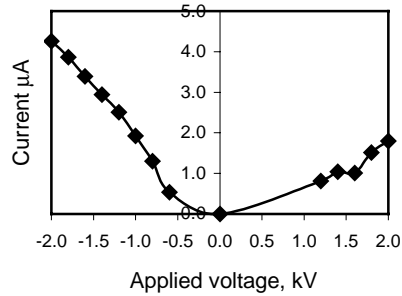
Figure 4. Absolute value of current vs. applied voltage. The current value of each test in the plot is averaged between 1.6 seconds to 1.8 seconds in free fall.

Figure 5. Distribution of charge number density for two tests, assuming each ion carries a single electric charge only. The peak of each curve is located at the flame radius.
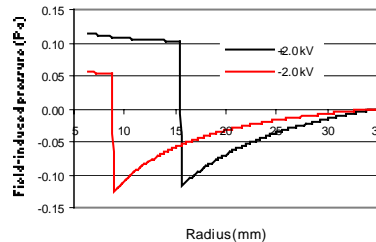
Figure 6. Distribution of the apparent pressure for two tests. The apparent pressure is always compressive (positive) in the inner electrode space and expansive (negative) in the outer electrode space because of different directions of the electric force in the two regions. The field-induced pressure is negligible in comparison with the atmospheric pressure for the current test conditions.

ELECTRIC FIELDS, FLAMES, AND MICROGRAVITY

Derek Dunn-Rankin
Mechanical and Aerospace Engineering, University of California, Irvine

Felix J. Weinberg
Chemical Engineering and Chemical Technology, Imperial College London

Introduction

The object of this paper is to review some of the recent investigations carried out at the University of California, Irvine and Imperial College London into the utilization of electric fields in combustion research, and their particular applicability to microgravity environments. In the absence of earth gravity, the use of such fields to manipulate dispersions and trajectories of electrically charged droplets and particles, and to control convection using the drag exercised on flame ions by electric fields, can be especially useful. The paper will explore several such topics in particular: The control of convection in diffusion flames, the spraying of liquid dispersions using a combination of electrohydrodynamics and gas assist atomization, and the use of ion winds to produce flow of a neutral gas. Because much of this work has appeared in archival publications, this paper briefly summarizes some of the findings and then references the more complete documentation.

Electric field-induced flame convection in the absence of gravity.

Under earth gravity, diffusion flames rely on natural or forced convection to replenish reactants and direct the hot products. The former is not available under microgravity conditions whilst the latter requires a compressor or keeping fuel under pressure in cylinders, entailing a considerable weight penalty. In microgravity, moreover, diffusion flames tend to become spherical and, as the result of blanketing by their own products, burn very slowly and become unsuitable for transferring heat to any object. Electric fields can control this convective environment by locally modulating an ion wind. Experiments show both steady and dynamic examples of this modulation, including a feedback control system that allows the flame system to track a desired luminosity behaviour. The main findings of our flame control work appear in Strayer (2001) and Strayer and Dunn-Rankin (2002). Briefly, the results have shown that flame luminosity responds on a timescale that is rather slow (tens of ms) relative to the instantaneous reaction of the ions to the field, and even relative to the time it takes for the ions to traverse the system. That is, the characteristic time for the ions to travel from the flame to the ground plane is given by $\tau_{ion} = L^2 / KQ$, where K is the ion mobility and Q is the potential applied across the electrode (flame capillary to ground plane) separation distance L. For our experiment, L is approximately 5 cm, K is 2.5 cm^2/sV, and Q is 2000 V, yielding an ion transport time of 4 ms. The system's measured response suggests, however, that the ion wind set up time is more on the order of 100 ms, so ion transport is not the limiting phenomenon. If we instead evaluate the time associated with a constant acceleration equivalent to g over a distance L, we find $\tau_g = \sqrt{L/g}$, or, again for $L = 5$ cm, τ_g is approximately 70 ms, matching very closely the time response of our flame to electric field forcing. Alternatively, we can equate the acceleration to the electric force per unit volume as in Lawton and Weinberg (1969), $F = j/K$, where j is the current density at the chosen

force or acceleration, which in our case is the buoyancy balancing body force so that, $a = F / \rho = j / K\rho$. The appropriate timescale associated with this force is then $\tau_{elec} = \sqrt{L / a} = \sqrt{\rho K L / j}$. At the balance condition, we find j to be approximately one microamp/cm^2, which yields a $\tau_{elec} = 35$ ms, within a factor of 2 of τ_g. These timescale calculations, along with the measured flame response, indicate that electric field forcing delay time will scale as the square root of the length scale and with the inverse square root of the current density. While this is better than a convective delay, which scales linearly with length (at fixed flow velocity), it is not the instantaneous response desired. The reason for the delay is that the flame is not actually responding to the movement of flame ions directly but to the ion wind that these ions produce as they try to accelerate through the neutral gas on their way to their terminating electrode. This momentum exchange builds a pressure gradient into the bulk gas, and the construction of this gradient takes time. Hence, while control can be used to help steady the flame in its balanced or fixed buoyancy configuration, it will not allow the kinds of high frequency flame manipulation that might affect kinetically dependent aspects such as soot and gaseous pollutant formation.

Figure 2. O$_2$ concentration profiles measured at 0 V, 2880 V, and 4300 V, corresponding to the naturally buoyant, microbuoyant, and negatively-buoyant conditions.
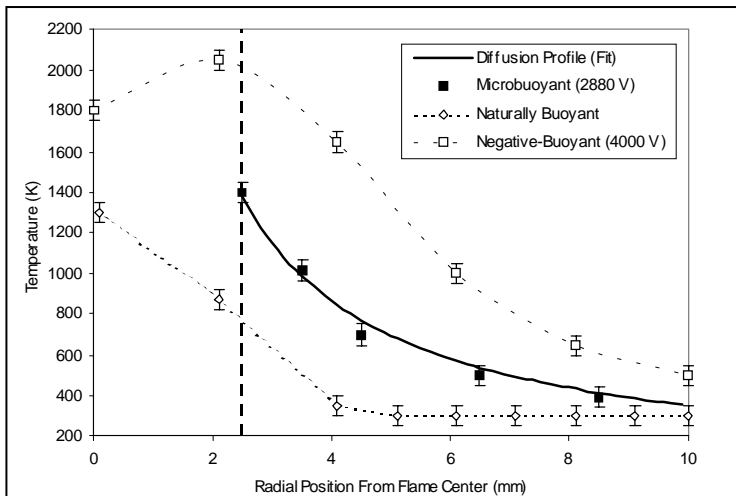
Figure 1.   Radial temperature profiles measured at 0 V, 2880 V, and 4000 V, corresponding to the naturally buoyant, microbuoyant, and negatively-buoyant conditions. The dashed line represents the flame boundary at microbuoyancy, which is 2.5 mm from the flame center

Simulation of microgravity by the application of electric fields to flames.

The effect for which microgravity is used in combustion research is generally only that of eliminating natural convection. To achieve such a microbuoyant condition, natural convection has been counterbalanced against the drag exercised on flame ions by electric fields. The object of such benchtop simulation is to facilitate a wide range of optical and laser diagnostic methods that can probe the structure of small diffusion flames without the considerable experimental obstacles and costs involved in drop tower or flight tests. To demonstrate this methodology, the temperature field of a small methane-air diffusion flame under electric field control was probed with

holographic interferometry and N_2 coherent anti-Stokes Raman spectroscopy (CARS). Oxygen concentration was also recorded using planar laser induced fluorescence.

Our previous work, where both shadowgraph images and CARS measurements were employed, revealed that the shadowgraph image disappears near the bottom of the flame in the microbuoyancy condition, and CARS temperature measurements down the vertical axis of the flame obey a diffusion profile, corresponding to the flame structure predicted by theory in the absence of convection (Strayer et al., 2002). We have recently extended this work to include oxygen concentration measurements. Figures 1 and 2 show, respectively, the temperature and molecular oxygen concentration profiles for the naturally buoyant, microbuoyant, and negatively-buoyant cases. In Fig. 1, the microbuoyant temperature profile is in good agreement with the theoretical profile within CARS measurement uncertainty, reaffirming previous findings. For the naturally buoyant case, the temperature profile drops to room temperature over a shorter distance than in the microbuoyant case,

Figure 3. Mass median diameter D50 for air-assisted electrosprays with various liquid flow rates. Dashed lines are results with high voltage on and solid lines are pure air-blast atomization.

as expected. This is a result of natural convective flows producing a stagnation point relatively close to the capillary tip, as implied by the shadowgraph images. Flame inversion is clearly evident in the negatively-buoyant case. The electric field pulls the flame away from the capillary tube, thereby reducing the heat loss to the capillary, and producing a hot gas plume directed downward. Hence, the maximum temperature recorded at this condition is much higher, nearing the adiabatic flame temperature for CH_4-air combustion. In Fig. 2, measured O_2 concentration profiles are plotted along with the theoretically derived diffusion profile for comparison. As with temperature, the microbuoyant profile matches the derived profile to 8 mm from the flame surface within the measurement uncertainty of the LIF system. Beyond this point, the measurement error increases as the distance from the flame increases because the fluorescence signal approaches the detection limit. Because the O_2 fluorescence depends on both the temperature and the O_2 concentration, the fluorescence signal decreases as the distance from the flame increases even though the O_2 concentration is increasing. For the naturally buoyant case, the flame is drawn upwards by convective influences, which causes the flame front to move closer to the capillary. In this case, the concentration profile of O_2 is controlled by both diffusion and convection driven motion. As a result, the concentration gradient is steeper and the O_2 partial pressure approaches 0.21 atm faster than in the microbuoyant case. Conversely, in the negatively-buoyant case, the flame is pulled downward. Further details of this work appear in Papac et al. (2003a). Incidentally, as part of this CARS study, we discovered an interesting method that can be used to align this complex laser diagnostic (Papac, et al., 2003b).
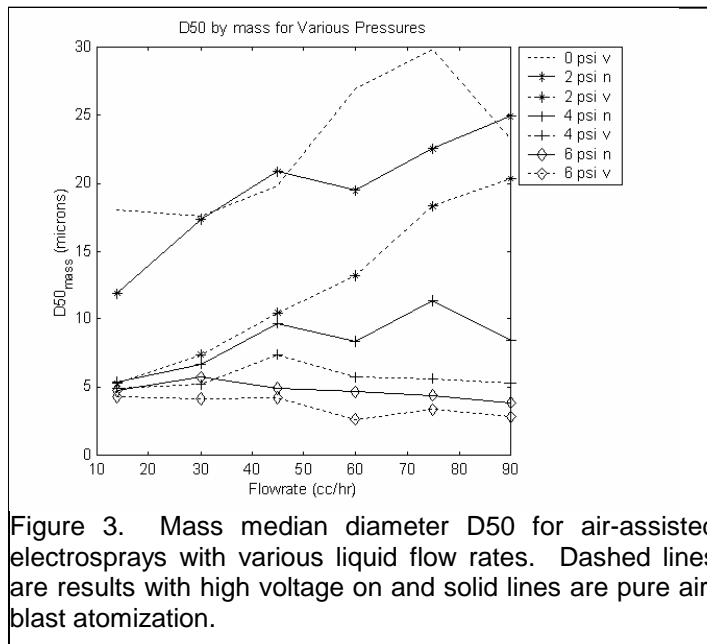
Electrically charged dispersions of extinguishants for use in microgravity environments.

Techniques for electrically charging and spraying dispersions of extinguishant droplets and particles have been developed in prior work, with a view to subsequent guidance of particle

trajectories under electric field control, especially in microgravity environments (Weinberg et al., 2002). We here discuss the use of combined electric fields and gas assist atomization to increase the flow rate of extinguishant that can be supplied through a single charged capillary needle. Charged sprays offer an alternate transport mechanism as well as the potential for controlled dispersion through focusing guide electrodes. While we found that sodium bicarbonate powder is a powerful flame suppressant, water was superior for extinguishing smoldering fire. The challenge of water electrospray, however, is the low flow rate. Although there have been attempts to create electrospray arrays to overcome this challenge, the interacting electric fields compromise performance (Regele, et al., 2002). Alternatively, we have found that adding a small amount of air-assist to the otherwise conventional EHD system can increase flow rates 10-fold with little degradation in atomization performance. Figure 3, for example, shows the droplet size distribution measured with a PCSV instrument from an air-assist electrospray system. Without air assist, the mass median diameter (D50) droplet size increases with increasing liquid flow rate. Adding 2 psi air assist, however, nearly halves the D50. The combination of a little air with electrospray is particularly effective at low liquid flow rates. Additional details of this work appear in Rickard and Dunn-Rankin (2002).

Corona winds for convection control of electrically neutral environments.

Having studied sprays and powder suspensions for fire extinguishment, our next aim is to look at field-induced gas flows; ionic winds. To avoid any dependence on current density associated with particular flames, the work used corona discharges to create the ions. Hypodermic needles (0.5 mm O.D.; 0.42 mm I.D.) are used throughout because their sharp points produce corona discharges at minimum field strengths and they can simultaneously be used to inject gaseous fuels or spray liquids. Formal results of this work are in preparation.

References

Papac, M.J., Dunn-Rankin, D., Stipe, C.B., and Lucas, D. (2003a) "N2 CARS Thermometry and O2 LIF Concentration Measurements in an Electrically Induced Microbuoyant Flame," *Combustion and Flame*, accepted for publication, January, 2003.

Papac, M.J., Posner, J.D., and Dunn-Rankin, D. (2003b) "Two Beam X-CARS in Dispersive Media," *Applied Spectroscopy*, **57**, 93--99.

Regele, J., Papac, M., Rickard, M., and Dunn-Rankin, D. (2002) "Effects of Capillary spacing on EHD Spraying from an Array of Cone-Jets," *Journal of Aerosol Science*, Volume 33, Issue 11, Pages 1471-1479.

Rickard, M. and Dunn-Rankin, D. (2002) "Experimental Study of Hybrid Electrohydrodynamic, Air-Assisted Atomizer," SAE paper 02-FFL-15, Powertrain and Fluid Systems Conference, San Diego.

Strayer, B.A., Posner, J.D., Dunn-Rankin, D., and Weinberg, F.J. (2002) "Simulating microgravity in small diffusion flames by using electric fields to counterbalance natural convection," *Proceedings of the Royal Society of London*, **458**, 2021, 1151—1166.

Strayer, B.A. and Dunn-Rankin, D. (2002) "Closed-Loop Electric Field Control of a Non-Premixed Flame," submitted to *Combustion and Flame*, June 2002.

Weinberg, F.J., Carleton, F.A., and Dunn-Rankin, D. (2002) "Electrically Charged Dispersions of Extinguishants for use in Microgravity Environments," Proceedings of the Second Mediterranean Combustion Symposium, Sharm El-Sheikh, Egypt, January 6—11; also submitted to *Combustion Science and Technology*.

ELECTRIC FIELD EFFECTS IN SELF-PROPAGATING HIGH-TEMPERATURE SYNTHESIS
UNDER MICROGRAVITY CONDITIONS

Unuvar, C.[1]; Fredrick, D[1]. M.; Shaw, B. D.[2]; Munir, Z. A.[1],
[1]Department of Chemical Engineering and Materials Science,
[2]Department of Mechanical and Aeronautical Engineering,
University of California, Davis

INTRODUCTION

Self-propagating high-temperature synthesis (SHS) has been used to form many materials [1]. SHS generally involves mixing reactants together (e.g., metal powders) and igniting the mixture such that a combustion (deflagration) wave passes though the mixture. The imposition of an electric field (AC or DC) across SHS reactants has been shown to have a marked effect on the dynamics of wave propagation and on the nature, composition, and homogeneity of the product (e.g., [2-5]). The use of an electric field with SHS has been termed "field-assisted SHS".

Combustion wave velocities and temperatures are directly affected by the field, which is typically perpendicular to the average wave velocity. The degree of activation by the field (e.g., combustion rate) is related to the current density distribution within the sample, and is therefore related to the temperature-dependent spatial distribution of the effective electrical conductivity of reactants and products. Furthermore, the field can influence other important SHS-related phenomena including capillary flow, mass-transport in porous media, and Marangoni flows. These phenomena are influenced by gravity in conventional SHS processes (i.e., without electric fields) [6-9]. As a result the influence of the field on SHS under reduced gravity is expected to be different than under normal gravity. It is also known that heat loss rates from samples, which can depend significantly on gravity, can influence final products in SHS (e.g., [10]).

This research program is focused on studying field-assisted SHS under reduced gravity conditions. The broad objective of this research program is to understand the role of an electric field in SHS reactions under conditions where gravity-related effects are suppressed. The research will allow increased understanding of fundamental aspects of field-assisted SHS processes as well as synthesis of materials that cannot be formed in normal gravity.

RESEARCH EFFORTS

The research will investigate the following topics.

(a)   The effect of the field on the dynamics of SHS waves in the absence of gravitationally induced buoyancy and phase separation effects. This aspect of the work includes the effect of the field on wave velocity and temperature, on the mode of propagation (e.g., planar or spinning) and its transition, and on the conversion profile. Implied in this part of the research is a significant effect of the field on interfacial energies, capillary spreading, mass transport in porous media, and electrically-induced Marangoni flows.

(b)   The effect of the field on phase formation and structure evolution in SHS. This research has practical implications as well as fundamental implications. We plan to investigate the role of the field on product formation (nature of the product, composition of phases, homogeneity of the phase(s), and grain size).

The work includes both terrestrial and reduced gravity experiments. The latter will be carried out in parabolic flights and in drop towers. The parabolic flight experiments will use existing facilities (COSYM™, developed by Guigne International, Ltd.) in NASA's KC-135 aircraft. Experiments will also performed at the NASA Glenn Research Center 2.2 Second Drop Tower.

The research will employ systems that produce varied amounts of liquid. For example, the systems Si + C and Mo + Si$_2$ allow investigation of the case where one reactant melts and the other does not, the system Ta + C allows investigation of a system where neither the reactants not the products melt, and the systems Fe + Al or Ti + Al allow investigation of the case where both reactants and products melt with high field activation. These systems are expected to respond to the gravity level in different ways, e.g., through liquid transport effects.

NORMAL GRAVITY EXPERIMENTS

Normal-gravity experiments have been performed to elucidate the effects of gravity by using different sample orientations for ignition: bottom, top or side. In all cases, reactant powder mixtures were pressed into pellets. The pellets were ignited at one end using a tungsten coil that was heated with current. In addition, a layer of chemical igniter material was sometimes placed on the end of a sample. This layer was composed of Ti, B and Fe$_2$O$_3$ and was typically about 3.2 mm thick. Sample pellets had dimensions of $25.5 \times 6.5 \times 15.5$ mm. Samples were generally ignited in ultrahigh-purity argon environments at 1 atm.

Investigation of the Si + C system with a high-speed camera (HSC) and a long-range microscope allowed us to examine microscale phenomena associated with combustion waves. Reactions with pulsating combustion fronts showed droplets of liquid silicon forming on the surface before the reaction and enlarging as the reaction wave pauses before the next pulse. Most of these droplets disappeared with the next pulse. All ignition orientations showed this behavior. In bottom ignition samples, reactant outgassing usually blocked the view of the wave front in the HSC because of buoyant flows. This was not observed in top ignition because the wave propagation was in the opposite direction of the convective flow.

The Ti + Al system was investigated with and without the use of an igniter layer for both top and bottom ignition orientations. The wave dynamics were investigated using Tracker 3, which is an Object Tracking and Image Processing software package supplied by NASA [11]. Tracker 3 is able to track the wave front position, which enables us to obtain wave velocity data. In the case of coil-only ignition (no igniter layer) at low applied fields, higher reaction temperatures and velocities existed for the bottom ignition orientation compared with top ignition (figure 1). This is likely a result of buoyant flows that would have been caused by the igniter coil in addition to the heated sample surface and flows inside the porous samples. These flows would have preheated the entire sample before ignition, causing higher wave velocities. This difference decreased as the applied field was increased (figure 1). It is hypothesized that this is because Joule heating within samples was dominant at higher field levels.

Ignition with an igniter layer is more robust and reliable then ignition achieved with just the tungsten coil. Therefore experiments were performed with the igniter layer, which showed similar effects at low applied fields. Velocity magnitudes converged at lower fields relative to results without the igniter layer with increasing fields. At high fields, the results from top ignition experiments showed increased velocity magnitudes relative to bottom ignition (figure 2).

Although the reactants are intrinsically electrically conducting, the green pellets were electrically insulating due to the low reactant density, which was about 59% of the theoretical maximum.

Figure 3 shows sample resistance data that were calculated using voltage and current data obtained during the experiments. The resistance falls quickly with formation of a molten phase and formation of the reaction zone. The resistance data show interesting results that can be related to changes in velocity at different fields. Resistances in certain ignition orientations tend to cluster together (figure 3). At low fields, resistances for the top ignition experiments had lower values than for bottom ignition. As the field was increased, resistances for both orientations became similar. However, at high fields, resistance of the top ignition experiments exceeded the bottom, similar to the velocity measurements (figure 3). These effects are believed to be due to the dominance of melting of the reactant (aluminum) at low fields and product at high fields.

Other efforts have involved quenching studies and development of gas flow visualization systems. Quenching experiments are performed by turning off the electric field during the combustion process, which causes the deflagration wave to quench under certain conditions, essentially freezing the structure of the wave. Wave structure will be analyzed using XRD, SEM and EPMA for both ignition orientations. For flow visualization, Schlieren and shadowgraph systems have been constructed at UC Davis using small, low-power components that can be employed in the reduced-gravity experiments.

We are also pursuing modeling studies. Computational efforts involve extending previous numerical models [3,12,13] to account for phenomena such as melting, capillary flows, buoyant flows and 3-d effects. We are evaluating use of the FlexPDE commercial finite element code [14] that may have the capability to model 3-d combustion with complex geometries. The asymptotic studies will be concerned with determining the influences of electric fields on stability and extinction of field-assisted SHS waves.

REDUCED GRAVITY EXPERIMENTS

Development of hardware for the reduced gravity experiments is proceeding. It is anticipated that parabolic-flight and drop-tower experiments will be performed during the current year of this cooperative agreement. These experiments will provide data on wave velocities, sample temperatures and sample microstructures for comparison with the normal-gravity experiments that have been performed.

REFERENCES

1. *Combustion and Plasma Synthesis of High-Temperature Materials*, edited by Z. A. Munir and J. B. Holt, VCH Publishers (1990).
2. Z. A. Munir, W. Lai, and K. Ewald, *U.S. Patent* No. 5,380,409, January 10, 1995.
3. A. Feng and Z. A. Munir, *Metall. Mater. Trans.*, **27B**, 581 (1995).
4. Z. A. Munir, *Z. Phys. Chem.*, **207**: 39 (1998).
5. H. Xue and Z. A. Munir, *J. Euro. Ceram. Soc.*, **17**: 1787 (1997).
6. K. G. Shkadinsky, G. V. Shkadinskaya, and B. J. Matkowsky, *Combust. Sci. Tech.,* **118**: 313 (1996).
7. O. Odawara, K. Mori, A. Tanji, and S. Yoda, *J. Mater. Synth. Process.,* **1**: 203 (1993).
8. K. R. Hunter and J. J. Moore, *J. Mater. Synth. Process.,* **2**: 355 (1994).
9. A. Mukasyan, A. Pelekh, A. Varma, A. Rogachev, and A. Jenkins, *AIAA J.,* **35**: 1821 (1997).

10. H. C. Yi, T. C. Woodger, J. J. Moore, and J. Y. Guigne, *Metall. Mater. Trans.,* **29B**: 889 (1998).
11. R. B. Klimek, T. W. Wright, and R. S. Sielken, NASA TM-107144 (1996).
12. A. Feng, O.A. Graeve, and Z. A. Munir, *Comput. Mater.Sci.*, **12**: 137 (1998).
13. E. M. Carrillo-Heian, O.A. Graeve, A. Feng, J. A. Faghih, and Z. A. Munir, *J. Mater. Res.,* **14**: 1949 (1999).
14. PDE Solutions, Inc., Antioch, CA 94531-4217.
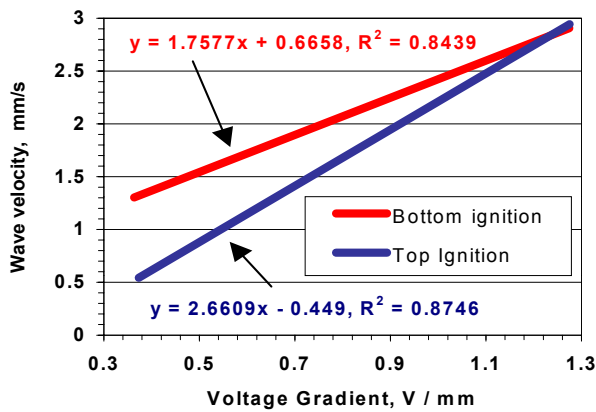
Figure 1. Wave velocity vs. field with coil-only ignition (no igniter layer) in the Ti + Al system.
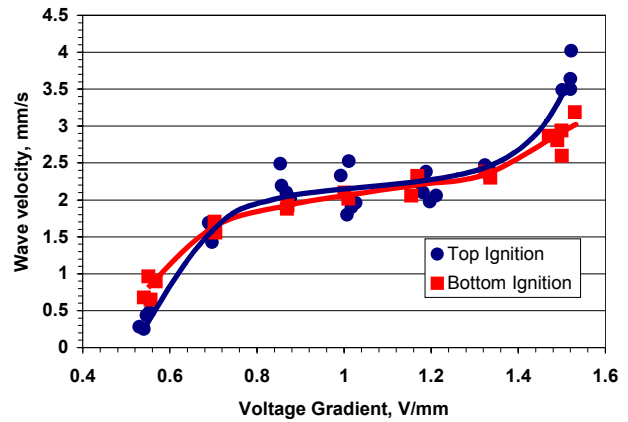
Figure 2. Wave velocity vs. field with coil and igniter layer in the Ti + Al system.
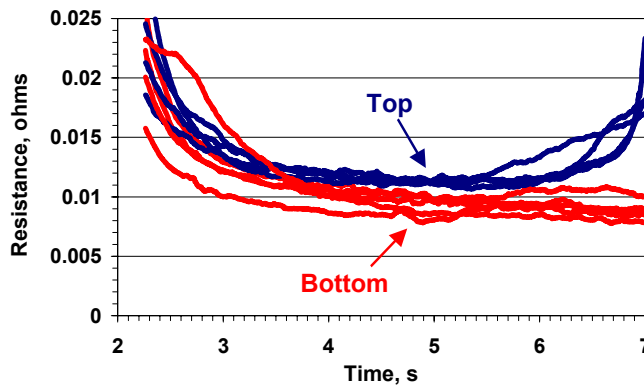
Figure 3. Comparison of resistances for bottom and top ignition at high field strengths (Ti + Al, voltage gradient ≈1.5 V/mm).

MODELS AND EXPERIMENTS OF LAMINAR DIFFUSION FLAMES IN NON-UNIFORM MAGNETIC FIELDS

J. Baker and R. Varagani
Department of Mechanical Engineering, University of Alabama, Tuscaloosa, AL 35487-0276
K. Saito
Department of Mechanical Engineering, University of Kentucky, Lexington, KY 40506-0108

INTRODUCTION

Non-uniform magnetic fields affect laminar diffusion flames as a result of the paramagnetic and diamagnetic properties of the products and reactants. Paramagnetism is the weak attraction to a magnetic field a material exhibits as a result of permanent magnetic dipole moments in the atoms of the material. Diamagnetism is the weak repulsion to a magnetic field exhibited by a material due to the lack of permanent magnetic dipole moments in the atoms of a material. The forces associated with paramagnetic and diamagnetism are several orders of magnitude less than the forces associated with the more familiar ferromagnetism. A typical example of a paramagnetic gas is oxygen while hydrocarbon fuels and products of combustion are almost always diamagnetic. The fact that magnets can affect flame behavior has been recognized for more than one hundred years. Early speculation was that such behavior was due to the magnetic interaction with the ionized gases associated with a flame. Using a scaling analysis, it was later shown that for laminar diffusion flames the magnetic field/ionized gas interaction was insignificant to the paramagnetic and diamagnetic influences.

In this effort, the focus has been on examining laminar diffusion slot flames in the presence of non-uniform upward decreasing magnetic fields produced using permanent magnets. The principal reason for choosing slot flames was mathematical models of such flames show an explicit dependence on gravitational body forces, in the buoyancy-controlled regime, and an applied magnetic field would also impose a body force. In addition, the behavior of such flames was more easily visualized while maintaining the symmetry of the two-dimensional problem whereas it would have been impossible to obtain a symmetric magnetic field around a circular flame and still visually record the flame height and shape along the burner axis. The motivation for choosing permanent magnets to produce the magnetic fields was the assumption that space-related technologies based on the knowledge gained during this investigation would more likely involve permanent magnets as opposed to electromagnets. While no analysis has been done here to quantify the impact that an electric field, associated with an electromagnetic, would have relative to the paramagnetic and diamagnetic interactions, by using permanent magnets this potential effect was completely eliminated and thus paramagnetic and diamagnetic effects were isolated.

MATHEMATICAL MODELING RESULTS

A modification of Roper's slot flame model [1] was used to develop an expression for the magnetically controlled flame height. To include the influence of a non-uniform magnetic field in Roper's formulation, the expression for the axial velocity must be modified. Assuming a magnetic field that is a linear function of the distance above the burner port, the expression for the axial velocity, v_z, is

$$v_z^2 = v_{fO}\left(1 + \frac{2}{Fr}\frac{z}{L_f} + \frac{1}{Fr_m}\left(\frac{\Delta B}{B_o}\right)\frac{z^2}{L_f^2} + \frac{1}{Fr_m}\frac{z}{L_f}\right)^{1/2} \qquad (1)$$

where v_{fO} is the initial speed of the fuel leaving the burner, z is the distance above the burner exit, L_f is the flame height, and $\Delta B / B_o$ is the change in the magnetic induction along the length of the flame divided by the initial magnetic induction at the burner exit. In addition, definitions of the Froude number and the magnetic Froude number used in the above expression may be found in a recent paper by Baker and Calvert [2]. For a magnetically controlled flame, the first two terms in the above expression may be dropped. The resulting expression for the magnetically-controlled flame height requires the solution to a nonlinear algebraic equation. Under the assumption that $\Delta B / B_o \ll 1$, a closed form solution is possible. As one would expect, this expression for a flame in the magnetically-controlled regime is similar to Roper's expression for a buoyancy-controlled flame, with the forces associated with gravity replaced by the forces associated with the magnetic field. While the closed form expression does provide insight into the fundamental relationships between the various dimensionless parameters, the associated assumption regarding the shape of the magnetic field does limit its practical value. At the time of writing, flame height information has been generated using solutions to the full nonlinear equation and a mathematical model for magnetically-controlled flame shape is been developed.

EXPERIMENTAL METHODS AND RESULTS

The initial experimental component of the Magnetically-Assisted Combustion Experiment (MACE) program examined, in a laboratory environment, the behavior of very small diffusion flames not exposed to an applied magnetic field [3]. The reason for this was that such flames, while in the buoyancy-controlled regime as defined by Roper, exhibit behavior qualitatively similar to microgravity flames. A scaling analysis conducted as part of this investigation provided insight into the role axial diffusion plays in determining slot flame height for these micro-flames and showed that micro-flames were not dynamically similar to microgravity flames. The initial microgravity results for slot flames with no applied magnetic fields were obtained through participation in the NASA Reduced Gravity Student Flight Opportunities Program. Examining laminar slot diffusion flames in both reduced gravity and in elevated gravity showed the Roper's expression for buoyancy-controlled flame height did, in fact, predict the flame heights for the conditions examined [4]. These initial investigations have laid the groundwork for the reduced gravity experiments involving laminar diffusion flames in non-uniform magnetic fields that are to be conducted in July 2003.

In parallel to the above investigations, a laboratory-based investigation of laminar diffusion flames in the presence of non-uniform upward decreasing magnetic fields has been conducted and experimental correlations of flame behavior have been developed [2,5]. This component of the MACE program also provided information as to the appropriate dimensionless parameters for a study of the impact magnetic fields have on diffusion flame behavior. During the past year, a holographic interferometer has been used to examine the temperature field in the vicinity of the flames exposed to non-uniform magnetic fields. Figure 1 provides a schematic diagram of the

holographic interferometry test cell. The two-exposure holographic interferometry technique provides images showing fringe patters that are directly related to temperature variations. For the present study, these fringe patters are only qualitative in nature due to the fact that the exact spatial concentration distribution of the product and reactant species is not known. This technique does provide qualitative information, however. Figure 2 shows sample results of optical flame images, holographic interferograms, and the temperature fields produced using the holographic interferograms. A preliminary examination of the holographic interferometry data indicated that that application of a non-uniform upward decreasing magnetic field decreased the maximum flame temperature with only a few exceptions [6]. This was somewhat unexpected as previous researchers have generally reported an increase in flame temperature, although there have been reports of investigations where the flame temperature decreased with the application of a non-uniform magnetic field. The exact reason for this unexpected behavior has yet to be resolved. It could be possible that, as a result of the geometric configuration of the magnetic prisms, a magnetic curtain was formed reducing the amount of oxygen available to the flame. Note also that the variation in the magnetic field was accomplished by moving the prisms in or out relative to the burner. The close proximity of the prisms would serve as a heat sink and thus could also be responsible for the observed temperature decreases. Additional investigation into this behavior is on-going.

CONCLUSIONS

The Magnetically-Assisted Combustion Experiment (MACE) program is examining the fundamental interaction between non-uniform magnetic fields and laminar diffusion flames. Both mathematical and experimental models have been constructed as part of the investigation thus far. Holographic interferometry has been used to examine the temperature field in the vicinity of the flame and has produced some unexpected results. Reduced gravity data has provided insight into the behavior of laminar slot flames when no magnetic field is applied and this information is being used to guide upcoming reduced gravity experiments involving an applied non-uniform magnetic field.

ACKNOWLEDGEMENTS

REFERENCES

1. Roper, F. G., 1977, "The prediction of laminar jet diffusion flame sizes: Part I. Theoretical Model," *Combustion and Flame,* Vol. 29, pp. 219-226.
2. Baker, J. and Calvert, M.E., 2003, "A Study of the Characteristics of Slotted Laminar Jet Diffusion Flames in the Presence of Non-Uniform Magnetic Fields," accepted for publication, *Combustion and Flame*.
3. Baker, J., Calvert, M.E., and Murphy, D.W., 2002, "Structure And Dynamics Of Laminar Micro-Slot Jet Diffusion Flames," *Journal of Heat Transfer*, Vol. 124, No. 4, pp.783-790.
4. Srireddy, M. and Baker, J., 2003, "Influence of Gravitational Level on Laminar Diffusion Slot Flames," accepted for presentation, 41st Aerospace Sciences Meeting and Exhibit, AIAA Paper No. AIAA-2003-0806, Reno, Nevada.

5. Calvert, M.E., Baker, J., and Saito, K., 2002, "Laminar Slot Diffusion Flames in Non-Uniform Magnetic Fields: Experimental Flame Height Correlation," proceedings of the 2002 Spring Technical Meeting of the Central States Section of the Combustion Institute, 7-9 April 2002, Knoxville, Tennessee.

6. Varagani, R. and Baker, J., 2003, "Temperature Measurements of Laminar Diffusion Flames in Non-Uniform Magnetic Fields Using Holographic Interferometry," proceedings of the 2003 Third Joint Meeting of the U.S. Sections of the Combustion Institute, 16-19 March 2003, Chicago, Illinois, USA.
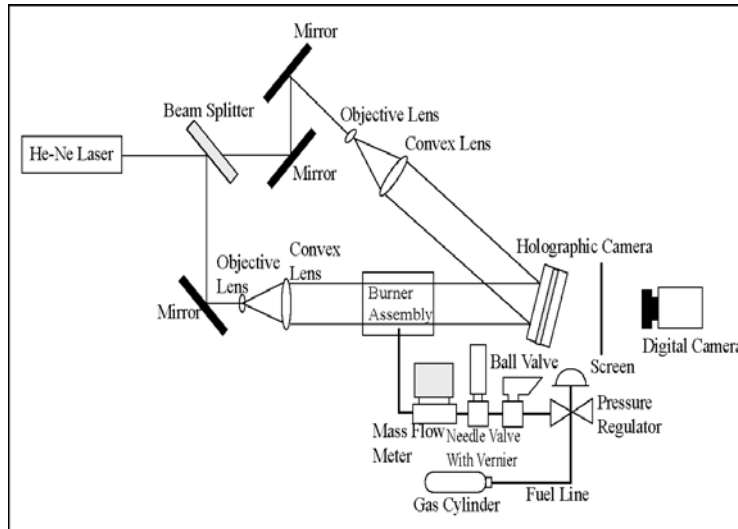
Figure 1: A shematic diagram of the holographic interferometer test cell.

$B_o(dB/dy)=244.26 \ T^2/m$

$B_o(dB/dy)=0 \ T^2/m$
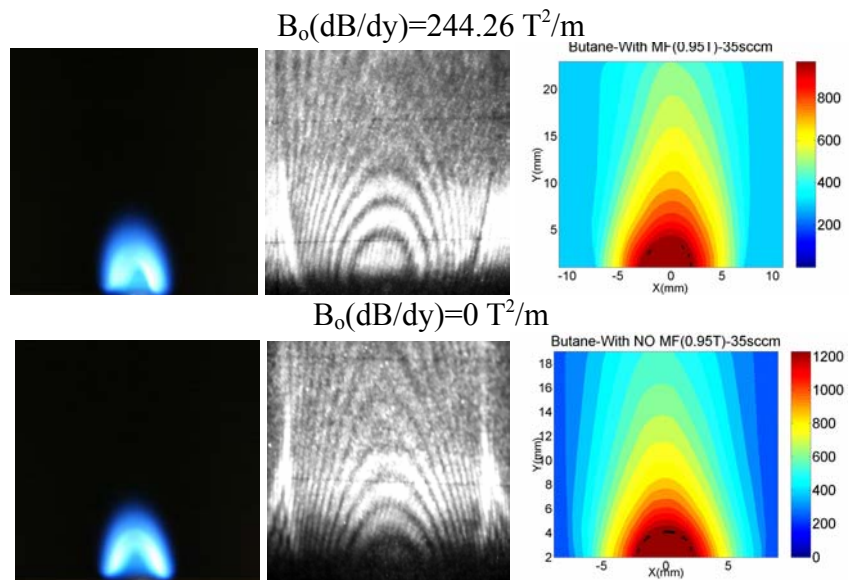
Figure 2: Sample butane flame data obtained from (left to right) : visual images, holographic interferograms, and temperature contours. The flow rate for both cases is 35 cm^3/min.

SOME RESPONSES OF SMALL DIFFUSION FLAMES TO ULTRASONIC RADIATION

David B. Thiessen, Wei Wei, and Philip L. Marston
Department of Physics, Washington State University, Pullman, WA 99164-2814

INTRODUCTION

As an extension to our NASA supported research on the stabilization of liquid bridges with acoustic radiation pressure [1], we examined some aspects of the response of gaseous flames to the radiation pressure of ultrasound. The radiation pressure is the result of the time-averaged (2nd order) stresses of ultrasound. Radiation pressure has been widely used to manipulate liquid drops in air [2] and to a lesser extent liquid bridges in air [3]. Our observations show that flames have significant responses to ultrasonic radiation pressure and this is supported by approximations for the radiation pressure. Ultrasound is expected to alter some aspects of the dynamics of flames in reduced gravity because the radiation force-per-volume on the flame may be made to be similar in magnitude to the buoyant force-per-volume on flames in normal gravity. Thus it may prove possible to use ultrasound to reintroduce some aspects of buoyancy on non-premixed (diffusion) flames in reduced gravity. Aspects of the radiation pressure on flames are also relevant to understanding the acoustic control of hot fluid objects. We observed in normal gravity the responses of small diffusion flames to standing ultrasonic waves. The direction of the response was found to agree with calculations of the radiation pressure on flames. In agreement with our predictions of the distribution of ultrasonic radiation stress on the flame, the flame is attracted to an acoustic pressure antinode and becomes slightly elliptical with the major axis in the plane of the antinode. The radiation pressure distribution and the direction of the radiation force follows from the dominance of the dipole scattering of sound by a small flame. We also observed that steady or modulated ultrasonic traveling waves modified the flicker of small diffusion flames.

DEMONSTRATION OF DEFORMATION AND DEFLECTION OF SMALL DIFFUSION FLAMES IN AN ULTRASONIC STANDING WAVE

In the following demonstration, high-intensity ultrasound is produced by a compact transducer operating at 29.8 kHz which has been developed for capillary-bridge stabilization [3]. Sound radiates from a rectangular aluminum plate driven in an anticlastic bending mode with two nodal lines approximately parallel to the long edges of the plate. This produces a fairly uniform sound field over the long dimension of the plate. An ultrasonic standing wave is established with a carefully positioned curved reflector. The standing wave of two wavelengths in width is produced between the transducer plate and a curved reflector positioned parallel to the plate with a spacing of 2.4 cm (see schematics in **Fig. 1**). A microphone embedded in the reflector is used to tune both the transducer frequency and the distance between the plate and reflector to achieve the highest amplitude standing wave. In order to demonstrate some of the effects of a high-intensity ultrasonic standing wave on a flame we used a very small flame to avoid detuning of the standing

wave resonance. Heating of the air in the gap between the plate and reflector changes the sound speed which leads to detuning if the frequency and/or spacing are not adjusted. A small natural gas diffusion flame is produced from gas released by a hypodermic needle (with square end) with gas flow rates on the order of 1 cm^3/s. The inside diameter of the needle was 0.4 mm.

In one experiment the configuration shown in the top schematic of **Fig. 1** is used where the flame is positioned at the pressure antinode of the standing wave. The gas flow rate was 0.8 cm^3/s. This configuration should minimize the volume of air within the standing wave which is heated by the flame and thereby minimize detuning. The flame is vertically positioned in the most intense part of the standing wave. **Figure 1(a)** shows a flame of circular shape when viewed from above in the absence of sound. In **Fig. 1(b)** the ultrasonic standing wave is turned on and the flame shape becomes elliptical with long axis lateral to standing wave direction. The orientation of the observed ellipse is in agreement with our predictions based on the spatial distribution of the radiation stress on a small flame that is positioned at the pressure antinode.

If the needle is translated away from the plane of the pressure antinode, the flame tilts back toward the pressure antinode. Thus the flame appears to be attracted to the pressure antinode of the standing wave. **Figures 1(c)** and **(d)** show a side view of the flame without and with sound respectively. The flame height is seen to decrease somewhat with the sound on. Note that the images in **Figs. 1(b)** and **(d)** are for nearly the same sound level but the configuration was slightly different as shown in the corresponding schematics to the right of the images. The same phenomenon is seen in either configuration and detuning was not serious for either case.

For the configuration of **Fig. 1(d)** it was found that when the gas flow rate was increased significantly, the ultrasound could stabilize the flame against blowout. With a stabilized flame in the standing wave the sound field could be gradually turned down until the flame would lift off the needle and blow out. The degree to which the natural blow-out limit could be exceeded has not been measured. The last observation with a standing wave is that a lifted flame could be stabilized with the ultrasound for a gas flow rate which was below the natural lift-off value.

EFFECTS OF CW ULTRASONIC TRAVELING WAVES ON FLAME FLICKERING DYNAMICS

A high-intensity ultrasonic traveling wave is produced by using the 29.8 kHz transducer without the reflector. Sound radiates from the rectangular aluminum plate producing a fairly uniform sound field over a vertical dimension of about 3 inches. A vertical natural gas diffusion flame was produced from a 2 mm diameter nozzle with a gas flow rate of 5 cm^3/s so that the flame is initially parallel to the transducer plate. The center of the nozzle was positioned about 3.6 cm from the transducer plate, with a vertical position level with the bottom of the plate. The apparatus is contained within a cubic box with dimensions of 60 cm on a side to avoid the effect of drafts on the flame. The box is ventilated at the top. A large steel sphere is positioned at 14 inches from the transducer plate to scatter the sound and avoid setting up a planar standing wave between the transducer and the wall of the box. Flame dynamics are monitored with a video CCD camera with a shutter speed set at 1/1000th of a second and 60 video fields per second. The camera alignment is tilted slightly from the perpendicular with the sound direction.

In the absence of a sound field the flame flickers in a varicose mode as seen in **Fig. 2(a)**. A small region on the edge of the flame was imaged with a lens onto a photodetector, the optical

axis being at 90º to the sound beam. An FFT of the photodetector signal gave a main peak of the flicker at 13.0 Hz. For a continuous sound field, the flame deflects away from the transducer as seen in **Fig. 2(b)**, the flicker is somewhat reduced and the average height of the flame is also reduced. The flame is narrower from the viewpoint of the camera, however it is actually being flattened somewhat so that its width increases in the direction perpendicular to the sound direction. For **Fig. 2(b)** the peak acoustic pressure above the nozzle at the vertical center of the plate was measured to be 192 Pa. The flame in **Fig. 2(b)** is tilted at an angle of $\vartheta = 25°$ from the vertical. By neglecting the inertia of the jet the ratio of radiation-to-buoyant force density is estimated to be $\tan\vartheta = 0.47$ which is the general magnitude estimated for a flame of this size.

We also observed that the flame flickering dynamics could be modified by amplitude modulation of the ultrasound. The transducer drive could be amplitude modulated at different frequencies with a square wave in order to investigate the effect on flame dynamics. The flickering dynamics (as recorded by the video images and the photodetector signal) was significantly modified in response to the modulated ultrasound.

CALCULATED RADIATION PRESSURE DISTRIBUTION AND RADIATION FORCE

Calculations explain some aspects of these observations of the response of small flames to standing and traveling ultrasonic waves. The flame is approximated as a homogeneous hot region of gas having an abrupt boundary. Calculations in which the flame is modeled as a sphere (leading to 3-dimensional scattering of sound) or a cylinder (leading to 2-dimensional scattering), give similar conclusions. The hydrostatic pressure within the flame is nearly the same as that of the surrounding air. It may be shown that the ratio of the adiabatic compressibility β of the flame to that of the air is approximately the reciprocal of the ratio of the polytropic exponents γ of these gases. Since γ is dominated by the large volume fraction of nitrogen in both the flame and the surrounding air, it follows that $\beta_{flame}/\beta_{air}$ is close to unity. Consequently from the theory for the scattering of sound from fluid objects at long wavelengths [4], it follows that the scattering should be primarily that of an acoustic dipole when ka is small where a is the radius of the flame and $k = 2\pi/\lambda$ where λ is the acoustic wavelength in air. Calculations of the scattering by small flames indicated scattering is similar for the range of flame temperatures anticipated for small diffusion flames (1500 K - 2200 K).

The observed result in **Fig. 1(b)** that small flames at an acoustic pressure antinode become oblate is consistent with the sign of the quadrupole projection of the radiation pressure for spheres (Eq. (2) of [5] and [6]). The radiation pressure distribution on a cylinder was evaluated by applying the formulation for scattering, summarized in [3] and [7]. The experiments show that when the flame is displaced slightly from the pressure antinode, the radiation force is established that tilts the flame toward the antinode. This is in agreement with the sign of the force predicted for small hot fluid spheres [8] and by extension of the cylinder formulation [7].

The radiation pressure on fluid spheres in a traveling or "progressive wave" is characterized by a dimensionless force function commonly denoted by Y_p [9]. Evaluation of Y_p for small flames indicates that it should not be difficult to obtain a ratio of radiation force-to-flame volume of 20 N/m^3. Consequently, radiation forces similar in magnitude to buoyancy present in normal gravity should be achievable. This is consistent with the observations shown in **Fig. 2(b)**.

REFERENCES

[1] Our research on the radiation pressure on fluids is supported by NASA grant NAG3-2378.

[2] E. H. Trinh, P. L. Marston, & J. L. Robey, J. Colloid and Interface Sci. **124**, 95-103 (1988).

[3] M. J. Marr-Lyon, D. B. Thiessen, & P. L. Marston, Phys. Rev. Lett. **86**, 2293-2296 (2001); **87** (20) 9001 (2001).

[4] L. D.Landau & E. M. Lifshitz, *Fluid Mechanics* (Pergamon Press, London, 1959).

[5] P. L. Marston, et al., J. Acoust. Soc. Am. **69**, 1499-1501 (1981); **71**, 511 (1982).

[6] P. L. Marston, J. Acoust. Soc. Am. **67**, 15-26 (1980); **71**, 511 (1982).

[7] M. J. Marr-Lyon, Ph. D. Thesis (Washington State University, Pullman WA, 2000).

[8] K. Yosioka & K. Kawasima, Acustica **5**, 167-173 (1955).

[9] T. Hasegawa, J. Acoust. Soc. Am. **65**, 32-40 & 41-44 (1979).
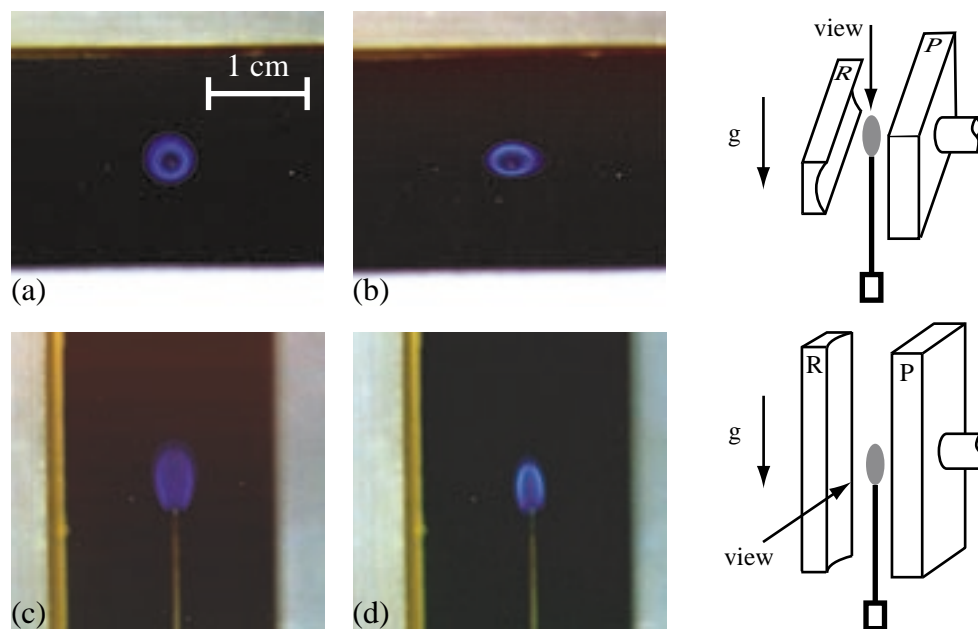
Figure 1: (a) & (b) Top view of flame for configuration shown at top right, (a) without sound and (b) with sound. (c) & (d) Side view of flame for configuration at bottom right, (c) without and (d) with sound. In schematics, R=reflector, P=transducer plate.

Figure 2: (a) Flickering flame in absence of sound and in (b) with CW sound (traveling wave) showing the deflection of the flame by the sound field and the reduction in flicker. The transducer plate is visible at the right side of the figures with the sound traveling from right to left in (b).
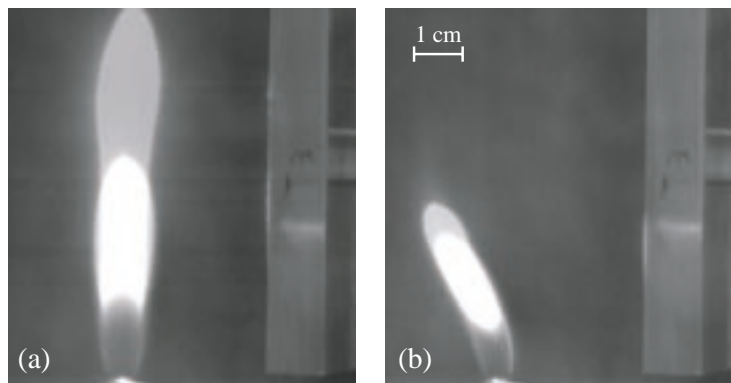
THE CIR INSERT EHPI (former: DCI)
EUROPEAN HIGH PRESSURE / HIGH TEMPERATURE INSERT

Ch. Eigenbrod, J. Siemer
ZARM-Technik GmbH, Bremen, Germany
M. Jordan[#], F. Bellossi[❖], Ch. Schmidt-Harms[◆]
[#]Astrium GmbH, Space Infrastructure, Friedrichshafen, Germany
[❖]EADS Launch Systems, Bordeaux, France
[◆]ESTEC, Noordwijk, The Netherlands

Abstract

The European Space Agency (ESA) has performed a feasibility study for an experiment insert to NASA´s CIR enabling experiments under conditions of elevated pressure and/or temperature. Initially based upon a European microgravity research program on droplet- and spray vaporization and combustion, the industrial study team was additionally collecting the different interests of scientists from Europe, Japan and the U.S.A. on such a facility in order to enhance the applicability of the inserts basic design. As the outcome of the study an insert appears to be feasible that allows for experiments on droplet and droplet array vaporization-, autoignition- and combustion investigations under pressure conditions up to 50 bar and initial temperature conditions up to 1000 K. The insert´s structure is modular to enable later modifications for other experiments needs. These experiments could be on spray- and particle cloud combustion or on investigations on autoignition of prevaporized premixtures. The study was also regarding the compatibility of the experiments with the CIR´s diagnostic environment.

Introduction

Technical combustion is mostly performed under elevated pressure and temperature conditions. This is not only to increase the volumetric power of machinery thus making it smaller, but also affects the physical and chemical interactive combustion processes. Basic research on generic partial problems, e.g. in microgravity conditions, therefore sometimes requests for an experiment environment of elevated pressure and/or temperature conditions. As on one hand the European microgravity combustion research program focuses on high pressure and high temperature related problems and the development of an insert allowing for such investigations is currently not foreseen on NASA´s side on the other hand, sharing of capabilities appears to be reasonable.

Interests on such a facility are ranging over the whole area of combustion research. As a EHPI insert cannot be realized by only confining the existing or planned inserts in a heatable and pressurizable vessel a re-assessment and redesign of all experiment specific equipment is required. As attempts for an all-in-wonder will fail for different reasons, such an insert needs to be specialized in application as the already scheduled inserts. The insert described hereafter is foreseen to enable experiments on droplet combustion issues. Nevertheless, the modular structure of the insert shall allow for modifications in order to later facilitate experiments that are presently not represented by the insert, its experiment specific equipment or the diagnostics and measurement environment.

Process Chamber (PrC)

The process chamber depicted in fig.1 is a pressurized component consisting of two parts. The yellow section contains the experiment furnace and is equipped with four sapphire windows to allow for optical access. The blue section contains the experiment specific equipment (see chap. ESE). After opening the door of the CIR chamber, the insert can be maintained in three ways. 1. The maintenance access can be opened to exchange fuel reservoirs, suspender rigs or the suspender lift. 2. The blue section can be removed for exchange to another experiment specfic equipment or can be transferred to e.g the microgravity science glove box (MSG) for cleaning, repair or modifications. 3. After removing the blue section, the experiment furnace can be withdrawn from the yellow section and be exchanged. The cooling circuits serve for balancing heat losses.
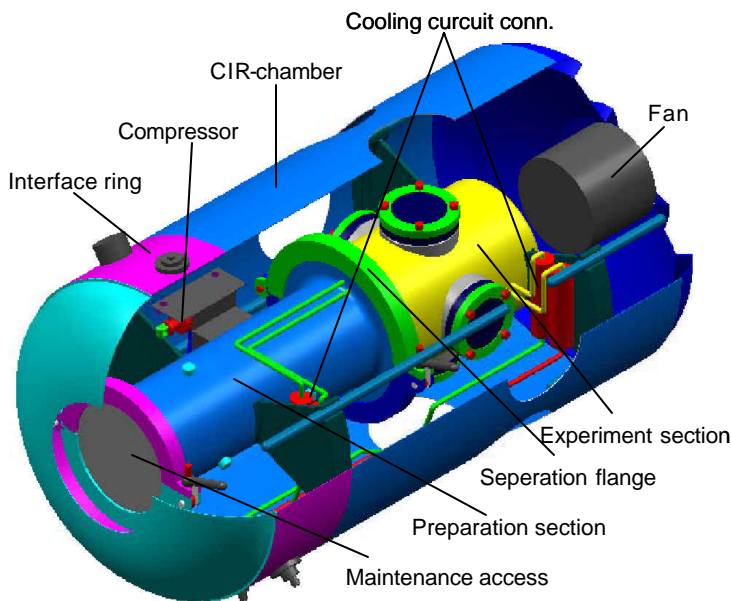
Fig. 1: EHPI process chamber installed to the CIR combustion chamber

Exhaust gases from a single experiment shall be released into the CIR combustion chamber. The CIR-fan will be used to homogenize the gases in the CIR combustion chamber before the compressor refills the gas into the insert. After several single experiments, the whole gas is circulated through adsorber cartridges and the CIR mass spectrometer back into the CIR combustion chamber. Exhausts are exchanged to oxygen. By doing so, initial experiment conditions can be kept mostly constant without exceeding the limitations in oxidizer consumption.

The experiment section is foreseen to contain two different experiment cells (see fig.2). A small cell of internal dimensions of 50 mm diam. and 80 mm in length is heatable up to 1000 K and is foreseen for droplet and droplet group experiments on transcritical vaporization and autoignition. The large cell of 100 mm diam. and 200 mm length is heatable up to 370 K and is foreseen for droplet array combustion experiments. Both cells are heated by means of resistance heaters, equipped with an appropriate thermal insulation and encapsulated by two cooling circuits. The cooling circuit also facilitates to keep the experiment preparation section (containing e.g. the fuel reservoir) at room temperature. A flipping door prevents from radiation losses towards the preparation section.

Resistance heated cores

Thermal insulation

Cooling loops
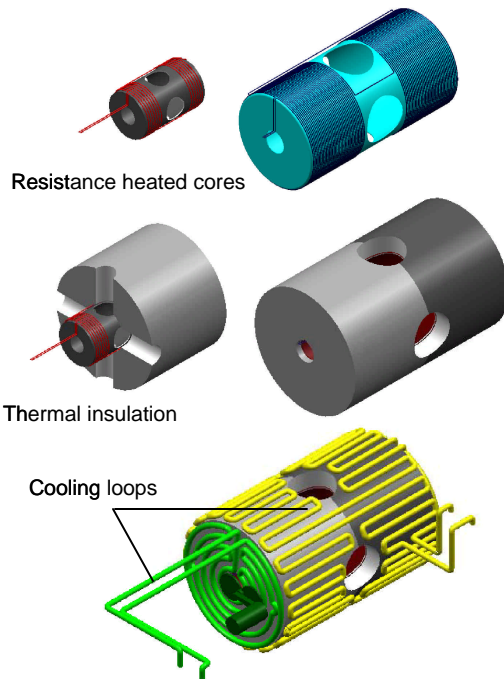
Fig. 2: Two experiment cells
50mm diam. x 80mm (1000 K max.) 100mm diam. x 200mm (370 K max.)

The dimensions of the large cell were chosen in order to allow for droplet arrays of maximum length or number of droplets respectively. The fig.3 shows that it is not the experiment section to determine the maximum experiment volume but that it is given by the length of the preparation section to fit between experiment section and the CIR-access door. The sketch shows a 12 droplet array suspender (10mm center spacing) at three positions. The position mostly left is for fuelling of the right end droplet, the intermediate position is for generation of the left end droplet and the right position is the experiment position.
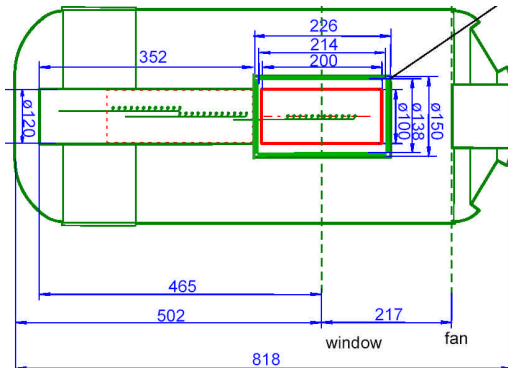
Fig. 3: Dimension of the largest practicable droplet array (e.g. 12 droplets, 10mm center spacing) is given by the distance between windows and CIR-access door

Even though for experiments on droplet array combustion applying the assisted ignition technique another insert layout could be possible, it needs to be compatible with droplet vaporization- and autoignition experiments where a mostly stepwise transfer of the droplets from the fuelling area into the experiment section is most important and thus a linear layout is inevitable.

A thermal analysis of the insert was performed showing that both variants are in-line with the power budget of the CIR.

Experiment Specific Equipment (ESE)

The study on ESE items was assessing the droplet suspension technique, the droplet transfer, the accurate droplet generation, methodes to monitor fueling, droplet sizes, suspender and window conditions. Some suggestions for window cleaning attempts were made that might be necessary when applying laser diagnostics. Fig.4 depicts a possible droplet transfer unit. The unit consists of a precision rail, a toothed belt drive and a stepper device. The transfer of a single droplet into the experiment position can be performed within 155 ms, 40 ms of which are in the

heat affected area. The optimal ramps for acceleration and deceleration need to be programmed in accordance with temperature, pressure, fuel type, droplet size, suspender type etc. the fig. also depicts a droplet generation device consisting of a piezo driven injector head mounted to a x-y microtranslator that is required when 3D suspender arrays shall be fuelled. Injector can be doubled in order to facilitate online blending of fuels. Monitoring tasks in the preparation section shall be taken over by a CCD-camera. The images shall be autonomously captured and evaluated by the experiment control unit (CU). The CU will transfer single images to outside of the facility for crew or to-ground information.

Fig. 4: Experiment Specific Equipment
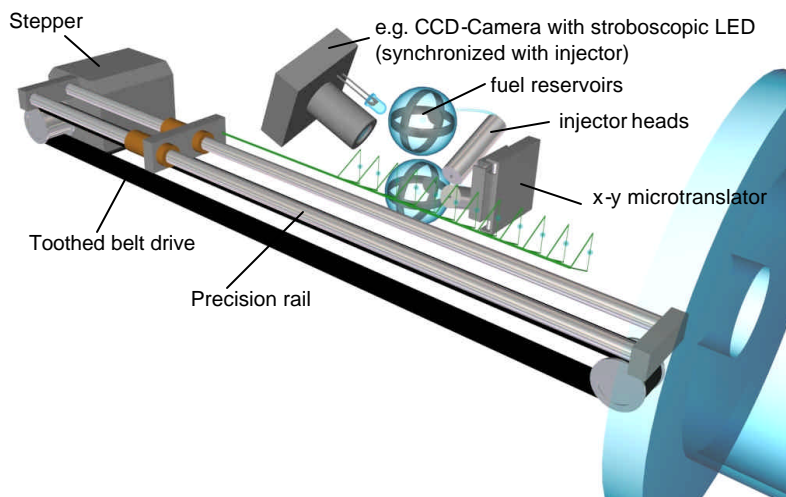
Diagnostics

All equipment of the CIR-optical bench will be also suitable for the EHPI experiments. Additional interest in the Advanced Disc Laser (ADL) is given through the wanted information on precursor reactions in autoignition (HCOH-LIF) and flame propagation (HCOH- and OH-LIF) through droplet arrays. Experiments on transcritical droplet vaporization will make use of the IR-camera system with additional IR-backlit illumination and differential optics for Differential Optical Absorption Spectroscopy purposes.

References

M. Jordan, Ch. Schmidt-Harms, "Droplet Combustion Insert - Investigator Working Group Meeting Report" Phase A Study, 2002

J. König, Ch. Eigenbrod, W. Triebel, D. Müller, M. Jordan, "EHPI and ADL: Instrumentation for Combustion Research onboard the ISS derived from Drop Tower Experiments", Proc. Drop Tower Days, 2002

S. Schnaubelt, O. Moriue, T. Coordes, C. Eigenbrod, H.J. Rath, "Detailed Numerical Simulations of the Multi-Stage Self-Ignition Process of n-Heptane Isolated Droplets and Their Verification by Comparison with Microgravity Experiments", Proc. Combust. Inst. 28, pp. 953-960, 2000

O. Moriue, C. Wendt, Ch. Eigenbrod, H. Rath, "Measurement of Vapor Concentration around an Evaporating Fuel Droplet by Infrared Absorption Technique", Proc. Combust. Inst. 29, to be published

EXPERIMENTAL STUDY OF CLOTHING FLAMMABILITY AND ASSOCIATED SKIN BURN DAMAGE IN MICROGRAVITY

Jane M. Cavanagh, David A. Torvi[1] and Kamiel S. Gabriel
Department of Mechanical Engineering, University of Saskatchewan
Saskatoon, SK S7N 5A9, Canada

INTRODUCTION

This research is an experimental study of flame spread over fabrics and the resulting burn injury which can occur. The experiment is intended to simulate the fire behaviour of test fabrics used in clothing in a microgravity environment such as a shuttle or the international space station. Previous fabric flammability tests done in microgravity are not numerous. In fact, most of the flammability data used is from ground-based tests that are then assumed to be the worst-case scenario in microgravity. Past experiments in microgravity have used the NASA NHB8060.1 Upward Flammability apparatus, the NIST lateral ignition and flame-spread tester (LIFT), and a cone calorimeter. Information was gathered from these tests on flammability, ignitability and lateral flame spread, and rate of heat release. While most of the materials passed the NASA test, which is often used to obtain flammability data, some materials did not perform well in the other tests. Therefore, a single test may not be an accurate representation of the performance of a material. No substantial experimental work has been done to give information about burn injury of skin in microgravity. Some research has been done in this area under normal gravity (e.g., Backer, et. al. [1]).

EXPERIMENTAL APPARATUS AND PROCEDURE

This experiment is being designed to fit in the Spacecraft Fire Safety Facility (SFSF), which is an experimental rig flown on NASA's KC-135 aircraft. It will make use of the existing specimen holder, which is a steel plate 250 mm by 470 mm by 0.4 mm. There will be a cut-out in the centre of the specimen holder, slightly smaller than the specimen itself. This will allow the specimen to be open to the flame for the test. The specimen holder will also have four corner pins to attach the specimen to the holder. The size of the specimen is taken from the Canadian General Standards Board (CGSB) Vertical Flame Resistance Test [2]. This test was chosen as it places the fabric in a vertical orientation, and the dimensions of the fabric specimen (200 mm by 80 mm) are close to the size of the opening in the existing SFSF specimen holder. The apparatus is shown in Figures 1 to 3.

At the onset of the experiment, the specimen will have to be ignited for flame spread to begin. For this purpose, the SFSF's hot wire ignition source will be used. Use of the hot wire allows control over the time which heat is applied to the fabric specimen, which ensures that ignition will occur. The ignition wire will be placed across the middle of the specimen to allow flame spread in any direction.

---

[1] Corresponding Author: Phone (306) 966-5493, Fax (306) 966-5427,
Email: David.Torvi@usask.ca
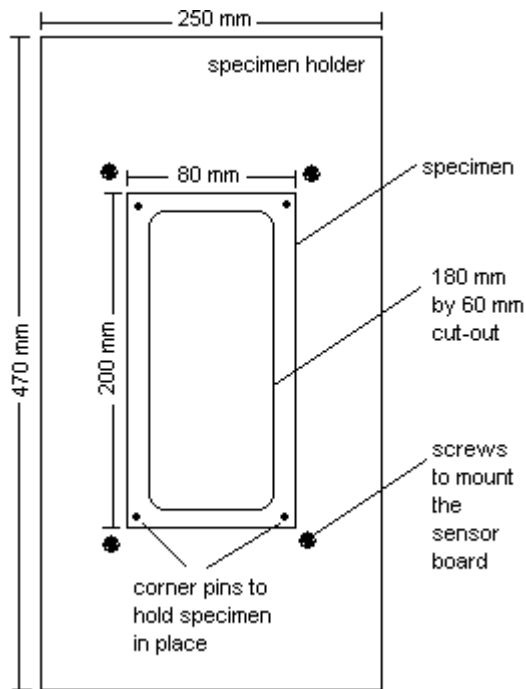
Figure 1: Specimen Holder

Figure 2: Sensor Board

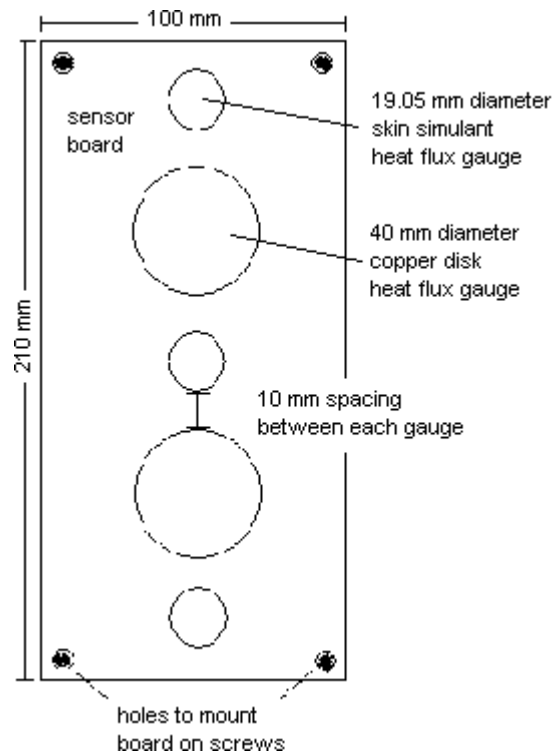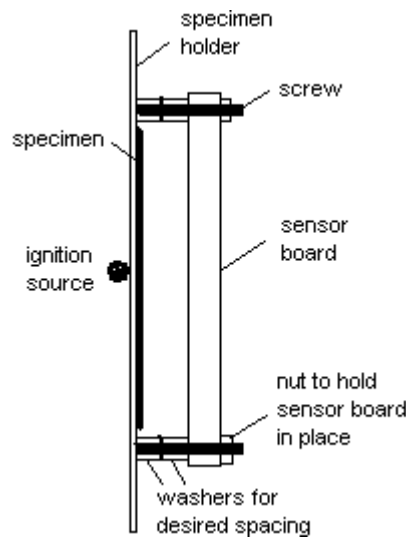Figure 3: Side View of the Experimental Apparatus

Measurements taken during the experiment include temperatures and heat fluxes. Thermocouples located on the backside of the fabric specimens will be used to obtain a temperature profile along the fabric. Due to the high temperature exposure, 36 and 40 gauge type K thermocouples will be used. Heat flux gauges will gather the data needed to compute

time to second and third degree burn of human skin. The heat flux gauges will be mounted in an insulating kaowool sensor board, located a specified air gap distance away from the back of the specimen. The locations of the gauges on the sensor board are shown in Figure 2. Two types of heat flux gauges will be used. Skin simulants can be used to provide information on time to both second and third degree burns, using Henriques' burn integral [3]. They have been successfully used in thermal mannequin tests of protective clothing (e.g., Dale et al. [4]). The other heat flux gauge used is a copper disk that acts as a calorimeter. These sensors can provide information on time to second degree burn of human skin by using the Stoll criterion [5]. The copper disks are used in various standards, including the radiant protective performance test [6]. Using both skin simulants and copper disks in these tests will allow a comparison to be made between the performance of each of the two types of sensors in microgravity fabric tests.

The sensor board has been designed to be easily positioned different distances from the back of the fabric specimen. This will allow the test to simulate cases when a fabric is in contact with skin or when there is an air space between fabric and skin. This is accomplished using four screws, mounted on the specimen holder just outside the corners of the specimen. Multiple washers, 1/8 in. thick, can be placed on the screws to maintain a desired spacing between the sensor board and specimen holder. A side view of the apparatus is shown in Figure 3.

During an experiment, temperature, pressure, air flow, and oxygen concentration within the combustion chamber will be kept constant using the control system on the SFSF. Experimental variables will include fabric types and weights, as well as fabric-skin spacing.

A few different types of fabrics will be tested, such as cotton and flame resistant aramids, which are worn at different times during missions. Various fabric weights, typical of those worn by astronauts, will be used. It has been found in previous ground-based tests [1] that varying the weight of cotton fabrics will affect flame spread and skin burn damage.

The width of the air gap between the fabric and the skin will be varied in this experiment by adjusting the location of the sensor board. The size of the air gap can determine whether or not convective cells will form at normal gravity levels. This study will examine the differences in heat fluxes in microgravity in the absence of convection cells. From previous ground-based tests [1], it is expected that varying the air gap width will also affect skin burn damage.

EXPECTED RESULTS

Data obtained from these microgravity experiments will include flame spread rates, heat fluxes, and temperatures. The flame spread rates will be visually observed, both during the experiment, and from the videotape afterwards. Heat fluxes will be obtained at various locations along the path of flame spread. As mentioned above, this information can be used to predict burn damage to human skin. A group of temperature readings on the fabric will also be gathered along the path of flame spread. This information may prove important for future modelling of flame spread over fabrics in microgravity.

Results from this experiment will also be compared to ground-based experiments. The identical test will be conducted in normal gravity, so that the microgravity results can be directly

compared with results under normal gravity. This should indicate if flame spread and burn injury increases or decreases in microgravity. The ignition source will then be changed from a hot wire to a burner, as used in many standards (e.g., [2]). By running the test with both the burner and the hot wire ignition sources, the results of the microgravity testing can be tied back to an existing standard that is typically used to provide information on the fire performance of fabrics.

CONCLUSIONS

This paper describes an experiment designed to investigate the flammability of various fabrics used by astronauts and the skin burn damage that can result if these fabrics ignite. This research will provide important information on the similarities and differences between the fire performance of textiles when subjected to the same conditions under normal gravity and in microgravity. This information can be used to assess the suitability of current testing procedures and if necessary, to develop new tests more appropriate to the microgravity environment. The overall goal is to ensure astronauts will be sufficiently protected from possible fires while in orbit.

ACKNOWLEDGMENTS

REFERENCES

[1] S. Backer, G.C. Tesoro, T.Y. Toong and N.A. Moussa, "Textile Fabric Flammability", The MIT Press, Cambridge, Massachusetts, 1976.
[2] National Standard of Canada, CAN/CGSB-4.2 No.27.10-2000, "Textile Test Methods: Flame Resistance – Vertically Oriented Textile Fabric or Assembly Test", September 2000, Canadian General Standards Board, Ottawa, Canada.
[3] F.C. Henriques Jr., "Studies of Thermal Injury V. The Predictability and the Significance of Thermally Induced Rate Processes Leading to Irreversible Epidermal Injury", Archives of Pathology, Vol. 43, 1947, pp. 489-502.
[4] J.D. Dale, E.M. Crown, M.Y. Ackerman, E. Leung and K.B. Rigakis, "Instrumented Mannequin Evaluation of Thermal Protective Clothing", Performance of Protective Clothing: Fourth Volume, ASTM STP 1133, J.P. McBriarty and N.W. Henry, Eds, American Society for Testing and Materials, West Conshohocken, PA, 1992, pp. 717-733.
[5] A.M. Stoll and M.A. Chianta, "Method and Rating System for Evaluation of Thermal Protection", Aerospace Medicine, Vol. 40, 1969, pp. 1232-1238.
[6] "ASTM F1939-99a Standard Test Method for Radiant Protective Performance of Flame Resistant Clothing Materials", American Society for Testing and Materials, West Conshohocken, PA.

Size and Residence Time Effects of Fine-Water Droplets in Suppressing Non-premixed and Premixed Methane-Air Flames

Harsha K. Chelliah

Department of Mechanical and Aerospace Engineering

University of Virginia, Charlottesville, VA 22904

Objectives:

On a mass basis condensed-phase fire suppressants, such as fine-water droplets, are equally as effective as some well known gaseous fire suppressants. They are known to promote fire suppression/inhibition primarily through thermal effects (because of the relative large latent heat associated with phase-change). However, full realization of thermal effects of condensed-phase agents depends heavily on the flame structure, velocity field, and the size of the condensed-phase agent used. This paper reports a detailed numerical modeling effort aimed at quantifying the flow residence time and size effects by considering two widely used laboratory flow fields. The two flame configurations considered are the non-premixed counterflow flames and freely-propagating premixed flames, with fine-water droplets as the condensed-phase flame suppressant. Comparisons with previously reported experiments are also presented.

In the present work, the previously developed two-phase model by Lentati and Chelliah [1] for a counterflow flame (see Fig. 1) is modified to analyze one-dimensional, freely propagating two-phase premixed flame with fine-water droplets (see Fig. 2). By varying the initial droplet size at the inflow boundary, it is shown that differences in the flow residence time between premixed and counterflow flames lead to varying flame suppression results. In other words, the optimal fine-water droplet size suppressing a non-premixed flame can be different from that of a premixed flame. The differences observed imply that extension of laboratory scale flame suppression results to large-scale fires, or to fires in a microgravity environment with entirely different flow residence times, must carefully consider the droplet/particle size effects.
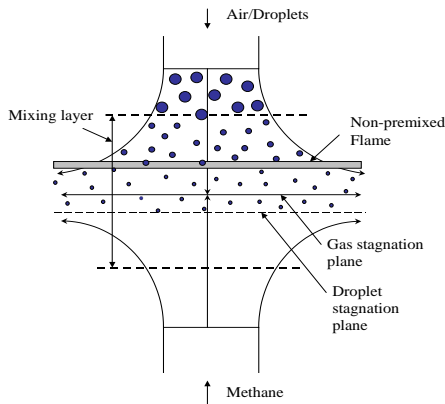
Figure 1: Illustration of the nonpremixed counterflow flames with water-mist added to the air stream.
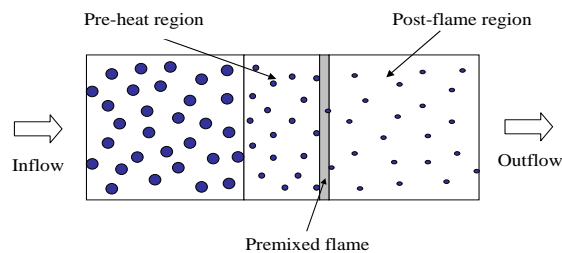
Figure 2: Illustration of the premixed flames with water-mist added to the fresh mixture.

Gas-Phase Conservation Equations:

The gas-phase equations for species and energy of steady, planar axisymmetric counterflow flames (along the axis of symmetry) and one-dimensional premixed flames, in the presence of evaporating droplets, are the same, and can be written as,

$$\rho v \frac{dY_i}{dx} + \frac{d}{dx}(\rho Y_i V_i) = W_i \dot{\omega}_i + (\delta_{i\alpha} - Y_i)S_m, \quad i = 1, ..., N, \tag{1}$$

$$\rho \sum_{i=1}^{N} (v + V_i) Y_i c_{pi} \frac{dT}{dx} = \frac{d}{dx} \left(\lambda \frac{dT}{dx} \right) - \sum_{i=1}^{N} W_i \dot{\omega}_i h_i + S_h - h_\alpha S_m, \tag{2}$$

where x is the distance, ρ the density, v the gas velocity (axial for counterflow field), V_i the diffusion velocity of species i (normal to the flame), T the gas temperature, λ the thermal conductivity, c_{pi} the specific heat at constant pressure of species i, $\dot{\omega}_i$ the molar production rate of species i, W_i the molecular weight of species i and h_i the enthalpy of species i. Here S_m is the mass-source term due to evaporating water droplets, S_h is the associated enthalpy source term and $\delta_{i\alpha}$ is the Kronecker delta function, where subscript α identifies the evaporating species (in this case water).

The determination of the velocity field depends on the flow configuration, i.e. counterflow or one-dimensional flow, and is well described in the literature, including the boundary conditions. The inflow boundary conditions are assumed to be at room temperature with constant atmospheric pressure. The fuel considered is methane, while the inflow streams with water droplets are assumed to be saturated with water vapor, similar to the experiments. The droplet size is assumed to be monodispersed across the transverse plane, while their size will decay along x because of evaporation.

Lagrangian Equations of Droplets:
The droplet source terms, eg. S_m and S_h above, must be described based on their trajectory through the flame structure. In the counterflow field, previous studies have indicated that integration of Eulerian equations describing the droplet transport can lead to singular behavior at the droplet stagnation plane (see Fig. 1). In addition, for small droplet number density (or dilute droplet loadings), because of the concerns about the validity of continuum approximation for the condensed phase, the Lagrangian description of droplet transport is used here. The relevant Lagrangian conservation equations, for example for mass and energy, can be written as [1],

$$\frac{dm_d}{dt} = -Q, \tag{3}$$

$$\frac{d}{dt}(m_d h_d) = -Q(h_d + L) + H, \tag{4}$$

where the subscript d refers to droplet properties. Here, d_d is the droplet diameter, $m_d = (\pi/6)\rho_d d_d^3$ the droplet mass, Q the mass evaporation rate of the droplet, $h_d = h_d^0 + c_{p,d}(T - T_0)$ the specific enthalpy of the droplet, L the specific latent heat of vaporization, and H the heat flux to the droplet from the gas. Both Q and H are estimated using analytical formula derived assuming d^2-law [2], which is applicable for isolated evaporating droplets under quasi-steady evaporation conditions. For droplet mass loading of 3% or less considered here, the droplet-to-droplet separation distance is over 20 times the droplet diameter [1], and under such conditions, the isolated droplet assumption is reasonable. The droplet velocities are allowed to deviate from that of the gas, and Lagrangian momentum conservation equations are used to obtain the droplet velocity based on Stokes drag force for low droplet Reynolds number.

For counterflow flames, the normalized droplet number per unit transverse surface area is denoted as the flux fraction $\mathcal{F}(t)$, which will decrease rapidly as the droplets approach the stagnation plane because of the flow straining. By defining the droplet source term as S_ϕ for the property ϕ transported, the mass, momentum and energy transferred to the computational

volume element j per unit volume, can be written in the general form,

$$S_{\phi j} = -(1/dx_j)n_{d_0}v_{d_0}\sum_{k=1}^{K_j}\int_{t_k}^{t_k+dt_k}\mathcal{F}(t)\phi dt, \qquad (5)$$

where n_{d0} is the droplet number density at the air nozzle exit and v_{d0} is the velocity of droplets (assumed to be same as the gas-velocity). For the one-dimensional premixed flow, $\mathcal{F} = 1$ because of the constant cross-sectional area.

Numerical Method:
In the presence of evaporating water droplets, a modified-Newton approach has been used to integrate the gas-phase equations numerically, with the coupled solution of Lagrangian equations of droplet motion for source terms ($\mathbf{S} = \{S_m, S_U, S_h\}$) [1,3]. In particular, the approach adopted by Lentati and Chelliah [1] has introduced a relaxation parameter $\gamma < 1$ to facilitate the convergence solution matrix to the steady-state solution. The droplet source terms $\mathbf{S}$ are functions of unknown solution vector $\mathbf{s} = \vec{v}, Y_i, T$, consequently, the inclusion of droplet source terms can lead to less-sparse Jacobian and unable to use the tridiagonal feature of the matrix. As a compromise, a less accurate conditional Jacobian matrix $J_{\mathbf{s}}$ based on the conservation equations without the droplet source terms is used here to march towards the steady-state solution. The Lagrangian equations describing the droplet motion are integrated via a mixed explicit-implicit scheme, as described in Lentati and Chelliah [1].

Inhibition of Premixed Flames with Fine Water Droplets:
If water droplets are introduced sufficiently upstream of the premixed flame, the fuel-air mixture is expected to be saturated with water vapor. At inflow pressure and temperature of 1 atm and 300K, the saturation mass fraction of water vapor is 0.0224. The resulting dilution of the fuel-air mixture with water vapor can reduce the burning velocity of the premixed flame. Based on the chemical kinetic model employed, the predicted burning velocity of a stoichiometric, dry methane-air flame is $S_L^0 = 40.8$ cm/s. With addition of water vapor, the predicted stoichiometric methane-air flame reduces to $S_{L,vap} = 34.9$ cm/s, i.e. about 14% reduction. All the flame burning velocity results reported here with addition of fine-water droplets are normalized by $S_{L,vap}$, not S_L^0. An important implication of imposing saturated vapor condition is that the droplets entering the computational domain (i.e. $x = -\infty$) do not evaporate until they reach the preheat (convective-diffusive) region of the premixed flame, as illustrated in Fig. 2. Therefore, the droplet residence time in the cold upstream region of the flame structure is of no consequence in terms of mass evaporation.

When a significant mass fraction of water droplets is introduced, the flame burning velocity is expected to reduce significantly, depending on the droplet loading and size. Figure 3 shows a plot of normalized burning velocity vs. droplet mass fraction, for several monodispersed size droplets introduced with the fresh mixture. For a selected droplet mass fraction, it is seen that the decrease in burning velocity of the premixed flame varies monotonically with decreasing droplet size. The higher flame inhibition with 10 μm droplets can be related to the higher surface area to volume, resulting in complete evaporation of the droplets within the diffusive-reactive layer of the flame structure.
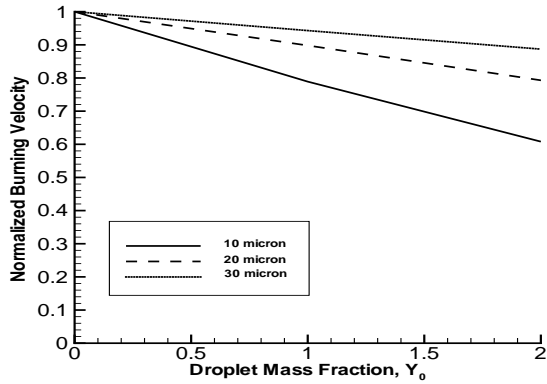
Figure 3: Normalized premixed burning velocity vs. droplet mass fraction, for several droplet sizes.

Figure 4: Comparison of premixed and non-premixed flame strengths as a function of droplet mass loading.

Extinction of Non-premixed Flames with Fine-Water Droplets and Comparisons with Premixed Flames:

The premixed flame burning velocity is proportional to the square-root of the overall chemical reaction rate. The non-premixed flame extinction strain rate (a_{ext}), however, is *directly* proportional to the chemical reaction rate. A formal asymptotic analysis [4], assuming that the overall reaction of the form $Fuel + Oxidizer \rightarrow Products$, yields the following relationship between the burning velocity and extinction strain rate,

$$(\rho_0 S_L^0)^2 \propto \left(\frac{\rho \lambda}{c_p Z^2} \right)_{st} a_{ext}, \tag{6}$$

where Z_{st} is the stoichiometric mixture fraction (assumed to be a small parameter). Based on this relationship and assuming that the mixture fraction, transport and thermodynamic properties are not affected by the small fraction of condensed-phase agent added, a direct comparison of the extinction/inhibition of non-premixed and premixed flames can be achieved by defining normalized flame strength as $\mathcal{S} = (S_L/S_{L,vap})^2 = (a_{ext}/a_{ext,vap})$. Figure 4 shows a comparison of the normalized flame strength for premixed and non-premixed flames as a function of droplet mass fraction, based on experimental and numerical data (predicted with 20 μm droplets).

The differences observed between the inhibition of non-premixed and premixed flames by pure water droplets, can be explained based on the flow residence time associated with each flame structure and its effect on the evaporation of fine-water droplets. The estimated flow residence time of these droplets through the thermal layer, from the cold boundary up to the peak flame temperature differs substantially, 4 msec for the premixed vs. 14 msec for the non-premixed. This implies that the time available for the droplets to vaporize in premixed flames is considerably less, and that the 20 μm droplets are not necessarily the ideal size for inhibiting the premixed flame considered. Consequently, the maximum thermal cooling is not achieved compared to the counterflow flame, resulting in the lower flame inhibition observed in Fig. 4 for premixed flames.

REFERENCES:

[1] Lentati, A.M. and Chelliah, H.K., *Combust. Flame,* **115**:158 (1998).
[2] Law, C.K., *Prog. Energy Combust. Sci.* **8**:171 (1982).
[3] Chen, N.-H., Rogg, B., and Bray, K.N.C., *Twenty-Fourth Symposium (Int.) on Combustion,* The Combustion Institute, p. 1513, 1992.
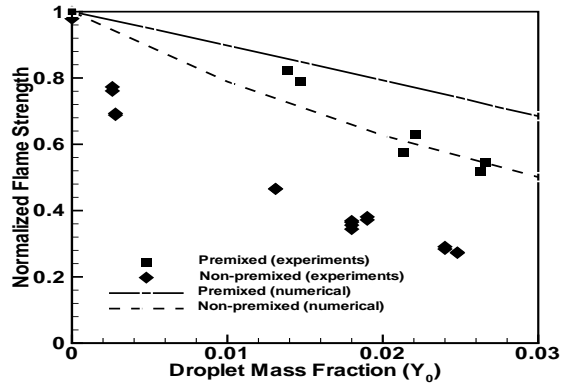[4] Peters, N.: *Combust. Sci. Tech.* **30**:1 (1983).

CHEMICALLY-PASSIVE SUPPRESSION OF PREMIXED FLAMES IN SPACECRAFT ENVIRONMENTS AT MICROGRAVITY

C. H. Kim, L. Qiao and G. M. Faeth
The University of Michigan, Ann Arbor, Michigan

O. C. Kwon
Sungkyunkwan University, Suwon, Kyunggi-do, Korea

INTRODUCTION

The effects of flame suppressants on outwardly-propagating spherical laminar premixed flames at atmospheric pressure were studied, emphasizing changes of both unstretched laminar burning velocities and flame response to stretch due to the presence of a flame suppressant. Experimental and computational methods were used to study laminar $H_2/O_2/N_2$ premixed flames, considering helium, argon, nitrogen, water vapor, carbon dioxide and water mist as suppressants with the reactants at normal temperature (see Refs. 1-15 for the details of experimental and computational methods).

FLAME/STRETCH INTERACTIONS

It is widely recognized that flame/stretch interactions, due to effects of preferential diffusion, can significantly affect the properties of laminar premixed flames [1-15]. Thus, the present flames were analyzed to account for flame/stretch interactions by relating the laminar burning velocity, S_L, and the flame stretch, K, using an early proposal of Markstein [16] and the local conditions hypothesis of Kwon et al. [1], to yield:

$$S_{L\infty}/S_L = 1 + MaKa \tag{1}$$

where S_L and $S_{L\infty}$ are the stretched and unstretched laminar burning velocities and Ma and Ka are dimensionless Markstein and Karlovitz numbers, defined as follows:

$$Ma = L/\delta_D, \quad Ka = KD_u/S_L^2 \tag{2}$$

where L is the Markstein length, δ_D is the characteristic flame thickness given by D_u/S_L, and D_u is the mass diffusivity of the fuel in the unburned gas. The values of S_L and K were found by observing the flame radius, r_f, as a function of time, t, for outwardly-propagating spherical laminar premixed flames and computing S_L and K following Strehlow and Savage [17] for both the measured and the numerically simulated flames, as follows:

$$S_L = (\rho_b/\rho_u)dr_f/dt, \quad K = (2/r_f)dr_f/dt \tag{3}$$

where ρ_b and ρ_u are the densities of the burned and unburned gases and the radii of the hot and cold boundaries of present flames were essentially the same because they were thin. Computation of ρ_b/ρ_u used the adiabatic equilibrium algorithm of McBride et al. [18], assuming the same concentrations of elements in the burned and unburned gases, because effects of preferential diffusion of heat and mass on the flame density ratio were small for present conditions.

EXPERIMENTAL AND COMPUTATIONAL METHODS

Measurements of S_L and K were obtained from shadowgraph motion pictures of outwardly-propagating spherical flames that were spark ignited at the center of a windowed pressure vessel containing the unburned gas mixture. The flames propagated rapidly for the conditions considered here and were not affected by buoyancy. The flames were also numerically simulated using either the one-dimensional time-dependent laminar flame code RUN1DL, of Rogg [19] or the one-dimensional steady flame code, PREMIX, of Kee et al. [20].

Thermochemical transport data were obtained from Kee et al. [21,22] except as noted by Kim et al. [14]. H/O chemistry was treated using mechanisms reported by Mueller et al. [23], Sun et al. [24], Marinov et al. [25] and Frenklach et al. [26].

RESULTS AND DISCUSSION

Unsuppressed Flames. Measured and predicted values of S_L were extrapolated to $K \rightarrow 0$ to find $S_{L\infty}$ is discussed in Refs. 1-15. Subsequently, measured and predicted values of $S_{L\infty}/S_L$ were plotted as a function of Ka as suggested by Eq. (1); such results for hydrogen/air laminar premixed flames at normal temperature and pressure (NTP) are plotted in Fig. 1. These results use the Mueller et al. [23] chemistry. Both measurements and predictions exhibit a linear relationship between $S_{L\infty}/S_L$ and Ka, implying a constant Ma through Eq. (1) for each fuel-equivalence ratio, ϕ. This behavior has been observed for all flames studied thus far; as a result Ma is a concise and convenient measure of flame/stretch interactions. The results in Fig. 1 exhibit the strong effects of flame/stretch interactions, with modest Ka < 0.2 causing S_L variations by as much as 50%. This behavior implies that flame/stretch levels must be quantified in order to properly evaluate the effects of suppressants on laminar premixed flames. Finally, measurements and predictions are in good agreement in Fig. 1.

Measured and predicted values of Ma and $S_{L\infty}$ for hydrogen-fueled laminar premixed flames are illustrated in Figs. 2 and 3. For these results, predictions are based on the H/O kinetics of Refs. 13-26 whereas measurements from Refs. 27-30 are shown along with the present results. The comparison between measurements and predictions is very good, even when N_2 is replaced by helium or argon as diluents.

Suppressed Flames. Given encouraging numerical simulations of unsuppressed hydrogen-fueled flames, evaluations of the numerical simulations were extended to consider effects of suppressants on such flames. The effects of chemically-passive suppressants, N_2 and CO_2, on the unstretched laminar burning velocities of laminar premixed H_2/air flames at NTP are illustrated in Fig. 4. The concentrations of suppressants are shown in two ways in Fig. 4: as the mole fraction of the diluent and as the oxygen index. The latter parameter is a common measure of chemically-passive flame suppressant concentrations [31]; it is defined as the concentration of O_2 in the suppressed nonfuel mixture in percent by volume. First of all, it is evident that the predictions are in good agreement with the measurements for the full range of conditions illustrated in Fig. 4. Next, the improved suppression performance of CO_2 compared to N_2, due to its larger heat capacity, is evident and is modeled very well. Predictions of the behavior of CO_2 suppressed flames at microgravity, however, did not indicate that limit conditions had been reached even at an oxygen index of 10 which is smaller than values of flammability limits at an oxygen index of 15 which is typical of hydrocarbon fuels at microgravity [37]. On the other hand, measurements of CO_2 suppressed flames near an oxygen index of 10 indicated strong buoyant distortion and extinction at normal gravity at these conditions. This provides evidence that flames are more robust at microgravity conditions than at normal gravity conditions — clearly demonstrating the need for carrying out suppression experiments at microgravity in order to better understand flame suppression for microgravity environments.

Finally, the simulations showed that the addition of a suppressant reduced the Markstein number of the flames tending to make them more unstable to preferential diffusion instabilities. Thus, using a suppressant tends to reduce laminar burning velocities, which is a desirable suppression effect, but at the same time promotes flame instabilities, which is an undesirable suppression effect.

REFERENCES
1. Kwon, S. et al., *Combust. Flame* 90:230 (1992).
2. Tseng, L.-K. et al., *Combust. Flame* 95:410 (1993).
3. Aung, K.T. et al., *Combust. Flame* 102:526 (1995).

4.   Aung, K.T. et al., *Combust. Flame* 109:101 (1997).
5.   Aung, K.T. et al., *Combust. Flame* 112:1 (1998).
6.   Aung, K.T. et al., *Combust. Flame* 113:282 (1998).
7.   Hassan, M.I. et al., *J. Prop. Power* 13:239 (1997).
8.   Hassan, M.I. et al., *Combust. Flame* 115:539 (1998).
9.   Hassan, M.I. et al., *J. Prop. Power* 14:479 (1998).
10. Aung, K.T. et al., *Combust. Sci. Tech.* 174:1 (2001).
11. Kwon, O.C. et al., *Combust. Flame* 116:310 (1999).
12. Kwon, O.C. et al., *J. Prop. Power* 16:513 (2000).
13. Kwon, O.C. and Faeth, G.M., *Combust. Flame* 124:590 (2001).
14. Kim, C.H. et al., J. *Prop. Power* 18:1059 (2002).
15. Faeth, G.M. et al., *Int. J. Environ. Combust. Tech.*, in press.
16. Markstein, G.H., *Non-Steady Flame Propagation*, Pergamon, New York, p. 22, 1964.
17. Strehlow, R.A. and Savage, L.D., *Combust. Flame* 31:909 (1978).
18. McBride, B.J. et al., NASA Report No. TM4557, 1994.
19. Rogg, B., Report No. CUED-THERMO/TR39, Univ. Cambridge, 1996.
20. Kee, R.J. et al., Sandia National Laboratories Report No. SAND85-8240, 1993.
21. Kee, R.J. et al., Sandia National Laboratories Report No. SAND87-8215B, 1992.
22. Kee, R.J. et al., Sandia National Laboratories Report No. SAND86-8246, 1992.
23. Mueller, M.A. et al., *Int. J. Chem. Kinetics* 31:113 (1999).
24. Sun, C.J. et al., *Combust. Flame* 118:108 (1999).
25. Maninov, N.M. et al., *Transport Phenomena in Combustion* (S.H. Chan, ed.), Vol. 1, Taylor & Francis, Washington, p. 118, 1996.
26. Frenklach, M. et al., www.me.berkeley.edu/giu.mech/Version 2.1, 1995; *Ibid*., Version 3.0, 1999.
27. Karpov, V.F. et al., *Combust. Flame* 109:436 (1996).
28. Taylor, S.C., Ph.D. Thesis, University of Leeds, U.K., 1991.
29. Vagelopoulos, C.M. et al., *Proc. Combust. Inst*. 25:1341 (1994).
30. Egolfopoulos, F.M. and Law, C.K., *Proc. Combust. Inst*. 23:333 (1990).
31. Tuhtar, D., *Fire and Explosion Protection: A System Approach*, John Wiley and Sons, New York, p. 127, 1989.
32. Babrauskas, V., *Fire Protection Handbook*, (A.E. Cote and J.L. Linville, eds.), 16th ed., NFPA, Quincy, MA, p. 5, 1986.
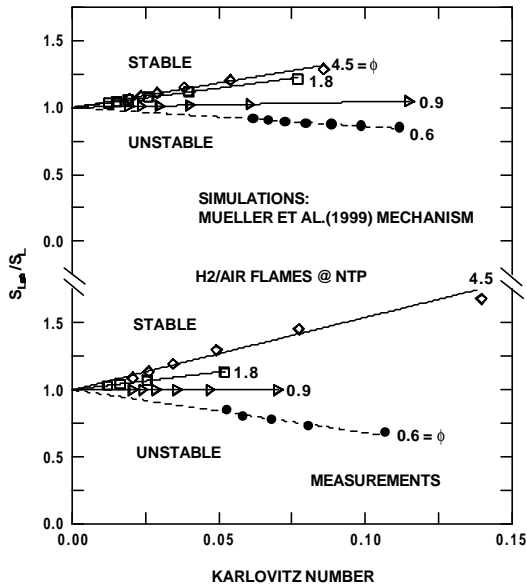
Fig. 1. Measured and predicted laminar burning velocities as a function of Karlovitz number and fuel-equivalence ratio for hydrogen-air laminar premixed flames at NTP. From Kwon and Faeth [13].

Fig. 2. Measured and predicted Markstein numbers as a function of fuel-equivalence ratio for laminar premixed hydrogen-fueled flames at NTP. From Kwon and Faeth [13].

Fig. 3. Measured and predicted unstretched laminar burning velocities as a function of fuel-equivalence ratio for hydrogen-fueled laminar premixed flames at NTP. From Kwon and Faeth [13].

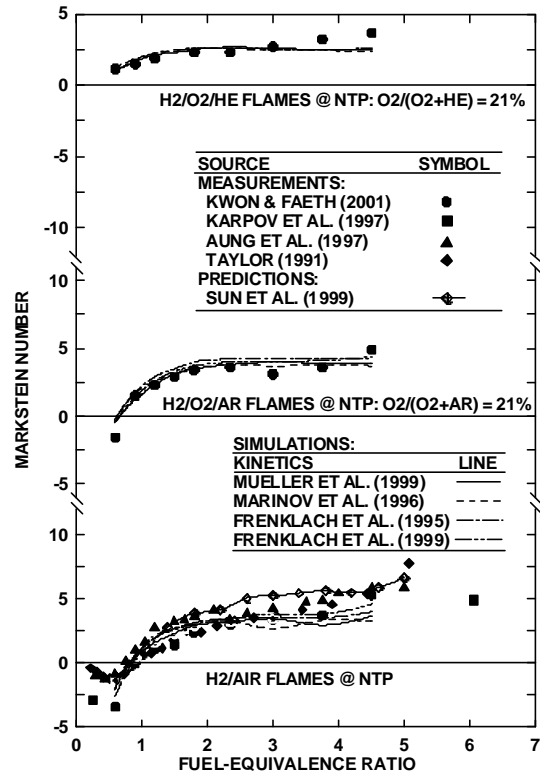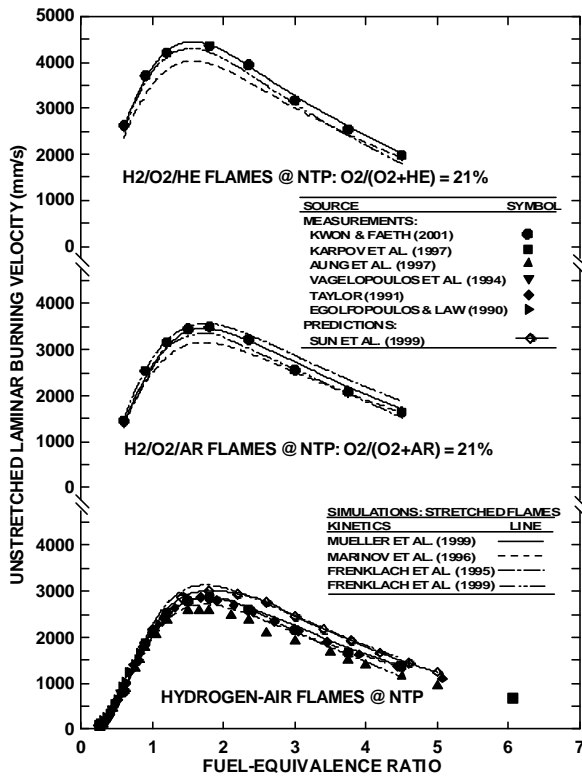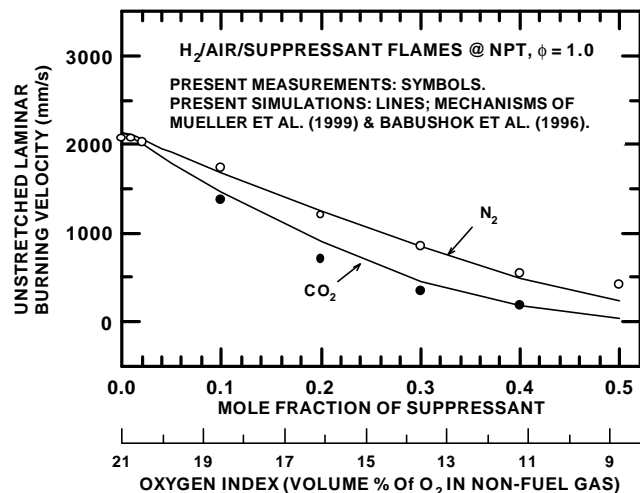Fig. 4. Measured and predicted unstretched laminar burning velocities as a function of concentrations of nitrogen and carbon dioxide suppressants for stoichiometric hydrogen-air flames at NTP. From Kim et al. [14].

Microgravity Apparatus and Ground-Based Study of the Flame Propagation and Quenching in Metal Dust Suspensions.

Sam Goroshin, Massimilliano Kolbe, Julie Bellerose, and John Lee
McGill University, Montreal, Quebec, Canada

Introduction

Due to particle sedimentation and relatively low laminar flame speeds in dust suspensions, microgravity environment is essential for the observation of laminar dust flames in a wide range of particle sizes and fuel concentrations [1]. The capability of a reduced-gravity environment to facilitate study of dust combustion was realized by researchers long before current microgravity programs were established by the various national Space Agencies. Thus, several experimentalists even built their own, albeit very short-duration, drop tower facilities to study flames in particle and droplet suspensions [2,3]. About ten years ago, authors of the present paper started their dust combustion reduced gravity research with the investigation of the constant volume dust flames in a spherical-bomb on board a parabolic flight aircraft [4]. However it was soon realized that direct observation of the constant-pressure flame might be more beneficial. Thus, microgravity apparatus, permitting examination of the freely propagating flames in open-end tubes, was tested in parabolic flights three years later [5]. The improved design of the newly-constructed apparatus for the experiments on board the NASA KC-135 aircraft is also based on the observation of the dust flame propagating in semi-opened tubes with free expansion of the combustion products that are continuously vented overboard. The apparatus design and results of its extensive ground-based testing are presented below.

Description of the Microgravity Apparatus.

The microgravity experimental package (Fig 1) is assembled in two separate frames. The first frame contains the control panel, computer data acquisition system, magazine of 8 combustion tube assemblies, and spare dust filters. The second frame (Fig. 1B) contains the combustion system and consists of three major components: the dust dispersion system, the combustion tube assembly, and the filtering and venting system. The dust fluidization system is modeled after our dust dispersion device that was used in numerous ground-based experiments [6,7] and has also demonstrated the ability to produce a uniform and well disaggregated dust suspension in the microgravity environment [5].
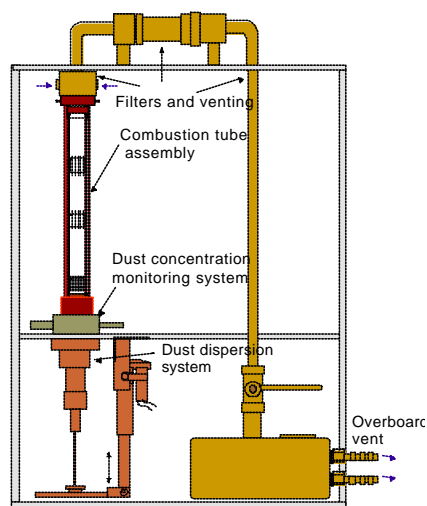

Figure 1 Photograph of the microgravity experimental package and schematic of the frame containing the dust combustion assembly.

The dust concentration is monitored directly within the dust supply tube by a laser light extinctiometer (Fig. 2). The use of the focused laser beam in combination with the pinhole aperture minimizes collection of the scattered light and makes deviation from the Beer-Lambert light attenuation law negligible even for optically-thick dust clouds. A narrow bandwidth interference filter protects the photodetector from ambient light.
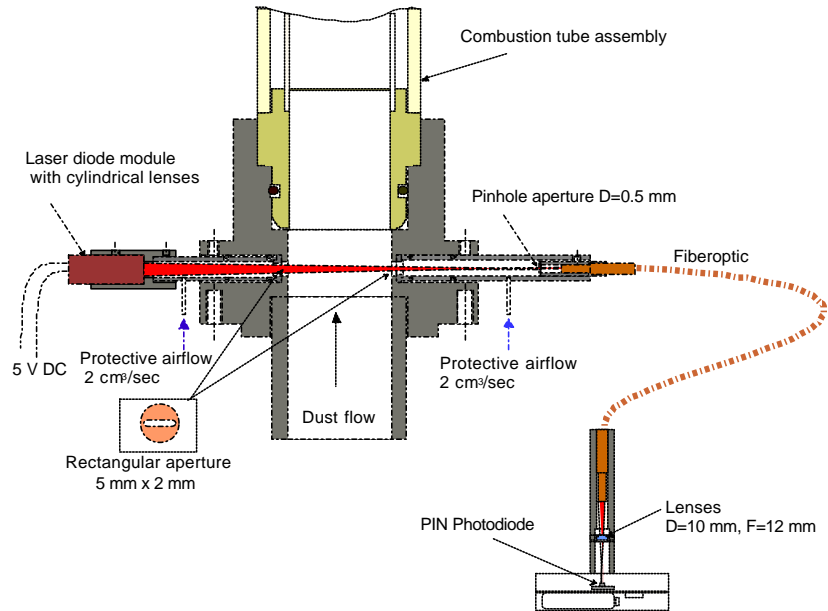
Figure 2. Laser dust concentration monitoring system.

For every powder used, the light extinctiometer was calibrated in the laboratory. For this a complete aspiration of dust from the flow was performed with a set of fine filters and a vacuum pump for a known time. Dust mass concentration in the flow is then determined by dividing total mass of aspired dust by the volume of the gas that passes through the dust dispersion during the same time. The example of the dust concentration measurements by the extinctiometer during the dispersion process is shown in Fig. 3
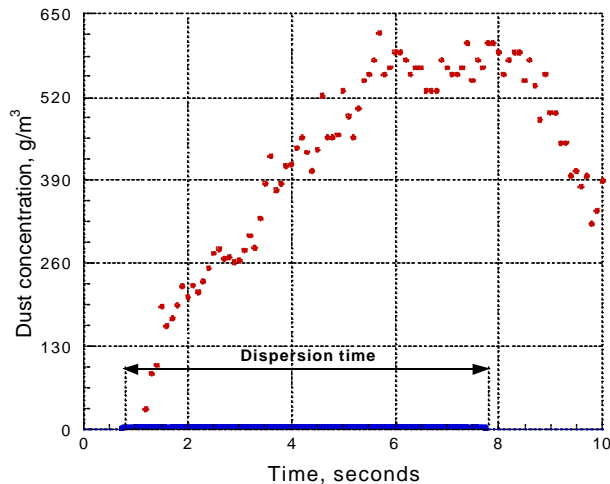
Figure 3 Results of dust concentration measurements by the extinctiometer during the dust dispersion process. Note that the ignition in ground-based experiments is usually performed 0.5 seconds after dispersion is switched off.

As it can be seen from Fig. 3, in approximately 5 seconds after the start of the dispersion process, the dust concentration in the flow reaches a plateau. The plateau extends for about 3 seconds until the end of the dispersion process. With a flow speed in the combustion tube of about 30 cm/s, the plateau duration is sufficient to fill the full length of the tube with a suspension of known and uniform dust concentration.

The flame propagates in 70-cm long, 5-cm ID Pyrex tube that is sealed inside another concentric transparent acrylic tube. An electrically heated ignition coil made from 0.25-mm tungsten wire is used to ignite dust at the open end of the tube. An O-ring seal at the lower end of the combustion tube provides a hermetic connection of the tube assembly with the dispersion system and allows its fast replacement in flight. Up to three sets of the steel quenching plates can be installed within the single combustion tube. The plates are about 0.8 mm thick and are soldered at equal distances with the help of thin stainless-steel rods. More than 40 quenching sets with quenching distances that range from 3 to 15 mm are prepared. Nine combustion tube assemblies that contain, in total, about 27 quenching assemblies will be prepared and used in each flight.

Figure 4 Combustion tube assembly and photograph of the aluminum dust flamelets propagating between quenching plates.

MotionScope[?] high-speed digital video camera records the flame propagation process at rate of about 1000 frames/sec before and inside the first set of quenching plates. The second, regular digital camera records the flame along the total length of the tube. A miniature microphone with enhanced low frequency response is installed near the exit of the dispersion system and allows registration of pressure oscillations in acoustically-exited flames.
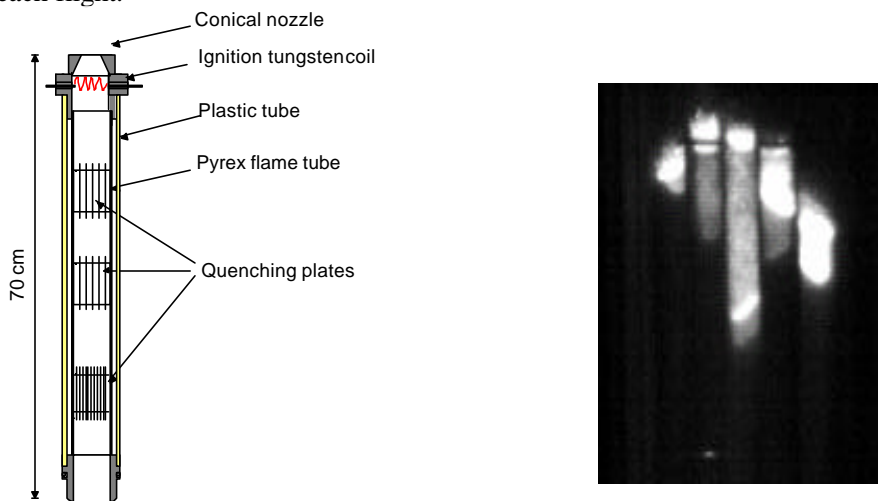
Flame propagation and quenching in micron-size metal particle suspensions.

Microgravity apparatus was extensively tested on the ground using gaseous methane-air mixtures and micron-size (d_{32} = 3-5?m) suspensions of pure metal powders of Al, Fe, Cr, and Ti. The tests with methane-air stoichiometric compositions found flame propagation speeds and quenching distances that are very close to those reported in the literature [8] (see Table). Experiments with aluminum and titanium powders revealed the existence of strong acoustic flame oscillations that appear almost immediately after the ignition. The frequency of the oscillations was close to the basic acoustic mode of the combustion tube, (100-120 Hz) and the flame behavior was similar to the dust oscillatory combustion previously observed by the author in longer tubes [9]. It was found that the intensity of coupling between flame and acoustic wave is not uniform along the tube length (see Fig. 5A). The amplitude of pressure oscillations was the highest at the open end and in the lower section of the tube. At moderate, close to stoichiometric dust concentrations, the upper section of the tube was often free of acoustic coupling. It is also interesting to note that if the acoustic coupling above quenching plates is not very intense, pressure oscillations nearly disappear when the flame travels between quenching plates. They, however, reach the maximum amplitude almost instantly as soon as the flame emerges out of the quenching plate assembly (Fig. 5B). Special experiments were performed to investigate the influence of the intensity of acoustic oscillations on flame quenching distance.
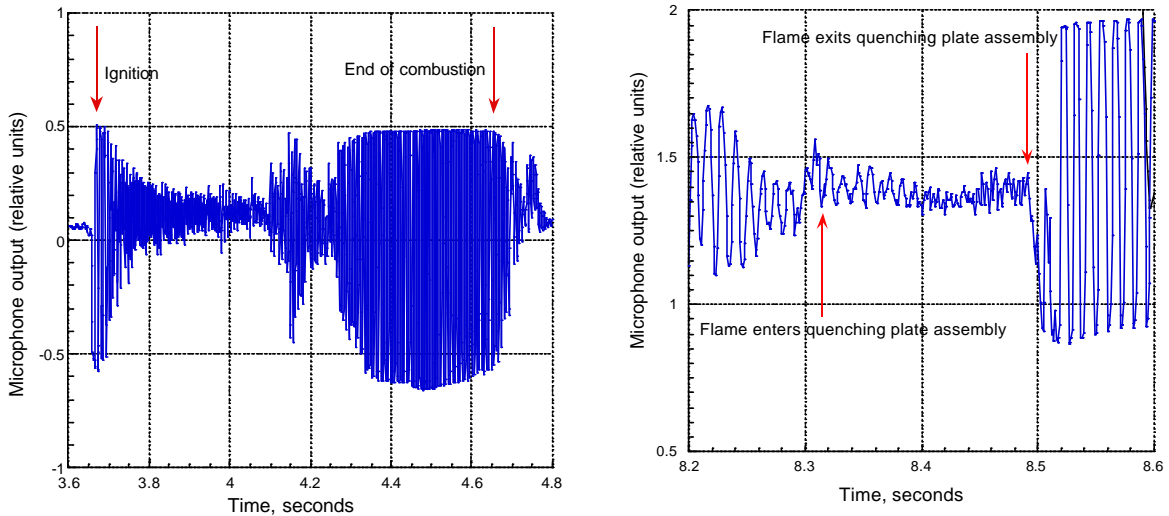
Figure 5 - (A) Acoustic oscillations during flame propagation along combustion tube; (B) Acoustic oscillations before, inside and after flame passes quenching plate assembly.

It was found that the quenching distance of the dust flame does not depend on the position of the quenching plates along the tube length and accordingly on the intensity of the acoustic flame oscillations outside quenching plates. Oscillating flames, however, demonstrate much lower average flame speed than an unperturbed one. Thus only flame speeds measured in the absence of acoustic coupling are shown in the table below. The table also summarizes obtained experimental data on flame quenching distances in methane-air mixtures and metal-air suspensions at fuel concentrations close to stoichiometric. Note that no acoustic coupling was observed for flames in Fe and Cr dust suspensions.

Fuel	Aluminum Al	Titanium Ti	Iron Fe	Chromium Cr	Methane CH$_4$
Metal density, g/m^3	2.70	4.59	7.87	7.19	-
Metal boiling point, K	2792	3550	3134	2944	
Stoichiometric concentration, g/m^3	310	415	725	600	160
Adiabatic flame temperature, K	3540	3300	2295	2800	2170
Quenching distance: Flame propagates, mm Flame quenches, mm	4 3	3 2	8 7	7 6	3 2
Flame speed in 5 cm ID tube (? 5 cm/s)	55	60	20	30	80

References.
1. Goroshin, S., Lee, J.H.S., *NASA/CP-1999-208917*, 123-126, 1999
2. Kumagai, S., *Combustion,* Iwanami Shoten Pub., Japan, 1976 (in Japanese)
3. Ballal, D.R., *Proc. Royal Soc. London, Ser. A,* 385:21-51, 1983
4. Peraldi, O., Lee, J.H.S., Landry, C., Shemie, M., *Proc. Spacebound'93,* Ottawa, 95-96, 1993
5. Goroshin, S., Kleine, H., Lee, J.H.S., Frost, D., *NASA/ CP –1995-10174*, 141-146, 1995
6. Goroshin, S., Bidabadi, M., Lee, J.H.S., *Combustion and Flame* V.105, 147-160, 1995
7. Goroshin, S., Fomenko, I., Lee, J.H.S, *Proc. Comb. Inst*, V. 26, pp. 1961-1967, 1996
8. Lewis, B. and von Elbe. G., *Combustion, Flames, and Explosions of Gases,* Ac. Press, NY, 1961
9. Goroshin, S., Shevchuk, V., Ageyev, N. *Comb., Expl., and Shock Waves,*, V.17, 595- 600, 1982

LOW REYNOLDS NUMBER DROPLET COMBUSTION IN
CO$_2$ ENRICHED ATMOSPHERES IN MICROGRAVITY

M. C. Hicks
NASA Glenn Research Center
21000 Brookpark Rd.
Cleveland OH, 44135

INTRODUCTION

The effect of radiative feedback from the gas phase in micro-gravity combustion processes has been of increasing concern because of the implications in the selection and evaluation of appropriate fire suppressants. The use of CO$_2$, an optically thick gas in the infrared region of the electromagnetic spectrum, has garnered widespread acceptance as an effective fire suppressant for most ground based applications. Since buoyant forces often dominate the flow field in 1-g environments the temperature field between the flame front and the fuel surface is not significantly affected by gas phase radiative absorption and re-emission as these hot gases are quickly swept downstream. However, in reduced gravity environments where buoyant-driven convective flows are negligible and where low-speed forced convective flows may be present at levels where gas phase radiation becomes important, then changes in environment that enhance gas phase radiative effects need to be better understood. This is particularly true in assessments of flammability limits and selection of appropriate fire suppressants for future space applications. In recognition of this, a ground-based investigation has been established that uses a droplet combustion configuration to systematically study the effects of enhanced gas phase radiation on droplet burn rates, flame structure, and radiative output from the flame zone.

BACKGROUND

It appears that the radiative feedback effects of CO$_2$, as well as other potential fire suppressants, have been largely un-quantified in the selection and ranking of fire suppressants for spacecraft fires. Since the extinction mechanism of many micro-gravity flames is radiation dominated it is reasonable to expect that the emissive and absorptive properties of the surrounding gases would play a role. Mention of the radiative interplay between flame and surroundings was made in discussing ranking criteria of fire suppressants in an earlier work; however, it was then reasoned that CO$_2$, for the very reasons that this suppressant may be problematic in micro-gravity, should be ranked the highest. The paper stated:

> *"For a suppressant to be effective radiatively, it must decrease flame luminosity, act as a radiation sink itself, and **remain transparent between the flame and its surroundings**. On this basis CO$_2$ was favored because CO$_2$ decreases sooting in diffusion flames by 20-30 percent more than does N$_2$ and CO$_2$ is more active radiatively (infrared) than N$_2$."* [1]

It has not been established that CO$_2$ is "transparent" in the distances, temperatures, and concentrations which may come into play in the event of a release in the *International Space Station*. Additionally, it is not clear that consideration was made of the possibility that radiative

emissions from heated gases, following a substantial fire, could potentially serve more as a radiative "source" rather than a radiative "sink" with respect to the fuel surface.

Recent work has highlighted this concern and is, in part, the focus of a current investigation funded under an NRA'99 solicitation. There, it was proposed to experimentally assess the efficacy of CO_2 as a fire suppressant in space environments by observing extinguishment characteristics of a burning PMMA test sample using various blends of CO_2/Air. This work is, in part, motivated by the recognized need to provide a better understanding of the radiative effects of CO_2 as stated in the following excerpt from the investigation's proposal listing concerns with fire suppression practices and policies in space:

> *"Carbon Dioxide, the suppressant of choice for ISS, behaves differently than other diluent, in regard to its impact on the range of oxygen concentrations that will support a flame. Whereas the range of flammable conditions narrows substantially in quiescent microgravity as compared to normal gravity for most diluent, the range is unaffected when carbon dioxide replaces nitrogen [Honda and Ronney 1997]. This is due to the fact that carbon dioxide absorbs radiation from a flame more readily than nitrogen, helium, or argon. Thus, the additional margin itself is absent in atmospheres diluted with carbon dioxide."* [2]

This work will provide a means of quantifying the effects of an enriched CO_2 environment through measurements of the changes in droplet burn rates, flame structure, and radiative losses. The droplet, in this case, serves as a proxy for a burning fuel particle and should provide a reasonable index of the concerns associated with fires surrounded by participating gases without the added complexities typical in many solid fuel experiments (e.g., changes in surface geometries, changes in surface emissivities, temperature dependencies, poorly characterized burn rates, etc.). Measurements of droplet burn rates and flame structure will subsequently be used in a 2-D axisymmetric numerical model, incorporating gas phase radiation, to further refine the distinctions between radiative heating and other changes in transport phenomena due to changes in CO_2 concentrations.

Use of a droplet test configuration is advantageous in two ways; first, a wealth of experimental data on droplet burn rates and flame structure already exists and this will serve as a convenient baseline for comparison. Secondly, the axisymmetric geometry of a droplet burning in a flow field lends itself to numerical modeling and subsequent verification more readily than other geometries.

SCIENTIFIC OBJECTIVES
The primary motivation behind this research is to provide an easily quantifiable and repeatable measure of the effectiveness of CO_2 as a space based fire suppressant. Previous work with radiatively participating gases indicate that high CO_2 concentrations in oxidizing environments may result in broader flammability limits due to radiative feedback to the fuel source and absorption in the surrounding gas phase combined with a lack of buoyant forces that normally minimize this effect in normal gravity environments [3,4]. A secondary motivation is to provide a database from tests performed in μg that will provide well-defined "test cases" to be used in the validation of droplet models that include gas phase radiation phenomena.

As such, this investigation will provide a test configuration that will allow indirect measurement of the gas phase radiative effects of a CO_2 enriched environment. This is accomplished by measuring variations in burn rates and flame structure of large fuel droplets (i.e., approaching 2.5 mm in diameter) in an environment with varying levels of CO_2 concentration. Additionally, because of the droplet's relatively simple axisymmetric geometry it is expected that an accurate correlation can be made with a 2-D axisymmetric droplet model in low speed flows that incorporate gas phase radiation. The model, once validated with the experimental results, will subsequently be used to provide predictions of the effects of gas phase radiation in enriched CO_2 environments for larger scale geometries and boundary conditions more representative of existing space habitats relying on CO_2 fire suppressants.

Two overarching science objectives are stated as follows:

- Measure the effect that an enriched CO_2 environment has on the burn rate and flame structure of a liquid droplet in a low convective environment by performing tests at various CO_2/Air mixture levels for a range of pressures and temperatures in both 1-g and micro-gravity.

- Develop a 2-dimensional numerical model of a burning droplet with a sufficiently detailed gas phase radiation model and use the experimental results to validate the model.

EXPERIMENTAL APPROACH

The first objective will be accomplished through a series of tests using two fuel types; a non-sooting fuel such as methanol and a sooting fuel such as n-heptane. A benchmark data base will initially be established in dry air (i.e., 21% O_2 and the balance N_2) at 1-g and 0-g in a quiescent environment at 25°C. Initial fuel droplet sizes will be approximately 2.5 mm in diameter and the burn rate will be precisely measured from recorded backlit images of the droplet. Two radiometers, a wide band and a narrow band (set to capture the predominant water line) will be used to obtain comparative information on the flame's intensity. The flame temperature will be measured by insertion of a thermocouple or by thin-filament pyrometry.

During the first phase of testing the combustion environment will be altered between tests by changing the ambient pressure from 1 atm to 3 atm. The increased pressure will effectively increase the optical thickness of the gases and will allow test chamber results to be extrapolated to geometries involving greater distances in 1 atm environments, such as may be evident in the *International Space Station*.

The second phase of testing will use a translating device (i.e., previously designed and built for use in ground testing performed for an on-going flight investigation[1] [5]; refer to Figure 1) to move the burning droplet at a precisely controlled speed (i.e., 5 cm/sec). The desire for a relative velocity between the oxidizer and droplet is to provide a test configuration that replicates a more likely combustion environment. On the *International Space Station* air flow behind the

---

[1] Flight investigation entitled "*Dynamics of Droplet Combustion and Extinction in Slow Convective Flows*" and directed by Vedha Nayagam (i.e., Principal Investigator).

experimental racks and in ventilation ducting is designed to be less than 20 cm/sec. Using this test configuration will provide an axisymmetric flame geometry and will establish a basis for relative comparisons of the combined convective and radiative heating effects. It is expected that due to the alteration of the inner region's temperature field resulting from the presence of the radiatively participating gases the convective heating effects will be greater than that observed without the radiatively participating gases.

The third and final phase of testing will be conducted at elevated ambient temperatures of 80°C (or higher if practicable). It is expected that the thermal effects of the gas phase radiation will increase with CO_2 concentration and with ambient temperature resulting in measurable differences in the droplet burn rates, flame stand-off distances, and the flame's radiative intensity. Further, it is expected that the radiative feedback effect will be more pronounced with the non-sooting fuel since the presence of a soot shell (e.g., with n-heptane droplets), which typically forms around the droplet in quiescent environments or in low convective flows, already functions as a radiative medium in the inner region between the flame and the droplet.

ACKNOWLEDGEMENT

REFERENCES
1. Reuther, J. J., "*Definition of Experiments to Investigate Fire Suppressants in Microgravity*", NASA CR-185295.
2. Ross, H.D., Research Proposal "*Secondary Fires: Initiation and Extinguishment*", NRA-99-HEDS-04.
3. Ju, Y., Masuya, G., and Ronney, P.D., "*Effects of Radiative Emission and Adsorption on the Propagation and Extinction of Premixed-Gas Flames*", Proceedings of Combustion Institute, 27, pp. 2619-2626, 1998.
4. Ronney, P.D., *Ch. 2 Premixed-gas Flames*, Microgravity Combustion: Fire in Free Fall, Academic Press, pp. 35-81, 2001.
5. Nayagam,V., Hicks, M.C., Kaib,N., Ackerman, M., Haggard, J.B., Williams, F.A., "*Droplet Combustion in a Slow Convective Flow*", pp. 237-240, NASA/CP 2001-210826.
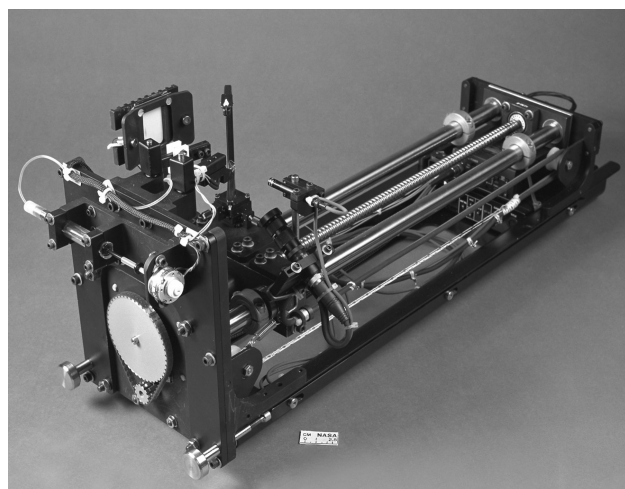
Figure 1(a) Translating sub-assembly designed for the "*Dynamics of Droplet Combustion and Extinction in Slow Convective Flows*" flight investigation led by Vedha Nayagam (i.e., Principal Investigator) for use in the Zero Gravity Facility (i.e., "5 Second Tower").
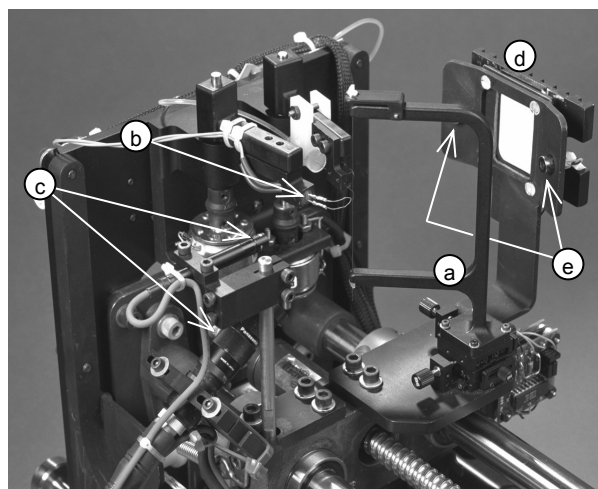

Figure 1(b) Close-up of the "translating subassembly" showing the (a) fiber support fixture, (b) ignitor wire, (c) remote camera heads, (d) LED backlight panel, and (e) radiometer locations.

AN APPROACH FOR ADDRESSING FIRE SAFETY IN REDUCED GRAVITY ENVIRONMENTS

K. Kailasanath
Laboratory for Computational Physics and Fluid Dynamics
Naval Research Laboratory, Washington DC 20375

Angel Abbud-Madrid
Center for Commercial Applications of Combustion in Space
Colorado School of Mines, Golden, CO 80401

INTRODUCTION

The accidental fire aboard the space ship Mir and the difficulties encountered in fighting it have been well documented[1]. While this was a unique event and the occurrence of a serious fire on board the space station is considered to have a very low probability[1], the difficulty of evacuating the occupants to a safe environment make it a critical issue for microgravity combustion research. The problem becomes even more critical during Lunar and Martian missions, which are for extended durations and could involve human-occupied bases on the Moon and Mars. Furthermore, fire behavior and hence preventive and responsive safety actions are strongly influenced by the low-gravity environments in flight and on planetary surfaces[2]. Understandably, NASA has decided to place "considerable emphasis on fire safety on extraterrestrial vehicles", and more specifically on, "extinguishment of fires with minimal residual damage" under the Microgravity Combustion Science and Chemically Reacting Systems program[3].

If there is an accidental fire, there is a need to detect it as soon as possible. Currently, a project on characterization of smoke from microgravity fires for improved fire detection[4] is underway. Once the fire is detected, timely release of a fire suppressant and confidence that it would suppress the incipient fire is needed. Research projects focused on the local physical and chemical interactions of a suppressant with a flame or fire[5-7] will provide valuable insight. In these projects, the suppressant is introduced adjacent to the flame such as using a co-flow. In most situations, it will not be practically feasible to introduce the suppressant in a co-flow adjacent to the fire. The suppressant will be delivered from a distance and will be significantly affected by the flow field in the compartment. In fact, a recent work workshop[8] and article[9] have emphasized the need for additional research on characterizing the flow field in space compartments, investigating the transport of fire-fighting agents and their interaction with the air and fuel surrounding the fire.

One direct approach to addressing the above fire safety issues in reduced gravity environments would be to conduct experiments in large-scale compartments in space. However, this is not practical at this time, because of the very safety issues that need to be addressed as well as the costs involved. A better understanding of the behavior of fires and their response to suppressants in a reduced gravity environment is needed before such large-scale experiments are contemplated. In order to provide timely answers, an alternate approach is needed.

AN ALTERNATE APPROACH FOR ADDRESSING FIRE SAFETY ISSUES

An interim approach for addressing safety issues with compartment fires in spacecraft could be to conduct numerical simulations. In general, to gain sufficient confidence in the results from numerical simulations, comparisons with at least limited experimental data is needed. However, it would be too risky to conduct such validation experiments in space without a fairly good idea of the expected results. Therefore, an alternate approach is needed.

In this alternate approach, Earth-based experiments are combined with numerical simulations and analysis of potential fire scenarios in various gravitational environments. The credibility of the numerical simulations is an important issue to be addressed in order to gain confidence in this approach. It is generally agreed that confidence in the results of simulations can be gained by the processes of "verification" and "validation". According to the AIAA guidelines[10], verification can be defined as: The process of determining that a model implementation accurately represents the developer's conceptual description of the model and the solution to the model. Validation is defined as: The process of determining the degree to which a model is an accurate representation of the real world from the perspective of the intended uses of the model.

Verification can be achieved solely by numerical testing. For example, verification of the simulations for different gravitational environments can be conducted by assessing the role of the spatial and temporal resolutions, boundary conditions and other numerical parameters. Validation tests conducted by comparing to Earth-based experiments will ensure that the results from the model are "valid" for at least one value of gravity. When simulations of different gravitational environments are conducted, only the numerical value of gravity is changed explicitly. No new terms representing additional physics or chemistry are needed for simulating reactive flows in a reduced gravity environment. This gives added validity to the Earth-based experimental validation process suggested. What does change when the gravity term changes is the nonlinear interactions among the various physical and chemical processes. Hence, the actual effectiveness of the suppressants could be different in different gravitational environments. Ideally, comparisons to experimental data obtained under several different gravitational conditions are needed to gain added confidence. For the reasons discussed earlier, such experiments are premature. Hence, the results of the simulations for reduced gravity environments will be predictions that will have to be compared with future experimental observations from space.

NUMERICAL SIMULATIONS OF FIRES IN LARGE COMPARTMENTS

The detailed simulation of a fire requires the representation of a number of physical and chemical processes that evolve over a range of spatial and temporal scales. The inclusion of suppressants such as water-mist introduces additional parameters such as droplet-size, droplet number density and distribution that need to be kept track of. Direct Numerical Simulation (DNS) of the suppression of fires in a large compartment is prohibitively expensive. Therefore, an alternate approach such as large eddy simulations is needed to make the problem tractable.

An advanced simulation approach is currently being developed at NRL for shipboard fire suppression and damage control[11]. In this approach, the compartment is divided into multiple blocks or regions. Finely resolved blocks are used only where the fire or suppressant injectors are located. Vastly different time-steps can be used in the different blocks. Typical results[11] from the model for a compartment fire are shown below.
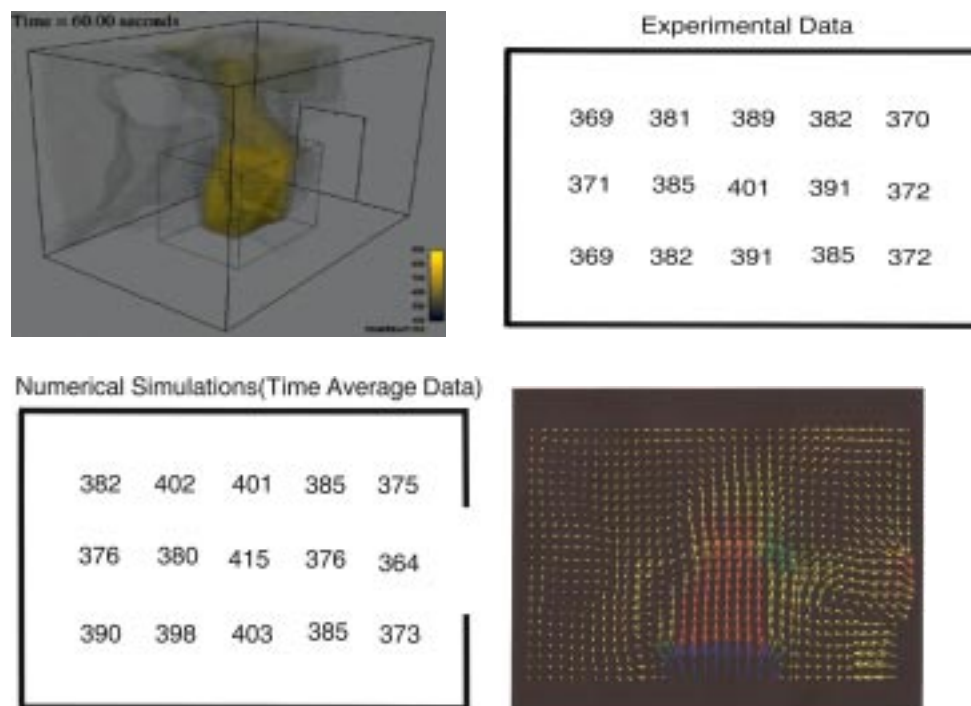
Fig. 1 The figure in the top left shows an instantaneous snap shot of the three-dimensional flow in a compartment with a fire in the center. The figure in the top right gives the measured temperature (°C) and the figure in the bottom left shows the computed temperature at the corresponding locations (all 10 cm below the ceiling). The final figure shows that the simulations capture the complex vortical flow field in the compartment. The velocity vectors in this figure have been color coded with the local temperature.

VALIDATION EXPERIMENTS

The validation experiments need to be conducted in rack-scale facilities such as at the Colorado School of Mines (CSM). The CSM facility is a rack-scale chamber with an 80 cm square footprint and 1.6 m in height, as shown in the Figure. Three of the vertical walls are glass to allow visual observation and videotape recording of the suppression events. The chamber exhaust is connected to a fume-hood ventilation system through a variable damper to allow control of the ventilation rate. Air enters the chamber through three controllable damper panels near the floor. Temperature is monitored with an array of Type-K thermocouples linked to a LabView data acquisition system. A Cohu video camera placed outside the chamber records the visual event on a digital video recorder. Oxygen and carbon
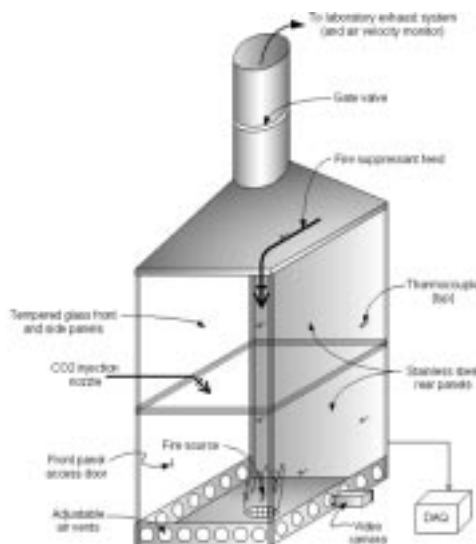
monoxide levels are measured at several points with a flue gas analyzer. Several arrays of water mist atomizers with a variety of droplet size distributions from 10- to 100-micron mean diameters are used. The chamber is fitted with a rapid CO_2 total flooding system as a backup to the water mist fire suppression system.

CONCLUDING REMARKS

Incipient fires and flames in space will be small and if tackled effectively can be prevented from growing into large ones. However, these small flames or fires are likely to occur in larger enclosures. Typically, the suppressant will need to travel some distance before reaching the incipient fire and interacting with it. A workshop[8] on "Spacecraft Fire Safety" identified, determination of flow in compartments, agent distribution, and characterization of transport phenomena from discharge outlets to the fire sites as key research topics. In this paper, a combined experimental and computational approach has been presented to tackle such fire safety issues in a reduced gravity environment. One of the key advantages of the proposed approach is that valuable and timely information for designing better space-based experiments can be gained in a cost-effective manner.

REFERENCES

1. Ross, H.D., "Burning to Go: Combustion on Orbit and Mars", Fall Technical Meeting of the Eastern States Section of the Combustion Institute, pp. 29-36, 1997.
2. Friedman, R., "Fire Safety in Extraterrestrial Environments", NASA/TM 1998-207417, 1998.
3. NASA, "Research Opportunities in Physical Sciences", NRA 02-OBPR-03, App. B, 2002.
4. Urban, D.L., Mulholland, G., Yuan, Z.G., Yang, J., and Cleary, T., "Characterization of Smoke Particulate for Spacecraft Fire Detection," Proceedings of the Sixth International Microgravity Combustion Workshop, NASA/CP-2001-210826, pp. 401-404, May 2001.
5. Abbud-Madrid, A., Riedel, E.P., and McKinnon, J.T., "A Study of Flame Propagation on Water-Mist Laden Gas Mixtures in Microgravity," Proceedings of the Fifth International Microgravity Combustion Workshop, NASA/CP-1999-208917, pp. 65-68, May 1999.
6. McKinnon, J.T., Abbud-Madrid, A., Riedel, E.P., Gokoglu, S., Yang, W., Kee, R.J., "The Water-Mist Fire Suppression Experiment: Project Objectives and Hardware Development for the STS-107 Mission," Proceedings of the Sixth International Microgravity Combustion Workshop, NASA/CP-2001-210826, pp. 105-108, May 2001.
7. Takahashi, F., Linteris, G.T., and Katta, V., "Physical and Chemical Aspects of Fire Suppression in Extraterrestrial Environments," Proceedings of the Sixth International Microgravity Combustion Workshop, NASA/CP-2001-210826, pp. 417-420, May 2001.
8. Workshop on Research Needs in Fire safety for the Human Exploration and Utilization of Space, Cleveland, OH, June 25-26, 2001.
9. Fire and Radiation Safety Get New Emphasis from Space Research, Space Research, Vol. 1, No. 1, pp. 6-11, Fall 2001, NASA.
10. "Guide for the Verification and Validation of Computational Fluid Dynamics Simulations," AIAA-G-077, 1998.
11. Prasad, K, Patnaik, G, and Kailasanath, K, "A Numerical Study of Water-Mist Suppression of Large Scale Compartment Fires," Fire Safety Journal, Vol. 37, pp. 569-589, 2002.

PARTICLE GENERATION AND EVOLUTION IN SILANE (SiH$_4$) /ACETYLENE (C$_2$H$_2$) FLAMES IN MICROGRAVITY

D. G. Keil

Titan Corporation, AeroChem Research Laboratory, Princeton, NJ 08543

INTRODUCTION

The objective of this experimental program is to advance the understanding of the coupling of particle formation with gas phase combustion processes. The work utilizes the unique SiH$_4$/C$_2$H$_2$ combustion system which generates particulate products ranging from high purity, white SiC to carbonaceous soot depending on equivalence ratio (Ref. 1). A goal of this work is to identify gas phase or particle formation processes that provide the enthalpy release needed to drive the combustion wave, and to locate the steps of the particle formation process that determine SiC stoichiometry and crystallinity. In a real sense, these SiH$_4$/C$_2$H$_2$ flames act like "highly sooty" hydrocarbon flames, but with simpler chemistry. This simplification is expected to allow them to be used as surrogates to advance understanding of soot formation in such rich hydrocarbon flames. It is also expected that this improved understanding of SiC particle generation and evolution in these self-sustaining flames will advance the commercial potential of the flame process for the generation of high purity SiC powders.

BACKGROUND

We previously investigated SiH$_4$/C$_2$H$_2$ flames in constant volume combustion experiments. In that work (Ref. 2), we found that SiH$_4$/C$_2$H$_2$ flames propagate over a wide range of stoichiometry ratios from 0.05 (C$_2$H$_2$-rich) to 2.5 (SiH$_4$-rich). Burning velocities extracted from the pressure histories of combustion events exhibited an unusual double maximum as a function of the SiH$_4$/C$_2$H$_2$ reactant ratio. The major products of the combustion are H$_2$ and fine powder containing most of the reactant mass of carbon and silicon. For a narrow range of SiH$_4$ /C$_2$H$_2$ mixture ratios near 2.0 (equal silicon and carbon atomic concentrations), the powder product of the combustion was found to be stoichiometric, nanocrystalline, cubic silicon carbide (SiC), consistent with intimate mixing on the atomic level. Processes which can contribute to the production of the silicon carbide powder include parallel formation of silicon- and carbonaceous particles that agglomerate with rapid interparticle diffusion to produce stoichiometric SiC; formation of silicon- (or carbonaceous) nuclei which grow by chemical vapor deposition with the proper ratio of gas phase Si$_x$H$_y$ and C$_x$H$_y$ species; or direct condensation of Si$_x$C$_y$H$_z$ on SiC nuclei. We have presented evidence (Ref. 2) for coupling of the silicon and carbon chemistries, i.e., that the silicon-carbon bonds form early in the flame and suggested that the such gas phase species determine the stoichiometry and crystallinity of the final product, indicating an important role of the third process. The kinetics of the overall mechanism is important in propagating the flame. Based on available thermochemical data for known and predicted gas phase intermediates, most of the combustion energy (~80%) is released in the particle formation processes.

Insight into the mechanism of SiC formation may be gained through comparisons of flame data and the product properties for a series of related flames. It is difficult to obtain detailed flame structure information from the constant volume combustion experiments described above. A steady-state, burner-supported flame is more suitable for accurate flame

diagnostics. In the present microgravity studies, the complex effects of buoyancy, buoyancy induced mixing, and gravitational settling are substantially reduced or eliminated, giving rise to undistorted and steady flames that reflect the combustion chemistry and particle formation processes. Accurate correlations are expected among, e.g., reactant stoichiometry, added gases, burning velocities, flame temperatures, and the resultant powder properties. Particle formation and growth mechanisms and their coupling will be addressed in this work.

EXPERIMENTAL APPROACH AND DESIGN

The program focus is on fundamental flame properties (burning velocity, particle and gas temperatures, flame species, and product characterizations). The key experimental challenges are to make reliable burning velocity measurements and to make measurements (e.g., gas/particle temperatures, concentrations) near the flame front to relate to the burning velocities of these particle-laden premixed flames. To make burning velocity measurements that reflect the adiabatic combustion chemistry, energy loss and thermophoretic transport to the burner must be minimized. In addition, flame front diagnostics require a geometry in which the pre-flame region is not obscured by the highly luminous particle cloud. A useful geometry that satisfies these requirements is that of inverted cone flame stabilized above a rod coaxial with the reactant flow and extending out of the burner outlet. The angle the flame makes relative to the flow direction is related to the ratio of the flow and to burning velocities. A related geometry is a "vee" flame stabilized above a transverse rod downstream of the burner outlet.

The SiH_4/C_2H_2 combustion system presented challenging design issues which have been addressed. The major features of the resultant design are described here. Both the reactants and the flame products are flammable and must be isolated from air exposure. The pyrophoric properties of the SiH_4 reactant are of particular concern, and for safety reasons, the allowable onboard quantity is limited. H_2, the gas phase flame product, also presents potential hazards related to its wide flammability limits in air. Because neither can be exposed to air, the apparatus design provides for the entire experiment to be performed in a sealed N_2-filled system. Means to maintain a constant pressure flame environment in the burner chamber is provided by a large back-pressure regulator connected to a dump tank which is evacuated before the experiment. To prevent N_2 bleed from the atmospheric pressure flame chamber through the regulator into the evacuated dump tank before the drop is initiated, they are separated by a high Cv solenoid valve which is opened only when the burner and N_2 (shroud and auxiliary chamber) flows begin. Both the solenoid valve and the back-pressure regulator are protected from the silicon carbide powder product with a high throughput, high efficiency filter. To assure safe operation in the unlikely event of a chamber seal failure during the experiment, the flame product H_2 is diluted with N_2 to below its flammability limit. The total quantity of onboard pressurized gas (N_2, SiH_4, and SiH_4/C_2H_2 reactant mixture) is limited so that the chamber pressure cannot exceed its pressure rating with complete gas release into the chamber and complete reaction of the reactants.

The reactant SiH_4/C_2H_2 mixtures will be prepared (by partial pressure) and stored in a reservoir with a feed line to the burner. To assure complete use of the reactant mixture (and hence to minimize the total quantity required), an inert flexible bag in the reservoir will be inflated with N_2 "piston" gas, feeding the reactant mixture to the burner by displacement. Constant mass (molar) flow of the piston gas will be provided by regulating the fixed pressure

upstream of critical flow orifices. The molar feed rate of the reactant mixture is essentially equal to that of the piston gas. When not being fed to the burner, the reactants and the piston bag will be isolated in the reservoir by solenoid valves. The reservoir will have a high pressure rating to withstand unintended ignition of the stored mixture.

DESIGN VALIDATION EXPERIMENTS

A laboratory prototype apparatus was assembled to test the design concepts and as a design aid for the microgravity drop tower apparatus. Normal gravity experiments investigated the feasibility of rapidly (~1 sec) establishing a steady flame in simulated drop experiments. One of the major questions was whether the back pressure regulator could maintain chamber pressure stable enough that steady flames could quickly be established in the presence of flow changes comparable to those expected in the microgravity experiments.   For the initial laboratory experiments, we chose to use CH_4(methane)-air "vee" flames supported above a transverse rod at the exit of a 3 cm diameter nozzle burner. The CH_4-air flames have comparable burning velocities to those previously measured for SiH_4/C_2H_2, without the complication of producing particles which would need to be filtered upstream of the back-pressure regulator. The burner was housed in a 15 cm (6") diameter Pyrex cross (~10 L), and the flame was viewed and recorded with a video camera through a window on one of the 10 cm (4") diameter side arms. The product gases from the chamber were exhausted into an evacuated 30 L tank through a solenoid valve and the dome-loaded back pressure regulator (Tescom 26-2900). The other critical aspect of the design is the burner feed method. As planned for the microgravity experiments, premixed burner reactants (CH_4-air) were displaced from a constant volume reservoir by filling a flexible bladder in the reservoir with a constant mass flow rate of N_2 supplied through a critical orifice. To maintain constant volume flow rate through the burner, it was critical that the chamber pressure remain constant. If the chamber pressure momentarily exceeded the reservoir pressure, the burner flow rate decreased and even reversed.

Experiments clearly showed that flow restrictions must be minimized between the chamber and the back pressure regulator for the regulator to function optimally.   The experiments confirmed that the response and throughput of the back pressure regulator was sufficient to dampen out pressure pulses (the largest are generated by the ignition of the flames) to minimize burner flow attenuation. For comparison, near-stoichiometric (9% CH_4 in air) flames were ignited and attached in under 1 second from initiation of flow (~600 scc/s) from the reservoir to the burner. Leaner flames (6.5% CH_4) have half the burning velocity and were fed at ~300 sccs. Attached flames were observed in about 1 second. Rich flames with comparable experimental burning velocities to the lean flames (i.e., 12.9% CH_4) required longer times (> 2 seconds at the same flow velocities) to stabilize. This behavior would make the intended microgravity measurements more difficult.

To better understand the observed differences in the lean and the rich flame ignition behavior, recorded chamber pressures and flame images were compared. From the pressure records, it was found that the rich mixture experiments showed larger pressure excursions in the ignition period than the lean mixtures.   The flame images revealed that once they were stabilized, the standoff distance of the rich flames above the flame holder was larger than that of the lean flames. The distance fluctuated periodically (15-30 Hz). It is likely that the two sets of

observations (pressure and flame fluctuations) are related and not coincidental. The flame holding observations can be understood on the basis of Lewis number effects.

Sung, Law, and Umemura [Ref 3] investigated inverted flame stabilization of C_3H_8(propane)-air flames and found differing behavior of lean and rich flames. For the rich flame, the height above the holder that the flame adopted was nearly independent of flow velocity, while the lean flame was stabilized over a wide range of heights above the holder, even though the laminar burning velocities of the two mixtures are nearly identical. A similar behavior characterizes our observations from the 6.5% and 12.9% CH_4-air flame recordings. However, in our case, the lean flame was stabilized at a fixed height, and the rich flame standoff distance fluctuated widely. These trends are seen to be identical if one compares the dimensionless Lewis numbers, Le, characteristic of the reactant mixtures. Sung et. al. calculate Le as the thermal diffusivity of the mixture divided by the mass diffusion coefficient of the deficient reactant (the inverse is also used by others). In their nomenclature, the observations are: rich C_3H_8/lean CH_4 - Le < 1 (small, stable standoff distance); lean C_3H_8/rich CH_4 - Le > 1 (large, variable standoff distance). Sung et. al. argue that the latter case is amenable to "adiabatic stabilization" when positioned at a great distance from the holder (heat sink). We also found the Le>1 flame to be susceptible to "waving" motions. These instabilities and the large pressure excursions we observed with these rich CH_4 flames are probably related to the "weaker" flame stabilization. Similar behavior could require longer microgravity times (as available in the 5 second drop tower) to stabilize the SiH_4/C_2H_2 flames in planned experiments. We estimated (Ref 4) that SiH_4 and C_2H_2 have similar thermal diffusivities (0.088 cm^2/s) and self-diffusion coefficients (0.11 cm^2/s). The computed Lewis number is less than 1 (Le ~ 0.81) for both rich and lean flames. The Lewis number predicts a tendency to stabilize near the holder (non-adiabatic). Thus, a more stable flame would be observed, but in the vicinity of the holder surface. It is not clear how valid this is for stoichiometric SiH_4/C_2H_2 mixtures. We are pursuing experimental measurements to answer this question.

ACKNOWLEDGMENTS

REFERENCES
1. Keil, D. G., Calcote, H. F. and Gill, R. J., *Mat. Res. Soc. Symp. Proc. Vol. 410*, Materials Research Society, Pittsburgh, 167 (1996).
2. Calcote, H.F. and Keil, D.G., "Combustion Synthesis of Silicon Carbide Powder," in Proceedings of the Joint NSF-NIST Conference of Nanoparticles: Synthesis, Processing into Functional Nanostructures, and Characterization, Arlington, VA, 12-13 May, 1997 p. 28.
3. Sung, C. J., Law, C. K., and Umemura, A., *Proceedings of the Combustion Institute*, *Vol. 24*, p.205 (1992).
4. Reid, R. C. and Sherwood, T. K., The Properties of Gases and Liquids, Their Estimation and Correlation, 2nd Ed. (McGraw-Hill, NY, 1966) pp. 460, 526.

A Characterization of Alcohol Fuel Vapor for Wavelength Modulation Spectroscopy Applied to Microgravity Flame Spread

Michael J. Kulis & Prof. David S. Perry
University of Akron, Department of Chemistry, 190 East Buchtel Commons,
Akron, OH 44325-3601

Fletcher Miller
National Center for Microgravity Research, NASA Glenn Research Center, MS 110-3,
Cleveland, OH 44135-3191

Nancy Piltch
NASA Glenn Research Center, MS 110-3, Cleveland, OH 44135-3191

Introduction

A diode laser diagnostic is being developed for use in an ongoing investigation of flame spread in microgravity at NASA Glenn Research Center. Flame spread rates through non-homogenous gas mixtures are significantly different in a microgravity environment because of buoyancy and possibly hydrostatic pressure effects. These effects contribute to the fuel vapor concentration ahead of the flame being altered so that flame spread is more rapid in microgravity [1]. This paper describes spectral transmission measurements made through mixtures of alcohol, water vapor, and nitrogen in a gas cell that was designed and built to allow measurements at temperatures up to 500 °C. The alcohols considered are methanol, ethanol, and n-propanol.

The basic technique of wavelength modulation spectroscopy for gas species measurements in microgravity was developed by Silver et al [2,3]. For this technique to be applicable, one must carefully choose the spectral features over which the diode laser is modulated to provide good sensitivity and minimize interference from other molecular lines such as those in water. Because the methanol spectrum was not known with sufficient resolution in the wavelength region of interest, our first task was to perform high-resolution transmission measurements with an FTIR spectrometer for methanol vapor in nitrogen, followed recently by ethanol and n-propanol. A computer program was written to generate synthesized data to mimic that expected from the experiment using the laser diode, and results from that simulation are also presented.

Experimental Apparatus and Procedure

In order to record alcohol spectra at low concentrations and elevated temperatures, we built a gas cell and fuel vapor filling system. The gas cell is a cylindrical stainless steel body with sapphire windows sealed at both ends using flanges and aluminum washers, Fig 1. The transmission path length is 9.83 cm. The cell can be heated up to 500 °C using a heating mantle wrapped around the cell. The heating mantle and cell are partially enclosed with ceramic plating. The temperature is displayed, set, and maintained using a temperature controller connected to the heating mantle and a thermocouple attached to one flange of the cell. A second thermocouple is welded through to the inside of the cell body (shown in Fig. 1) to accurately measure the temperature within the cell.
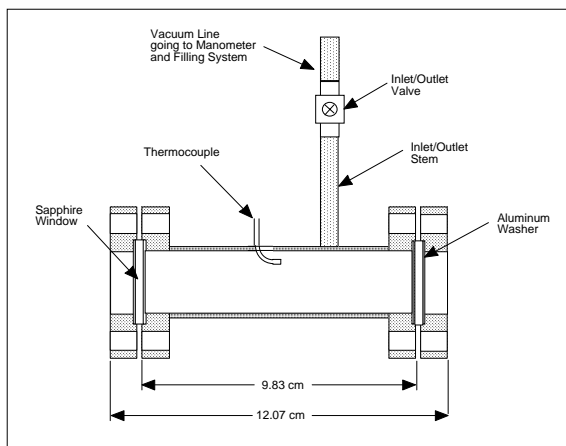
Fig 1. Gas cell without heating mantle and ceramic plating

The fuel vapor filling system is used to precisely fill the cell with alcohol vapor at the desired pressure while the cell is at the temperature at which the transmission will be recorded. The system and gas cell are evacuated for about thirty minutes to clear all inner surfaces from contamination of previous experiments. The alcohol vapor is introduced into the filling system and gas cell by opening one of the valves leading to a test tube containing alcohol in its liquid state and its corresponding vapor pressure at room temperature. The pressure in the cell is measured using a capacitance manometer on a vacuum line. The approximate error of the pressure measurement is 0.25 torr. The pressure is adjusted by partially opening the system to vacuum. The inlet/outlet valve on the cell is then closed, and the capacitance manometer in addition with the vacuum line going to the cell is evacuated. Nitrogen is introduced into the system up to the inlet/outlet valve. Once the pressure of nitrogen is above the vapor pressure of the alcohol in the cell, the inlet/outlet valve is opened. The pressure in the cell is increased to approximately one atmosphere to give a pressure broadened spectrum that resembles a spectrum obtained in a combustion environment.

The spectra were obtained with a Nicolet Nexus 870 FTIR spectrometer over a range of 2100 to 8000 wavenumbers, with a resolution of 0.05 wavenumbers. The cell was specifically designed to fit inside the open sample compartment with its heating mantle in place. Ambient air was purged from cell windows with nitrogen to avoid interference with overlapping water lines in the alcohol spectrum.

Experimental Results

Spectra of methanol, ethanol, n-propanol and water recorded at 30 °C are shown in Fig 2 for a limited wavelength range that we determined had the optimal peaks for methanol detection. Each spectrum is normalized by its partial pressure and the pathlength in order to directly compare signal strengths with other spectra. Of the three alcohols, methanol provides the sharpest and most intense peaks. Along with alcohol concentration information, the spectra obtained for the experimental combustion system will contain overlapping water lines and also encode temperature information. Fig. 2 shows that methanol peak 1 has an overlapping water line that could be used for water concentration and/or temperature determination; methanol peak 2 has no overlapping water lines. As temperature dependence is weak, it may prove impossible to extract temperature reliably. A typical diode laser has a temperature tuning range of near 3 nm and a current tuning range of near 0.4 nm. Due to the thermal time constant, only current tuning is used during a given experiment, while temperature tuning can be used as a coarse adjustment in the set-up phase.
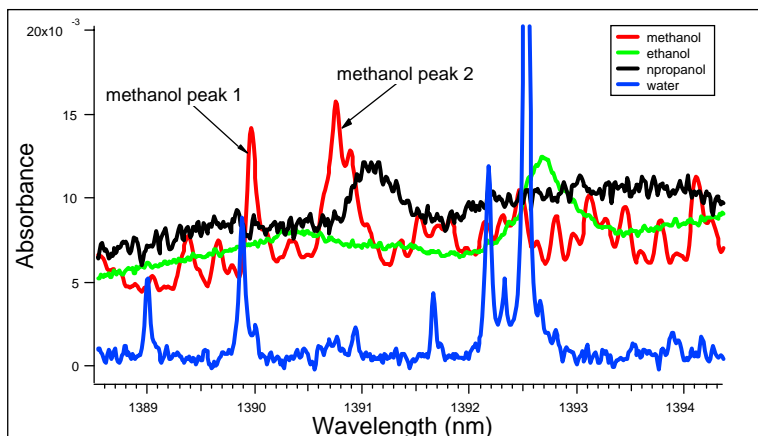
Fig 2.The first overtone OH stretch vibration of methanol, ethanol, n-propanol, and water per torr of pressure and per meter pathlength at 30 °C

In order to determine if the large methanol peaks shown in Fig. 2 are diagnostically useful, experimental spectra were recorded using the FTIR spectrometer in a range of conditions with temperature varying from 30 to 300 °C, pure methanol pressure from 10 to 70 torr, pure water pressure from 5 to 18 torr and select mixtures of the of two. Fig. 3 shows the concentrations of the species in each spectrum obtained at 30 °C.

Simulated Wavelength Modulated Spectra

The FTIR spectra were translated into wavelength modulation spectra with a routine designed to simulate the data acquisition of the diode laser system developed by Silver et al. This system uses a modulation frequency f, demodulated at $2f$, and modulation depth, which represents the amplitude of the applied modulation signal. Simulated $2f$ spectra of methanol are shown in Fig. 4 with modulation depths of 0.04 nm, and 0.06 nm. This figure illustrates that, for modulation depths small compared to the linewidth, increasing the modulation depth improves the signal to noise ratio [4].
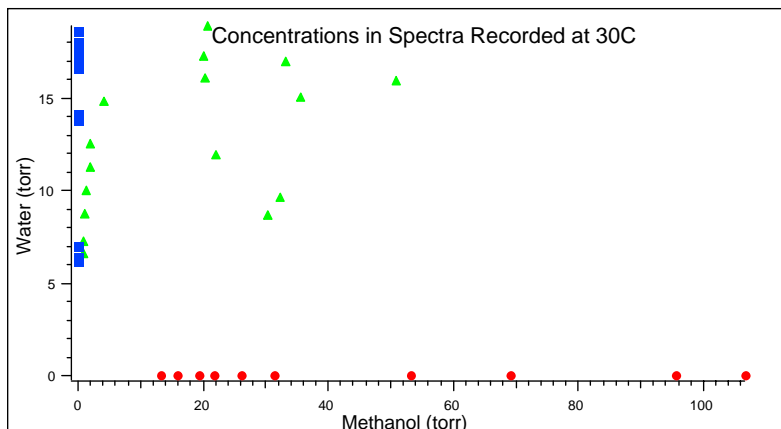

Fig. 3. Concentration of the methanol and water in each spectrum at 30 °C

The intensities of both peaks correlate well with methanol concentration; peak 1 correlates only marginally with temperature. Using the wavelength modulation technique, the detection limits of these peaks are expected to be near 10 ppm with a 10cm pathlength. The correlation with temperature may improve with the spectra obtained using the wavelength modulation technique. With this technique, the detection sensitivity is limited by the detector quantum noise instead of by laser $1/f$ noise, as is the case with direct absorption. The signal to noise for wavelength-modulation spectra is expected to be approximately three times larger than that for the FTIR spectra if the detector quantum noise limit is reached.
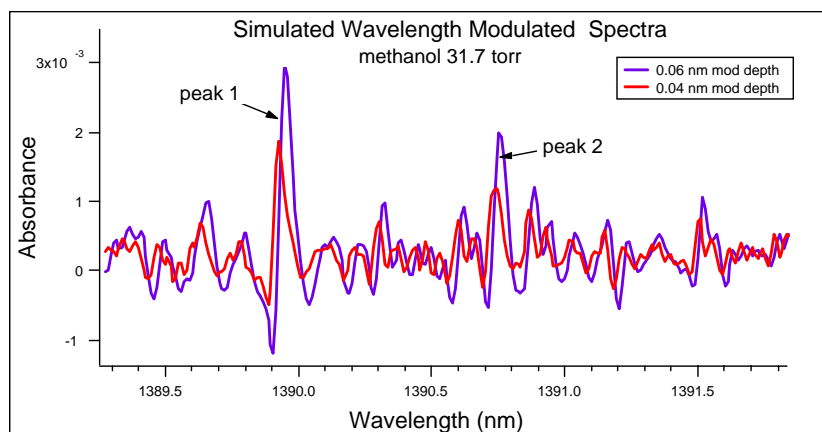
Fig. 4. Simulated 2*f* spectra from FTIR spectra.

Conclusions

In preparation for diode laser measurements of methanol for use in flame spread investigations, an extensive study of the spectra of methanol and water in the region of available diode lasers was performed. A heated cell was constructed to allow measurements of heated methanol vapor. High-resolution FTIR spectra were obtained for vapor-phase methanol, water, and mixtures from 30 to 300 °C and various concentrations. From these measurements two methanol features were identified that show minimal interference from water and that have sufficient amplitude for detection by diode laser spectroscopy. Similar spectra were also recorded for ethanol and n-propanol.

A computer program was written to simulate wavelength-modulated diode laser spectra using the experimental FTIR spectra as input. The output is displayed as a *2f* spectrum (that is, demodulated at twice the modulation frequency) and effects of varying the modulation depth were examined.

Acknowledgements

References

1. F.J. Miller, J. W. Easton and A.J. Marchese, "Gravitational effects on flame spread through non-homogeneous gas layers," *Proc. Comb. Institute*, **29**, 2003 (to appear)
2. Joel A. Silver, Daniel J. Kane and Paul S. Greenberg, "Quantitative species measurements in microgravity flames with near-IR diode lasers" *Applied Optics*, **34**, 2787 (1995)
3. Joel A. Silver and Daniel J. Kane, "Diode laser measurements of concentration and temperature in microgravity combustion," *Meas. Sci. Technol.* **10**, 845 (1999)
4. Joel A. Silver, "Frequency-modulation spectroscopy for trace species detection: theory and comparison among experimental methods," *Applied Optics*, **31**, No. 6, 707, (1992)

FUEL DILUTION STUDIES OF COFLOW LAMINAR DIFFUSION FLAMES IN A MICROGRAVITY ENVIRONMENT

Marshall B. Long and Mitchell D. Smooke
Department of Mechanical Engineering
Yale University
New Haven, CT 06520-8284

INTRODUCTION

While computational and experimental studies of diffusion flames have become increasingly sophisticated over the past ten years, they have also helped to illustrate areas in which improvement in both the chemical and physical modeling of these systems is needed. Two specific areas in which further research is warranted are the effects of fuel dilution on flame lift-off and stability, and the formation of combustion generated soot-particulates. The unique characteristics of the microgravity environment are useful for studying both of these phenomena, which occur at opposite ends of the fuel dilution spectrum. Microgravity enables the stabilization of very weak flames with high levels of dilution. For undiluted fuels, microgravity flames have increased soot residence times (and therefore greater soot volume fractions) compared to their normal-gravity counterparts. Studying these flames will enable us to better understand the factors that affect diffusion flame lift-off height and extinction. It will also enable us to quantify the roles of inception, surface growth and oxidation processes in combustion-generated soot particulates. The goals of the research will be the development of modified kinetic mechanisms for hydrocarbon fuels that are able to model effectively diffusion flame structure under a larger parameter range than existing mechanisms. We will also pursue the development of submodels for soot formation that are capable of predicting both high and low soot loading levels in hydrocarbon flames of various fuels.

PREVIOUS MICROGRAVITY EXPERIMENTS

A number of diffusion flame studies have been carried out in a microgravity environment [1-9]. These studies have ranged from methods to evaluate flame structure [1-5], to observations of soot processes [6-9]. The studies indicated that while computational models employing parabolic approximations to the governing equations gave qualitative agreement with experimental observations, a better understanding of kinetic effects and axial diffusion in these flames is needed. In addition, only minimal temperature and species composition measurements were made in these systems. The series of studies that investigated soot processes in nonbuoyant flames [6-9] focused on the measurement of soot volume fractions and soot structure investigations. Our own study of microgravity laminar coflow diffusion flames, carried out between 1996 and 2000, sought to investigate many of these issues while bringing a combined computational/experimental program to bear on these problems [10-13]. The microgravity (μg) combustion experiments proceeded in two phases. The first phase involved extracting reliable, quantitative information from flame chemiluminescence measurements and using this technique in a microgravity flame study aboard the KC-135 reduced-gravity aircraft. After this work had increased our

experimental expertise and understanding of microgravity diffusion flame behavior, a variety of two-dimensional laser diagnostics were brought to the KC-135 to allow for the measurement of temperature, major species, and soot distributions. These μg measurements afforded the most rigorous set of comparisons with flame computations to date.

BURNER CONFIGURATION

The flame chosen for investigation consists of nitrogen-diluted methane fuel surrounded by an air coflow. The burner was designed to have well-defined velocity and temperature boundary conditions to facilitate comparisons between computations and experiments. The burner has a central fuel jet (4 mm inner diameter, 0.4 mm wall thickness) surrounded by coflowing air (50 mm inner diameter). The standard flow conditions, which have been measured and modeled extensively in normal gravity [14], consist of fuel composed of 65% CH_4 diluted with 35% N_2 by volume (denoted 65/35 in later discussions). The plug flow exit velocity of both fuel and coflow was 35 cm/s. These conditions produce a blue flame roughly 3 cm in length with a lift-off height of 5.5 mm in normal gravity. A wide range of fuel dilution levels was measured in this study. The CH_4/N_2 fuel composition varied from 100% CH_4 (denoted 100/0) to 30% CH_4 (denoted 30/70) in 5% increments, with fuel and air exit velocities held fixed at 35 cm/s. For all conditions, the flame was lifted from the burner surface so that the assumption of negligible heat loss to the burner is an excellent one.

COMPUTATIONAL APPROACH

The computational model used to compute the temperature field, velocities, and species concentrations solves the full set of elliptic two-dimensional governing equations for mass, momentum, species, and energy conservation on a two-dimensional mesh. The resulting nonlinear equations are then solved by a combination of time integration and Newton's method. The chemical mechanism employed contained 26-species (C_2) and 83 chemical reactions [14]. Similar results have been obtained using GRI Mech 2.11 and GRI Mech 3.0. Flame structure was calculated over a range of flow conditions in both μg and normal gravity. These computations were performed for CH_4/N_2 mixtures ranging from 30/70 to 75/25. Calculations were not performed at flow conditions less dilute than 75/25 since these flames were observed to produce soot, which was not included in the computational model.

EFFECTS OF DILUTION ON FLAME LIFT-OFF

Flame emission measurements were performed in μg and 1g over a wide range of dilution levels, from 50/50 to 100/0. The base of the flame, where the chemiluminescence signal is strongest, remained extremely stable over the 10 s integration time for all conditions studied. Measured flame shape, as indicated by the spatial distributions of the CH* and OH* radicals, can change significantly between normal gravity and microgravity. In general, a microgravity flame is shorter, wider, and has a higher flame front curvature relative to its normal gravity counterpart. Furthermore, since methane is lighter than air, density effects produce a normal gravity flame with a higher lift-off than the corresponding μg flame. These effects can be seen in both computed CH profiles and measured CH* profiles. For flames with modest dilution levels (e.g.,

65/35) the structural agreement is excellent for lift-off and flame shape, in both normal and microgravity.

We define the measured lift-off as the height above the burner where the CH*/OH* maximum occurs, and similarly for CH in the computations. All three peaks occupy the same spatial location, as shown in earlier work [10]. The measured and computed lift-off heights, both in µg and normal gravity, can now be plotted as a function of methane level in the fuel stream as shown in Fig. 1. In addition to the lift-off heights derived from the emission measurements, Fig. 1 shows lift-off heights for greater dilution levels obtained from temperature measurements in the same flame. Uncertainties in measured lift-off at higher dilution levels arise from flame asymmetries and are likely responsible for the discrepancies between the two measurement techniques.
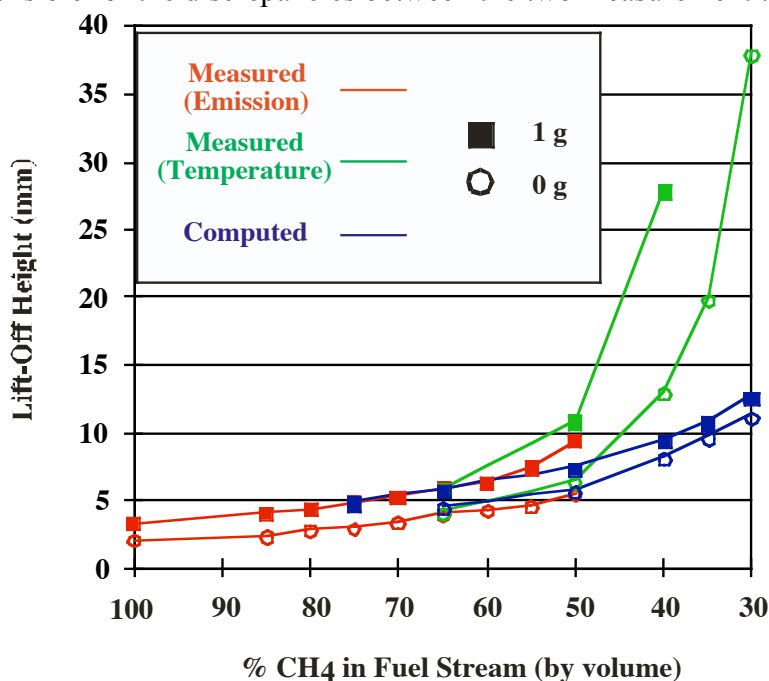
The predicted lift-off height agrees well with measurement in 1g at the 75/25 and 65/35 fuel mixtures. As the methane level decreases from 65% to 50%, the computed and measured curves begin to separate. When the fuel mixture is diluted below 50% CH_4 in 1 g, the lift-off height becomes increasingly under-predicted, until the code computes a stable flame at fuel mixtures (35% and 30% CH_4) beyond the 1 g experimental blow-off limit (40% CH_4). Further, the difference between computed normal and µg lift-offs does not match the measured curves, which separate increasingly as the fuel mixture is diluted. The measured and computed µg lift-offs show reasonable agreement up to a dilution level of 50% and then depart significantly. The discrepancy between measured and predicted lift-off suggests that there are unresolved kinetic issues, i.e., reaction pathways that may become increasingly important in highly diluted flames, which must be studied further in cooler, more dilute methane-air diffusion flames.

SOOT MEASUREMENTS

For undiluted coflow flames, laser-induced incandescence (LII) measurements of the soot volume fraction were made in both normal and µg conditions [13]. In each case, the LII signal was

measured as a function of laser intensity to ascertain the optimum per-pulse energy for the determination of soot volume fraction. Since the soot field was observed to fluctuate during "g-jitter" on the KC-135, the LII images taken in µg are single-shot. These time-resolved images are indexed with the local acceleration to assess the behavior of these flames in an unsteady gravitational field. Flame luminosity background measurements were made in µg but could not be subtracted from measured LII signals due to the unsteadiness present in the flames. Single-shot LII measurements were made successfully in the 100% CH_4 (100/0) flame, where five measurements can be made during a given low-g parabola. For normal gravity measurements, the soot levels present in methane flames were insufficient to allow for single-shot measurements, so a 100-shot integration was used.

In making LII measurements on the KC-135, single-shot measurements were repeated at multiple times to assess the fluctuations in soot volume fraction and distribution in relation to the time-varying local acceleration. In a given 15 mm region above the burner surface, the peak soot volume fraction can vary by as much as 50% over the course of a low-g parabola. However, the measured soot concentration and distribution is repeatable for measurements made during similar g-levels and g-histories. Therefore, the distribution which results after a long (> 3s) period of "g = 0" is considered to be the best available soot measurement in the noisy gravitational field available aboard the KC-135. For this best-case µg measurement, the peak soot volume fraction increases by a factor of 15 while the soot-containing region contracts axially and expands radially [13]. In future work, these measurements need to be compared with the predictions of computations to assess the validity of the soot models being developed. Additionally, a low-noise µg environment with long time scales may be necessary to allow the flame to reach steady state, as observed in sooty flames by other researchers [5,9].

REFERENCES
1. Cochran, T.H. and Masica, W.J., *Proc. Comb. Inst.*, 13, 1970, pp. 821-829.
2. Klajn, M., and Oppenheim, A.K., *Proc. Comb. Inst.*, 19, 1982, pp. 223-235.
3. Sunderland, P.B., Mendelson, B.J., Yuan, Z.-G., and Urban, D.L., *Comb. Flame*, 116, 1999, pp. 376-386.
4. Hegde, U., Zhou, L., and Bahadori, M.Y., *Comb. Sci. Tech.*, 102, 1994, pp. 95-113.
5. Lin, K.-C., Faeth, G.M., Sunderland, P.B., Urban, D.L., and Yuan, Z.-G., *Comb. Flame*, 116, 1999, pp. 415-431.
6. Bahadori, M.Y., Edelmann, R.B., Stocker, D.P., and Olson, S.L., *AIAA Journal*, 28, No. 2, 1990, pp. 236-244.
7. Megaridis, C.M., Griffn, D.W., and Konsur, K., *Proc. Comb. Inst.*, 26, 1996, pp. 1291-1299.
8. Konsur, B., and Megaridis, C.M., *Comb. Flame*, 116, 1999, pp. 334-347.
9. Urban, D.L., Yuan, Z.-G., Sunderland, P.B., Lin, K.-C., Dai, Z., Sun, K., and Faeth, G.M., *AIAA Journal*, 36, No. 8, 1998, pp. 1346-1360.
10. Walsh, K. T., Long, M. B., Tanoff, M. A., and Smooke, M. D., *Proc. Comb. Inst.*, 27, 1998, pp. 615-623.
11. Walsh, K.T., Fielding, J. and Long, M. B., *Opt. Lett.*, 25, 2000, pp. 457-459.
12. Luque, J., Jeffries, J. B., Smith, G. P., Crosley, D. R., Walsh, K. T., Long, M. B. and M.D. Smooke, *Comb. Flame*, 122, 2000, pp. 172-175.
13. Walsh, K. T., Fielding, J., Smooke, M. D. and Long, M. B., *Proc. Comb. Inst.*, 28, 2000, pp. 1973-1980.
14. Smooke, M. D., Xu, Y., Zurn, R. M., Lin, P., Frank, J. H., and Long, M. B., *Proc. Comb. Inst.*, 24, 1992, pp. 813-822.

COUPLED RADIATION AND THERMOPHORETIC EFFECTS IN SOOTING MICROGRAVITY FLAMES

D. W. Mackowski
Department of Mechanical Engineering, Auburn University, AL

V. Nayagam and P. B. Sunderland
National Center for Microgravity Research, Cleveland, OH

INTRODUCTION

The objective of our research program is to investigate, both theoretically and analytically, the effects of coupled radiation emission and thermophoretic transport on the dynamics of soot particles in flames. The effect of this coupling would be familiar to anyone who has emersed a thermocouple into a sooting flame. As is well recognized, radiative cooling of the bead creates a conductive flow of heat from the gas to the bead, and the resulting temperature gradient in the gas drives a thermophoretic motion of soot particles towards the bead, leading to soot deposition onto the bead. We propose that this effect can occur among the soot particles themselves; soot is an efficient radiator of heat, and in high temperature gases the soot, via radiative emission, will create a heat sink in the gas. The temperature gradients in the gas that result from this sink will act, through thermophoresis, to 'compress' the soot particles into regions of increasing concentration. The ultimate effect of this coupling would be the accelerated growth of large soot aggregates via the scavenging of smaller particles.

There is some evidence that the coupled radiation/thermophoretic (CRT) mechanism affects the dynamics of the soot fields in microgravity gaseous jet and droplet diffusion flames. Images of such flames show the formation and growth of large (visible to the eye) soot aggregates within the soot 'shell' that is formed between the flame and the source of fuel. Brownian diffusion or fluid shear mechanisms of coagulation cannot account for the formation of such particles in the time span ($\sim 2.2 - 5$ s) of the experiments.

Aside from developing a better understanding of the processes which govern soot growth, an additional motivation for our research stems from the fact that the CRT mechanism could lead to new methods for controlling particle agglomeration, via manipulation of the radiation environment.

The tasks of the research consist of 1) predicting the thermophoretic, diffusive, and radiative properties of realistic soot aggregates; 2) modelling the effects of CRT on the dynamics of the soot field; and 3) developing experimental methods in which the CRT mechanism can be identified and manipulated.

TRANSPORT PROPERTIES OF AGGREGATES

Soot particles invariably form as aggregates of spheres. An accurate understanding of the effects of CRT will require an equally accurate prediction of the transport properties (thermophoretic, diffusive, radiative) of the aggregate. Of course, such properties are relevant beyond the scope of this research (i.e., soot deposition studies, radiative transfer in flames, interpretation of LII measurements).

Prediction of the thermophoretic and hydrodynamic forces on a soot aggregate is made

difficult by the unique Knudsen characteristics of the particle. The momoners in the aggregate (radii ~ 0.02 μm) will be considerably smaller than the gas mean free path in atmospheric pressure, high temperature gases, yet the overall size of the aggregate could be comparable to or greater than the mean free path.

As a first approximation, we developed a Monte–Carlo, molecular dynamics method to predict the free–molecular thermophoretic and hydrodynamic forces acting on fractal–like aggregates of spheres [1]. This model assumes that all characteristic sizes of the aggregate are significantly less than the prevailing mean free path. A modification of the sampling procedure that is used to assign velocities to the computational molecules was developed, which allowed for a relatively fast and accurate determination of the particle transport properties for small Mach number (i.e., slow–moving) conditions. Aggregate targets in the simulation were generated using an algorithm which mimics cluster–cluster aggregation, and simulations were performed on aggregates with a range of fractal dimensions and structure factors. The results indicate that for fractal dimensions in the range of $D_f = 1.7 - 2.0$, the hydrodynamic radius of the aggregate scales as $a_m \sim a N_S^{0.47}$, in which a is the sphere radius and N_S is the number of spheres. This result is consistent with experimental findings of Wang and Sorensen [2]. Results also show that the thermophoretic velocity of a randomly–oriented aggregate will be slightly larger than that of the isolated spheres. The enhancement in velocity increases with N_S, yet for relatively large–scale aggregates with $N_S = 3000$ the increase is only around a factor of 1.08. This is also consistent with previous analytical work, based on rod–like particles in the free–molecular limit and clusters of spheres in the near–continuum approximation, of Rosner et al. [3].

We have developed an electrostatics model to accurately predict the visible–IR absorption properties of fractal–like aggregates of spheres. In the near to mid–IR, our model indicates that the absorption of an aggregate can be considerably greater than that predicted from a Rayleigh–Gans–Debye model. Details will be presented at the meeting.

MODELLING THE EFFECTS OF CRT

As mentioned previously, microgravity diffusion flame experiments show the presence of rapid particle growth in the soot shell. To demonstrate a possible connection between this effect and CRT, we have performed simulations of particle dynamics in non–reacting (i.e., constant total mass) cloud of soot with combined conduction, convection, and radiation. A hybrid method is used to model the evolution of the soot, with the energy equation cast in the usual Eulerian formulation, yet with a discrete particle (Lagrangian) model representing the soot field. Details of the model will be described in [4].

To present a simple illustrative calculation, we applied the model to a plane layer of soot in a stationary, high temperature gas. To model an infinite expanse of the layer, we chose a cubic computational domain and imposed periodic boundary conditions at the x and y normal surfaces. The computational particles were initially distributed randomly in a layer of thickness d in the x, y plane. Surfaces normal to z were isothermal. Assuming optically thin conditions and a cold radiative environment, the dimensionless governing equations for
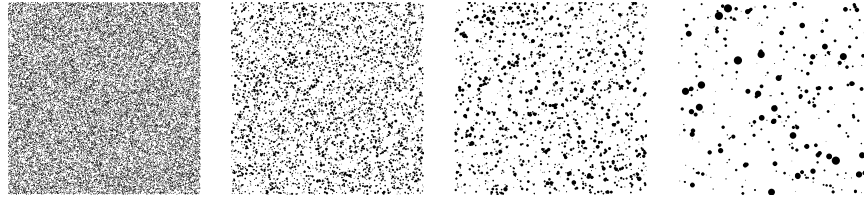
Figure 1: Soot field evolution

the system are

$$\frac{\partial T}{\partial t} = \nabla^2 T - N_R\, f\, T^4 \tag{1}$$

$$\frac{d\mathbf{r}_i}{dt} = -c_T\, Pr\, \nabla\, T, \quad i = 1, 2, \dots N_P \tag{2}$$

in which f is the volume fraction of the particles, N_R is a radiation–conduction number, c_T is a dimensionless thermophoretic diffusion factor (order unity), Pr is the Prandtl number, and $\mathbf{r}_i$ is the position vector of the ith computational particle. The energy equation was discretized in space using a standard finite volume approach, and the particle volume fraction in each cell was computed from the number of particles in the cell. A time–splitting procedure was used to integrate the coupled system forward in time.

Figure (1) gives an indication of the evolution of the soot field in the layer as predicted by the model. The random initial distribution of the particles in the layer, shown in the leftmost plot, results in a small degree of nonuniformity in the initial local volume fraction. These nonuniformities create 'dimples' in the temperature field, which results in the thermophoretic transport of particles towards regions of relatively high concentration. These illustrative calculations, while simple in nature, indicate that the CRT mechanism creates an instability in the soot cloud, in that nonuniformities (or perturbations) in the concentration field will become amplified.

Further discussion on the stability of the layer – including the effects of particle diffusion – will be discussed at the meeting and in Ref.[4].

EXPERIMENT

To experimentally examine the effects of CRT, we have devised a ground based experiment involving a laminar flow of soot particles through a heated, yet radiatively transparent, tube. The basic hypothesis is that the particles will radiate heat from the flow to the cold environment (owing to the transparency of the tube), which will be balanced by the conduction of heat from the heated tube walls to the gas. The temperature at the center of the tube will therefore be lower than the temperature at the walls, and thermophoresis will drive the particles towards the tube centerline.

The experimental design is illustrated in Fig. (2). A 2 cm ID quartz tube is used to contain the particle/gas stream. The tube wall is maintained at a high temperature by a annular CH_4/air premixed flame, mounted at the base of the tube and contained within an 8 cm ID quartz tube. In current experiments we are using a C_2H_2/air jet diffusion flame on the inside of the tube to generate the soot particle stream. We are also examining the use of
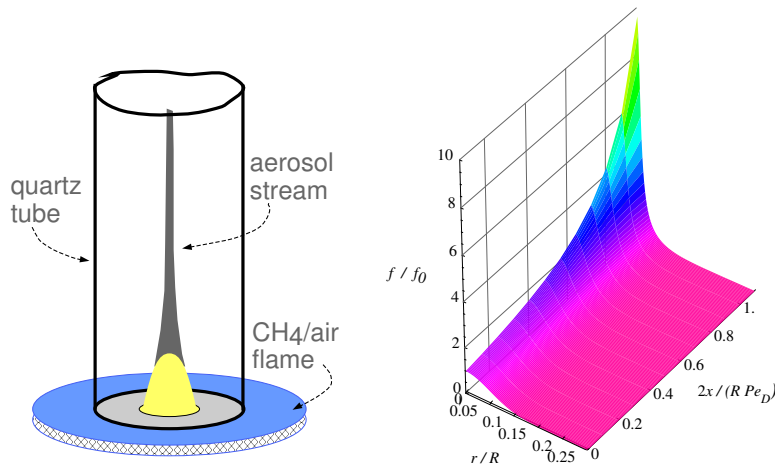
Figure 2: Tube flow CRT experiment and predictions

an aerosol generator to feed the particles into the stream, which would provide for a more dispersed initial distribution of particles than the flame.

To predict the rate of compression of the soot field, we modelled the flow as axisymmetric, non–reacting and with constant properties, and adopted an Eulerian formulation for the soot concentration field. Wall temperatures and inlet temperatures were uniform and equal, and the radial distribution of soot volume fraction at the inlet was specified. The tube wall is taken to be transparent up to a fixed cutoff wavelength (~ 3 μm for quartz), beyond which the material is opaque. An optically thin radiative model was used for the particles, with spectral absorption properties characteristic of soot.

Predictions of the evolution of the soot field are given in Fig. (2), which shows the volume fraction distribution (normalized with respect to the inlet centerline volume fraction) as a function of dimensionless radial ($= r/R$) and axial ($= 2x/(R\,Pe_D)$, where Pe_D is the Peclet number of the flow) coordinates. The predictions correspond to a tube wall temperature of 1200 K, an inlet centerline volume fraction of 10^{-5}, and a Gaussian inlet f distribution with $\sigma/R = 0.005$. For these conditions, the model predicts that the centerline volume fraction will increase by a factor of 10 within an axial distance of $x \sim R\,Pe_D$. Experimental results will be discussed at the meeting.

[1] D. W. Mackowski. Monte–carlo simulation of hydrodynamic drag and thermophoresis of fractal aggregates of spheres in the free–molecule flow regime. *J. Aerosol Sci.*, 2003. Submitted for publication.

[2] G. M. Wang and C. M. Sorensen. Diffusive mobility of fractal aggregates over the entire knudsen number range. *Phys. Rev. E*, 60:3036–3044, 1999.

[3] D. E. Rosner, D. W. Mackowski, , and P. Garcia-Ybarra. Size– and structure–insensitivity of the thermophoretic transport of aggregated soot particles in gases. *Combust. Sci. Tech.*, 80:87–101, 1991.

[4] D. W. Mackowski, V. Nayagam, and P. B. Sunderland. The effects of radiation and thermophoretic coupling on the dynamics of soot in flames. 2003. In preparation.

HIGH PRESSURE COOL FLAMES AT MICROGRAVITY

David L. Miller, Nicholas P. Cernansky, Howard Pearlman
Drexel University

Jens König and Hans Rath
University of Bremen

INTRODUCTION

Research on subatmospheric pressure cool flames and low-temperature oxidation at microgravity has been conducted by Pearlman and co-workers (Pearlman, 1999, 2000) during the past six years at NASA GRC. Both laboratory (1g) and KC-135A reduced-gravity experiments have been performed in a spherical, quartz reactor, housed in a preheated furnace (classical Mallard-LeChatlier apparatus).

To summarize the results, four different reaction modes have been observed. They include: (1) slow reaction, (2) cool flame(s), (3) multi-stage ignition and (4) single-stage ignition. *Slow reaction* is a mode characterized by a weak pressure and temperature excursion accompanied by no detectable light emission. *Cool flames* are characterized by a weak pressure and temperature excursion along with weak spectral emission, presumably due to excited formaldehyde. *Multi-stage ignition* occurs when a cool flame transitions into a hot ignition and *single-stage ignition* is a hot ignition, not preceded by a cool flame. A brief description of each mode is presented below.

At 1g, the cool flame starts at the top of the reaction vessel due to the presence of convective currents that arise as a result of self-heating associated with slow reaction. In contrast, the cool flame originates at the center of the vessel at reduced gravity and subsequently propagates radially outward in a one-dimensional fashion. One-dimensional, radial propagation is expected at reduced gravity, since diffusive fluxes govern the transport of heat and species.

Multiple cool flames are also observed in a static configuration at 1g for a select range of test parameters. However, only one cool flame has been observed in the n-butane-oxygen system at reduced gravity within the available 23s reduced-gravity test time on the KC-135 aircraft. While additional test time is needed to determine whether or not multiple cool flames occur in this system at μg, it was hypothesized (Griffiths, 1999) that the time needed for thermal relaxation in ground-based facilities may be insufficient for multiple cool flames to develop. To test this hypothesis, an equimolar mixture of n-C_4H_{10}-O_2 was diluted with equal volumes of helium or argon (monotonic inert gases) to vary the thermal diffusivity of the mixture (αHe-mix~4αAr-mix) and thus adjust the thermal relaxation time (τ_{th}~L2/α). Under reduced gravity conditions the mixture with helium produced as many as five sequential cool flames.

Multi-stage ignition -- one (or more) cool flames followed by a hot ignition -- has also been observed at 1g and reduced gravity. Similar to the cool flames, both the cool flame and hot flame associated with the two-stage process originate at the top of the vessel at 1g and near the center at reduced gravity. Note also that the second induction period (the time between the cool flame and the hot flame) is also shorter at μg than at 1g, perhaps due to the shorter transport times at μg (diffusion times~L^2/α and L^2/D, where α and D are the thermal and mass diffusivities, respectively) compared to 1g (buoyant rise time scales as $(gL)^{1/2}$).

Single-stage ignition, not preceded by single or multiple cool flames, has been observed at reduced gravity. Analogous to the proceeding modes, the ignition kernel develops at the center of the spherical volume and propagates radially outward in a one-dimensional manner.

RESEARCH PROGRAM

Overview: The primary objective of this program is to extend subatmospheric work on low-temperature oxidation reactions, cool flames, and auto-ignition in unstirred, static reactors to higher pressures (1atm<P<10atm). Specifically, the work will:

(1) Develop ignition diagrams (phase-plots of temperature versus pressure and mixture stoichiometry) for heavy hydrocarbon-air and hydrocarbon-oxygen mixtures at elevated pressures in the range of 1-10atm,

(2) Measure and record the one-dimensional flame speed, integrated spatial distribution of uv and visible light, 2D formaldehyde and temperature distribution, and induction times(s) associated with high pressure cool flames and auto-ignition fronts,

(3) Develop chemical kinetic models for high pressure, low-temperature reactions in a microgravity environment and compare the results to the experimental measurements,

(4) Compare the results to those obtained by other researcher efforts that have used CSTR's, heated flow tubes, and motored engines.

To accomplish these objectives, a team of researchers with experimental and modeling experience in low temperature oxidation and cool flames has developed a program that includes laboratory and reduced gravity experimental development and testing, detailed kinetic modeling, and LIF diagnostic development and implementation. The U.S. participants will focus on the experiment development and modeling, while the German Co-Investigators will focus on LIF diagnostics and testing. This study will be a testbed for a LIF disk laser system being developed by the German Space Agency.

Apparatus: The experimental apparatus will consist of a quartz vessel jacketed by a high pressure stainless-steel vessel housed in a furnace, a gas mixing and delivery system, a vacuum pump, and diagnostics that include intensified video imaging, thermocouple and pressure measurements, and a diagnostic setup for LIF imaging. It is envisioned that some of the subsystems developed previously for low-pressure studies (under NASA sponsorship) can be modified, while others must be developed.

A high pressure, high temperature reaction vessel outfitted with a thermocouple rake, gas delivery/ evacuation ports, a pressure tap/ transducer, and windows for optical access will be designed, built and used to conduct the proposed experiments. It is envisioned that the reaction vessel will be made from quartz or fused silica to minimize heterogeneous surface effects and housed within a 10cm i.d. (or larger) stainless steel vessel. The steel shell will be outfitted with optical access, such that spectral imaging and LIF can be performed. During the experiments, the annulus between the high pressure reaction vessel and the stainless steel shell will be filled with pressurized inert gas to minimize the pressure gradient across the quartz vessel.

The stainless steel shell and reaction vessel will be housed in a furnace and preheated to uniform temperature prior to gas entry. It is envisioned that a new furnace with optical access, diagnostic feedthroughs, and high pressure gas delivery be designed and procured. To hold the reaction vessel and housing, a low-thermal conductivity, machinable ceramic will be used. A thermocouple rake and pressure transducer(s) for high-pressure operation are also needed. It is envisioned that a stainless-steel jacketed quartz tube will be used for gas supply to the reactor. Inert gas at the same pressure as the

reactants will flow in the annulus between the quartz supply tube and the stainless-steel jacket to minimize the pressure difference across the quartz supply tube. This technique eliminates the need for high temperature quartz to metal transitions, which are not readily available for temperatures in excess of 250°C.

Radial temperature and pressure measurements are planned using a thermocouple rake and pressure transducer. Video records will also be obtained with filtered intensified video cameras. In addition, an LIF disk laser system, provided by the German Space Agency, will be used to non-intrusively map the 2D temperature and formaldehyde species concentration fields.

It is proposed that the LIF system be used to acquire 2D species maps of select fluorescence emission lines. While the device is capable of targeting OH, NO, C_2, HCO and HCHO, HCHO (formaldehyde) is the primary species of interest, since it is a key intermediate product in low-temperature alkane oxidation. Due to its relatively high concentration and well-known uv-spectral properties, formaldehyde is a sensitive tracer for both low- and high temperature ignition. More information on the spectral approach to exciting formaldehyde and its use in studying staged-hydrocarbon ignition can be found in (König et al., 1999). Electronic excitation of formaldehyde by means of an Advanced Disc Laser (ADL) source is further described in Grebner, 2001. The acquired two-dimensional temporal formaldehyde-LIF maps will be compared to the results of detailed kinetic models.

While challenging, OH-LIF will be explored as part of this project, yet it is recognized that the typical number density of OH in low temperature oxidation regimes ranges from 10^{-9} to 10^{-6}. Currently, this is at the detection limit of the system.

As discussed above, gas temperature measurements are critical to follow the path of chemical reaction. Moreover, it is highly desirable to measure the temperature non-intrusively, to an accuracy of at least 10°C. Thus, it is proposed that in addition to using a thermocouple rake, the formaldehyde-LIFTED technique, recently developed to study cool flames by one of the co-authors (Burkert et al., 2002) be used. This technique has the advantage that it can be accomplished using the same formaldehyde-LIF diagnostic setup with few modifications (i.e., a second intensified camera and a few optical components).

With respect to the management plan, it is proposed that the LIF system and support personnel refine the system in Germany, and then test the system at NASA and aboard the KC-135 aircraft, if available. Also note that use of ESA's Airbus and the Bremen drop tower will also be available, as provided by the German Co-I's.

Modeling: The modeling effort will have three, equally important focuses. The first will be to provide support for the design of the experimental test plan with respect to reactant mixture selection, initial temperatures and initial pressures. The second will be to further our understanding of cool flame chemistries through comparison of the detailed model predictions to the temperature, pressure and spectroscopic profiles measured during the reaction periods before cool flames or ignitions. The third will to develop an appropriate model with sufficient spatial information to allow simulation of the low gravity, cool flames; as indicated by the data obtained with the temperature rake, pressure measurements and spatially defined measurements.

In all of these modeling efforts pressure effects must be included and considered. Over the range of pressures to be tested, several key reactions are expected to traverse their fall-off region and approach their high pressure limit, such that the chemistry and the system behavior will be affected/.

Understanding and appropriately modeling these pressure effects is crucial if critical combustion system applications are to be handled. This is one of the primary motivations for the proposed work.

Experimental Program: The experiment, modeling, and diagnostic development efforts will be conducted in parallel. The modeling effort will also continue coincident with the integration and testing of the experimental hardware and provide guidance to optimize the test parameters (compositions, temperature, pressures) as well as help explain the results.

With respect to the experiments, the fuels that will be tested include propane, n-butane, iso-butane, and heptane. All of these fuels have been investigated in well-stirred reactors (Pilling, 1997), yet there is no data at high pressure in an unstirred, reduced gravity environment. Moreover, n-heptane will be tested as a representative technical liquid fuel. The oxidizers will be pure oxygen and oxygen:inert mixtures.   Both lean and rich stoichiometries will be tested.   For a given mixture composition, temperatures ranging from 250 to 500°C and pressures ranging from 1 to 10atm will be mapped. Table 1 is a preliminary test matrix.

Reactants	P (atm)	T (^{o}C)	Vessel I.D. (cm)
Propane: Oxygen: Inert	1-3	250-500	5
"	1-10	250-500	2.5
n-Butane: Oxygen: Inert	1-5	250-500	5
"	1-10	250-500	2.5
iso-Butane: Oxygen: Inert	1-5	250-500	5
"	1-10	250-500	2.5
Heptane: Oxygen: Inert	1-5	250-500	5
"	1-10	250-500	2.5

Table 1: Preliminary Test Matrix

REFERENCES

Burkert, A., Triebel, W., Stafast, H., König, J (2002) "Single shot imaging of gas temperatures in low temperature combustion based on laser induced fluorescence of formaldehyde," Proceedings of the Combustion Symposium, 29:1024-1056.

Grebner, D., Müller, D., Triebel, W., König, J., Johannsen, I., Giesen, A. (2001) "The advanced disk laser (ADL): instrumentation for laser diagnostic in microgravity Combustion Research," 6th Intl. Microgravity Combustion Workshop.

Griffiths, J. (1999) Personal communication.

König, J., Eigenbrod, C., Rath, H.J., Grebner, D., Hein, J., Triebel, W. (1999) "Formaldehyde-PLIF detection of cool-flame reactions during two stage ignition of alkane droplets", 5th Intl. Microgravity Combustion Workshop, Cleveland, OH, May 18-20, 1999.

Pearlman, H. (1999) "The role of buoyant convection on cool flames and low-temperature reactions," *Combustion and Flame 121*,390-3.

Pearlman, H. (2000) "Isolating the role of conduction heat transfer on cool flames and autoignitions -- studies at microgravity," Presented at the Third International Seminar on Fire and Explosion Hazards of Substances, Lake Windermere, UK, April 10-14, 2000.

Pilling, M.J., ed. (1997) *Low Temperature Combustion and Autoignition 35*, 545-653, Elsevier Science.

THERMAL TRANSPIRATION BASED MICROSCALE PROPULSION AND POWER GENERATION DEVICES

F. Ochoa, C. Eastwood, P. D. Ronney,
Dept. of Aero. & Mech. Eng., Univ. of Southern California, Los Angeles, CA 90089-1453

B. Dunn
Dept. of Materials Sci. & Eng., Univ. of Calif. at Los Angeles, Los Angeles, CA 90095-1595

Motivation

With the continually decreasing size and weight of communication, control and instrumentation systems for aerospace vehicles due to advances in microelectronics and micro electro-mechanical systems (MEMS), there is considerable interest in miniaturizing the propulsion and power systems as well. While many miniature space and airbreathing propulsion system concepts have been proposed, e.g. [1], most require moving parts. All miniaturized propulsion devices with moving parts experience more difficulties with heat and friction losses due to higher surface to volume ratios than their macroscale counterparts. Moreover sealing, fabrication and assembly are much more difficult at small scales because microfabrication processes have much poorer relative precision than convectional macroscale processes.

Additionally, all air and space vehicles, regardless of size, require electrical power. The use of combustion processes for electrical power generation provides enormous advantages over batteries both in terms of energy storage per unit mass and in terms of power generation per unit volume, even when the conversion efficiency in the combustion process from thermal energy to electrical energy is taken into account. Most current micro-scale power generation concepts employ scaled-down versions of existing macroscale devices, in particular internal combustion engines, though again such micro-devices experience more difficulties with heat losses, friction, sealing, fabrication, assembly etc. than their macroscale counterparts. Consequently, the advantages of combustion processes over batteries for small-scale electrical power sources have not yet been exploited, though research is ongoing [2, 3].

Approach

Because of these difficulties, we propose a microscale or mesoscale propulsion system with no moving parts and not requiring precision manufacturing, applicable to either space or airbreathing vehicles, based on a catalytic combustion-driven thermal transpiration pump. Thermal transpiration occurs in gases in porous membranes or capillary tubes when (1) the mean free path of the gas molecules is comparable to the pore or tube diameter and (2) a temperature gradient is imposed in the solid phase along the length of the pore or tube. Under such conditions, a pressure gradient is induced in the gas, which causes a flow from the cold to hot end of the pores or tubes. A pumping device based on this principle is sometimes called a "Knudsen compressor" after M. Knudsen who first studied thermal transpiration in the early 1900's [4]. Requirement (1) indicates that using conventional MEMS materials and machining techniques producing pore sizes of microns or larger, Knudsen compressors can only be used for very low-pressure gases. However, aerogels and nanoporous oxides have pore sizes of typically 10 nm, which is comparable to the mean free path of air molecules at ambient conditions, thus they are ideal for constructing Knudsen compressors operating at near-ambient pressures. Moreover, aerogels have very low thermal conductivity, thereby enabling a temperature gradient to be sustained across the aerogel with minimal thermal power requirement. Aerogel-based thermal transpiration devices have recently been demonstrated for vacuum pump applications by Vargo *et al.* [5] using electrical heating to sustain the temperature gradient.

We propose to take the concept introduced by Vargo *et al.* [5] one step further by using heat release from catalytic combustion instead of electrical heating. Such a pump/propulsion system has *no moving parts, no supplemental working or pressurization fluids, very low mass and integrates pressurization and thrust generation*. Figure 1 (left) shows the basic building block unit. As in Vargo *et al.*, the reactants first flow through a low-temperature "thermal guard" consisting of a plate with microchannels (not nanoscale pores as in the aerogel). The thermal guard material has a thermal conductivity much higher than that of the aerogel and is non-catalytic to the fuel, plus the thermal guard pore size is much larger than the mean free path of the molecules so that no thermal transpiration occurs in this region. The reactants then pass through the aerogel membrane where the pumping occurs due to the temperature difference across the membrane. The reactants then pass through a second catalytic thermal guard and are converted into products, resulting in heat production. The heat release in the high-temperature thermal guard, combined with the low thermal conductivity of the aerogel, sustains the temperature gradient and thus the pumping action is self-sustaining. Catalytic combustion is ideal for this application because it is localized on catalytic surfaces that can be
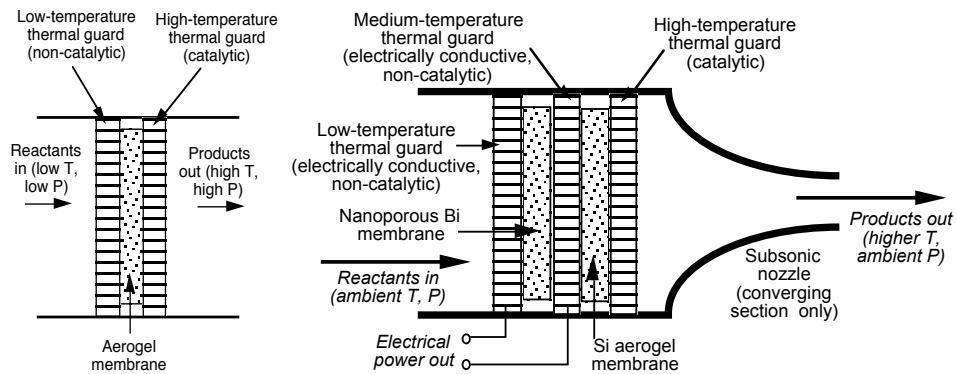
Figure 1. Schematic diagrams of thermal transpiration pumps. Left: single-stage device, stand-alone or incorporated into the center of a Swiss-roll combustor; right: possible integrated power generation and propulsion device.

located on the hot side of the Knudsen compressor, making the thermal resistance between the combustion gases and the hot side of the compressor negligible.

Recently the UCLA group investigated nanoporosity for improving thermoelectric properties [6]. It was found that the thermoelectric figure of merit was higher for nanoporous bismuth than for the bulk material under some conditions. Thus it is possible that by using this material rather than more conventional nanoporous materials such as silica aerogel, *both propulsion and power generation could be obtained in one device with no moving parts* (Fig. 1, right). In the design shown, the lower temperature pumping is accomplished with nanoporous bismuth whereas the higher temperature pumping is accomplished with silica aerogel. A third thermal guard is inserted between the two materials to extract the electrical power from the bismuth stage.
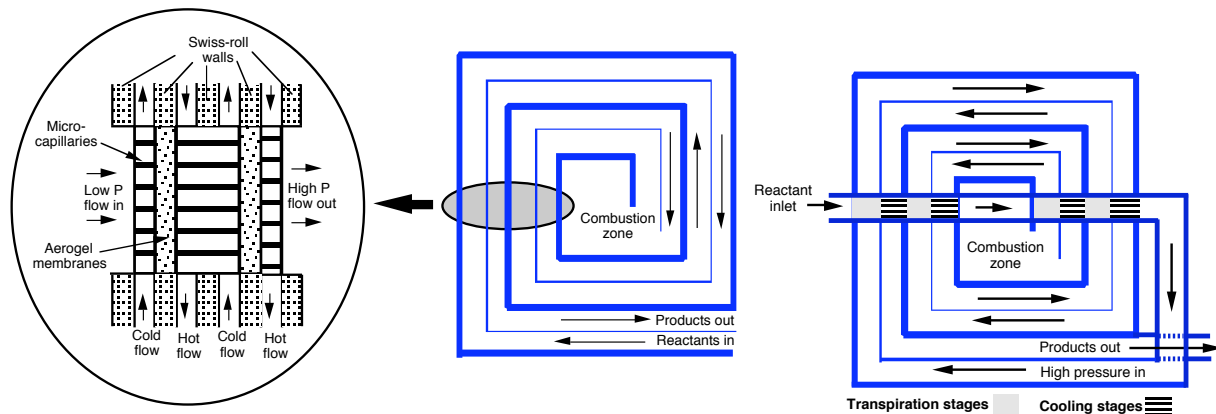
Figure 2. Proposed implementations of thermal transpiration pumps into Swiss roll combustors. Generic "Swiss roll" combustor (center) and multi-stage thermal transpiration pump integrated into the turns of a Swiss-roll combustor (left and right) (note transpiration and cooling stages are reversed going toward vs. away from center of combustor.)

Vargo *et al.* [5] showed that it is possible to construct a staged Knudsen compressor where the aerogel membranes are separated by cooling stages with pore sizes much larger than the mean free path of the molecules (so that no reverse thermal transpiration occurs in the cooling stages.) In this way a larger pressure rise can be obtained than is possible from a single stage. This pattern of alternating heating and cooling sections is readily available within a spiral counter-current "Swiss roll" heat exchanger and combustor [7], in which multiple adjacent hot (product) and cold (reactant) channels are present. Figure 2 shows how Knudsen compressors could be incorporated into a Swiss roll combustor for multi-stage pressurization. The microchannels of the thermal guards would instead be microcapillary tubes that are exposed to the flow in the channels of the Swiss roll device. The system acts as sets of cross-flow heat exchangers for providing the alternating temperature gradients with temperature increasing (in the direction of flow) in the aerogel membranes and decreasing in the microchannels.

Vargo and collaborators [5] developed a model of the performance of thermal transpiration pumps. This model can be used to predict the performance of thermal transpiration pumps for propulsion using the

usual thrust equation based on a 1D momentum balance and the standard isentropic compressible 1D flow equations [8] for gas expansion to ambient pressure (matched exit condition). The predictions (Fig. 3) are expressed in terms of standard figures of merit, e.g. the dimensionless thrust $\equiv F/\mathbf{m}a_1$, where F is the thrust, $\mathbf{m}$ the total mass flow rate and a_1 the sound speed at ambient conditions, and the dimensionless thrust specific fuel consumption $\equiv$ (thermal power)/Fa_1, where the thermal power is simply the product of the membrane thermal conductivity, area and temperature gradient of the aerogel. Figure 3 (left) shows that an optimal pore diameter exists, but the maximum of pumping efficiency and minimum of thrust specific fuel consumption are relatively shallow so that precise matching of pore diameter to operating conditions is not required. Figure 3 (right) shows that there is a substantial benefit to higher hot-side temperatures, *e.g.* beyond the temperature limit of nanoporous bismuth (270°C). For this reason the hybrid system of Fig. 1 (right) is preferable when combined propulsion and power generation is required and maximum performance of both is desired. Interestingly, the predicted performance data are of the same order of magnitude as that calculated theoretically for commercial aircraft gas turbine engines; for a typical idealized turbojet cycle the values of specific thrust and thrust specific fuel consumption are 2 and 3, respectively [8].
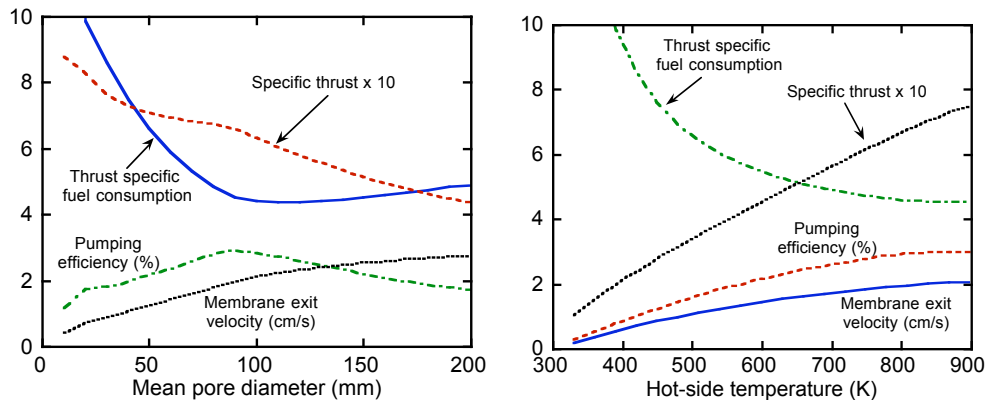
Figure 3. Predicted performance of Knudsen pumps and propulsion devices. Left: effect of mean pore diameter of nanoporous membrane; Right: effect of temperature on hot side of membrane. Membrane thickness 1 mm, cold-side temperature 300K, cold-side pressure 1 atm, hot-side temperature 800K.

Preliminary results

Although NASA funding has not yet begun, an initial test of the stand-alone thermal transpiration system was made using commercially available silica aerogel with thermal conductivity of 0.016 W/m°C and density 0.1 g/cm^3, machined using traditional techniques into a disk 4 mm thick x 30 mm diameter. The test fixture is shown in Fig. 4 (left). The thermal guards were sealed into inlet and outlet plenums with o-rings. On the outlet-side (hot-side) thermal guard, an additional sub-plenum with a platinum gauze catalyst screen was installed, though in the tests described below only air was used as the test gas and an electrical heater was wrapped around the outlet-side plenum to create the temperature gradient across the aerogel membrane. K-type thermocouples were attached to both thermal guards to measure the temperature differential across the aerogel. Steady-state flow rates were measured by displaced water in a graduated cylinder. This simple test fixture was found to produce steady pumping for at least several hours of continuous operation. Figure 4 (center and right) shows typical quantitative results. The measured pressure differences and flow rates obtained are about a factor of two lower than the predicted values from the analytical model, almost certainly because the aerogel membrane is not sealed on the outside surface. Nevertheless, it does demonstrate the possibility of thermal transpiration pumping in a configuration similar to that shown in Fig. 1. Means for sealing the sides of the aerogel without causing a thermal or electrical short circuit have been identified and will be pursued in this work.

Project objectives

The goal of this work is to test the feasibility of creating miniature propulsion and power generation devices employing nanoporous materials for four purposes relevant to space applications:

(1) Thermal transpiration based propulsion, integrating nanoporous materials with a catalytic combustor having lower thermal contact resistance with the hot side of the nanoporous membrane to create a combustion-driven thermal transpiration pump for propulsion applications. This will employ SiO$_2$ aerogels and nanoporous materials to accomplish thermal transpiration along with conventional catalyst materials and supports. Both simple linear designs (Fig. 1) and multi-stage Swiss-roll designed (Fig. 2) will be tested.

(2) Combustion catalysts encapsulated in nanoporous material for use with (1) above as a possible (but not required) integrated performance enhancement.

(3) Thermal insulation. The use of nanoporous materials *sealed with low thermal conductivity materials to prevent gas leakage and patterned using fabrication processes borrowed from MEMS technologies* is an important performance enhancing technology.

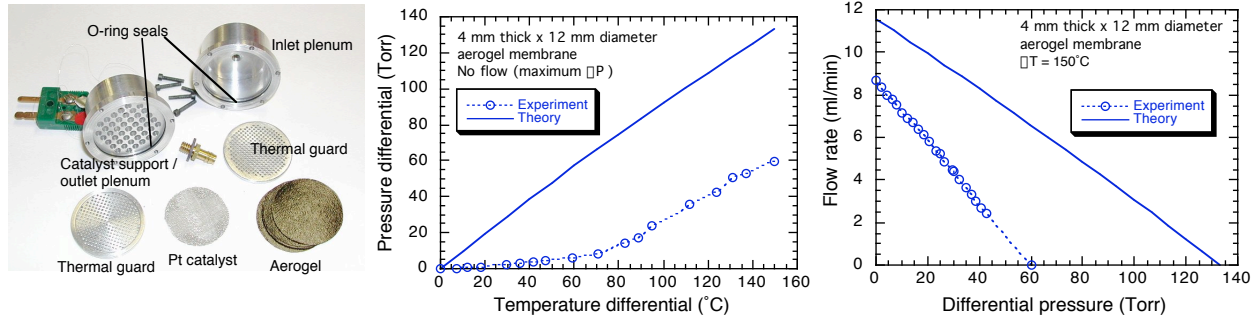*(4) Integrated power generation and thermal transpiration pumping using nanoporous bismuth.*

Figure 4. Left: Disassembled view of catalytic combustion driven thermal transpiration pump test fixture. Center: maximum (zero flow) pressure differential as a function of temperature difference across the aerogel membrane. Right: volume flow rate as a function of pressure differential for 150˚C temperature difference across the aerogel membrane.

Potential applications of the results

In addition to the self-pressurizing propulsion/power generation application proposed in the current work, catalytic combustion driven thermal transpiration compressors could also be used for virtually any small-scale pumping application such as microscale gas sampling instrumentation (e.g. a micro-mass spectrometer), pneumatic accumulators for mechanical actuators and active cooling systems for dense microelectronics. Combustion-driven thermal transpiration pumps have a distinct advantage for these applications in that fuel, rather than electricity that must be generated at very low efficiency, provides the power for the pump. One particularly useful spinoff might be to non-propulsive miniature power generation. Many such methods have been proposed, *e.g.* [1, 2, 3], but most leave unresolved critical "balance of plant" issues, in particular pressurization for fuel and air. In the case of thermoelectric-type systems, even if sufficient fuel and air pressure are available to push the reactants through the generator, additional pressure enables more aggressive fins to be attached to the thermoelectric devices. This reduces the thermal resistance between the gases and the thermoelectric elements, which increases the temperature difference across the elements (as opposed to the temperature difference between the gases and the surfaces of the elements), which in turn improves thermoelectric device performance greatly.

References

1. Waitz, I. A., Gauba, G., and Tzeng, Y. *Journal of Fluids Engineering* 120:109 (1998); Mehra, A., Ayon, A. A., Waitz, I. A. and Schmidt M. A., *IEEE Journal of MEMS* 8:152 (1999).
2. Fu, K., Knobloch, A. J., Cooley B. A., Walter, D. C., Fernandez-Pello, C., Liepmann, D. and Miyaska, K., *ASME 35th National Heat Transfer Conference*, NHTC2001-20089 (2001).
3. Sitzki, L, Borer, K., Schuster, E., Ronney, P. D., Wussow, S., *Third Asia-Pacific Conference on Combustion*, Seoul, Korea, June 24-27, 2001.
4. M. Knudsen. *Ann. Physik* 31:205–229 (1910); *Ibid.. Ann. Physik*, 33:1435–1448 (1910).
5. S. E. Vargo and E. P. Muntz, in*: Proceedings of the 21st International Symposium on Rarefied Gas Dynamics*, 711–718, (1999); S. E. Vargo, E. P. Muntz, G. R. Shiflett and W. C. Tang, *J. Vac. Sci. Technol. A* 17, 2308-2313 (1999).
6. W. Shen, B. Dunn, F. Ragot, M. Goorsky, C. Moore, D.W. Song, G. Chen, R. Gronsky, T. Radetic, W. Fuller-Mora, A. Ehrlich, *Proc. 18th Intern. Conf. on Thermoelectrics,* (IEEE, Piscataway, NJ, 1999) pp. 562-564; W.-N. Shen, B. Dunn, C.D. Moore, M.S. Goorsky, T. Radetic and R. Gronsky, J. Mater. Chem (2000) **10**, 657.
7. Lloyd, S. A. and Weinberg, F. J., *Nature* 251, 47-49 (1974); Lloyd, S. A. and Weinberg, F. J. (1975), *Nature* 257, 367-370 (1975).
8. Hill, P. G., Peterson, C. R., *Mechanics and Thermodynamics of Propulsion*, 2nd Ed., McGraw-Hill, 1998.

OXYGEN AND FUEL JET DIFFUSION FLAME STUDIES IN MICROGRAVITY MOTIVATED BY SPACECRAFT OXYGEN STORAGE FIRE SAFETY

P.B. Sunderland and Z.-G. Yuan
National Center for Microgravity Research, Cleveland, OH 44135.

S.S. Krishnan and J.M. Abshire
Department of Mechanical Engineering, IUPUI, Indianapolis, IN 46202.

J.P. Gore
School of Mechanical Engineering, Purdue University, W. Lafayette, IN 47907.

INTRODUCTION

In 1997 there was a fire on the Mir space station that threatened the lives of everyone aboard. The fire involved an oxygen jet leaking from a lithium-perchlorate oxygen generator, as described by Ross [1]. The fire was unusual in that it involved three factors not normally encountered in terrestrial fires: enhanced oxygen, inverse flames (where the oxidizer is surrounded by fuel), and microgravity. Further, there were the following characteristics of these fires that were noted by the astronauts: They produced large amounts of soot and were difficult to extinguish. Therefore it is important to examine the effects of these three factors on laminar diffusion flames and the characteristics of these flames in comparison to normal flames in normal gravity.

Inverse flames have mixture-fraction/temperature/time trajectories for soot processes that are different from those of normal flames. Inverse diffusion flames were reported in 1928 by Burke and Schumann [2]. Sidebotham and Glassman [3], Kaplan and Kailasanath [4] and Blevins et al. [5, 6] have studied inverse diffusion flames. Sunderland et al. [7] used inverse spherical flames to distinguish the effects of convection direction and stoichiometry on soot formation.

OBJECTIVES

Owing to the absence of past work involving flames similar to the Mir fire – namely oxygen-enhanced, inverse gas-jet diffusion flames in microgravity – the objectives of this work are as follows:

1. Observe the effects of enhanced oxygen conditions on laminar jet diffusion flames with ethane fuel.
2. Consider both earth gravity and microgravity.
3. Examine both normal and inverse flames.
4. Compare the measured flame lengths and widths with calibrated predictions of several flame shape models.

This study expands on the work of Hwang and Gore, [8,9] which emphasized radiative emissions from oxygen-enhanced inverse flames in earth gravity, and Sunderland et al., [10] which emphasized the shapes of normal and inverse oxygen-enhanced gas-jet diffusion flames in microgravity.

MICROGRAVITY EXPERIMENTS

The present experiments involve ethane reacting with oxygen/nitrogen mixtures with oxygen mole fractions of 0.21, 0.3, 0.5 and 1. The flames were attached to a round stainless-steel burner with an inside diameter of 5.5 mm and a knife-edge tip. The burner tube was straight and unobstructed for a length of 25 cm upstream of its tip. The ambient gas was quiescent at 0.98 bar and 298 K and was contained in a cylindrical windowed pressure vessel.

The earth-gravity tests were conducted with the burner gas injecting vertically upward. The microgravity tests were performed in the NASA Glenn 2.2-second drop tower. Details of the rig were reported in Sunderland et al. [10]. The flames were imaged using a color CCD camera with a 25 mm manual-iris lens, recorded on analog color video and analyzed subsequently.

The lengths and widths of the microgravity flames were measured from the video recordings. Where blue contours were not obscured by soot, flame sheet lengths were measured from the burner tip to the peak of blue intensity. Where contours were obscured, flame luminosity lengths were measured from the burner tip to the end of the yellow region. Flame sheet widths were not obscured by soot for any flame and were defined as the width of the contour of peak blue intensity at its widest. Repeatability of the flame length and width measurements was ±5%.

Four oxidizer compositions each for normal and inverse flames in earth gravity and microgravity i.e., a total of 16 flames, were studied. The burner gas velocity for the inverse flames was held constant at 866 mm/s. The ethane flowrates for the normal flames were chosen to match the heat release rates of the corresponding inverse flames, such rates being determined using a lower heating value of ethane of 47 KJ/g. This choice of flowrates yielded a relatively small variation in flame sheet length for all flames. The present Reynolds numbers confirm that the discharge conditions were laminar.

FLAME SHAPE PREDICTIONS – APPROACH

Descriptions of the different models used in the present study are described in Sunderland et al. [10]. One of the models used, the Roper model following Roper [11] and its results are described in better detail here and in Sunderland et al. [10]. A Matlab code was developed to predict the flame shape using the governing equation for the conserved scalar, C which is a non-dimensionalized mixture fraction. Romberg integration and Newton-Raphson iterative methods were used to solve for the flame shape for a given C_{st} which defined the flame sheet. A uniform velocity profile of magnitude equal to the burner exit velocity is assumed at all axial locations. The resulting flame shape was obtained in terms of r and z coordinates. A plot of the flame shape curve was obtained in Matlab.

The flame images from the experimental results in JPG format and the flame shape curve predicted by the Roper model from Matlab were copied into AutoCAD. The CCD image used square pixels. The Matlab-generated curve was spline-fitted in AutoCAD after magnification to preserve the shape. The scales of a ruler image from the flame image and the scale of the flame shape curves were matched in AutoCAD.

RECENT RESULTS

Only the most recent results are shown here. Other results have been reported in Sunderland et al. [10, 12]. Figures 1 (a) and 1(b) show still color images of eight microgravity normal and inverse flames respectively. The Roper model predictions are shown overlaid on the images and show excellent agreement with the experimental flame shapes. The shift in the prediction for

the first two normal flames in figure 1(a) is due to the neglect of axial diffusion effects which become predominant in these flames. In these images soot is identified by white, yellow, or orange coloration, and stoichiometric flame sheets are identified by blue emissions.

In general, the earth-gravity flames were reported earlier as much narrower than their microgravity counterparts owing to buoyantly induced entrainment [10]. The normal flames have undiluted C_2H_6 flowing from the burner. With the exception of microgravity normal flame 21, which is blue, all these flames contain soot, which first appears inside the flame sheet near the burner. Increasing oxidizer concentration yields brighter flames, as revealed by the images and their relative exposures. The normal microgravity flames were seen to increase in length and width and to decrease in brightness throughout the 2.2 s tests. Large soot aggregates, on the order of 1 mm, are seen being emitted from microgravity flames 30 and 50.

Figure 1(b) shows color images of the present inverse flames in microgravity. All these flames contain soot, which forms and resides on the fuel side of the flame sheet and which is emitted into the ambient ethane gas. Increasing oxidizer concentration yields brighter flames, as revealed by the images and their relative exposures. Unusual variations in blue intensity in the inverse flames, also noted in Hwang and Gore [8], complicate the precise identification of the stoichiometric contours of these flames.

The present microgravity inverse flames have annular soot layers which start near the burner tip, expand with axial distance until just below the stoichiometric flame tip, and contract above this. Most of the soot formation in these flames occurs on the rich side of the flame near the stoichiometric flame sheet. The newly-formed soot is then driven radially outward by thermophoresis and volumetric expansion caused by heat release overcoming the inward flow caused by the action of viscosity and resulting in a soot annulus. The contraction of the annulus above the flame is attributed to radial inflow in a region with significantly lower thermophoresis and volumetric expansion. Finally, in figure 1(b), the agreement with the Roper prediction is seen to be excellent in these flames. The area near the burner tip is not shown due to the invalidity of the far-field assumption.

Figure 2 shows the quantitative comparisons of inverse flame lengths and widths using the Roper and Spalding models. The inverse diffusion flame widths are predicted better by the Roper model. More work is needed to understand the models and how they work for the different cases. A detailed computational model is planned as part of future work.

CONCLUSIONS

Ethane fueled laminar gas-jet diffusion flames were observed, emphasizing the effects of oxygen enhancement, gravity, and inverse burning on flame appearance and sooting behavior. The major findings were:

1. Oxygen-enhanced conditions caused increases in soot production, soot emission, and luminosity for both normal and inverse flames. This attests to the increased fire hazards associated with oxygen-enhanced combustion.

2. Microgravity flame shape predictions with Roper and Spalding models were considered. The shapes captured by the Roper model closely agree with the experimental photos. However, a proper evaluation can be accomplished only by additional measurements such as peak temperature and location of the stoichiometric mixture fraction contours and a more detailed computational model.

ACKNOWLEDGEMENT

REFERENCES

[1] H.D. Ross, in: H.D. Ross (Ed.), Microgravity Combustion, Academic Press, San Diego, 2001, pp. 1-34.
[2] S.P. Burke, T.E.W. Schumann, Ind. Eng. Chem. 20 (10) (1928) 998-1004.
[3] C G.W. Sidebotham, I. Glassman, Combust. Flame 90 (1992) 269-283.
[4] C.R. Kaplan, K. Kailasanath, Combust. Flame 124 (2001) 275-294.
[5] L.G. Blevins, R.A. Fletcher, B.A. Benner, E.B. Steel, G.W. Mulholland, Proceedings of the Combustion Institute, Vol. 28, The Combustion Institute, Pittsburgh, 2002, p. 29.
[6] L.G. Blevins, N.Y.C. Yang, M.A. Mikofski, G.W. Mulholland and R.W. Davis, AIAA 41st Aerospace Sciences Meeting and Exhibit, Reno, January 2003.
[7] P.B. Sunderland, R.L. Axelbaum, D.L. Urban, B.H. Chao, S. Liu, Combust. Flame, 132 (2003) 25-33.
[8] S.S. Hwang, J.P. Gore, KSME Intl. J. 16 (9) (2002) 1156-1165.
[9] S.S. Hwang, J.P. Gore, Proc. Inst. Mech. Eng. A - J. Power Energy, 216 (2002) 379-386.
[10] P.B. Sunderland, S.S. Krishnan, and J.P. Gore, AIAA 41st Aerospace Sciences Meeting and Exhibit, Reno, January 2003.
[11] F.G. Roper, Combust. Flame 29 (1977) 219-226.
[12] P.B. Sunderland, S.S. Krishnan, and J.P. Gore, Combust. Flame, submitted (2003).
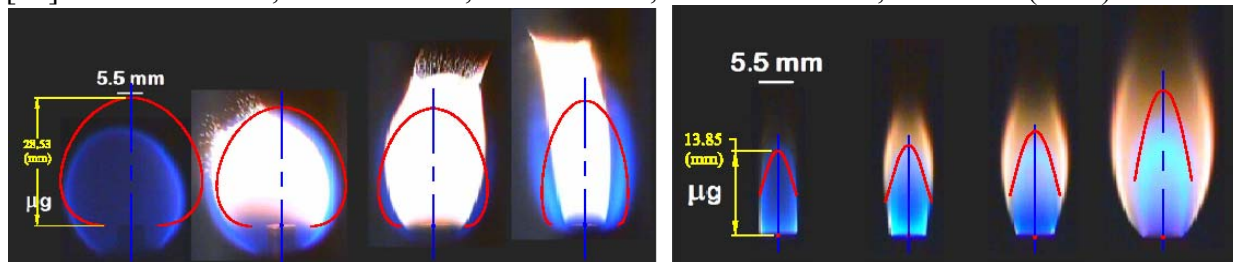
Figure 1. Comparisons between Roper model predictions and microgravity experimental results – (a) Normal and (b) Inverse Diffusion Flames (ethane with 21, 30, 50 and 100 % oxygen) (NOTE: Figure 1(b) is not to the same scale as Figure 1(a)).
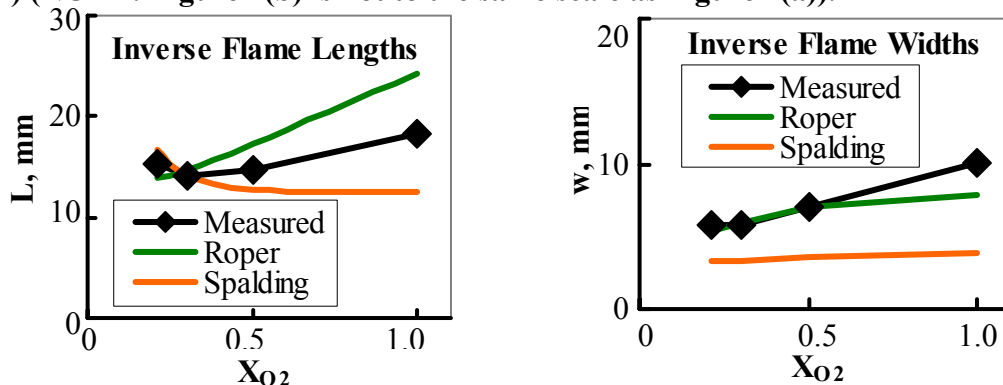
Figure 2 Inverse Flame length and Width comparisons with model predictions.

DEVELOPMENT OF PIV FOR MICROGRAVITY DIFFUSION FLAMES

**Paul S. Greenberg[1], Mark P. Wernet[1], William Yanis[2],
David L. Urban[1], and Peter B. Sunderland[2]**

[1]NASA Glenn Research Center
Cleveland Ohio

[2]National Center for Microgravity Research
Cleveland Ohio

INTRODUCTION

Despite numerous experimental investigations, the characterization of microgravity laminar jet diffusion flames remains incomplete. Measurements to date have included shapes, temperatures, soot properties, radiative emissions, and compositions, but full-field quantitative measurements of velocity have been limited. Kato et al. (1998) performed flame Particle Image Velocimetry (PIV) measurements in the JAMIC drop facility and Most et al. (2000) performed similar measurements on the AirBus A300 microgravity aircraft, but advanced PIV systems such as these have yet to be utilized in the NASA Glenn microgravity facilities. The present work concerns the development of a drop rig capable of performing PIV tests in diffusion flames in the 2.2 second drop tower.

Because the differences between normal-gravity and microgravity diffusion flames arise from changes in velocities, it is essential to measure velocity fields in microgravity flames. Velocity measurements in nonbuoyant flames will be helpful both in validating numerical models and in interpreting past microgravity combustion experiments. The importance of such measurements is mentioned in Law and Faeth (1994).

Pointwise velocity techniques, such as Laser Doppler Velocimetry, are inadequate for full-field velocity measurements in microgravity facilities. In contrast, the PIV system described here can capture an entire flowfield in 33 ms. Although PIV is a mature diagnostic for normal-gravity flames (Goss et al., 1991; Mungal et al., 1995; Driscoll and Mueller, 2002), restrictions on size, power and data storage complicate these measurements in microgravity.

Results are presented here from the application of PIV to the overfire region of a laminar gas jet diffusion flame in normal gravity. A methane flame burning in air at 0.98 bar was considered. The apparatus demonstrated here is packaged in a drop rig designed for use in the 2.2 second drop tower.

EXPERIMENTAL METHODS

The present flame was established in a windowed pressure vessel. The chamber internal width × depth × height were 25 × 25 × 50 cm. The tests were conducted in quiescent ambient air at 0.98 bar.

The burner was a 23 cm long stainless tube with an inside diameter of 5.5 mm. This length ensured fully developed laminar flow at the jet discharge. The burner was placed on the chamber centerline and oriented such that the methane injected vertically upward. The methane flowrate was maintained at approximately 1.1 mg/s. Fuel flowrate was controlled with a pressure regulator followed by a critical-flow metering valve. The chamber air was seeded prior to testing and the fuel was seeded during the tests.

The present PIV system is described in detail in Wernet et al. (2000). A dual-head mini-Nd:YAG laser operating at 532 nm was used to generate 50 mJ pulses. A 50×0.1 mm light sheet was generated using a 25 mm cylindrical lens and a 300 mm spherical lens.

The imaging system consisted of a 1008×1018 pixel Kodak ES 1.0 camera equipped with a 50 mm Schneider lens (set at f/2.8) and an interference filter (532 ± 10 nm). The first exposure had a 0.25 ms integration period. The second frame was integrated for 33 ms (while the first frame was being read from the sensor). Each pixel corresponded to a region of 51×51 μm in the object plane.

The PIV system hardware is based on custom designed in-house software, which provides the unattended operation required for the drop rig. All commercial PIV systems utilize graphical user interfaces, which are not amenable to automation. A Kodak ES 1.0 camera is coupled with an EPIX framgrabber board for "frame-straddling" image pair acquisition. The laser firing and camera timing are controlled via a National Instruments NI-6602 counter timer board. The NASA Glenn developed PIV system acquires image frame pairs at 15 Hz. The present velocity vector maps were obtained by averaging 100 instantaneous vector maps. Estimated velocity uncertainties are ±1% near the flame centerline and slightly higher in regions of lower velocity.

The data were multi-pass cross-correlation processed using 64×64 pixel subregions followed by 32×32 pixel subregions. The resulting velocity vector maps had horizontal and vertical spacings of 16 pixels, corresponding to grid point separations of 0.8 mm in the velocity vector maps. The analysis of the present PIV images used the correlation software of Wernet (1999).

The seed was 2.5 μm silica particles. These particles scatter sufficient light for these tests and are not expected to be significantly affected by thermophoresis. Microgravity rules out traditional seeders such as fluidized or packed beds, which can produce uncontrolled or overseeded conditions in microgravity. The present apparatus uses orifice-inlet seeders, which have been demonstrated in the microgravity facilities at NASA Glenn (Greenberg et al., 1997).

RESULTS AND DISCUSSION

A color image of the present flame is shown in Fig. 1. The flame was the longest nonflickering methane flame that could be obtained using the present burner in quiescent ambient air.

Figure 2 shows the velocity vectors and representative streamlines determined by PIV. The spatial resolution of the PIV measurements is the same as the spacing of the vectors in this figure. The streamline starting points are equally spaced at the upstream boundary. In this and subsequent figures, *HAB* is height above burner and the burner centerline corresponds to $r = 0$. Note that the present PIV measurements are in the overfire region but the present system also is capable of making velocity measurements within flames.

Figure 3 is a color contour plot of the velocity vectors of Fig. 2. Figure 4 is the corresponding contour plot of vorticity (assuming negligible gas velocities normal to the plane of the laser sheet). The present measurements took advantage of steady burning conditions by averaging over 100 PIV image pairs. Tests in the 2.2 second drop tower will not permit such extensive averaging. Nevertheless, Figs. 2-4 are representative of the velocity and vorticity measurements anticipated in upcoming microgravity combustion tests.

REFERENCES

Driscoll, J.F. and Mueller, C.J., Velocity Profiles Measured Across Wrinkled Flames – To Assess Flamelet Assumptions," *Combust. Sci. Technol.*, 179:9 (2002).

Goss, L.P., Post, M.E., Trump, D.D., and Sarka, B., "Two-Color Particle Image Velocimetry," *J. of Laser Applications*, winter, pp. 36-42 (1991).

Greenberg, P.S., Griffin, D.W., Weiland, K.J., and Yanis, W., "Selected Diagnostics for Microgravity Combustion Science;" Fourth International Workshop on Microgravity Combustion, Cleveland, pp. 275-280 (1997).

Kato, H., Kunieda, S., Enomoto, H., Okai, K., Kaneko, T., Chauveau, C., GöKalp, I., Sato, J., Tsue, M. and Kono, M., "Effects of Co-Flowing Air on Behavior of Gas Jet Diffusion Flames Under Normal- and Micro-gravity Fields," Drop Tower Days, JAMIC, paper 12-B-11, Sapporo, Japan (1998).

Law, C.K. and Faeth, G.M., "Opportunities and Challenges of Combustion in Microgravity," *Prog. Energy Combust. Sci.* 20:65 (1994).

Most, J.-M., Most, A., Susset, A., Baillargeat, J. and Joulain, P., "Flame Characterization by PIV in Microgravity Conditions," Tenth International Symposium on the Application of Laser Techniques in Fluid Mechanics, Lisbon (2000).

Mungal, M.G., Lourenco, L.M., and Krothapalli, A., "Instantaneous Velocity Measurements in Laminar and Turbulent Premixed Flames Using On-Line PIV," *Combust. Sci. Technol.*, 106:239 (1995).

Wernet, M.P., "Fuzzy Logic Enhanced Digital PIV Processing Software," 18th International Congress on Instrumentation for Aerospace Simulation Facilities, Toulouse, France (1999).

Wernet, M.P., Greenberg, P.S., Sunderland, P.B., and Yanis, W., "A PIV Investigation of Weakly Buoyant Laminar Get Diffusion Flames," AIAA-2000-0694, Reno (2000).
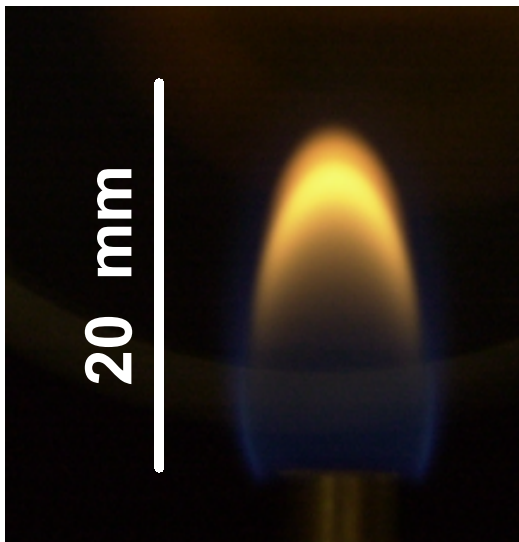
Figure 1. Color image of the present flame and burner.
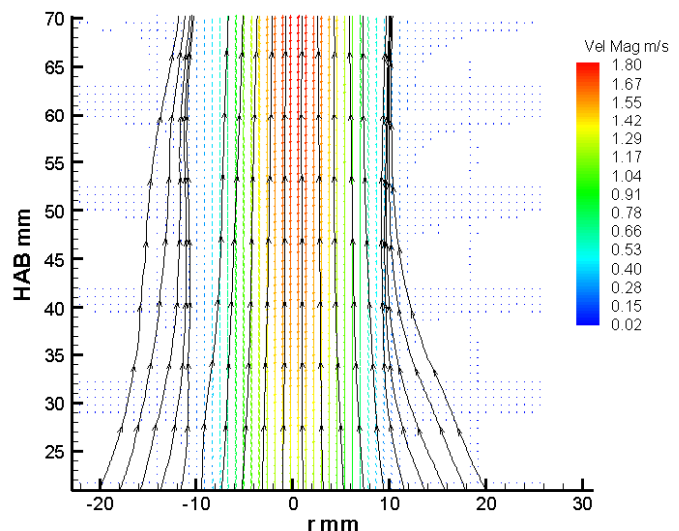
Figure 2. Color velocity vectors and representative streamlines.
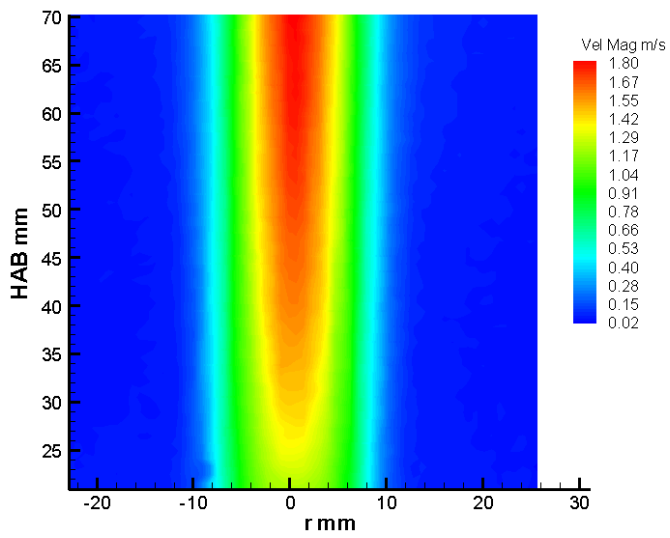
Figure 3. Color velocity contours.
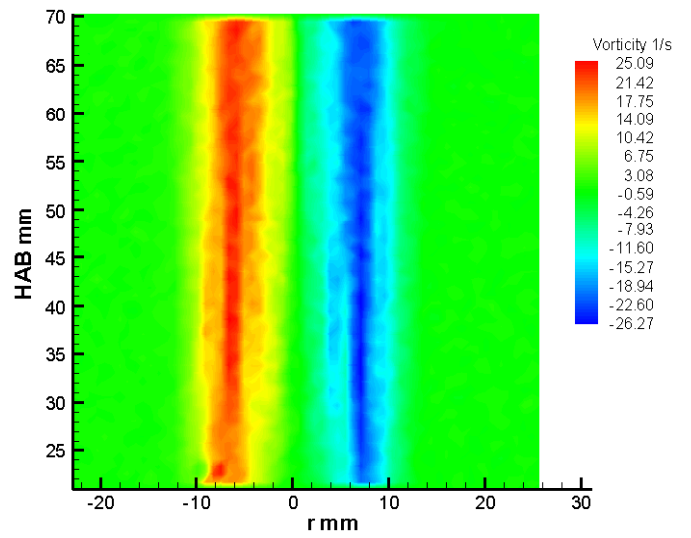
Figure 4. Color vorticity contours.

CATALYZED COMBUSTION IN MICRO-PROPULSION DEVICES – PROJECT STATUS

C. J. Sung

Department of Mechanical and Aerospace Engineering, Case Western Reserve University, Cleveland, OH 44139
National Center for Microgravity Research on Fluids and Combustion, Cleveland, OH 44135

S. J. Schneider

NASA Glenn Research Center, Cleveland, OH 44135

INTRODUCTION

In recent years, there has been a tendency toward shrinking the size of spacecraft. New classes of spacecraft called micro-spacecraft have been defined by their mass, power, and size ranges [1]. Spacecraft in the range of 20 to 100 kg represent the class most likely to be utilized by most "small sat" users in the near future. There are also efforts to develop 10 to 20 kg class spacecraft for use in satellite constellations. More ambitious efforts will be to develop spacecraft less than 10 kg, in which MEMS fabrication technology is required. These new micro-spacecraft will require new micro-propulsion technology. Although micro-propulsion includes electric propulsion approaches, the focus of this proposed program is micro-chemical propulsion which requires the development of micro-combustors. As combustors are scaled down, the surface to volume ratio increases. The heat release rate in the combustor scales with volume, while heat loss rate scales with surface area. Consequently, heat loss eventually dominates over heat release when the combustor size becomes smaller, thereby leading to flame quenching. The limitations imposed on chamber length and diameter has an immediate impact on the degree of miniaturization of a micro-combustor. Before micro-combustors can be realized, such a difficulty must be overcome. One viable combustion alternative is to take advantage of surface catalysis.

Micro-chemical propulsion for small spacecraft can be used for primary thrust, orbit insertion, trajectory-control, and attitude control. Grouping micro-propulsion devices in arrays will allow their use for larger thrust applications. By using an array composed of hundreds or thousands of micro-thruster units, a particular configuration can be arranged to be best suited for a specific application. Moreover, different thruster sizes would provide for a range of thrust levels (from μN's to mN's) within the same array. Several thrusters could be fired simultaneously for thrust levels higher than the basic units, or in a rapid sequence in order to provide gradual but steady low-g acceleration. These arrays of micro-propulsion systems would offer unprecedented flexibility and redundancy for satellite propulsion and reaction control for launch vehicles.

A high-pressure bi-propellant micro-rocket engine is already being developed [2] using MEMS technology. High pressure turbopumps and valves are to be incorporated onto the rocket "chip". High pressure combustion of methane and O_2 in a micro-combustor has been demonstrated without catalysis, but ignition was established with a spark. This combustor has rectangular dimensions of 1.5 mm by 8 mm (hydraulic diameter 3.9 mm) and a length of 4.5 mm and was operated at 1250 kPa with plans to operate it at 12.7 MPa. These high operating pressures enable the combustion process in these devices, but these pressures are not practical for pressure fed satellite propulsion systems. Note that the use of these propellants requires an ignition system and that the use of a spark would impose a size limitation to this micro-propulsion device because the spark unit cannot be shrunk proportionately with the thruster.

Currently, cold gas and small monopropellant N_2H_4 systems represent the state-of-the-art in micro-propulsion. It is generally recognized that reduced-scale versions of these conventional systems will not be practical for micro-satellites. In addition, these propulsion systems will benefit greatly from the use of non-toxic propellants, which will require ignition. Systems fabricated using MEMS technology and catalyzed ignition/combustion are proposed. Once catalyzed ignition is established in a microtube, the reacting gases can be used for micro-propulsion device or they can be propagated into the combustion chamber for ignition in larger thrust class rockets. This benefits all rocket propulsion systems through the elimination of high voltage electrical discharges to achieve spark ignition.

Results presented in this paper consist of an experimental evaluation of the minimum catalyst temperature for initiating/supporting combustion in sub-millimeter diameter tubes. The tubes are resistively heated and reactive premixed gases are passed through the tubes. Tube temperature and inlet pressure are monitored for an indication of exothermic reactions and composition changes in the gases.

CHARACTERIZATION OF GASSEOUS H_2/O_2 COMBUSTION

Figure 1 plots the spatially resolved profiles of temperature and heat release rate for an atmospheric, freely-propagating, stoichiometric H_2/O_2 flame in the flame coordinates, which are computed using a detailed mechanism of Mueller *et al.* [3]. The corresponding laminar flame speed is 1029 cm/s. It is seen from Fig. 1 that the overall flame thickness based on the temperature profile is of sub-millimeter. If we define the reaction zone thickness as the

full-width-half-maximum of the heat release profile, the corresponding reaction zone thickness is 0.16 mm. Hence, it is expected that a minimum size for micro-combustors using stoichiometric H_2/O_2 premixed combustion would be limited to 0.1 mm, below which the flame is expected to be quenched due to excessive loss to the wall.

To further demonstrate the above concept, we have carried out numerical experiments on flame propagation in various two-dimensional channels. The numerical tool chosen for this study is the SPARK Navier-Stokes Code [4], with 2nd-order accurate MacCormack explicit predictor-corrector scheme. The two-dimensional channel is 10 cm in length, and is closed at the left-hand side, while open at the right-hand side. Initially, the channel is filled with an atmospheric stoichiometric H_2/O_2 mixture at 300 K. No-slip wall is assumed and the wall temperature is fixed at 600 K. Ignition is achieved using a 0.6 mm zone (full channel height) of H_2O at 4000 K and 1 atm.

Figure 2 shows the temperature contours for the 1.0 mm × 10 cm channel at time of 61.6 μs. It is seen that the maximum flow field temperature is greater than 3000 K, indicating that combustion is fairly completed within the present combustor volume. Additionally, at t=61.6 μs, the propagation front is near the channel exit. Furthermore, the present condition actually leads to detonation. The results clearly demonstrate that for the given premixture stable combustion can be established with a channel height of 1.0 mm.

When the channel height is reduced to 0.1 mm, which is comparable with the characteristic reaction zone thickness, Fig. 3 shows that flame propagation cannot be sustained. Especially, the ignition front eventually dies out. Further increasing the ignition zone to 6 mm length shows no change in results. These results substantiate the concept that a simply scaled-down micro-combustor will be limited by the quenching distance, which is an intrinsic property of the given fuel/oxidizer mixture.

A plot of H_2/O_2 flame thickness as a function of equivalence ratio for atmospheric pressure and pressure of 34.5 kPa (approximately 5 psia) is given in Fig. 4. It is seen that flame thickness increases with decreasing pressure and the calculated flame thickness at the test pressure of 34.5 kPa and an equivalence ratio of 10 (mixture ratio MR=0.8) is 4 mm, which is greater than the diameter of either the 0.4 mm platinum or the 0.8 mm palladium micro-tubes used in this catalytic micro-combustion experiment.

Figure 4 also shows the corresponding reaction zone thickness. At the equivalence ratio of 10 (mixture ratio=0.8), the reaction zone thickness is ~1 mm at atmospheric pressure and initial temperature of 300 K and increases to ~3 mm when the pressure is reduced to 34.5 kPa. Experimental tests in the micro-tubes were run mostly between 1.2 and 0.4 mixture ratios (equivalence ratios of 6.7 to 20, respectively). At these mixture ratios and the low pressure of the tests the reaction zone thicknesses are greater than the diameter of either the 0.4 mm platinum or the 0.8 mm palladium micro-tubes used in this catalytic micro-combustion experiment.

The rich flammability limits of the H_2/O_2 flames at various pressures are compared in Fig. 5. At a given pressure, it is seen that the burning rate decreases with increasing equivalence ratio. The turning point, beyond which steady flame propagation is not possible, defines the rich flammability limit. We further note that for near rich limit hydrogen flames, in which the Lewis number is greater than unity, pulsating instability has been observed to take place in mixtures with fuel concentrations slightly below that of the rich limit [5-7] and the flame was found to oscillatorily extinguish well ahead of the static extinction limit [6,7]. Thus, the flammability range of a H_2/O_2 mixture is expected to be narrowed when the intrinsic oscillatory nature of flame propagation is taken into account.

APPARATUS AND TEST PROCEDURES

Miniature flame tube apparatus is chosen for study because microtubes can be easily fabricated from known catalyst materials and their simplicity in geometry can be used in fundamental simulations to more carefully characterize the measured heat transfer and pressure losses for validation purposes. Experimentally, we investigate the role of catalytically active surfaces within microtubes, with special emphases on ignition and extinction. The experimental apparatus involves the microtube, along with a mass flow control system, electrical power supply to heat a section of tube, and a data acquisition system. A schematic of the instrumented microtubes is shown in Fig. 6. Two capillary tubes were available for testing. One was a 0.4 mm I.D. platinum tube with a 0.15 mm wall thickness and an overall length of 100 mm of which 70 mm was resistively heated. The other tube was 0.8 mm I.D. and was made of palladium with a wall thickness of 0.1 mm and an overall length of 190 mm of which 160 mm was resistively heated. Three thermocouples were spot welded to the outside of the tubes at the 20%, 50%, and 80% positions of the heated section as shown in the schematic. The tubes were tested in a small rocket test facility at the NASA Glenn Research Center. The facility maintains an ambient pressure of 1.38 kPa during the tests. These initial tests were conducted with gaseous oxygen and gaseous hydrogen propellants at low mixture ratios (high equivalence ratios) to test the rich flammability limits of the propellants, to avoid melting the catalysts and to avoid oxidation loss of catalyst material. These propellants are non-toxic and can be produced on-orbit by water electrolysis [8].

PRELIMINARY EXPERIMENTAL RESULTS

Experimental results consist of a determination of the minimum catalyst preheat temperature for initiating/supporting combustion in the two sub-millimeter diameter tubes. Data are obtained with the tubes resistively heated by the power supply in voltage control mode and with reactive premixed gases passed through the tubes. Tube temperature and inlet pressure are monitored for an indication of exothermic reactions and composition changes in the gases.

Temperature data for the 0.8 mm I.D. tube preheated to a peak temperature of 477 K and showing an exothermic reaction is given in Fig. 7. The total mass flow is 0.00123 g/s of gaseous oxygen and gaseous hydrogen at an oxidizer to fuel mixture ratio of 0.8 (equivalence ratio 9.92). The resistivity of palladium at these temperatures is 17.2×10^{-8} Ω-m and the voltage drop across the tube is 1.21 Volts, giving an estimated power input of 15 Watts. At 10 seconds into the test TC1 has dropped to 338 K, TC2 has dropped to 412 K as the gas picks up heat, but TC3 has risen to 511 K as the gases are heated by catalyzed reactions between TC2 and TC3. At 10 seconds into the test TC3 starts a rapid rise to 750 K. Heat from this reaction is conducted through the tube upstream toward TC2 which starts a rapid temperature rise to 815 K at 16 seconds into the test. Further conduction to the TC1 position is indicated by its rapid temperature rise at 40 seconds into the test. Steady state is reached at TC3 at approximately 60 seconds into the test. The test was terminated at 100 seconds, however, before steady state was reached at TC1.

Temperature data for the 0.8 mm I.D. tube preheated to a peak temperature of 422 K and showing no reaction is given in Fig. 8. The total mass flow is 0.00123 g/s of gaseous oxygen and gaseous hydrogen at an oxidizer to fuel mixture ratio of 0.8 (equivalence ratio 9.92). Some reactions between TC2 and TC3 cause the temperature of TC3 to rise to a peak of 430 K at 6 seconds into the test, otherwise all of the temperatures fall to a steady state profile of TC1 at 321 K, TC2 at 351 K, and TC3 at 377 K.

Data at other mass flows and fuel rich mixture ratios are shown on mass flow rate versus preheat temperature plots in Fig. 9 for the 0.8 mm I.D. palladium tube and Fig. 10 for the 0.4 mm platinum tube. Using temperature and pressure rise as an indication of reactions the solid symbols indicate those test conditions where reactions were observed. As mass flow decreases the preheat temperature required to initiate reactions decreases. For the 0.8 mm palladium tube the lowest preheat temperature for reactions was 340 K at a mixture ratio of 0.8 and a mass flow of 0.000128 g/s. Above a mass flow of 0.0022 g/s reactions did not occur at any preheat temperature in the 0.8 mm I.D. palladium tube, 190 mm long with 160 mm resistively heated. For the 0.4 mm I.D. platinum tube, the lowest preheat temperature for reactions was 480 K at a mixture ratio of 1.0 and a mass flow of 0.000187 g/s. Above a mass flow of 0.00054 g/s reactions did not occur at any preheat temperature in the 0.4 mm I.D. platinum tube, 100 mm long with 70 mm resistively heated.

REFERENCES

1. Mueller, J., AIAA 97-3058, 1997.
2. London, A. P., Epstein, A. H., and Kerrebrock, J. L., *Journal of Propulsion and Power*, Volume 17, No. 4, pp. 780-787, 2001.
3. Mueller, M. A., Yetter, R. A., and Dryer, F. L., *International Journal of Chemical Kinetics* **31**, pp. 705-724 (1999).
4. Drummond, J. P., NASA TM-103480, 1990.
5. He, L. and Clavin, P., *Combustion and Flame* **93**, pp. 408-420, 1993.
6. Christiansen, E. W., Sung, C. J., and Law, C. K., *Proceedings of the Combustion Institute* **27**, pp. 555-562, 1998.
7. Christiansen, E. W., Law, C. K., and Sung, C. J., *Combustion and Flame* **124**, pp. 35-49, 2001.
8. de Groot, W. A. et., al., AIAA 97-2948, 1997.
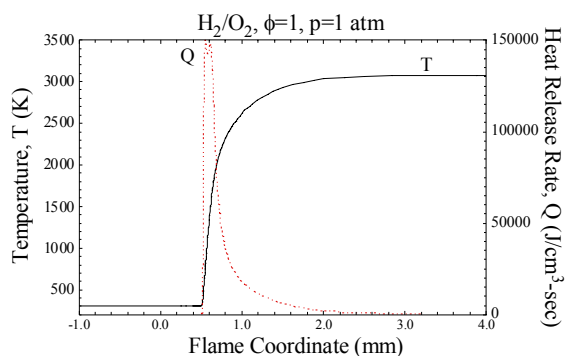
Figure 1. Spatially resolved profiles of temperature and heat release rate of an atmospheric stoichiometric H_2/O_2 flame with initial temperature of 300 K.
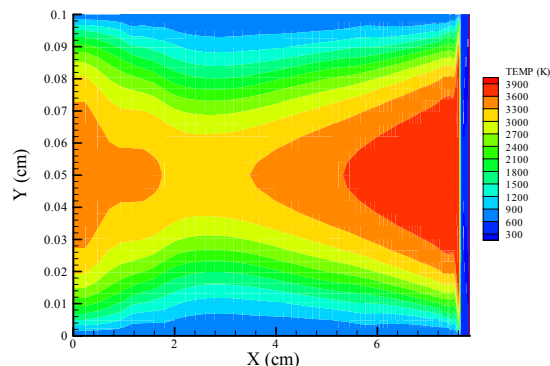
Figure 2. Temperature Contours from closed end of tube through the combustion zone at t=61.6 μs, for the case of 1.0 mm channel height.
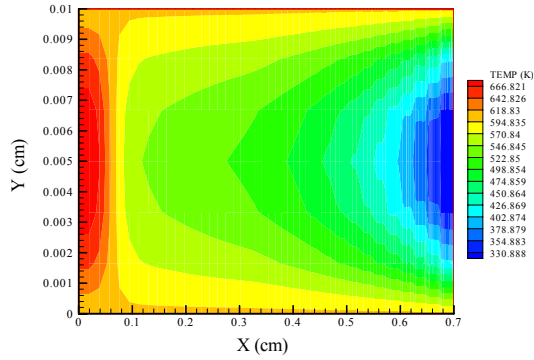
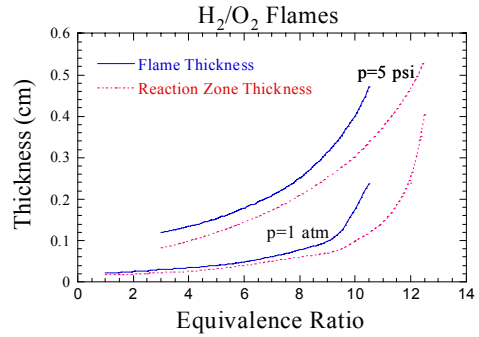**Figure 3**. Temperature Contours at t=4.6 μs, showing no incipient combustion, for the case of 0.1 mm channel height.

Figure 4. Plot of flame thickness and reaction zone thickness versus equivalence ratio for p=1 atm and 5 psia.

Figure 5. Plot of mass burning flux versus equivalence ratio for rich H_2/O_2 flames at various pressures. The turning point of the response curve defines the rich flammability limit.
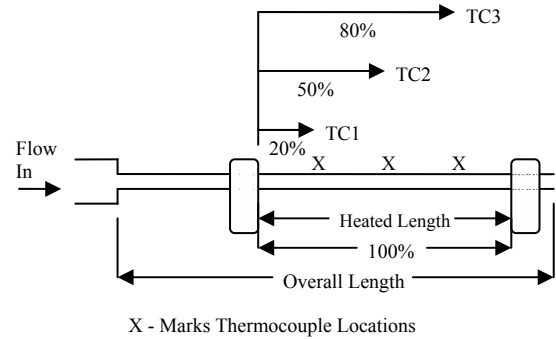
Figure 6. Schematic of microtube test articles.

Figure 7. Temperature data for 0.8 mm I.D. palladium tube, MR=0.8, 0.00123 g/sec.
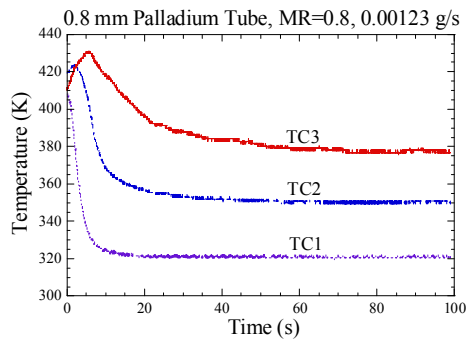
Figure 8. Non-ignition temperature data for 0.8 mm I.D. palladium tube, MR=0.8, 0.00123 g/sec.

Figure 9. Ignition data for 0.8 mm I.D. palladium tube – open symbols are non-ignition and solid symbols are ignition as indicated by tube temperature rise.
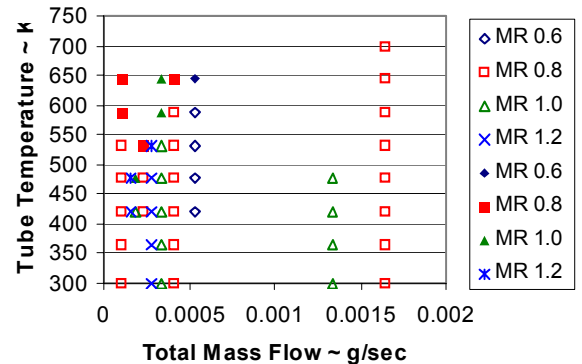
Figure 10. Ignition data for 0.4 mm I.D. platinum tube – open symbols are non-ignition and solid symbols are ignition as indicated by tube temperature rise.

Quantification of Fire Signatures for Practical Spacecraft Materials

Randy L. Vander Wal[1], Gary A. Ruff[2] and Aaron J. Tomasek[1]
[1]National Center for Microgravity Research in Fluids and Combustion
[2]Microgravity Combustion Science Branch
NASA John H. Glenn Research Center, 21000 Brookpark Road
Cleveland, OH 44135

BACKGROUND

Fire protection strategies and procedures on the Space Shuttle and International Space Station has been developed primarily through the modification of standard practices in terrestrial fire safety applications and experience gained throughout the history of the U.S. manned space program. These procedures address all aspects of fire safety including fire prevention, detection, suppression, and post-fire clean up. Because of dire consequences of a major fire on a manned spacecraft, the procedures have been developed to first, reduce the risk that a fire can occur and second, if a fire occurs, to minimize the spread rate so that it can be extinguished before it transitions into a major fire with potentially catastrophic consequences. Reducing the risk that a fire occurs is accomplished through the strict limitations on the use of flammable materials and the minimization of potential ignition sources. If a fire would start, the best way to ensure that the fire remains small and does minimal damage is through the rapid detection and response. On the Space Shuttle and ISS, fire detection is accomplished by smoke detectors that essentially mirror well-established terrestrial designs and operating procedures.

Several factors indicate that the use of smoke detectors alone may be inefficient for fire detection. First, smoke detectors are sensitive to airborne particulates meaning that they are not only sensitive to smoke but also to dust. In both Shuttle and ISS missions, there have been numerous nuisance alarms because of dust in the cabin atmosphere. Second, of the potential fire-causing incidents that have occurred on the Space Shuttle, all were first detected by the crew, not the smoke detectors (Friedman, 1992). In a large spacecraft with a limited crew, not all modules will be constantly inhabited. Based on these previous events, a fire incident could have existed longer than it did if the smoke detectors were the only means to detect and annunciate the fire. Lastly, research has shown that smokes produced in microgravity have different size and morphology than smokes produced in normal gravity (Urban *et al*., 1998). Therefore, the presumed margin of safety that exists with smoke detectors developed based on experience in terrestrial applications is reduced when applied to the microgravity environment. Even though there have been no major fires on U.S. manned spacecraft, it is difficult to say that this has resulted from an efficient fire detection system.

There are currently at least three research projects aimed at developing improved fire detectors based on the measurement of combustion gases. These include several SBIR projects developing sensitive laser absorption techniques as well as the development of MEMS gas sensors being conducted at the NASA John H. Glenn Research Center. While these sensors are promising in spacecraft because of their small size and low power requirements, a more basic problem exists – to make use of these sensors to detect fires, one must know what chemical species and concentrations are expected.

Studies conducted in 1-g environments have measured the yield and identity of partial decomposition products as functions of the rate of heating and oxygen concentration. Though insightful, buoyancy convolves the rate of heating with oxidizer entrainment and combustion product removal. Thus, variability in the partial decomposition products (identity and yield) and the occurrence of secondary reactions of evolved volatiles may be obscured. The non-buoyant or weakly convective flows characteristic of a microgravity environment will alter the rates of oxidizer entrainment and combustion product removal. The tenet of this research is that the specific chemical reactions (and their products) can differ substantially in microgravity environments from their normal gravity counterparts. Given that smoldering or pyrolysis are generally characteristic pre-fire and "fire" events, variability in the evolved partial decomposition products and their concentration has direct consequences for both early fire detection and toxicological assessment. While it may seem logical to conduct this experiment in space experiment, it is not practical at this time because of uncertainties in test procedures, measurement techniques, products produced and their concentrations, and the sheer number of tests that would be required to adequately quantify the fire signatures. As with the 1-g tests performed to screen material flammability, a 1-g method to obtain pre-fire signatures must be developed.

The hypothesis of this proposal is that by comparing the 1-g time history of the smoldering and pyrolysis products produced at different heating rates, convective velocities, oxygen concentrations, and ambient pressures, we will be able to quantify the variation of these signatures with operating conditions. These time histories will be compared to pre-fire signatures obtained in ground-based low-gravity test facilities. The Zero-Gravity Facility and the KC-135 aircraft are the most likely candidates for these tests because these provide the longest low-gravity periods. Even though the periods of low gravity are very short, we can determine (1) whether the low gravity signatures exhibit the same dependence on heating rates, oxygen concentrations, and ambient pressures as their 1-g counterparts, and (2) how the signatures compare to those obtained in the 1-g tests over similar durations. This information will help to assess candidate species for fire signatures, anticipated concentration ranges, and the applicability of the 1-g data to represent 0-g performance.

OBJECTIVE

The overall objective of this project is to measure the fire signatures of typical spacecraft materials in 1-g and determine how these signatures may be altered in a microgravity environment. During this project, we will also develop a test technique to obtain representative low-gravity signatures. The specific tasks that will be accomplished to achieve these objectives are to:

(1) measure the time history of various fire signatures of typical spacecraft materials in 1-g at varying heating rates, temperatures, convective velocities, and oxygen concentrations,

(2) conduct tests in the Zero-Gravity Facility at NASA John H. Glenn Research Center to investigate the manner that a microgravity environment alters the fire signature,

(3) compare 0-g and 1-g time histories and determine if 0-g data exhibits the same dependence on the test parameters as experienced in 1-g

(4) develop a 1-g test technique by which 0-g fire signatures can be measured.

The proposed study seeks to investigate the differences in the identities and relative concentrations of the volatiles produced by pyrolyzing and/or smoldering materials between normal gravity and microgravity environments. Test materials will be representative of typical spacecraft materials and, where possible, will be tested in appropriate geometries. Wire insulation materials of Teflon, polyimide, silicone, and PVC will be evaluated using either cylindrical samples or actual wire insulation. Other materials such as polyurethane, polyimide, melamine, and silicone-based foams will be tested using cylindrical samples, in addition to fabric materials, such as Nomex. Electrical components, such as resistors, capacitors, circuit board will also be tested.

Gas and particulate sampling will be performed and evaluated as a function of method and rate of pre-heating, convective flow velocity, and oxygen concentration. Values of these parameters will be typical of those found in spacecraft microgravity environments. Chemical analysis will consist of mass spectrometric (MS) analysis, gas chromatography and infrared absorption of collected volatiles and particulate matter. Tests will be conducted in the 2.2-sec drop tower for experiment check-out and development of procedures, the 5-sec drop tower to further increase the available time while maintaining a good, low-gravity event. Additional tests are planned for the KC-135 aircraft.

STATUS

Funding for this project will not begin until at least Fall 2003 however, planning and design for the 1-g test facility is underway. The objective of the initial 1-g tests will be to develop and verify the test procedures and conditions that will be investigated in low-gravity. An existing combustion chamber will house the flow tunnel in which the samples will be located, as shown in Fig. 1. The inlet flow will pass through a plenum, a volume of packed beads, and finally a honeycomb flow-straightener before entering the flow chamber. The samples will be placed within the flow tunnel and will be heated either by direct contact with an electric heater or by a hot air flow. Because of the different sample materials and configurations to be investigated, it is anticipated that several different heating methods will be required. Determining a method for the different samples will be one of the objectives of the initial tests.

Gas samples will be drawn from the top of the flow tunnel and directed to a mass spectrometer to provide initial information on pyrolysis/smoldering products. The effect of heating method, heating rate, and flow condition will be evaluated which will help define the 1-g test matrix. Additional diagnostics will be added when the 1-g testing commences in FY04. The low-gravity facility will be developed during FY04 with the tests beginning early in FY05.

REFERENCES

Friedman, R. (1992) "Fire Safety Practices and Needs in Human Crew Spacecraft," *Jour. Appl. Fire Sci.*, Vol. 2, No. 3, 1992-1993, pp. 243-259.

Urban, D. L., Griffin, D. W., and Gard, M.Y. (1998) "Comparative Soot Diagnostics: 1 Year Report," *Third United States Microgravity Payload: One Year Report*, edited by P. A. Curreri, D. McCauley, and C. Walker, NASA/CP-1998-207891, Nov. 1998, pp. 119-134.
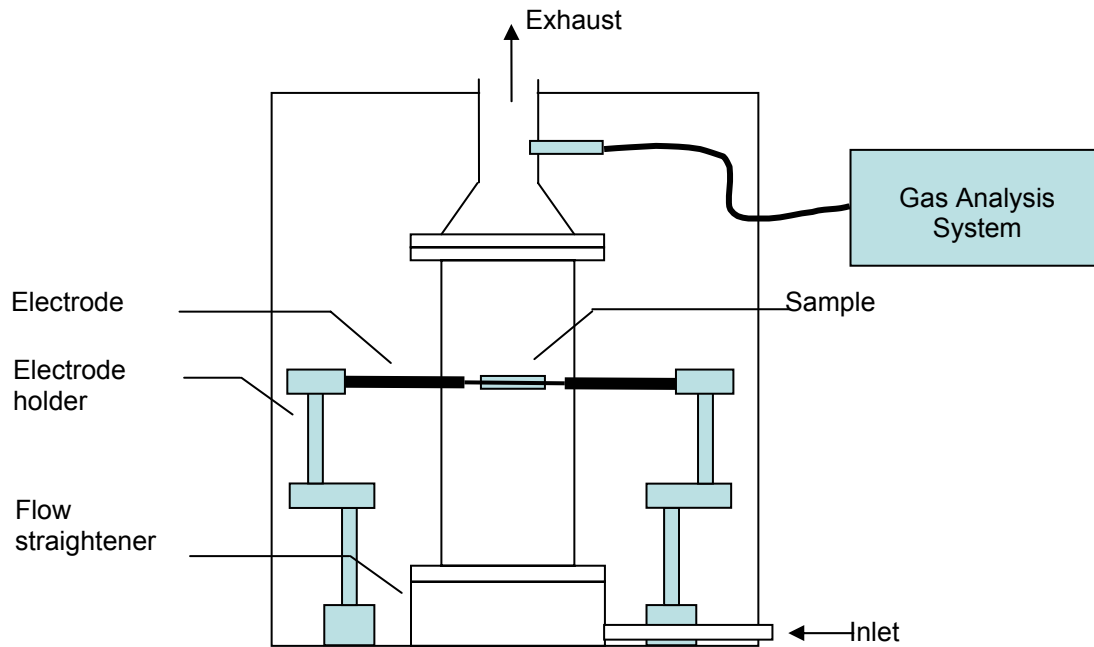
Figure 1. Schematic of the normal-gravity test facility

Author Index

REPORT DOCUMENTATION PAGE

1. AGENCY USE ONLY (Leave blank)	2. REPORT DATE August 2003	3. REPORT TYPE AND DATES COVERED Conference Publication

4. TITLE AND SUBTITLE

Seventh International Workshop on Microgravity Combustion
and Chemically Reacting Systems

6. AUTHOR(S)

Kurt Sacksteder, Compiler

5. FUNDING NUMBERS

WBS–22–101–52–01

7. PERFORMING ORGANIZATION NAME(S) AND ADDRESS(ES)

National Aeronautics and Space Administration
John H. Glenn Research Center at Lewis Field
Cleveland, Ohio 44135–3191

8. PERFORMING ORGANIZATION REPORT NUMBER

E–13952-1

9. SPONSORING/MONITORING AGENCY NAME(S) AND ADDRESS(ES)

National Aeronautics and Space Administration
Washington, DC 20546–0001

10. SPONSORING/MONITORING AGENCY REPORT NUMBER

NASA CP—2003-212376-REV1

11. SUPPLEMENTARY NOTES

Proceedings of a conference sponsored by NASA Microgravity Science Division hosted by NASA Glenn Research Center, Cleveland, Ohio, June 3–6, 2003. Responsible person, Kurt Sacksteder, organization code 6711, 216–433–2857.

12a. DISTRIBUTION/AVAILABILITY STATEMENT

Unclassified - Unlimited
Subject Category: 29   Distribution: Nonstandard

Available electronically at http://gltrs.grc.nasa.gov

This publication is available from the NASA Center for AeroSpace Information, 301–621–0390.

12b. DISTRIBUTION CODE

13. ABSTRACT (Maximum 200 words)

This conference proceedings document is a compilation of papers presented orally or as poster displays during the Seventh International Workshop on Microgravity Combustion and Chemically Reacting Systems held in Cleveland, Ohio, on June 3–6, 2003. The purpose of the workshop is to 1) present and exchange research results from theoretical and experimental work in combustion science using the reduced-gravity environment as a research tool, and 2) inspire and discuss new research efforts to improve spacecraft fire safety and support the future exploration of space. The research results were contributed by researchers funded by NASA throughout the United States at universities, industry, and government research agencies, and by researchers from international partner countries. Prospects for new research were contributed by additional participants from outside the traditional combustion community with expertise in Earth-based development of potential exploration technologies. The product of the workshop is intended for use by public and private sector organizations for academic and technology development purposes in combustion science, fire safety on Earth and in habitable spacecraft, and for the future exploration of space.

14. SUBJECT TERMS

Microgravity; Combustion; Fires; Flammability

15. NUMBER OF PAGES
411

16. PRICE CODE

17. SECURITY CLASSIFICATION OF REPORT	18. SECURITY CLASSIFICATION OF THIS PAGE	19. SECURITY CLASSIFICATION OF ABSTRACT	20. LIMITATION OF ABSTRACT
Unclassified	Unclassified	Unclassified	